
Linear Co-polymer Photocatalysts: From Fundamental Design to Organic/Inorganic Hybrids

Thesis submitted in accordance with the requirements of the
University of Liverpool for the degree of Doctor of Philosophy

Submitted by Ian Coates
Day of submission: 02.07.2023

1. Primary Supervisor: Prof. Paul Chalker
2. Secondary Supervisor: Prof. Andrew Cooper
3. Secondary Supervisor: Dr John Ward



School of Engineering
Materials Science
Leverhulme Trust



Ian David Coates
Student number: 200840765

PhD Thesis
Topic: Linear Co-polymer Photocatalysts: From Fundamental Design to Organic/Inorganic Hybrids

Submitted: 02/07/2023

Supervisor: Prof Paul Chalker
Prof Andrew Cooper
Dr John Ward

School of Engineering
Mechanical, Materials & Aerospace Eng
University of Liverpool
Brownlow Hill
Liverpool L69 3GH

Thesis Statement

I herewith formally declare that I have written the submitted thesis independently. I did not use any outside support except for the quoted literature and other sources mentioned in the paper. I clearly marked and separately listed all of the literature and all of the other sources which I employed when producing this academic work, either literally or in content. This thesis has not been handed in or published before in the same or similar form.

Date: 02/07/2023 Signature: Ian David Coates

Abstract

Linear Co-polymer Photocatalysts: From Fundamental Design to Organic/Inorganic Hybrids

Ian David Coates

Hydrogen gas will likely play an important role in the decarbonisation of hard-to-abate sectors and the overall global race to net zero. Organic photocatalysts offer a route to cheap and sustainable production of green hydrogen by using solar energy to split water. Indeed, significant advances in using semiconducting conjugated polymers to produce hydrogen from water under sacrificial conditions have been made in recent years. However, examples of polymeric photocatalysts capable of achieving overall water splitting have been limited. Since the chemical space constructed from simple organic building blocks is almost infinite, there is enormous potential for further enhancements via the rational design of polymer structures. It is well known that small structural changes can enable the fine-tuning of physical, chemical, and optoelectronic properties of organic semiconductors. This thesis focuses on understanding the structure-activity relationships of linear organic co-polymer photocatalysts, designing new polymers based on these understandings, and then using these polymers to design hybrid organic/inorganic photocatalysts for overall water splitting.

First, an in-depth analysis of the structure-activity relationships of linear co-polymers is performed using data from previously published high-throughput experimental results. This leads to new insights into the detrimental effects of residual palladium, low synthesis yields, short fluorescence lifetimes, and small predicted oscillator strengths. Structural features, physical properties, and photocatalytic activities are correlated with computationally predicted properties, which are used to identify 78 new promising organic photocatalysts. Improved predictions for the optical bandgaps of these materials are also made based on newly devised methodology. A particular focus is placed on understanding the varied results obtained for structurally similar polymers upon adding a platinum co-catalyst.

A series of co-polymers based on dibenzothiophene sulfone (DBTS) and fluorinated phenylene (PhF_x) monomers are synthesised via a microwave-assisted high-throughput reaction. These studies demonstrate that fine-tuning the reaction conditions and co-catalyst content can dramatically enhance photocatalytic activity. The resulting polymers consistently outperformed all 99 co-polymers reported in the previous high-throughput study. Some polymers outperformed the Pt-loaded DBTS-DBTS homopolymer under optimal conditions for the first time. Statistical ternary co-polymers combining the DBTS-PhF_x co-polymers with the electron-accepting benzodithiophene (BDT) moiety are also reported. This work is reinforced with DFT calculations and demonstrates that fluorination can be used to fine-tune electronic structure and influence molecular packing.

Finally, organic/inorganic hybrid photocatalysts are prepared via *in-situ* polymerisation. This includes the first known attempts to form a direct heterojunction interface between a conjugated polymer and flux-mediated Al:SrTiO₃. Attempts to form a polymer/BiVO₄ hybrid S-scheme photocatalyst were also made. These initial experiments show promising signs as proof of concept and indicate that further experiments should be conducted.

Acknowledgements

Thank you, Professor Paul Chalker, for the opportunity to work with you, for your patience, compassion, support, supervision, input, and guidance throughout the last five years

I would like to thank Professor Andy Cooper for the meetings, input, and discussions throughout my studies. I would also like to thank Dr John Ward for the meetings and discussions throughout and for helping me to find a way to continue my studies from home during the personal challenges I faced during the pandemic. More generally, I would also like to thank the rest of the Cooper group for welcoming me and making me feel like one of the team. Thank you, Zuzka, Rob, Xiaobo, Linjinag, Veronica, and Haofan, for the accommodations, organisation, training, advice, and support.

Thank you to the Rosseinsky group for letting me use your furnaces, to the technicians of the Open Access Area who have trained me on countless pieces of equipment, and to the Domen group from the University of Tokyo for providing a reference sample of your state-of-the-art photocatalyst.

To Natalie, Ben, Matt, and Richard: Thank you all for the help and community you provided when I was working on ALD. I would also like to thank all of the other PhD students I have been lucky enough to work alongside in the last few years: Ram, Rich, Liang, Miaojie, Thukshan, and Yuan. Your support and friendships have been invaluable. Thank you also to the Leverhulme Trust for funding my research and to Ben, Lucy, Adele.

To Duncan, Sarah, Ewan, and my brother, Pete, thank you for all the board game nights and pub quizzes that provided the perfect outlet away from the lab. Similarly, thank you to Tom W, Sarah C, Natasha, Gianluca, and Carl: lockdown wouldn't have been the same without such great housemates. Morgan and Kevin – I always have and always will value you, your friendship, and your advice.

Mum, Dad, Pete, your unconditional love and unwavering support knows no bounds. I am constantly reminded of how wonderful you are and how lucky I am to have you all. Thank you for everything. R.I.P. Pops, you will be sorely missed.

Finally, to my incredible girlfriend, Sarah. Words cannot express how amazing you are. You've stood by me every single step of the way and kept me sane, despite going through some of the toughest times. You are my rock, and I could never have done this without you. Thank you for always being there for me, encouraging me, listening to me, motivating me, and inspiring me at every stage.

P.S. Thank you to my cat, Hoopoe, who frequently insisted on trying to write my thesis for me.

Table of Contents

ABSTRACT.....	V
ACKNOWLEDGEMENTS.....	VI
TABLE OF CONTENTS.....	VII
CHAPTER 1: INTRODUCTION & LITERATURE REVIEW.....	2
1.1 OVERVIEW.....	2
1.2 GREEN HYDROGEN: PROMISE AND CHALLENGES.....	3
1.2.1 Applications.....	3
1.2.2 Green Hydrogen Production.....	7
1.2.3 The Potential of Solar Energy.....	7
1.3 PHOTOCATALYTIC HYDROGEN PRODUCTION.....	8
1.3.1 Photocatalytic Cycle.....	8
1.3.2 Atoms, Molecules, and Semiconductors.....	9
1.3.3 Photocatalysis.....	12
1.4 INORGANIC PHOTOCATALYSTS.....	16
1.4.1 Oxide Photocatalyst.....	16
1.4.2 (Oxy)Nitride and (Oxy)Sulfide Photocatalysts.....	17
1.4.3 Al-doped SrTiO ₃	18
1.5 ORGANIC PHOTOCATALYSTS.....	19
1.5.1 Organic Semiconductors.....	20
1.5.2 Polymer Photocatalysts.....	24
1.6 Z-SCHEME AND S-SCHEME PHOTOCATALYSTS.....	33
1.7 CONCLUSIONS.....	34
1.8 AIMS, OBJECTIVES, AND THESIS OUTLINE.....	34
CHAPTER 2: LITERATURE ANALYSIS AND POLYMER DESIGN.....	1
2.1 INTRODUCTION.....	1
2.2 SUMMARY OF ORIGINAL FINDINGS.....	2
2.3 ANALYSIS OF METHODS.....	6
2.3.1 High Throughput Synthesis.....	6
2.3.2 High Throughput Photocatalysis.....	14
2.3.3 Predicted vs Optical Bandgap.....	17
2.4 GENERAL TRENDS.....	39
2.4.1 Fluorescence Lifetime.....	39
2.4.2 Oscillator Strength.....	43
2.5 ROLE OF PT CO-CATALYST.....	47
2.5.1 IP, EA and Pt Loading.....	49
2.5.2 High Throughput Screening Parameters.....	53
2.6 STRUCTURE/ACTIVITY RELATIONSHIPS.....	59
2.6.1 Structure and Oscillator Strength.....	64
2.6.2 Phenylene Co-monomers.....	74
2.6.3 Heterocycles.....	92
2.7 COMPUTATIONAL SCREENING.....	97
2.7.1 Methods.....	98
2.7.2 Synthesised DBTS Co-polymers.....	99
2.7.3 Screening of Remaining Co-polymers.....	106
2.8 CONCLUSIONS.....	120
CHAPTER 3: ORGANIC PHOTOCATALYSTS.....	126
3.1 INTRODUCTION.....	126

3.2	CHAPTER OUTLINE	129
3.3	METHODS	129
3.3.1	<i>DFT Calculations</i>	129
3.3.2	<i>Organic Synthesis</i>	130
3.3.3	<i>Optoelectronic Characterisation</i>	131
3.3.4	<i>Photocatalytic Activity Testing</i>	134
3.4	PHOTOCATALYSIS METHOD VALIDATION.....	137
3.5	DFT COMPUTATIONAL MODELLING.....	146
3.5.1	<i>DBTS-PhFx</i>	146
3.5.2	<i>BDT-PhFx and DBTS-PhFx-BDT</i>	152
3.6	DIBENZOTHIOPHENE SULPHONE CO-POLYMERS.....	155
3.6.1	<i>Initial Synthesis Conditions</i>	155
3.6.2	<i>Lower Reaction Temperature</i>	158
3.6.3	<i>Residual Palladium from Suzuki-coupling Catalyst</i>	159
3.6.4	<i>Updated Synthesis Procedure</i>	163
3.6.5	<i>Alternative Reaction Conditions</i>	166
3.6.6	<i>Alternative Photocatalytic Reactions</i>	173
3.7	BENZO[1,2-B:4,5-B']DITHIOPHENE CO-POLYMERS (BDT-PHFx)	177
3.7.1	<i>Organic Solvent: Toluene (3 ml), Aqueous Base: 2M K₂CO₃ (2 ml)</i>	177
3.7.2	<i>Reaction Condition Screening</i>	180
3.7.3	<i>Organic Solvent: 1,4-Dioxane (4.375 ml), Aqueous Base: 2M TBAA (0.625 ml)</i>	184
3.7.4	<i>Alternative Sacrificial Reagents: Ascorbic Acid / DMF</i>	186
3.7.5	<i>Photocatalytic Hydrogen Peroxide Production</i>	188
3.8	TERNARY POLYMERS	190
3.8.1	<i>Synthesis of Br-PhFx-BDT-PhFx-Br Intermediate</i>	190
3.8.2	<i>Ternary Statistical Random Co-polymer (DBTS)_n-(PhFx)_m-(BDT)_o</i>	192
3.9	OPTOELECTRONIC CHARACTERISATION	195
3.9.1	<i>DBTS-PhFx</i>	196
3.9.2	<i>BDT-PhFx</i>	207
3.9.3	<i>DBTS-PhFx-BDT</i>	214
3.9.4	<i>Binary vs Ternary Polymers</i>	221
3.9.5	<i>Optoelectronics Discussion</i>	224
3.10	CONCLUSIONS AND FUTURE WORK.....	226
3.10.1	<i>DBTS-PhFx</i>	226
3.10.2	<i>Binary vs Ternary Polymers</i>	230
CHAPTER 4: HYBRID PHOTOCATALYSTS		233
4.1	INTRODUCTION	233
4.2	RATIONALE AND HYBRID DESIGN.....	234
4.2.1	<i>Design</i>	235
4.2.2	<i>Polymer/Oxide Energy Level Alignment</i>	237
4.2.3	<i>Type of Heterojunction</i>	238
4.3	SIDE CHAINS AND OXIDE ANCHORING GROUPS: A DFT STUDY.	242
4.4	CHAPTER OUTLINE	248
4.5	METHODS	248
4.5.1	<i>Inorganic Photocatalysts</i>	248
4.5.2	<i>Hybrid Organic-Inorganic Photocatalysts</i>	250
4.6	FLUX SYNTHESISED AL:STO	251
4.6.1	<i>Purity of Reagents</i>	253
4.6.2	<i>Temperature</i>	254
4.6.3	<i>Al:STO Co-catalysts</i>	255
4.7	IN-SITU POLYMERISATION REACTION OPTIMISATION.....	261
4.7.1	<i>Reaction Conditions</i>	261
4.8	DBTS-DBTS/AL:STO	278
4.8.1	<i>Synthesis and Physical Characterisation</i>	278
4.8.2	<i>Area-normalised vs Mass-normalised Photocatalytic Activities.</i>	282

4.8.3	<i>Sacrificial Hydrogen Evolution</i>	285
4.8.4	<i>Change of Sacrificial Reagent</i>	287
4.8.5	<i>Overall Water Splitting</i>	290
4.8.6	<i>Photocatalytic Hydrogen Peroxide Production</i>	291
4.8.7	<i>Discussion</i>	292
4.9	DBTS-PH/AL:STO	296
4.9.1	<i>Pt-loading Study</i>	297
4.9.2	<i>Sacrificial Reagent-Dependent Activity</i>	298
4.9.3	<i>Sequential Photodeposition of Co-catalysts</i>	299
4.9.4	<i>Overall Water Splitting</i>	300
4.10	DBTS-DBTS/BIVO ₄	303
4.10.1	<i>Synthesis and Characterisation</i>	303
4.10.2	<i>Photocatalytic Activity</i>	306
4.11	DBTS-BDT/BIVO ₄	309
4.12	CONCLUSIONS AND FUTURE WORK.....	311
CHAPTER 5: CONCLUSIONS AND FUTURE WORK		315
5.1	SUMMARY OF CONTENT	316
5.2	RESEARCH OUTCOMES	317
5.3	IMPACT AREA I: POLYMER DESIGN	317
5.3.1	<i>Predicted Optical Bandgap</i>	317
5.3.2	<i>Optical Bandgap, Fluorescence Lifetime, and Photocatalytic Activity</i>	320
5.3.3	<i>Acceptors, Donators and Orbital (De)localisation</i>	320
5.3.4	<i>Delocalisation, Co-planarity, and Oscillator Strength</i>	323
5.3.5	<i>New Polymer Designs</i>	324
5.4	IMPACT AREA II: OPTIMISED ORGANIC PHOTOCATALYSTS	324
5.4.1	<i>DBTS-PhFx Polymers</i>	325
5.4.2	<i>Co-catalysts</i>	327
5.5	IMPACT AREA III: BDT-PHFx AND TERNARY POLYMERS	328
5.5.1	<i>Polymer Design</i>	328
5.5.2	<i>DBT-PhFx Outcomes</i>	329
5.5.3	<i>DBTS-PhFx-BDT Outcomes</i>	330
5.6	IMPACT AREA VI: ORGANIC/INORGANIC HYBRID PHOTOCATALYSTS	333
5.6.1	<i>Hybrid Photocatalyst Design</i>	333
5.6.2	<i>Hybrid Preparation</i>	333
5.6.3	<i>Hybrid Photocatalysis</i>	334
5.7	RECOMMENDED FUTURE WORK	336
REFERENCES.....		340

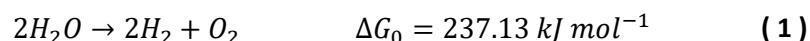
List of Abbreviations

AA	Ascorbic Acid
BDT	Benzodithiophene
BHJ	Bulk Heterojunction
CB	Conduction Band
CBM	Conduction Band Minimum
CC(U)S	Carbon Capture (Usage) and Storage
CMP	Conjugated Microporous Polymer
COF	Conjugated Organic Frameworks
CP	Conjugated polymer
CTF	Conjugated Triazine Frameworks
DBTS	Dibenzo[b,d]thiophene-S,S-dioxide
DFT	Density Functional Theory
DMF	N,N-Dimethylformamide
DoS	Density of States
DRS	Diffuse Reflectance Spectroscopy
FCEV	Fuel Cell Electric Vehicles
GC	Gas Chromatography
GCN	Graphitic Carbon Nitride
GHC	Greenhouse Gas
HER	Hydrogen Evolution Reaction
HOMO	Highest Occupied Molecular Orbital
HOR	Hydrogen Oxidation Reaction
HT	High throughput
IRF	Instrument Response Function
LEES	Local Excited Exciton State
LEGS	Local Exciton Ground State
LP	Linear Polymer
LUMO	Lowest Unoccupied Molecular Orbital
OER	Oxygen Evolution Reaction
OLED	Organic Light Emitting Diode
OOR	Oxygen Oxidation Reaction
OPV	Organic Photovoltaics
OWS	Overall Water Splitting
PGM	Platinum Group Metals
QEEs	Quasiextended Exciton State
SMR	Steam-Methane Reforming
SOMO	Singly Occupied Molecular Orbital
SR	Sacrificial Reagent
TCSPC	Time-Correlated Single Photon Counting
TEA	Triethylamine
THF	Tetrahydrofuran
VB	Valence Band
VBM	Valence Band Maximum

Chapter 1: Introduction & Literature Review

1.1 Overview

The body of research presented in this thesis focuses on photocatalytic water splitting. Photocatalysts are semiconductor materials that absorb light and use the photon's energy to drive photochemical reactions. Photocatalysts are not consumed by the photochemical reactions they participate in; they are regenerated as part of a catalytic cycle. In the context of photocatalytic overall water splitting, photocatalysts absorb photons and use that energy to split water into its constituent elemental components: hydrogen and oxygen.¹ Resultingly, two molecules of water are converted into one molecule of oxygen and two molecules of hydrogen. This reaction is presented in equation (1). As indicated by the positive change in Gibbs free energy, this reaction is endothermic and does not occur spontaneously.



Just as the water-splitting reaction is endothermic, the reverse reaction is exothermic, and when hydrogen and oxygen are combined to form water, energy is released. The resulting energy can be harnessed by controlling when, where, and how this reaction occurs. In this context, hydrogen gas can be combined with ambient oxygen in the atmosphere and used as a clean fuel that produces water as the only byproduct.

Compared with the combustion of oil and gas, which currently dominate the global energy supply, hydrogen does not produce nitrous oxides, volatile organic compounds, carbon monoxide, carbon dioxide, or other byproducts that may result from incomplete combustion. Therefore, not only can hydrogen be used to tackle the energy sector's carbon footprint by decreasing the amount of CO₂ released, but it can also contribute to cleaner air quality and consequently improve public health.²

Importantly, since photocatalytic water splitting is powered by light, solar energy can be harnessed directly to drive this process. As such, it is possible to use renewable energy to produce clean hydrogen fuel and ultimately replace hydrocarbons. Hydrogen produced by photocatalysis is, therefore, considered a solar fuel.

Solar fuels are not novel concepts. After all, photosynthesis relies on a photocatalytic process to convert carbon dioxide and water into complex carbohydrates and oxygen. However, with the ever-worsening climate crisis and recent technological advancements, research in this field is accelerating

at a tremendous pace. At the research scale, photocatalysts and photoelectrocatalysts are being developed to produce other value-added products such as ammonia, methanol, and hydrogen peroxide.³ They are also used for CO₂ reduction, wastewater purification, and other environmental remediation processes.⁴⁻⁶

However, significant challenges must be overcome before such solar-powered systems become scalable and commercially viable. These challenges include efficiency, stability, reliability, cost, scalability, sustainability, and safety.

1.2 Green Hydrogen: Promise and Challenges

Although hydrogen has incredible potential as a green replacement for fossil fuels, significant challenges currently prevent its widespread adoption. In many cases where hydrogen could theoretically be applied, it competes with alternative approaches to decarbonisation. This section discusses which sectors could adopt hydrogen technology and identifies those in which this adoption is most likely. The remaining challenges inhibiting that adoption are also discussed.

1.2.1 Applications

1.2.1.1 Substitution of Natural Gas

In its simplest form, hydrogen gas can be added to natural gas supply lines. This gas mixture can be used to provide hot water, heat homes, and power gas-fired cooking appliances. By supplementing natural gas in this way, the residential energy sector can slowly be weaned off its dependence on this fossil fuel. This approach has been highlighted within the UK's hydrogen strategy.⁷ The government will be progressing with trials of this approach on the scale of a whole village of 1,000 – 2,000 homes by 2025.⁸

At low concentrations, this approach could have an immediate impact on the carbon footprint of the residential energy sector. Hydrogen could be mixed into existing gas pipelines and utilised by existing household appliances. However, at higher concentrations, household boilers and cooking appliances would need to be modified or replaced entirely to ensure compatibility and safety. Furthermore, the national gas supply infrastructure would need to be replaced. Hydrogen is a light gas that leaks easily and forms explosive mixtures with oxygen at high concentrations.⁹

Although the oil and gas industry is enthusiastic regarding this approach, the investment required to completely eradicate the use of natural gas is arguably unreasonable, and it has been argued that blending small volumes of hydrogen with methane may prolong the use of the latter. Furthermore, this approach would consume vast quantities of hydrogen, and it is unlikely such volumes could be produced cost-effectively using renewable energy.

Electrification provides an alternative route for heating households via renewable energy. This approach can be achieved by using renewable electricity to power heat pumps and may be a more cost-efficient approach to the decarbonisation of residential heating.

1.2.1.2 Fuel Cell Electric Vehicles

The second most widely-touted application for green hydrogen is that of fuel-cell electric vehicles. Hydrogen fuel cells operate by recombining hydrogen and oxygen via an electrochemical process that generates electricity. For this to be widely adopted, however, significant infrastructure investment is required to ensure hydrogen fuelling stations are easily accessible. Without such public investment, the private sector is equally unlikely to invest heavily in advancing fuel cell technology.

Whilst such investment is being made in countries such as South Korea, China, the US, and Japan,¹⁰ European nations are primarily focussing on electric vehicles (EVs) using lithium-ion battery technology and the associated changes in infrastructure required. Whilst EVs can also operate via renewable energy, questions remain regarding the environmental and humanitarian impact of an often unregulated, exploitative, and potentially unsustainable supply chain that is susceptible to disruption by geopolitical factors.¹¹

Whilst hydrogen-powered cars and vans are unlikely to become mainstream in Europe. There remains considerable interest in using the same technology to power trains, buses, and HGVs. The heavy nature of these vehicles makes the large batteries required less economically viable. As such, hydrogen may play an important role in decarbonising these subsectors of the transport market.¹²

1.2.1.3 Precursor to Synthetic Fuels

As for heavy land-based vehicles, the aviation and long-distance shipping sectors are incompatible with electrification. Powerful batteries are large, expensive, heavy, and require frequent recharging that can often be slow. However, hydrogen-powered jumbo jets, container ships, and passenger

ferries would also require very large and very heavy canisters of compressed gas. As such, hydrogen fuel cells are also widely considered incompatible with the decarbonisation of these sectors.

Here, the envisaged route to decarbonisation involves the use of synthetic E-fuels.¹³ E-fuels are typically hydrocarbon fuels like petrol and diesel that are considered carbon-neutral based on how they are synthesised. Instead of extracting and refining fossil fuels to isolate these chemicals, E-fuels are synthesised from CO₂ extracted from the atmosphere via carbon capture technology and green hydrogen produced from water using renewable energy.

Although theoretically carbon neutral, the environmental impact of this technology remains net negative. For example, this does not consider the increased environmental cost of burning fuels at high altitudes or the immediate impact on air and water quality. To ensure complete carbon neutrality, the energy input required to synthesise these fuels must also originate from renewable sources. Nevertheless, E-fuels are shaping up to play an incredibly important role in reaching net zero as both governments and the private sector are investing in this technology.

A similar technology being considered for long-distance shipping is to power them using green ammonia-powered combustion engines or green methanol-powered fuel cells. The power densities of these fuels are significantly higher than gaseous hydrogen and hence remove the necessity for giant heavy gas cylinders. As with E-fuels, green ammonia and green methanol can be synthesised from green hydrogen. An additional benefit to using ammonia as a fuel is that it does not release greenhouse gasses when combusted.

Aside from the increased cost of E-fuels compared with fossil fuels, another challenge is that they rely on global adoption such that ships and jets can re-fuel at all global ports and airports. Ammonia combustion engines and methanol fuel cells also require further technological innovation to become economically viable.

1.2.1.4 Steel Manufacturing

Arguably, the most significant area in which green hydrogen can facilitate decarbonisation is in the steel manufacturing industry. Steel manufacturing currently consumes approximately 8% of the global energy supply and is responsible for approximately 7% of global energy sector CO₂ emissions.^{14,15}

The most common steel manufacturing process involves heating coal in the presence of iron oxide. This results in the simultaneous reduction of iron oxide into metallic iron and the incorporation of carbon. Coal is environmentally unsustainable as an energy source for this process since it does not burn cleanly and produces excess amounts of carbon dioxide.¹⁶

An alternative process that shows significant promise is one in which the direct reduction of iron oxide is achieved using green hydrogen.¹⁴ By using hydrogen to produce iron and an electric arc furnace to heat the process using renewable energy, it is theoretically possible to reduce the carbon emissions from this process by 90%. While this technology already exists and has been implemented in several pilot plants, it is expensive to implement. The method is also not compatible with existing infrastructure. As such, conversion of existing production sites would require significant public and private sector investment.

1.2.1.5 Chemical Industry

Currently, the vast majority of hydrogen is either produced from the steam-methane reformation reaction or from coal. The major byproduct of these processes is CO₂. An IEA report from 2018 estimates that 6% of annual natural gas and 2% of annual coal supply is used to produce hydrogen.² Demand for hydrogen is also expected to continue to increase over the coming decades, even for existing demands not covered by the above-mentioned future uses for green hydrogen. As such, significant reductions in CO₂ emissions can be attained by replacing this so-called 'grey' hydrogen with green hydrogen produced from renewable energy sources.

The current global production level of hydrogen is 120 Mth₂/yr. This is equivalent to approximately 3% of the global energy demand.² Most of this supply is used in industrial processes such as oil refining and ammonia production. A significant portion is also used as part of an unrefined mixture of other gasses to produce methanol and in some direct reduction processes in iron manufacturing.

It is worth noting that, whilst E-fuels and other fine chemicals can be synthesised using green hydrogen and CO₂ extracted from the atmosphere, it may be cheaper and equally beneficial to use CO₂ that is produced and captured during the industrial manufacturing process of cement. Cement production is currently responsible for approximately 7% of global CO₂ emissions.¹⁷ Most of this arises as a direct byproduct resulting from the thermal decomposition of calcium carbonate, CaCO₃. Clearly, cement manufacturing is inherently difficult to decarbonise and will be heavily reliant on the development of carbon capture technologies.

1.2.2 Green Hydrogen Production

Clearly, there is a wide range of potential applications for green hydrogen. However, for these processes to become a reality, the cost of green hydrogen must become competitive with that of grey hydrogen. For green hydrogen to be widely adopted, several factors are required: technological advancements, governmental initiatives, changes to domestic policy regarding taxation and subsidies, and increased international collaboration on energy policy and trade.

Currently, most green hydrogen is produced by electrolysis using excess renewable electricity. However, electrolysis only accounts for 4% of global hydrogen production, and it is estimated that only 33% of that is produced using electricity from renewable energy sources.² This is because energy from green hydrogen is approximately 2-3 times more expensive than that from oil and gas.

Whilst the price of hydrogen from electrolysis is expected to decrease over the next few decades, it will remain challenging to compete with the steam-methane reforming reaction coupled with carbon capture and storage solutions.¹⁸ This is because the cost and efficiency of renewable electricity generation must first be considered in addition to the cost of the electrolyser unit. Both alkaline electrolysers and proton exchange membrane electrolysers require complex structures and operating conditions that add to their costs. Alkaline electrolysis, the most established technology, is also not well suited to the unreliable variational supply of electricity that is associated with renewable energy sources such as wind and solar.

By contrast, photocatalysts and photoelectrocatalysts can harness solar energy directly and use it to drive the water-splitting reaction. In the case of photocatalysts, no complicated device structure is required beyond suspending the particulate material in water and a gas separation membrane to separate the resulting gaseous mixture of hydrogen and oxygen. A technical analysis from 2013 predicted that overall water-splitting photocatalysts could produce hydrogen at a cost of \$1.60 kg⁻¹.¹⁹ The US Department of Energy at that time had identified a target cost of green hydrogen at \$2.0-\$4.0 kg⁻¹. This cost analysis assumed an overall solar-to-hydrogen energy conversion efficiency (STH) of 10% for a single-particle photocatalyst.

1.2.3 The Potential of Solar Energy

Solar energy is considered the most promising of the various renewable energy resources. According to an analysis carried out by the US Department of Energy, the global energy consumption rate is

predicted to reach 43 TW by the year 2100.²⁰ Meanwhile, the technical potential of harvestable solar energy using solar cells to convert solar energy into chemical energy via electrical energy is determined to be 7,500 TW. Similarly, the potential for direct conversion of solar to chemical energy, assuming a 10% solar-to-hydrogen efficiency, is 2,500 TW. These values eclipse the expected future energy demand and would only require a small percentage of land use to be dedicated to solar energy. The report also draws a comparison with other renewable resources and highlights that solar energy has considerably more potential than wind, tide, hydropower or geothermal energy.

1.3 Photocatalytic Hydrogen Production

1.3.1 Photocatalytic Cycle

To a simple approximation, two possible photocatalytic cycles for overall water splitting are presented in Figure 1. In the first case, the photocatalyst, P, absorbs a photon, generating an excited state, P*. P* is a stronger reducing agent than P since its highest-energy electron has more energy. This electron is then used to reduce hydrogen ions to form molecular hydrogen. This is known as the hydrogen evolution reaction, HER. In the first cycle, the HER generates a positively charged photocatalyst, P⁺. This photocatalyst subsequently oxidises water to form molecular oxygen in the oxygen evolution reaction, OER, and reforms the ground state photocatalyst. These two half-reactions can take place in the opposite order, as demonstrated by Figure 1b. A negatively charged photocatalyst intermediate, P⁻, is formed in this case.

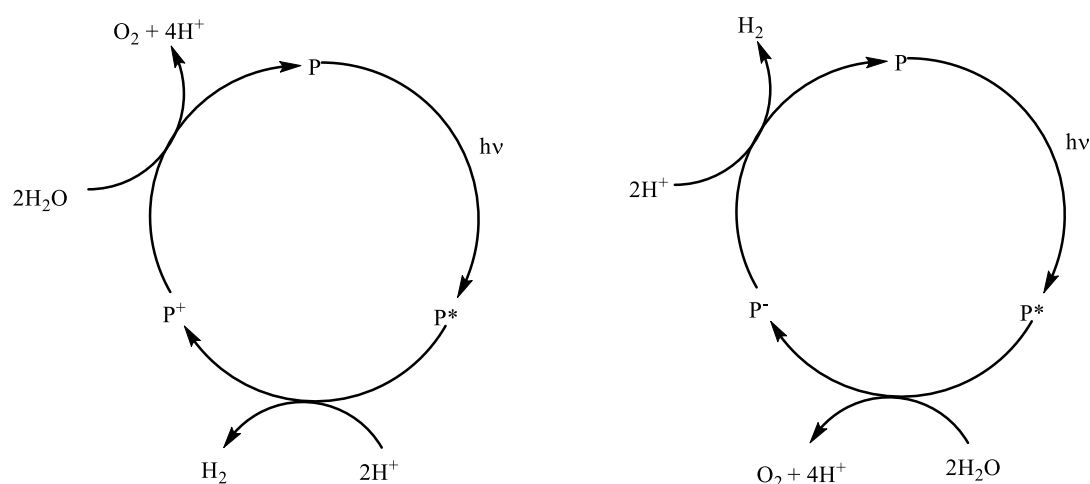
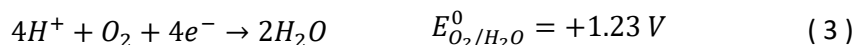


Figure 1: Photocatalytic cycle for overall water splitting with a positively (left) and negatively charged (right) photocatalyst intermediate.

Importantly, the overall water-splitting reaction is split into two independent electrochemical half-reactions: the reduction of protons and the oxidation of water. The standard reduction potentials for

these two processes are presented in equations (2) and (3). The standard reduction potentials assume standard conditions, including a temperature of 273 K, pressure of 1 bar, concentration of 1 mol dm⁻³, and pH=0. Standard reduction potentials are reported relative to the reduction potential of H⁺ at standard conditions. Therefore, the standard cell potential for the overall water-splitting reaction (equation (4)) is also +1.23 V.



It should be noted that the HER and OER are two-electron and four-electron processes. This is one reason the catalytic cycles in Figure 1 are oversimplified since photocatalysts must absorb four photons and transfer all of the photogenerated charges to split two molecules of water. As such, several intermediary mechanistic steps involving additional photon absorptions, charge transfers, and adsorbed reaction intermediates are not presented in these cycles.

1.3.2 Atoms, Molecules, and Semiconductors

Electrons in a ground-state atom fill up atomic orbitals according to Hund's rule and the Pauli exclusion principle. The energies of these atomic orbitals are discrete and quantised and can be determined with quantum mechanics by solving the Schrodinger equation for a hydrogen atom. Negatively-charged electrons are stabilised by electrostatic interactions with the positively charged nucleus. Orbital energies are, therefore, reported as negative values relative to the energy of a free electron in a vacuum. The ground state is the lowest-energy electron configuration of an atom in which all of the lowest-energy orbitals are doubly occupied. Optical transitions occur when an atom absorbs a photon, and an electron is excited from an occupied low-energy orbital into an unoccupied orbital with more energy. The atom is transformed from its ground state into an excited state.

When atoms come together to form a molecule, the highest-energy valence electrons in each atom are redistributed and shared. Atomic orbitals overlap to form molecular orbitals. This is associated with a net decrease in the overall ground-state energy. Quantum mechanics reveals the formation of bonding orbitals and anti-bonding orbitals. As with atomic spectroscopy, when molecules absorb a photon, an electron in a ground-state molecular orbital will be promoted into a higher-energy

unoccupied orbital to transform the molecule into an excited state. Molecular orbitals are also discrete and quantised. The total number of molecular orbitals formed equals the number of constituent atomic orbitals. An example of how two hydrogen atoms come together to form bonding and anti-bonding orbitals in an H₂ molecule is presented in Figure 2.

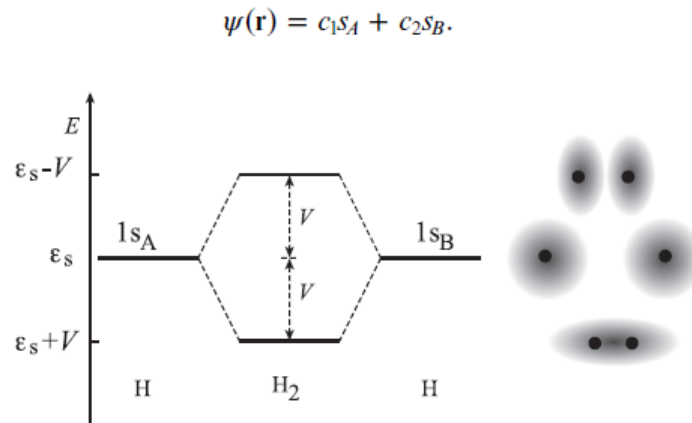


Figure 2: Energy level diagram of a hydrogen molecule. The two 1s of the two hydrogen atoms come together to form two molecular orbitals. A σ -bonding orbital and a σ^* anti-bonding orbital. The two electrons occupy the bonding orbital to result in a net lowering of the molecular energy relative to the non-bonded hydrogen atoms. Figure reproduced from reference ²¹.

From a simplified electronic structure perspective, solid-state materials can be considered as molecules containing billions of atoms. This results in the formation of billions of 'molecular' orbitals spanning a distribution of energies. In these materials, energy levels lie so close in energy to one another that they form a continuous distribution of electronic states called bands. The density of states provides information regarding how these states are distributed with respect to their energy.

Metals contain partially filled bands. Electrons can be excited into empty states by thermal fluctuations or by external electric fields. This accounts for most of their physical properties, such as high electrical and thermal conductivity. An example of how a linear chain of N hydrogen atoms comes together to form a half-filled metallic band is shown in Figure 3.

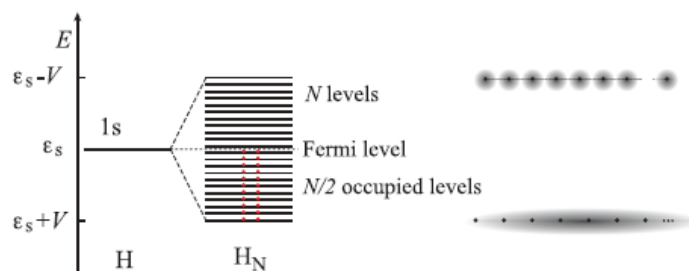


Figure 3: A 1D chain of N hydrogen atoms bond together to form N molecular orbitals with a wide quasi-continuous distribution of energies. This is known as an energy band. Since each hydrogen atom contributes one electron and each molecular orbital can contain two paired electrons, the ground state of this system contains $N/2$ occupied levels, and $N/2$ unoccupied levels. This theoretical system therefore has a half-filled electronic band resulting in metallic properties. Figure reproduced from reference ²¹

By contrast, semiconductors and insulators contain two electronic bands. A fully occupied band called the valence band (VB), and an empty band, located at a higher energy, called the conduction band (CB). The two electronic bands are separated by the bandgap, in which there are no energetic states that can be occupied by an electron. This is represented in Figure 4.

Whether a material is a semiconductor or an insulator depends on the size of the bandgap. In narrow bandgap semiconductors at room temperature, some electrons have enough thermal energy to be excited from the valence band into the conduction band. This results in two partially-filled bands. As in the case of a metal, partially-filled electronic bands result in a material that is electrically conductive. Electrons are conducted through the conduction band, whereas the vacancy left behind in the valence band can be considered as a positively-charged quantum mechanical quasiparticle called a hole.

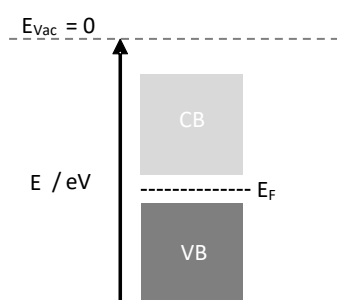


Figure 4: Schematic diagram to explain the steps involved in photocatalytic water splitting. Absorption, excitation, charge separation, charge migration, charge transfer, and redox half-reactions.

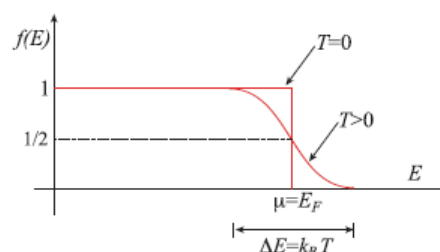


Figure 5: Fermi-Dirac distribution to determine the population of an energetic state relative to its distance from the Fermi level. Figure reproduced from reference ²¹

In wide bandgap semiconductors, the energy difference between the valence band maximum, VBM, and the conduction band minimum, CBM, is too wide for an electron to be thermally excited across the bandgap. However, the bandgap in these materials is small enough such that absorption of a

photon will promote an electron from the VB into the CB to generate an electron-hole pair. Insulators have even wider bandgaps.

The Fermi energy, E_F , marks the energy at which 50% of the states are occupied and 50% are unoccupied. In a metal, this point lies in the middle of a band, whereas in an intrinsic semiconductor, it lies in the middle of the bandgap. More generally, the temperature-dependent Fermi-Dirac equation provides the probability that a quantum state with energy E_α would be occupied at a given temperature.

$$f(E_\alpha) = \frac{1}{1 + e^{\frac{E_\alpha - E_F}{kT}}} \quad (5)$$

The Fermi energy, E_F , is defined as the energy at which a state would be exactly half occupied. The Boltzmann constant, k , is the amount of kinetic energy an electron gains per degree increase in temperature. This equation is represented in Figure 5.

When a semiconductor is doped with impurities or defects, additional energy levels may form inside the forbidden zone of the bandgap. These defect levels can be fully occupied, partially occupied, or completely unoccupied. Depending on the energy of these defect levels and their occupancy, the Fermi level will shift away from the middle of the bandgap accordingly. It is, therefore, possible to increase the number of electrons in the CB or holes in the VB at thermal equilibrium by doping a semiconductor to introduce the desired defect levels. This is the origin of p- and n-doping in silicon.

1.3.3 Photocatalysis

Thermodynamically, for a photocatalyst to be capable of driving the OWS reaction, its band edge potentials must straddle the redox potentials of the two half-reactions involved in overall water splitting. This is represented in Figure 6a.

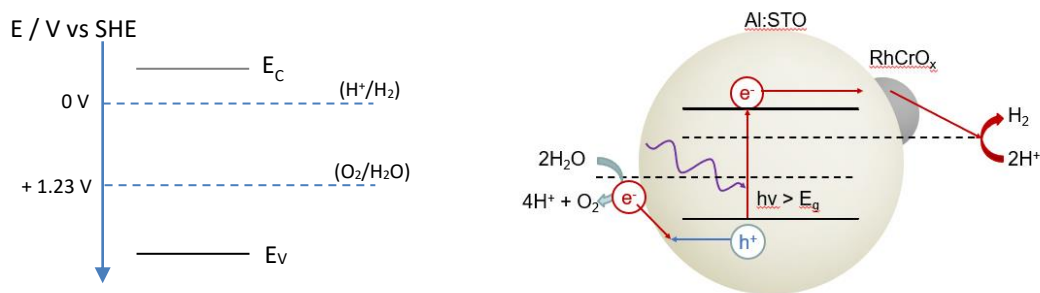


Figure 6: a) Energy level band diagram to show that the CBM and VBM potentials must straddle the HER and OER half-cell potentials to be able to drive overall water splitting. b) Schematic diagram to explain the steps involved in photocatalytic water splitting. Absorption, excitation, charge separation, charge migration, charge transfer, and redox half-reactions.

Figure 6b summarises the overall photocatalysis process using a particle of Al-doped SrTiO₃ loaded with a RhCrO_x co-catalyst as an example. Firstly, a photon with energy greater than the bandgap is absorbed, resulting in the photoexcitation of an electron from the VB into the CB. The photogenerated charges will be coulombically attracted to one another. Together, this electron-hole pair can be considered together as a quantum mechanical quasiparticle known as an exciton.

Depending on the structural and electronic properties of the semiconductor, this exciton pair will either dissociate into free charges and subsequently migrate through the bulk material or remain bound and migrate through the material together before charge separation occurs at the surface. Once at the surface, electrons and holes will participate in the water-splitting half-reactions. This is often mediated by an intermediary step in which charges are first extracted from the photocatalysts and injected into a co-catalyst, from which they subsequently participate in the half-reactions.

The efficiency of a photocatalyst is dependent on many factors. However, the most important is recombination, in which electrons and holes recombine, and the energy provided by an absorbed photon is lost. This is typically associated with the fluorescence of a photon or energy transfer from the semiconductor into the environment. The rate at which these recombination events occur determines the lifetime of an excited state. The longer photogenerated charges survive, the greater the chances of migrating to the surface and subsequently participating in a reaction.

Co-catalysts are incredibly useful because they can enhance the rate of charge separation at the surface and facilitate charge extraction. Once a photogenerated charge has been removed from the semiconductor, the probability of photogenerated charge recombination is minimised. Co-catalysts are also designed to have optimal electronic structures and overpotentials specific to the desired half-

reactions. They also have optimal binding energies with reagents and intermediates. As such, they catalyse the reactions taking part on their surfaces, resulting in enhanced rates of reaction.

The apparent quantum yield, AQY, presents the percentage of incident photons of a certain energy which produce photoexcited charges that subsequently participate in the desired redox reaction. This is given by equation (6), where n is the number of electrons involved in the photocatalytic reaction, R is the molecular production rate, and I is the rate of incident photons.

$$AQY(h\nu) = \frac{nR}{I} \quad (6)$$

Whilst the AQY is incredibly useful in determining the probability of converting a photon's energy into chemical energy, it is specific to the wavelength tested. For a photocatalyst to attain a solar-to-hydrogen efficiency, STH, greater than 10%, high AQYs must be maintained over all absorbable wavelengths. The wavelengths that can be absorbed primarily depend on the optical bandgap of the semiconductor. The equation to determine the STH is given in equation (7). r_{H_2} is the rate of hydrogen evolution, ΔG is the change in Gibbs free energy for the overall water splitting reaction, P_{Sun} is the energy flux of sunlight, and S is the area of irradiation.

$$STH = \frac{\text{Output energy}}{\text{Energy of incident solar light}} = \frac{r_{H_2} \times \Delta G}{P_{Sun} \times S} \quad (7)$$

Clearly, a wide bandgap semiconductor that can only absorb high-energy photons in the UV portion of the solar spectrum ($\lambda < 400$ nm) will have a limited maximum STH efficiency, even if it exhibits an AQY of 100%. This is exemplified in Figures 7 and 8, which present the spectral output of the sun at the earth's surface (AM 1.5 G irradiation) and the maximum theoretical STH efficiencies that can be achieved by an overall water-splitting photocatalyst depending on the AQY and maximum wavelength of light accessible, as calculated by Hisatomi *et al.*¹

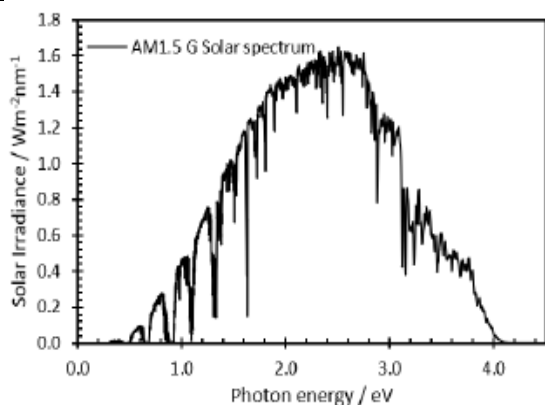


Figure 7: Average solar irradiance reaching the earth's surface. Obtained from ASTM open-source data.²²

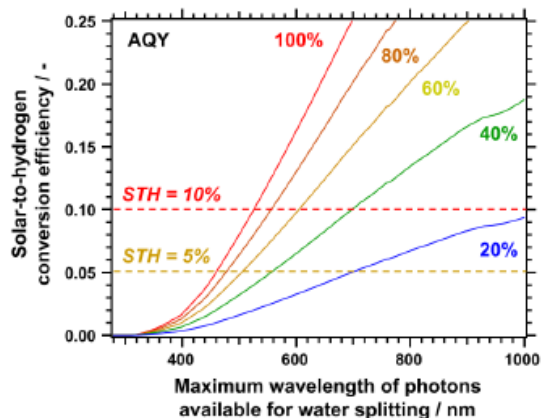


Figure 8: Relationship between AQY and STH ratios with respect to the range of wavelengths that a photocatalyst is capable of harvesting. Figure reproduced from reference¹

After converting the wavelengths into optical bandgaps, Figure 8 demonstrates that a 10% STH efficiency rating could either be achieved by a photocatalyst with a 2.4 eV bandgap in which the AQY is 100% for all wavelengths shorter than 520 nm. Meanwhile, if a semiconductor has an optical bandgap of 2.05 eV, then an STH efficiency of 10% could be obtained if it exhibits an AQY of 60% for all accessible wavelengths ($\lambda < 605$ nm). Wide bandgap semiconductors that only absorb UV radiation are limited to a theoretical maximum of just 1.7% STH.

It should also be noted, however, that there is a fundamental limit on the maximum efficiency that can be achieved by a single bandgap semiconductor photocatalyst. Following a similar logic as that devised by Shockley and Quessier to determine the thermodynamic limit of efficiency in photovoltaics,²³ Ross *et al.* determined that the maximum theoretical efficiency for a single absorber is approximately 29%.²⁴ Pinaud *et al.* took this one step further to determine what they deemed to be "reasonably achievable" STH values after considering the requirement of kinetic overpotentials and energy losses from material defects.¹⁹ They concluded that optimum STH efficiencies of 11.2% can be obtained from a semiconductor with a bandgap of 2.26 eV, which equates to a semiconductor that absorbs all wavelengths shorter than 550 nm. Their analysis has been reproduced in Figure 9.

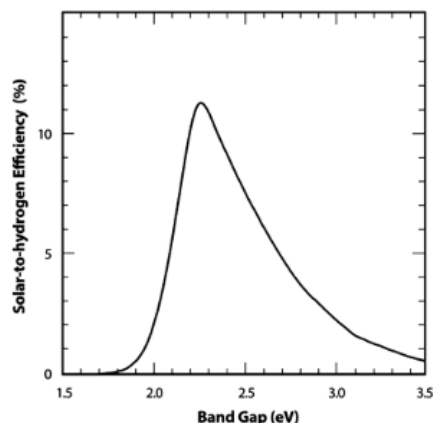


Figure 9: Reasonably achievable STH efficiencies with respect to bandgap energy. Reproduced from reference ¹⁹.

As Pinaud's analysis goes on to discuss, photocatalysis has the potential to produce hydrogen cheaply enough that green hydrogen can compete directly with hydrogen produced from fossil fuels, assuming a device lifetime of 10 years. Indeed, from an engineering perspective, overall water splitting panels showing good stability have successfully been constructed and tested on a 100 m² scale.²⁵ However, current state-of-the-art systems are still only achieving STH efficiencies under 2%. As such, more work is required at the research and discovery phase to design and test new materials.

1.4 Inorganic Photocatalysts

1.4.1 Oxide Photocatalyst

The first reports of photon induced overall water splitting was observed by Fujishima and Honda in 1972.²⁶ In their seminal work, hydrogen and oxygen was observed from a TiO₂ photoanode irradiated with UV light. Since then, a huge proportion of the subsequent literature has focussed on TiO₂. The main challenge regarding this material is that its conduction band is formed from oxygen 2p orbitals that are very low in energy and results in a large overpotential for the OER but only a small overpotential for the HER. As such, it has a wide bandgap which limits its overall STH efficiency.

Many approaches have focussed on ways in which TiO₂ can be modified to enable the absorption of longer wavelengths of light.²⁷ This has included loading with gold nanoparticles that can inject charges into the CB via the surface plasmon effect.²⁸ These nanoparticles may also introduce an electric field at the interface that facilitates charge separation. Dye-sensitisation is a common method in which a dye molecule, adsorbed to the oxide surface, absorbs visible wavelengths of light and transfers the photoexcited electron to the TiO₂ particles. Meanwhile, doping is also a common practice for enhancing the optoelectronic properties of TiO₂. Doping is also considered band gap engineering since

new energy levels are introduced into the bandgap to modify the oxide's inherent electronic structure. Doping may involve the introduction of metal cations, non-metal anions, or even intrinsic doping, such as the introduction of oxygen vacancies.^{29,30}

In addition to TiO₂, many other oxide photocatalysts have also demonstrated photocatalytic activity. However, all such materials suffer from low energy valence bands that limit their applicability. For example, BiVO₄ and WO₃ have narrower bandgaps than TiO₂, which enable these materials to absorb visible wavelengths of light. However, narrow band gaps combined with a deep valence band result in an unsuitable conduction band potential for driving the hydrogen evolution reaction. Nevertheless, these oxides can be used as oxygen evolution photocatalysts in multi-component systems, as discussed later. Another wide bandgap oxide photocatalyst that has been widely investigated for its photocatalytic applications is strontium titanate, SrTiO₃. This photocatalyst will also be discussed in more detail later.

1.4.2 (Oxy)Nitride and (Oxy)Sulfide Photocatalysts

Since the primary issue associated with oxide photocatalysts is their deep valence band energies, many other non-oxide materials have also been investigated. Of particular interest are nitrides such as Ta₃N₅³¹ and sulfides such as CdS.³² These materials are predicted to exhibit suitable band edges for overall water splitting and narrow bandgaps that allow for extensive visible light absorption; both are highly susceptible to photodegradation.³³ These photocatalysts also currently exhibit extremely low quantum yields. It is, therefore, challenging to envisage these materials maintaining high efficiency over a ten-year lifespan, as required for commercial applications. Nonetheless, their stability can be improved by applying protective coatings, using efficient co-catalysts that rapidly extract photogenerated charges, controlling particle size, and controlling particle morphology.^{32,34}

A similar approach is to combine the narrower bandgaps introduced by the nitrogen and sulfur atoms with the increased stability of the oxides by investigating oxynitrides and oxysulfides. These are particularly promising photocatalyst materials for which OWS has recently been observed when irradiated by light with wavelengths up to 600 nm.^{35,36} A good review of recent progress in these materials has recently been published by the leading academic in the field, Prof Kazunari Domen.³⁷ However, the AQYs over the absorbable wavelengths are low, and STH efficiencies still fall substantially short of the minimum target of 5%.

1.4.3 Al-doped SrTiO₃

As mentioned above, SrTiO₃ is another wide bandgap oxide semiconductor that is capable of driving the overall water splitting reaction. The bandgap of SrTiO₃ is 3.2 eV, which means it can only absorb UV-light. However, the most significant recent advances in our understanding of the fundamentals of photocatalytic water splitting stem from studies of this material. Indeed, in 2020, Domen *et al.* reported an AQY at 365 nm of over 90%.³⁸ Cheap, scalable water-splitting panels have been constructed using this material³⁹ and subsequently scaled up to a pilot study over 100 m².²⁵ This photocatalyst has also proven its stability and efficiency when tested over 1000 hrs of constant illumination.⁴⁰

The breakthroughs regarding this material have been steady over the course of the last 15 years. Initially, it was discovered in 2009 that aliovalent doping resulted in improvements in photocatalytic activity by an order of magnitude.²⁹ It was hypothesised that triply-charged cation dopants result in the reduction of Ti³⁺ defects. These defects introduce energy levels below the CB, acting as electron traps and charge recombination centres.^{41,42}

The AQY was substantially improved by preparing SrTiO₃ via a flux-synthesis method. This resulted in highly crystalline faceted particles with extended photoexcited charge lifetimes.^{43,44} This study also serendipitously incorporated Al³⁺ dopants into the particles due to the alumina crucibles and an AQY of 30%. In 2018, Al₂O₃ nanoparticles were added to the flux mixture, which resulted in enhanced Al³⁺ content and nanosized crystals. Combined, these features resulted in an AQY of 56%.³⁹ Fine tuning of the flux process enabled the selective exposure of anisotropic crystallographic facets on the nanocrystals.³⁸

Meanwhile, additional developments were being made regarding the role of co-catalysts. Firstly, dual-loading of Rh and Cr in the form of a RhCrO_x co-catalyst was shown to enhance water-splitting activities on a photocatalyst made of a solid solution of GaN and ZnO.⁴⁵ Co-loading flux-synthesised Al-doped SrTiO₃ with this co-catalyst and an additional MoO_x co-catalyst enhanced the AQY to 69%.⁴⁶ This AQY was increased to over 90% only after changing the co-catalyst loading method. Sequential photodeposition of Rh followed by Cr₂O₃ resulted in a core-shell structured hydrogen evolution co-catalyst in which the chromium oxide layer prevents oxygen diffusion to the Rh site, and inhibits the competitive oxygen reduction back-reaction.⁴⁷ Further photodeposition of an additional CoOOH oxygen evolution co-catalyst enhanced the rate of overall water splitting further. An AQY of 96% was observed.³⁸ TEM images revealed that the hydrogen evolution and oxygen evolution co-catalysts were

selectively deposited on different crystallographic facets. Computational studies revealed that this arises from different surface energies and work functions in different crystallographic directions that generate an internal electric field within the particles. This electric field leads to rapid charge separation.

These discoveries indicate the importance of crystallinity, particle size, morphology, defect structure, and co-catalyst selection. Many of these factors are currently driving the research amongst other inorganic photocatalysts. For a relatively comprehensive review of the current state of inorganic semiconductor photocatalysts, see the review article published by Wang and Domen in 2019.⁴⁸

1.5 Organic Photocatalysts

In direct contrast to inorganic photocatalysts are their organic counterparts. Whilst some organic molecular photocatalysts exist,⁴⁹ the vast majority of reports in the literature focus on polymeric semiconductors.^{50,51} Whereas inorganic semiconductors are typically highly crystalline with long photogenerated charge lifetimes and long photogenerated charge diffusion lengths, inorganic semiconductors are highly disordered with typically semicrystalline or amorphous structures.

Excitons are very weakly bound in inorganic semiconductors due to the high dielectric constants and coherent delocalisation of photogenerated charges throughout the spatial confines of a single crystal. Meanwhile, excitons in organic semiconductors are tightly bound due to their localisation on a single polymer chain. An additional exciton binding energy of 0.1 – 1 eV must typically be overcome to achieve charge separation. Resultingly, observed exciton lifetimes are on the timescale of nanoseconds, and exciton diffusion lengths are 5-10 nm. As such, achieving high AQYs is incredibly difficult.⁵²⁻⁵⁵

Nonetheless, these boundaries and limitations are constantly being pushed and surprising advancements have been made. For example, covalent organic frameworks can introduce larger domains of crystallinity,⁵⁶ nanostructures can enable long-range exciton transport,⁵⁷ and polymer structures can be modified to decrease binding energies and promote charge separation.⁵⁸⁻⁶¹ Once charge separation and, importantly, charge extraction has occurred, evidence suggests that the remaining photogenerated charges can survive for orders of magnitude longer than the excitons.⁶²⁻⁶⁴

Organic semiconductor photocatalysts suffer from many of the same limitations as other devices constructed using organic semiconductors, such as organic photovoltaics (OPV) and organic light

emitting devices (OLEDs), and in flexible wearable electronics. However, these applications have already been commercialised, and the cost efficiencies of these materials are ever-improving.

OPVs are the closest technology to photocatalysts since they also function by harvesting photogenerated charges. Indeed, these devices overcome the problems associated with short exciton diffusion lengths by building bulk heterojunction (BHJ) photoactive layers in which polymeric absorbers form a biphasic immiscible mixture with a second organic component into which photoelectrons are rapidly extracted. Phase separation within the bulk of the absorber layer in these devices is on the scale of the exciton diffusion lengths. As such, single-junction OPV-based solar cells have recently achieved over 19% efficiency, making them even more competitive with the more expensive silicon-based solar cells.⁶⁵ Similar bulk heterojunction photocatalysts have also recently been reported to achieve high-efficiency hydrogen evolution rates.^{66–71}

Overall, organic semiconductors are not limited by deep valence bands. There are also an infinite number of polymer structures that can be made from common organic building blocks. This allows for fine-tuning of the optoelectronic and physical properties to ensure optimal band gaps and band edge potentials for the desired application. They can also be synthesised at scale relatively cheaply.

Despite showing significant promise and ever-increasing efficiencies for driving the hydrogen evolution reaction, there are very few reports of organic materials that are capable of driving the oxygen evolution reaction and even fewer capable of achieving overall water splitting.⁷² When testing for activity with respect to hydrogen evolution, holes in the VB are consumed by sacrificial reagents rather than by the oxygen evolution reaction.

1.5.1 Organic Semiconductors

Inorganic crystalline semiconductors form electronic band structures as a result of the periodic distribution of atoms according to the crystal structure. Their derivations are beyond the scope of this thesis, but there are several excellent textbook resources that can be consulted for more information.^{73,74}

The electronic structure that gives rise to the semiconducting properties of conjugated polymers is far less obvious. Two opposing theoretical approaches are typically considered when considering organic semiconductors. The first is that of band theory. This builds on the basis that a single linear polymer chain is a one-dimensional semiconductor. Each conjugated atom along the backbone contributes one

delocalised p-orbital electron. Bands form from the constructive interference that arises from the periodic spacing of carbon atoms in each repeat unit over the length of the entire polymer chain. This model is comprehensively discussed in the 2018 book by Luís Alcácer.²¹ Organic semiconductors formed from molecular crystals can also be explained in this way.

The second theoretical approach to consider the electronic structure of conjugated polymers is to consider them as large organic molecules. In this approximation, polymers have a highest occupied molecular orbital (HOMO) and a lowest unoccupied molecular orbital (LUMO) rather than a valence band and conduction band.⁷⁵

In reality, however, the true electronic structure of conjugated organic polymers lies somewhere between the two extremes. It is also extremely structure and phase-dependent. The approach used by Prof William Barford in his textbook titled "*Electronic and Optical Properties of Conjugated Polymers*" neatly combines both theoretical approaches and develops a practical understanding that correlates with experimental results.⁷⁶ This is the approach which will be used to describe the photophysical and photochemical processes of the conjugated polymers discussed in this thesis.

1.5.1.1 Absorbing Chromophores and Local Excitons

The band structure model of organic polymers describes the electronic wavefunctions distributed over the entire polymer chain. In reality, disorder along the polymer backbone will create breaks in conjugation. However, optical absorption events are also not localised to a single repeat unit or chemically distinct monomeric unit.

Upon absorption, an exciton is formed. This exciton can be considered as a quantum mechanical quasiparticle with its own wavefunction. This exciton will be delocalised over several adjacent polymeric repeat units. According to Anderson's rule, the energetic and spatial extent of this wavefunction is determined by the degree of disorder.⁷⁷

As for all quantum particles, the energy of the resulting exciton is quantised and defined by an associated quantum number. Importantly, the ground state of an exciton can be described by a wavefunction without any nodes. The exciton can be conceptualised as a particle in a box. At the edges of the box, the square of the wavefunction is zero. In the context of a polymer chain, the start and end point for this box is determined by structural disorder such as bond rotations or defects that prevent extended delocalisation over the entire chain.

Every π -bond along the backbone of a conjugated polymer can interact with a photon and lead to photoexcitation. Therefore, each monomeric unit will be located within the spatial confines of one ground state exciton. Hence, the entire polymer chain can be separated into distinct, non-overlapping ground-state excitons. Malyshev and Malyshev first predicted this.^{78,79} These exciton states are now typically called Local Exciton Ground States (LEGSs).⁸⁰

The spatial extent of each LEGS defines an absorbing chromophore. Therefore, the energy of each exciton ground state will vary according to the number of repeat units contained within it, the local polymer backbone geometry, and the local environment around that segment. When considering all chromophores across all polymer chains within a given sample, it quickly becomes apparent that there is a wide distribution of possible energetic states.

It should be noted that LEGS represent exciton ground states. It is also possible for a chromophore to absorb a photon of higher energy to generate a Local Excited Exciton State (LEES). Each LEES is confined to a chromophore defined by its underlying LEGS. As for a particle in a box, the LEES wavefunction will have an increased number of nodes relative to the ground state. It is also possible for a conjugated polymer to absorb a high-energy photon and generate a so-called Quasiextended Exciton State (QEES). QEES are node-containing excitons that are delocalised over several adjacent chromophores. In the condensed phase, it is also possible that these excitons are delocalised over several adjacent polymer chains, particularly inside the crystalline domains of semicrystalline polymers.

Following the absorption of a photon and the generation of an exciton, several processes occur over several timescales, from femtoseconds to nanoseconds. These involve exciton wavefunction decoherence, energy relaxation from a LEES or QEES to a LEGS, and further localisation of the exciton onto a smaller section of the polymer chain as it relaxes on its potential energy surface to form a vibrationally relaxed state. Whereas LEGSs make up all the potential absorption chromophores, vibrationally relaxed states, VRSs, correspond to the emissive chromophores. For an excellent summary and further reading on this topic, please see Barford *et al.*⁸¹

1.5.1.2 Exciton Diffusion

Given the different electronic structures of organic and inorganic semiconductors, it becomes clear that the mechanism by which excitons and free charges migrate through the two materials also differ.

Whereas the conduction band of an inorganic semiconductor is delocalised over a single crystal, an exciton in a conjugated polymer is localised onto a single portion of a specific polymer chain.

Excitons migrate through the conjugated polymer via one of two energy transfer mechanisms: Dexter Energy Transfer, and Förster Resonance Energy Transfer (FRET). Both of these mechanisms make use of the fact that there is a large energetic distribution of exciton states available as the exciton is transferred from one chromophore (a donor) to another (an acceptor). These mechanisms are best understood by considering a molecular orbital approach.

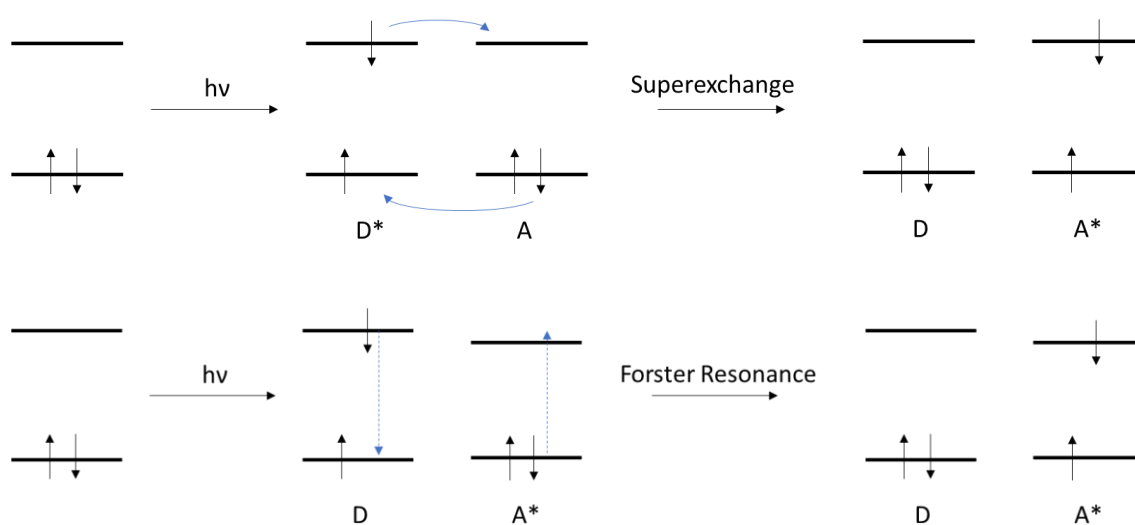


Figure 10: Representative examples of Dexter (Top) and Forster (Bottom) energy transfer mechanisms. Photoexcitation of a chromophore is associated with the excitation of an electron from the HOMO to the LUMO.

These two mechanisms are represented in Figure 10. The Dexter mechanism involves the direct transfer of the higher-energy electron from the excited donor chromophore into the LUMO of an accepting chromophore. This is accompanied by the transfer of a HOMO electron on the accepting chromophore into the HOMO of the donor. The net effect of this exchange is the donating chromophore in its ground state, D, and the acceptor in its excited state, A*. As with photocatalytic processes, the two electron transfer processes can occur sequentially. As such, the charge transfer steps may occur via either a $[D^+ - A^-]$ or $[D^- - A^+]$ transition state. For this energy exchange process to occur, the donating and accepting chromophores must have overlapping orbitals. As such, the rate of energy transfer decays exponentially with distance.

By contrast, FRET occurs through space and does not rely on orbital overlap. As such this process is long range and the rate of energy transfer decay as a function of $1/R^6$. This process enables exciton diffusion through a polymer photocatalyst particle on the nanometre scale. In the FRET process, the

excited donating chromophore, D^* , relaxes back down to the ground state. However, instead of releasing a photon, as in the case of fluorescence, the energy is transferred to a nearby accepting chromophore. For this process to occur, the ground state exciton of the donating chromophore must have more energy than that of the accepting chromophore.

Applied to the theory of local exciton ground states, this means that the excited chromophore will relax to its LEGS, and subsequently into its emissive VRS. For FRET energy transfer to occur, the energy of the donating VRS must be larger than that of the accepting LEGS. Consequently, the energy from the absorbed photon is transferred from the absorbing chromophore to the lowest energy emissive LEGSs that lie in the low energy tail end of the total distribution. This occurs via a process involving several sequential charge transfer events into increasingly lower-energy exciton states.

As the exciton migrates between chromophores and lowers in energy, there become fewer and fewer LEGSs with lower energy into which further energy transfer can occur. At this point, FRET must occur over longer distances. Resultingly the exciton hopping distance increases, but the rate of energy transfer decreases. In this regime, the rate constant for FRET begins to compete with that of fluorescence. This results in fluorescence spectral diffusion in which the fluorescence photon energy is shifted to lower energies (and longer wavelengths) over the course of its lifetime.

It should be noted that the probability, and hence rate, of FRET occurring does not only depend on the distance between chromophores. It also relies on the coupling between the transition dipole moments associated with the relaxation and excitation transitions on the emissive and absorbing chromophores, respectively. For a discussion of exciton diffusion from the perspective of molecular orbitals, please see reference ⁸² For a more comprehensive discussion in terms of exciton ground states, please see references ^{80,81,83–86}.

1.5.2 Polymer Photocatalysts

The first conjugated polymer reported to produce hydrogen photocatalytically was poly(*p*-phenylene) (PPP), first synthesised in 1985.⁸⁷ The polymer has an optical bandgap of 3 eV and, as such, is only active under UV irradiation. This polymer also exhibited limited stability and a relatively short lifetime. These experiments were conducted in the presence of sacrificial electron donors and exhibited an

AQY of only 0.03% at 365 nm. Early studies also investigated the role of noble metal co-catalysts and a range of sacrificial reagents.^{88,89}

Despite a growing interest in organic semiconductors for photovoltaic devices, electronic devices, and superconducting applications, which led to the Nobel Prize being awarded in 2000, little progress was made with respect to polymeric photocatalysts for water-splitting applications. In 2009, however, a breakthrough was made after overall water splitting was observed on graphitic carbon nitride, g-C₃N₄, and further enhanced upon loading with a Pt co-catalyst.⁹⁰ This discovery resulted in a significant shift in research focus as the library of materials expanded from a domain mainly dominated by inorganic materials, particularly TiO₂.⁹¹

Since 2009, g-C₃N₄ has remained a primary focus for much of the subsequent research into organic photocatalysts.^{92–96} This is primarily due to its abundance, stability, moderate bandgap (2.7 eV), and favourable band potentials. However, the bulk material is an inefficient photocatalyst that suffers from high recombination rates of photocarriers, poor electrical conductivity, low surface area, and lack of active sites.

Building upon the discovery of photocatalytic activity in g-C₃N₄, other active polymeric organic materials were rapidly realised. The most widely studied family of organic semiconductors are linear conjugated polymers (LPs). However, many other families also exist, including covalent triazine frameworks (CTFs),^{97–104} covalent organic frameworks (COFs),^{105–115} and conjugated microporous polymers (CMPs)^{116–133}. Whilst each has its merits, such as increased surface area, porosity, crystallinity, and multidimensional band structures, discussion and investigations in this thesis focus on linear conjugated polymers, since these materials arguably offer the most information regarding structure/activity relationships.

Organic photocatalysts for hydrogen evolution is an incredibly active field of research. An analysis of Web of Science search results for the field is presented in Figure 11. Clearly, there has been a rapid increase in publications over the last decade, and there are currently over 2000 new publications relating to organic photocatalysts for hydrogen evolution being published in the 2022 calendar year. A total of 14,086 publications were identified by the search. Over 8,000 of these have been published since the start of this PhD project.

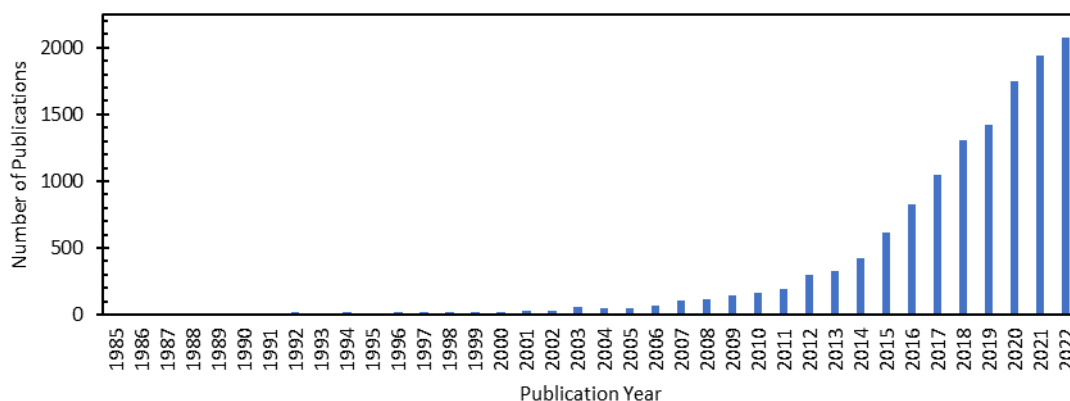


Figure 11: Web of Science Search Analysis for Papers containing the terms "polymer" or "organic", "hydrogen" or "H2", and "Photocat*". In total, 14,086 publications were found. Search performed on 29/06/2023. Results for 2023 publications have been omitted from the chart.

1.5.2.1 Linear Polymers

In terms of linear conjugated polymers, one of the earliest breakthroughs was made in 2016 when Sprick *et al.* investigated a series of linear co-polymers in which the para-phenylene unit was co-polymerised with several planarised macrocyclic monomer units.¹³⁴ This led to the discovery of the linear conjugated co-polymer **P7**, which contains a phenylene moiety and a dibenzo[b,d]thiophene sulphone (DBTS) co-monomer. Compared with the UV-active poly(p-phenylene) polymer, **P1**, each p-phenylene co-polymer containing planarised co-monomers exhibited increased photocatalytic activities under sacrificial conditions. However, **P7** exhibited an increase in activity over 10 times. This is the first reported work using the DBTS monomer unit in organic photocatalysts, which has since become a staple of some of the most active organic photocatalysts to date.¹³⁵

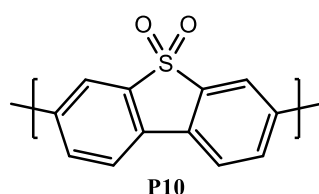
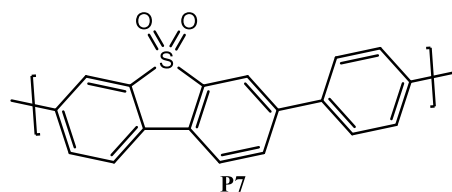


Figure 12: Linear polymers investigated in reference ¹³⁴.

Subsequent work investigated the DBTS homopolymer, **P10**, which exhibited improved photocatalytic hydrogen evolution rates compared to the phenylene-DBTS co-polymer.⁶⁴ Transient absorption spectroscopy (TAS) identified a long-lived polaron state on the order of milliseconds for both **P7** and **P10**.^{64,136} This was ascribed to a negatively charged electron polaron resulting from reductive quenching of holes by the sacrificial reagent, TEA. The long lifetime of the polaronic state highlights that once charges have been separated, polarons are more likely to survive long enough to diffuse to participate in the hydrogen evolution reaction.

Molecular modelling was used to highlight the interaction of various polymers with the H₂O, MeOH, and TEA solvent mixture and calculate the relative proportions in the closest contact with the polymer backbone.⁶⁴ It was found that a greater proportion of water came into close contact with the backbone in polymers containing the DBTS monomer thanks to the polar sulfone groups. The IP, EA, IP* and EA* of each polymer in each solvent were also calculated via DFT and highlighted that proton reduction is only thermodynamically favourable when situated in water. However, this does raise an important question about the use of TEA as a sacrificial electron donor when testing for hydrogen-evolving polymers since the energy levels are considerably influenced by its presence in the solvent mixture. Furthermore, TEA is strongly basic, which will affect water redox potentials and may complicate commercial adoption.

Linear polymers **P11** – **P17** constituted a family of 1,4-phenylene/2,5-thiophene co-polymers with various mole fractions.¹³⁷ The bandgap inversely correlated with the thiophene fraction as a range of visible light-sensitive polymers were prepared. Though greater thiophene fractions increased the range of visible absorbable wavelengths, they also reduced the IP such that greater thiophene fractional weighted polymers had unsuitable orbital energies to react with the TEA SED. As such, the optimal fraction was discovered to be that containing 33 mol% thiophene. Interestingly, the HER seems to also depend on the sequence of phenylene/thiophene units, whereby a 50/50 molar ratio polymer **P13** with alternating units exhibited a slightly improved HER compared to the 50/50 molar ratio **P14**, with a diphenyl-thiophene structured backbone. This discrepancy is likely related to the optimised conformational structure of the backbone and the extent to which charge is delocalised in a single given chain.

Computational high throughput studies have also investigated the impact of statistical copolymerisation between two linear co-polymers.¹³⁸ Here, thiophene, pyridine and phenylene copolymers were considered in terms of fractional distribution, degree of separation and range of conformations. This work confirms earlier reports that the band gap of the overall polymer can be finely tuned with relative proportions of monomers, whereby the IP and EA values vary between the limits of the two co-monomers. The degree of segregation between A and B monomers along the backbone and the conformation of that backbone only has a minimal impact on the IP and EA values. However, this work highlights that there are currently no high-throughput electronic calculations capable of investigating charge transport properties along the polymer backbone, which is likely to impact the exciton's natural lifetime.

The introduction of nitrogen into the linear polymer backbone was also investigated by Cooper *et al.*¹³⁹ co-polymers combining p-phenylene and pyridine monomers resulted in improved HER compared to poly(p-phenylene) homopolymers. The best-performing polymer was a co-polymer containing phenyl and pyrazine monomers, exhibiting a HER of 24 $\mu\text{mol h}^{-1}$ under visible light irradiation. The co-polymer containing phenyl and pyridine monomeric units and the homopolymer poly(p-pyridine) both also performed substantially better than the poly(p-phenylene) homopolymer. Polymers in which one 6-membered ring was linked via the meta position did not show any signs of hydrogen evolution despite their IP and EA energies being theoretically aligned to allow for proton reduction and oxidation of the SED. This might have been due to limited delocalisation via electron resonance in the meta-position. A linear polymer based on triphenylamine was also investigated and found to demonstrate very limited to no activity. As for the meta-linked polymers, π -electron delocalisation may not have been

favoured along the backbone due to no backbone-conjugated resonance structures. The torsion angle between phenyl groups would also make it difficult to overlap between π -orbitals for efficient delocalisation, stabilising the exciton and minimising the exciton binding energy.

Benzothiadiazole-containing conjugated linear polymers (CLP) and conjugated microporous polymers (CMP) were investigated by Wang *et al.*¹⁴⁰, who found that the activity of the linear polymer was more significant than any cross-linked derivative. Meanwhile, Cooper's group also identified a similar pattern within pyrene-linked CMPs, which performed only marginally better than the linear derivatives of the same design.¹⁴¹ For both linear polymers, reasonable porosity was still observed, despite the absence of cross-linking. This is in line with other linear porous CMPs previously investigated.¹⁴² Xiang and Chen synthesised derivatives of these linear polymers via Sonogashira–Hagihara cross-coupling reaction, which incorporated triple-bonded ethynyl separators into the polymer backbone.¹⁴³ This resulted in red-shifted absorption and photoluminescence spectra attributed to an extended π conjugated system. This narrowing of the bandgap led to improved HER for all investigated polymers. Upon photodepositing 3 wt% Pt on the **P7** derivative with ethynyl linkers (**P7-E**), this polymer exhibited an AQY of 7.2% at 420 nm.

Following this research, B-BT-E was modified further via the incorporation of fluorine and methoxy functional groups on the BT unit to aid charge separation and exciton stabilisation.¹⁴⁴ Interestingly, the addition of one fluorine group was considerably more beneficial than the addition of two. Still, the co-functionalisation of one fluorine group and one methoxy group provided the largest increase in HER. Polymer **B-FOBT-1,4-E** exhibited an AQY of 5.7% compared to the 0.85% reported for the non-functionalised **B-BT-1,4-E** linear polymer. As with the earlier research, linear derivatives consistently performed better than the 1,3,5 tri-linked phenyl monomer.

One of the main advantages of linear polymers over other organic variants is the option to generate soluble polymers. This has been particularly beneficial in organic photovoltaic devices where solution processing of the photosensitising organics significantly benefits competing technologies and allows for easily scalable processing methods such as spin coating and dye slot printing. An initial paper based on poly(*p*-phenylene)-carbazole co-polymers look at the effects of introducing aliphatic side chains on the carbazole nitrogen to introduce solubility in organic solvents.¹⁴⁵ This work found that, below a particular molecular weight threshold, both branched and linear hydrocarbon side chains result in soluble polymers capable of photocatalytic proton reduction under visible light in the presence of TEA with the branched polymer performing better of the two. As with most linear polymers, this hydrogen

evolution rate improved significantly under full-spectrum irradiation. However, the soluble polymers were found to evolve hydrogen at a slower rate compared to their insoluble derivatives of higher molecular weight.

Soluble linear co-polymers containing dibenzothiophene[b,d]sulfone and side chain-modified polyfluorene have also been investigated.¹⁴⁶ Alongside a range of linear and branched aliphatic side chains, Woods *et al.* also introduced polyethylene glycol (PEG) side chains, significantly improving the polymer's interaction with water and surface wettability. This improved contact with water is claimed to be responsible for the improved photocatalytic activity of this particular polymer, **FS-TEG**, which had a HER of 72.5 $\mu\text{mol h}^{-1}$. Transient absorption measurements highlighted that reductive quenching occurs rapidly in the presence of TEA, leaving long-lived polaronic states available to reduce protons on the millisecond timescale. Benzodithiophene-benzothiadiazole co-polymers were also functionalised with oligoethylene glycol side chains by Cao *et al.* This was also found to improve wettability, dispersion in water, and the interaction with Pt co-catalysts.¹⁴⁷

Given the short exciton diffusion lengths in polymer photocatalysts and the requirement of a surface or interface to facilitate charge separation, a novel approach to produce polymer nanodots (pdots) was devised utilising the fact that polymers can be made to be soluble in organic solvents.¹⁴⁸ Tian *et al.* used a poly(fluorene-benzothiadiazole) PFBT polymer whereby the fluorene moiety was modified with octane side chains. This polymer was combined with a PEG-chain modified polystyrene polymer, which contracts to nanosized dots and forms a micelle-like structured pdot with a narrow size distribution between 20 and 100nm. These pdots can easily be dispersed in water. Further optimisation of this polymer led to very significant weight normalised HER of over 50 $\text{mmol h}^{-1} \text{g}^{-1}$.¹⁴⁹ However, it should be noted that increased rates were only observed when decreased photocatalyst masses were used for the reaction, and so this is not consistent with increased STH rates. There is also limited evidence for sustained activity over the lifetime of these pdots. Pdots incorporating cycloplatinated units into the backbone have also been investigated, with rates reaching 12.7 $\text{mmol h}^{-1} \text{g}^{-1}$.¹⁵⁰

Another route to forming water-dispersible nanoparticles from soluble linear conjugated co-polymers is to introduce ionic side chains onto the fluorene units and hence make redundant the need for PS-PEG-COOH polymer for dispersability.¹⁵¹

Recently, mini-emulsion polymerisation has been used to synthesise nanoscale powder distributions of otherwise insoluble polymers such as the previously highly photoactive **P10**.¹⁵² Reagents were contained in nano-emulsion particles stabilised by surfactants so that polymerisation, and hence particle sizes, were contained on the microscale. **P10** synthesised via this emulsion method displayed an HER of over 60 mmol h⁻¹ g⁻¹ and an AQE of 20.4% at 420 nm. Unlike previous p-dot photocatalysts, these polymers are not diluted by PS-PEG-COOH polymer chains, are more stable under irradiation for longer timescales, and their activity scales with concentration.

Recently, McCullough *et al.* have demonstrated the use of this mini-emulsion method to synthesise nanoparticles of an OPV-like bulk heterojunction.⁶⁷ In this material, a polymer photocatalyst sensitiser is blended with a molecular electron acceptor, and the two organic materials phase-separate on the nanoscale. This allows exciton charge separation within a few nanometres of the excitation event and significantly reduces the recombination rate. Record hydrogen evolution rates over 60 mmol hr⁻¹ g⁻¹ were obtained. Furthermore, AQY values of 6.2% were observed at 700 nm excitation. Simultaneously, Cooper's group also investigated the fabrication of nanohybrid bulk heterojunction polymer nanoparticles.¹⁵³ Using a slightly different synthetic approach, 237 different molecular donor-acceptor pairs were explored using a high throughput experiment. This also resulted in photocatalysts capable of achieving HER values over 50 mmol h⁻¹ g⁻¹.

It is worth mentioning that Suzuki cross-coupling reactions, by which the vast majority of these polymers are synthesised, leave residual traces of Pd incorporated into the polymer after synthesis. In most cases, this residual palladium acts as a natural co-catalyst.^{62,154,155} However, in the case of **P10**, charge transfer to palladium, as measured by transient absorption spectroscopy, is determined to be surprisingly slow compared to other polymers.⁶³ **P10** also exhibits significant increases in activity when loaded with photodeposited platinum as a co-catalyst, indicating a co-catalyst-dependent charge transfer rate.¹⁵⁶

Pd concentrations vary in every batch according to the synthesis conditions, and residual Pd cannot be separated from insoluble polymers. Comparing polymer activities based on their structures alone is, therefore, challenging. Furthermore, comparing values between different research groups is also challenging. Research teams use different setups, testing conditions, and reporting methods. As such, many calls have been made for standardised testing protocols and a certification system to be implemented.¹⁵⁷

The light source, intensity, and filter system must be reported for comparable results. Furthermore, the irradiation surface area, polymer concentration, and reaction mixture path length should also be reported. Experiments should also be conducted on dispersions containing polymer concentrations in the saturation regime. This would result in slower mass-normalised hydrogen evolution rates since adding more polymer would increase the mass but not the absolute amount of hydrogen produced. However, area-normalised rates are inherently more comparable. This would be particularly beneficial since future photocatalysis systems will be best judged according to their ability to convert the solar irradiation per unit surface area, as is the standard for solar panels.

1.5.2.2 Oxygen Evolution and Overall Water Splitting

As discussed in section 1.4, inorganic oxide photocatalysts are well-suited to drive the four-electron oxygen evolution reaction due to deep valence bands and photogenerated holes with large oxidation overpotentials.¹⁵⁸ This also results in more inorganic materials capable of driving the overall water-splitting reaction. Although organic photocatalysts have made significant advances in their hydrogen evolution rates using sacrificial reagents, reports of oxygen evolution and overall water-splitting remain extremely rare.^{72,159}

Nonetheless, recent progress in this regard has been made. For example, Bai *et al.* achieved overall water splitting on **P10** by loading it with an iridium oxide co-catalyst.¹⁶⁰ This result followed earlier work in which water oxidation was achieved by loading with a cobalt-based co-catalyst.¹⁶¹ More recently, a conjugated microporous polymer containing 1,3,5-triazine and benzodithiophene has demonstrated very low activity for overall water splitting.¹⁶²

Similarly, molecular photocatalysts based on perylene diimide (PDI) have shown promise as oxygen evolution photocatalysts. One particular paper has reported a seemingly remarkable oxygen evolution rate of $27 \text{ mmol hr}^{-1} \text{ g}^{-1}$.¹⁶³ However, the scalability of such mass-normalised values should be viewed with caution. In this case, reactions were performed by dispersing just 1 mg of material in 100 ml of water, so evolution rates on absolute or area-normalised terms are much lower. Nonetheless, PDI polymers and photodeposited FeOOH co-catalysts have since been used in other organic overall water-splitting systems.¹⁶⁴

Possibly the most remarkable result, however, was published by Ye *et al.* A first publication demonstrated that it is possible to incorporate small amounts of a 5 mol% of a peryleno[1,12-bcd]thiophene sulfone unit into the P10 structure to narrow the bandgap and enhance the

photocatalytic hydrogen evolution activity.¹⁶⁵ This polymer has since demonstrated stoichiometric overall water splitting after loading it with a FeOOH co-catalyst.¹⁶⁶

1.6 Z-scheme and S-scheme Photocatalysts

A commonly investigated alternative approach to developing single particulate photocatalysts capable of driving the overall water splitting is to couple two photocatalyst materials together that can drive the HER and OER reactions independently. For these systems to work, a pathway must be available through which unused photoelectrons from the oxygen-evolving photocatalyst, OEP, can be combined with the unused holes from the hydrogen evolution photocatalyst, HEP. This type of system is called a Z-scheme photocatalyst and is outlined in Figure 13.¹⁶⁷

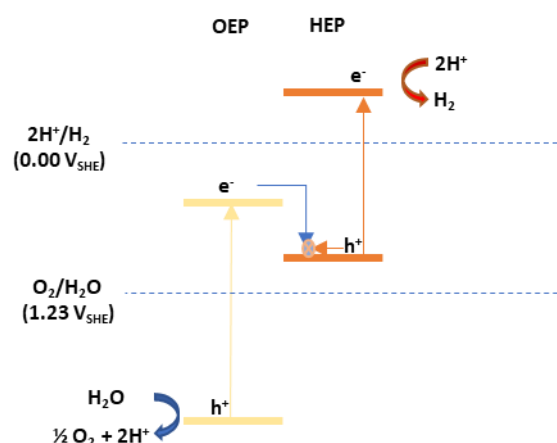


Figure 13: Z-scheme photocatalyst for overall water splitting

Compared to single-type photocatalysts for OWS, Z-schemes benefit from fewer restrictions to the electronic band edges of each component, as no single component has to straddle both the HER and OER half potentials. As a result, there is far more flexibility when selecting the two components, enabling the use of semiconductors with narrower bandgaps. In turn, a greater proportion of the solar spectrum can be harnessed. However, compared to a single semiconductor system, the main downside to these systems is that two photons must be absorbed for each electron-hole pair that reacts with water, amounting to a halving of efficiency.

Several approaches have been used to ensure electron-hole transport between the two components. The simplest involves using a solution-based reversible redox mediator such as IO_3^-/I^- .^{168–171} However,

the redox mediator can absorb light or extract charges from the wrong photocatalyst and compete with the water-splitting half-reactions. A second approach requires the use of a solid-state conductive mediator, such as gold or reduced graphene oxide.¹⁷²⁻¹⁷⁷ However, embedding two particulate photocatalysts onto a single continuous conductive matrix is challenging and not always easily reproduced.

A third approach is to create a direct heterojunction interface between the OEP and HEP components. This approach removes the requirement for any third electron mediator component. However, these systems require a good direct interface between the two components and optimal alignment of the energy bands and Fermi levels. In the cases where this is achieved, charge separation and extraction across the interface can be enhanced by internal electric fields that arise from band bending and Fermi level alignment. Photocatalysts belonging to this subset of Z-scheme heterojunctions are sometimes called S-scheme heterojunctions.¹⁷⁸⁻¹⁸¹

1.7 Conclusions

Research into particulate photocatalysts has rapidly accelerated over recent years. Novel designs and innovative approaches are constantly being developed. Advances in inorganic photocatalysts have resulted in materials with AQYs approaching 100%. However, overall water splitting efficiencies from these materials still suffer due to the wide bandgaps and deep valance bands that limit the hydrogen evolution reaction. Developments in organic photocatalysts have demonstrated remarkably high hydrogen evolution rates under visible light when paired with sacrificial reagents. The optical bandgap and band edge potentials can also be finely tuned by design. However, these materials lack the overpotentials and active sites to efficiently drive the four-electron oxygen evolution reaction. It is, therefore, logical that hybrid organic/inorganic photocatalyst systems for overall water splitting should be considered for their complementary characteristics.

1.8 Aims, Objectives, and Thesis Outline

The primary focus of this work is to develop an understanding of the structure-activity relationships of linear organic polymer photocatalysts and subsequently design and synthesise new ones. It is hoped that these polymers not only function as efficient standalone hydrogen evolution photocatalysts but can also be paired with various oxide photocatalysts to generate hybrid organic/inorganic photocatalyst systems.

The work presented in Chapter 2 builds upon previous research conducted in the group. In 2019, Bai *et al.* published research in which a library of 6,354 theoretical linear co-polymers was investigated computationally using a high-throughput virtual screening method.¹⁵⁶ High-throughput microwave synthesis was subsequently used to attempt the synthesis of 127 these co-polymers containing the DBTS monomer unit. Ninety-nine polymer photocatalysts were successfully synthesised, tested for their photocatalytic activity, and characterised. Most of these were previously unreported in the literature.

The supplementary information of their publication provides the largest available library of polymer photocatalysts synthesised and tested under identical conditions. Resultingly, these results can be directly compared with one another. The original analysis presented in the original publication was limited in scope and methodology. The results were analysed globally using a machine learning algorithm and only focussed on the HER rates without a platinum co-catalyst. Her rates after the photodeposition of Pt were also recorded, but this data set was not analysed or dicussed in the original publication.

Chapter 2 presents a more detailed analysis of these results. There is a particular focus on structure-activity relationships and the change in photocatalytic activity associated with loading the polymers with a platinum co-catalyst. Screening parameters are also applied to the 705 DBTS co-polymers investigated as part of the wider computational study of the same publication. This analysis is used to identify target co-polymer photocatalysts for future investigations.

Chapter 3 investigates the effects of incorporating fluorinated phenylene monomers into the backbone of linear conjugated polymer photocatalysts. Seventeen linear conjugated polymers are first investigated by density functional theory (DFT) calculations and subsequently synthesised using a microwave-assisted synthesis method. Discussions focus on the impact of fluorination, synthesis conditions, and co-catalysts on the resulting photocatalytic activities. This work also introduces the possibility of designing ternary co-polymers for greater control over physical and optoelectronic properties.

Work presented in Chapter 4 attempts to prepare organic/inorganic hybrid photocatalysts by combining polymers from Chapter 3 with high-performance inorganic oxides from the literature via *in-situ* polymerisation. Two hybrid systems are targeted: a Type-II heterojunction based on

polymer/Al-SrTiO₃ photocatalysts for polymer-sensitised hydrogen evolution and an S-scheme polymer/BiVO₄ hybrid for overall water splitting. Theoretical polymer designs that could be used to enhance the performances of future hybrid photocatalysts are also considered by DFT calculations.

Chapter 2: Literature Analysis and Polymer Design

2.1 Introduction

In 2019, a collaboration between Professors Cooper and Zwiijnenburg demonstrated how high throughput computational screening and high throughput experiments can be combined to identify new polymers capable of water splitting.¹⁸² In this pioneering paper, 6,354 different copolymers were screened computationally. A library of 127 different linear copolymers, based on the DBTS monomer, was subsequently synthesised via a high-throughput microwave synthesis method. The resulting polymers, of which 99 were obtained in yields over 30%, were characterised and tested for sacrificial photocatalytic hydrogen production from water.

This work contains the largest data set of structurally similar polymeric photocatalysts synthesised and characterised under identical conditions to date. This publication identified several key relationships between photocatalytic activity and computationally predicted optoelectronic properties. However, further detailed analyses may gain additional information from this data.

This chapter commences with an analysis of the published findings. Subsequently, it explores how this large dataset can be further analysed to advance the scientific community's understanding of linear organic polymeric photocatalysts containing the DBTS moiety. Special consideration is given to the limitation of the methodology used, and polymers for which the synthesis conditions may have had a detrimental impact on the resulting photocatalytic activities are highlighted.

Novel structure-activity relationships are identified and related to properties that may be predicted computationally. The computational methods used to predict optoelectronic properties are also improved upon. This improved methodology is used to identify a brand new set of co-polymers as promising candidates for photocatalytic water splitting. A specific focus is placed on polymers that exhibited a significant enhancement in activity following the photodeposition of platinum, as this data was recorded in the initial study but not reported on.

2.2 Summary of Original Findings

The computational screening part of this study considered the 6,345 co-polymers that arise through the combination of nine dibromonic acid monomers with 705 possible dibromide monomers. The electron affinity, ionisation potential, optical bandgap, and oscillator strength were predicted computationally for each combination. Given its prominence in many water-slitting polymeric photocatalysts, one of the nine diboronic acid moieties considered was dibenzo[b,d]thiophene sulfone (DBTS). This building block was selected as the basis of the subsequent high-throughput experiment.

DBTS-(B(pin))₂ was reacted with 127 different aromatic dibromide moieties to form DBTS-based linear co-polymers via a microwave-assisted Suzuki coupling reaction. Ninety-nine of these reactions resulted in solid products, assumed to be the target co-polymers, with yields over 30%. The reaction scheme is presented in Figure 14. The aromatic dibromide reactants studied are shown in Figure 15.

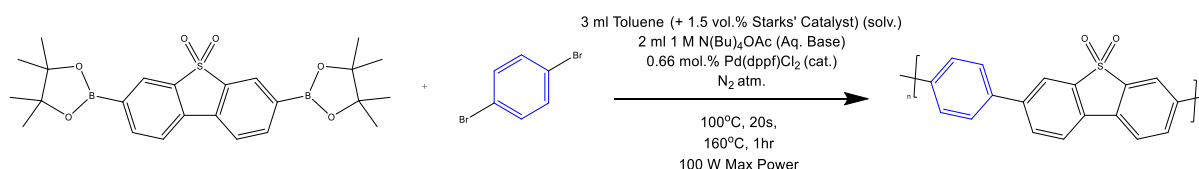


Figure 14: Microwave-assisted Suzuki-Miyaura Polycondensation reaction conditions used to synthesise the library of polymers discussed in this chapter.

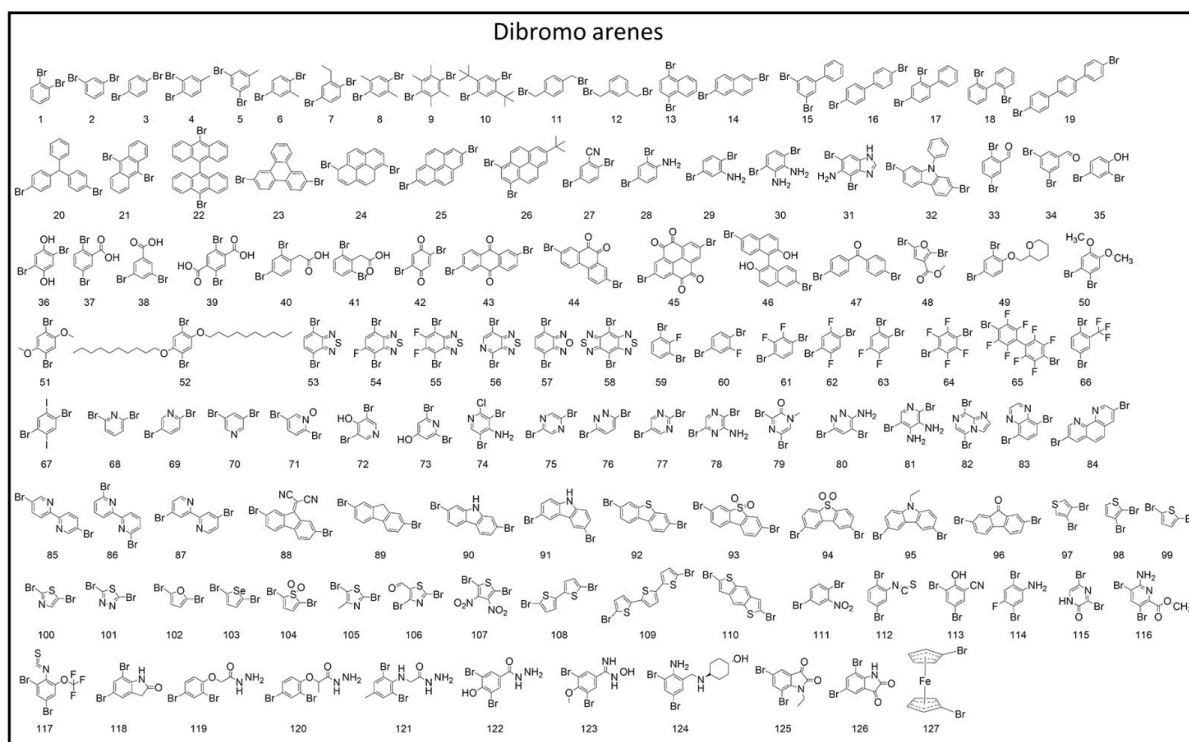


Figure 15: List of 127 dibromide monomers that were co-polymerised alongside dibenzo[b,d]thiophene sulfone *via* a high throughput synthesis approach. Figure reproduced from reference ¹⁸².

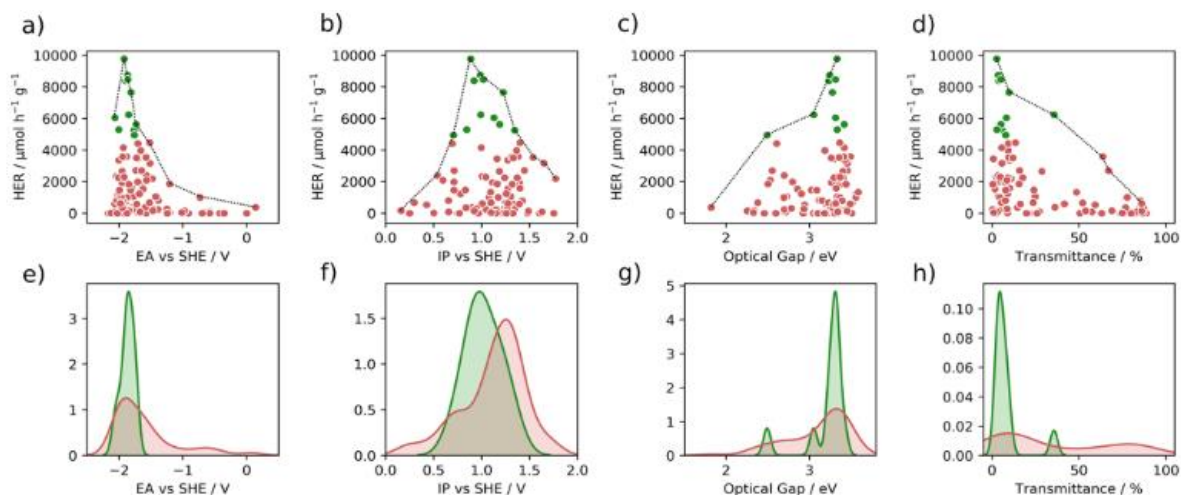


Figure 16: Observed relationships between predicted properties and observed hydrogen evolution rates. Reproduced from reference ¹⁸²

The sacrificial photocatalytic performance of each sample was tested using a 1:1:1 mixture containing equal volumes of TEA, MeOH, and water. Each sample was tested with and without 1 wt.% of photodeposited Pt as a co-catalyst. Additional photocatalytic hydrogen evolution measurements were performed using aprotic aqueous Na₂S as the sacrificial reagent. Residual Pd content was determined via ICP-OES. Each sample was physically characterised via FTIR, UV-Vis diffuse reflectance spectroscopy, PXRD, TCSPC fluorescence lifetime, transmissivity, and gas sorption analysis.

The resulting data was analysed using a machine-learning (ML) algorithm to determine any correlation between the computationally predicted properties, physical properties, and the resulting photocatalytic activity. The ML algorithm was trained on four variables: predicted EA, predicted IP, optical gap, and dispersibility in a 1:1:1 sacrificial reagent solution. Considering these four variables, a multivariate analysis revealed that 68% of the variation in observed photocatalytic activity could be accounted for. The dependencies of the photocatalytic activity on these four properties are presented in Figure 16. Incorporating additional datasets led to no statistically significant improvement in this correlation.

The paper resulted in the discovery of many new active photocatalysts, including 19 other polymers that exceeded the photocatalytic activity of the DBTS-DBTS homopolymer (P10) in the absence of a Pt co-catalyst. However, the most active polymer following the photodeposition of a Pt co-catalyst was

P10. P10 increased significantly from 3.4 mmol hr⁻¹ g⁻¹ to 16.7 mmol hr⁻¹ g⁻¹ when 1 wt.% of Pt was loaded onto its surface.

In addition to preparing the library of linear DBTS-based copolymers, the researchers selected six of the most efficient DBTS-based co-polymers and attempted to synthesise 48 additional co-polymers by using these six dibromides and reacting them with the eight alternative boronic acid precursors. The selected diboronic acids and dibromides are presented in Figures 17 and 18. Thirty-seven of these additional co-polymers were successfully synthesised using the same reaction conditions as the initial high throughput study.

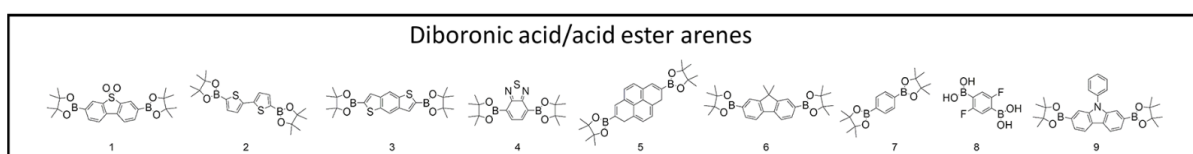


Figure 17: Diboronic acids used to synthesise 48 additional co-polymers using the eight alternative diboronic esters

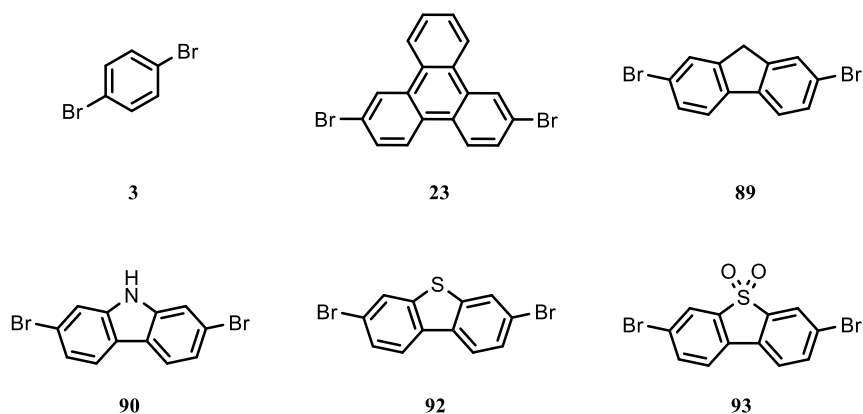


Figure 18: Group of diboronic acids used to synthesise 48 additional co-polymers using the eight alternative diboronic esters highlighted in Figure 17.

The trends of the resulting photocatalytic activities mirrored those observed in the DBTS copolymerisation study. The most influential factors included predicted electron affinities (EA), ionisation potentials (IP), and measured optical bandgaps. Interestingly, despite not being highlighted in the initial publication, polymer P8-92 produced hydrogen at a rate of 9.8 mmol hr⁻¹ g⁻¹ in the absence of additional platinum. Although this co-polymer does not contain the DBTS monomer, this hydrogen evolution reaction (HER) rate exceeds all of the 99 DBTS-based co-polymers investigated in the initial high throughput study when tested under the same conditions.

Unsurprisingly, large-magnitude IP and EA values correspond to the most-active photocatalysts since these properties lay the foundational thermodynamic requirements for photocatalytic redox reactions. The more negative the EA, the stronger the thermodynamic driving force for proton reduction, and a more positive IP corresponds to a thermodynamic overpotential driving force for TEA oxidation. Likewise, the wider the optical bandgap, the larger these overpotentials are likely to be.

Although these correlations are not unexpected, it is worth noting that the EA, IP, and E_g values were calculated using a computationally cheap extended tight-binding method that allowed properties of a very large compositional space to be calculated over a relatively short period.^{183,184} These correlations, therefore, imply that this computational model can correctly identify which polymers will have larger bandgaps and stronger photoredox potentials relative to one another in minutes rather than requiring several tens of minutes per polymer.

Overall, this paper has demonstrated that cheap, scalable computational tools based on tight-binding models can be used in the place of energy- and time-intensive DFT calculations to rapidly screen thousands of potential polymers and identify those which possess suitable bandgaps and band edge potentials to drive the photocatalytic water splitting reactions. It has also shown how high-throughput computational screening can be combined with automated systems to run high-throughput synthesis and characterisation experiments. In particular, it has demonstrated how an automated microwave synthesis approach, in which reactions take an hour each and can be sequenced to run automatically, can replace traditional reaction methods that require reaction times of 2+ days per sample and are limited to only running a very small number samples at a time. Finally, their work resulted in the most extensive library of directly comparable polymer photocatalysts in the literature.

The ML model approach to analysing the resulting library identified relationships between the HER rates and the IP, EA, bandgap, and transmittance data. The authors claim these properties account for 68% of the variation observed within the resulting HER activities. However, understanding and explaining the remaining 32% requires scientists to manually study the results to draw further conclusions.

This database includes the HER rates for all of the polymer samples when 1 wt.% of metallic platinum has been photodeposited onto their surfaces as a co-catalyst. Most samples exhibited a slight increase in activity following photodeposition, some experienced a significant increase, and the activity decreased for others. Beyond attributing this variation to the presence of residual palladium, the

published work does not attempt to investigate which materials reacted positively to the presence of Pt or why.

Consequently, this database of results provides an ideal opportunity to further advance our understanding of polymeric photocatalysts for hydrogen evolution as a result of further analysis. As such, this chapter provides additional, previously unreported insights into the data gathered as part of the published research, with a particular focus on the underlying structure-activity relationships.

2.3 Analysis of Methods

Unlike in the field of photovoltaics,¹⁵⁷ standardised testing methods have yet to be fully established for water-splitting photocatalysts. As such, comparisons between different research groups remain challenging. Different photocatalysis testing setups use different light sources, photocatalyst concentrations, temperatures, pressures, pHs, additives, dispersal methods, sacrificial reagents, co-solvents, irradiation times and other discrepancies. These polymers have all been tested for their photocatalytic activity under identical conditions. Resultingly, their activities are directly comparable with one another.

However, the high-throughput nature of this work also generates an issue whereby the hierarchy of photocatalytic activities of the resulting polymers only applies to the precise conditions under which the polymers were synthesised and tested. Here, the HT synthesis and H₂ evolution testing conditions are analysed critically to identify potential issues regarding the reliability of the results.

2.3.1 High Throughput Synthesis

The polymer photocatalysts were synthesised using a microwave-assisted polymerisation method that reduced the reaction time from two days, using the conventional solvothermal method, to under two hours. Following the optimisation of synthesis conditions when preparing poly(p-phenylene), the final synthesis conditions are presented in Figure 19. The blue phenyl ring dibromide is used to represent all of the 127 different aromatic dibromides tested in this experiment.

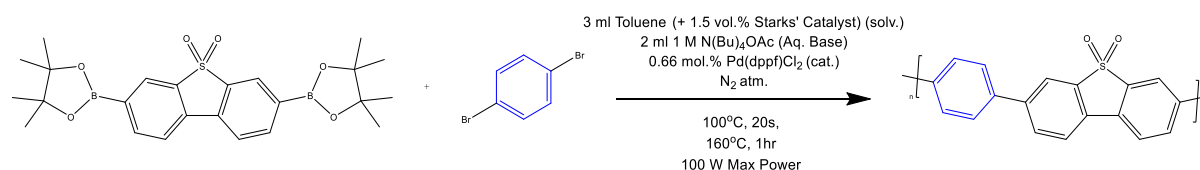


Figure 19: Microwave-assisted Suzuki-Miyaura Polycondensation reaction conditions used to synthesise the library of polymers discussed in this chapter.

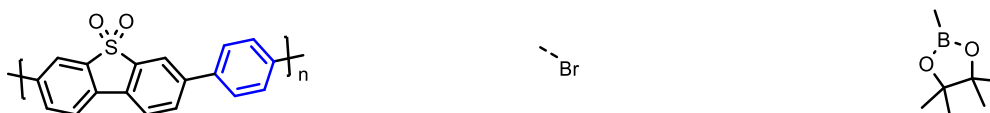
2.3.1.1 Yield

For each sample synthesised, a yield is reported. This section examines the relationship between this yield and the photocatalytic activity. However, a discussion of what the reported yield means and its limitations must first be considered.

Importantly, the insoluble precipitate resulting from the Suzuki coupling reaction is assumed to be the pure polymeric product. Each product was isolated by washing with deionised water and methanol before drying in a vacuum oven. As such, the resulting product is fairly crude, having undergone limited purification steps. Typically, 50% of the mass of the starting reagents' masses belong to the boronate and bromide leaving groups. As such, incomplete purification may leave behind large masses of byproducts. Despite the potential for low purity products, the mass of the isolated product is used for the subsequent yield calculations. As such, the masses of impurities are included in the mass used for yield calculations.

Functional groups at the polymer chain ends further complicate the yield calculation. The theoretical mass of the product is calculated with the assumption that the masses of the chain ends are negligible relative to the combined mass of the repeating units within each polymer chain. However, since the polymeric products are insoluble, there is no reliable way to determine the degree of polymerisation. In fact, short chains are highly probable since the products are highly insoluble and are likely to crash out of the reaction mixture before they grow too large.

Chains are likely to be terminated by boronic esters and bromine functional groups, which have large molecular weights. These groups likely contribute a significant proportion of the mass of the final product. As such, the yield calculation, which is only based on the molecular mass of the repeat unit, will be artificially inflated. As such any yield values were often greater than 100% and should be considered as approximations. The theoretical impact that brominated oligomers may have on the yield calculation of an example co-polymer (DBTS-Ph) are summarised in Figure 20 and Table 1.



Repeat Unit MW: 293.25 g mol⁻¹

End Group MW: 79.90 g mol⁻¹

End Group MW: 127.28 g mol⁻¹

Figure 20: Molecular weight of a polymeric repeat unit used in theoretical yield calculations and the molecular weights of leaving groups that typically cap the polymeric chain ends.

Table 1: Impact of brominated chain ends on the yield calculations when end groups are neglected and the degree of polymerisation is very low (oligomeric products).

N repeat units	Polymer chain MW (Brominated chain ends)	Weight % Br	Theoretical maximum yield %
1	453.05	35%	154%
2	746.30	21%	127%
3	1,039.55	15%	118%
5	1,626.05	10%	111%
10	3,092.30	5%	105%
100	29,325.00	0.5%	100.5%

Under these reaction conditions, 99 of the 127 polymers were successfully synthesised with approximate yields above 30%. The synthesis yield distribution is presented in Figure 21. Many polymers (21) were obtained with yields above the theoretical maximum due to unreacted boronate and dibromide functional groups at the polymer chain ends, which were not accounted for in theoretical yield calculations.

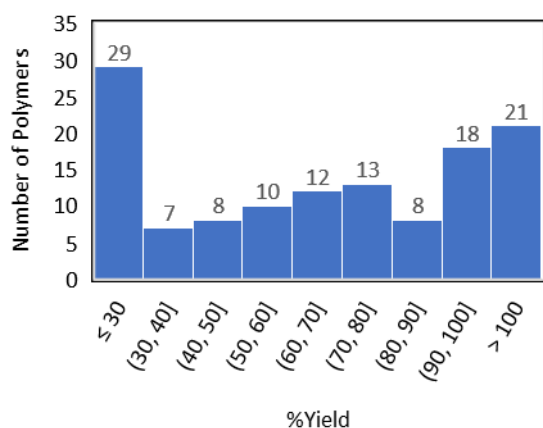


Figure 21: Histogram depicting the distribution of synthesis yields obtained for the 99 synthesised DBTS-based polymers. Many samples were obtained with yields over 100%. The extent to which these samples weighed more than the theoretical maximum is not reported in the original publication. Here, all such samples have arbitrarily been assigned a yield of 105%.

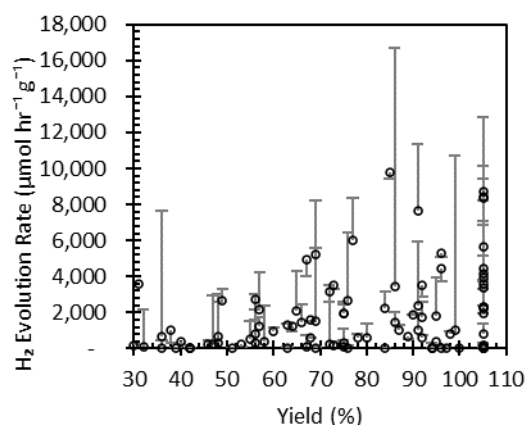


Figure 22: Photocatalytic hydrogen evolution rates vs approximate synthetic yield. Data points represent photocatalytic activity before platinum deposition. Error bars represent the change in photocatalytic activity after the photodeposition of 1 wt.% Pt.

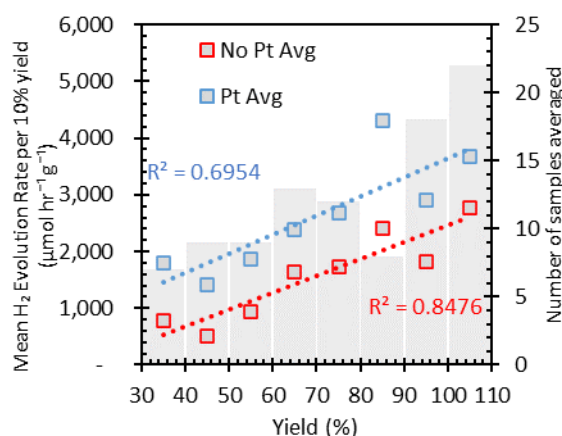


Figure 23: Average hydrogen evolution rates for all samples before and after the photodeposition of 1 wt.% Pt. Each data point represents the average HER obtained for all samples produced within a window of $\pm 5\%$ yield. The grey histogram (secondary axis) represents the number of samples included in the calculation for each data point.

Figure 22 contains the data for photocatalytic activity for 5 mg of the polymers dispersed in 5 ml of a 1:1:1 mixture of $\text{H}_2\text{O}/\text{MeOH}/\text{TEA}$, in which MeOH acts as a dispersing agent, and TEA is the sacrificial electron donor. The error bars represent how the photocatalytic activity of each polymer changed after the photodeposition of 1 wt.% Pt as a co-catalyst. Figure 23 represent the average activity for all samples within each 10% yield distribution. The blue and red datapoints represent the linear best fit for data averaged with and without the Pt co-catalyst, respectively. Samples obtained with approximate yields greater than 100% have been ascribed a value of 105% since the exact measured values were not provided.

These charts demonstrate that the photocatalytic hydrogen evolution rates were, on average, higher for polymers obtained with higher yields. This trend remains true after Pt photodeposition, where the average increase in activity appears to be largely independent of the yield. Polymers obtained at lower yields may possess a greater concentration of impurities and byproducts trapped in the polymer matrix. These could act as traps or recombination centres for excitons, decreasing the polymers' apparent quantum yields. Byproducts and unreacted precursors may also be susceptible to photoreduction by the polymer photocatalysts and limit the availability of electrons for hydrogen evolution.

Low yields are not necessarily indicative of low purity and vice versa. Instead, the Suzuki coupling may be more likely to fail for some structurally related dihalides than others. For example, the oxidative addition step in which the halide bonds to the Pd catalyst, the rate of reaction is enhanced by using an electron-deficient aromatic dihalide. As such, electron-withdrawing substituents on the aromatic dihalide (acting either by either mesomeric or inductive pathways) may increase the likelihood of achieving a high yield. These electronic effects, will also have a significant impact on the optoelectronic properties of the resulting polymers and hence also, their photocatalytic activities. As such, lower activities from polymers may result from related structural effects rather than because of impurities.

To determine whether the samples produced with low yields perform poorly because of inappropriate synthesis conditions or because of their inherent structure would require further investigations. However, low yields may also indicate the traces of undesirable byproducts, higher concentrations of residual palladium, and lower degrees of polymerisation compared samples produced with higher yields.

2.3.1.2 Residual Palladium

One impurity that may be particularly impactful is residual palladium. A common reason why the Suzuki reaction fails is due to the decomposition of the palladium catalyst and the formation of metallic palladium nanoparticles, commonly called palladium black. Residual palladium may be beneficial since it is known to act as a co-catalyst for photocatalytic hydrogen evolution in these materials. However, excess Pd immobilised inside the bulk polymer matrix may also act as an electron trap that cannot drive the HER due to the absence of a Pd/H₂O interface.

There is no clear correlation between the synthesis yield and the relative concentration of residual palladium, as shown in Figure 24. Polymers obtained at low yields did not always contain high levels of Pd, and likewise, polymers obtained at high yields did not always contain low levels of palladium. This may be because residual Pd is also present in its ligated catalytic form, either trapped in the bulk polymer matrix or bonded to the polymer's chain ends. Ultimately, the exact source of Pd in the photocatalysts may not be relevant as residual traces of Pd(II)(dppf)Cl₂ would likely be reduced to Pd(0) via photocatalysis.

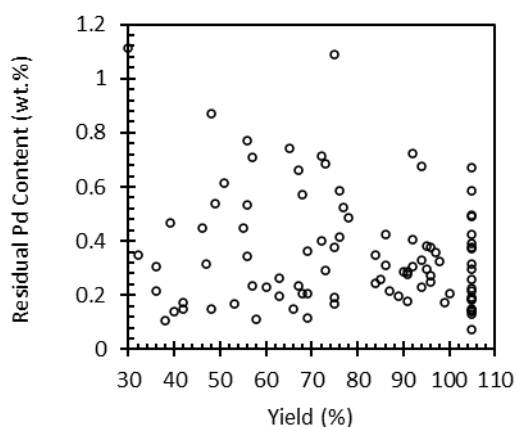


Figure 24: Plot of synthesis yield vs residual palladium concentration. The scattered data indicates that any correlation between these two properties is very low.

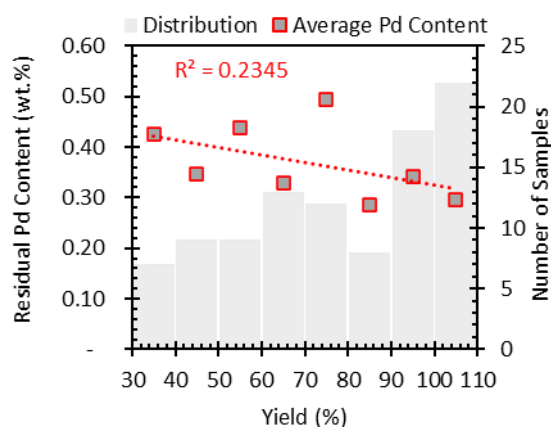


Figure 25: Weight averaged plot of the yield vs residual palladium content. Pd contents have been averaged out for every 10% yield to account for the asymmetric distribution of sample yields (grey bars, secondary axis). The small R^2 value and negative gradient indicates a possible weak negative correlation.

However, some interesting trends appear when we compare the residual palladium content with the photocatalytic activity. Figure 26 plots the photocatalytic hydrogen evolution rates all 99 co-polymers relative to their residual palladium content. The data points represent the activity before Pt photodeposition, whereas the error bars represent the change in activity afterwards. Whilst a visual inspection of these data appear to suggest that low palladium content correlates with high hydrogen evolution rates, this is a little misleading as it does not account for the natural distribution of the sample population. In reality, over two thirds of all samples were found to have residual palladium concentrations lower than 0.4 wt.%, as demonstrated by Figure 27. Therefore, statistically, the most active samples are likely to be naturally located in this region.

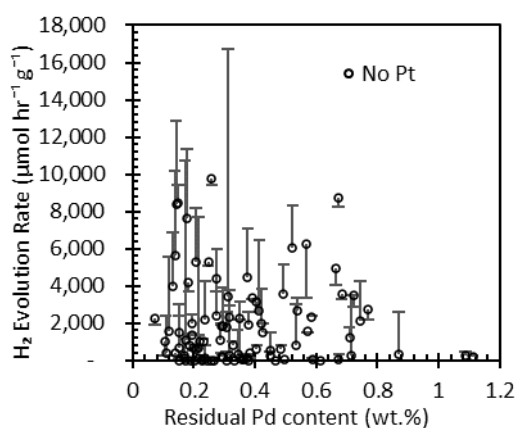


Figure 26: HER rate vs residual palladium concentration. Points represent activity before platinum deposition, error bars represent activity after.

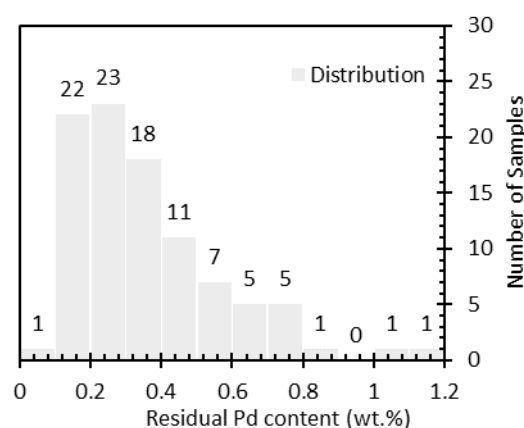


Figure 27: Residual palladium content distribution. Each bar represents the number of samples within an envelope of 0.1 wt.% of Pd.

To navigate this, Figure 32 plots the average HER rate for all samples within each discrete window of 0.1 wt.% Pd. Figure 32a presents these data for samples before Pt photodeposition, whereas Figure 32b presents the same data after the photodeposition of 1 wt.% Pt. In both cases, these weighted averages demonstrate no clear correlation between residual palladium content and the photocatalytic performance.

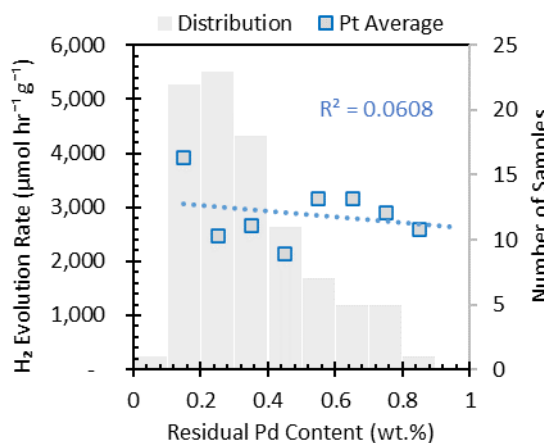
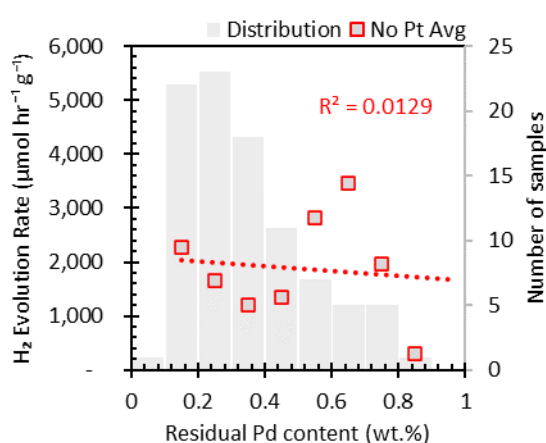


Figure 28: Weighted average HER rates for all polymer samples a) without Pt (red) and b) with 1 wt.% Pt (blue) relative to their residual palladium content. A low R^2 of below 0.1 indicates there is no linear correlation between the two when considering all samples. Grey histogram indicates the distribution of samples with different Pd content.

However, since the most active photocatalysts are of particular interest, it is important to find trends amongst these samples, specifically. Figure 29 contains the equivalent data to Figure 28 with the exception that these graphs only consider the 56 most active samples. The subset of samples contains the combined population of the 50 most active polymers before Pt photodeposition and the 50 most

active photocatalysts afterwards. Before adding Pt, there was no clear correlation between the residual Pd content and the photocatalytic activity.

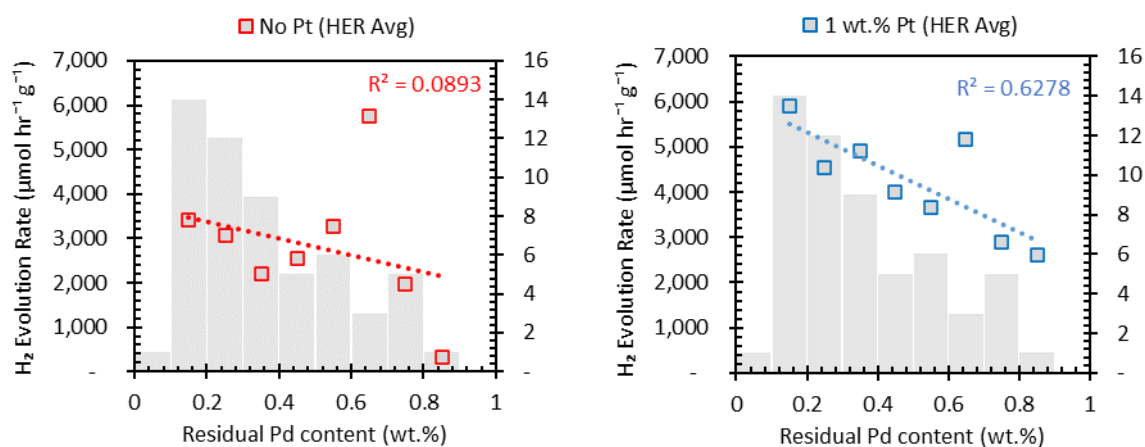


Figure 29: Weighted average HER rates for the top 56 polymer photocatalyst samples a) without Pt (red) and b) with 1 wt % Pt (blue) co-catalyst relative to their residual palladium content. Grey histogram indicates the distribution of the top 56 samples with different Pd content. The R² value for Pt-loaded samples indicates that a negative linear correlation between these two only exists after loading with a Pt co-catalyst.

Although several highly-active photocatalysts have low Pd content, others with higher Pd content also produce significant amounts of hydrogen under sacrificial conditions. In these polymers, palladium likely acts as an intrinsic co-catalyst and some polymers may benefit from its presence at higher concentrations. Whilst attempting to fit this data with a linear equation results in a negative gradient, the quality of the fit is very poor. An R² value of less than 0.1 implies that there is no clear and obvious correlation between the two.

However, after the photodeposition of 1 wt.% Pt, significant increases in activity are observed for many samples containing small amounts of Pd. In contrast, several samples with high residual Pd concentrations decreased in activity. A negative correlation between the residual Pd content and their photocatalytic activity after loading with Pt is, therefore, established. This is confirmed by the far stronger linear fit of the data, as represented by an R² value of greater than 0.5.

These results suggest that high Pd concentrations may enhance the photocatalytic activity of the polymers in the absence of other co-catalysts but are detrimental to further enhancement by additional co-catalysts. However, this rule has several exceptions, as with all these generalised trends. The rate at which electrons are transferred to either palladium or platinum will depend heavily on the polymer structure, as will be explored in more detail in section 2.6.

Ultimately, the reaction conditions will have significant impacts on the properties of the resulting photocatalysts. Yields, purity, Pd content, degree of polymerisation, degree of crystallinity and other physical characteristics could be tuned for optimal photocatalytic activity by fine-tuning the synthesis conditions for each polymer. Variables include the total reaction volume, aqueous-to-organic phase ratios, base selection, base concentration, organic solvents, palladium catalyst, catalyst concentration, reaction temperature, reaction time, microwave power, and others. Even when different reaction conditions produce the same polymers with a 100% yield, significant variation in photocatalytic activity is likely.

Understandably, finding one set of reaction conditions that produce an optimised polymer photocatalyst for all 127 dihalide monomers would have been impossible. However, the reaction conditions were only optimised to achieve the maximum yield of poly(p-phenylene). Not only did this not provide any information regarding how effective the reaction mixture would be for DBTS-based polycondensation reactions, but it also did not optimise the reaction conditions with respect to their impact on the resulting photocatalytic activity. As such, many of the polymers reported here may be capable of achieving photocatalytic hydrogen evolution activities that are substantially higher than recorded, had a slightly different generic recipe been used for all synthesis reactions.

2.3.2 High Throughput Photocatalysis

Hydrogen evolution experiments were run using a high-throughput setup. Briefly, 5 mg of each polymer was loaded into GC headspace vials, which were subsequently charged with 5 mL of degassed scavenger solutions. Where relevant, H_2PtCl_6 (8 wt.% Aq. solution) was added as a Pt precursor for photodeposition, and the vials were capped under inert conditions. Vials were ultrasonicated before being irradiated for one hour under AM1.5G solar simulated light from a wide surface area (12 x 12 inches) AAA-rated solar simulator. The resulting gas headspace was sampled and tested for H_2 and O_2 via gas chromatography and quantified by GC-peak area calibration curves. For a complete description of these methods, please see the supplementary material of the original publication.

While effective as a high-throughput photocatalysis setup that provides comparative results, some questions remain regarding how accurate this system is when used to test highly active polymers. Questions remain regarding how the HER rate is affected by the corresponding increase in pressure that accompanies the hydrogen evolution inside a closed environment over an hour. It is possible that, at a high partial pressure of H_2 , the HER rate is significantly reduced or the back reaction rate increases.

Likewise, gas is more likely to escape the headspace at high pressures at a rate at equilibrium with that of hydrogen evolution.

Furthermore, H₂ evolution studies of polymers conducted over several hours have frequently demonstrated that H₂ evolution rates can be inconsistent and sluggish over the first hour. This may be due to the preferential reduction of impurities or co-catalyst precursors instead of H⁺ ions. As such, some questions remain regarding whether the observed H₂ evolution rates are accurate or comparable to others in the literature, particularly when loaded with the Pt co-catalyst.

It is also worth noting that the trends of photocatalytic activity discussed primarily concern the experiments involving TEA as the hole scavenger and which use MeOH as a dispersant. Though these conditions give rise to some of the most active photocatalysts in the literature (particularly those containing the DBTS subunit), this approach also risks overlooking polymers that would perform better with alternative sacrificial reagents and dispersants.

Figure 30a plots the measured optical bandgap for each co-polymer against their respective IP and EA potentials. The area of each data point represents the associated HER rate when using TEA as the sacrificial reagent. For TEA to act as an effective hole scavenger, the polymer's IP must be more positive than the TEA to TEA^{•+} reaction potential. This reaction potential is marked as a dotted grey line.

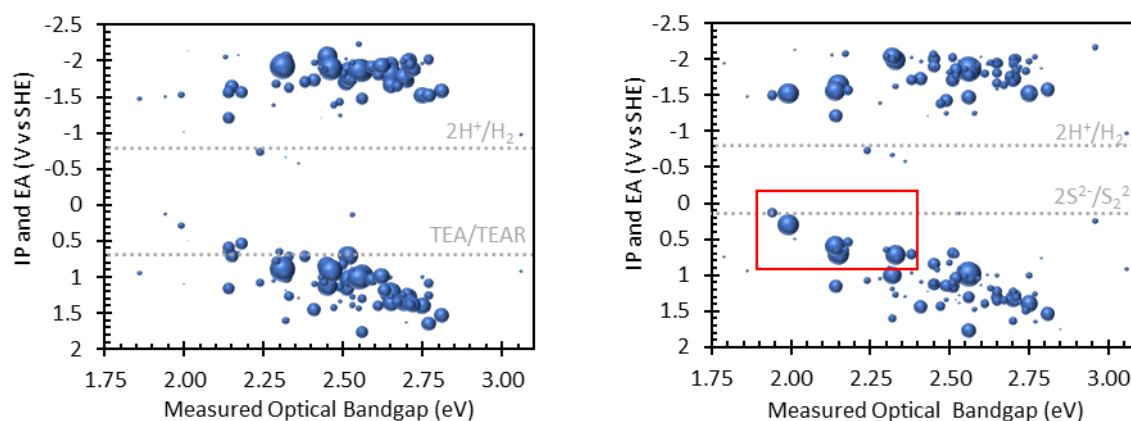


Figure 30: xTB-IPEA predicted IP and EA values for each DBTS copolymer plotted against the measured optical bandgap. The area of each data point represents the HER rate of the polymer without a Pt co-catalyst. a) Sacrificial Reagent conditions using 1:1:1 v/v mixture of H₂O/MeOH/TEA. 5 mg polymer dispersed in 5 ml. 1 hr irradiation. b) Sacrificial Reagent conditions using 0.026 M aqueous solution of Na₂S. 5 mg polymer dispersed in 5 ml. 1 hr irradiation. The red box highlights the copolymer polymers with small oxidation potentials that perform better with an alternative sacrificial reagent. Grey dotted lines indicate the proton reduction potential (-0.8 V vs SHE pH=14) the TEA/TEAR⁺ charge transfer oxidation potential (+0.7 V vs SHE), and the sulfide ion oxidation potential (+0.14 V vs SHE).

All samples in this experiment were also tested for their activity when using Na₂S as the sacrificial reagent. Figure 30b contains the same information as Figure 30a, except the data point areas represent the photocatalytic activity when using this alternative hole scavenger. Interestingly, when tested under these conditions, four of the five most active polymers have IPs below +0.7 V vs SHE. This is only possible because the oxidation potential of the sulfide ion is only +0.14 V vs SHE and demonstrates that using TEA as a scavenger may lead to highly active hydrogen evolution photocatalysts with narrow bandgaps being overlooked or screened out.

Amongst this group of polymers are some of the narrowest bandgap materials synthesised and, as such, are promising candidates to maximise the utilisation of visible light irradiation. The best-performing co-polymer in Na₂S solution contained thiophene (P1-99). Another group has since synthesised this copolymer.¹⁸⁵ In their report, DMF is used as a cosolvent to aid dispersion and ascorbic acid is used as the sacrificial reagent. Rates as high as 147 mmol hr⁻¹ g⁻¹ were reported, representing one of the highest activities for any single-phase linear organic polymer photocatalyst to date. However, concentrations of the photocatalyst were reduced to 0.1 mg ml⁻¹, which is ten times more dilute than the concentrations in the high-throughput study currently being discussed. Such methodology would inevitably lead to artificially enhanced mass-normalised hydrogen evolution rates. The irradiation area was not reported. By contrast, using the high throughput setup, the same polymer achieved rates of 0.6 and 2.1 mmol hr⁻¹ g⁻¹ using Na₂S and MeOH/TEA systems.

All samples were significantly less active in an Na₂S solution compared to the mixture of MeOH/TEA. Such reduced activity is expected since the interaction of the DBTS subunit with the latter is directly responsible for the rapid charge transfer and charge separation processes that lead to high activities. MeOH content improved the surface wettability, and TEA oxidation is predicted to occur on the ps-timescale.¹³⁵

As with the use of TEA, higher performances of photocatalysts using Na₂S also correlate with high-magnitude electron affinities and high synthetic yields. These are presented in Figures 31 and 32. Palladium concentration also appears to impact the HER positively, as shown in Figure 33. The Na₂S system was not investigated with an additional photodeposited Pt co-catalyst. Since each polymer has a different amount of Pd, direct comparison of different structure/activity relationships according to the comonomer is challenging. Transmittivity experiments were only completed in the 1:1:1 solution mixture. As such, their dispersibility in the absence of methanol as a co-solvent has not been measured for the Na₂S system.

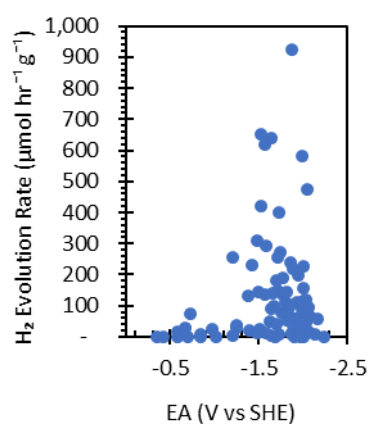


Figure 31: Photocatalytic HER rates for 99 DBTS co-polymers dispersed in an Na₂S solution with respect to predicted electron affinity potential vs SHE

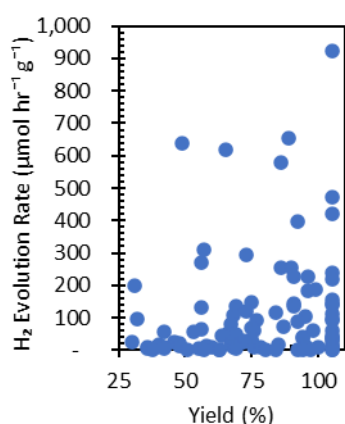


Figure 32: Photocatalytic HER rates for 99 DBTS co-polymers dispersed in an Na₂S solution with respect to the synthesis yield.

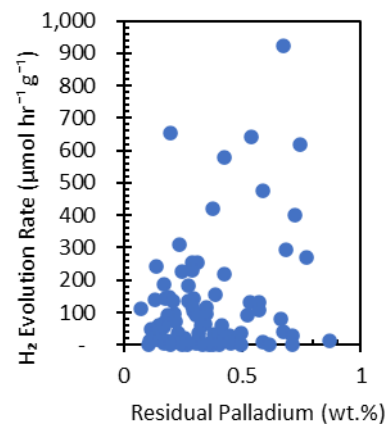


Figure 33: Photocatalytic HER rates for 99 DBTS co-polymers dispersed in an Na₂S solution with respect to residual palladium concentration.

The ideal conditions to produce the maximum amount of hydrogen will vary for each polymer. As such, this paper can only provide a rough guide for which polymers will most likely be successful, and it is not a guarantee. This point is reinforced by the 2020 nature study in which an autonomous robot optimised the sacrificial reagent conditions for the DBTS-DBTS homopolymer over the course of several hundred iterative experiments.¹⁸⁶ This study demonstrated that factors such as the solution's ionic strength and pH, the sacrificial reagent, and the surfactant content could all impact the resulting photocatalytic activity. Furthermore, the HT paper also only loaded with 1 wt.% Pt when loading a co-catalyst. In reality, an optimal co-catalyst loading could vary for each polymer and is likely higher for some and lower for others. The choice of co-catalyst could also have a significant impact.

2.3.3 Predicted vs Optical Bandgap

The authors used an extended tight-binding model to enable a high-throughput approach to screen the optoelectronic properties of over 6,000 polymers via computational means. Values obtained using the xTB code¹⁸⁷ were then adjusted to match those that would have been obtained from more comprehensive DFT models using a previously developed linear calibration function trained on 40 linear polymers.¹⁸⁸ The properties were averaged over 500 different randomly-generated conformations for each polymer. In this section, the accuracy and validity of this method are discussed critically. A brief overview of the fundamentals underpinning the methodology is provided to aid later discussion.

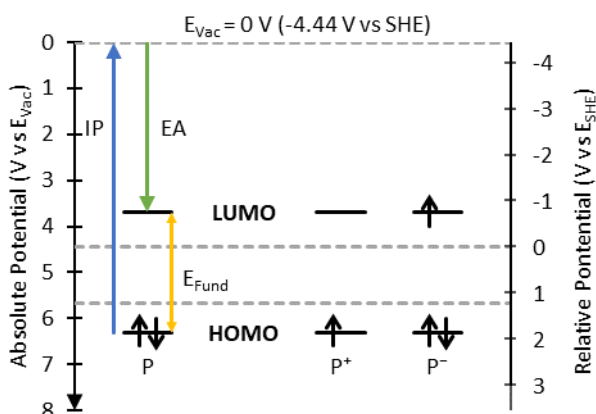


Figure 34: Diagram relating how the ionisation potential (IP) and electron affinity (EA) relate to the HOMO and LUMO orbital energies in the ground state. The two scales highlight how the absolute potential scale relates to the potential scale relative to the Standard Hydrogen Electrode (SHE).

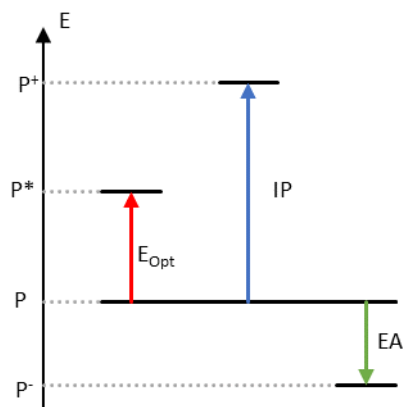


Figure 35: Energy level diagram highlighting relative energies of the neutral ground state polymer, the positively charged polymer, the negatively charged polymer, and the polymer's first photoexcited state. Energy differences between the different states and the neutral ground state polymer are given by the arrows.

2.3.3.1 Fundamentals

To estimate the reduction and oxidation potentials of a polymer's frontier molecular orbitals, ionisation potentials (IP) and electron affinities (EA) are calculated for each polymer. Ionisation energies tell us how deep the highest occupied molecular orbital (HOMO) lies relative to the vacuum level. Likewise, the electron affinity determines the position of the Lowest Unoccupied Molecular Orbital (LUMO) relative to the vacuum level. The difference in magnitude between these energies can be considered an approximation of the HOMO-LUMO bandgap for the polymer in its ground state, as illustrated in Figure 34. This bandgap is known as the fundamental bandgap, E_{Fund} .

The IP and EA are determined by first calculating the energies of the neutral polymer (P), the positively charged polymer (P^+), and the negatively charged polymer (P^-). The calculations are performed by quantum mechanical *ab initio*¹⁸⁹ or semi-empirical¹⁸⁷ methods based on the constituent atoms, their relative positions, and the overlap of their atomic orbitals. The redox potentials for the HOMO and LUMO are then calculated from the IP and EA energies by converting them into electronvolts and dividing by the elemental charge of an electron. The relative energies of these species are presented in Figure 35. The optical bandgap, E_{Opt} , is given by the difference in energy between the ground state of the polymer and its first excited state, P^* , and describes the minimum photon energy required to drive this transition via absorption.

However, it is important to note that the two values that describe the bandgap, E_{Opt} and E_{Fund} , are not equal, as highlighted in Figure 36. This is because the energy of P^* is stabilised relative to the theoretical level predicted from the IP and EA values due to the exciton binding energy, E_{B} . The exciton binding energy arises from the electrostatic interaction between the photogenerated electron and hole pair. As such, the reduction and oxidation potentials of the exciton are slightly smaller than those predicted by the EA and IP values alone, as presented in Figure 37. However, the oxidation and reduction potentials of the charged polarons, P^+ and P^- , are expected to remain unchanged, as the exciton binding energy must be overcome to achieve charge separation. These potentials are also provided in Figure 34. The exciton binding energy is typically predicted to be smaller in polymers with Donor-Acceptor type structures that maximise the electron and hole spatial separation along the polymer backbone. Excitons in materials with high dielectric constants, such as traditional crystalline inorganic semiconductors, experience negligible exciton binding energies because the e^-h^+ interactions are strongly screened.

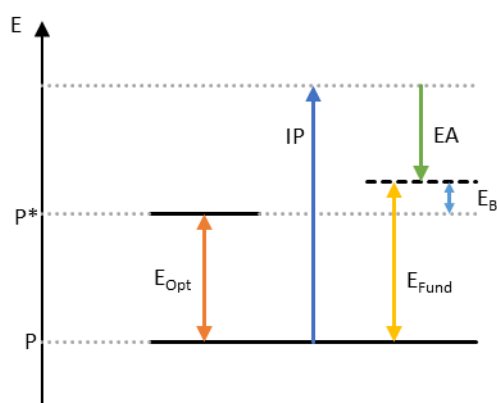


Figure 36: Energy level diagram to highlight that the fundamental gap, E_{Fund} , should always be larger than the optical bandgap, E_{Opt} . These two energies differ by the Exciton Binding Energy, E_{B} .

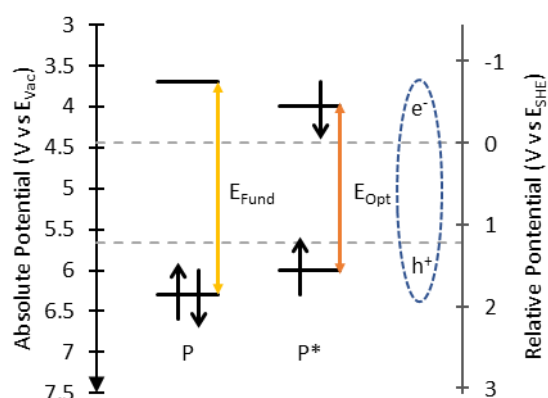


Figure 37: Orbital energy level diagram to highlight the origin of the exciton binding energy. Photoexcitation generates an electron-hole pair that interact via their electrostatic attraction. Less energy is therefore required to form an exciton than two non-interacting oppositely charged ground state polarons.

Generally, excited state calculations are not performed using simple DFT calculations on the ground state molecules. Instead, computationally intensive time-dependent DFT (TD-DFT) is used to determine the response of the underlying wavefunctions to an external potential (such as an electromagnetic field) over time. As such, this allows for calculations regarding the energy of orbitals in the excited state and the interaction of material with light.

In the high throughput work published by Bai *et al.* the optical bandgaps are predicted using an extended tight binding calculation model (sTDA-xTB).^{184,190} These results are adjusted to reproduce the values expected from TD-DFT calculations via a linear calibration function. The DFT-calculated values for E_g were corrected to match values predicted using the CAM-B3LYP hybrid functionals in combination with the 6-31G(d,p) basis set.¹⁸⁸ The CAM-B3LYP functionals were selected since they are range-separated and, unlike traditional B3LYP, do not erroneously predict extended delocalisation. B3LYP calculations typically lead to underestimates of the bandgap and do not accurately predict the relationship between optical properties and oligomer length.¹⁹¹

2.3.3.2 Accuracy of Predicted Optical Bandgap

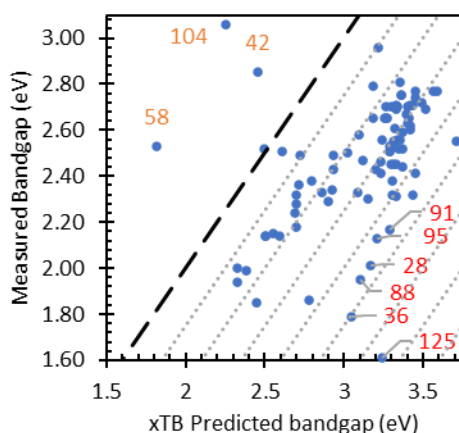


Figure 38: Optical Bandgaps predicted by sTDA-xTB calculations vs the measured optical bandgaps determined by UV/Vis diffuse reflectance spectroscopy (DRS). Points on the dashed black line indicate an accurate prediction in which the xTB values and experimental values match. Each parallel dotted grey line represents an overestimation of the optical bandgap by 0.25 eV. Experimental outliers are labelled with the dibromide monomer number to which they correspond.

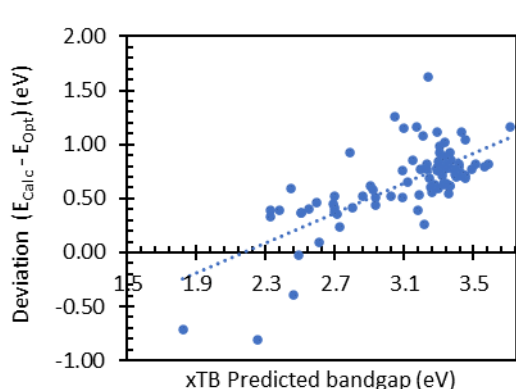


Figure 39: Relationship between the overestimation of the predicted optical bandgap with respect to the predicted value. Polymers predicted to have wider bandgaps are overestimated by more than those predicted to have narrower bandgaps.

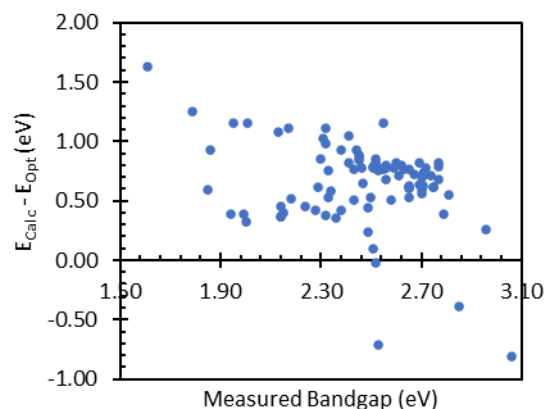


Figure 40: Relationship between the overestimation of the predicted optical bandgap with respect to the experimentally determined value.

Since the xTB bandgaps were corrected to match those predicted by CAM-B3LYP, they are, as expected, over-overestimated.¹⁹¹ Figure 38 contains a scatter plot of the predicted bandgaps and the corresponding experimentally observed optical bandgap, as determined by diffuse reflectance spectroscopy. The black dashed line represents where the points would lie in the case of a perfect prediction, and each dotted line represents an overestimation of an additional 0.25 eV. The average deviation from the measured value is +0.65 eV.

The extreme outliers in Figure 38 can be classified according to two sets: those with measured bandgaps significantly larger than expected (orange data labels) and those with measured bandgaps significantly smaller than expected (red data labels). According to the paper's SI, the wide bandgaps of polymers P1-104 and P1-42 result from noisy absorption spectra with very irregular shapes. The wide bandgap of P1-58 is determined to have arisen from an incomplete polymerisation reaction that led to short-chain oligomers with a wider bandgap. The narrow bandgaps of P1-125 and P1-36 are attributed to poorly-defined absorption spectra that do not produce linear regions in the Tauc plot analysis.

A Tauc plot analysis assumes that the shape of the absorption spectrum close to the bandgap follows that of a traditional amorphous semiconductor.¹⁹² Typically, this involves weak absorption from sub-bandgap states in what is known as the Urbach Tail, followed by a steep rise in absorption above the bandgap. However, the absorption spectra of organic photocatalysts are complicated by the presence of distinct chromophores along the polymer chain, which results in an absorption spectrum with additional features. Furthermore, any contamination of samples with light-absorbing species, such as unreacted reagents or products from side reactions, will also appear in the absorption spectrum. Such features are known to distort the measurement of the bandgap by traditional means.¹⁹³

Further analysis of the UV-Vis DRS data presented in the initial paper's SI reveals that many samples exhibit non-standard absorption spectra. For example, the absorption spectra of samples P1-28, P1-91, and P1-95 are dominated by sub-bandgap absorption in the tail. As such, no steep increase above the bandgap is visible, and an accurate extrapolation of the linear regions in a Tauc plot would be challenging. Additionally, the absorption spectrum of P1-88 contains distinct absorption bands around 500 and 700 nm that are inconsistent with a typical semiconductor's absorption profile. These erroneous bandgap measurements have been easily identified because the miscalculations resulted in outlying data points. However, poor experimental data may have also resulted in erroneous bandgap values for other samples.

Generally, these calculations overestimated the measured value by 0.25 eV - 1 eV. As shown in Figure 39, polymers predicted to have a larger bandgap were likely to be overestimated by a greater magnitude than those predicted to have a smaller bandgap. Resultingly, it is possible to generate an additional linear calibration function to modify the predicted bandgaps to match the experimental values more closely. After omitting the most significant outliers, the final calibration function was

obtained using the Excel Solver add-in to using a least-squares method. This function is presented in equation (8).

$$E_{New} = E_{Calc} - (0.41E_{Calc} - 0.65) \quad (8)$$

The graphs corresponding to Figures 38-40 are reproduced following the calibration correction in Figures 41 - 43. Following this calibration, 71% (64/90) of the measured bandgaps are within ± 0.15 eV of their predicted value. This increases to 79% within an error margin of ± 0.25 eV. Most of the data points outside this window likely belong to poor-quality absorption spectra.

To test this hypothesis, a qualitative screening of these spectra (as presented in Figures S-4 to S-17 in the SI of the original publication) has been performed to identify those without an obvious linear region from which an absorption onset can be extrapolated. These data points have been highlighted in orange in Figure 43.

It should be noted that this analysis is highly subjective and that bandgaps are best determined from Tauc plots rather than a direct interpretation. However, a more comprehensive analysis is impossible without a copy of the original data files or the Tauc plots from which bandgaps were determined. Despite this, a clear trend becomes apparent in which all of the polymers with predicted bandgaps greater than their measured values by 0.27 eV or more belong to this sub-set of polymers.

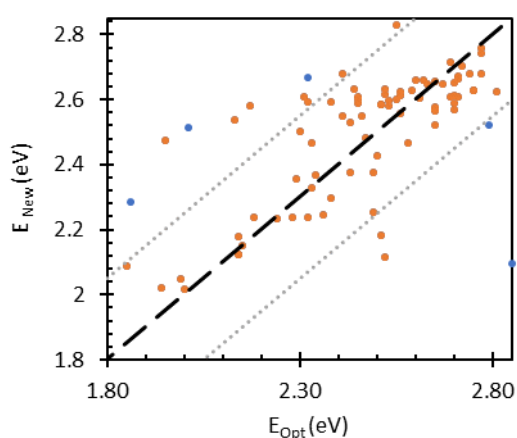


Figure 41: Correlation between the measured optical bandgap, E_{Opt} , and the predicted optical bandgap after applying a linear correction term, E_{New} . Points on the dashed black line indicate an accurate prediction in which the xTB values and experimental values match. Each parallel dotted grey line represents a deviation from the measured optical bandgap by ± 0.25 eV. Blue dots highlight experimental outliers shown to be unreliable in the original publication.¹⁸²

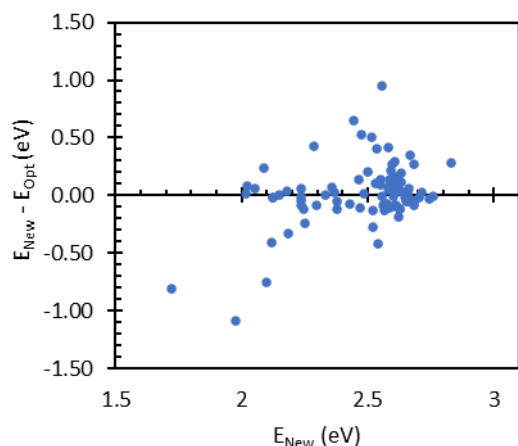


Figure 42: Difference between the predicted optical bandgap after applying a linear correction term, E_{New} , and the experimentally-determined optical bandgaps, E_{Opt} , relative to E_{New} .

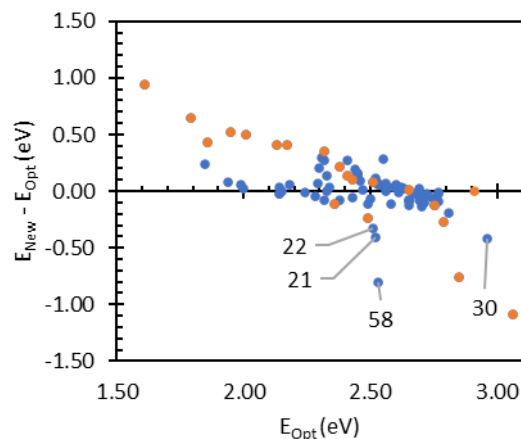
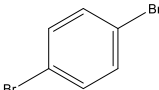
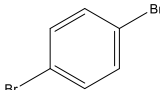
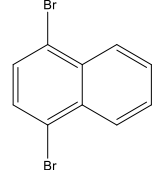
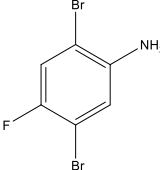
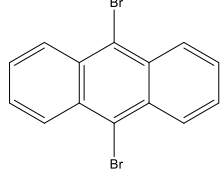
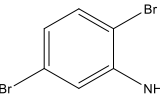
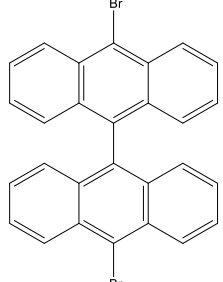
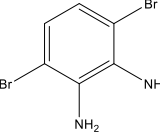


Figure 43: Difference between the newly predicted optical bandgap after applying a linear correction term, E_{New} , and the experimentally determined optical bandgap, E_{Opt} . Orange data points highlight samples with poor quality or atypical DRS spectra. Data labels highlight the remaining outliers discussed in the text.

Four polymers exhibited substantially wider bandgaps than predicted despite seemingly high-quality spectra. These samples are labelled with their monomer number in Figure 43, and their co-monomer structures are presented in Table 2 alongside some of the most closely related co-polymers. As discussed above, P1-58 was shown to have been synthesised as a short oligomer. It is, therefore, possible that the remaining three polymers have also been unsuccessfully synthesised.

This is particularly likely for P1-30 since the optical bandgap becomes substantially larger after adding a second amine substituent to the para-linked phenyl ring, despite the measured and calculated data for P1-3, P1-114, and P1-29 suggesting that bandgaps should be narrower after adding amine groups. These copolymers are represented in Table 2. The same explanation is possible for P1-21 and P1-22, in which the anthracene-copolymers exhibit wider bandgaps than the Phenylene (P1-3) and naphthalene (P1-13) co-polymers, despite the prediction that larger polycyclic units would lead to narrower bandgaps. This prediction, supported by E_{New} and E_{Fund} calculations, is reasonable. Increased delocalisation typically leads to the absorption of longer wavelengths of light. However, whilst short-chain oligomers can explain the wider-than-expected bandgaps, it is also possible that delocalisation in the polymer backbones of these polymers is reduced due to a lack of co-planarity resulting from steric effects.

N°	Structure	$E_{Opt}^{[a]}$	$E_{New}^{[b]}$	$E_{Fund}^{[c]}$	N°	Structure	$E_{Opt}^{[a]}$	$E_{New}^{[b]}$	$E_{Fund}^{[c]}$
3		2.45	2.59	3.02	3		2.45	2.59	3.02
13		2.43	2.53	2.91	114		2.33	2.47	2.70
21		2.52	2.12	2.47	29		2.3	2.50	2.69
22		2.51	2.18	2.40	30		2.96	2.54	2.41

[a] Optical bandgap measured from UV-VIS DRS measurements.

[b] Optical Bandgap calculated by sTDA-xTB and corrected following the calibration equation outlined in the main text.

[c] Fundamental bandgap obtained from IP and EA potentials calculated by the IPEA-xTB code.

Table 2: Table of outliers for P1-21, P1-22, and P1-30, whose measured optical bandgaps are notably wider than those predicted by E_{New} , despite regular DRS spectra. Data pertaining to P1-3, P1-13, P1-29, and P1-114 are provided as references to structurally-similar co-polymers.

While the calibration function to convert E_{Calc} to E_{New} appears to work well for this family of DBTS-based co-polymers, verifying that the relationship also holds for structurally dissimilar co-polymers is essential. Therefore, the veracity of equation (8) was tested by application to the remaining polymers synthesised from alternative boronic acid pinacol esters (see Figures 15 and 18). The resulting correlations between predicted and measured optical bandgaps before and after calibration are presented in Figures 44 and 45, respectively.

This data set contains 43 polymers that were successfully synthesised, six of which were synthesised from the DBTS diboronic ester and were part of the initial training set. Eight of the remaining polymers (PX-93) also contain the DBTS monomer unit from the dibromide source, and hence equivalent polymers were also contained in the initial training set. However, differences in optical gaps for these polymers depending on the synthesis route are possible. The remaining 29 are new polymers that did not form part of the calibration data. The measured bandgaps of all 43 polymers lie within ± 0.25 eV of the predicted value after calibration. Neglecting the P1 repeat set of polymers, the predictions deviated by an average magnitude of 0.12 eV, corresponding to an average deviation of -0.05 eV when

also accounting for the sign. This presents a remarkable level of accuracy that can be obtained for a highly diverse dataset considering the level of theory of the underlying calculations and the speed at which different structures can be screened.

It is worth noting, however, that the sTDA-xTB approach is still limited and should only be used to predict general trends in the bandgap. Clustering of different monomer units on either side of the dotted trendline can be observed in Figure 45. This trendline represents an ideal case in which the calculated bandgaps equal those measured experimentally. The calculation consistently under-evaluated the bandgaps of polymers synthesised from the P2, P3, P5, and P8 boronic esters, whereas polymers made from P4 were over-evaluated. However, this appears to be a fault of the initial computation rather than an issue with the calibration. It should be noted that the co-monomers were all selected from an initial set of P1-based polymers with very similar band gaps. Despite being trained on a data set containing 90 P1-based polymers, all six containing the DBTS unit here are clustered and over-evaluated. The fact that the other polymers are clustered according to their boronic ester unit is unsurprising.

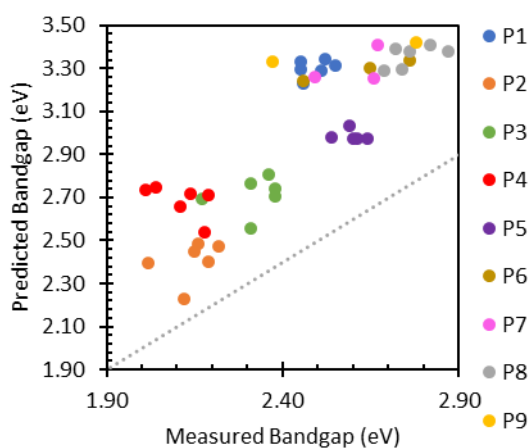
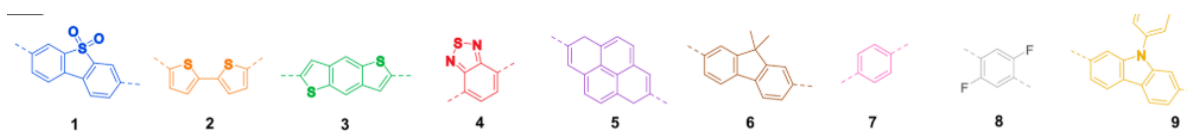


Figure 44: Predicted (E_{Calc}) vs measured optical bandgaps (E_{Opt}) for the co-polymers synthesised from a range of diboronic acid precursors. The dotted grey line represents an accurate prediction in which the xTB values and experimental values match. Data points are colour-coordinated to match the relevant diboronic acid precursor, as shown in the top image.

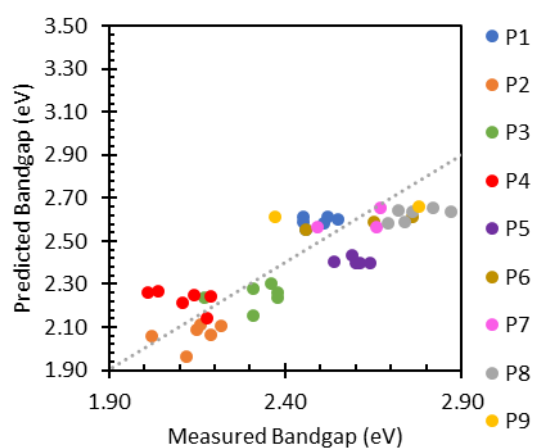


Figure 45: Predicted (E_{New}) vs measured (E_{Opt}) optical bandgaps for the linear co-polymers synthesised from alternative diboronic acid precursors after applying the linear correction term to the predicted values. The dotted grey line represents an accurate prediction in which the xTB values and experimental values match. Data points are colour-coordinated to match the relevant diboronic acid precursor, as shown in the top image.

As mentioned above, each cluster contains a PX-93 co-polymer synthesised with the DBTS-Br₂ monomer reagent. These polymers are structurally equivalent to some P1-X polymers synthesised from the DBTS-(Bpin)₂ monomer reagent. These results present an opportunity to investigate if the synthesis conditions can influence the resulting optical bandgap and photocatalytic activity.

Figure 47 demonstrates that, regardless of the synthesis route, all of the equivalent co-polymers containing the DBTS monomer maintain the same bandgap. However, the selection of dibromide and boronic ester precursors can significantly impact the resulting photocatalytic activities, as shown in Figure 48. Whilst P8-93 exhibited significantly higher rates of H₂ production compared to the identical polymer P1-62, other polymers (P3-93, P6-93, and P9-93) performed significantly worse.

These results suggest significant differences in the physical properties of the polymers prepared via opposite synthetic routes. In general, the synthetic yields were higher when using the (DBTS-Bpin)₂ precursor. The only exception is the pyrene-based polymer, P5-93, which was successfully synthesised with a 91% yield. In contrast, the synthesis of the equivalent polymer using the DBTS boronic ester, P1-25, failed.

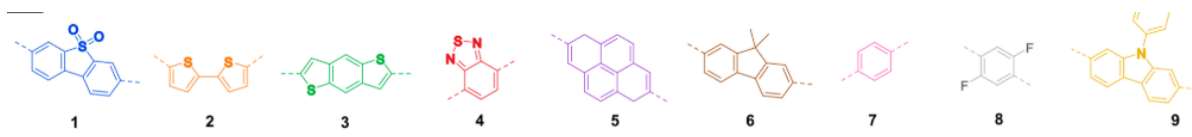


Figure 46: DBTS and eight alternative diboronic acid precursors used for copolymer syntheses.

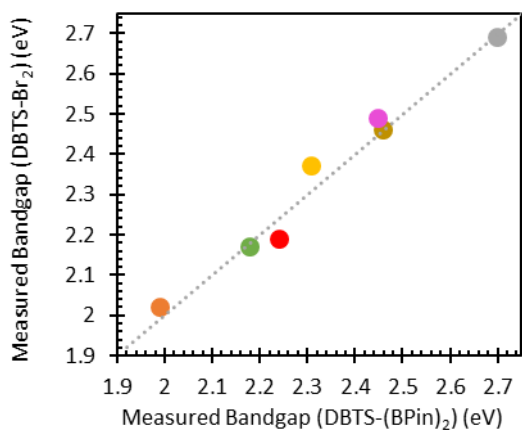


Figure 47: Measured optical bandgaps for the DBTS-containing co-polymers, when synthesised via the DBTS diboronic acid vs when synthesised from the DBTS dibromide. Data points are colour-coordinated to match the relevant diboronic acid precursor, as shown above.

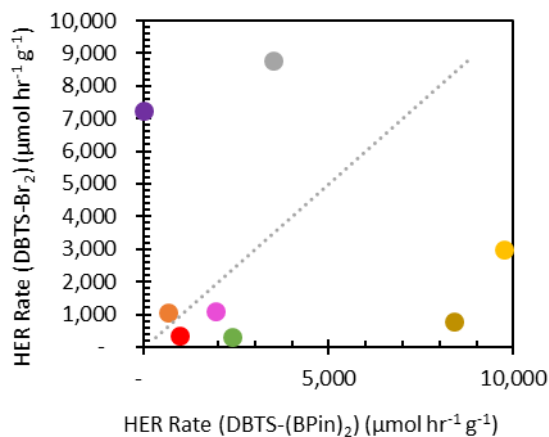


Figure 48: Hydrogen evolution reaction rates for the DBTS-containing co-polymers when synthesised via the DBTS diboronic acid vs when synthesised from the DBTS dibromide. Data points are colour-coordinated to match the relevant diboronic acid precursor, as shown above.

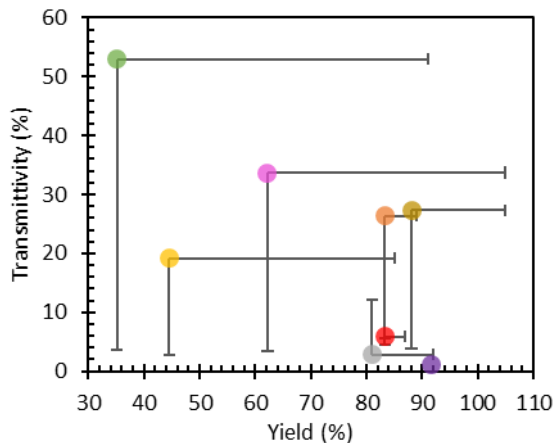


Figure 49: Polymer transmissivity and synthetic yield values of DBTS-based co-polymers when synthesised from the DBTS dibromide. Error bars indicate the relative values for the equivalent co-polymers when synthesised from the DBTS diboronic ester. Data points are colour-coordinated to match the relevant diboronic acid precursor, as shown in the top image.

Figure 49 contains a scatter plot of yield vs transmissivity data for the PX-93 polymers using the boronic esters P2 to P9. The horizontal error bars denote the change in yields compared with equivalent P1-X co-polymers. Likewise, the vertical error bars show the equivalent change in transmissivity. These data strongly reinforce the observations made earlier in this chapter that low yields and poor dispersibility (high transmissivity) correlate with reduced photocatalytic activities.

These results also highlight that dispersibility is not an inherent property of the polymer structure but also depends on the synthetic route. The exact reason is unclear, but it possibly originates from increased concentrations of hydrophobic byproducts associated with decreased yields. The polymer chain length, particle size, morphology, and crystallinity can also impact dispersibility.

2.3.3.3 Reliability of IP, EA and Fundamental Gap

Unlike E_{Calc} , which could be modified using experimentally derived values to produce E_{New} , the calculated redox potentials of the charged polarons, P^+ and P^- , corresponding to IP and EA, respectively, have no corresponding experimental data.

However, the fundamental bandgap E_{Fund} , defined as the difference in energy between the ionisation potential and the electron affinity, should be the same as, or greater than, the optical bandgap. The difference between E_{Fund} and E_{Opt} , corresponding to the exciton binding energy, should also typically be approximately a few tenths of an electronvolt for organic semiconducting materials.

A plot of the measured optical bandgap against the predicted fundamental gap is presented in Figure 50. The black dashed line represents where the points would lie if these two values were identical, and the dotted grey lines represent ± 0.25 eV compared to this value. The orange data points represent some polymer samples with poor-quality absorption spectra that may have led to erroneous optical bandgap readings and, in the case of P1-58 and P1-30, samples that appear to have been synthesised as oligomers with wider bandgaps.

Concerning the first measure of reliability, the fundamental gap is not consistently wider than the optical gap for all samples. The fundamental gaps of the narrowest bandgap polymers appear smaller than their experimentally-derived optical gaps. This result cannot be theoretically explained by the exciton binding energy alone and indicates EA and IP values that require additional calibration terms similar to that applied to the calculated optical gaps.

The plot of differences between E_{Fund} and E_{Opt} versus the fundamental gap in Figure 51 reinforces this hypothesis. The linear correlation with a large R^2 value confirms that the narrowest fundamental bandgaps are underestimated, whilst the widest fundamental gaps are overestimated. As such, this difference, which would typically represent a measure of the exciton binding energy for accurate values of IP and EA, is unreliable.

Compared with the measured and calculated optical gaps, the overestimation at one end of the spectrum and underestimation at the other result in a very broad distribution of fundamental gaps, as shown by the cumulative frequency curves in Figure 52. However, it is worth noting that the fundamental gaps are closer to the true optical gaps than the initial results from the sTDA-xTB calculations of the latter (E_{Calc}).

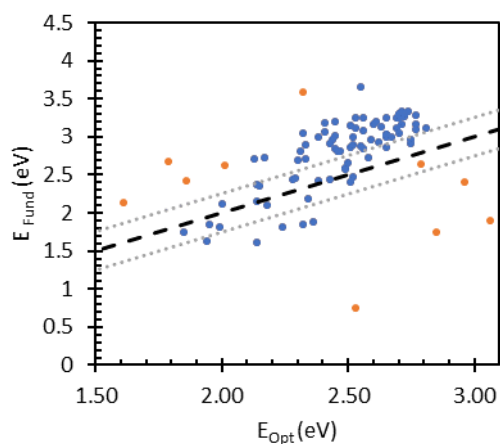


Figure 50: Predicted fundamental bandgaps calculated from IP and EA energies from xTB-IPEA calculations vs the measured optical bandgaps determined by UV/Vis diffuse reflectance spectroscopy (DRS). Points on the dashed black line indicate samples for which the predicted fundamental gap matches the experimentally-determined optical bandgap. The parallel dotted grey lines represent a deviation of the two values by ± 0.25 eV. Experimental outliers ignored when determining the calibration equation are highlighted in orange.

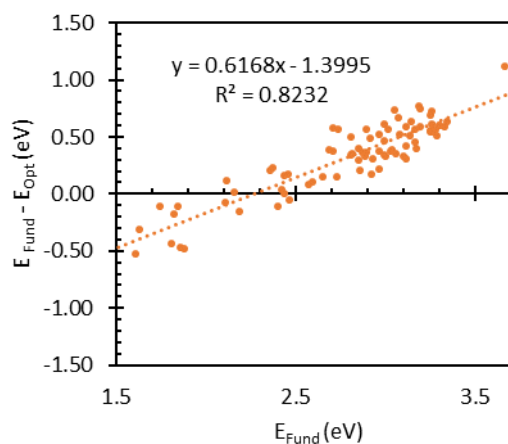


Figure 51: Differences between the calculated fundamental gap and the measured optical bandgap relative to the calculated fundamental gap. Outliers highlighted in Figure 50 have been omitted from this analysis.

As discussed above, accurate calibration equations to modify the predicted values cannot be determined without experimental values for the IP and EA. While values for these properties can be determined by photoelectron spectroscopy methods or approximated by electrochemical measurements, both are time-consuming and cannot easily be scaled up for high-throughput experiments.

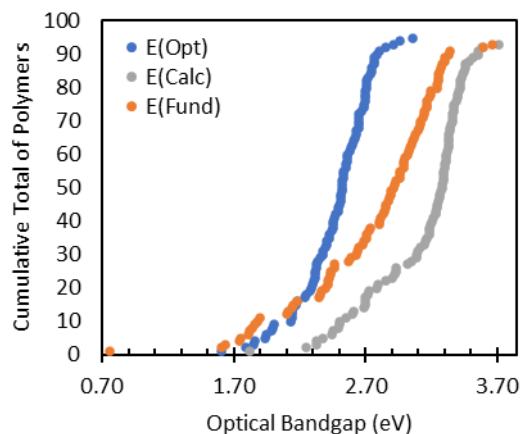


Figure 52: Cumulative distributions of the measured optical bandgap, E_{Opt} , sTDA-xTB predicted optical bandgaps, E_{Calc} , and the xTB-IPEA determined fundamental gaps for the synthesised and tested polymers, E_{Fund} .

By performing TD-DFT calculations, it is possible to calculate the IP and EA for the polymer in its excited state. These values are typically referred to as IP^* and EA^* , and the energy difference between them is assumed to be equivalent to the optical bandgap, as shown schematically in Figure 53. Many reports in the literature show these calculations being performed on polymeric photocatalysts.¹⁹⁴ Typically, for DBTS-containing linear polymers, the predicted exciton binding energy is on the order of 0.1 – 0.5 eV.^{58,60,195}

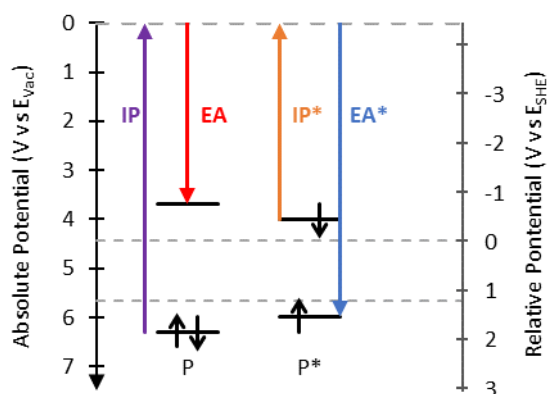


Figure 53: Energy level diagram to highlight the difference between the ionisation potentials and electron affinities of the polymer in its ground state vs those in the excited state. Ground state calculations enable the determination of the fundamental gap, whereas excited state calculations can be used to calculate the optical bandgap.

Since the polymers investigated in this study are structurally similar, they likely exhibit similar exciton binding energies to one another. It may, therefore, be possible to accurately predict the optical bandgaps of these polymers from the xTB-calculated IP and EA energies without requiring the additional TDA-xTB calculation. This was investigated by developing individual linear correction

functions for the IP and EA values such that the difference between the E_{Fund} and E_{Opt} is minimised by a least squares method. As such, the exciton binding energy is neglected, and it is assumed that $\text{IP}=\text{EA}^*$ and $\text{EA}=\text{IP}^*$.

As shown in Figure 51, the broad distribution of IP and EA values results in underestimating the fundamental gap of small bandgap polymers and overestimating that of wide bandgap polymers. Figures 54 and 55 demonstrate that this error predominantly originates from an erroneous evaluation of the EA.

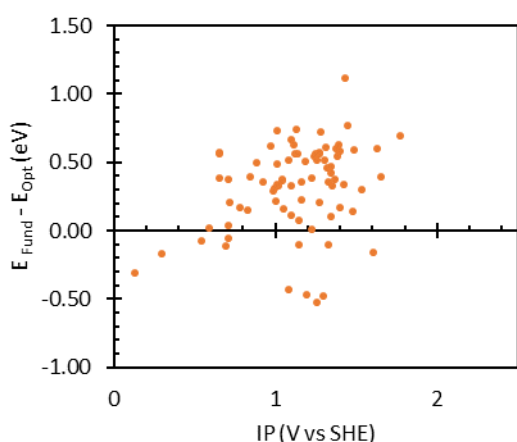


Figure 54: Differences between the calculated fundamental gap and the measured optical bandgap relative to the calculated ionisation potentials. Outliers highlighted in Figure 50 have been omitted from this analysis.

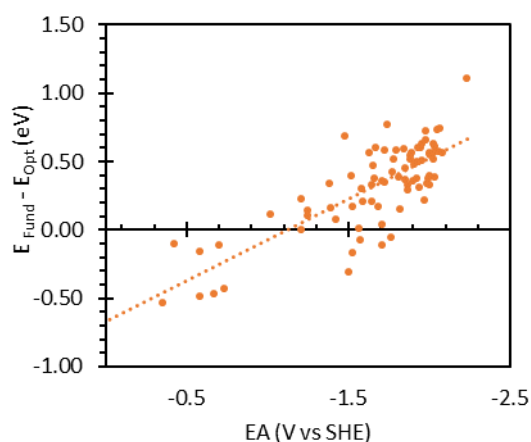


Figure 55: Differences between the calculated fundamental gap and the measured optical bandgap relative to the calculated electron affinities. Outliers highlighted in Figure 50 have been omitted from this analysis.

After applying a correction function to the calculated EA values, the difference between the gap from IP/EA values and the experimentally determined optical gap is significantly decreased from ± 0.75 eV to ± 0.50 eV. Plots of the new errors relative to the optical measured gap vs IP and EA are presented in Figures 56 and 57. The correction of the EA term reveals that a similar linear trend exists amongst the calculated IP values. Deep levels result in over-estimated gaps, and shallow levels result in underestimated ones.

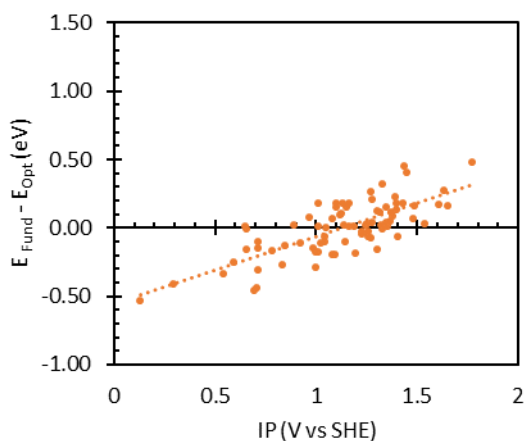


Figure 56: Differences between the modified fundamental gap and the measured optical bandgap relative to the calculated ionisation potentials. The modified fundamental gap is calculated after applying a linear correction term to the electron affinity values. Outliers highlighted in Figure 50 have been omitted from this analysis.

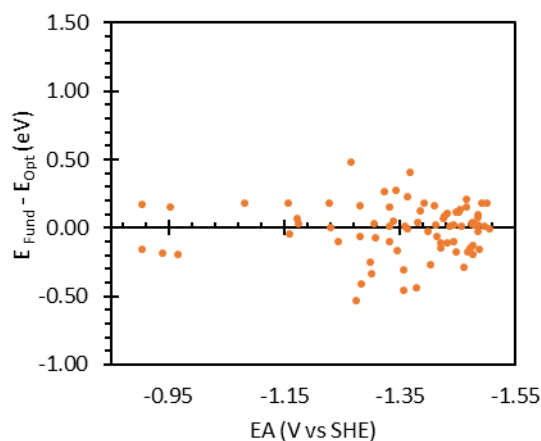


Figure 57: Differences between the modified fundamental gap and the measured optical bandgap relative to the calculated electron affinities. The modified fundamental gap is calculated after applying a linear correction term to the electron affinity values. Outliers highlighted in Figure 50 have been omitted from this analysis.

Applying a linear correction function to both the IP and EA values (optimised using a least-squares fitting method) results in an optical bandgap estimation, here referred to as E_{IPEA} , in which the optical bandgaps of all polymers can be accurately predicted to within ± 0.25 eV, as demonstrated by Figure 58. It should be noted that E_{IPEA} can no longer be considered the fundamental bandgap and that the modified IP and EA potentials are more representative of EA^* and IP^* than those of the ground-state polymer. The linear dependence of the differences on the IP/EA gap has also been resolved (Figure 59).

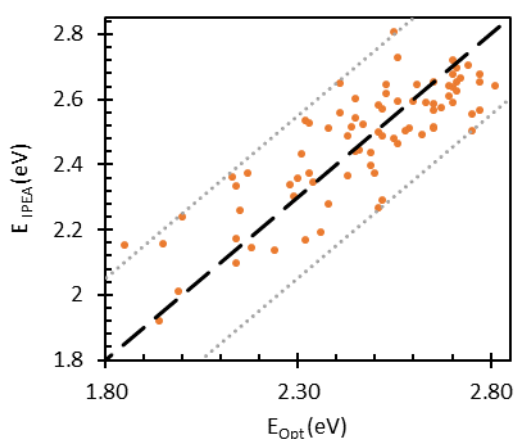


Figure 58: Predicted optical bandgaps (E_{IPEA}) determined from estimated IP^* and EA^* vs the measured optical bandgaps. Excited state potentials were approximated by applying linear calibration functions to the calculated ground state IP and EA values. Points on the dashed black line indicate samples for which the predicted fundamental gap matches the experimentally-determined optical bandgap. The parallel dotted grey lines represent a deviation of the two values by ± 0.25 eV.

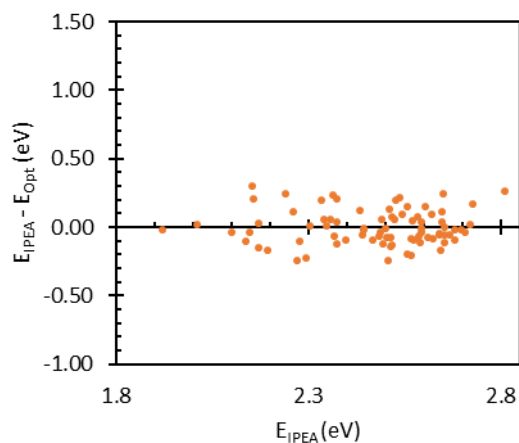


Figure 59: Differences between the predicted optical bandgaps (E_{IPEA}) and the measured optical bandgaps relative to E_{IPEA} . Excited state potentials were approximated by applying linear calibration functions to the calculated ground state IP and EA values.

Compared with the bandgap prediction obtained by calibrating the sTDA-xTB results, calibration of the IP and EA values also produces highly accurate predictions of the optical bandgaps, despite not accounting for the exciton binding energy. In fact, several of the outliers unaccounted for by the former (Figure 41) now lie inside the ± 0.25 eV limit, implying that this secondary method is more accurate.

These calibration terms also dramatically improve the predicted optical bandgaps of the validation set of polymers based on the alternative P2 to P9 diboronic acid monomers (Figure 60). However, after removing the polymers that contain the DBTS monomer unit, the remaining optical bandgaps are underestimated by approximately 0.125 eV (Figure 61). This is a result of the fact that all 90 polymers in the initial training set are based on the DBTS-based co-polymers.

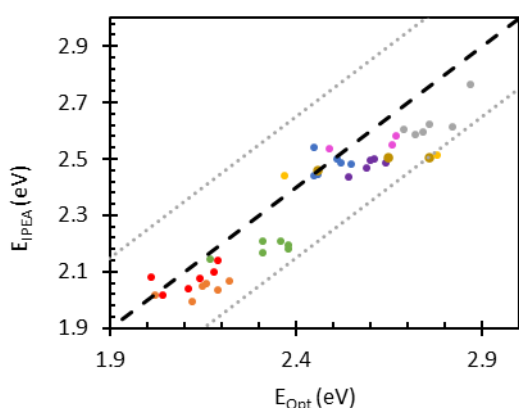


Figure 60: Predicted (E_{IPEA}) vs measured (E_{Opt}) optical bandgaps for the linear co-polymers synthesised from alternative diboronic acid precursors after applying the linear correction terms to the calculated IP and EA values. The dashed black line represents an accurate prediction in which the predicted values and experimental values match. Data points are colour-coordinated to match the relevant diboronic acid precursor, as shown in the text.

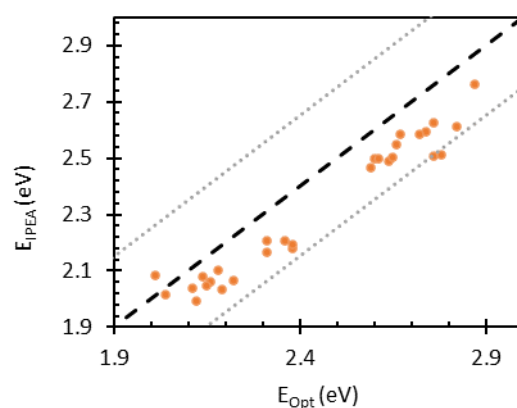


Figure 61: Predicted (E_{IPEA}) vs measured (E_{Opt}) optical bandgaps for the linear co-polymers synthesised from alternative diboronic acid precursors after applying the linear correction terms to the calculated IP and EA values. Relative to Figure 60, all copolymers containing the DBTS moiety have been omitted.

When compared with other co-polymers, those containing the DBTS unit (blue data points Figure 62) are consistently predicted to have shallower EA potentials than the equivalent co-polymers based on P2-P9 (orange data points Figure 62). This results in a slight shift in the EA correction equation for all DBTS polymers compared to non-DBTS polymers, as seen in Figure 63.

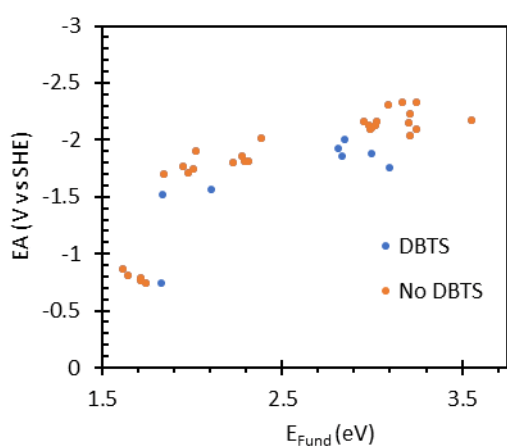


Figure 62: xTB-IPEA predicted EA values for linear co-polymers synthesised from alternative diboronic acid precursors vs the fundamental gap. Data points relating to co-polymers containing the DBTS moiety have been coloured in blue.

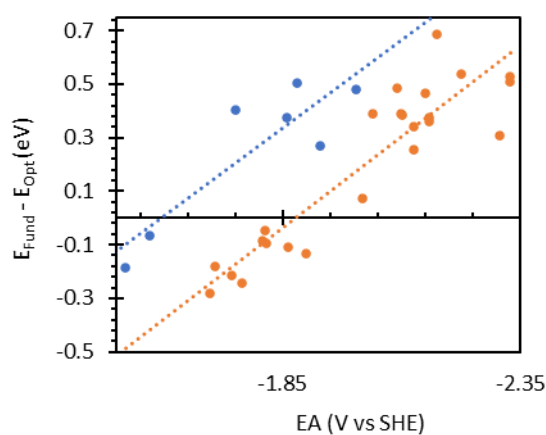


Figure 63: Difference between the fundamental bandgap and the measured optical bandgap relative to the xTB-IPEA predicted EA values. Data points relating to co-polymers containing the DBTS moiety have been coloured in blue. Parallel trendlines imply that the EA correction equation for non-DBTS differs from that of DBTS-containing co-polymers by a constant.

The difference between the predicted values for DBTS-based co-polymers and those that do not contain the DBTS unit can be explained by considering the local environment surrounding the chromophore. The IPEA-xTB screening approach calculates the IP and EA energies for oligomers containing an equivalent of 12 phenylene rings.¹⁸⁸ However, the local environment around the oligomer unit will influence the energies of the P, P⁺, and P⁻ units considered in the calculations. A high dielectric environment such as water, which is strongly polar and has a high dielectric constant of $\epsilon=80.1$, stabilises charges and excitons and minimises exciton binding energy. Meanwhile, a non-polar environment, such as benzene with a dielectric constant of $\epsilon=2$, produces the opposite effect.

Since IP and EA potentials must be considered at the polymer-water interface, these values were calculated (and calibrated to match DFT calculations) according to a high-dielectric environment. However, this approach is simplified compared to the actual situation in which polymer chains are in contact with water at the surface but are only in contact with other polymer chains in the bulk. This is particularly problematic if IP and EA values are used to predict the optical bandgap since most absorption events occur in the polymer bulk.

Since the DBTS unit contains strongly polar sulfone groups, polymers containing this unit are likely to experience a higher dielectric environment than those without it, particularly compared to those with non-polar monomer units. This would explain why, amongst the P1-P9 data, the PX-93 polymers consistently exhibited smaller bandgaps than the others and why these polymers require more significant correction terms than the others relative to the other polymers with equivalent EA potentials. However, the constant shift in the optical gap of these polymers appears to be small and predictable. This implies that future High-Throughput Virtual Screening approaches may be able to introduce an additional correction term based on the polymer polarity or its predicted dielectric constant in the bulk.

In Prof. Zwijnenburg's seminal paper, which first outlined this high-throughput screening approach,¹⁸⁸ IPEA-xTB calculations were more closely correlated to the B3LYP calculations in high-dielectric environments than those in low-dielectric environments, despite using the generalised Born surface area solvation model for water and benzene in these calculations for the xTB calculations. DFT calculations predicted wider fundamental gaps for high dielectric environments and narrower fundamental gaps for low dielectric environments, with the fundamental gap shifting by approximately 1 eV between the two scenarios. Meanwhile, the change in fundamental gaps across different environments when using the IPEA-xTB code was significantly smaller on the order of 0.2 eV.

Without a correction term that can be applied according to the polymer's polarity, it is important to derive a global-fit calibration equation that is not biased by only considering the DBTS co-polymers that can be used in future bandgap predictions where the dielectric constant in the bulk material is not known. Repeating the calibration process for the P1-P9 set of co-polymers containing both DBTS and non-DBTS co-polymers results in an exceptional fit for this data set, as shown in Figure 64. Amongst this set of samples, the optical bandgap is predicted with a mean absolute deviation of just ± 0.06 eV. As expected, the non-DBTS polymers deviate by an average of -0.03 eV, and the DBTS polymers deviate in the opposite direction by an average of $+0.06$ eV. The quality of this fit demonstrates a clear improvement in predictive power compared to the calibration of the E_{Calc} results, despite not accounting for the exciton binding energies (beyond any potential linear dependence on the predicted IP and EA values) or the local dielectric environment in the polymer bulk.

Applying these global-fit calibration equations to the calculated IP and EA potentials of the complete set of P1-X polymers results in a quality of fit represented in Figure 65. As expected, there is a minor bias towards over-estimating these polymers' optical gaps as they all contain the DBTS unit. The mean absolute deviation is 0.11 eV, and only five of the predicted bandgaps deviate by more than $+0.25$ eV. This approach also results in a more accurate prediction of the optical gaps for the widest-gap materials, which were all underestimated when correction factors were only based on the DBTS co-polymer dataset.

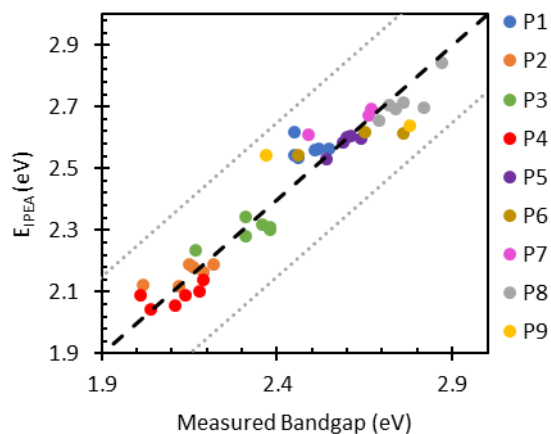


Figure 64: Predicted (E_{IPEA}) vs measured (E_{Opt}) optical bandgaps for the linear co-polymers synthesised from alternative diboronic acid precursors after applying the modified linear correction terms to the calculated IP and EA values. The modified calibration equations are derived from a broader set of co-polymer structures, including both DBTS and non-DBTS co-polymers. The dashed black line represents an accurate prediction in which the predicted values and experimental values match. Data points are colour-coordinated to match the relevant diboronic acid precursor, as shown in the text. The dotted grey lines represent error margins of ± 0.25 eV.

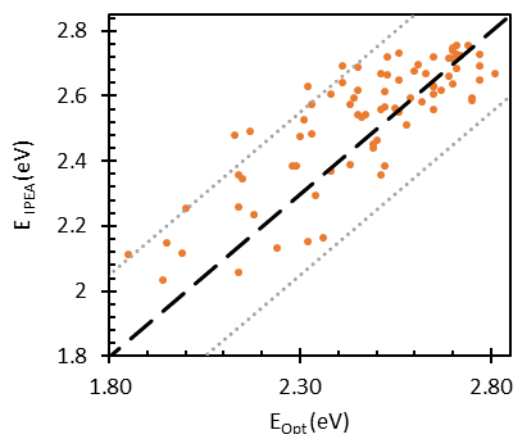


Figure 65: Predicted (E_{IPEA}) vs measured (E_{Opt}) optical bandgaps for the DBTS-based linear co-polymers synthesised from DBTS-B(pin)₂. E_{IPEA} values were determined after applying modified linear correction terms to the calculated IP and EA values. The modified calibration equations are derived from a broader set of co-polymer structures, including both DBTS and non-DBTS co-polymers. The dashed black line represents an accurate prediction in which the predicted values and experimental values match. The dotted grey lines represent error margins of ± 0.25 eV.

A summary of the different correction functions discussed in this section is presented in Table 3 below. It should be noted that there are an infinite number of combinations for the '+c' constants in the IP and EA calibration equations. These equations optimise the difference between the two values and do not consider the absolute position of the potentials relative to the SHE.

Since the calibration function is linear with a gradient of less than 1, the positions of the IP and EA potentials for each polymer relative to one another remain unchanged compared to those predicted by the xTB calculations. In reality, due to the different exciton binding energies of different polymers, this hierarchy would be expected to change slightly if EA* and IP* had been calculated directly using TD-DFT models.

Table 3: Summary of constants used for the various calibration equations discussed in this chapter. a) Constants derived by only considering DBTS-co-polymers. b) constants derived from a broader but smaller set of co-polymer structures, including both DBTS and non-DBTS co-polymers.

$$E_{Opt} \approx E_{New} = E_{Calc} - (mE_{Calc} + c) \quad \begin{array}{l} m \\ m = 0.41 \end{array} \quad \begin{array}{l} C \\ c = -0.65 \end{array} \quad (9)$$

$$E_{Opt} = EA^* - IP^*$$

$$EA^* \approx IP_{New} = IP - (m_1(IP) + c_1) \quad \begin{array}{l} m_1 = 0.51^a \\ m_1 = 0.57^b \end{array} \quad \begin{array}{l} c_1 = -0.47^a \\ c_1 = -0.69^b \end{array} \quad (10)$$

$$IP^* \approx EA_{New} = EA + (m_2(EA) + c_2) \quad \begin{array}{l} m_2 = -0.67^a \\ m_2 = -0.60^b \end{array} \quad \begin{array}{l} c_2 = -0.89^a \\ c_2 = -0.69^b \end{array} \quad (11)$$

2.4 General Trends

So far, by analysing the supplementary data from this paper, it has been highlighted that a reduced reaction yield can be associated with poor photocatalytic performance, that swapping the dibromide and diboronic ester functional groups for a given pair of monomers can impact both the yield, dispersibility and photocatalytic activities despite unchanged optoelectronic properties, and that the presence of residual palladium at high concentrations may significantly inhibit potential gains in photocatalytic activity associated with the photodeposition of a platinum co-catalyst. None of these associations were addressed in the initial study and, to the best of this author's knowledge, have not been explicitly identified in the literature before. This section discusses the trends amongst the additional data gathered in this publication, focusing on the fluorescence lifetime data and the predicted oscillator strengths.

2.4.1 Fluorescence Lifetime

One key optoelectronic property that was tested for all P1-X polymers as part of this experiment was the fluorescence lifetime. In theory, a slower fluorescence decay implies a longer lifetime of the photogenerated excitons. Longer lifetimes should lead to higher apparent quantum yields as the exciton has a higher probability of diffusing to a reaction site rather than recombine (radiatively) within the bulk of the polymer particles. Hence, the extended lifetime allows the rate of radiative decay to compete with the rate of redox reactions, and hence improves the AQY.

2.4.1.1 Background

For a perfect fluorescent material, every absorbed photon would result in a corresponding emitted photon. The ratio of emitted photons to those absorbed is considered the photoluminescence quantum yield (PLQY). In such systems where the PLQY = 1, assuming only one emissive state, it should be possible to fit a single exponential function to the time-resolved fluorescence decay. However, real systems are considerably more complicated since the excited state can also relax back to the ground state via several different pathways.

An electron in an excited state can also decay via non-radiative pathways in which the energy is released to the environment as phonons (vibrations) instead of photons. The singlet exciton state can also transfer into a triplet excited state manifold via intersystem crossing (ISC). Importantly, in the context of conjugated polymers, energy can also be transferred from one chromophore to another, either by Forster resonance energy transfer (FRET), or by the Dexter (superexchange) energy transfer mechanism. Likewise, energy transfer via coupling to the environment may also occur. This could include energy transfer to solvents, impurities, and co-catalysts. The energy in the excited state could also be consumed in photoredox reactions that result in charge separation/extraction and the formation of ground-state polarons.

Since there is no single exponential decay pathway, a three-component multi-exponential fit is used to approximate the overall decay, as represented by equation (12). However, instead of reporting three fluorescence lifetimes for the three components, (τ_i), a single weighted average lifetime value is presented instead, $\langle \tau \rangle$. The lifetime reported is the intensity average, as calculated by equations (13) and (14). Typical values for fluorescence lifetimes of linear polymeric semiconductors are on the order of 0.1 – 10 ns.

$$I(t) = A + B_1 e^{-\frac{t}{\tau_1}} + B_2 e^{-\frac{t}{\tau_2}} + B_3 e^{-\frac{t}{\tau_3}} \quad (12)$$

$$f_i = \frac{B_i \tau_i}{\sum B_i \tau_i} \quad (13)$$

$$\langle \tau \rangle_{int} = \sum f_i \tau_i \quad (14)$$

2.4.1.2 Photocatalytic Activity vs Lifetime

In their attempts to correlate measured properties with the observed photocatalytic activities via machine learning, the initial publication did not identify any association between the fluorescence

lifetime and the photocatalytic activities. However, this process was only performed using the data for the DBTS co-polymers without adding a platinum co-catalyst.

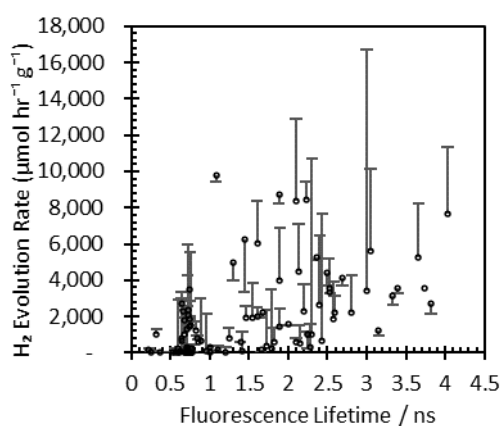


Figure 66: HER rates for the 99 DBTS-copolymers plotted against their fluorescence lifetimes. Error bars represent the change in HER rates after the photodeposition of 1 wt.% Pt as a cocatalyst.

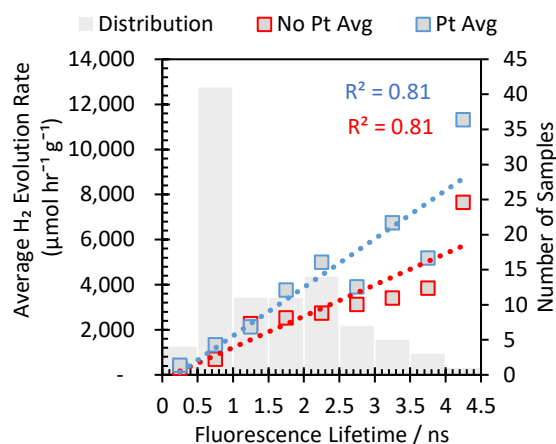


Figure 67: Average H₂ evolution rates for all samples with similar fluorescence lifetimes (± 0.25 ns). Data is plotted separately for photocatalytic activities with and without photodeposited platinum. The number of samples averaged for each data point is displayed as a histogram read from the secondary axis.

Figure 66 plots the photocatalytic activity of the polymers without Pt against the measured fluorescence lifetime. The error bars represent the change in photocatalytic activity after the photodeposition of 1 wt.% Pt. Remarkably, of the 99 polymers, 46 have a weighted fluorescence lifetime of less than 1 ns. Of these polymers, none produced hydrogen at a rate above 4 mmol hr⁻¹ g⁻¹ before Pt addition or above 6 mmol hr⁻¹ g⁻¹ afterwards. The remaining set of 53 polymers contains all of the top ten and 22 of the top 25 photocatalysts after Pt photodeposition. Furthermore, a direct correlation shows that longer lifetimes result in faster photocatalytic rates.

The distribution of polymer sample populations with different fluorescence lifetimes are presented on the secondary axis of Figure 67. The average photocatalytic performance of samples within each 0.5 ns envelope are presented as the red and blue data points to represent before and after Pt photodeposition, respectively. A clear linear trend with a strong positive correlation can be observed in both cases. On average, samples with 1 wt.% Pt photodeposited on the surface produced 2.15 mmol hr⁻¹ g⁻¹ more hydrogen for every additional ns of fluorescence. This highlights the importance of producing high-purity polymers with low defect densities that may lead to accelerated recombination rates of photogenerated charges. Understanding which chemical design elements lead to longer fluorescence lifetimes is also essential.

2.4.1.3 Lifetime vs Residual Palladium Content

In general, some of the most significant improvements in photocatalytic activity after adding platinum can be observed in samples with the longest lifetimes. Four samples with lifetimes longer than 3 ns see increased significant performance after Pt photodeposition. However, four other samples exhibit minor decreases in performance. Interestingly, the most active photocatalysts before Pt photodeposition are the same samples that exhibited increased activity afterwards. To understand if these observations are linked with those made regarding residual palladium in section 2.3.1.2, the fluorescence lifetime is plotted against palladium content in Figure 69.

The area of the data points represents the change in hydrogen evolution rates after adding the platinum co-catalyst. It is observed that the samples exhibiting longer lifetimes are typically the same ones that are lower in residual palladium. This suggests that charge transfer to residual palladium quenches the fluorescence via charge extraction in agreement with transient absorption measurements in the literature.⁶²

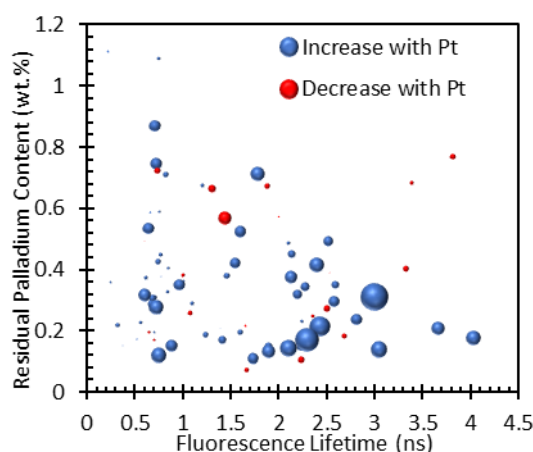


Figure 68: Relationship between the weight-averaged fluorescence lifetimes and the residual palladium concentration. Data point areas correspond to the change in HER rates following the photodeposition of 1 wt.% Pt. Red data points show a decrease in activity, whereas blue data points indicate increases in photocatalytic activity.

The only data points that break this trend are the two samples that are situated in the upper right quadrant of the chart. However, these samples, with long lifetimes and high palladium content, exhibit decreased photocatalytic performances after loading with platinum. The third sample with a long lifetime and decreased activity also contains more palladium than the other samples with lifetimes longer than 3 ns. The Pd content was not measured for the remaining sample in this region.

These results are interesting since residual palladium does not appear to quench the fluorescence lifetime for these samples. Some potential hypotheses for this phenomenon include the slow transfer of charges to palladium, the back transfer of electrons from residual palladium into the polymer

excited state, or direct radiative recombination of a Pd-based electron and a positively charged polaron P⁺. Since adding platinum does not improve the HER rate, unlike most other samples, this implies that Pd clusters retain their charge-trapping properties and function as radiative recombination sites. Alternatively, charge transfer to Pt is as inefficient for these particular polymer structures as the transfer to residual palladium.

Overall, these results demonstrate that the fluorescence lifetime does have a significant impact on photocatalytic activity. The lifetime is linked to residual palladium content, and the most significant improvements upon Pt photodeposition are observed when an exciton has both a long lifetime and low palladium content. These results suggest the potential for interesting transient absorption experiments in which exciton and polaron lifetimes are monitored as a function of residual Pd and photodeposited Pt.

2.4.2 Oscillator Strength

The oscillator strength, f , can be considered the ratio between a quantum mechanical transition rate and the classical absorption rate of a single electron oscillator with the same frequency. For symmetry allowed electronic transitions, large values of $f \approx 1$ can be observed. Large values of f indicate that these transitions take place rapidly with a high probability.

The oscillator strength is closely related to the transition dipole moment associated with a transition, μ_{fi} . f is proportional to μ_{fi}^2 multiplied by the energy of the transition represented as a wavenumber. Briefly, μ_{fi} represents the degree of similarity between the wavefunction corresponding the final energetic state and that of the initial energetic state when perturbed by an external electromagnetic force (i.e. a photon). The oscillator strength can also be linked to the molar absorption coefficient, ϵ , and the rate of fluorescence, k_e^0 . Resultingly, it can be calculated for each transition from absorption and emission spectra.

$$f \propto \bar{\nu} |\mu_{fi}|^2 \quad (15)$$

$$f \propto \epsilon_{max} \Delta \bar{\nu}_{fwhm} \quad (16)$$

$$f \propto \frac{k_e^0}{\bar{\nu}^2} \quad (17)$$

Importantly, when considering large, conjugated molecules such as these polymers, the absorption spectrum cannot be defined by distinct features corresponding to a single electron transitions between specific well-defined quantised energy levels. Instead, absorption bands correspond to transitions from one continuum of states (the valence band) into another (the conduction band). Therefore, the f value reported in these calculations do not represent a single electron transition but sum together the oscillator strengths for many different transitions originating from quasi-degenerate orbitals located at the band edges. Resultingly, oscillator strengths much greater than one are observed.

Estimated oscillator strengths for each polymer were calculated as part of the sTDA-xTB calculations of the optical gaps. The optical gap is defined by the lowest energy electronic transition that has a non-zero oscillator strength. A high oscillator strength depends on substantial ground and excited state orbital mixing when perturbed by electromagnetic radiation. The oscillating dipole moment induced by this interaction is proportional to the transition dipole moment, which determines the degree of mixing.

The magnitude of the induced oscillating dipole depends on the strength of the incident electric field and the polarisation of light relative to the transition dipole moment. It is also dependent on the molecule's polarisability. π -conjugated electrons along a conjugated polymer backbone can be considered delocalised. As such, valence electrons in conjugated polymers are strongly polarisable, resulting in very strong absorption and emission spectra.

In the context of photocatalysis, large oscillator strengths are preferable for a couple of reasons. Firstly, a large absorption coefficient implies that less material is required to absorb all incident light fully. It also means that most light is absorbed near the particle surface. Therefore, excitons do not have to diffuse as far, and the probability of bulk recombination is minimised.

The transition dipole moment is also an essential parameter concerning the Forster Resonance Energy Transfer by which excitons diffuse through the polymer particles. In this process, instead of emitting a photon upon deexcitation, the oscillating dipole from the donor chromophore induces an oscillating dipole (and hence an excitation event) in the acceptor chromophore via a long-range dipole-dipole interaction. This results in energy transfer from Donor to Acceptor. As such, the rate of energy transfer depends on the transition dipole moment of the relaxation transition in the donating chromophore

and the transition dipole moment of the excitation transition of the acceptor chromophore. As such, increased diffusion lengths may be observed in polymers predicted to have large oscillator strengths.

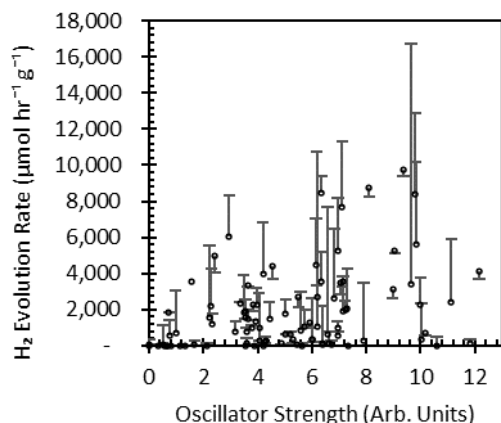


Figure 69: HER rates for the 99 DBTS-copolymers plotted against their calculated oscillator strengths, f . Error bars represent the change in HER rates after the photodeposition of 1 wt.% Pt as a cocatalyst.

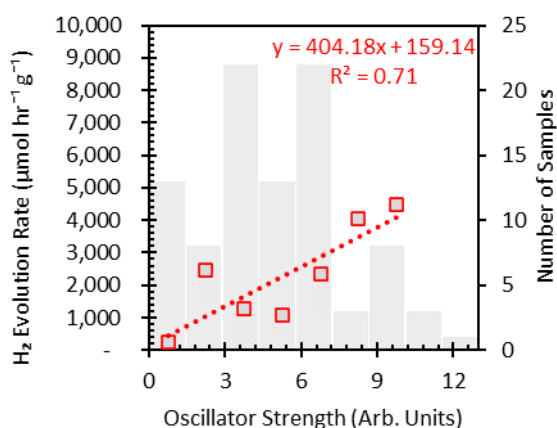


Figure 70: Average hydrogen evolution rate (No Pt) per 1.5 a.u. oscillator strength. Grey histogram presents the distribution of predicted oscillator strengths for all synthesised samples.

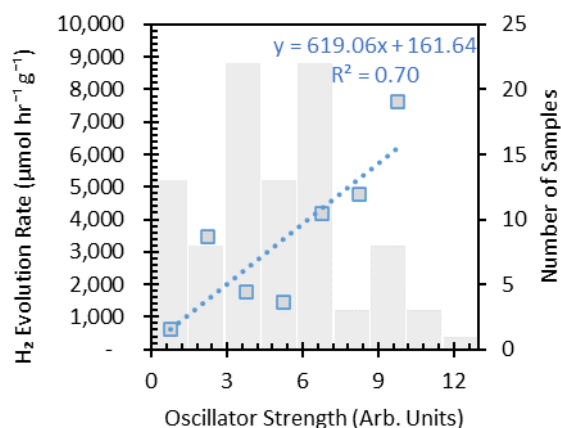


Figure 71: Average hydrogen evolution rate (1 wt.% Pt) per 1.5 a.u. oscillator strength. Grey histogram presents the distribution of predicted oscillator strengths for all synthesised samples.

Figure 69 plots the H_2 evolution rate vs the predicted oscillator strengths for each polymer. As with previous charts, data points represent the activity before Pt photodeposition and error bars represent the activity after photodeposition. As expected, improved oscillator strengths are accompanied by improved HERs.

It is important to note the relationship between the rate constant for emissive relaxation, k_e , and the oscillator strength as outlined in equation (17). To a first approximation, this appears to highlight two conflicting mechanisms regarding fast HERs: large oscillator strengths and shorter excited state

lifetimes. However, this does not consider the fact that the electronic states associated with the absorption and emission events are not necessarily the same.

The oscillator strength associated with a transition from S_0 to S_n may be very large, implying a significant molar absorption coefficient. However, S_n will rapidly relax into the S_1 excited state via internal conversion. The oscillator strength associated with the $S_1 \rightarrow S_0$ transition may be significantly smaller, thus resulting in a high absorption coefficient and a long lifetime. However, as discussed above, absorbing chromophores in conjugated polymers are rarely the same as the emitting chromophores. An S_1 excited state of an absorbing chromophore will transfer its energy to neighbouring chromophores before a photon is emitted. In this case, the rate of radiative emission will depend on the transition dipole moments associated with the emitting chromophore.

Equally, a short fluorescence lifetime does not necessarily mean a significant emissive decay rate constant and a large oscillator strength. The change in the excited state population results from the combination of radiative and non-radiative relaxation processes. Photoluminescence quantum yield measurements are required to provide more information regarding the relative rates of these processes.

Finally, the absorption and emission rates depend significantly on the vibronic coupling of vibrational and electronic energy levels. In particular, the vibrational wavefunctions of the initial and final states must exhibit an appreciable overlap integral (Frank-Condon factor) to allow a transition to take place. Since absorption takes place from the vibrationally-relaxed ground state, and emission takes place from the vibrationally-relaxed excited state, the FC factors associated with the $S_0^{v=0} \rightarrow S_1^{v'=n}$ transition may differ from those for the $S_1^{v'=0} \rightarrow S_0^{v=n}$ transition, despite relating to the same electronic energy levels. The vibrationally-relaxed geometries of the ground and excited states are likely to be similar for rigid co-planar structures and differ in polymers with increased degrees of rotational and vibrational degrees of freedom. The relationships between specific structures and photocatalytic performance will be discussed in more detail later.

2.5 Role of Pt co-catalyst

So far, we have identified specific associations between photocatalytic activities and measured properties that are more prominent after the photodeposition of a Pt co-catalyst. These appear to be particularly apparent regarding the residual Pd content, excited state lifetime, and oscillator strength. In this section, consideration is given to why some polymers experience significant improvements in activity following Pt addition and others do not. Likewise, explanations for why some polymers are sensitive to residual Pd content are considered.

First, some possible catalytic pathways must be considered, as shown in Figure 72. Along the first pathway, the reductive pathway, rapid oxidation of the sacrificial electron donor produces a negatively charged polaron (the reduced polymer). The negative charge is then transferred to the metallic co-catalyst, where the HER occurs. The second pathway, the oxidative pathway, considers the reverse situation in which an electron is initially injected into the co-catalyst, and the resulting positively-charged polaron is reduced by the sacrificial electron donor.

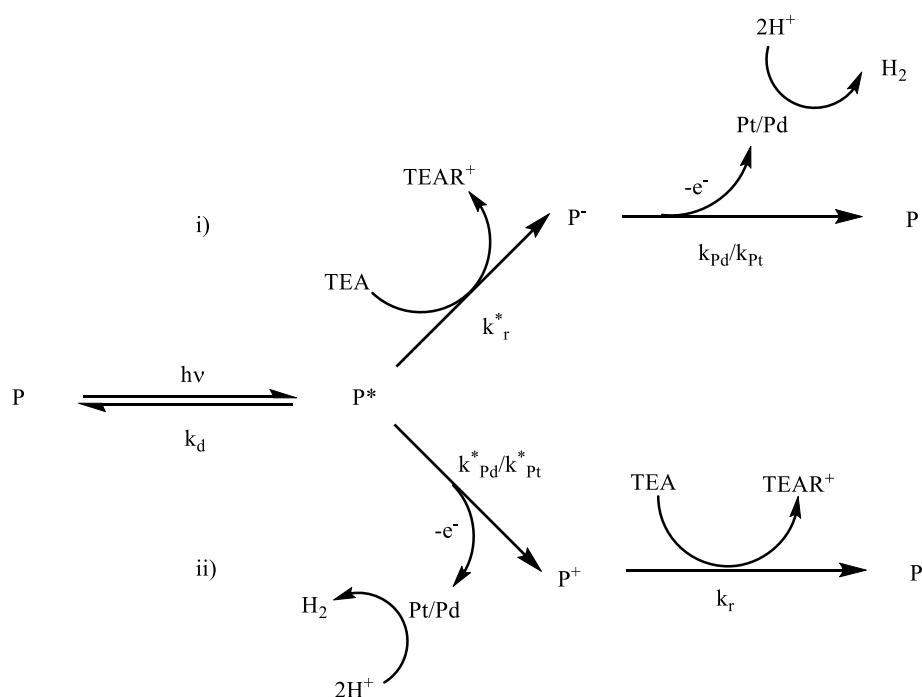


Figure 72: Possible reaction pathways to regenerate the polymeric photocatalysts following excitation. Pathway i) represents a reductive pathway in which the excited polymer is reduced by the sacrificial electron donor, TEA before transferring an electron to a metallic co-catalyst. Pathway ii) involves initial oxidation of the excited polymer by transferring an electron to a co-catalyst followed by reduction by a sacrificial electron donor. The excited polymer may also relax back to its ground state via various radiative or non-radiative pathways. Each electronic process is associated with a rate constant. The overall rate of reaction will be determined by these constants, and the relative concentrations of the species involved. Which step is rate determining will depend on the selection of the polymer, co-catalyst, and sacrificial reagent.

It must be stated that this reaction schematic is dramatically simplified since not all possible side reactions can be considered. For example, P^* , P^+ , and P^- may undergo photodegradation, react with one another, react with neutral polymer molecules, or react with impurities. We also assume that the HER takes place on the co-catalyst surface. However, structure-dependent reaction mechanisms involving the polymer itself may also be possible.

The rate constant k_d represents the various deactivation pathways from the excited state back to the initial ground state, including fluorescence, phosphorescence, and internal conversion. The rate constant k_r^* represents the rate of reduction of the excited polymer. k_r is the rate constant for the reduction of the positive polaron. These rates depend on the EA^* and IP potentials relative to the oxidation potential of TEA. EA^* and IP differ by half of the exciton binding energy. The rate constants for charge transfer from the negative polaron and exciton to the Pd/Pt co-catalysts are represented by $k_{Pd/Pt}$ and $k_{Pd/Pt}^*$, respectively. These rates will depend on EA and IP* potentials and their relative positions to the Pd and Pt work functions.

Following the mechanistic investigations conducted by Sachs *et al.*, the homopolymer DBTS-DBTS (P1-93, also known as P10) has been demonstrated to follow the first pathway. However, the negatively-charged polaron is long-lived due to the slow transfer of electrons to residual palladium clusters.^{62,63} The population of this negatively charged polaron has also been demonstrated to scale with the number of DBTS units in the backbone.¹³⁵ The long-lived negatively-charged polaron is also present in the DBTS-Ph (P7) polymer.¹⁹⁶

However, none of these studies have also considered the impact of adding a Pt co-catalyst. Sachs *et al.* concluded that despite the slow transfer of electrons to residual Pd, palladium remains essential for improved HER rates.⁶³ They go on to claim that future polymeric catalysts require long-lived stable polarons and rapid charge transfer to palladium. However, this HT study, in which the activity of P10 increases from $3.4 \text{ mmol hr}^{-1} \text{ g}^{-1}$ to $16.7 \text{ mmol hr}^{-1} \text{ g}^{-1}$ following Pt addition, implies that charge transfer to platinum is considerably faster than to palladium.

In reference to Figure 72, P1-93 likely progresses through the reductive quenching pathway (i.e. $k_r^* \gg k_{Pd}^*$). The rate-determining step controlling the HER is, therefore, the charge transfer to residual palladium ($k_r^* > k_{Pd}$). It is apparent that $k_{Pt} > k_{Pd}$, and this process is likely responsible for the improved activity after loading with Pt.

Compared with palladium, platinum has a larger work function ($\phi_{\text{Pt}}=5.64$ V, $\phi_{\text{Pd}}=5.12$ V).¹⁹⁷ This means there is a greater thermodynamic driving force for electron extraction into Pt than there is into Pd. Pt also has a lower binding energy for protons and hydrogen, enabling rapid adsorption and desorption processes. As such, Pt is considered the optimal co-catalyst for hydrogen evolution and typically results in faster HER rates than Pd.

When acting as an electron sink, it is preferable to form a Schottky barrier at the co-catalyst/semiconductor interface.¹⁹⁸ This enables the injection of photoelectrons into the metal but introduces a barrier to prevent their back-transfer and enhances charge separation. The size of this junction depends on the bandgap and the alignment of the semiconductor's Fermi Energy, E_{F} , relative to the metal's work function. Assuming that the polymer photocatalysts are intrinsic semiconductors, their Fermi levels would lie in the middle of the bandgap. We can approximate this potential as the mid-point between the IP and EA.

2.5.1 IP, EA and Pt Loading

Relating IP, EA, and E_{F} to Figure 72, we can predict certain trends regarding how the activity might change following the photodeposition of Pt relative to these parameters. Firstly, the more negative the EA potential, the greater the driving force for charge extraction into residual palladium clusters. As such, the HER rate increases with this metric. This trend was observed and discussed in the original publication and is shown in Figure 73a.

Likewise, charge transfer to platinum is also expected to follow this trend for the same reasons. This is also observed for the polymers after loading with Pt, as shown in Figure 73c. In general, the biggest increases in activity are also observed for polymers with the most negative EA potentials, as shown in Figure 73b. This pattern is consistent with the notion that the charge transfer of electrons into Pd, described by k_{Pd} , defines the rate-determining step in the HER.

A more interesting shift is observed when comparing the photocatalytic activities before and after Pt photodeposition relative to the IP potential. For the as-prepared photocatalysts in which residual Pd is the only co-catalyst, Figure 73d demonstrates the photocatalytic activity peaks at 0.9 V vs SHE. At potentials more negative than this, there is a limited driving force for TEA oxidation, particularly considering the exciton binding energy. In this situation, the rate-determining step may be defined by the rate constant k^*_{r} , rather than k_{Pd} . In cases where the IP is considerably more negative, the reaction

may progress via the photooxidation pathway (i.e. $k^*_{pd} > k^*_r$), in which charge extraction into Pd precedes TEA oxidation via the P^+ polaron.

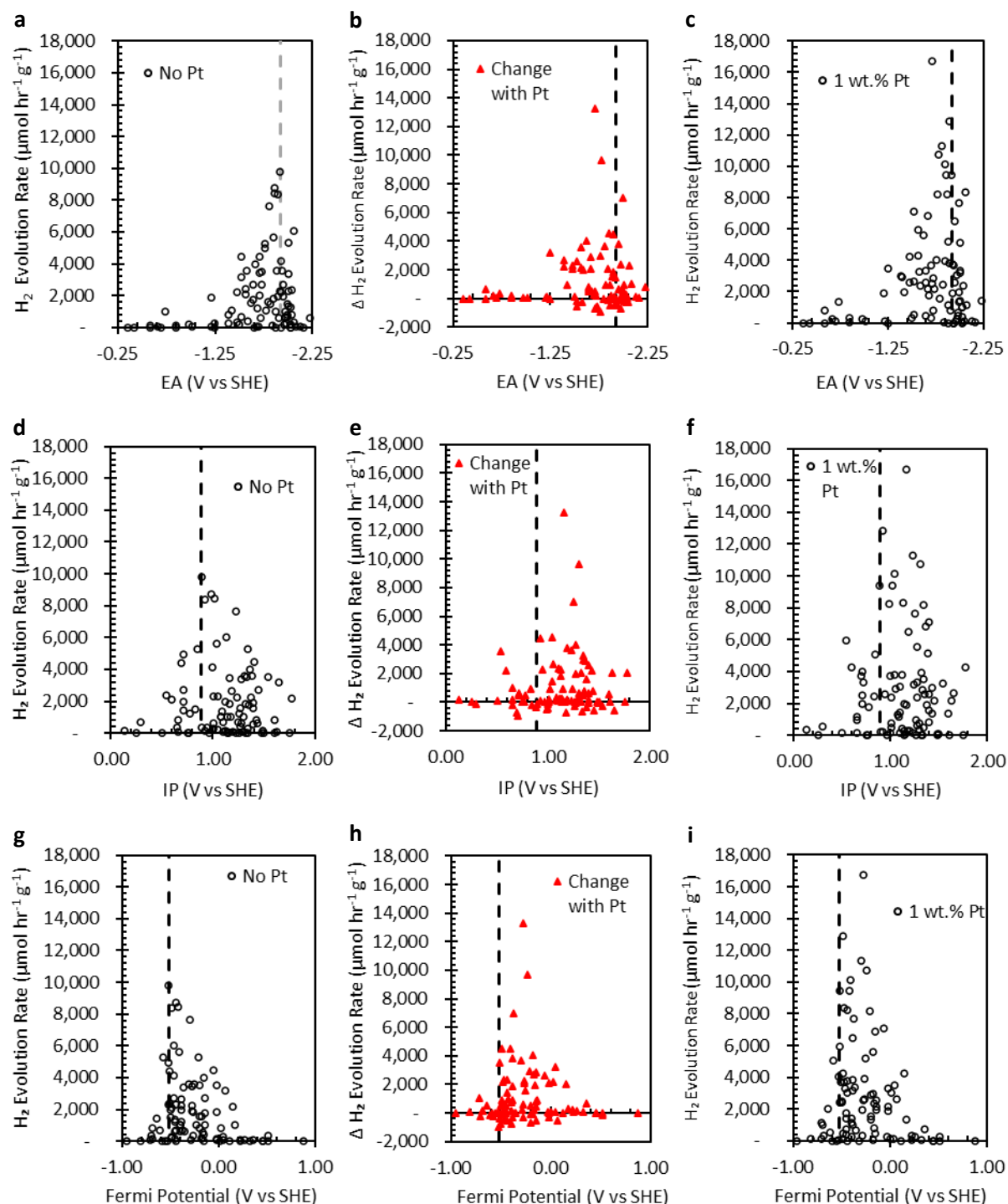


Figure 73: Hydrogen evolution rates for the 99 DBTS co-polymers before (left) and after (right) photodeposition of 1 wt.% Pt. Central graphs represent the change in photocatalytic activity observed for each polymer associated with photodepositing the 1 wt.% Pt co-catalyst. Top, middle, and bottom rows plot these values relative to the EA, IP, and Fermi potential, respectively. The Fermi Potential is approximated as the mid-point between the xTB-IPEA calculated IP and EA values. Dashed vertical lines represent the maxima before the addition of platinum.

The resulting photocatalytic activity also decreases for IP potentials more positive than 0.9 V vs SHE. It can be argued that this trend provides evidence that the HER rate is limited by k_{pd} . If the rate was limited by k^*_r , a more-positive IP potential should result in an increased HER. Those with deeper (more positive) IP potentials are also expected to have either deeper EA potentials or wider bandgaps. The latter would result in a smaller proportion of the incident light being harnessed. It is also possible that rapid TEA oxidation in these polymers results in the rapid accumulation of negative charges in the polymer backbone that inhibits further absorption events. Such charge accumulation may also promote the rate of back-transfer of electrons into TEA^+ to reform TEA.⁶⁴

In contrast with the EA-related graphs, the optimal IP potential for polymers loaded with photodeposited Pt is shifted to more positive voltages relative to the SHE, as shown in Figures 73e and 73f. This observation can be rationalised by considering that $k_{Pt} > k_{Pd}$. If charge transfer to platinum becomes competitive with the rate of reductive quenching, k^*_r , then the rate-determining step for the reaction could be either step. In the case where reductive quenching is limiting, a more positive IP potential would generate a stronger thermodynamic driving force for TEA oxidation. Rapid charge extraction would also limit the negative charge accumulation in the form of excess P^- polarons and mitigate any accompanying competing charge-transfer reactions.

It is also worth considering the relative HER rates with respect to the polymer's Fermi level, which lies at the midpoint between the IP and EA potentials, assuming they are intrinsic, undoped semiconductors. The respective charts are plotted in Figures 73g - 73i. In the case of a Pd co-catalyst, the most photoactive polymers have the most negative Fermi levels relative to the SHE. Such polymers would provide the largest thermodynamic driving force for electron extraction and form the most significant Schottky barriers that prevent the back transfer of electrons from Pd into the polymer matrix.

Conversely, after Pt photodeposition, the optimal Fermi Level is shifted to more positive potentials vs the SHE, and the most active photocatalysts span a wider range of Fermi Level potentials. This agrees with the theory that the thermodynamic driving force is more substantial, and the Schottky barrier is taller at the semiconductor-Pt junction than the semiconductor-Pd junction due to its more considerable work function.

There is a substantial cluster of data points in Figure 73h close to the baseline at -0.5 V vs SHE. This implies that the samples with the most negative Fermi levels do not exhibit significant increases in

photocatalytic activities following Pt deposition. In such samples, it is possible that $k_{Pd} \approx k_{Pt}$ or even that $k_{Pd} > k_{Pt}$. Since Pd is known to be a less-effective cocatalyst and some clusters will be immobilised inside the bulk of the polymer particles, the photocatalytic activities of these polymers could be increased by improving synthesis conditions to limit residual Pd content.

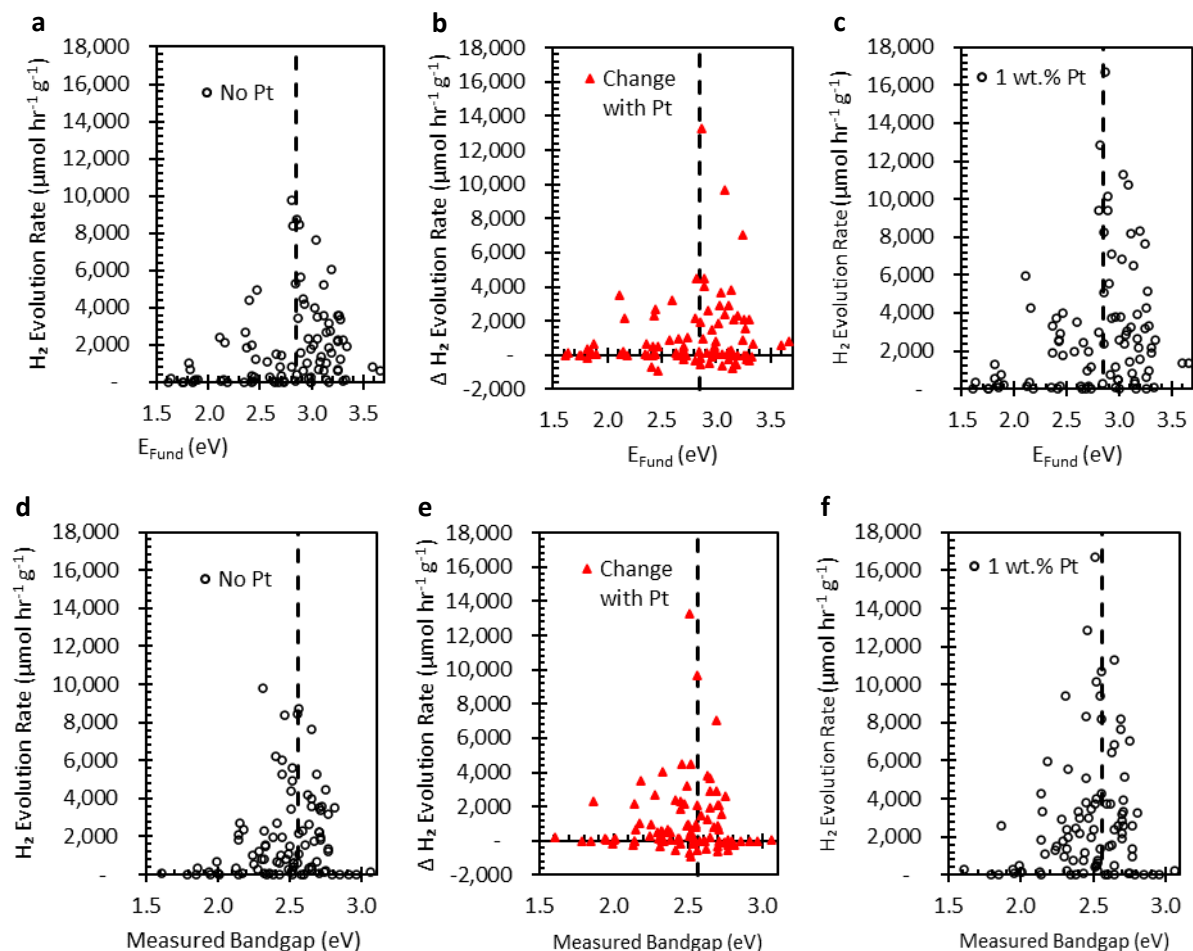


Figure 74: Hydrogen evolution rates for the 99 DBTS co-polymers before (left) and after (right) photodeposition of 1 wt.% Pt. Central graphs represent the change in photocatalytic activity observed for each polymer associated with photodepositing the 1 wt.% Pt co-catalyst. Top and bottom rows plot these values relative to the fundamental gap and measured bandgap, respectively. Dashed vertical lines represent the maxima before the addition of platinum.

The equivalent charts corresponding to the calculated fundamental and measured optical gaps are presented in Figures 74a to 74f. The vertical dashed lines ($E_F = 2.85$ eV and $E_g = 2.53$ eV) correspond to the peak activities in the Pd-catalysed distribution of samples (Figures 74a and 74d). Interestingly, the optimal gaps before and after Pt addition remain unchanged, as demonstrated by the alignment between the peak activity and the dashed line in Figures 74c and 74f. However, samples with wider fundamental gaps still exhibit larger increases in activity on average, as demonstrated by the substantial number of data points on the right-hand side of the dashed line in Figure 74b, indicating a change in the HER rate of greater than $1,000 \mu\text{mol hr}^{-1} \text{g}^{-1}$ following Pt photodeposition.

These results suggest that wider bandgap materials will most likely have favourable EA and IP potentials. However, wider bandgaps may also correspond to decreased activities because they can absorb a smaller portion of the solar spectrum. Thus, this highlights the importance of fine-tuning the optical properties of photocatalysts, which is considerably easier for organic semiconductors than inorganic ones.

In summary, the relative rates of hydrogen evolution before and after Pt photodeposition is a complicated phenomenon. However, it is possible to establish some parameters that can be incorporated into any future high-throughput computational screening experiments when searching for new linear copolymers. Such screening experiments should aim to predict the most active polymers when paired with Pt rather than Pd since the charge transfer to Pt appears to be considerably faster for most linear copolymers.

2.5.2 High Throughput Screening Parameters

Ensuring that the predicted EA potential lies as negatively as possible is important. Therefore, a suitable screening parameter would be to identify polymers for which the EA value lies between -2.2 and -1.5 V vs SHE. The criteria for an ideal IP potential is more complicated since this oxidation potential determines the rate of oxidation of the sacrificial reagent, SR, the selection of which is an important variable. For these reaction conditions, which utilise TEA as the SR, the most active photocatalysts were predicted to possess IP values between +0.9 and +1.4 V vs SHE. Given the oxidation potential of TEA to form TEA^{•+} ($E_{\text{TEA}} = +0.7$ V vs SHE), this suggests that screening hypothetical polymers according to their IP potential should prioritise samples which provide at least 0.2 – 0.7 V of overpotential relative to the SR to be used.

By taking the extremes of each range, the resulting fundamental gaps of the screened polymers should lie between $2.4 < E_{\text{Fund}} < 3.6$ eV when screening for suitable polymers that function well with TEA. Likewise, the Fermi level will be predicted to lie between $-0.05 > E_{\text{Fermi}} > -0.65$ V vs SHE. If presented with a lot of samples, these values could be narrowed further by only considering fundamental gaps wider than 2.8 eV and prioritising the remaining samples with the most negative Fermi energies. However, these parameters must also be adjusted for alternative sacrificial reagents accordingly.

The remaining polymers could undergo an additional screening step in which only polymers with oscillator strengths greater than 6 ($f > 6$) since this value can also be predicted computationally and is an important factor amongst the most active polymers.

The modified calibration curve relating IP/EA potentials and the optical bandgap also allows us to predict the optical bandgap to within ± 0.15 eV of their experimental values and rank them relative to the optimal experimental value of 2.56 eV.

Of the 99 synthesised polymers, 21 meet these criteria based on theoretical calculations. Their photocatalytic activities before and after Pt addition are presented in Figure 75. Nine of the top ten polymer photocatalysts after Pt photodeposition fall into this subspace of predicted properties. This subset of 21 polymers also contains 16 of the top 25, 18 of the top 50 photocatalysts, and only three samples from the 50 least active photocatalysts.

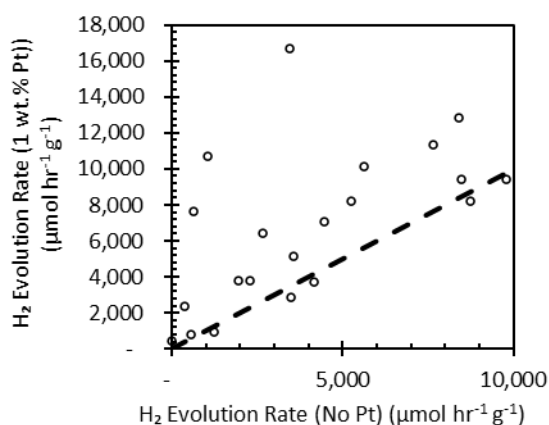


Figure 75: Hydrogen evolution rates for the 21 synthesised polymers that meet the screening criteria outlined in the text. Rates before Pt deposition are plotted against rates after Pt photodeposition.

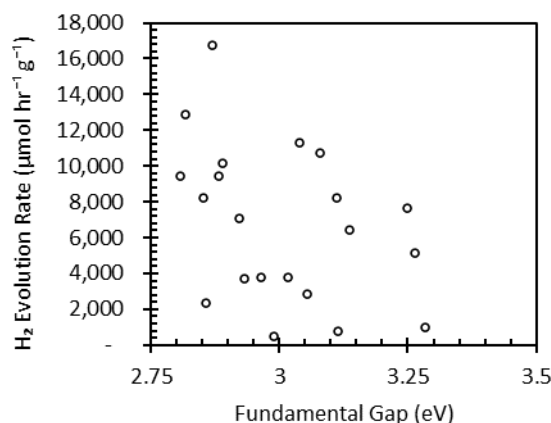


Figure 76: Hydrogen evolution rates (with 1 wt. Pt) for the 21 synthesised polymers that meet the screening criteria outlined in the text. HER rates are plotted against the calculated fundamental gap.

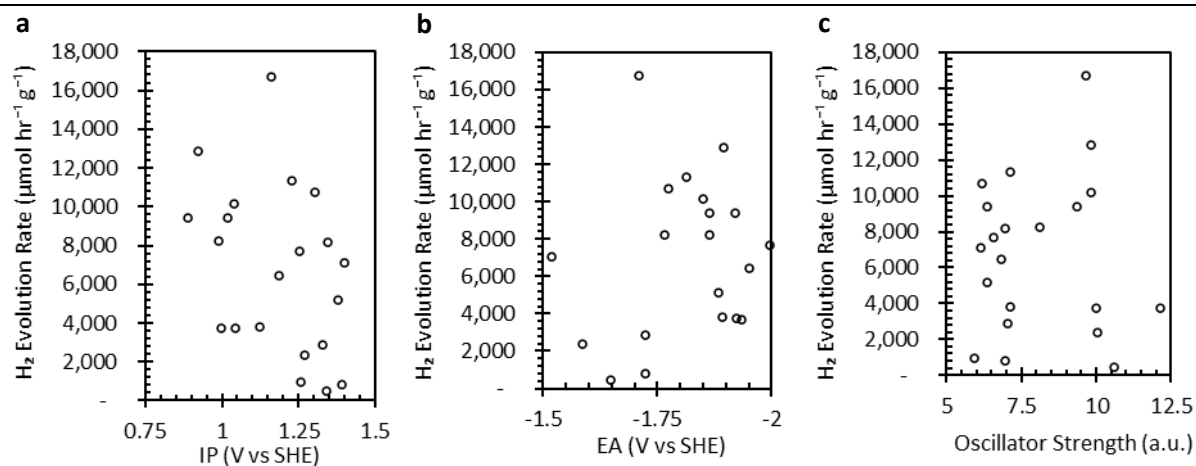


Figure 77: Hydrogen evolution rates (with 1 wt. Pt co-catalyst) for the 21 synthesised polymers that meet the screening criteria outlined in the text. HER rates are plotted against the predicted IP (a), EA (b), and oscillator strength (c) values. These results show that there is no clear correlation between these computationally-determined values and the photocatalytic activities after applying general screening criteria.

Although samples within these screening parameters are more likely to be highly active photocatalysts under specific testing conditions, these calculations cannot predict which will be the most active. Alone, they also cannot identify which polymers will exhibit the largest increases in activity after Pt photodeposition.

With the possible exception of the fundamental gap (Figure 76), in which wider fundamental gaps appear to correlate with lower activities, any dependence of the activity on the other parameterized properties is no longer apparent, as seen in Figures 77a-c. However, correlations between the photocatalytic activity, the yield, and the residual palladium remain relatively strong (Figures 78a-b).

The correlation between the fluorescence lifetime and the photocatalytic activity of this subset of polymers is less clear (Figure 78c). However, it should be noted that only two polymers within this refined subset have fluorescence lifetimes shorter than 1 ns. This is in direct contrast to the unfiltered sample library in which nearly 50% of all samples exhibited fluorescence lifetimes of 1 ns or shorter. As such, there is a clear implication that IP, EA, and the oscillator strength directly impact the excited state lifetimes.

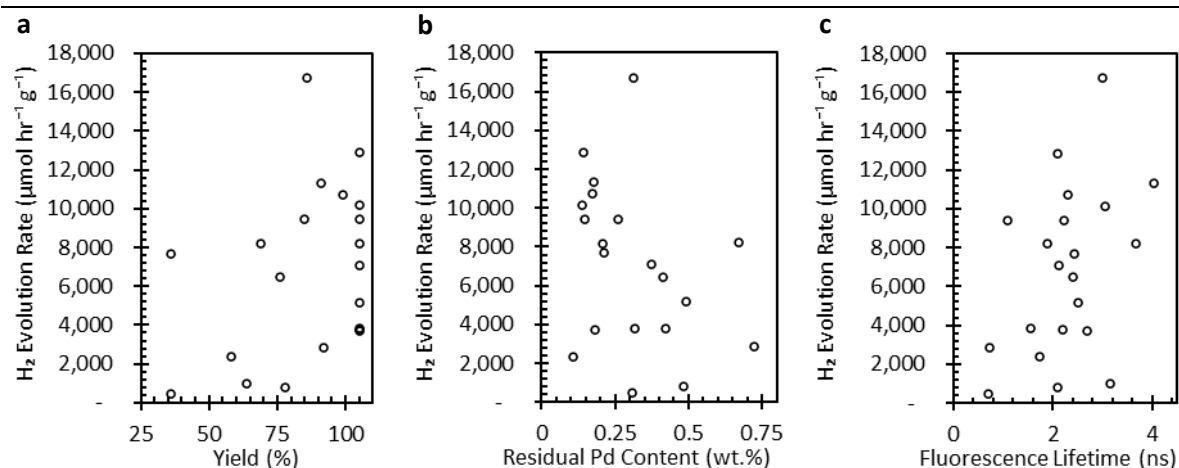


Figure 78: Hydrogen evolution rates (with 1 wt. Pt co-catalyst) for the 21 synthesised polymers that meet the screening criteria outlined in the text. HER rates are plotted against the synthesis yield (a), residual palladium content (b), and the weighted fluorescence lifetime (c). These results show that experimental factors may be most influential in determining the photocatalytic activities of the screened polymers.

Of these factors, the fundamental gap (i.e. the difference between the IP and EA potentials) likely has the most significant impact. The inverse energy gap law states that non-radiative decay from the excited state will be faster when the energy difference between the ground and excited states is small. This process takes place via internal conversion in which ground and excited state wavefunctions mix due to perturbations from molecular vibrations. This results in a horizontal energy transfer from the excited state into a vibrationally-hot ground state. The wider the energy gap, the poorer the vibrational wavefunction overlap will be, so the internal conversion rate slows down considerably.

When comparing the fluorescence lifetime of all polymers with the predicted fundamental gaps, we can see that this relationship holds true, as shown in Figure 79a. Importantly, this also holds true for the measured optical gap, as shown in Figure 79b. This has important implications regarding the design of future linear organic photocatalysts as there is a clear trade-off between the optical bandgap, which should be as narrow as possible to maximise the portion of harvestable solar irradiation, but also needs to be wide enough such that the excited state lifetime is long enough to ensure that exciton migration and charge extraction processes can compete on with the non-radiative decay pathways.

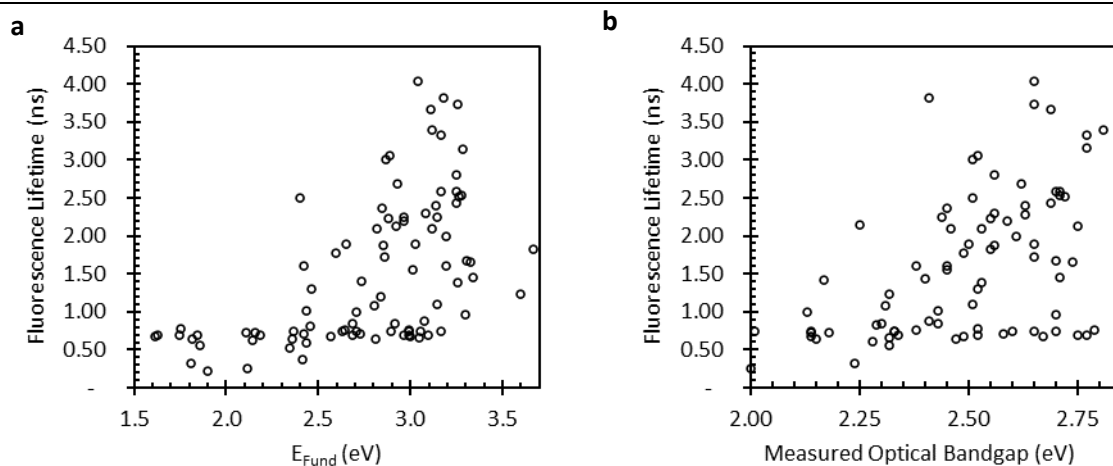


Figure 79: Direct correlational relationship between the fluorescence lifetimes and the polymer's calculated fundamental gap (a), and measured optical gap (b).

Figure 80a reaffirms that the residual Pd content does not depend on the synthesis yield. However, Figure 80c, in which the width of the bubbles represents the HER rates after the addition of Pt, demonstrates how efficient photocatalytic activity independently depends on both the high yield and low Pd content. Meanwhile, Figure 80b shows that the residual Pd content and the excited state lifetime are strongly correlated. Longer lifetimes appear to be considerably more likely when there are lower levels of Pd. Figure 80d highlights those samples exhibiting long fluorescence lifetimes and low Pd concentrations exhibit the fastest HER rates when using Pt as a co-catalyst. Of the eight samples that demonstrate lifetimes between 2 and 2.5 ns, the four most active possess lower levels of palladium. It is also worth noting that several of the 21 selected polymers disperse poorly in the water/methanol/triethylamine solution (Figure 81), which will also detrimentally affect the resulting photocatalytic activity.

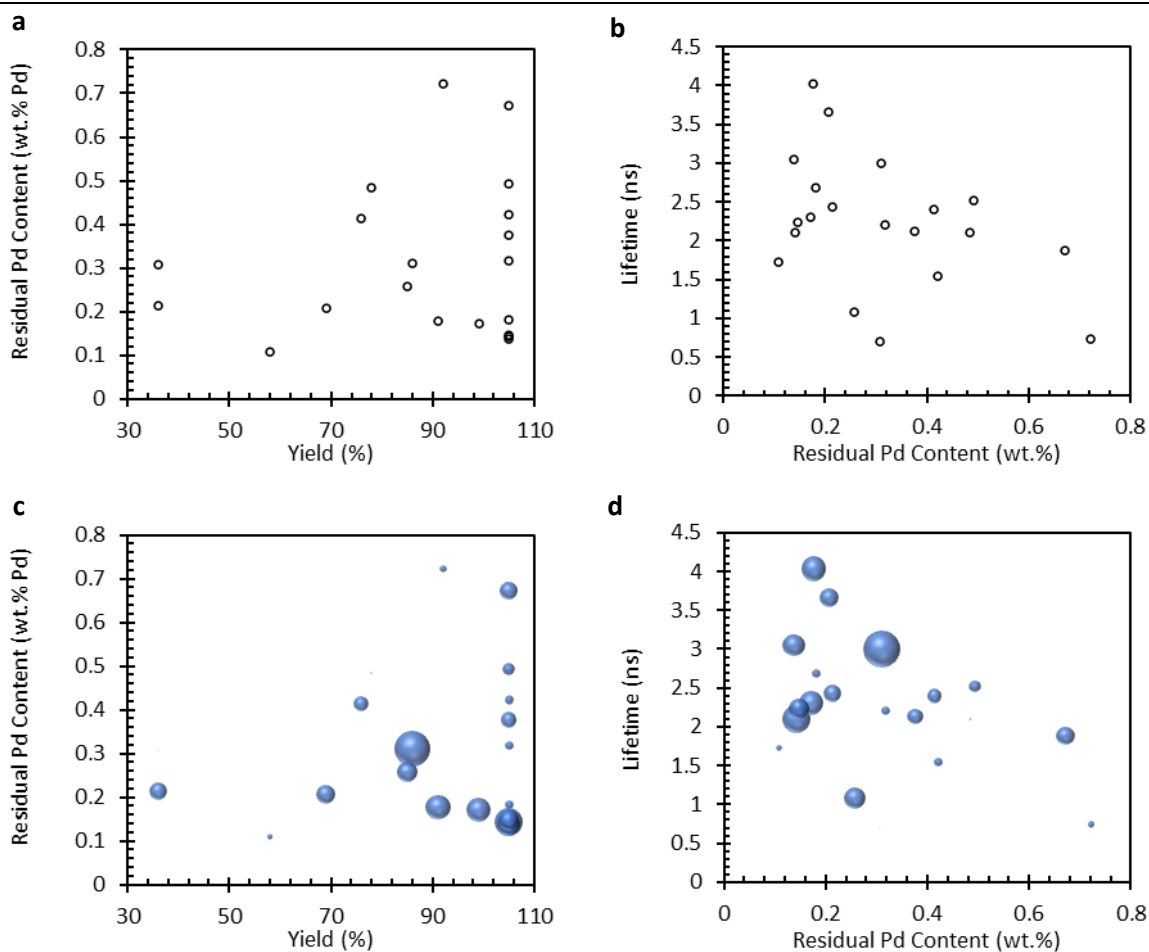


Figure 80: Left) Relationship between residual palladium content and synthesis yield for the 21 identified polymers after screening. Right) Relationship between residual palladium content and the fluorescence lifetime for the same samples. Data point widths in the charts c) and d) represent the hydrogen evolution activities after the photodeposition of 1 wt.% Pt.

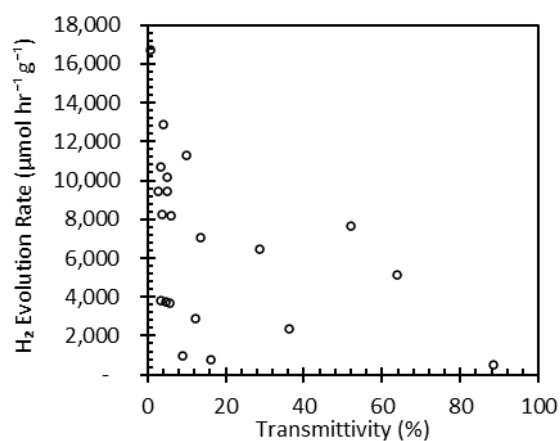


Figure 81: Hydrogen evolution rates (1 wt.% Pt) vs transmittivity data for the 21 DBTS co-polymers identified after screening all 99 synthesised polymers according to their computationally-determined properties.

Although the 21 polymers identified produce hydrogen at a range of rates from $480 \mu\text{mol hr}^{-1} \text{g}^{-1}$ to $16,720 \mu\text{mol hr}^{-1} \text{g}^{-1}$, restricting the subspace of computationally-screened polymers according to the desired EA, IP, and E_{Fund} can effectively highlight polymers with a high likelihood of achieving fast photocatalytic hydrogen evolution under sacrificial conditions after loading with a Pt co-catalyst.

Furthermore, these data strongly indicate that modifying the synthesis conditions could lead to improved photocatalytic activities amongst the underperforming samples as a result of better synthetic yields and decreased residual palladium concentrations.

However, despite this, it remains challenging to predict which polymers will be the best photocatalysts specifically. Amongst the very top photocatalysts, their activities cannot be distinguished or ranked according to these computational and experimental data alone. In reality, further information regarding the structure-activity relationships is required.

Unfortunately, the crystallographic data was only assessed qualitatively, and the gas sorption data were not tabulated. Computational calculations were also performed to determine the solvation energies in the original study, but these results were not tabulated either. However, particle size, particle porosity, crystallinity, and wettability are likely to be important factors in determining the photocatalytic activity of these polymers.

2.6 Structure/Activity Relationships

Until now, the discussion has focussed on identifying global trends from the recorded data with respect to this library of photocatalysts. In addition to those identified in the original publication (IP, EA, E_g , and %T), several other trends have been identified in this chapter (yield, residual palladium content, fluorescence lifetime, and oscillator strength).

Whilst these parameters can be used to identify polymers that are likely to perform well, such metrics cannot guarantee an efficient photocatalyst. Nor can they reliably predict the resulting hierarchy of the polymers that do meet all of the criteria.

The top 12 performing polymers before Pt addition are presented in Table 4. Whilst most of these polymers meet the majority of criteria outlined in the previous sections, there are notable exceptions. These values have been highlighted in the table in bold. For example, P1-32, the most active polymer before Pt photodeposition, exhibits a relatively short fluorescence lifetime and the smallest bandgap

of the set. As exemplified by larger transmittance values, P1-72 and P1-47 are less dispersible than an ideal system would be but retain their activities. P1-61 and P1-71 were also synthesised in yields below 70%, and P1-74 only has an oscillator strength of 2.95, well below the cut-off value used for screening in the previous section. Four of the top 12 polymers also had very high residual palladium content. However, only one of these polymers, P1-74, exhibited an enhanced activity following Pt deposition.

Table 4: Top 12 DBTS-X co-polymers for photocatalytic hydrogen evolution before Pt photodeposition. Values in bold represent outliers typically associated with lower photocatalytic activities.

Polymer	Monomer	HER No Pt ($\mu\text{mol hr}^{-1}$ g^{-1})	HER Pt ($\mu\text{mol hr}^{-1}$ g^{-1})	E_g (eV)	Yield (%)	T (%)	τ (ns)	Pd (wt. %)	IP (V vs SHE)	EA (V vs SHE)	<i>f</i>
1	P1-32	9,772	9,422	2.31	85	2.68	1.08	0.258	0.89	-1.92	9.36
2	P1-14	8,742	8,228	2.56	>100	3.63	1.88	0.672	0.99	-1.87	8.11
3	P1-92	8,462	9,422	2.55	>100	5.1	2.23	0.147	1.02	-1.86	6.36
4	P1-89	8,390	12,869	2.46	>100	3.88	2.1	0.142	0.92	-1.90	9.81
5	P1-60	7,649	11,320	2.65	91	9.85	4.03	0.177	1.23	-1.81	7.11
6	P1-72	6,232	3,348	2.40	#N/A	35.62	1.44	0.569	#N/A	#N/A	#N/A
7	P1-74	6,038	8,341	2.45	77	8.33	1.6	0.522	1.13	-2.06	2.95
8	P1-23	5,631	10,155	2.52	>100	5.12	3.05	0.138	1.04	-1.85	9.83
9	P1-90	5,288	5,089	2.45	96	2.8	2.36	0.247	0.85	-2.00	9.06
10	P1-61	5,248	8,195	2.69	69	5.94	3.66	0.207	1.35	-1.77	6.95
11	P1-21	4,954	4,020	2.52	67	7.86	1.3	0.664	0.71	-1.76	2.43
12	P1-47	4,462	7,076	2.75	>100	13.52	2.13	0.376	1.40	-1.52	6.16

Table 5: Top 12 DBTS-X co-polymers for photocatalytic hydrogen evolution after Pt photodeposition (1 wt.%). Values in bold represent outliers typically associated with lower photocatalytic activities.

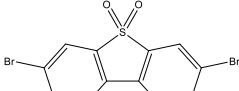
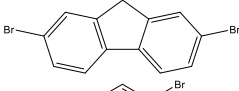
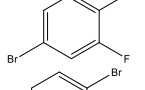
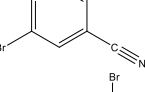
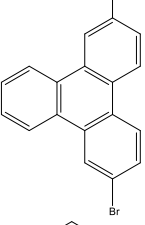
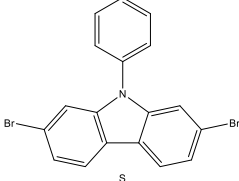
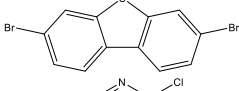
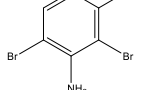
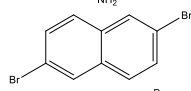
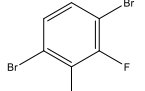
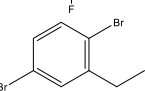
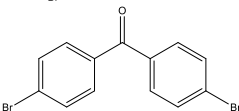
Polymer	Monomer	HER No Pt ($\mu\text{mol hr}^{-1} \text{g}^{-1}$)	HER Pt ($\mu\text{mol hr}^{-1} \text{g}^{-1}$)	E_g (eV)	Yield (%)	T (%)	τ (ns)	Pd (wt. %)	IP (V vs SHE)	EA (V vs SHE)	f	
1	P1-93		3,443	16,719	2.51	86	0.79	3	0.311	1.16	-1.71	9.64
2	P1-89		8,390	12,869	2.46	105	3.88	2.1	0.142	0.92	-1.90	9.81
3	P1-60		7,649	11,320	2.65	91	9.85	4.03	0.177	1.23	-1.81	7.11
4	P1-27		1,053	10,721	2.56	99	3.46	2.3	0.171	1.30	-1.78	6.19
5	P1-23		5,631	10,155	2.52	105	5.12	3.05	0.138	1.04	-1.85	9.83
6	P1-32		9,772	9,422	2.31	85	2.68	1.08	0.258	0.89	-1.92	9.36
7	P1-92		8,462	9,422	2.55	105	5.1	2.23	0.147	1.02	-1.86	6.36
8	P1-74		6,038	8,341	2.45	77	8.33	1.6	0.522	1.13	-2.06	2.95
9	P1-14		8,742	8,228	2.56	105	3.63	1.88	0.672	0.99	-1.87	8.11
10	P1-61		5,248	8,195	2.69	69	5.94	3.66	0.207	1.35	-1.77	6.95
11	P1-7		652	7,671	2.69	36	52.04	2.43	0.214	1.25	-2.00	6.58
12	P1-47		4,462	7,076	2.75	105	13.52	2.13	0.376	1.40	-1.52	6.16

Table 5 presents the top 12 DBTS-X co-polymers following the photodeposition of 1 wt.% Pt. Whilst this set contains 9 of the most active polymers from Table 4, the order has changed dramatically. The remaining polymers ranked 1st, 4th, and 11th in Table 5 result from significant increases in the HER and are only ranked 20th, 46th, and 56th before Pt photodeposition. Generally, the magnitude of change in HER following Pt photodeposition does not appear to depend on the initial HER. This is exemplified in Figure 82.

As was the case before co-catalyst addition, most of the characteristics of polymers in Table 5 align with the general trends identified in the previous sections of this chapter, with most of the same notable exceptions. P1-7 (Rank 11th with Pt) is the only new exception, synthesised at a very low yield and exhibiting a high transmissivity value, indicating that it does not disperse well in the reaction medium.

Despite a general agreement with the overall trends, such as an oscillator strength greater than 6, lifetimes greater than 1 ns, yields above 70%, and suitable IP, EA and transmittance values etc., it is impossible to identify which polymers will be the most efficient from these properties alone.

Clearly, a study of the structure-property relationships is required to better understand which polymers performed best relative to one another beyond these global trends. Initial inspection of these two tables already provides some indication of how structure and activity are related. For example, several of these monomers can be considered fused macrocycles in which the delocalisation runs parallel to the backbone of the polymer chain. Para-linked phenylene chains also feature heavily and appear to be particularly effective when containing electron-withdrawing functional groups. However, the presence of polymers such as P1-72, P1-74, and P1-47 indicates that designing polymers on these principles alone may result in the omission of other highly-effective polymer structures. It is also worth noting that the fused macrocycle monomers may contain electron-withdrawing or electron-donating groups. This section will break down the 99 synthesised polymers into various subsets according to the structures and attempt to rationalise the observed trends accordingly.

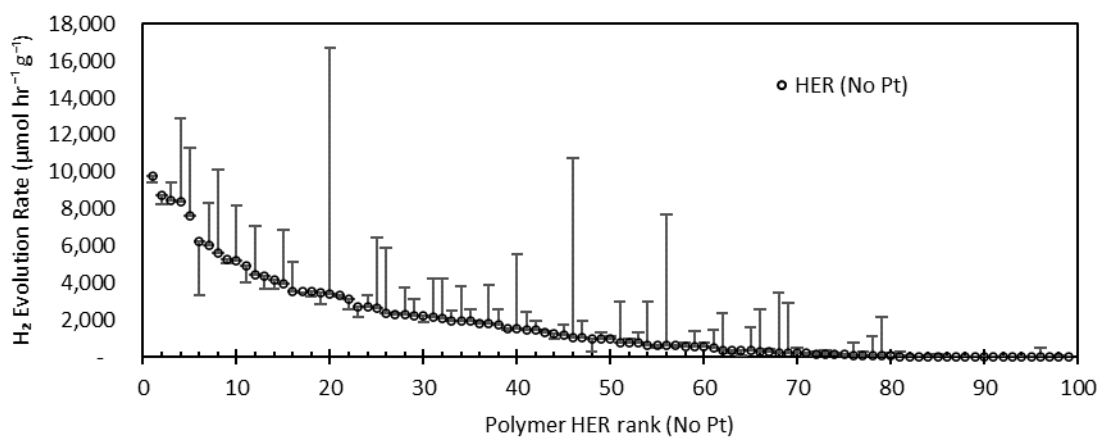


Figure 82: Distribution of photocatalytic activities of all polymers before photodeposition of Pt. Error bars represent the change in HER rates after the photodeposition of Pt. Samples are ordered according to their initial HER rate.

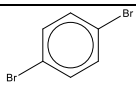
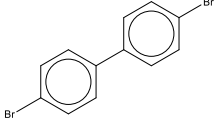
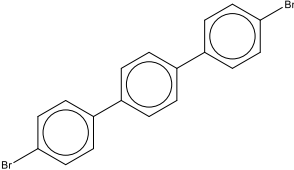
2.6.1 Structure and Oscillator Strength

The first thing to establish is which structural features give rise to large oscillator strengths. The most active photocatalysts have large oscillator strengths greater than six. However, most samples have oscillator strengths lower than this. Therefore we must consider which structural elements should be incorporated into the polymer design to increase the likelihood of large oscillator strength.

2.6.1.1 Number of conjugated bonds

Consider polymers P1-3, P1-16, and P1-19, as presented in Table 6. Clearly, the oscillator strength increases as the number of conjugated π -bonds along the direction of the backbone increases. This is because the upper limit of the oscillator strength is equal to the total number of delocalised electrons at the band edge. Although a molecular orbital can only contain two electrons according to Pauli's exclusion principle and Hund's rule, conjugated semiconductors contain many degenerate energy levels close to the band edge.

Table 6: Table to highlight association between number of p-phenyl rings and oscillator strength.

Polymer	Monomer	HER No Pt ($\mu\text{mol hr}^{-1} \text{g}^{-1}$)	HER Pt ($\mu\text{mol hr}^{-1} \text{g}^{-1}$)	E_g (eV)	Yield (%)	T (%)	τ (ns)	Pd (wt. %)	IP (V vs SHE)	EA (V vs SHE)	f	
1	P1-3		1,948	3,815	2.45	Quant	3.51	1.55	0.42	1.12	-1.89	7.14
2	P1-16		2,295	3,764	2.59	Quant	4.74	2.2	0.32	1.04	-1.92	9.99
3	P1-19		4,155	3,703	2.62	Quant	5.63	2.69	0.18	1.00	-1.93	12.16

However, these samples demonstrate that the oscillator strength alone cannot determine the HER after Pt photodeposition, as all three samples exhibit very similar HER rates between 3.70 and 3.82 $\text{mmol hr}^{-1} \text{g}^{-1}$ under these conditions.

This trend is in direct contrast with the photocatalytic HER rates when the only co-catalyst is residual palladium. In this case, the HER rate is significantly dependent on the residual Pd concentration, as shown in Figure 83a. As observed on the global scale, the excited state lifetime is also inversely proportional to the residual palladium content, such that P1-19 benefits from both low Pd content and long excited state lifetimes (Figure 83b). The fluorescence lifetimes also track inversely with the measured optical bandgap.

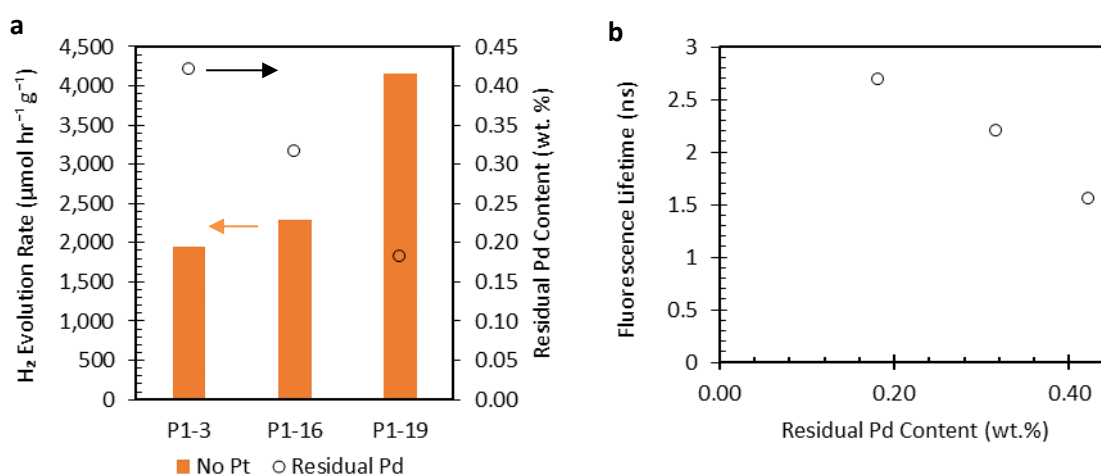


Figure 83: a) Association between photocatalytic activity co-polymers highlighted in Table 6 (No Pt), and the residual palladium concentration. b) Relationship between residual palladium concentration and fluorescence lifetime for the same three samples.

One surprising trend here is that, despite the lower Pd content and longer excited state lifetime, P1-19 decreases in activity upon Pt addition, whereas the other two samples increase in activity. This may arise because the Pt loading concentration has not been optimised. It is well known that the presence of too much co-catalyst can inhibit photocatalytic activity by covering active sites, shielding light absorption, decreasing the surface area, and in some cases, increasing the charge recombination rate.¹⁹⁹

2.6.1.2 Perpendicular Conjugation

Table 7: Computationally and experimentally derived values relating to the DBTS-Anthracene co-polymers relative to the DBTS-DBTS homopolymer.

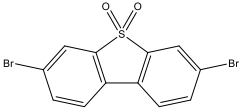
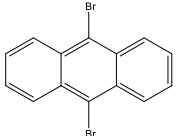
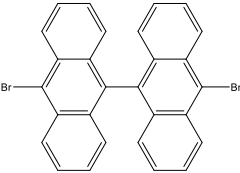
Polymer	Monomer	HER No Pt ($\mu\text{mol hr}^{-1} \text{g}^{-1}$)	HER Pt ($\mu\text{mol hr}^{-1} \text{g}^{-1}$)	E_g (eV)	Yield (%)	T (%)	τ (ns)	Pd (wt. %)	IP (V vs SHE)	EA (V vs SHE)	f
P1-93		3,443	16,719	2.51	86	0.79	3	0.31	1.16	-1.71	9.64
P1-21		4,954	4,020	2.52	67	7.86	1.3	0.66	0.71	-1.76	2.43
P1-22		4,413	3,703	2.51	96	9.45	2.5	0.27	0.69	-1.71	4.56

Table 7 contains the data for the anthracene-based co-polymers P1-21 and P1-22 and the DBTS homopolymer P1-93. Despite the extended π -conjugated system on the anthracene units, these polymers are predicted to have considerably lower oscillator strengths than the equivalent phenylene co-polymers P1-3 and P1-16. This is because the additional π -electrons do not contribute to delocalisation along the direction of the polymer backbone and would predominantly interact with an orthogonal polarisation of light. Furthermore, the less-positive IP values for these molecules relative to P1-93 indicate that the HOMO is predominantly located on the anthracene unit, and the EA values remain unchanged and are probably located on the DBTS unit. As such, the HOMO-LUMO orbital mixing during the interaction with light will be minimal, resulting in a smaller transition dipole moment and smaller oscillator strength.

It is worth noting that the measured optical bandgaps of the DBTS-anthracene co-polymers are similar to those for all the other co-polymers discussed in this section, despite the considerably narrower

fundamental gap ($E_{\text{Fund}} = q(\text{IP} - \text{EA})$). This reinforces the idea that the HOMO-LUMO transition does not occur with any appreciable probability. It also indicates that the lowest energy transition likely involves deeper molecular orbitals that lie lower in energy than the HOMO.

Given the structural similarities between P1-21/P1-3 and P1-22/P1-16, the orbitals involved in the optical transitions are likely very similar. This would explain the similar optical band gaps. The lack of overlap between the HOMO and LUMO orbitals also indicate a spatial separation of photogenerated electron and holes. It would also explain why achieving longer excited state lifetimes is possible despite a small fundamental gap.

2.6.1.3 Fused macrocycles

As indicated above, larger oscillator strengths do not always lead to enhanced photocatalytic rates after Pt deposition. To understand why so many samples with large oscillator strengths are effective photocatalysts, we must also consider fused macrocycles in which torsional rotation of phenylene groups along the direction of the polymer backbone is not possible.

Table 8: Computationally and experimentally derived values relating to the DBTS co-polymers containing two p-phenylene units along the polymer backbone.

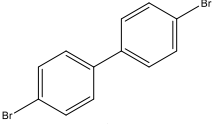
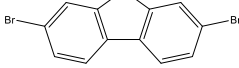
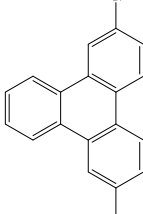
Polymer	Monomer	HER No Pt ($\mu\text{mol hr}^{-1}$ g^{-1})	HER Pt ($\mu\text{mol hr}^{-1}$ g^{-1})	E_g (eV)	Yield (%)	T (%)	τ (ns)	Pd (wt. %)	IP (V vs SHE)	EA (V vs SHE)	f
P1-16		2,295	3,764	2.59	Quant	4.74	2.2	0.32	1.04	-1.92	9.99
P1-89		8,390	12,869	2.46	Quant	3.88	2.1	0.14	0.92	-1.90	9.81
P1-23		5,631	10,155	2.52	Quant	5.12	3.05	0.14	1.04	-1.85	9.83

Table 8 compares three DBTS co-polymers in which the second monomer contains a biphenyl unit along the direction of the backbone. All three were synthesised with over 100% yield and are predicted to have very similar oscillator strengths. However, the para-linked phenyl rings in P1-89 and P1-23 are co-planar, i.e., they have a dihedral angle of 0° due to their fused ring structures. In both cases, the

HER rate is considerably higher than the biphenyl co-polymer P1-16. Both samples also exhibit significant increases in activity following the addition of a Pt co-catalyst.

In general, co-planar backbones in linear conjugated polymers have been associated with decreased exciton binding energies, which lead to increased exciton dissociation yields and increased charge carrier mobility.^{60,134,200,201} In general, the improvements can be attributed to enhanced spatial delocalisation along the polymer backbone, which is broken by rotation around the dihedral bond.

Given that co-planar monomers must contain multiple rings along the direction of the backbone by definition, it is important to reconsider the role of the oscillator strength with respect to the high HER rates. Figure 84 plots the HER rate against the oscillator strength for monomers that contain two or more aromatic rings along the polymer backbone and separates them according to whether they are co-planar or if torsional angles can be introduced via non-coplanar dihedral bonds. Clearly, large coplanar rings are essential to obtain active photocatalysts with large oscillator strengths. However, this graph also highlights that a coplanar structure does not guarantee large oscillator strengths and those with large oscillator strengths are not guaranteed to be active.

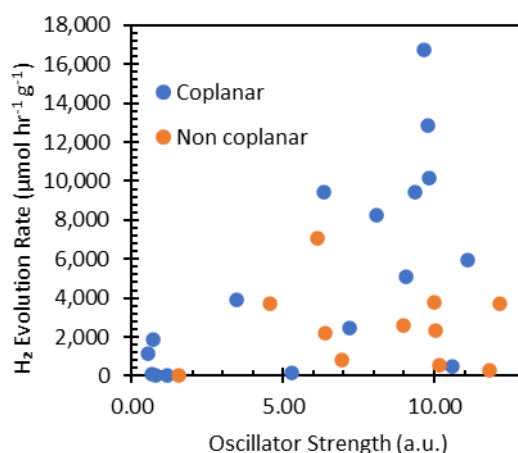
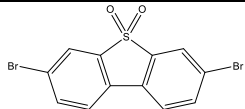
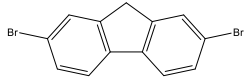
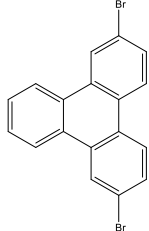
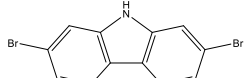
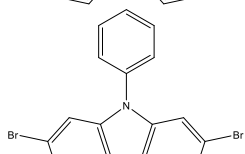
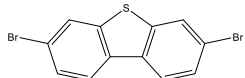
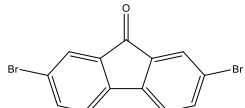
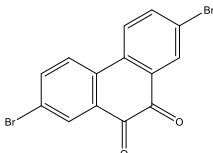
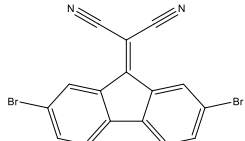


Figure 84: Impact of co-planarity on the photocatalytic hydrogen evolution activities in co-polymers containing two or more para-linked phenylene units along the direction of the polymer backbone. HER rates are plotted against their predicted oscillator strengths.

Table 9 summarises the measured and predicted properties of several co-planar monomers. P1-96, P1-44, and P1-88 each have very small oscillator strengths despite coplanar biphenyl structures. In all three cases, this can be attributed to the more positive EA potentials, which indicate that the LUMO is located on the variable monomer unit. This is related to the presence of easily-reducible electron-withdrawing functional groups that are directly conjugated with the polymer backbone. As for the anthracene-containing polymers, this likely results in localised electron density perpendicular to the

direction of the backbone and poor overlap between HOMO and LUMO orbitals and hence small oscillator strengths. Their narrow bandgaps and small EA potentials result in very short lifetimes and a weak driving force for charge separation at the polymer/co-catalyst interface.

Table 9: Coplanar monomers

Polymer	Monomer	HER No Pt ($\mu\text{mol hr}^{-1}$ g^{-1})	HER Pt ($\mu\text{mol hr}^{-1}$ g^{-1})	E_g (eV)	Yield (%)	T (%)	τ (ns)	Pd (wt. %)	IP (V vs SHE)	EA (V vs SHE)	f
P1-93		3,443	16,719	2.51	86	0.79	3	0.31	1.16	-1.71	9.64
P1-89		8,390	12,869	2.46	Quant	3.88	2.1	0.14	0.92	-1.90	9.81
P1-23		5,631	10,155	2.52	Quant	5.12	3.05	0.14	1.04	-1.85	9.83
P1-90		5,288	5,089	2.45	96	2.8	2.36	0.25	0.85	-2.00	9.06
P1-32		9,772	9,422	2.31	85	2.68	1.08	0.26	0.89	-1.92	9.36
P1-92		8,462	9,422	2.55	Quant	5.1	2.23	0.15	1.02	-1.86	6.36
P1-96		1,854	1,869	2.14	90	15.55	0.74	0.29	1.16	-1.21	0.72
P1-44		0	1	1.85	94	3.21	0.69	0.33	1.33	-0.42	1.15
P1-88		0	81	1.95	63	19.83	0.69	0.27	1.15	-0.70	0.67

P1-90, P1-32, and P1-92 contain electron-rich 5-membered heterocyclic groups that act as electron donors. When paired with the DBTS unit, push-pull dynamics are engaged in the resulting D-A polymer structure. This process is summarised in Figure 85a, using P1-92 as an example. These resonance

structures also demonstrate that these D-A polymers can stabilise both positive and negative charges, indicating that stable polarons of either charge can be formed. Furthermore, resonance forms also indicate that conjugation and delocalisation along the backbone remain intact for both polaronic species, as shown in Figure 85b.

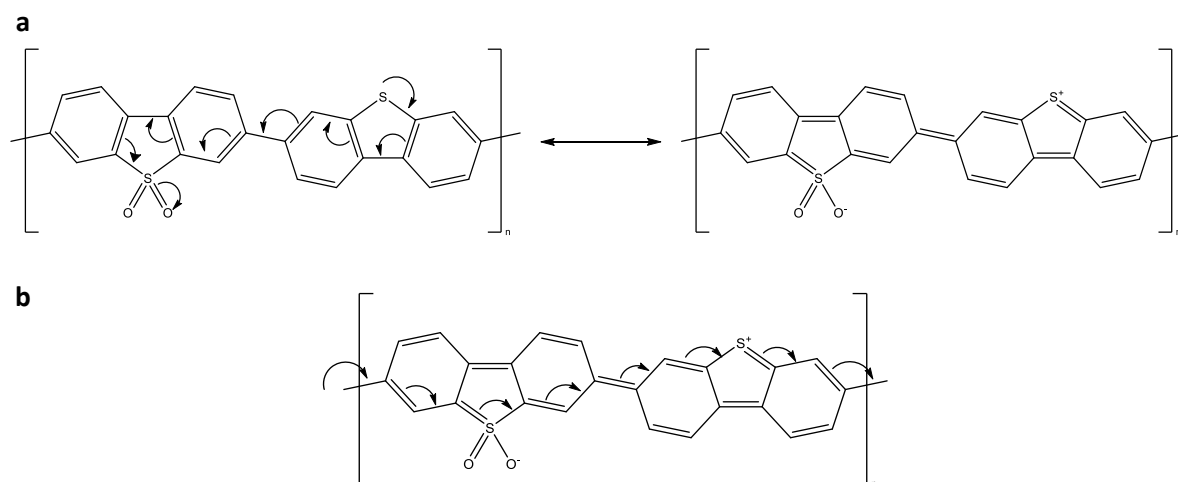


Figure 85: Resonance structures P1-92, a D-A polymer, demonstrating the ability of 5-membered heterocycles to act as electron donors capable of stabilising a positive charge. Figure b) shows that the delocalisation of electrons along the polymer backbone is maintained in polaronic and zwitterionic forms.

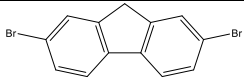
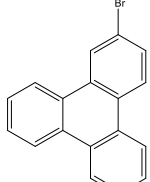
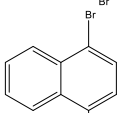
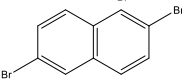
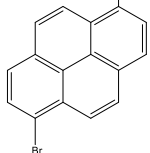
Interestingly, the photocatalytic activities of these D-A copolymers are not significantly improved by adding platinum compared to their activities from residual palladium. In contrast, the HER rates of P1-89 and P1-23, which do not contain electron-donating heteroatoms, significantly improve upon Pt addition.

Here three possible explanations for this discrepancy are described: i) $k_{Pt} \approx k_{Pd}$, i.e. the rate of charge transfer from the D-A polymers to platinum is insufficient to compete with that to palladium; ii) The D-A polymers are more sensitive to Pt concentration and lower loadings are required to obtain optimal improvements in photocatalytic activity; iii) If $k_r^* < k_{Pd}$, the HER rate is limited by TEA oxidation rather than by the charge transfer to co-catalyst. The shallower oxidation potentials (less positive IP) of D-A polymers suggest that photogenerated holes are concentrated on the donor monomers. The lower oxidation potential combined with the different reactive sites compared to P1-93 could result in slower oxidation of TEA. Furthermore, k_{Pd} is more likely to be relatively fast in these systems since the upward shift in the IP value also results in a negative shift of the Fermi potential, resulting in faster charge separation, as shown in Figure 73g.

Table 10 compares some other hydrocarbon monomers with large oscillator strengths. In P1-14, the conjugation pathway along the polymer backbone travels along the naphthalene axis, whereas in P1-13, the axis of the naphthalene is perpendicular to the backbone, resulting in a smaller f and lower activity. This sample also did not disperse well in the reaction solution. P1-14 contains a significant amount of residual palladium, which may explain why its activity did not improve upon adding Pt.

P1-24 has a surprisingly small oscillator strength, given that it contains four conjugated phenylene rings. However, pyrene is a highly symmetric chromophore known for its weak symmetry-forbidden optical transitions that result from small transition dipole moments.²⁰² Furthermore, the lateral displacement of the two bromine groups indicates that the conjugation pathway of electrons along the polymer backbone, which is ideally linear and aligned with the polarisation of the incident light, may be hindered by the change in direction and also hinders the induction of a large oscillating dipole. These factors may account for the relatively poor photocatalytic performance despite its large oscillator strength and co-planar structure.

Table 10: Comparison of experimentally- and computationally-determined values relating to DBTS co-polymers containing macrocyclic hydrocarbon co-monomers.

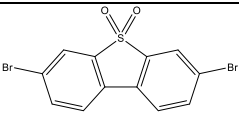
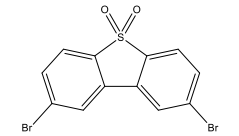
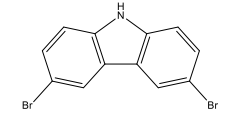
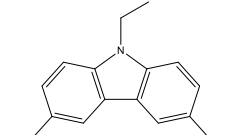
Polymer	Monomer	HER No Pt ($\mu\text{mol hr}^{-1}$ g^{-1})	HER Pt ($\mu\text{mol hr}^{-1}$ g^{-1})	E_g (eV)	Yield (%)	T (%)	τ (ns)	Pd (wt. %)	IP (V vs SHE)	EA (V vs SHE)	f
P1-89		8,390	12,869	2.46	Quant	3.88	2.1	0.14	0.92	-1.90	9.81
P1-23		5,631	10,155	2.52	Quant	5.12	3.05	0.14	1.04	-1.85	9.83
P1-13		613	764	2.43	92	42.3	0.85	0.41	1.01	-1.91	5.21
P1-14		8,742	8,228	2.56	Quant	3.63	1.88	0.67	0.99	-1.87	8.11
P1-24		1,986	2,484	2.38	75	7.5	1.6	0.19	0.71	-1.71	7.22

2.6.1.4 Oscillator Strength as an Indicator of Conjugation

As discussed above, the oscillator strength depends on the number of conjugated π -bonds delocalised along the polymer backbone. It is considerably larger when both the HOMO and LUMO orbitals involved in a transition are parallel to the backbone. However, the oscillator strength, as a metric for the prediction of photocatalytic activity, does not account for the structural disorder that torsional angles around freely-rotating dihedral bonds may introduce.

A break in conjugation can explain the remaining group of coplanar monomers with smaller oscillator strengths. These polymers are presented in Table 11. In the cases of P1-91, P1-94, and P1-95, the polymer backbone will have a bent structure, preventing the formation of extended molecular orbitals delocalised over several monomers.⁶⁰ This would limit the magnitude of any oscillating dipole induced by incident electromagnetic radiation, resulting in smaller transition dipole moments.

Table 11: Comparison of experimentally- and computationally-determined values relating to DBTS co-polymers containing macrocyclic co-monomers without complete delocalisation of charges along the backbone. P1-93 provided as a point of comparison.

Polymer	Monomer	HER No Pt ($\mu\text{mol hr}^{-1} \text{g}^{-1}$)	HER Pt ($\mu\text{mol hr}^{-1} \text{g}^{-1}$)	E_g (eV)	Yield (%)	T (%)	τ (ns)	Pd (wt. %)	IP (V vs SHE)	EA (V vs SHE)	f
P1-93		3,443	16,719	2.51	86	0.79	3	0.31	1.16	-1.71	9.64
P1-94		1,836	3,932	2.71	95	0.49	2.58	0.30	1.32	-1.85	3.49
P1-91		84	1,130	2.17	75	57.35	1.41	0.17	0.66	-2.08	0.53
P1-95		350	127	2.13	95	76.76	1	0.38	0.65	-2.06	5.29

The break in conjugation can also be rationalised qualitatively by considering the resonance structures of some of these monomers, as shown in Figure 86. Here, we see that conjugation through the monomer along the backbone of the neutral monomer is possible for P1-93, but not for P1-94.

P1-94 still retains a reasonable level of photocatalytic activity due to the favourable IP and EA potentials. The additional sulfone functional group should also enhance the interaction with the solvent mixture and provide additional reactive sites for TEA oxidation. The predicted IP values for P1-91 and P1-95 indicate that these polymers provide no obvious thermodynamic driving force to initiate the TEA oxidation reaction ($E_{\text{TEA}/\text{TEAR}} = 0.7 \text{ V vs SHE}$). This may explain why their photocatalytic activities are an order of magnitude smaller than P1-94.

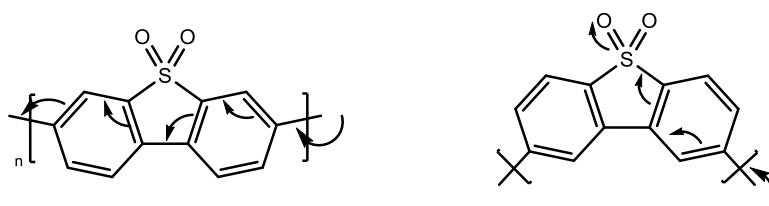


Figure 86: Example of how resonance structures can be used to show when conjugation is partially broken along the polymer backbone in the neutral state according to the linkage positions. Poor backbone delocalisation is connected with smaller oscillator strengths and poorer photocatalytic activities.

2.6.1.5 Special case: Benzophenone

Polymer	Monomer	HER No Pt ($\mu\text{mol hr}^{-1}$ g^{-1})	HER Pt ($\mu\text{mol hr}^{-1}$ g^{-1})	E_g (eV)	Yield (%)	T (%)	τ (ns)	Pd (wt. %)	IP (V vs SHE)	EA (V vs SHE)	f
P1-47		4,462	7,076	2.75	Quant	13.52	2.13	0.38	1.40	-1.52	6.16

P1-47, containing the benzophenone unit, is a particularly interesting case. It does not have a fused macrocyclic structure. Instead, it is bent, and there is no one-step delocalisation pathway along the polymer backbone. The redox potentials also indicate a deep HOMO and a shallow LUMO that are typically not conducive to highly active photocatalysts. Despite these features, P1-47 is the 12th best photocatalyst both before and after Pt photodeposition. It also exhibits a large increase in activity following Pt deposition whilst containing relatively high levels of residual palladium. As such, this polymer is an outlier in many regards and would not necessarily have been identified from the database according to the criteria outlined in this chapter so far.

Benzophenone is a well-studied chromophore and is often used as a photocatalyst in organic synthesis reactions due to the efficient and rapid formation of a long-lived triplet state. The rate of ISC is fast because the transition from the $(n,\pi^*)^1$ into the $(\pi,\pi^*)^3$ state involves a change in orbital angular

momentum as well as a shift in the electron spin such that total momentum is conserved. Molecular benzophenone has already demonstrated its propensity for rapid charge transfer to TEA in several solvents.²⁰³ This charge transfer was followed by a hydrogen abstraction reaction to form a ketyl radical. However, Graetzel *et al.* identified that the ketyl intermediate is readily oxidised back to the initial ketone by transferring an electron to particles of metallic platinum, where hydrogen evolution takes place.²⁰⁴

In Graetzel's paper, the electron transfer rate from the ketyl radical to platinum was only limited by diffusion. Similar reaction mechanisms underpin most of the molecular photocatalysts used for hydrogen evolution today.²⁰⁵ However, this reaction pathway, in which the rapid formation of triplet states prolongs excited state lifetimes, is not typically considered when designing conjugated polymer photocatalysts. This result indicates that such polymer designs might be worth considering in the future.

Compared with molecular photocatalysts, the polymeric derivatives should have narrower bandgaps and smaller exciton binding energies. It is also possible to improve the wettability by pairing them with suitable co-monomers such as DBTS. Radical intermediates are also stabilised by delocalisation over the extended π -conjugated system.

2.6.2 Phenylene Co-monomers

So far, the discussion of structure/activity relationships has focussed on co-monomers containing multiple aromatic rings since these are associated with the largest oscillator strengths and most of the highest photocatalytic hydrogen evolution rates. This section will focus on the individual phenylene rings and their substituents.

2.6.2.1 Para- vs Meta-linked Phenylene Units

For the co-planar monomers, bent structures prevented the formation of extended regions of delocalisation. The position of the monomer linkages also weakened the conjugation along the backbone since no resonance forms could be delocalised across multiple polymer repeat units. These factors led to smaller oscillator strengths and poorer photocatalytic activities.

An equivalent parallel can be drawn when considering para-linked and meta-linked phenylene monomers. As shown in Figure 87, p-phenylene generates a linear structure in which electrons are

completely delocalised along the polymer backbone, whereas the meta-linkage limits delocalisation through the m-phenylene monomer.

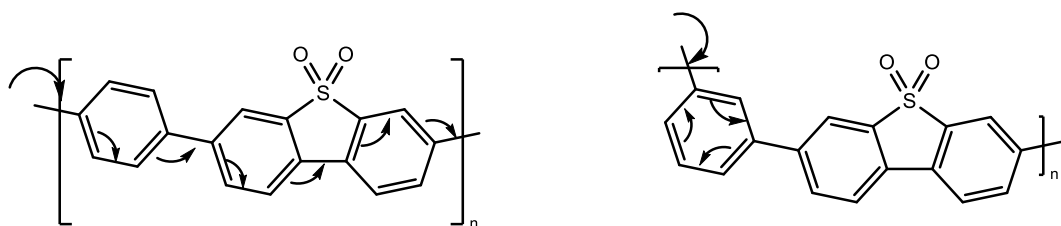


Figure 87: Example of how resonance structures can be used to show when conjugation is partially broken along the polymer backbone in the neutral state according to the linkage positions. Applied to a co-polymers containing meta-linked phenylene units. Poor backbone delocalisation relates to smaller oscillator strengths and poorer photocatalytic activities.

The data relating to a subset of related meta- and para-linked phenylene co-polymers are presented in Table 12. In the case of these two copolymers containing the unsubstituted phenylene units, P1-2 and P1-3, the oscillator strength of the m-Ph copolymer is substantially lower than that containing the p-phenylene unit. Despite this, the two sets of photocatalytic activities remain similar. However, P1-2 has a wider band gap, resulting in a more negative EA and a longer fluorescence lifetime, typically relating to improved activity, but still has a lower photocatalytic activity after loading with a Pt co-catalyst.

The exact relationship between residual palladium, structure, and photocatalytic activity remains unclear. However, both P1-2 and P1-3 contain high levels of palladium, which may also explain why they perform similarly.

The introduction of alkyl groups on the para-phenylene ring widens the bandgap, increases the fluorescence lifetime, and increases the photocatalytic activity when loaded with Pt. The optical and fundamental bandgaps of P1-6 and P1-7 are comparable to the meta-linked P1-2 and P1-5. This suggests that p-linked phenylene co-polymers can achieve higher photocatalytic activity relative to their m-linked equivalents.

Table 12: Comparison of DBTS co-polymers containing structurally similar m-linked phenylene units vs p-linked phenylene units.

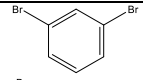
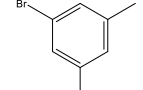
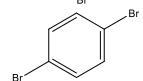
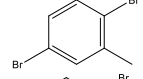
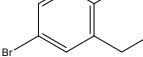
Polymer	Monomer	HER No Pt ($\mu\text{mol hr}^{-1} \text{g}^{-1}$)	HER Pt ($\mu\text{mol hr}^{-1} \text{g}^{-1}$)	E_g (eV)	Yield (%)	T (%)	τ (ns)	Pd (wt. %)	IP (V vs SHE)	EA (V vs SHE)	f
P1-2		2,254	3,166	2.7	84	9.11	2.59	0.35	1.24	-2.01	3.96
P1-5		3,363	3,350	2.71	Quant	10.05	2.53	0.39	1.27	-2.00	3.64
P1-3		1,948	3,815	2.45	Quant	3.51	1.55	0.42	1.12	-1.89	7.14
P1-6		2,658	6,463	2.63	76	28.67	2.4	0.41	1.18	-1.95	6.83
P1-7		652	7,671	2.69	36	52.04	2.43	0.21	1.25	-2.00	6.58

Figure 88a plots the HER rates of the Pt-loaded co-polymers containing m- and p-phenylene monomers against the oscillator strength. As expected, on average, polymers containing p-phenylene units have larger oscillator strengths and higher photocatalytic activities. However, as in the case of the co-planar monomers, the oscillator strength still depends on the nature of the functional groups on the phenylene ring.

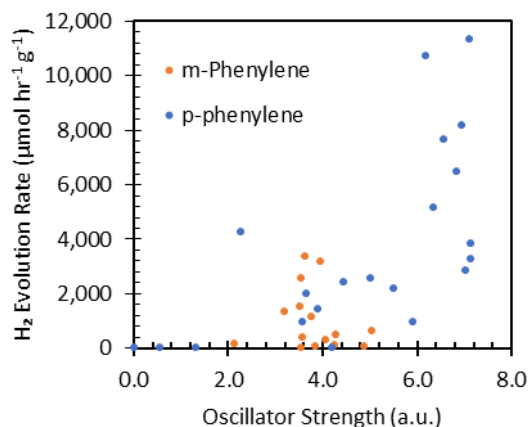


Figure 88: HER photocatalytic activities (1 wt. % Pt) for DBTS co-polymers containing m-linked and p-linked phenylene units and their associated oscillator strengths.

2.6.2.2 P-phenylene Co-monomers

The remainder of this section will focus on the polymers containing various p-phenylene monomer units. This subset of copolymers is the largest, containing structurally related polymers whose properties can be compared and contrasted directly.

This subset contains 21 polymers that can be categorised according to the nature of their functional groups, i.e. whether they are electron-donating or electron-withdrawing and whether they act via mesomeric or inductive pathways. Example structures of each are given in Figure 89. Electron-withdrawing groups (EWG) can stabilise a negative charge that is delocalised along the polymer backbone, whereas electron-donating groups (EDG) stabilise positive charges. Mesomeric groups enable the complete delocalisation of electrons onto the functional groups via extended pi-conjugated systems, whereas inductive functional groups do not.

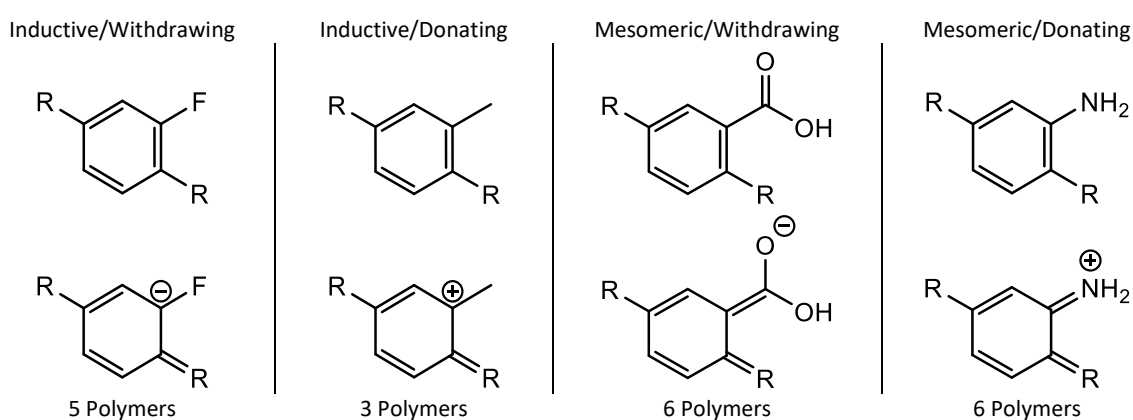


Figure 89: Examples of phenylene-based electron-donating and electron-withdrawing substituents. Top row reprints the neutral monomers and the bottom row demonstrates how these functional groups stabilise resonance structures and delocalised charges along the polymer backbone.

In terms of the electronic structure, these structural changes have predictable effects on the ground state. For example, EDGs destabilise the frontier orbitals (i.e. shifting their IP and EA potentials to more negative values), making oxidation more energetically favourable and reduction favourable. EWGs stabilise the frontier orbitals (i.e. making their energies more negative), increasing the probability of reduction and decreasing the probability of oxidation. These changes can be seen in variations of the IP and EA energies.

In terms of conjugated linear copolymers, the impact of changing the functional groups on one monomer on the overall HOMO and LUMO energies is less evident, as electron density is delocalised over both monomers in the repeat unit. The HOMO and LUMO are often spatially separated and concentrated on whichever unit has more donating or withdrawing character, respectively.

Figures 90a and 90b present the HER rates for each P1-X copolymer containing a derivative of a p-phenylene monomer unit relative to the IP and EA potentials. These rates represent those before Pt photodeposition. The polymers have been categorised according to the nature of the functional group on the phenylene unit.

Relative to P1-3, which contains the unsubstituted phenylene monomer, the IP is shifted to more positive potentials for polymers containing EWGs. When the polymer contains mesomeric EDGs, the IP is shifted to more positive values. However, with inductive EDGs, the IP only shifts marginally to more positive values relative to P1-3. Although this latter shift is in the opposite direction than expected, it is consistent with the wider bandgap observed for these alkyl-containing polymers (Figure 90c). This wider bandgap may arise from geometric constraints. The optimal conformation of the polymers containing bulky methyl and ethyl groups may result in larger torsional angles and reduced delocalisation along the backbone. The EA potential is shifted towards more positive values for polymers containing EWGs and more negative values for polymers containing EDGs.

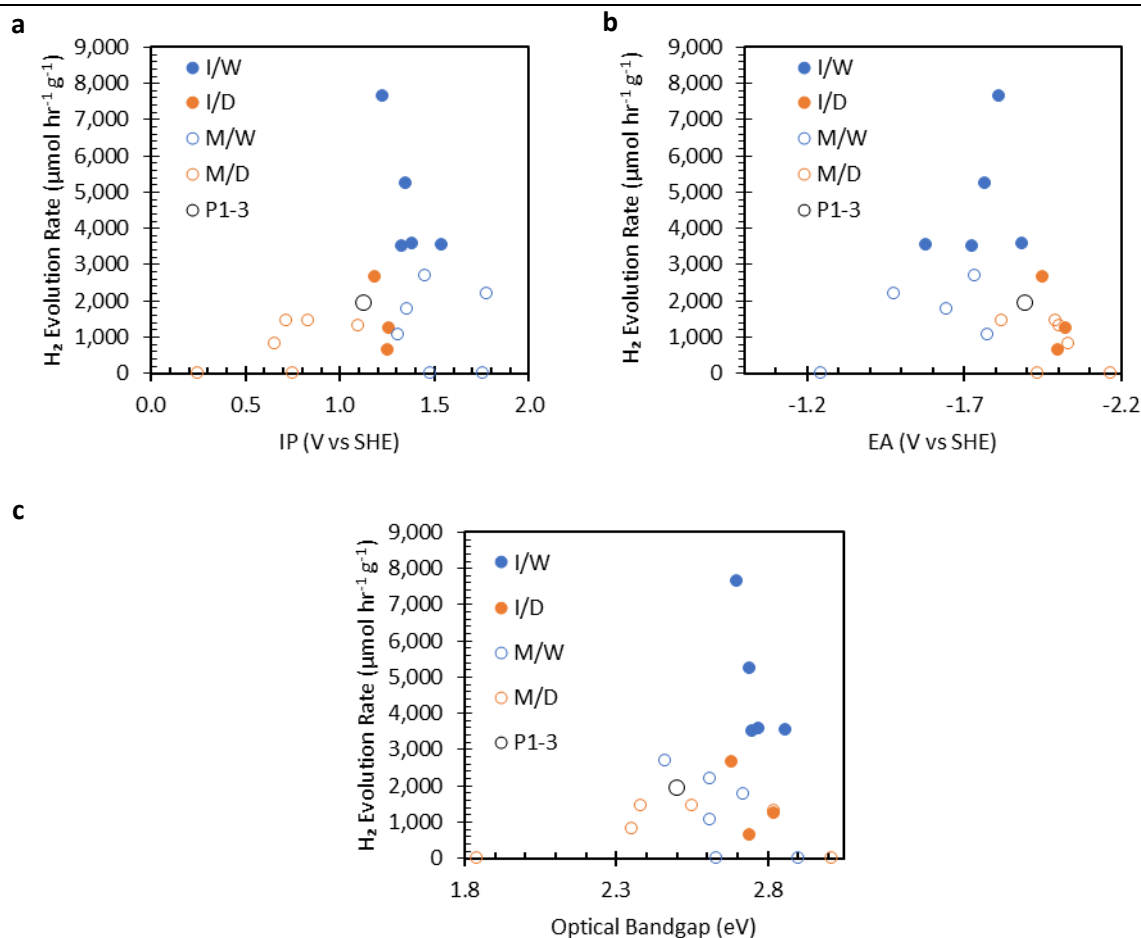


Figure 90: Photocatalytic hydrogen evolution rates (No Pt) of DBTS co-polymers containing p-phenylene comonomers. Polymers are categorised according to their electron donating (orange) and electron withdrawing (blue) characteristics, and according to whether that contribution is predominantly mesomeric (hollow) or inductive (filled). The unsubstituted para-phenylene copolymer (P1-3) is represented by a hollow black data point. The impact of functional groups on the IP, EA and optical bandgap are presented in graphs a, b, and c, respectively.

Inductive functional groups correspond to polymers with larger oscillator strengths (Figure 91). Since these functional groups do not contain conjugated π -electrons, the transition dipole moment will likely be oriented parallel to the polymer backbone and lead to larger oscillator strengths. Meanwhile, π -conjugated mesomeric substituents on the phenyl ring are more likely to result in spatially separated frontier orbitals and a transition dipole moment oriented perpendicularly to the polymer backbone, leading to smaller oscillator strengths.

Phenyl rings containing inductive electron-withdrawing groups perform the best when relying on the residual palladium as a co-catalyst. This can be attributed to the large oscillator strengths and the ability to stabilise the negatively-charged polaron that forms following the charge transfer to TEA and before the charge transfer to palladium.

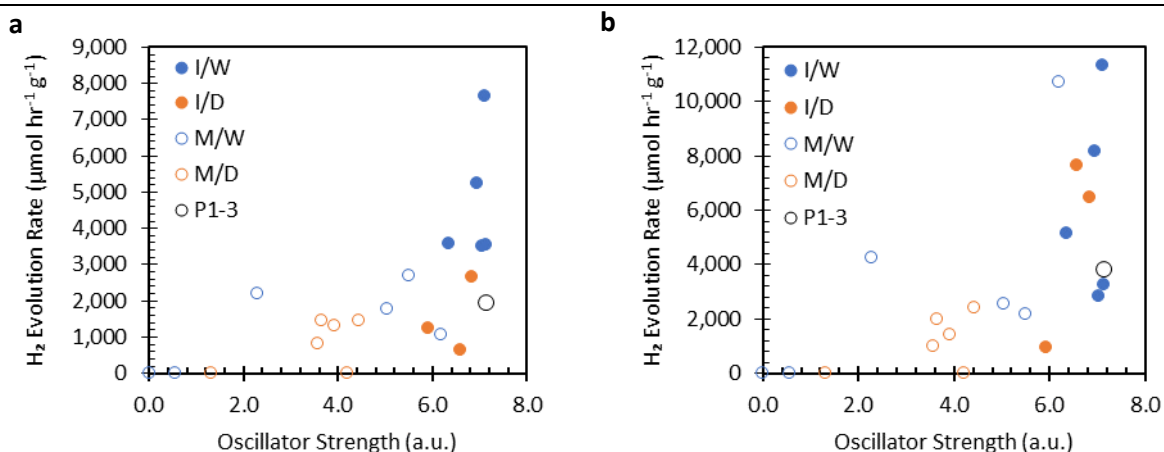


Figure 91: Photocatalytic hydrogen evolution rates of DBTS co-polymers containing p-phenylene comonomers before (left) and after (right) photodeposition of 1 wt.% Pt. HER rates are plotted against the predicted oscillator strengths.

After photodepositing Pt, the largest increases in photocatalytic activity are also observed amongst the polymers with the largest oscillator strengths. However, not all polymers increase their activity evenly. The most important factors determining which samples exhibit the biggest increases in activity with Pt appear to be the initial rate with Pd and the concentration of Pd. Figure 92a shows the change in activity relative to the residual palladium concentration. The biggest increases in photocatalytic activity arise in samples containing low concentrations of Pd. The activity of samples containing high Pd concentrations decreased after the photodeposition of Pt.

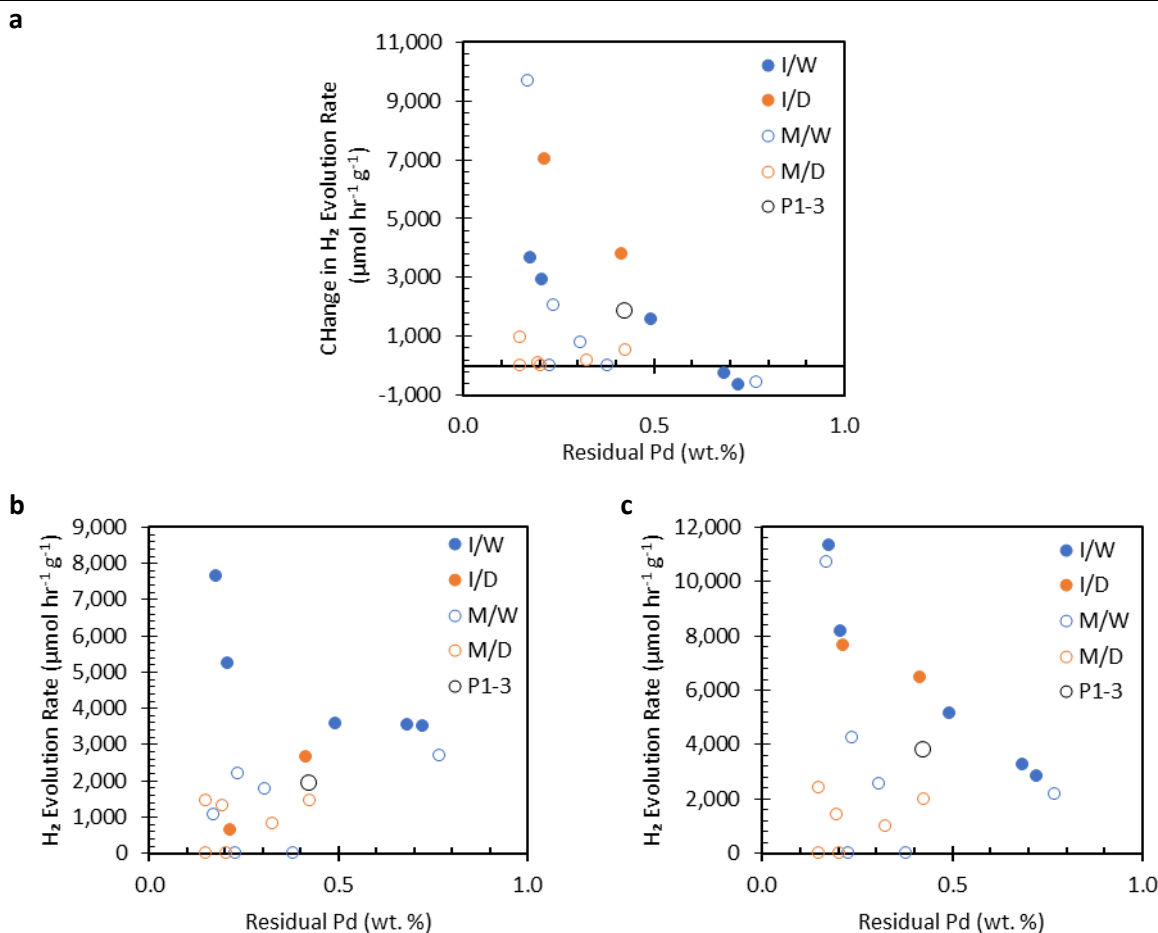


Figure 92: Photocatalytic hydrogen evolution rates of DBTS co-polymers containing p-phenylene comonomers before (b) and after (c) photodeposition of 1 wt.% Pt. HER rates are plotted against the residual palladium concentrations. Figure (a) plots the change in photocatalytic activity upon photodeposition of 1 wt.% Pt for each co-polymer.

Figures 92b and 92c demonstrate the relationship between photocatalytic activity before and after Pt photodeposition with respect to the residual Pd concentration. Whilst the I/W phenylene units demonstrate the highest photocatalytic activities when residual Pd acts as the only cocatalyst, the polymers' photocatalytic activities after Pt deposition appear to be limited by the residual Pd content, and the top performing polymers belong to both inductive groups and one mesomeric electron withdrawing polymer.

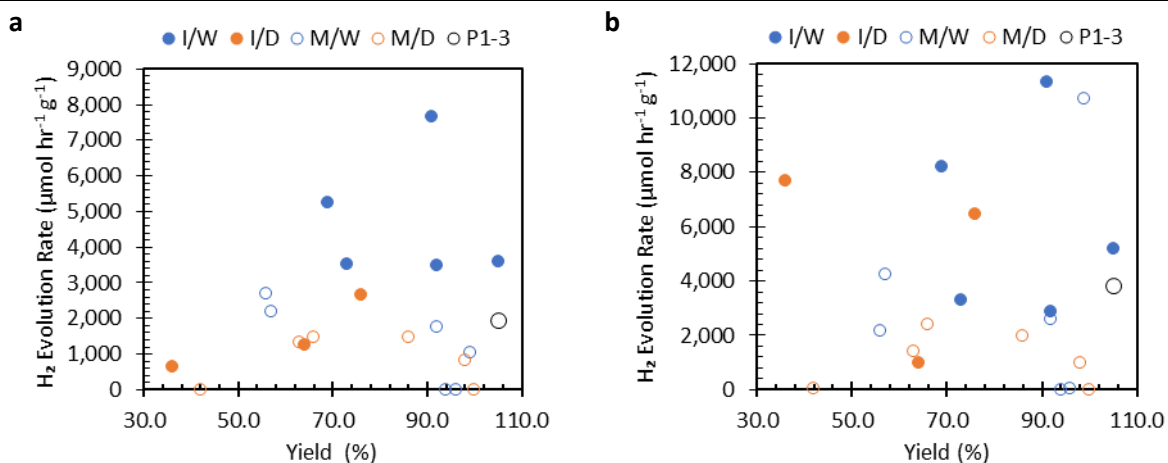


Figure 93: Photocatalytic hydrogen evolution rates of DBTS co-polymers containing p-phenylene comonomers before (a) and after (b) photodeposition of 1 wt.% Pt. HER rates are plotted against the synthesis yield.

Before Pt addition, the synthesis yield may have limited the photocatalytic activities of polymers containing inductive substituents on the phenyl ring (Figure 93a). However, this dependence on the yield appears to be relaxed upon adding Pt (Figure 93b). This would occur if charge transfer to residual Pd is slow and the photocatalyst reacts with impurities instead of water in the absence of Pt. Rapid transfer of electrons to Pt may preferentially drive the hydrogen evolution reaction after its photodeposition. After considering the low yield and low Pd content of P1-7, its slow Pd-catalysed HER rate and fast Pt-catalysed HER rate can be rationalised (see Table 12 for details).

Another important factor to consider when building an understanding of these structure-activity relationships is that of the fluorescence lifetime. As shown in Figure 94a, the samples exhibiting the longest lifetime also exhibited the highest photocatalytic activity. After the addition of Pt (as indicated by error bars), this trend becomes less clear, with the residual palladium concentrations defining the final photocatalytic activity. I/W polymers already achieve relatively fast HER rates with Pd, likely driven by longer excited state lifetimes and efficient transfer to Pd. As such, the I/D and M/W polymers with poor Pd-catalysed activities and shorter lifetimes benefit the most from Pt addition.

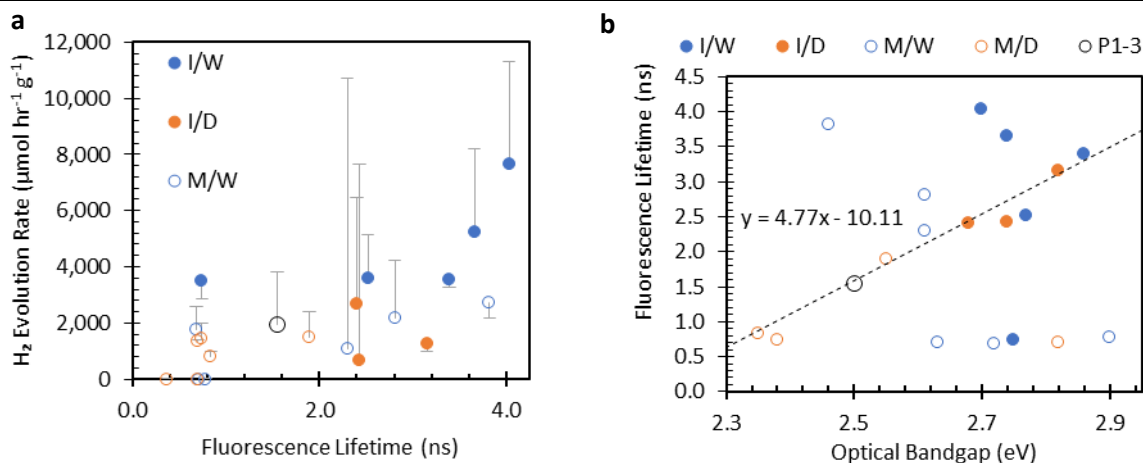


Figure 94: a) Photocatalytic hydrogen evolution rates of DBTS co-polymers containing p-phenylene comonomers before photodeposition of 1 wt.% Pt. HER rates are plotted against the fluorescence lifetime. Error bars represent the change in activity after photodeposition. Figure (b) plots the relationship between the optical bandgap and the fluorescence lifetime for the same polymers.

Generally, the longer lifetimes also correspond to the wider optical bandgaps (Figure 94b). However, there are some apparent exceptions to this rule. The lifetime is also related to the residual palladium concentration. As discussed earlier in section 2.4.1, high palladium concentrations typically result in shorter fluorescence lifetimes. However, of the 99 synthesised polymers, there are two exceptions to this rule: P1-64 and P1-37. Figure 95a presents the relationship between the fluorescence lifetime and residual palladium concentration for the p-phenylene copolymers. Figure 95b presents the same plot, but the data point areas correspond to the change in photocatalytic activity upon photodeposition of Pt.

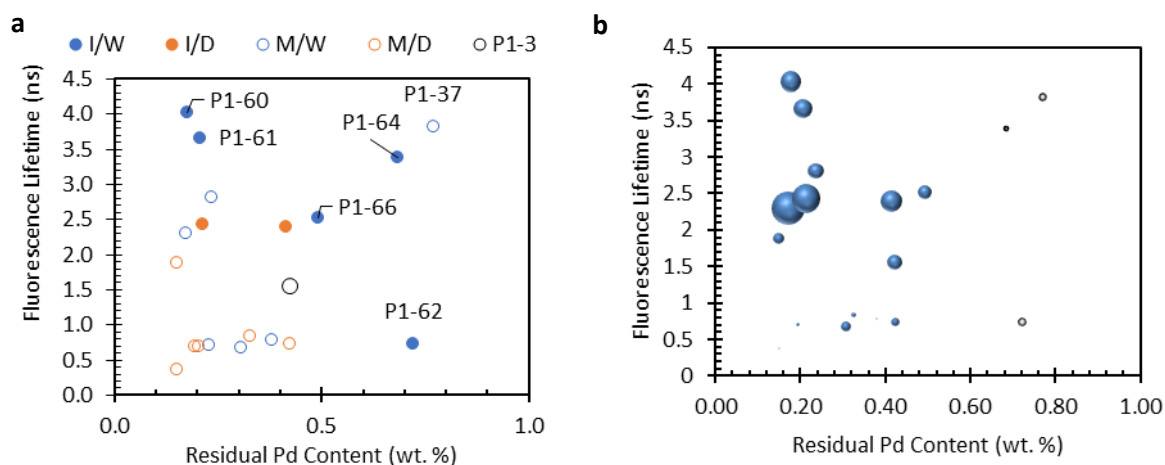
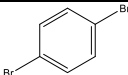
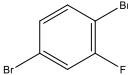
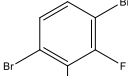
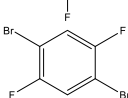
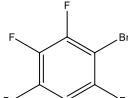
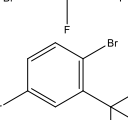
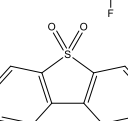


Figure 95: Relationship between fluorescence lifetime and residual palladium concentration. Data points in graph (a) are categorised according to the nature of the phenylene substituent. Data point areas in graph (b) represent the change in photocatalytic activity upon photodeposition of 1 wt. % Pt.

P1-60, P1-61, P1-62, and P1-66 all have similar optical bandgaps. However, their fluorescence lifetimes differ dramatically. The relative concentrations of residual palladium can likely explain this variation. However, P1-64 is structurally very similar. The optical bandgap dominates its fluorescence lifetime, which is unaffected by the polymer's high residual palladium content. Despite this, the photocatalytic activity of P1-64 appears to be significantly inhibited by the residual Pd.

To understand these trends, we must consider all properties together alongside the specific structures. Table 13 contains the tabulated data for the p-phenylene co-polymers containing inductive electron-withdrawing substituents. P1-3 and P1-93 are also presented for reference.

Table 13: Comparison of DBTS co-polymers containing inductive electron-withdrawing p-phenylene co-monomer. P1-93 is presented for comparison of values with the DBTS-DBTS homopolymer.

Polymer	Monomer	HER No Pt ($\mu\text{mol hr}^{-1} \text{g}^{-1}$)	HER Pt ($\mu\text{mol hr}^{-1} \text{g}^{-1}$)	E_g (eV)	Yield (%)	T (%)	τ (ns)	Pd (wt. %)	IP (V vs SHE)	EA (V vs SHE)	f
P1-3		1,948	3,815	2.45	Quant	3.51	1.55	0.42	1.12	-1.89	7.14
P1-60		7,649	11,320	2.65	91	9.85	4.03	0.18	1.23	-1.81	7.11
P1-61		5,248	8,195	2.69	69	5.94	3.66	0.21	1.35	-1.77	6.95
P1-62		3,501	2,862	2.7	92	12.08	0.74	0.72	1.33	-1.72	7.04
P1-64		3,534	3,274	2.81	73	9.6	3.39	0.68	1.54	-1.58	7.13
P1-66		3,581	5,162	2.72	Quant	63.72	2.52	0.49	1.38	-1.88	6.35
P1-93		3,443	16,719	2.51	86	0.79	3	0.31	1.16	-1.71	9.64

As shown in Figure 96a, the improved photocatalytic activity of P1-60 and P1-61, relative to the other inductive withdrawing phenylene groups, correspond with their low residual palladium content. These polymers also exhibit the most significant increases in photocatalytic activity after Pt addition. Meanwhile, P1-62 and P1-64 are poor Pd-catalysed photocatalysts, and their activities decrease with Pt addition. These trends can be associated with their high residual Pd content.

These polymers' weighted average fluorescence lifetimes range from 4 to 0.7 ns. Except for P1-64, these can also be inversely correlated with the residual Pd content, as shown in Figure 96b. The fluorescence lifetime of P1-64 matches that which would be expected based on the optical bandgap alone (as shown by the trendline of Figure 94b). The optical bandgap also explains why P1-3 and P1-66 exhibit different lifetimes despite similar palladium concentrations.

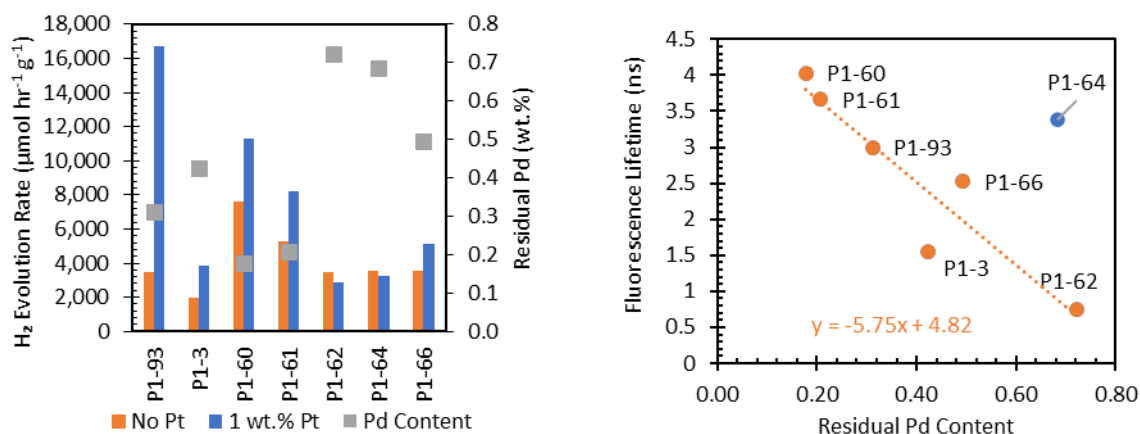


Figure 96: a) HER rates for DBTS co-polymers containing p-phenylene co-monomers substituted with fluorinated functional groups that are inductively electron-withdrawing. P1-93 (the DBTS-DBTS homopolymer) and P1-3 (DBTS-Ph co-polymer containing an unsubstituted phenylene unit) are presented for comparison. HER rates are presented before and after photodeposition of 1 wt.% Pt. Residual palladium concentrations are plotted on the secondary axis. **b)** relationship between residual palladium concentration and fluorescence lifetimes for these samples.

One possible explanation for the unusually-long fluorescence lifetime of P1-64 arises from consideration of the polymer's redox potentials. Although only by a small degree, P1-64 has the lowest-energy LUMO and the deepest Fermi level, assuming undoped intrinsic semiconductor characteristics. This results in a small space-charge region at the semiconductor-metal interface and minimises the energy barrier for the transfer of electrons from reduced Pd back into the polymer.

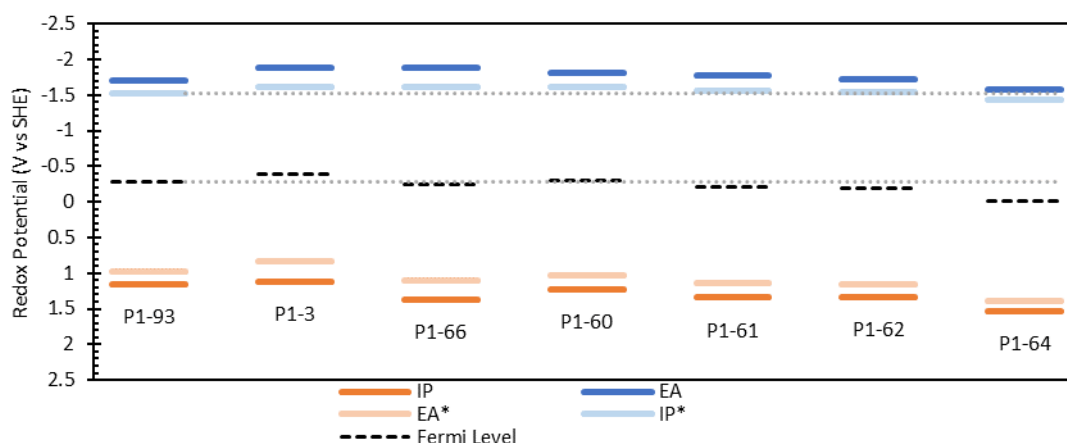


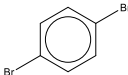
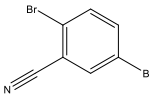
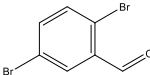
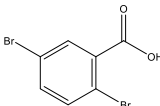
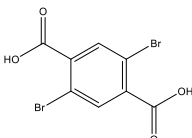
Figure 97: IP and EA values for several co-polymers containing fluorinated p-phenylene moieties. P1-93 and P1-3 are also presented for reference. Fermi potentials for each polymer are presented as dashed black lines. IP* and EA* potentials are estimated from the EA values, IP values, and the measured optical bandgap.

Despite the extended excited state lifetime of P1-64 compared with P1-62, there is no clear advantage to the photocatalytic HER rate before or after Pt deposition. This implies that the exact causal relationship between Pd concentration and photocatalytic activity is complicated and cannot be explained by the impact of Pd on the excited state lifetime alone. It is important to note that fluorescence lifetimes only provide limited information. Photoluminescence quantum yields could provide important information regarding the proportion of absorption events that lead to non-radiative decay. This could provide important information if palladium assists intersystem crossing via the (internal or external) heavy atom effect.

These systems should be considered in more detail to understand the exact relationship between fluorinated phenylene rings and photocatalytic activity. For example, further optimisation of the synthesis procedure could produce polymers with higher synthetic yields, lower palladium levels, and improved dispersibility. Identifying optimal platinum loading concentrations may also lead to enhanced photocatalytic activities since these polymers appear to be particularly sensitive to co-catalyst loading concentrations.

Although P1-60 performed the best in this high throughput experiment, it also exhibited the longest fluorescence lifetime, the lowest residual palladium concentration, and was obtained with a 91% yield. P1-61, meanwhile, was obtained with a 69% yield. This difference alone may explain why it performed worse despite containing a similarly low Pd concentration and exhibiting an equally long excited state lifetime.

Table 14: Comparison of DBTS co-polymers containing electron-withdrawing mesomeric functionalised p-phenylene comonomers.

Polymer	Monomer	HER No Pt ($\mu\text{mol hr}^{-1}\text{g}^{-1}$)	HER Pt ($\mu\text{mol hr}^{-1}\text{g}^{-1}$)	E_g (eV)	Yield (%)	T (%)	τ (ns)	Pd (wt. %)	IP (V vs SHE)	EA (V vs SHE)	f
P1-3		1,948	3,815	2.45	Quant	3.51	1.55	0.42	1.12	-1.89	7.14
P1-27		1,053	10,721	2.56	99	3.46	2.3	0.17	1.30	-1.78	6.19
P1-33		1,772	2,579	2.67	92	1.13	0.68	0.31	1.35	-1.64	5.03
P1-37		2,710	2,161	2.41	56	15.92	3.82	0.77	1.45	-1.73	5.51
P1-39		2,191	4,245	2.56	57	10.97	2.81	0.24	1.77	-1.48	2.29

Of the mesomeric electron-withdrawing phenylene polymers, the only polymer that competes with the inductive photocatalysts is P1-27. This polymer was synthesised with 99% yield and only contained 0.17 wt.% residual Pd. In the case of inductive fluorinated phenylene monomers, this would result in a high HER rate when using Pd as the only co-catalyst. However, the photocatalytic activity of P1-27 is relatively low, producing only $1.1 \text{ mmol hr}^{-1}\text{g}^{-1}$ under these conditions. However, the HER rate increases significantly to $10.7 \text{ mmol hr}^{-1}\text{g}^{-1}$ following the addition of Pt.

The only other polymer to exhibit such a significant jump in performance upon the addition of Pt is P1-93, the DBTS homopolymer. For these polymers, charge transfer to palladium appears slow and ineffective, whereas charge transfer to Pt is efficient. Overall, the promising performance of these polymers may be attributed to the fact that they are not negatively impacted by palladium contamination like the fluorinated derivatives are.

Importantly, the cyano group is known to be an effective ligand for Pt and Pd and will likely contain a localised negative charge in negatively charged polaron. This could lead to selective photodeposition of Pt atoms at the cyano functions groups, in which the nitrogen atom acts as an anchor to connect the polymer to the metal cocatalyst and facilitate rapid charge transfer. Although further investigations are necessary to confirm this hypothesis, initial studies involving cyano functional groups have shown them to be very promising as polar electron acceptor groups in effective D-A polymers.²⁰⁶ In this study, the enhancements were ascribed to enhanced hydrophilicity, exciton charge separation along the backbone, and charge transfer to platinum.

The mesomeric electron-withdrawing delocalisation in P1-33, P1-37, and P1-39 arises from carbonyl bonds that are conjugated with the polymer backbone. As discussed in the case of the benzophenone monomer, carbonyls can complicate the resulting photochemistry due to the potential for intersystem crossing between (n,π^*) and (π,π^*) singlet and triplet states. Furthermore, the excited states of these functional groups are often also highly reactive, leading to photooxidation or photoreduction of the functional group itself.

P1-33 contains an aldehyde group which may be oxidised to the carboxylic acid or reduced to the alcohol. This reactivity may explain why its excited state lifetime is very short, despite medium levels of palladium and a relatively wide bandgap. Since fluorescence lifetime measurements were performed as dispersions in water under ambient conditions, oxygen may be involved in these reactions. Molecular oxygen is also known to effectively quench the triplet state.

P1-37 is the other outlier in which high palladium concentrations do not lead to short fluorescence lifetimes. However, this can be rationalised in the same way as P1-64. Figure 98 plots the IP and EA potentials for these mesomeric electron-withdrawing p-phenylene co-polymers and compares them with P1-93. Whilst the EA potential of P1-37 is almost exactly the same as in P1-93, its bandgap is substantially smaller than the fundamental gap. Shifting the IP and EA positions according to this difference presents an estimation of the IP* and EA* potentials. Here, the IP* of P1-37 lies below that of P1-93. The Fermi level of P1-37 is also below that of P1-93. Similar to the P1-64 case, this provides an avenue for the back transfer of electrons from residual palladium back into the polymer's LUMO, preventing quenching and extending the fluorescence lifetime. This charge transfer process with Pd may also explain why the excited state lifetime of P1-37 is so long despite its narrow bandgap.

P1-39 has a very similar electronic structure to P1-37. However, since it contains significantly less Pd, it is unknown whether its lifetime would remain unchanged at higher Pd concentrations. As in the cases of P1-62 and P1-64, the change in photocatalytic activity upon loading with Pt primarily depends on the residual Pd content. The photocatalytic activity of P1-39 (low Pd) increases, whereas that of P1-37 (high Pd) decreases, as shown in Figure 99. The smaller oscillator strength of P1-39 relative to P1-37 also agrees with previous observations that increased conjugation outside the direction of the polymer backbone results in smaller oscillator strength. The IP/EA potential alignment of P1-39 vs P1-93 is also the largest, indicating that HOMO and LUMO orbitals have substantially different spatial configurations in the two cases.

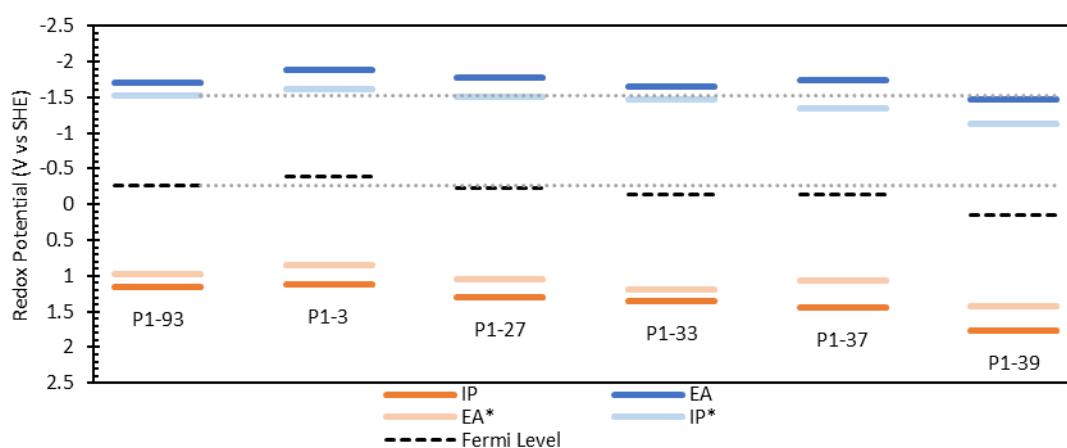


Figure 98: IP and EA values for several co-polymers containing p-phenylene moieties substituted with mesomeric electron-withdrawing groups. P1-93 and P1-3 are also presented for reference. Fermi potentials for each polymer are presented as dashed black lines. IP* and EA* potentials are estimated from the EA values, IP values, and the measured optical bandgap.

Consideration of the IP and EA levels also highlights the alignment of the LUMO energies of P1-93 and P1-27. This implies that the LUMO is more likely to be delocalised over both the Ph-CN and DBTS monomers, leading to a larger oscillator strength for P1-27 relative to the carbonyl-containing derivatives.

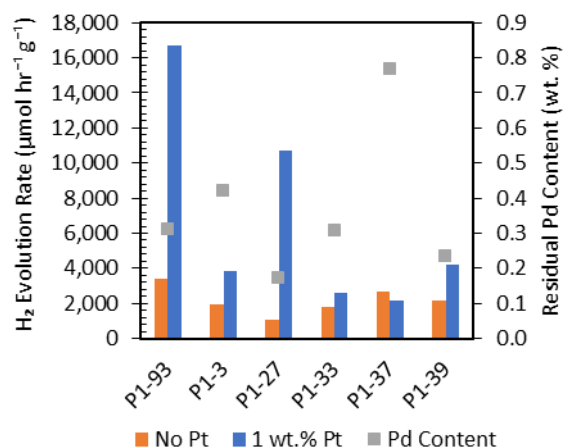
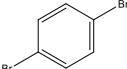
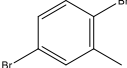
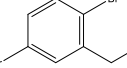
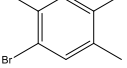


Figure 99: HER rates for DBTS co-polymers containing p-phenylene co-monomers substituted with mesomeric electron-withdrawing functional groups. P1-93 and P1-3 are presented for comparison. HER rates are presented before and after photodeposition of 1 wt.% Pt. Residual palladium concentrations are plotted on the secondary axis.

2.6.2.3 Inductive/Donating

Table 15: Comparison of DBTS co-polymers containing inductive electron-donating functionalised p-phenylene comonomers.

Polymer	Monomer	HER No Pt ($\mu\text{mol hr}^{-1} \text{g}^{-1}$)	HER Pt ($\mu\text{mol hr}^{-1} \text{g}^{-1}$)	E_g (eV)	Yield (%)	T (%)	τ (ns)	Pd (wt. %)	IP (V vs SHE)	EA (V vs SHE)	f
P1-3		1,948	3,815	2.45	Quant	3.51	1.55	0.42	1.12	-1.89	7.14
P1-6		2,658	6,463	2.63	76	28.67	2.4	0.41	1.18	-1.95	6.83
P1-7		652	7,671	2.69	36	52.04	2.43	0.21	1.25	-2.00	6.58
P1-8		1,244	973	2.77	64	9.01	3.15	#N/A	1.26	-2.03	5.92

Unlike the inductive/withdrawing polymers, for which the fluorescence lifetimes mirrored the residual palladium concentration, the fluorescence lifetimes of inductive/donating alkyl groups are most closely linked to the optical bandgap, as shown in Figure 100a. No clear relationship between the fluorescence lifetime and residual palladium can be obtained since there is no data regarding the residual Pd content of P1-8, leaving only two data points in addition to P1-3.

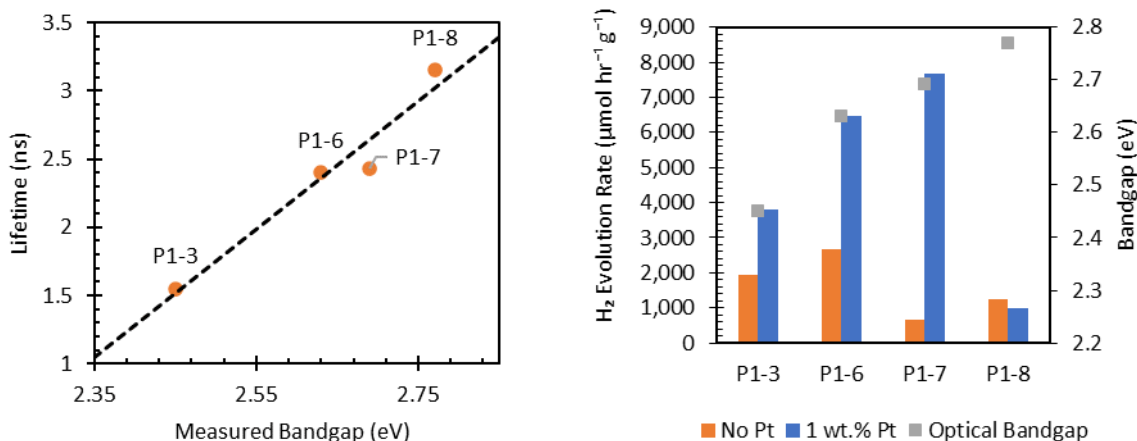


Figure 100: a) Dependence of fluorescence lifetimes on the optical bandgap for DBTS co-polymers containing p-phenylene moieties substituted with inductively electron-donating alkyl groups. b) HER rates of these co-polymers before and after Pt photodeposition. Grey data points represent the measured optical bandgaps for each polymer.

Figure 100b demonstrates how the photocatalytic activities after Pt addition also closely correlate to the optical bandgaps of P1-3, P1-6, and P1-7, and hence also the fluorescence lifetime measurements. P1-8 proves a clear exception to this rule. However, given its low initial photocatalytic activity decreases further upon the addition of Pt, it is highly likely that P1-8 contains a substantial amount of residual Pd.

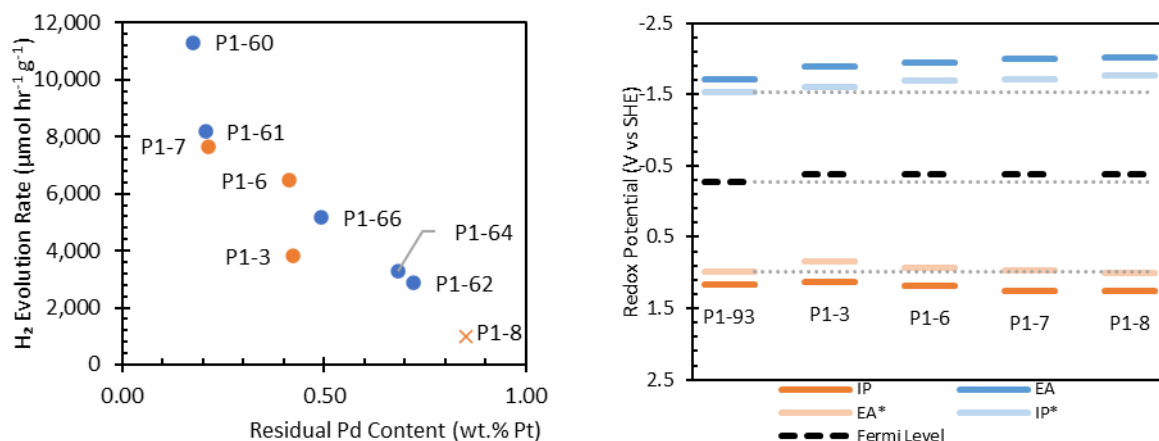


Figure 101: a) Correlation between HER rates after Pt photodeposition and residual palladium concentration in all DBTS co-polymers containing inductive functional groups. The residual palladium concentration of P1-8 is estimated according to this linear relationship. b) Energy level diagram for DBTS co-polymers containing p-phenylene moieties substituted with electron-donating inductive alkyl chains.

This is reinforced by Figure 101a, which shows that the photocatalytic activities of P1-6 and P1-7 fit the trend observed for the I/W polymers with regard to the dependence of HER rate following Pt

addition on the residual Pd content. If we assume a linear correlation according to this graph, we can assume that P1-8 would have a residual Pd concentration of approximately 0.85 wt.%.

Such an analysis would place P1-8 in a similar category to P1-37 and P1-64: long lifetime despite high concentrations of residual palladium. However, unlike P1-37 and P1-64, the LUMO of P1-8 is predicted to lie higher in energy than that of P1-93 (Figure 101b). However, the strong coupling of bandgap and lifetime appears to supersede any influence of Pd content on lifetime for all of the I/D co-polymers.

Analysis of the energy level diagrams (Figure 101b) reveals important information. The IP* of all I/D polymers are higher in energy than that of P1-93. This implies that the LUMO is likely to be preferentially localised on the DBTS unit, and the phenylene orbitals are not involved in the transfer of electrons to or from residual palladium. As such, changing the inductive/donating substituents will alter the bandgap, and hence the change lifetime, but will not influence the rate of charge transfer to and from palladium. Since electron-withdrawing groups lower the EA, the LUMO is more likely to be located on the phenylene groups. In these cases, the specific structure of the co-monomer is more influential in determining how charges are transferred to and from palladium.

2.6.3 Heterocycles

So far, we have only considered monomers that include phenyl or biphenyl sub-units. The final group of co-polymers to be considered in this chapter are those containing nitrogen or sulfur heteroatoms along the conjugated polymer backbone. Unlike for p-phenylene co-polymers, there were fewer heterocyclic polymers from which to draw definitive conclusions regarding structure-activity relationships.

2.6.3.1 Pyridines and Bipyridines

There are only 15 polymers that contain 6-membered N-heterocycles. As such, the same level of in-depth analysis as performed on the phenylene polymers is not possible. The N-heterocycle monomers can be meta- or para-linked. In the case of meta-linked monomers, the nitrogen atom may be ortho or meta to the two bromides. These 15 samples also include three bipyridine monomers and one coplanar bipyridine pyridine monomer.

Despite the absence of a comprehensive set of monomers, there are some notable exceptions to the trends observed amongst the phenylene polymers. For example, large oscillator strengths are not

associated with high HER rates (Figure 102a). Moderate increases in activity are also observed upon adding platinum, even for those containing high levels of Palladium (Figure 102b). However, the final hydrogen evolution rates of these polymers remain similar to others containing high palladium content, such as P1-62, P1-64, and P1-37. Finally, moderate HER rates between 2 and 6 mmol hr⁻¹ g⁻¹ are also observed for the polymers with short fluorescence lifetimes below 1 ns (Figure 102c). The maximum fluorescence lifetimes follow the same trendline with respect to bandgap as for the phenylene polymers (Figure 103).

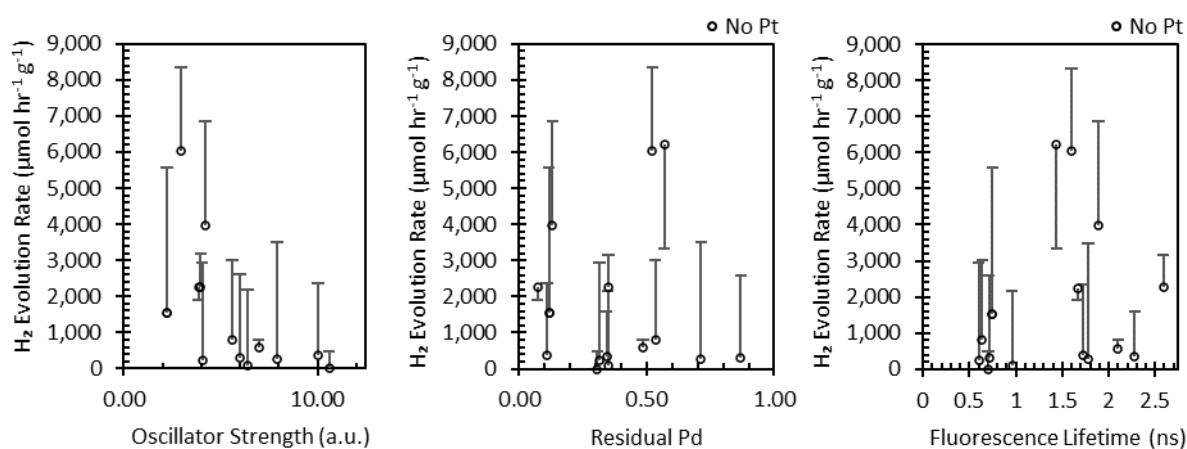


Figure 102: Counterintuitive behaviour of DBTS co-polymers containing pyridine-based co-monomers. Data points present HER rates before Pt photodeposition, error bars represent photocatalytic activity afterwards. HER rates are plotted against oscillator strengths, residual palladium and fluorescence lifetimes in the left, centre, and right hand graphs, respectively.

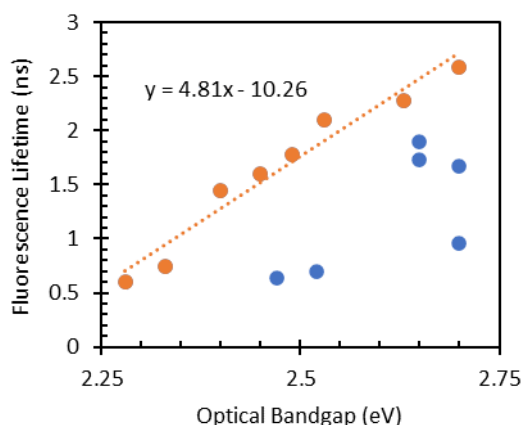
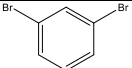
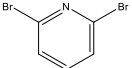
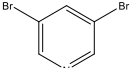
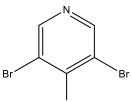
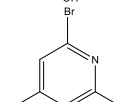
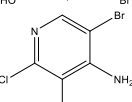
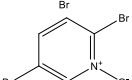
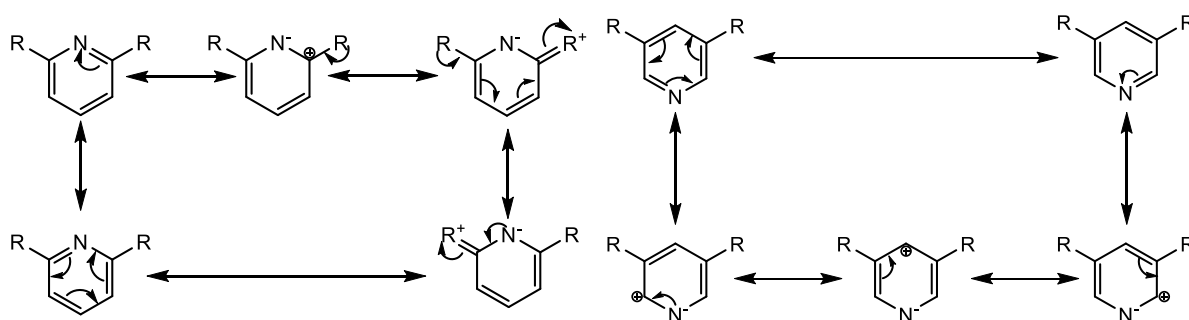


Figure 103: Relationship between fluorescence lifetime and optical bandgap for DBTS co-polymers containing pyridine-based comonomers.

Table 16: Comparison of some DBTS co-polymers containing pyridine-based co-monomers.

Polymer	Monomer	HER No Pt ($\mu\text{mol hr}^{-1}\text{g}^{-1}$)	HER Pt ($\mu\text{mol hr}^{-1}\text{g}^{-1}$)	E_g (eV)	Yield (%)	T (%)	τ (ns)	Pd (wt. %)	IP (V vs SHE)	EA (V vs SHE)	f
P1-2		2,254	3,166	2.7	84	9.11	2.59	0.35	1.24	-2.01	3.96
P1-68		3,969	6,858	2.65	Quant	9.34	1.89	0.13	1.36	-1.66	4.19
P1-70		2,246	1,918	2.7	Quant	17.66	1.67	0.07	1.37	-1.93	3.84
P1-72		6,232	3,348	2.4	44	35.62	1.44	0.57	#N/A	#N/A	#N/A
P1-73		347	1,596	2.63	56	86.63	2.28	0.34	#N/A	#N/A	#N/A
P1-74		6,038	8,341	2.45	77	8.33	1.6	0.52	1.13	-2.06	2.95
P1-71		1,536	5,572	2.33	69	1.67	0.75	0.12	1.27	-1.62	2.23

Data relating to the top-performing pyridine-based co-polymers are presented in Table 16. P1-68 and P1-70 are heterocyclic analogues of P1-2. However, P1-70 is less active than P1-2, whereas P1-68 is more active. This can be attributed to the relative positions of the monomer linkages relative to the nitrogen atom, which can stabilise a negative charge. The resonance structures in Figure 104 show that charges can be delocalised over the polymer backbone in P1-68 but not in P1-70. Therefore, P1-68 is a better electron acceptor with a lower energy LUMO than P1-70, as indicated by its more positive EA potential.

**Figure 104:** Comparative resonance structures for 2,6-linked (left) pyridine monomers and 3,5-linked pyridine monomers (right). Structures highlight how delocalisation along the backbone is maintained for the former when a negative charge is stabilised on the nitrogen atom.

Despite this relationship, the opposite trend is observed for P1-72 and P1-73. This is because the mesomeric electron-donating hydroxy group changes the nature of this monomer from electron-accepting to electron-donating. 4-hydroxypyridines are capable of tautomerisation to form 4-pyridone, as shown in Figure 105. Pyridone is considered the more stable tautomer, so the resonance forms are derived from this conformation. As these resonance diagrams demonstrate, P1-72 is capable of donating a negative charge onto neighbouring monomers, but P1-73 is not. The same delocalisation is also possible for P1-74, except 4-aminopyridine is more stable than its 4-pyridonimine tautomer (Figure 106). Amines are also stronger donating groups than hydroxyls, which may explain why P1-74 is a better photocatalyst than P1-72. However, the presence of the chlorine group complicates the final structure since Suzuki coupling is also possible with aryl chlorides.

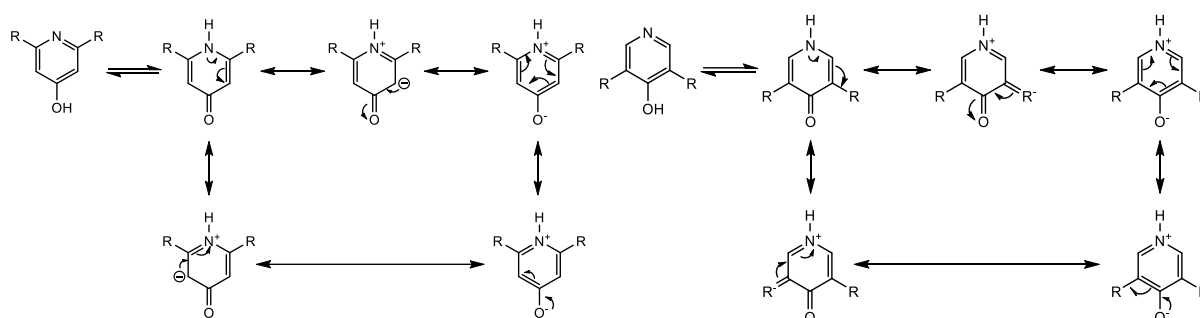


Figure 105: Comparative resonance structures for 2,6-linked (left) 4-pyridinol monomers and 3,5-linked pyridinol monomers (right). Figures also show tautomerisation from the 4-pyridinol to the 4-pyridone structures. Resonance structures highlight how negative charges are only delocalised over the polymer backbone in the 3,5-linked isomer.

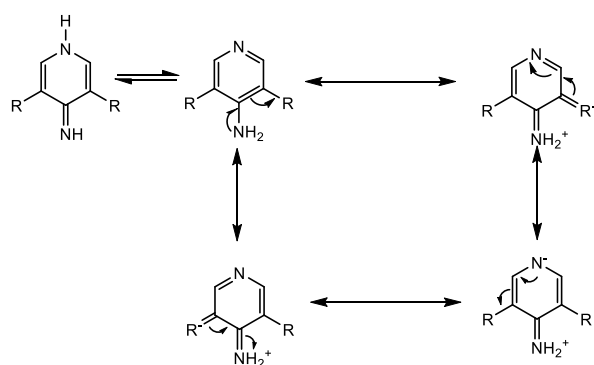


Figure 106: Tautomerisation between 4-pyridonimine and 4-aminopyridine and resulting delocalisation of negative charge along the polymer backbone in the 3,5-linked monomer.

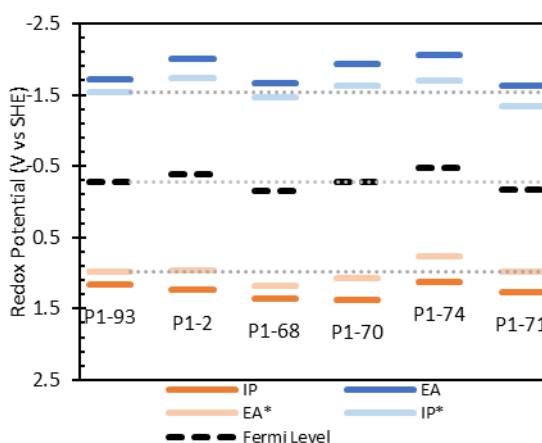


Figure 107: Energy level diagram for DBTS co-polymers containing pyridine-based co-monomers. P1-93 and P1-2 are presented for reference.

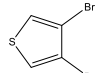
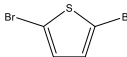
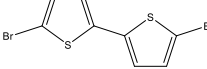
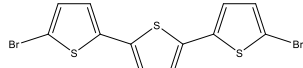
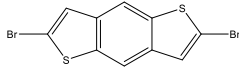
P1-72 and P1-73 were not part of the 705 DBTS co-polymers screened computationally. As such, predicted IP, EA, and f values are not available for these samples. The remaining EA and IP potentials are presented in Figure 107. The IP and EA levels relative to P1-93 highlight the electron-accepting nature of P1-68 compared to P1-70 and the electron-donating character of P1-74.

P1-71 is the only para-linked pyridine derivative synthesised. Its small bandgap results in very short lifetimes of less than 1 ns. Despite its short lifetime, as a result of its narrow bandgap, it achieves an HER rate of 5.6 mmol hr⁻¹ g⁻¹ after loading with Pt. This large increase is in agreement with its low residual palladium concentration. The high photocatalytic activity relative to the fluorescence lifetime indicates that charge transfer from this monomer unit to photodeposited Pt is very fast. The HER rate may also be enhanced due to the narrow bandgap, which results in a more significant portion of the solar spectrum being utilised.

2.6.3.2 Thiophene-based Heterocycles

The final group of polymers considered in this chapter are those containing thiophene units along the polymer backbone. Their properties are summarised in Table 17. Except for P1-97, the polymers are predicted to have oxidation potentials of less than 0.7 V vs SHE, whereas the reduction potentials remain very close to the value predicted for P1-93: -1.53 V vs SHE. This indicates that these polymers have a strong D-A character in which the HOMO is located on the thiophene donor unit. The IP of P1-108 and P1-109 is too small to efficiently drive the TEA oxidation reaction.

Table 17: Comparison of DBTS co-polymers containing thiophene-based co-monomers

Polymer	Monomer	HER No Pt (μmol hr ⁻¹ g ⁻¹)	HER Pt (μmol hr ⁻¹ g ⁻¹)	E _g (eV)	Yield (%)	T (%)	τ (ns)	Pd (wt. %)	IP (V vs SHE)	EA (V vs SHE)	f
P1-97		672	3,024	2.41	48	23.7	0.88	0.15	1.10	-1.97	0.99
P1-99		2,091	4,267	2.14	65	8.58	0.72	0.74	0.59	-1.56	7.30
P1-108		669	525	1.99	89	5.54	0.65	0.20	0.30	-1.52	10.17
P1-109		164	318	1.94	Quant	4.24	0.7	0.29	0.13	-1.50	11.82
P1-110		2,390	5,934	2.18	91	3.64	0.72	0.28	0.54	-1.57	11.12

As shown in Figure 108a, P1-99 and P1-110 also have small oxidation potentials, small bandgaps, and short fluorescence lifetimes, which are expected to decrease the photocatalytic activity. However, the HER rates with Pt remain remarkably high. Given that the reduction potential remains close for P1-93, P1-99 and P1-110, the LUMO is expected to be delocalised over both monomers, and the thiophene units may be involved in the charge transfer to Pt. The negative Fermi potential implies that the interface with the metal co-catalyst may induce a larger space-charge region at the interface and impact the charge transfer process.

The benzodithiophene unit in P1-110 benefits from a co-planar structure in which delocalised electrons run along the length of the backbone. As such, it has a remarkably large oscillator strength. Given its unfavourable overpotential for TEA oxidation, this polymer may operate via a different photocatalytic mechanism. In particular, photooxidation of the excited polymer by charge transfer to the co-catalyst may occur faster than TEA oxidation. The polymer's high activity and narrow bandgap make it a promising monomer to be considered in future linear conjugated polymer photocatalyst designs. Using alternative sacrificial reagents such as ascorbic acid could enhance its activity. Its narrow bandgap also makes it a promising candidate to be used as the hydrogen evolution component in a Z-scheme system where a second component can drive the oxygen evolution reaction.

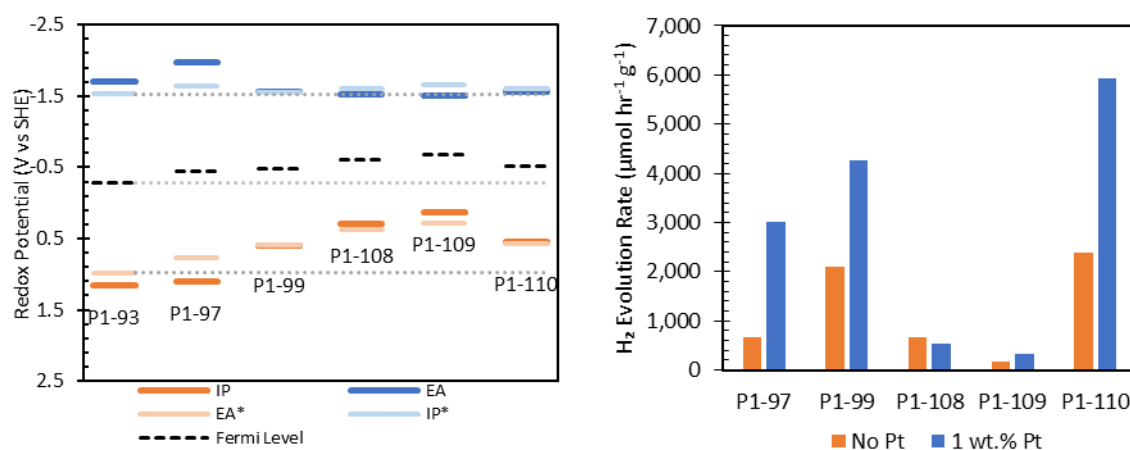


Figure 108: a) Energy level diagram for DBTS co-polymers containing pyridine-based co-monomers. P1-93 is presented for reference. b) HER rates of discussed co-polymers before and after photodeposition of 1 wt.% Pt.

2.7 Computational Screening

The computational screening considered nine different diboronic acids paired with 704 different dibromides. Of these theoretical co-polymers, attempts were made to synthesise 127. Of these, 99 were successfully synthesised with yields over 30%. However, many of the most successful polymers will exist within the subset of 605 co-polymers that were not synthesized.

2.7.1 Methods

In this section, the full set of 704 linear DBTS co-polymers will be assessed according to the trends observed and discussed in this chapter's earlier sections. Firstly, calibration equations derived in 2.3.3 are used to determine the optical bandgaps within a ± 0.11 eV mean average deviation from their experimentally derived values. The difference between these calculated bandgaps and the calculated fundamental bandgaps are then used to modify the IP and EA potentials to estimate values for EA* and IP*. The EA and IP potentials are shifted equally and in opposite directions to ensure the Fermi level remains unchanged. These modifications follow equations -18-23.

$$E_{IPEA} = IP_{New} - EA_{New} \approx E_{Opt} = EA^* - IP^* \quad (18)$$

$$IP_{New} = IP - 0.51(IP) + 0.47 \quad (19)$$

$$EA_{New} = EA - 0.67(EA) - 0.89 \quad (20)$$

$$EA^* = IP - \frac{E_{Fund} - E_{IPEA}}{2} \quad (21)$$

$$IP^* = EA + \frac{E_{Fund} - E_{IPEA}}{2} \quad (22)$$

$$E_{Fermi} = \frac{IP + EA}{2} = \frac{EA^* + IP^*}{2} \quad (23)$$

The most promising candidates are identified by screening the resulting polymers according to the EA*, IP*, and E_{Fermi} potentials and the predicted oscillator strengths, f . The screening parameters are outlined in Table 18. The resulting polymers are then categorised according to their electron-donating or electron-accepting character. This is estimated according to the height of the HOMO and LUMO potentials relative to P1-93.

Table 18: Screening parameters applied to the 704 DBTS co-polymers investigated via high-throughput virtual screening study and the number of samples that meet each criteria. The number of synthesised polymers meeting the criteria and the number of top-performing (top 25) photocatalysts meeting the criteria are also presented. Of the 99 polymers synthesised, 93 featured in the initial set of 704 polymers that were initially screened virtually.

Parameter	Theoretical Polymers (Max: 704)	Synthesised polymers (Max: 93)	N° Top 25 Photocatalysts (1 wt.% Pt)
$-1.8 < IP^* < -1.3$	471	66	24
$0.5 < EA^* < 1.25$	503	69	24
$-0.6 < E_{Fermi} < 0$	472	67	24
$f > 5.5$	153	43	19
All Criteria	107	29	19

2.7.2 Synthesised DBTS Co-polymers

2.7.2.1 Results

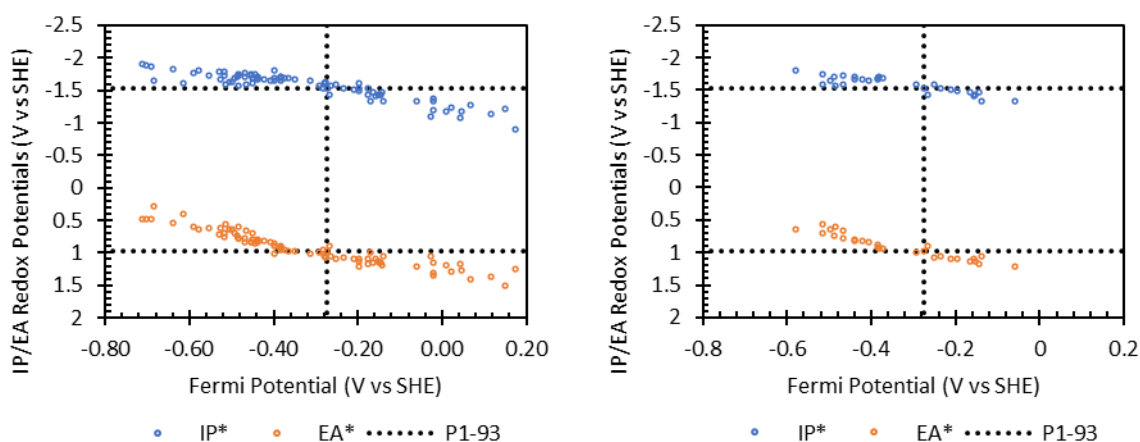


Figure 109: a) IP* and EA* values for the 99 synthesised DBTS co-polymers plotted against their calculated Fermi potential. IP* and EA* values are estimated from the xTB-IPEA calculated EA and IP values and the predicted optical bandgap (E_{IPEA}). b) An equivalent plot for the 29 polymers arising from the virtual screening process highlighted in the text.

Figure 109a presents the estimated IP* and EA* potentials for each of the synthesised polymers present in the computational database and plots them against the Fermi potential. Figure 109b contains the 29 remaining polymers after applying the screening criteria outlined in Table 18. Table 18 also highlights how many of these 29 polymers are amongst the most active photocatalysts after photodepositing Pt.

The dotted lines in Figures 109a and 109b represent the predicted IP*, EA*, and E_{Fermi} for the DBTS-DBTS homopolymer, P1-93. This point acts as an important reference since co-monomers used in polymers to the left can be considered electron donors, and those to the right are typically electron acceptors.

When the IP* is considerably more negative than that of P1-93 (-1.52 V vs SHE), the LUMO rises in energy. This happens because LUMO density (and hence photoexcited electrons) become increasingly localised on the DBTS acceptor unit. Likewise, as the EA* potentials become more negative, the HOMO (and photogenerated holes) becomes increasingly localised on the non-DBTS co-monomer. It is important to note that some copolymers with more-negative Fermi potentials are predicted to have a localised HOMO and a delocalised LUMO, whereas others can be considered to have a delocalised HOMO and a localised LUMO. The activity of polymers towards the left of these charts becomes

limited by insufficient driving forces for TEA oxidation. Rising HOMO energies can also be associated with narrower bandgaps and shorter fluorescence lifetimes.

For polymers that lie to the right of P1-93, the co-monomer becomes more electron-accepting than the DBTS unit. Since DBTS is an electron acceptor itself and provides an efficient catalysis site, it is unsurprising that there are few DBTS co-polymers in this region. Those that do meet the criteria for photocatalysis in this region can primarily be considered as having delocalised LUMOs across both units. In this case, charge transfer from the polymer to Pd and Pt cocatalysts will involve the co-monomer, and the relative rates will be structure-dependent.

2.7.2.2 Discussion

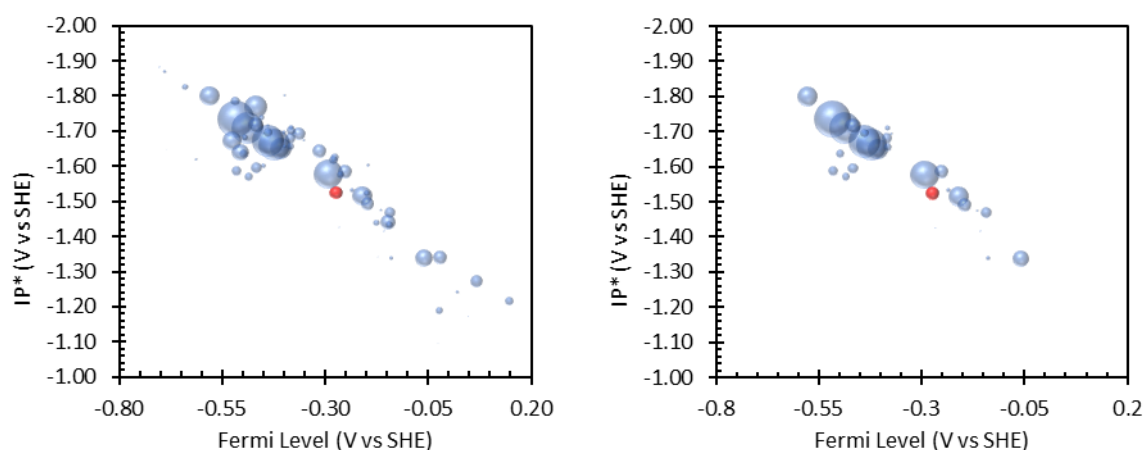


Figure 110: a) IP* vs the Fermi potential for the 99 synthesised DBTS co-polymers. The in width of each data point represents the photocatalytic activity **before** photodepositing Pt as a co-catalyst. b) The same plot after virtual screening according to the rules outlined in the text. Red data point represents P1-93, the DBTS-DBTS homopolymer.

Figure 110a presents the distribution of the most active photocatalysts before Pt addition and before excluding any samples via the screening parameters. Figure 110b is the same Figure after refining the computational results. As can be seen, the vast majority of the active photocatalysts are preserved, and the most inactive photocatalysts are removed. Figures 111a and 111b present the same data for the photocatalysts after Pt photodeposition. The red data point represents P1-93. The width of each bubble is proportional to the photocatalytic activity relative to the highest activity within the set.

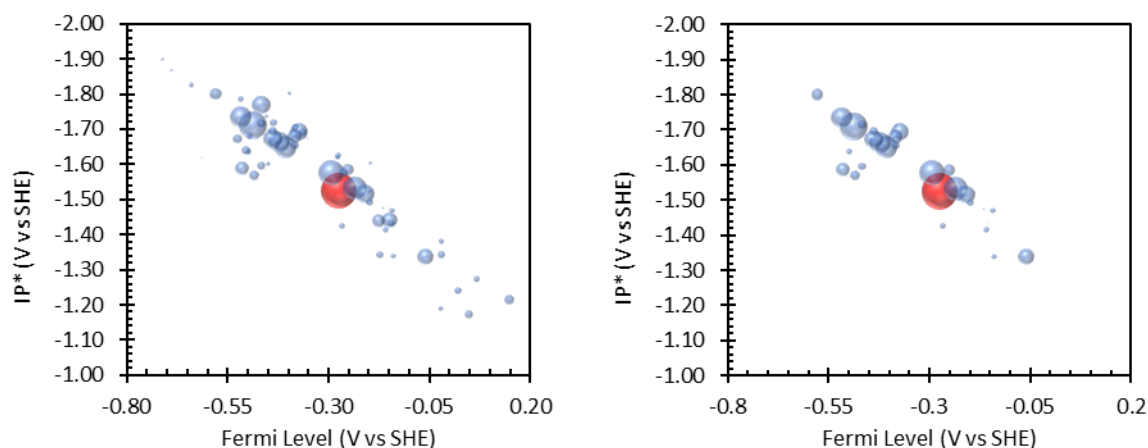


Figure 111: a) IP* vs the Fermi potential for the 99 synthesised DBTS co-polymers. The width of each data point represents the photocatalytic activity **after** photodepositing Pt as a co-catalyst. b) The same plot after virtual screening according to the rules outlined in the text. Red data point represents P1-93, the DBTS-DBTS homopolymer.

As highlighted in Table 18, 29 of the synthesised polymers are selected following the computational screening process. Nineteen of the top 25 photocatalysts after Pt photodeposition remain within this set.

Before Pt photodeposition, the most active photocatalysts have a Fermi level that is more negative than P1-93. However, many of the most active photocatalysts after Pt photodeposition have Fermi levels similar to that of P1-93. Figure 112 contrasts the photocatalytic activities of the polymers before Pt deposition (Figure 112a) with their relative increases in activity after Pt deposition (Figure 112b).

Interestingly, all of the polymers highlighted in the red box contain aromatic hydrocarbons without any heteroatoms. This means that monomers containing nitrogen and sulfur heteroatoms, whose resonance structures contribute to the electron-donating characteristics, do not benefit from platinum as a co-catalyst compared with palladium.

Polymers inside the grey box can be considered as having LUMOs delocalised over both monomer units. The lower IP* potentials may result in structure-dependent charge transfer rates to residual palladium and platinum. For example, excitons in P1-93 are long-lived. P1-27 also lies in this region and also appears to be very unreactive with palladium and highly active with platinum. However, the fluorescence lifetimes (and photocatalytic activities) of the polymers containing fluorinated phenylene rings: P1-60, P1-61, P1-62, and P1-66, are heavily dependent on the relative concentrations of residual palladium. Thiophene-containing polymers P1-110 and P1-99 lie to the left of this region, they have

strongly localised HOMOs, but the LUMO remains low in energy and delocalised. As such, they benefit from the favourable work function of platinum that enhances the rate of charge transfer.

The final region, denoted by the blue box, highlights polymers whose LUMOs are localised predominantly on the electron-accepting co-monomer. Since the DBTS unit is less involved in the electron transfer process, the response of these polymers to Pt and Pd is considerably more dependent on the structure of the acceptor unit. This also typically results in lower-activity photocatalysts. The samples in this region demonstrating the biggest increases in activity with Pt typically contain pyridine rings or carbonyl groups. However, these samples may operate via unique mechanisms.

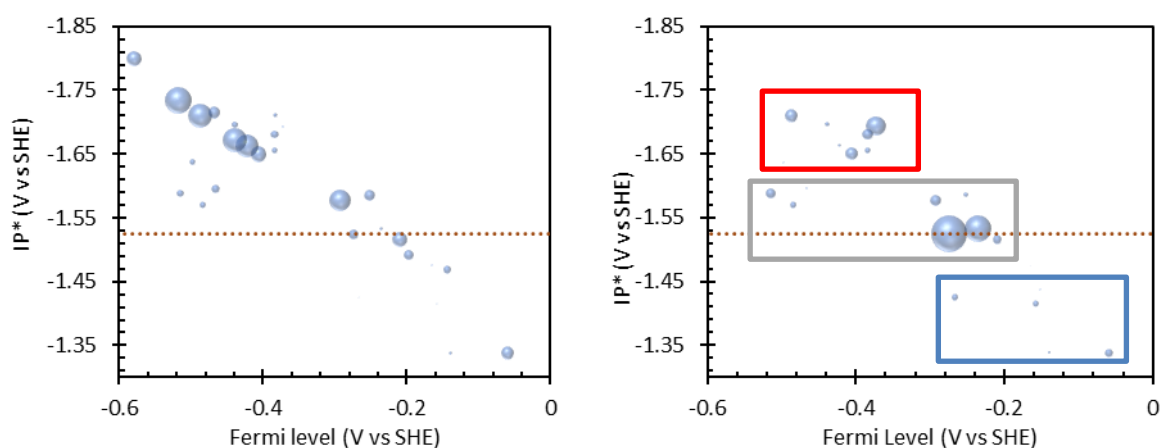


Figure 112: a) IP* of remaining synthesised polymers after virtual screening. Data point width represents HER rate before Pt photodeposition. b) Data point widths represent the change in photocatalytic activity upon photodeposition of 1 wt.% Pt. Dotted line represents IP* for P1-93. Three boxes in graph figure b) represent polymers with LUMO orbital density theoretically localised on the DBTS unit (red) delocalised over both monomers (grey) or localised on the co-monomer (blue). These also correspond with electron-donating, neutral, and electron-accepting co-monomers.

2.7.2.3 Inactive Polymers Included by Screening

The screening process identified ten polymers as potentially promising candidates, which performed poorly when tested. These polymers are summarised in Table 19. The poor photocatalytic activity can be accounted for in almost all of these cases by considering the structure-activity relationships explored above or the residual palladium concentration.

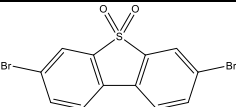
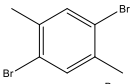
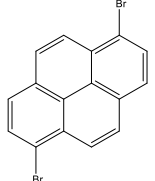
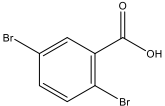
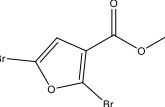
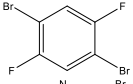
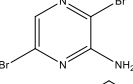
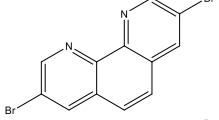
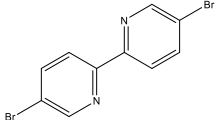
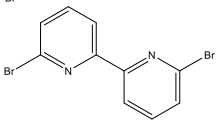
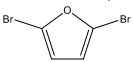
The copolymers P1-8, P1-62, and P1-37 are structurally similar to many other polymers with high activities. Their poor activities can be attributed to high palladium concentrations, as discussed in

section 2.6.2. P1-24 is the most surprising polymer that is not amongst the top 25. However, its low oxidation potential implies that there may be a limited driving force for TEA oxidation.

P1-78, P1-84, P1-85, and P1-86 contain pyridine rings that are electron-accepting. These polymers fit into a larger general trend in which pyridine-containing photocatalysts performed worse than their phenylene equivalents. Many of these polymers also dispersed poorly in the reaction mixture. P1-78 also has a very small bandgap, and the IP* and EA* levels indicate that HOMO and LUMO are both localised on the co-monomer unit.

P1-102 is ranked 30th for its photocatalytic activity with water. It is structurally very similar to P1-99 and has a poor overpotential for TEA oxidation. Unlike the thiophene-based P1-99, furans are more electronegative and do not donate their electrons as readily. It also dispersed very poorly in the reaction mixture. P1-48 also contains a furan unit. However, in this case, the ester group transforms the polymer into an electron-accepting group relative to P1-93. Typically, polymers containing carbonyl groups appear to have very unpredictable photocatalytic activities. This is likely due to their unique photophysical processes, as discussed in section 2.6.2.

Table 19: Comparison of Low-activity DBTS co-polymer photocatalysts included by screening criteria. P1-93 is presented for reference values.

Rank	Polymer	Monomer	HER No Pt ($\mu\text{mol hr}^{-1}$ g^{-1})	HER Pt ($\mu\text{mol hr}^{-1}$ g^{-1})	E_g (eV)	Yield (%)	T (%)	τ (ns)	Pd (wt. %)	EA* (V vs SHE)	IP* (V vs SHE)	E_{Fermi}	f
1	P1-93		3,443	16,719	2.51	86	0.79	3	0.31	0.98	-1.52	-0.27	9.64
62	P1-8		1,244	973	2.77	64	9.01	3.15	#N/A	0.94	-1.71	-0.38	5.92
41	P1-24		1,986	2,484	2.38	75	7.5	1.6	0.19	0.64	-1.64	-0.50	7.22
46	P1-37		2,710	2,161	2.41	56	15.92	3.82	0.77	1.18	-1.47	-0.14	5.51
48	P1-48		1,051	1,969	2.49	91	24.79	0.68	0.29	1.06	-1.34	-0.14	5.73
36	P1-62		3,501	2,862	2.7	92	12.08	0.74	0.72	1.10	-1.49	-0.20	7.04
38	P1-78		315	2,597	1.86	48	87.05	0.71	0.87	0.89	-1.43	-0.27	5.99
69	P1-84		0	477	2.52	36	88.54	0.7	0.31	1.13	-1.44	-0.15	10.59
44	P1-85		381	2,355	2.65	58	36.18	1.73	0.11	1.10	-1.41	-0.16	10.03
63	P1-86		578	796	2.53	78	16.26	2.1	0.49	1.14	-1.48	-0.17	6.95
30	P1-102		2,691	3,333	2.15	49	66.95	0.64	0.54	0.66	-1.60	-0.47	6.19

2.7.2.4 Active Polymers Excluded by Screening

Nineteen of the top 25 polymers are identified according to these criteria. The six remaining unidentified polymers with high activity are presented in Table 20. All of these polymers were omitted on the basis of their small oscillator strengths. P1-39 was additionally excluded on the basis of its IP* and EA* potentials that arise from the monomer's strong electron-withdrawing character.

P1-74 and P1-68 have small oscillator strengths due to the meta-linkages along the polymer backbone, as discussed in section 2.6.3. Clearly, this screening system will omit all other meta-linked pyridines that are potentially promising photocatalysts. However, these molecules make up a very small proportion of the catalyst library. Furthermore, no polymers containing para-linked pyridine monomers from the library were successfully synthesised. Such para-linked pyridine copolymers with higher oscillator strengths may be even more active.

Table 20: Comparison of high-activity DBTS co-polymer photocatalysts excluded by virtual screening process.

Rank	Polymer	Monomer	HER No Pt ($\mu\text{mol hr}^{-1}$ g^{-1})	HER Pt ($\mu\text{mol hr}^{-1}$ g^{-1})	E_g (eV)	Yield (%)	T (%)	τ (ns)	Pd (wt. %)	EA* (V vs SHE)	IP* (V vs SHE)	E_{Fermi}	f
8	P1-74		6,038	8,341	2.45	77	8.33	1.6	0.52	0.83	-1.77	-0.47	2.95
13	P1-68		3,969	6,858	2.65	Quant	9.34	1.89	0.13	1.14	-1.44	-0.15	4.19
16	P1-71		1,536	5,572	2.33	69	1.67	0.75	0.12	1.09	-1.44	-0.18	2.23
20	P1-39		2,191	4,245	2.56	57	10.97	2.81	0.24	1.51	-1.22	0.15	2.29
21	P1-21		4,954	4,020	2.52	67	7.86	1.3	0.66	0.62	-1.67	-0.53	2.43
22	P1-94		1,836	3,932	2.71	95	0.49	2.58	0.30	1.05	-1.58	-0.26	3.49

P1-71 contains the structurally-unique pyridine N-oxide monomer. In its molecular form, pyridine N-oxides are used in photochemical reactions for their rapid electron transfer from the non-bonded n-orbitals. The resulting radical has also demonstrated its ability to abstract hydrogen from water and catalyse water oxidation via a two-electron pathway to form hydrogen peroxide. As such, this is an interesting polymer for future consideration as an overall water-splitting photocatalyst. It is expected to have band potentials similar to P1-93, but its measured bandgap is much smaller than P1-93. This discrepancy indicates that xTB-IPEA calculations may not correctly interpret structures with complicated valence states, such as the charge-separated N-O bond in this case.

The LUMO of P1-39 is situated predominantly on the phenyl ring and contains carboxylic acid groups. As such, its photocatalytic activity may also depend on an entirely different mechanism than most other polymers in this dataset. Although P1-21 and P1-94 place amongst the top 25 photocatalysts, they place 21st and 22nd, respectively. These have been discussed in detail in earlier sections. Their small oscillator strengths correspond with these polymers performing considerably worse than their similarly-structured counterparts, which were not excluded by the screening criteria.

2.7.3 Screening of Remaining Co-polymers

Of the 704 DBTS co-polymers included in the high-throughput computational virtual screening stage of the work published by Bai *et al.*, 107 meet the criteria outlined in Table 18. The full datasets before and after screening for these properties are presented in Figures 113a and 113b, respectively. The majority of excluded samples result from the requirement for an oscillator strength greater than 5.5.

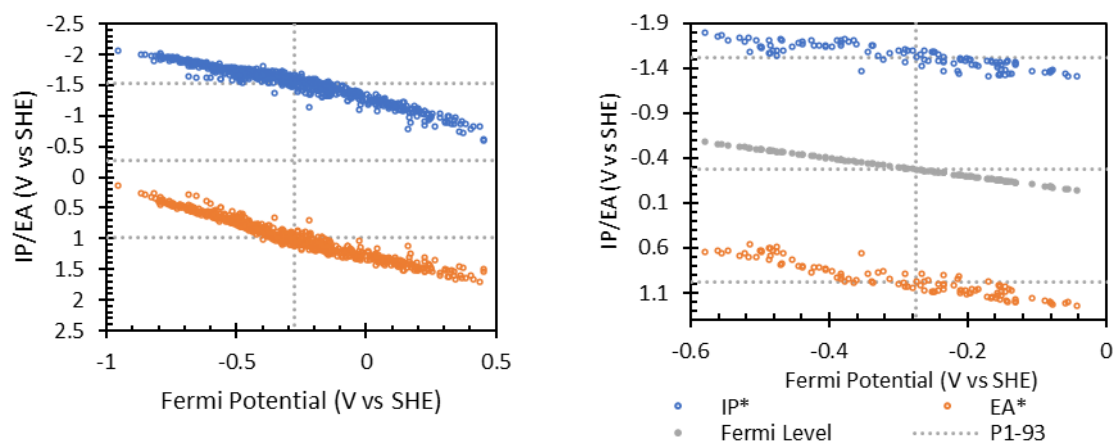


Figure 113: a) IP* and EA* values for the 704 theoretical DBTS co-polymers plotted against their calculated Fermi potential. IP* and EA* values are estimated from the xTB-IPEA calculated EA and IP values and the predicted optical bandgap (E_{IPEA}). b) An equivalent plot for the 107 DBTS co-polymers that meet the screening criteria.

The resulting polymers can also be assessed according to their predicted IP* and EA* potentials to indicate if the frontier orbitals are likely to be localised on the DBTS unit, delocalised over both monomers, or localised on the co-monomer. Furthermore, using the structure-activity relationships observed for the synthesised polymers, it should be possible to predict which polymers will be highly active and which will improve their photocatalytic activity after photodepositing Pt.

2.7.3.1 IP* and EA* relative to P1-93

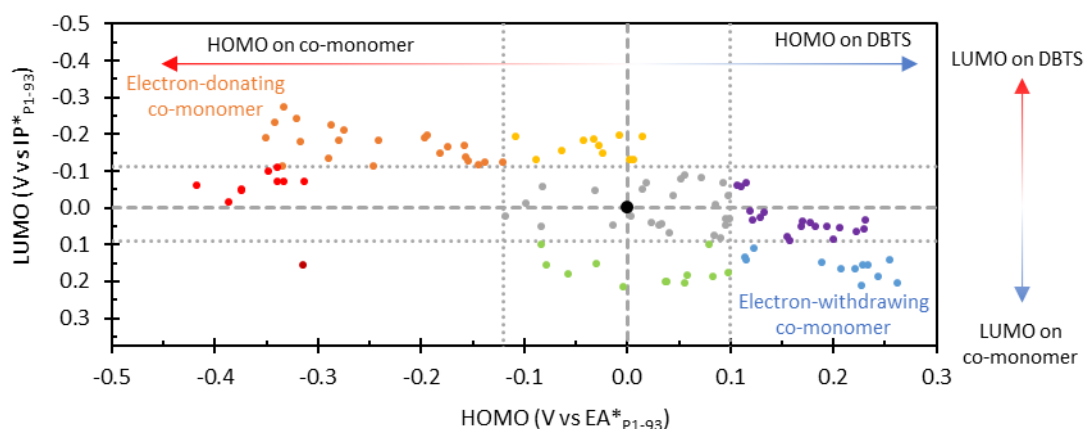


Figure 114: Plot of IP* vs EA* of the 112 screened DBTS co-polymers. Excited state band edge potentials are plotted relative to the IP* and EA* of the DBTS-DBTS homopolymer, P1-93, which is denoted by the black data point and the dashed grey lines. The theoretical polymers are categorised according to their HOMO and LUMO positions relative to P1-93. The graph split into 9 sections. Orange and yellow data points have more a negative IP* (<math>< -0.1\text{ V vs P1-93}</math>) green and blue have a more positive IP* (IP*>0.1 V vs P1-93). Red, grey, and Purple co-polymers have an IP* that is $\pm 0.1\text{ V vs IP}^*$ of P1-93. Similar analysis categorises the polymers according to the EA* potentials relative to the EA* of P1-93.

Figure 114 plots the estimated IP* and EA* values relative to the IP* and EA* of P1-93, and as such, P1-93 lies at the origin. The polymers meeting the screening requirements can be categorised according to their IP* and EA* potentials relative to this data point. As indicated by the arrows, the magnitude and direction of each data point relative to P1-93 provide information on whether the HOMO and LUMO are likely to be delocalised or if they will be spatially separated as for a true donor-acceptor structure.

Nine key regions of this graph have been identified and are marked by different colours accordingly. The polymers in the top left section, represented by orange data points, are predicted to be D-A type polymers in which the HOMO is located on the comonomer, and the LUMO is located on the DBTS monomer. These polymers have large negative Fermi potentials relative to P1-93 and are the best-performing photocatalysts when using residual palladium as a co-catalyst.

The polymers represented by red data points also contain strongly donating co-monomer units. In this case, the higher energy HOMO is paired with a LUMO whose energy is close to P1-93. As such, these polymers will have smaller bandgaps than P1-93. The matching LUMO energies imply that electron density is more likely to be delocalised over the polymer backbone, and the nature of the co-monomer will impact charge transfer rates to palladium and platinum.

Yellow data points represent polymers with HOMO energies close to P1-93, implying a delocalised HOMO. However, the higher-energy LUMO compared to P1-93 also indicates a slight electron-donating character, and that electron density is more concentrated on the DBTS unit.

Polymers represented by the grey data points have HOMO and LUMO energies that most closely resemble those of P1-93. In such cases, the HOMO and LUMO are both expected to be delocalised over the polymer backbone. For these polymers, charge transfer to palladium is expected to be slow, and the biggest increases in activity will be observed by photodepositing platinum. However, the rate of charge transfer to either noble metal will depend on the nature of the comonomer.

Purple polymers have Fermi potential more positive than that of P1-93, implying that the comonomers are relatively electron-withdrawing. The LUMO energy remains close to that of P1-93 and can hence be considered delocalised, but their HOMOs lie at lower energies. As such, electron transfer events to Pd/Pt may still occur via the DBTS unit, but the relative rates are considerably more dependent on the nature of the co-monomer. These polymers are expected to have wider bandgaps than P1-93.

Green data points represent polymers with a HOMO energy similar to P1-93 and a lower LUMO energy. LUMO electron density is expected to be more localised on the co-monomer unit rather than the DBTS one. As such, charge transfer to co-catalysts will be entirely structure dependent. However, the lower LUMO suggests there may be a lower driving force for charge separation and hydrogen evolution. These polymers are expected to be considerably more efficient with Pt than Pd. TEA oxidation rates are expected to be fast as the HOMO is delocalised over both monomer units.

Finally, the photocatalytic activities of the blue polymers are almost entirely dictated by the nature of the co-monomer. These polymers are expected to present as D-A polymers in which the HOMO (and hence photogenerated holes) is localised on the DBTS unit, which has become the donating moiety. The LUMO will become more concentrated on the co-monomer unit, and the nature of the co-monomer/metal interactions will dominate the rate of charge extraction. As for polymers in the green region, the lower energy LUMO implies a smaller driving force for proton reduction. Reactions are expected to be considerably faster with platinum instead of palladium. Although the DBTS moiety may be less involved in the electron transfer process to the co-catalyst, the polymer would still benefit from its fused linear macrocycle structure and polar functional groups.

2.7.3.2 Aromatic Heterocyclic Co-monomers

Structurally, the polymers can be grouped according to whether or not the comonomer contains heterocyclic aromatic rings. The resulting set of heterocyclic polymers is assessed in this section. The complete set of these polymers is presented in Figures 115 and 116. Following the conventions of the previous sections, the polymers are all DBTS copolymers and are represented by varying co-monomer dibromides. These monomers are colour-coordinated to indicate which region of Figure 114 they can be located in.

These polymers can be divided into four subsets according to the nature of the heterocycle. Polymers S1-S21 make up the first of these subsets and contain either a pyrrole, thiophene, or furan. These 5-membered heterocyclic rings contain a single electron-donating heteroatom in the ring. Resonance structures place a partial positive charge on the heteroatom and delocalize the negative charge evenly across the four remaining carbons. Resultingly, these monomer units are predicted to be easily oxidised and enable D-A-type polymers to be prepared. A clear pattern can be seen in which pyrrole-containing polymers have a higher energy LUMO and more electron-donating character than the thiophene and furan derivatives. This can lead to enhanced charge separation and minimised exciton binding energy. S1, S2 and S5 were synthesised in the initial set of polymers and shown to be highly efficient photocatalysts with residual palladium. However, these polymers did not improve after the addition of Pt since charge transfer to Pd is fast. By contrast, thiophene-containing polymers possess lower energy LUMOs with a lower driving force for charge transfer. When synthesised, the photocatalytic activities of S6, S11, and S13 improved after Pt deposition. However, due to small overpotentials, their high-energy HOMOs may limit the activity when TEA is used.

Many of these polymers were synthesised in the original study. However, this work suggests that alkyl chains may be added to thiophene units without dramatically impacting the electronic structure. Such modifications could allow for soluble derivatives to be synthesised. S3 was not synthesised but is predicted to perform similarly to S1 and S2. The photocatalytic activity of S4 is difficult to predict, given the presence of an ester functional group. This group has a mesomeric electron-withdrawing effect and is conjugated to the polymer backbone. Whilst this may stabilise the negatively-charged polaron, carbonyls can also introduce the potential for ISC to the triplet state and are often reactive photochemical reagents. S12 would be an exciting target since the oxygen ether groups are inductively electron-withdrawing and mesomerically donating. They also add polarity to the backbone, which may improve polymer-water interactions and dispersibility. S14 is the only polymer predicted to substantially lower the LUMO energy and raise the HOMO energy. This is possible because of its two

fused thiophene rings in tandem with the mesomeric electron withdrawing carboxylic acid. It is predicted to have the narrowest bandgap of 2.0 eV.

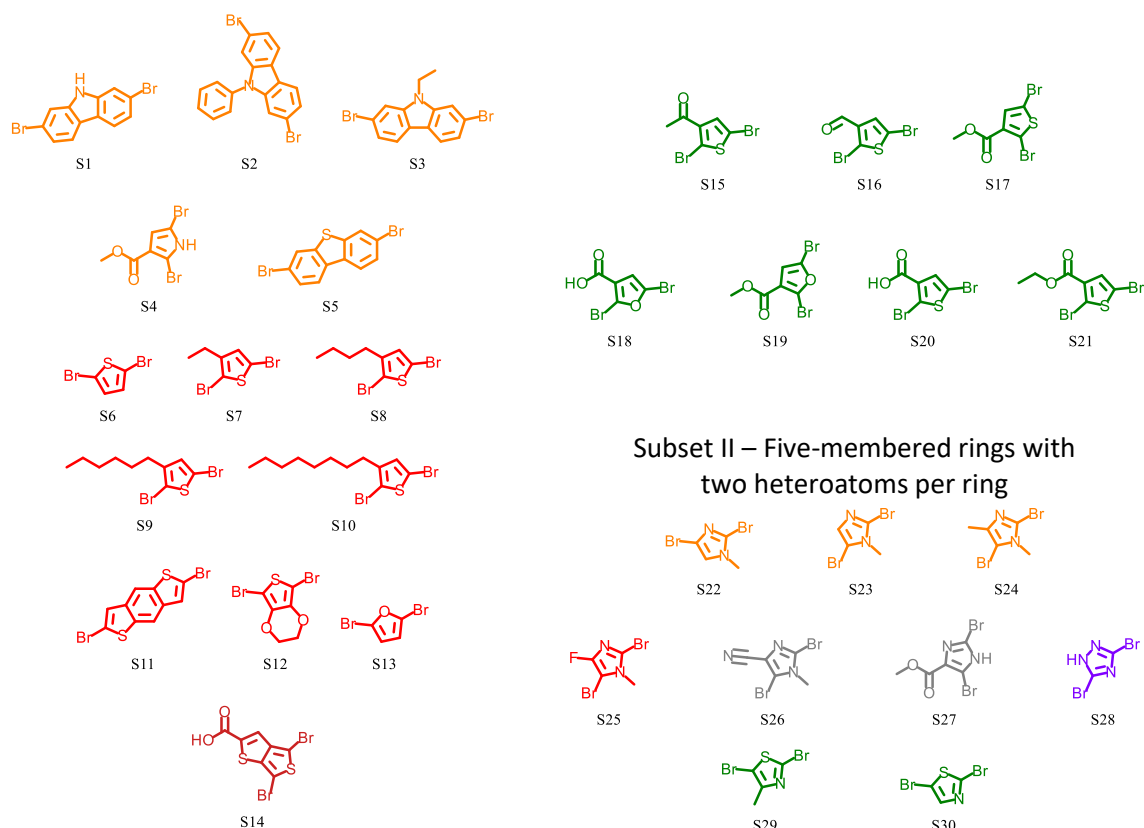
Polymers S15 to S21 also contain thiophene- and furan-based monomers. However, these monomers also contain electron-withdrawing carbonyl groups, giving rise to a LUMO energy that is lower in energy than P1-93. These monomers are, therefore, predicted to be more electron withdrawing than electron donating. The HOMO is also shifted to lower energies to align with the HOMO of P1-93. In this case, the photogenerated holes are expected to be more delocalised, implying that these thiophene units are no longer electron-donating.

Whilst potentially interesting polymers, aldehydes, ketones, carboxylic acids, and ester functional groups are prone to photooxidation or photoreduction reactions. Carbonyl chromophores also enable rapid ISC to form photoexcited triplet states. However, these functional groups are also polar and can potentially improve the energetics at the interface with water. These polymers are also expected to have narrow bandgaps.

The second subset of polymers is represented by the dibromides S22-S30. These contain 5-membered heterocyclic monomers with two or more heteroatoms. In this case, one heteroatom is pyrrole-like and donates a lone pair to the ring to complete aromaticity. In contrast, the second heteroatom is pyridine-like, and its lone pair of electrons are perpendicular to the π -electron system. As such, one heteroatom is electron-donating, and the other is electron-accepting.

Aromatic Heterocyclic Co-monomers

Subset I – Five-membered rings with one heteroatom per ring



Subset II – Five-membered rings with two heteroatoms per ring

Subset III – Fused polyaromatic monomers (5+6 membered rings) with two or more heteroatoms

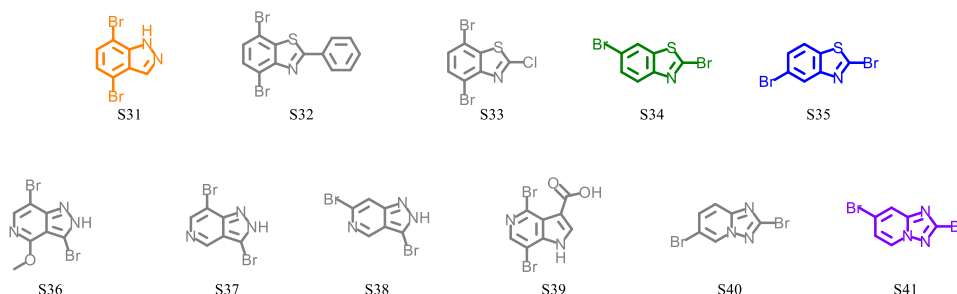


Figure 115: List of the most promising photocatalysts resulting from virtual screening of 704 theoretical DBTS co-polymers. Set I : Heterocyclic co-monomers. S1 - S21 (Subset I) contain 5 membered aromatic rings with a single mesomeric electron-donating heteroatom, S22 – S30 (Subset II) contain two heteroatoms within the 5 membered ring, one atom is electron donating, the other is electron accepting. S31 – S41 (Subset III) contain a 5 membered heterocycle with two heteroatoms fused to an additional 6-membered ring (benzene or pyridine). Polymers are colour coordinated according to their position on the IP* vs EA* chart relative to the DBTS-DBTS homopolymer. See Figure 114 for details.

S29 and S30 were both targeted in the high-throughput synthesis study. However, their synthesis was unsuccessful, and they were not tested. As such, none of the polymers in this subset have been synthesised so far, and their photocatalytic activities are uncertain. These polymers span a wide range of regions in the IP*/EA* plot (Figure 114), indicating how structural variations can modify the HOMO and LUMO positions relative to P1-93. Accordingly, the bandgaps of these polymers can also be finely tuned and are predicted to range from 2.26 to 2.62 eV. S25 – S28 would make interesting polymers

since their LUMO energies are similar to that of P1-93. Samples in this region show interesting dependencies on Pd and Pt concentrations.

The third subset of heterocyclic polymers contains monomers with a 5-membered aromatic heterocycle fused to a 6-membered aromatic ring. Each monomer contains at least two heteroatoms in the fused ring system, including an electron-donating heteroatom on the 5-membered aromatic ring. As in the second subset, the remaining aromatic heteroatoms are pyridine-like and electron-accepting. The heteroatom elements, heteroatom positions, and monomer linkage positions differ in each case, making this a problematic subspace to explore efficiently using a small number of potential monomers. However, this also generates a significant chemical space to expand further if these polymers show initial promise.

None of these theoretical polymers were present in the initial high throughput experiment, and their viability as components in photocatalytic systems so far remains untested. This subset represents a diverse set of polymers that range from electron-donating to electron-accepting relative to P1-93.

The dibromide linkages on S34, S35, S40, and S41 result in a polymer geometry in which the axis of the fused rings lies parallel to the polymer backbone. The previous sections show that this typically leads to significant oscillator strengths and efficient photocatalytic activity. However, each of these DBTS co-polymers makes a potentially exciting new photocatalyst.

Benzothiadiazole (BT) is structurally similar to these monomers and is commonly used as an acceptor monomer in D-A polymers and has shown promise in polymers for photocatalytic hydrogen evolution.^{114,207–209} Although DBTS-BT polymers and their derivatives were synthesised in the initial high throughput experiment, their photocatalytic activities were inferior. However, the screening process excluded these monomers due to their low EA, and their poor performance is unsurprising. Since DBTS is already an efficient electron acceptor, it would not make sense to pair it with another monomer that is considerably more electronegative than those highlighted here.

Polymers S42 – S64 cover the final subset of heterocyclic aromatic comonomers. These monomers all contain 6-membered pyridine rings in which the N-heteroatom is electron-withdrawing and can stabilise a negative charge. As such, the majority of these polymers span the grey-to-blue region of the IP* vs EA* plot.

Subset IV – Six-membered heterocyclic aromatic co-monomers

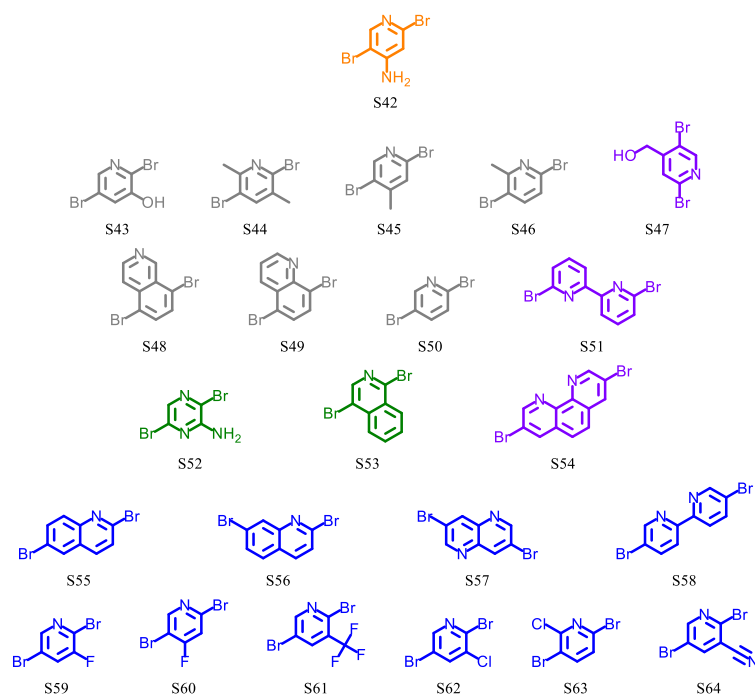


Figure 116: List of the most promising photocatalysts resulting from virtual screening of 704 theoretical DBTS co-polymers. Set I : Heterocyclic co-monomers (Contd.). S42 – S64 (Heterocycle Subset IV) represent all of the co-polymers containing 6-membered heterocycles with mesomeric electron-withdrawing nitrogen atoms and no 5-membered heterocyclic components. Polymers are colour coordinated according to their position on the IP* vs EA* chart relative to the DBTS-DBTS homopolymer. See Figure 114 for details.

Four of these polymers were synthesised in the initial study and tested for their photocatalytic activity: S51, S52, S54, and S58. All of these polymers resulted in photocatalytic activities outside of the top 25. However, each of these polymers contains two electron-accepting heterocyclic N-atoms. S51 and S58 contain rotational degrees of freedom around the dihedral bond. S52 is the only pyrazine moiety; the LUMO of the others are excluded in the screening process due to large magnitude positive Fermi energies indicating strong electron-accepting characteristics. Although S54 is a fused linear macrocycle with a large oscillator strength, it was only obtained with a 30% yield. The resulting photocatalytic performance may have been affected by its purity.

It is worth noting that S51 is present, but the polymer containing a single meta-linked pyridine unit is not. The oscillator strength of S51 may only have met the oscillator strength criteria due to the presence of two rings. However, in phenylene, biphenylene, and triphenylene-containing polymers, additional rings without a rigid co-planar structure do not lead to enhanced photocatalytic activities.

However, despite limited precedent for success amongst these polymers, meta-linked derivatives of several of these monomers were found to result in highly active photocatalysts that were excluded on the basis of their small oscillator strengths (see Table 20). It remains unclear if those polymers were active because of their meta-linked structure or if their para-linked isomers could be even more active.

The 4-aminopyridine co-polymer, S42, and the para-pyridine co-polymers should be synthesised, given the top 15 performances of their meta-linked derivatives, P1-74 and P1-68. S44, S45, and S46 are also interesting targets since the inductive donating methylene groups would raise the energy of the LUMO and make the pyridine ring less electron-accepting.

Among the blue electron-accepting co-monomers, S55 and S57 are potentially active since these monomers contain fused aromatic rings, which would extend the linear conjugation path along the polymer backbone. S64 also holds excellent potential since this monomer contains a mesomeric electron-withdrawing cyano group. The phenylene equivalent to this polymer achieved the third-highest photocatalytic activity of all the samples (P1-27). This indicates that the cyano group is excellent for selectively enhancing charge transfer to platinum cocatalysts. Since the cyano group in S64 is located on a pyridine ring, this unit becomes even more electronegative. A more significant proportion of the LUMO electron density will be localised on this unit compared to the Ph-CN unit of P1-27, potentially leading to even higher photocatalytic activities.

2.7.3.3 Aromatic hydrocarbon co-monomers

The second set of copolymers includes co-monomers that only contain aromatic hydrocarbon rings, i.e. no heteroatoms. Whereas heterocycles can stabilise positive and negative charges via their resonance forms and naturally include more significant intrinsic dipole moments, benzene rings are symmetric and contain no dipole moment before substitution. Benzene rings can be considered neutral, unlike heterocyclic molecules pyrrole and pyridine, which are mesomeric electron donors and acceptors, respectively. Phenylene rings are more stable, less reactive, and are good π -spacing units for conjugated systems. They also operate as a blank slate for structural modifications that can introduce dipoles and transform the electronic structure via substituent effects.

The aromatic hydrocarbon-based co-polymers can be subdivided into three subsets. The first subset (S65-S70) contains fused macrocyclic rings with extended delocalised π -systems spread over co-planar units. The second subset (S71-S97) includes phenylene units substituted with functional groups that do not contain π -electrons that are conjugated to the polymer backbone. These substituents only

contribute inductive electron donating or withdrawing effects. The third subset of copolymers contains phenylene rings with π -conjugated substituents that extend the π -electron network along the polymer backbone. These substituents contribute mesomerically to the electron-donating and withdrawing effects of the co-monomer. The variable co-monomers for each of these subsets are presented in Figures 117 and 118.

Aromatic Hydrocarbon Co-monomers

Subset I – Fused polycyclic aromatic hydrocarbons

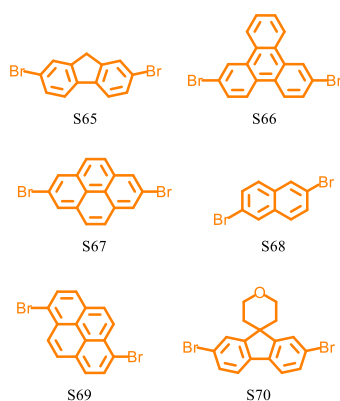


Figure 117: List of the most promising photocatalysts resulting from virtual screening of 704 theoretical DBTS co-polymers. Set II : Co-monomers containing aromatic hydrocarbon rings. S65 – S70 (Hydrocarbon Subset I) contains fused hydrocarbon macrocyclic comonomers. Polymers are colour coordinated according to their position on the IP* vs EA* chart relative to the DBTS-DBTS homopolymer. See Figure 114 for details.

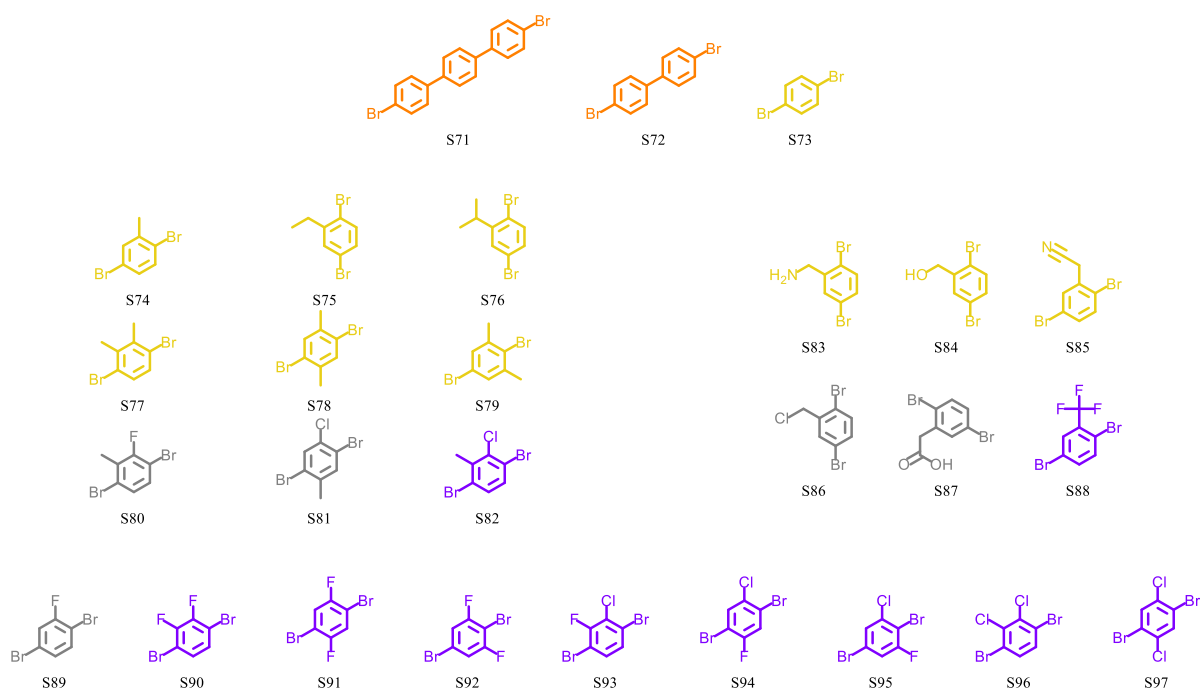
Most of the fused aromatic systems of subset 1 have already been synthesised in the initial high throughput experiment. These co-polymers performed very well with no additional co-catalyst. This is in line with their strong electron-donating character relative to DBTS, as indicated by their location in the orange region of the IP*/EA* plot (Figure 114). Their high-energy LUMO should generate an appropriate driving force for charge transfer to residual palladium. However, unlike the fused macrocyclic systems containing 5-membered heterocycles, the photocatalytic activity of S65 (P1-89) and S66 (P1-23) increased further upon the addition of a platinum co-catalyst. S68 (P1-13) contained substantial levels of palladium. Resultingly, this polymer demonstrated the highest activity before Pt, but the activity did not increase further following Pt addition.

S67 (P1-24) performed poorly, which is possibly attributable to the non-linear conjugation pathway along the polymer backbone and its particularly high energy HOMO that may result in slow TEA

oxidation rates. The pyrene unit is also symmetric and non-polar, which could potentially lead to weaker absorption coefficients and no permanent dipole-dipole interactions with the TEA reagents to aid charge transfer. Although the preparation of S67 (P1-25) was unsuccessful, this polymer may also perform poorly for similar reasons.

The remaining polymer, S70, would be an interesting candidate since the presence of the ether group introduces a dipole moment that may enhance the interaction with water and other polar solvents. However, it is unlikely to result in a significant improvement over the other similar polymers.

Subset II: Para-linked phenylene monomers with inductive functional groups



Subset III: Para-linked phenylene monomers with mesomeric functional groups

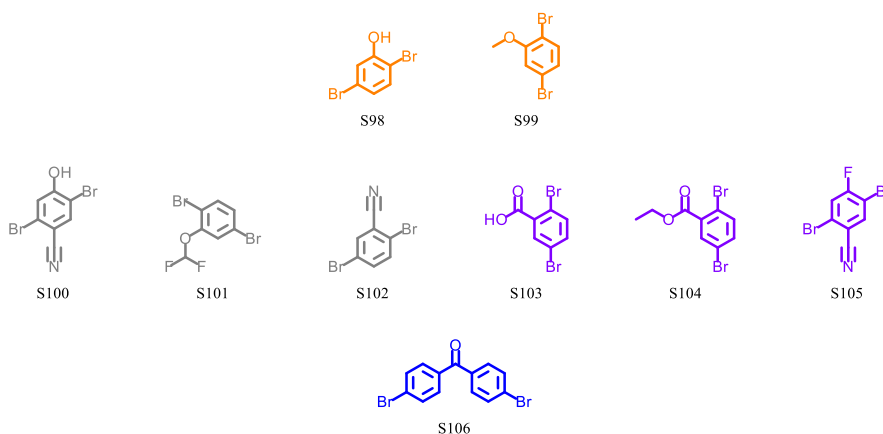


Figure 118: List of the most promising photocatalysts resulting from virtual screening of 704 theoretical DBTS co-polymers. Set II : Co-monomers containing aromatic hydrocarbon rings. S71 – S97 (Hydrocarbon Subset II) contains phenylene-based comonomers with inductive functional group substituents. S98-S106 (Hydrocarbon subset III) contains phenylene-based comonomers with mesomeric functional group substituents across which charge can be delocalised. Polymers are colour coordinated according to their position on the IP* vs EA* chart relative to the DBTS-DBTS homopolymer. See Figure 114 for details.

Subset 2 (S74 – S97) contains phenylene monomers with inductive substituents. An unsubstituted phenylene monomer (S73) is electron donating relative to DBTS. Increasing the number of phenylene units relative to the number of DBTS units (S71 and S72) increases this electron-donating character. As discussed earlier, adding hydrocarbon substituents produces an additional inductive donating effect. As with the fused hydrocarbon macrocycles, these polymers also exhibited improved photocatalytic activities with Pt deposition when residual palladium levels were low. Photocatalytic

activity before Pt also appeared to have been negatively impacted by impurities associated with low synthetic yields.

The addition of electron-withdrawing groups lowers the LUMO energy from the yellow region to the grey region, which is associated with a lower energy and more-delocalised LUMO. This would theoretically lead to the slower transfer of electrons to residual palladium. However, S89 (P1-60) was the second-best photocatalyst after Pt addition but was also unexpectedly efficient without Pt.

Whereas the fluorescence lifetimes of most polymers were predominantly dependent on the optical bandgap, polymers containing fluorinated phenylene rings S88, S89, S90, and S91 each exhibited fluorescence lifetimes that were predominantly dependent on the residual palladium content. S89 and S90 (P1-61) contained the least palladium, had longer lifetimes than expected for their bandgaps, and exhibited the fastest hydrogen evolution rates after Pt addition. These results imply that when the LUMO is delocalised, the chemical nature of the co-monomer becomes more influential regarding the charge transfer rates to palladium and platinum.

As such, the other phenylene-based co-polymers in the grey and purple regions make excellent candidates for future investigations to gain an improved understanding of residual palladium's role in the photocatalysis mechanism. Methyl groups will increase the LUMO energy, whereas chlorine appears to decrease the predicted LUMO energy. S92 is also a particularly interesting monomer relative to S90 and S91 since its permanent dipole lies parallel to the polymer backbone, whereas the permanent dipole of S90 is at 30 degrees relative to the backbone, and S91 has no net permanent dipole moment.

The third subset of phenylene-containing co-polymers includes those with π -conjugated mesomeric substituents (S98-S106). As discussed earlier, hydroxy, ether, aldehyde, carboxylic acid, and ester functional groups complicate photophysical properties since they are potentially unstable regarding auto-oxidation or reduction and can enhance rates of ISC.

However, very few of the polymers identified in this subset of polymers were successfully synthesised in the initial study. S103 (P1-37) performed poorly, but this can largely be attributed to the astonishingly high residual palladium concentrations. Meanwhile, S106 (P1-47) placed among the top 25 photocatalysts before and after Pt addition. The dihydroxy derivative of S98 was also synthesised (P1-36) and performed poorly. However, this polymer was deselected during the screening process

for its high electron-donating Fermi energy and poor oscillator strength. As such, the remaining oxygen-containing co-polymers presented in this subset should not be dismissed.

S102 (P1-27), which contains a conjugated cyano group and no oxygens, was the fourth-best photocatalyst with Pt and exhibited the second-largest change in HER rate relative to the test without Pt. S100 and S105 are more electron-donating and electron-withdrawing derivatives, respectively. They still contain the cyano group, but engineering the redox potentials by adding additional donating or withdrawing groups could lead to the discovery of an improved photocatalyst. S105 is particularly interesting since fluorobenzene is also an active polymer. The electron-withdrawing nature of this comonomer could lead to increased electron density on the phenylene unit and faster electron transfer to platinum via the cyano group.

It is worth noting that, of the 24 polymers whose HOMO and LUMO energies both lie close in energy to those of P1-93 (represented in grey), only two were synthesised in the high throughput experiment. Both of these polymers, P1-60 and P1-27, are within the top 3 highest performing photocatalysts after P1-93 when loaded with 1 wt.% Pt. As such, other polymers in this region should be targeted for future novel polymers since a delocalised HOMO and LUMO appear beneficial. The red and purple polymers should also be targeted as potential polymers that can significantly increase activity when using Pt as a co-catalyst.

2.8 Conclusions

In this chapter, previously published results from high-throughput computational calculations and high-throughput experiments have been analysed in detail. The original publication²¹⁰ reported ionisation energies, electron affinities, optical bandgaps, and oscillator strengths using low-cost computational methods for 6,354 linear copolymers. This library of potential polymers includes 705 theoretical linear co-polymers containing the DBTS monomer unit. The authors subsequently attempted to synthesise 127 of these copolymers using high-throughput experimental methods and produced 99 polymers with yields greater than 30%.

The first outcome of this work relates to the accuracy of the computational model in predicting the polymer's optical bandgaps. In the original paper, high throughput computations were performed using an extended tight-binding model. A correction term was added to the IP, EA, and E_g energies. These correction terms result from a linear correlation between xTB-determined values and those obtained from more advanced DFT calculations. However, despite this correction, substantial errors persist when the resulting E_g is compared with the measured values for the synthesised polymers.

The fundamental bandgap and the optical bandgap differ by the exciton binding energy. However, this exciton binding energy is typically on the order of tenths of an electron volt, which is substantially less than the error in the predicted bandgap relative to the measured bandgap. This work shows that it is possible to correctly predict the optical bandgap of these linear polymers within a mean absolute deviation of ± 0.11 eV of the measured value. This was achieved by applying correction terms to the IP and EA energies based on a linear correlation between the fundamental gap and the measured optical gap. Independent calibration equations were determined for the IP and EA values. The resulting calibration equations produced an estimation of the optical bandgap, E_{IPEA} , which exhibits a mean average deviation from the experimental values was ± 0.11 eV. This magnitude of error is excellent, considering that no information regarding the exciton binding energy is included.

These calibration equations were also tested on a blind set of polymers not used to determine the calibration equation. These polymers were also predicted within ± 0.25 eV. However, since the calibration equation was trained from data only relating to DBTS copolymers, optical bandgaps for the linear polymers that do not include the DBTS unit were systematically underestimated by small amounts.

The large differences between E_{Fund} and E_{IPEA} significantly exceed the exciton binding energies. This indicates that the IP and EA energy estimations, and hence the polymer oxidation and reduction potentials derived from these values, are unreliable. However, using the E_{IPEA} gap approximation, estimations of the excited state ionisation potentials and electron affinities, IP^* and EA^* , were made by equally shifting the predicted IP and EA levels in opposite directions such that the difference between IP^* and EA^* equals the predicted optical bandgap.

The predicted and measured optical properties of the 99 synthesised polymers have been examined with respect to the hydrogen evolution rates. Whereas the original research focussed on trends associated with the photocatalytic activity without an additional co-catalyst, this work explicitly considers the different performances before and after the photodeposition of platinum. Furthermore, this work also considers photocatalytic activity trends amongst subsets of similarly-structured co-polymers. In doing so, it has been possible to gain further insight into some property-activity trends that are not obvious when the complete data is analysed together as a whole.

Analysis in this chapter has revealed several previously-unidentified relationships. The first relates to the predicted oscillator strengths. Most of the top photocatalysts revealed in this study are predicted to have oscillator strengths larger than 5.5. The oscillator strength appears to be a good measure of the degree of orbital delocalisation along the polymer backbone. The oscillator strength is larger for monomers in which resonance structures show that electrons can flow in through one side of the monomer and out of the other. For example, this value can differentiate between para-linked and meta-linked phenylene. Electrons in p-phenylene polymers are more delocalised and usually result in higher HER rates. Molecules will also have larger oscillator strengths when the longest axis of the comonomer's conjugated π -electron system is oriented along the direction of the polymer backbone. These polymers also typically exhibit higher HER rates.

The main exceptions to this rule arise when co-monomers contain multiple aromatic rings that are not co-planar. In such systems, oscillator strengths are large because they contain extended linear regions of conjugated double bonds along the direction of the polymer backbone. However, when the sequential aromatic rings are not locked into a co-planar geometry, this conjugation may be weakened, and the delocalisation length shortened, due to non-zero dihedral angles between the planes of the adjacent aromatic π -systems.

Other exceptions appear to arise in polymers containing meta-linked pyridine co-monomers. These systems are also predicted to have small oscillator strengths due to the meta-linkages. However, in these systems, the photocatalytic HER rate remains relatively high when the N-atom is ortho to the two polymer linkage positions. Pyridine's resonance structures show that positive charges are delocalised onto the ortho and para positions relative to the heteroatom. These charges can be further delocalised along the polymer backbone, stabilising the negatively-charged nitrogen. As such, the co-polymer synthesised from 2,6-dibromopyridine can stabilise a negatively charged polaron without breaking the conjugation via resonance structure considerations. Similar rationales can be used to explain the high photocatalytic activities of other meta-linked pyridine-based co-polymers with small oscillator strengths.

The second unexplored relationship in the original study is the association between the fluorescence lifetime and the photocatalytic activity, particularly regarding enhancements after the photodeposition of Pt. Forty-five of the 99 polymers exhibited weighted-average fluorescence lifetimes shorter than 1 ns. Of these 45 polymers, only three produced hydrogen at rates faster than $4 \text{ mmol hr}^{-1} \text{ g}^{-1}$ after Pt addition, placing them in the top 25 polymers. For most polymers, long-lived fluorescence lifetimes appear essential for high-efficiency photocatalysis.

The original study noted that the optical bandgap is a highly influential factor in predicting polymers with high photocatalytic activities. This was counter to expectation since narrow bandgap polymers can absorb a greater proportion of incident photons by also absorbing those with lower energies. They attributed this discrepancy to wider bandgaps correlating with more negative EA potentials, another very influential predictive factor.

However, the analysis presented in this chapter has demonstrated that bandgap also directly correlates with the fluorescence lifetime. This is likely due to the inverse gap law for non-radiative relaxation from the excited state to the ground state via internal conversion. The wider the energy gap, the lower the probability of non-radiative relaxation events occurring. Since polymers are subject to many vibrational and rotational modes, the probability of IC is very high, even among wide bandgap organic semiconductors. Fast rates of non-radiative relaxation will significantly inhibit the maximum achievable efficiency.

Analysis in this chapter has also identified that the fluorescence lifetimes of certain co-polymers do not follow the same dependence on the optical bandgap. The fluorescence lifetimes of polymers

containing fluorinated para-phenylene monomers vary linearly with respect to their residual palladium content. Those with the lowest levels of palladium also exhibited fluorescence lifetimes longer than expected, given their measured bandgap. More generally, there also appears to be a weaker correlation between the residual palladium concentration and fluorescence lifetimes, but in most cases, this is less influential than the optical bandgap. P1-37, which contains a benzoic acid comonomer, also exhibited a particularly long fluorescence lifetime, given its optical bandgap. The polymers containing fused macrocyclic rings also exhibited longer fluorescence lifetimes, in agreement with their more rigid and strained geometries that would reduce the probability of IC.

This chapter has also highlighted the key relationship between photocatalytic activity and the residual palladium concentration. In the absence of a platinum co-catalyst, this relationship is not obvious since higher palladium content appears to result in higher photocatalytic activities in some cases. However, after the photodeposition of a Pt co-catalyst, the negative linear correlation between residual palladium content and HER rate becomes much clearer. The most significant increases in HER rate when comparing activity before and after Pt addition are observed in polymers with long lifetimes and low palladium concentrations. The activities of samples containing high levels of palladium are considerably more likely to decrease after adding Pt.

This work has also identified a clear correlation between the maximum photocatalytic activity and the synthesis yield. Polymers obtained with low yields were considerably more likely to exhibit lower photocatalytic activity than their similarly-structured counterparts with similar palladium levels when they were obtained with low yields. The exact relationship here is unclear, but photoreduction of impurities, short polymer chain lengths, and an increased probability of a high palladium content are all possible. Additionally, the high concentrations of unreacted bromine on chain ends could lead to faster intersystem crossing rates from a photoexcited singlet state into a triplet state via the heavy atom effect.

The original research also discusses the IP and EA potentials relative to the standard hydrogen electrode. This work presents an alternative frame of reference from which to consider these values: the IP and EA of the DBTS homopolymer P1-93. By considering the IP and EA potentials of the DBTS co-polymers with respect to those of the homopolymer, we gain considerably more insight into how the co-polymer electronic structures vary with respect to their physical ones.

The co-polymers in which the IP and EA are both more negative than those of P1-93 result from co-polymerising the DBTS unit with a strongly electron-donating co-monomer. Likewise, when DBTS is co-polymerised with an electronegative, electron-withdrawing co-monomer, the resulting HOMO and LUMO potentials are more positive relative to P1-93. It is useful to consider the electron-donating and accepting behaviours of the co-monomers in this way. This research has also highlighted how the Fermi potential, as represented by the point at the middle of the fundamental gap, can also be reported relative to that of P1-93 to determine whether the co-monomer should be considered an electron donor, acceptor, or neutral when paired with the DBTS unit. This approach to the analysis could also be adapted to the homopolymer potentials for the nine alternative co-polymer sets considered in the computational screening stage of this research rather than by analysing the absolute EA and IP of the polymers.

In this way, the DBTS co-polymers can be subdivided into several categories related to their IP (HOMO) and EA (LUMO) potentials relative to P1-93 to provide more information regarding their structure-activity relationships. In the absence of a platinum co-catalyst, the most efficient copolymers contain an electron-donating co-monomer. These resulting polymers have more negative IP and EA potentials relative to P1-93. In these cases, the thermodynamic driving force for electron injection into palladium and proton reduction is the greatest. Upon loading the polymers with a platinum co-catalyst, larger increases in photocatalytic activity are observed for polymers in which the co-monomer could be considered neutral or electron-withdrawing relative to P1-93. This is attributed to the fact that platinum is a more efficient co-catalyst for hydrogen evolution with a larger work function and hence requires a smaller thermodynamic overpotential to drive the hydrogen evolution reaction.

Many of the best photocatalysts after Pt addition are predicted to have EA potentials within ± 0.1 eV of P1-93. The best-performing polymer was P1-93 itself. With the exceptions of the thiophene-containing co-polymers, P1-99 and P1-110, the photocatalytic activities of polymers containing other electron-donating heterocyclic co-monomers did not improve upon Pt photodeposition. However, P1-99 and P1-110 are predicted to have EA potentials similar to P1-93, and their electron-donating character is only noticeable when considering the relative IP potentials.

Aromatic hydrocarbons are shown to be electron-donating co-monomers relative to DBTS since DBTS itself is electron-withdrawing. This donating effect is emphasised in polymers containing polycyclic aromatic hydrocarbon monomers. However, unlike the polymers containing electron-donating

aromatic heterocycles, the photocatalytic activity of these polymers improved upon photodepositing Pt, provided the palladium concentration was low.

Adding electronegative substituents to phenyl rings lowers the EA potential, making it closer in energy to that of P1-93. These samples, such as the fluorinated phenylene copolymers, exhibited some of the most interesting properties. The hydrogen evolution rate of P1-27, which contains the cyano-substituted phenylene co-monomer, increased from 1.1 mmol hr⁻¹ g⁻¹ to 10.7 mmol hr⁻¹ g⁻¹ after Pt addition.

A similar approach was then applied to analyse the 705 DBTS co-polymers for which the optoelectronic properties were calculated during the computational stage of the research. This analysis also used the new calibration equations to provide a closer estimate of the optical bandgaps compared to the xTB-based values initially provided. The new estimations of IP* and EA* were also used for this analysis.

The 705 theoretical polymers were reduced to 107 promising candidates via screening parameters based on IP, EA, the Fermi potential, and the oscillator strength. Of these 107 polymers, 29 had been synthesised in the 99-sample high-throughput study. Nineteen of these 29 ranked in the top 25 polymers for photocatalytic activity after Pt photodeposition, including nine of the top 10. Although these screening parameters are not perfect, they are highly effective. Six of the top 25 polymers were omitted based on their small oscillator strengths and included some structurally unique pyridine-based co-polymers. However, the remaining omitted polymers with high activities were structurally related to other highly effective polymer photocatalysts that had not been omitted and which were considerably more efficient. Likewise, several poor photocatalysts that had not been omitted contained large amounts of palladium or had been synthesised with low yields and may prove to be more efficient if synthesised under different conditions.

This analysis resulted in the prediction of 78 new DBTS co-polymers expected to be highly efficient photocatalysts. The structures of the resulting monomers were then assessed by eye to predict which should be targeted as the most promising based on their similarities and differences relative to the initial synthesised set.

Chapter 3: Organic Photocatalysts

3.1 Introduction

In the work published by Bai *et al.*, the DBTS-DBTS homopolymer, widely known as P10, produced the fastest photocatalytic hydrogen evolution rates.¹⁸² However, as demonstrated in Chapter 2, several other co-polymers showed immense promise, and the synthesis conditions may have inhibited their photocatalytic performances.

The work presented in this chapter focuses on three closely-related sets of linear copolymers. The first set, the DBTS-PhF_x set, reproduces a selection of dibenzothiophene sulfone (DBTS) co-polymers containing phenylene comonomers with varying fluorine substituents from the original high-throughput publication. The second set, BDT-PhF_x, includes benzodithiophene (BDT) co-polymers containing the same fluorinated phenylene co-monomers. The third set of co-polymers investigated, BDT-PhF_x-DBTS, contains a set of ternary co-polymers constructed from the first two sets. These three sets of polymers are outlined in Figure 119.

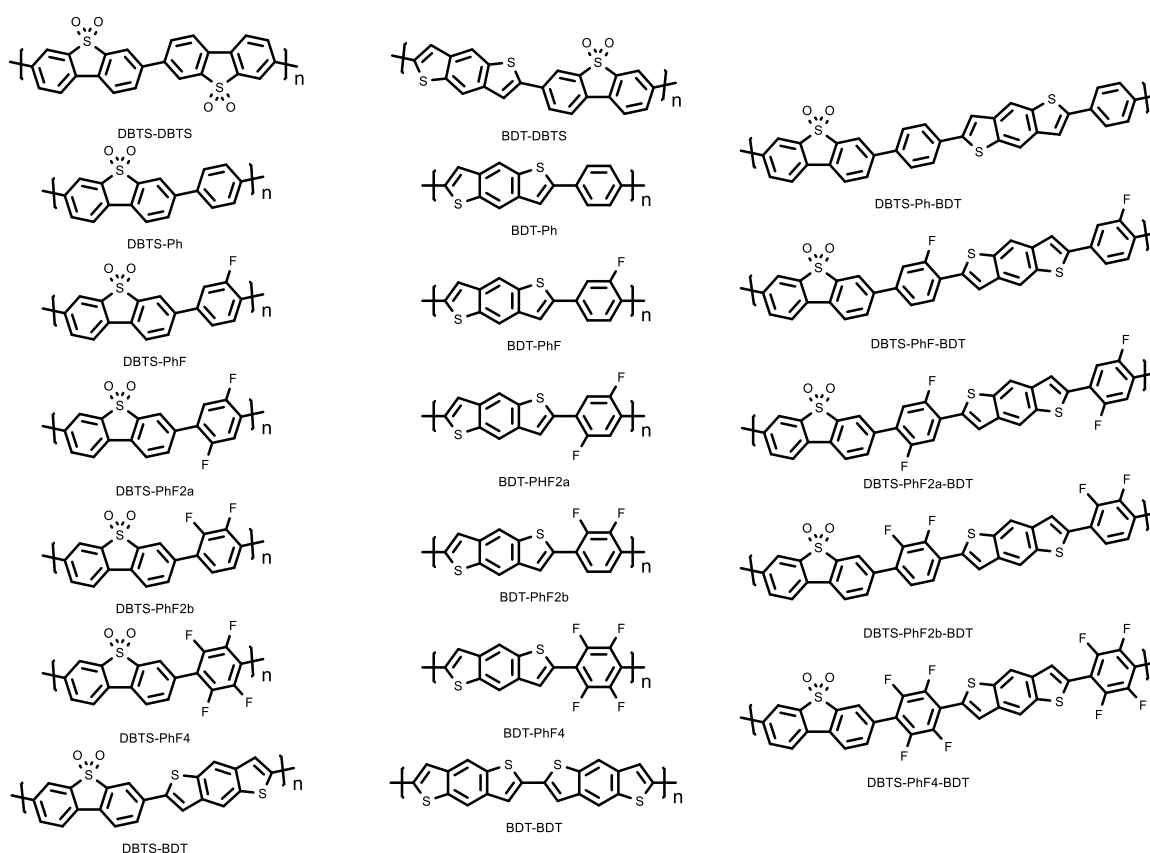


Figure 119: Target co-polymers investigated in this chapter. DBTS-PhF_x binary co-polymers (left), BDT-PhF_x binary co-polymers (middle), DBTS-PhF_x-BDT ternary co-polymers (right).

The DBTS-PhFx polymers were selected because the polymers DBTS-PhF (P1-60) and DBTS-PhF2b (P1-61) ranked within the top 10 photocatalysts for sacrificial hydrogen evolution in the high throughput research. However, the photocatalytic activities of DBTS-PhF2a and DBTS-PhF4 were significantly impacted by their high residual palladium concentrations and sub-optimal yields. Overall, it is hoped that, by optimising the synthesis conditions, it may be possible to enhance the photocatalytic activity of these polymers above that of P10.

From a bandgap-engineering perspective, the addition of fluorine substituents lowers the LUMO energy of the co-polymer such that the LUMO of DBTS-PhFx polymers lie close in energy to the DBTS-DBTS homopolymer. Theoretically, this should result in increased delocalisation of photogenerated electrons over the polymer backbone since the energetic barrier for transport between adjacent monomers is diminished. Resultingly, the LUMO is likely to be delocalised over several repeat units in the polymer backbone. In such systems, the chemical structure of the co-monomer becomes more influential in the rate of the photoreduction (hydrogen evolution) reaction.

Interestingly, amongst the DBTS-PhFx polymers, an inverse linear dependence of the fluorescence lifetimes and the residual palladium concentration was observed, unlike most of the other polymers in which the fluorescence lifetimes predominantly depended on the optical bandgap. This result suggests fluorinated phenylene units may facilitate rapid charge transfer to metal co-catalysts. By incorporating these units, it may be possible to synthesise efficient organic photocatalysts that require very low loading concentrations of noble metal co-catalysts.

The polymers of the second set are synthesised from the BDT-B(pin)₂ monomer. These have been selected because the DBTS-BDT co-polymer (P1-110) showed some unique characteristics in the high-throughput study. In particular, P1-110 ranked 15th amongst the most active photocatalysts after Pt photodeposition, despite exhibiting a fluorescence lifetime shorter than 1 ns. Its photocatalytic activity is also remarkably high, given its narrow bandgap.

The BDT unit comprises three fused aromatic rings resulting in a co-planar geometry, and its longest molecular axis, along which the π -electrons are delocalised, is oriented parallel to the polymer backbone. Resultingly, polymers containing the BDT unit are expected to have very large oscillator strengths, which correlate to high photocatalytic activities.

Thiophene rings are typically considered electron-donating monomers when incorporated into extended π -conjugated systems such as organic conjugated polymers. Resonance structures show that a positive charge can be localised on the sulfur atom while negative charges are delocalised along the polymer backbone. Since the thiophene unit can be easily oxidised, polymers containing the BDT have smaller (less positive) ionisation potentials relative to the SHE. This lower IP corresponds to BDT-containing co-polymers having higher-energy HOMOs compared to polymers without electron-donating moieties.

However, as discussed in Chapter 2, compared to co-polymers containing other electron-donating aromatic heterocycles such as furans and pyrroles, those containing thiophenes also have larger electron affinities (as represented by more positive EA potentials relative to the SHE), corresponding to lower-energy LUMOs. According to the predicted EA potentials, the DBTS-BDT LUMO is predicted to lie at a very similar energy to the DBTS-DBTS LUMO, and as such, the electron density of photogenerated electrons is also expected to be delocalised over the polymer backbone in these structures.

Unlike the polymers containing nitrogen-based electron-donating units, P1-110 and other thiophene-containing co-polymers exhibited increased photocatalytic activity upon the photodeposition of platinum. This increase indicates that the smaller reduction potential may correlate with slower charge transfer to residual palladium and enable preferential charge transfer to surface Pt. Incorporating fluorinated phenylene units may also influence the charge transfer rates to different co-catalysts.

The BDT unit is a common moiety that features in organic photovoltaics (OPV), where its strong electron-donating character and narrow bandgap are beneficial for rapid charge separation at the bulk heterojunction interfaces and harvesting large portions of the solar spectrum, respectively.²¹¹ One feature that makes the BDT unit particularly versatile is the relative ease with which the benzene unit can be further substituted. Modifications of this side chain can be used to exert additional control over the electronic structure,^{212,213} improve polymer solubility,¹⁴⁶ form conjugated crosslinks to form microporous polymers, or improve the interfaces with water, organic solvents, or inorganic solids.

The third set of co-polymers investigates the potential of ternary conjugated polymers. By introducing fluorinated phenylene linkers between the DBTS and BDT units, it is hoped that the resulting polymeric photocatalysts should benefit from the narrow bandgap and strong donating character of the

modifiable BDT unit, the improved co-catalyst charge transfer ability of the fluorinated phenylene units, and the inherent photocatalytic activity associated with the DBTS unit. Ternary polymers also enable fine-tuning of the electronic band structure by varying the component ratios statistically.^{165,214}

3.2 Chapter Outline

Following section 3.3, in which the experimental methodology is outlined and discussed, section 0 presents a computational investigation of the proposed linear polymers using DFT calculations. The oxidation and reduction potentials of each polymer are modelled relative to the standard hydrogen electrode to verify that the ternary polymers are thermodynamically capable of driving sacrificial hydrogen evolution. The electronic structures of the ternary co-polymers are compared with their binary equivalents. This section also includes an analysis of the frontier molecular orbitals.

Sections 3.6 - 3.8 focus on the synthesis, photocatalytic activities, and optoelectronic characterisation of the DBTS-PhFx, BDT-PhFx, and DBTS-PhFx-BDT co-polymers, respectively. The polymers are synthesised using a microwave-assisted Suzuki-Miyaura polycondensation reaction. By using this microwave-assisted approach for organic synthesis, a range of reaction conditions can be screened rapidly since each reaction is completed in under two hours. A particular focus is placed on the impact of synthesis conditions on the resulting photocatalytic activity. The three sets of fluorinated copolymers are compared and contrasted in section 3.9.5. Section 3.10 contains the overall conclusions and identifies future work that should be conducted in this field to continue this research and further verify the observed trends.

3.3 Methods

3.3.1 DFT Calculations

All calculations were conducted using the Materials Studio Software Package (*Dassault Systems, 2016*). For each polymer of interest, calculations were run on oligomeric analogues of the overall polymer. The oligomeric chain length in each case contains an equivalent of 12 phenylene units in accordance with previous DFT calculations of conjugated organic polymers.¹⁸⁹ These oligomers first undergo a conformer search in which 5000 conformations are searched based on random rotations of the dihedral bonds. Each conformation is then subsequently optimised using a pcff forcefield geometry optimisation calculation.²¹⁵ A geometry optimisation calculation using the semi-empirical density functional tight-binding (DFTB+) method was completed starting from the most stable conformer.²¹⁶

Single-point energy calculations using the Dmol³ package²¹⁷ were then calculated using a B3LYP hybrid functional^{218–221} in conjunction with the DNP+ basis set with basis file 4.4.^{222,223} oligomer chains were modelled in a high dielectric environment using the COSMO solvent model to mirror the potentials at the interface with water.²²⁴ Additionally, single-point energy calculations were conducted on the singly-charged oligomer chains (P⁺ and P⁻) without further geometry optimisation. The differences in absolute energies between P, P⁺, and P⁻ were then used to calculate vertical ionisation energies and electron affinities. These IP and EA energies were then used to calculate the absolute potentials of the HOMO and LUMO orbitals relative to the vacuum level from which oxidation and reduction potentials can be calculated relative to the standard hydrogen electrode, SHE ($V_{\text{SHE}} = 4.44 \text{ V vs } V_{\text{abs}}$).

3.3.2 Organic Synthesis

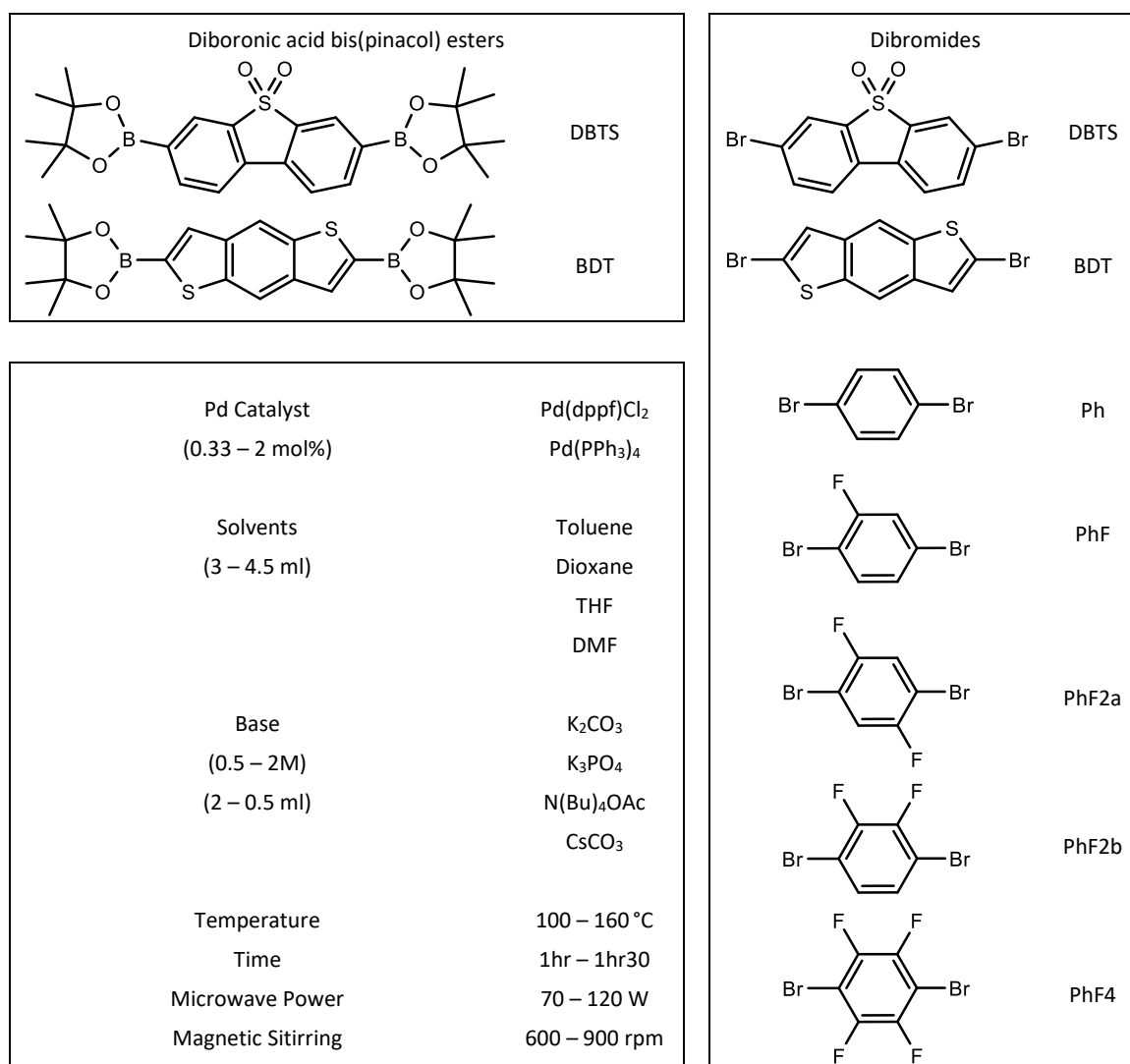


Figure 120: Reagents and conditions used for microwave-assisted Suzuki polycondensation reactions performed in this chapter.

Dibromide and diboronic acid bis(pinacol) ester reagents were purchased from Fluorochem, Sigma-Aldrich, TCI, and Manchester Organics. These reagents were used as purchased without further purification. A list of different boronates, halides, bases, solvents, and additives used in these reactions is presented in Figure 120. The phase transfer catalyst used in toluene-based reactions (PTC) is Aliquat 336 (Starks' catalyst).

The synthesis methodology was adapted from the high throughput microwave synthesis approach used by Bai *et al.*¹⁵⁶ Typically, a 2-5 ml microwave reaction vial (Biotage) is charged with the solid reagents and a magnetic stirrer bar. The aqueous base and organic solvent are added before the vial is capped with a lid containing a rubber septum. The reaction mixture is degassed by bubbling nitrogen through the solution for 10 minutes. The reaction mixture is vigorously stirred via magnetic stirring before being transferred to the microwave reactor (Biotage, Initiator+ robot sixty). Reactions are typically performed on the 0.25 mmol scale, producing approximately 90 mg of product.

Various reaction conditions were used throughout the study. Typically, 30 s of pre-stirring was followed by heating to 100 degrees for 15 minutes before increasing the temperature to 120 degrees for a further 60 – 90 minutes. The microwave absorption rate is set to very high, and the power is limited to 70-100 W to prevent sudden spikes of pressure. The reaction mixture is stirred at 600 - 900 rpm.

After the reaction's completion, the vial is de-capped, and the contents are emptied into methanol. The solid polymer is isolated by Buchner filtration and washed with water, methanol, and chloroform. The resulting powders are dried in a vacuum oven at 60°C overnight.

3.3.3 Optoelectronic Characterisation

3.3.3.1 UV-Vis Diffuse Reflectance Spectroscopy

An Agilent Cary 500 UV/Vis spectrometer was equipped with the Praying Mantis accessory to allow Diffuse Reflectance Spectroscopy, DRS, measurements to be acquired from small quantities of each sample.

A reflectance spectrum of high purity barium sulfate, BaSO₄, (Sigma Aldrich) was recorded as a reference spectrum equating to 100% reflectance. Due to its very wide bandgap of 4.0 eV and high purity, this sample reflects all light with wavelengths longer than 310 nm.

Since the polymers of interest are strong absorbers, 5 mg of the polymer was combined with 55 mg of BaSO₄ and ground together using an agate pestle and mortar. This prevents reflectance measurements of 0% or below and allows an accurate absorption spectrum to be recorded above the bandgap.

Reflectance measurements were recorded relative to pure BaSO₄. The reflectance was converted to an approximation of the absorbance via the Kubelka-Munk function,

$$F(R_{\infty}) = \frac{K}{S} = \frac{\left(1 - \left(\frac{R}{R_s}\right)\right)^2}{2\left(\frac{R}{R_s}\right)}.$$

In this equation, K is the absorption coefficient, and S is the scattering factor.²²⁵ R/R_s is the reflectance from the sample relative to the BaSO₄ standard. For amorphous and polycrystalline samples, F(R) can be used to approximate the absorption coefficient, α .

The bandgap of a semiconductor is determined using the Tauc method.¹⁹² This is based on the assumption that the following formula can be used to express the absorption coefficient at the absorption edge,

$$(\alpha \cdot hv)^{\frac{1}{\gamma}} = B(hv - E_g).$$

For direct semiconductors, $\gamma = \frac{1}{2}$, and for indirect semiconductors, $\gamma = 2$. The optical bandgap can therefore be determined from DRS data by plotting $(F(R_{\infty}) \cdot hv)^{\frac{1}{\gamma}}$ against hv and extrapolating the linear section at the band edge and calculating its intercept with the x-axis.

This method was initially elaborated for amorphous and polycrystalline inorganic semiconductors. Although this can also be used to approximate the bandgap of organic conjugated polymer semiconductors, the unusual semicrystalline properties of such semiconductors make it challenging to ascribe physical meaning to the value of γ that gives rise to the most linear band edge. A high density of optically-active sub-gap states belonging to excitons results in strong absorption at energies below the bandgap and gives rise to a significant Urbach tail.^{226,227}

Following the recommendations of Macyk *et al.*,¹⁹³ indirect bandgaps are determined from the intercept of the linear section of the band edge and the linear extrapolation of the tail to enable a more accurate measure of this value and prevent underestimating the bandgap.

It is worth noting that the Tauc method assumes that the density of states close to the band edge is proportional to the square root of the energy, \sqrt{E} . Conjugated polymers contain a distribution of chromophores, each with a distinctive absorption spectrum consisting of optically-allowed transitions between molecular orbitals.²²⁸ As such, there is much debate regarding how the density of states varies as a function of energy at the band edge.

3.3.3.2 Steady State Fluorescence

Fluorescence measurements were performed on an Edinburgh Instrument FLS1000 fluorescence spectrometer that allows for fluorescence excitation, emission, and lifetime measurements of the polymers in their solid state. In preparation for fluorescence measurements, powder samples were loaded into a quartz sample holder for powdered solids and loaded onto a rotational sample stage. The sample was rotated to an angle of approximately 45° from the incident light (450W Xe Arc lamp) to maximise the spot size and fluorescence intensity. Quick excitation and emission fluorescence measurements were taken to identify the respective maxima.

In steady-state excitation fluorescence measurements, the Xe lamp excitation source is scanned, and the emission is monitored at a set wavelength. By contrast, fluorescence emission spectra are recorded by setting the excitation source to a constant wavelength and scanning with the emission monochromator.

The excitation and receiving slit widths were adjusted for each sample such that the emission intensity was high enough for a high signal-to-noise ratio, S:N, but low enough to prevent the detector's saturation and potential damage. The equipped detector was a PMT900.

DBTS-PhFx polymers were the most fluorescent, and required narrow monochromator bandwidths of 0.5 nm, whereas BDT-PhFx polymers were the least fluorescent and required detection bandwidths of 3 nm. Emission intensity from the ternary system was between the two.

The emission spectra are recorded from excitation at 350 nm for the measurements presented in this chapter. This allowed the entire emission spectrum to be registered and resulted in a smooth peak shape. When excited at longer wavelengths, the emission peak was less reliable. Excitation spectra were recorded at the emission maximum.

TCSPC measurements were also conducted using the FLS1000 spectrometer. An EPL-405nm diode laser was used with a 50 ns pulse period, a pulse width of 60 ps, and a typical peak power of 110 mW. Each channel of the 2048-channel detector counted single incident photons in each 24 ps time interval. The Instrument response function, IRF, was measured at the emission wavelength (404.7 nm). Photoemission was measured at the peak identified from the steady-state emission spectrum. Fluorescence decay curves were fitted by reconvoluting a tri-exponential decay function with the IRF using the Fluoracle software.

3.3.4 Photocatalytic Activity Testing

3.3.4.1 GC Peak Calibration

A calibration curve was generated to enable the quantitative analysis of HER and OER rates. For this process, 10 ml headspace vials were loaded with 5 ml water, capped, and degassed. Specific volumes of pure hydrogen at 1 bar and air (assuming 20.95 vol.% oxygen) were then injected into the headspace vials. These were subsequently run on the GC system. The peak areas and corresponding concentrations of gas in the headspace of the vials are plotted in Figure 121. The number of moles of injected gas is calculated using the ideal gas equation. The calculation also assumes that all injected gas is present in the headspace. In reality, some gas will dissolve into the water leading to an inaccurate assumption of headspace concentration. However, the calibration was conducted in 5 ml of water to minimise errors arising from gas that dissolves in the solvent under operating conditions.

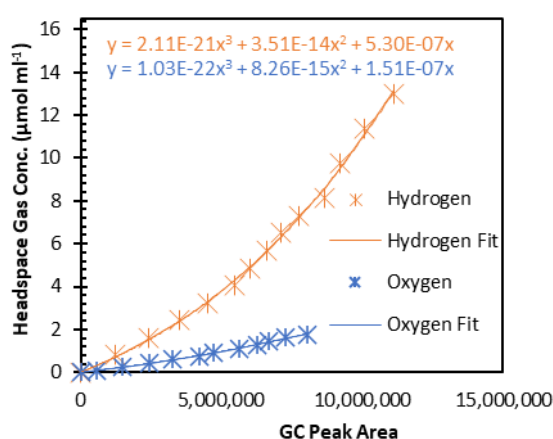


Figure 121: H₂ and O₂ calibration curves for Shimadzu GC system equipped with a BID 2010 detector.

The headspace vial caps contain a butyl rubber septum impermeable to gasses and rated up to pressures of 45 psi (3 atm). The upper end of the hydrogen calibration curve corresponds to a peak area of 11,000,000 when 1.6 ml of pure H₂ gas (65 µmol) is injected into the headspace vial. Given that

these vials only contain 5 ml of headspace, this increases pressure from 1 to 1.27 atm. The calibration assumes that no gas is lost in the injection process and that the septum is immediately re-sealed upon removing the needle. Errors arising from the solubility changes at different pressures are also reduced by including 5 ml of water in the calibration headspace vials. However, it is worth noting that repeat calibrations using empty vials yielded almost identical curves.

3.3.4.2 Hydrogen Evolution

5mL of 1:1:1 (volume) TEA/MeOH/H₂O solution was added to 5 mg of photocatalyst in 10 ml Agilent crimp-top clear glass headspace vials, which were then capped. The suspension was degassed by bubbling nitrogen gas through each vial for three minutes via inlet/outlet needles perforating the rubber septum.

The samples were dispersed for five minutes in an ultra-sonicator and subsequently exposed to AM 1.5G solar spectrum light for one hour under a 12"x12" solar simulator (Newport Instruments, Oriel Sol 3A, 94123A 1440W). Sample vials are placed on a sample roller to agitate the suspension and prevent sedimentation. Samples were subsequently degassed a second time, re-dispersed, and irradiated for an additional 15 minutes before testing the gas composition via gas chromatography, GC.

The irradiated samples were loaded into a headspace sampler (Shimadzu, HS-20) paired with a gas chromatography system (Shimadzu, GC-2010 Tracera) equipped with an Rt-MSieve 5A, 30m, 0.53 mm ID column using helium as the carrier gas. A split flow injection method was used to dilute the sample concentration. A purge flow was used to prevent volatile contaminants from the silicone septum from entering the column. The samples were heated to 80 °C before injecting into the column. Flow rates of 5 L min⁻¹ and a 10:1 split ratio were used. After 8 minutes, the column was ramped to 160 °C at a speed of 10 °C per minute, where it was held for five minutes to purge the line of contaminants. The eluting gas was detected using a BID-2010 plasma detector set to 200 °C. H₂ and O₂ peak areas were quantitatively analysed for hydrogen evolution rates by comparing them with calibration curves acquired from injecting different volumes of pure gasses into the system. The calibration equations are presented in Figure 121.

For samples involving in-situ photodeposition of a platinum co-catalyst, 8 wt.% H₂PtCl₆ (Sigma Aldrich) was added to the vials before they were capped. The volume of the solution was such that the mass

of platinum corresponded to 0.5 – 3 wt.% of the photocatalyst. For analysis purposes, complete photodeposition is assumed.

3.3.4.2.1 Disclaimer 1: Shortage of Vial Caps

A shortage of crimp-top caps for the headspace vials and long lead times for replacements resulted in a modified procedure for some samples. Typically, the butyl rubber septum is pierced twice during the degassing process, after which the sample is irradiated for 1 hr to photodeposit platinum and ensure further irradiations are more indicative of the steady-state HER rates. After this initial exposure, the vials are recapped and degassed for a second time.

Early experiments indicated that the second re-capping step was necessary to avoid piercing the rubber septum too many times over the two degassing stages. When the cap is not replaced, the seal may lose its integrity, as some samples demonstrated signs of leaked hydrogen and the introduction of oxygen. Since GC measurements take place over several hours, the integrity of this seal is essential to ensure reliable results.

To minimise the number of cap perforations and remove the requirement for cap replacement when the supply was low, the vials were not degassed before their initial 1-hour irradiation. Therefore, oxygen was present in the headspace for these measurements. These samples were subsequently degassed prior to the second irradiation, after which the headspace composition was tested. Samples tested in this manner are highlighted as such in the text. However, these results should be caveated with the fact that irradiation in an oxygenated atmosphere may have altered the properties of the photocatalyst. For example, oxygen opens the possibility of photooxidation and photodegradation pathways for the polymer. Unfortunately, due to time constraints, it was not possible to re-test these samples under normal conditions. Samples tested under these conditions are clearly identified in the main text.

3.3.4.3 Hydrogen Peroxide Production

To test for photocatalytic hydrogen peroxide production, 3 mg photocatalyst was dispersed in 5 ml deionised water, capped, and irradiated for 1.5 hours. Peroxide testing strips were used to test the water immediately after irradiation to gauge an approximate hydrogen peroxide production rate. The results of the test strips are analysed semi-quantitatively by inspecting the colour of the test strip and comparing it with the supplied colour chart.

3.4 Photocatalysis Method Validation

Before discussing the results gathered, this section is dedicated to discussing the advantages and limitations of the methodology used to determine the hydrogen evolution rates of the polymers synthesised in the subsequent sections. This discussion must be taken into consideration when comparing the results presented here with others presented in the literature, as there are key differences.

For example, different research groups will use different catalyst loading concentrations, irradiation areas, dispersion methods, light sources, co-catalysts, and sacrificial reagents. One of the most common photocatalysis testing setups used amongst the scientific community is the Photoreactor system produced by the Beijing Perfectlight Technology Company. This system uses a lower power light source (300 W Xe arc lamp), tests the photocatalytic system under reduced pressure, and regulates the temperature via water cooling.

Meanwhile, the high throughput system, in which hydrogen evolution occurs within a closed headspace vial and starts at ambient pressure. Whilst a fan is used to circulate air and cool the samples down during testing, this is less effective than water cooling.

3.4.1.1 Irradiation Time

The pressure within the vial's headspace during irradiation is a key consideration for the setup used for these studies. As more hydrogen is produced over time, the headspace pressure increases. The impact of this is twofold. The first consideration is that of thermodynamics. At high partial pressures of hydrogen, the hydrogen content in solution increases and the thermodynamic equilibrium is shifted towards the left-hand side of the reaction according to Le Chatellier's Principle and the hydrogen evolution rate will decrease. Secondly, at higher headspace pressures, the rate at which gas escapes from the vial into the surroundings will increase. This will not be constant for all samples, as the rate of gas exchange will depend on the quality of the manually-capped seal. Furthermore, each septum will be prone to leaking at high pressures as they are perforated during the degassing process.

Many photocatalysts investigated are highly active hydrogen evolution photocatalysts under sacrificial conditions (i.e. when dispersed in a MeOH/H₂O/TEA 1:1:1 mixture). Irradiating a sample for too long will result in the headspace pressure rising. In this case, the hydrogen evolution reaction rate decreases or may halt entirely.

To test this hypothesis, DBTS-DBTS (P10) was irradiated for three different durations: 30 mins, 1 hr, and 2 hrs. A repeat measurement was also made in which the photocatalysts were loaded with 3 wt.% Pt as a co-catalyst via in-situ photodeposition. The H₂ peak areas from the GC chromatograph are

presented in Figure 122. The Pt-loaded sample is highly active and in this case, the H₂ GC peak area after irradiation for two hours is the same size as when the sample is irradiated for one hour. This indicates that the system reaches equilibrium within one hour of irradiation. In this case, rate at which hydrogen is produced equals the combined rate at which rate at which it is consumed and/or escapes from the vial.

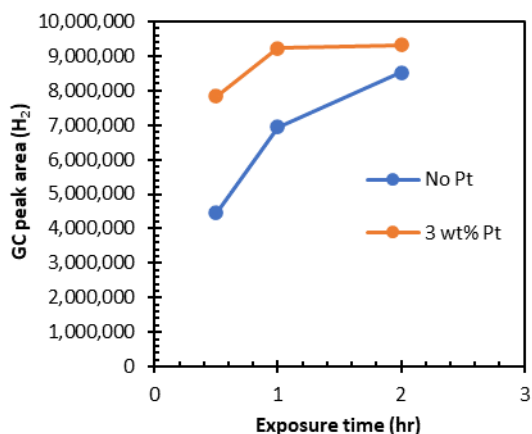


Figure 122: H₂ peak areas for 5mg DBTS-DBTS dispersed in 5mL of 1:1:1 TEA/MeOH/H₂O solution after 30 minutes, 1hr and 2 hours of exposure of AM1.5G irradiation.

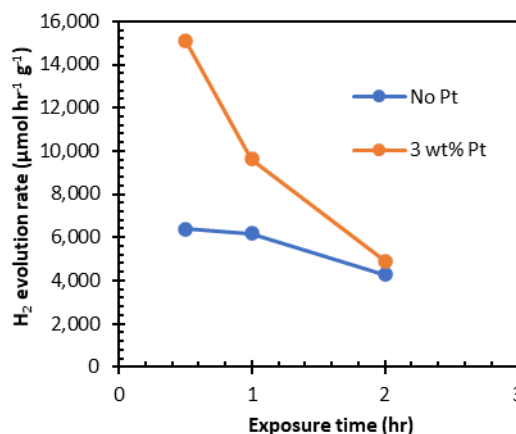


Figure 123: The corresponding mass-normalised HER rates when calculated after applying the calibration equation.

The peak areas were used to calculate HER rates using the calibration curve shown in Figure 121. These mass-normalised HER rates are shown in Figure 123. Without a Pt co-catalyst, the HER rate for P10 is ~6.4 mmol hr⁻¹ g⁻¹. This value was consistent for the measurements after 30 minutes and 1 hour of irradiation. However, over 2 hours of irradiation, the H₂ evolution rate is calculated to decrease to 4.2 mmol hr⁻¹ g⁻¹. Whilst it is possible that this decrease represents a degradation in polymer performance over time, it is more likely to be a result of building headspace pressure. The GC peak area corresponding to this data point was ~ 8,000,000 and lies close to the peak area of the Pt-loaded system under equilibrium.

Once loaded with a platinum co-catalyst, the hydrogen peak area is already close to the saturation regime (~ 8,000,000), and the corresponding HER of 15 mmol hr⁻¹ g⁻¹ is likely an underestimation of the true value. This is reinforced by the relatively small increase in peak area observed by doubling the exposure time from 30 minutes to 1 hour. As can be seen in Figure 123, HER rates for the platinum-loaded system decreases dramatically with irradiation time.

An irradiation time of 15 minutes was subsequently decided upon to ensure that other samples do not reach this saturation regime. However, the reaction rates in the first 15 minutes rarely accurately describe the inherent steady-state hydrogen evolution reaction rates. Many polymers, particularly when photodepositing co-catalysts, undergo an initialisation period. For example, when photodepositing metallic platinum, Pt⁴⁺ is preferentially reduced, and this photoreduction competes with the HER at the early stages under illumination. Even in the absence of photodeposition, polymer photocatalysts may undergo an initial period of low activity when impurities are preferentially reduced or the polymer self-oxidises. It was therefore decided that all samples would be irradiated for one hour and then degassed before conducting the final 15 minutes measurement.

3.4.1.2 Mass-normalised HER Rates

Much of the literature for photocatalytic water splitting reports the activity in a mass and time-normalised format: μmol of H₂ evolved per hour irradiated per gram of photocatalyst. Whilst mass-normalised metrics are helpful in considering how cheap a photocatalyst may be to scale up, they are often misused to inflate the reported HER rates artificially. Firstly, organic polymers are comprised of light elements and have a low mass density per mole of absorbing chromophores. Secondly, photocatalysts are loaded into reaction vessels at exceptionally low concentrations, which results in high activities per unit mass, but only utilises a small proportion of the incident light.^{148,229}

Furthermore, the mass-normalised reaction rates are further complicated when hybrid photocatalysts comprised of two or more absorbing materials are used. Depending on the relative concentrations of the multiple phases, normalising per unit mass of the overall hybrid photocatalyst may obfuscate the actual trends. For example, 1 g of a photoactive material dispersed on the surface of 9 g of support particles would result in lower activity per unit mass but may achieve a greater overall efficiency per unit of the irradiated area.

Standardised photocatalysis testing protocols are a significant area of discussion. A good review of the issues with current testing methods and how to avoid their pitfalls can be found in a recent publication produced by leading academics in the field.²³⁰

Several concentrations of DBTS-DBTS dispersed in a 1:1:1 solution were tested for hydrogen evolution rates after 15 mins of exposure. The absolute hydrogen evolution rate for each photocatalyst concentration is presented in Figure 124. Here, the principal issue surrounding the reporting of mass-normalised HER rates is highlighted, as the amount of hydrogen produced per vial does not trend

linearly with the photocatalyst mass within it, making this value redundant and incomparable. Whilst $51.9 \mu\text{mol hr}^{-1}$ is evolved by 0.5 mg of polymer in suspension, only $58.6 \mu\text{mol hr}^{-1}$ is evolved from five times the mass (2.5 mg). Likewise, 5 mg of polymer produces $60.2 \mu\text{mol hr}^{-1}$.

Therefore, at loadings above 2.5 mg ml^{-1} , additional mass of photocatalyst has a negligible effect on the absolute amount of hydrogen produced. Since these samples were only irradiated for 15 minutes, the headspace pressure is well below the threshold that dramatically affect the HER rates. Instead, this plateau results from the near complete absorption of incident light over the irradiated area. i.e. the HER is limited by the flux of incident photons, not by the amount of photocatalyst in suspension. To ensure that results reported in this thesis are comparable to one another, all samples are loaded with concentrations of 1 mg ml^{-1} . Given the structural similarity between the polymers of interest, it is assumed that this is a sufficient concentration to enable all polymers investigated to absorb all incident photons with energy greater than their bandgaps.

The mass-normalised HER rates of P10 loaded at different concentrations are presented in Figure 125. The resulting mass-normalised activities for the same sample therefore vary from $103.7 \text{ mmol hr}^{-1} \text{ g}^{-1}$ for 0.5mg, to $12.0 \text{ mmol hr}^{-1} \text{ g}^{-1}$ when loaded with 5 mg of polymer. It is, therefore, very difficult to compare mass-normalised photocatalytic activities in the literature. Mass normalised values reported in this thesis are, therefore, best used to compare with one another and with the high throughput study upon which this work is based. Further comparison with wider literature requires conversion of rates into area-normalised values.

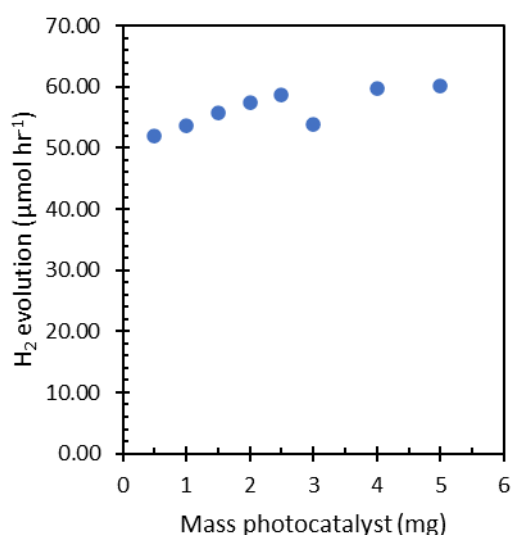


Figure 124: Absolute quantity of H₂ evolved from dispersions of DBTS-DBTS containing different masses of polymer. Irradiation time is 15 mins. Samples are not loaded with additional co-catalyst. Note: Y-axis starts at 12.5 μmol.

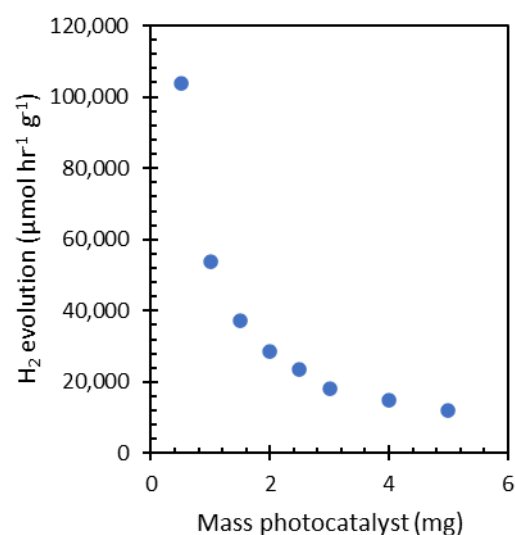


Figure 125: Corresponding mass-normalised HER rates for different masses of loaded photocatalyst. Polymer dispersed in 5 ml of a sacrificial reagent mixture inside a 12 ml headspace vial and irradiated for 15 minutes.

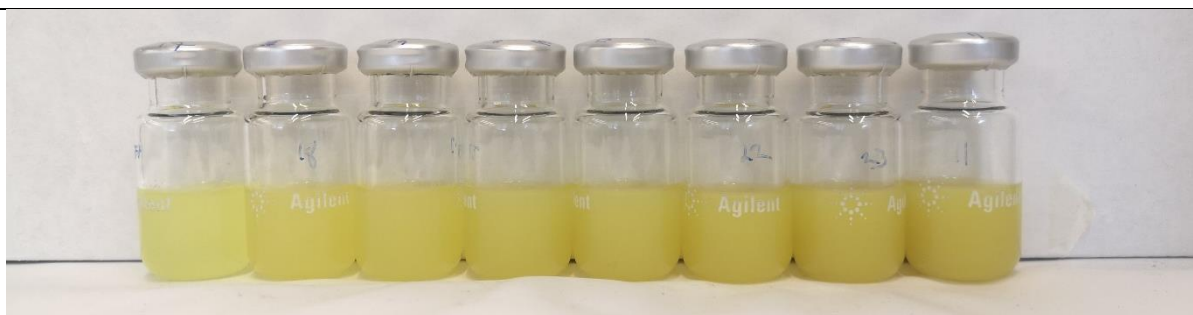


Figure 126: Photograph of P10 (DBTS-DBTS homopolymer) loaded at different concentrations in 10 ml headspace vials. Concentrations range from 0.1 mg ml⁻¹ to 1 mg ml⁻¹ from left to right as reported in Figures 124 and 125 above.

The sample vial loaded with 3 mg of polymer exhibited a lower HER rate than expected based on the other data points surrounding it. This highlights that additional sources of error in measurements must be considered when analysing the results reported hereafter. Firstly, errors in weighing are exacerbated when handling solids on the milligram scale. Incorrectly tared or contaminated balances can lead to significant mass errors. Likewise, small quantities of solid lost during the transfer steps will also have a significant impact on the resulting concentration. If the synthesised polymer is inhomogeneous with regards to particle size, morphology, purity, and polymer chain size distribution, one 5 mg sample may not behave identically to another taken from the same batch. Errors may also arise if there is any variation in the quality of the sealed cap between samples. There will also be some limited variation in irradiation intensity and spectral distribution over the 12x12" irradiation area. However, this factor is mitigated by the use of a AAA-rated system. Lastly, each GC measurement takes over 20 minutes. When testing a maximum of 48 samples in one batch, the final vial is tested 16 hours after the first. This leaves more time for gas equilibration with the surroundings, consumption of H₂ in a back-reaction, or the production of additional photocatalytic H₂ from ambient light in the laboratory.

3.4.1.3 Area-normalised HER Rates

Like organic photovoltaic devices, photocatalysts are ideally situated to operate embedded on panels. Early attempts by chemists and engineers have focussed on this approach to scaled-up operations.^{25,231} It is, therefore, more appropriate to report the photocatalytic rates according to their area-normalised values. This is particularly important when an excess of photocatalyst is added to generate high concentrations to ensure maximum absorption of incident light and achieve high STH efficiencies.

In the context of our experiments, area-normalised measurements are complicated by the cylindrical shape of the high throughput headspace vials, as demonstrated in Figure 127. The path length of incident light through the vial's centre differs from at its edge. This results in non-uniform absorption

across the lateral cross-section of the vial due to the Beer-Lambert law. Secondly, the irradiation area and incident light path length through the dispersion depend on the volume of liquid in the vial.

The surface area of the reaction mixture in the vial is approximated according to Figure 128. The volume of the vial and neck is approximated by a single cylinder with an unchanged radius. The volume of liquid inside the vial is then approximated as a cuboid, with its width calculated at the depth from which equal volumes of water lie above and below the line. This gives rise to a cross-sectional area equal to 6.7 cm^2 for the 10 ml crimp-top, round-bottomed clear glass Agilent headspace vials containing 5 ml of liquid. The path length of light through this liquid is approximated to be the depth of the cuboid, which equates to 0.75 cm when containing 5 ml of photocatalyst suspension. This volume of liquid was used for all measurements to ensure consistency of irradiation area and headspace volume.

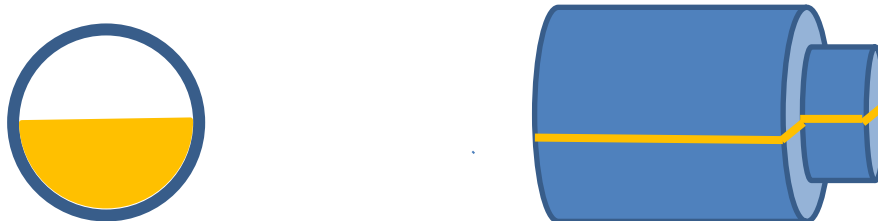


Figure 127: Schematic diagram showing the expected liquid level when 12 ml headspace vials are half-filled with a photocatalyst dispersion. Cylindrical nature of vial means surface area depends on the volume of liquid used, and the path length of incident light is not consistent across the entire surface area.

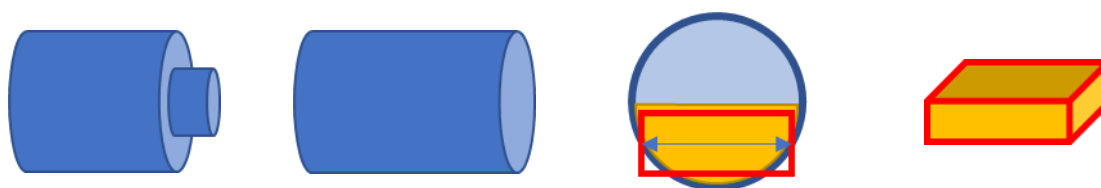


Figure 128: Series of diagrams to show how irradiation area and path length have been approximated. First the vial is approximated as a single cylinder. Secondly, the mid-point level is identified. This is the depth at which 50% of a given volume of liquid lies above and 50% lies below. The width of the vial at this point is used to calculate an average irradiation surface area. The average path of incident light through the dispersion is calculated by approximating the volume as a cuboid using the aforementioned surface area. For 5 ml liquid in a 10 ml Agilent crimp-top vial (typical conditions), the surface area is 6.7 cm^2 and path length is 0.75 cm.

3.4.1.4 Glass Absorption

It is also essential to consider the spectral absorption of the glass vial itself, especially since headspace vials are not designed for optical applications. To test this, the solar spectrum was recorded under direct sunlight from both outside and inside a glass headspace vial. The results are presented in Figure

129 alongside the spectral output of the solar simulator.¹ These data demonstrate no significant losses due to absorption by the glass in the wavelengths of interest.

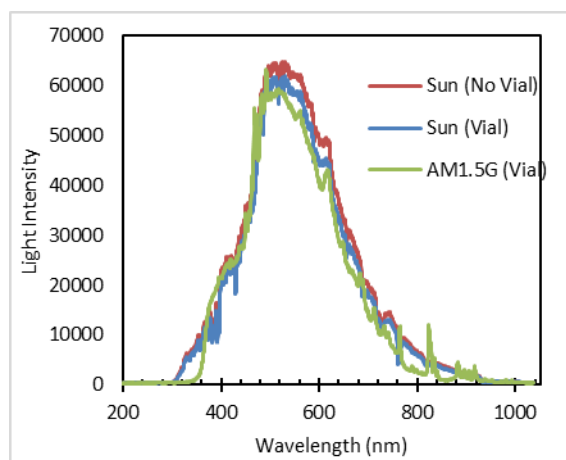


Figure 129: Spectral output from the sun as recorded from outside (red) and inside (blue) of an Agilent headspace vial, compared with the spectral output from the 12" x 12" solar simulator (green), which was also recorded from inside a vial.

3.4.1.5 Comparison to Literature Values

Due to the lack of standardisation for photocatalytic water splitting measurements, drawing direct comparisons between experimental results obtained from different research groups is challenging. Groups may use various light sources, irradiation areas, temperatures, pressures, concentrations, irradiation times, and dispersal methods. Furthermore, the choice of sacrificial agents, cosolvents, and their concentrations relative to water are also not standardised.

The AQY and STH metrics are the most reliable and comparable between groups and give the best measure of absolute efficiency compared to other photocatalyst materials. However, these experiments are time-consuming and cannot easily be conducted on hundreds of samples. Since the polymers prepared in this thesis are of most interest when compared with one another and the previously-published high-throughput work, which used the same experimental setup, mass-normalised units are used. However, such values reported here should not be directly compared with values published by other research groups.

The approximate surface area of the 5 ml dispersion when loaded into these specific headspace vials is 6.7 cm². This area can be used to convert the reported rates into area-normalised values for saturated solutions. However, differences in experimental setups must still be considered when

¹ Spectra recorded by Dr Clowes (group technician). Data retrieved from shared group drive. Experimental details not provided.

comparing with results from other research groups, which rarely report the surface irradiation area and often perform photocatalysis experiments below the absorption saturation concentration.

3.4.1.6 Quantitative GC Analysis for Determining HER Rates

The GC system is equipped with a Dielectric-Barrier Discharge Ionisation Detector (BID). The helium carrier gas is ionised under a high voltage to form a plasma. Upon relaxation to the ground state, the helium plasma emits a broad distribution of high-energy photons (X-Ray spectrum). These photons then ionise the substrate as it is eluted from the capillary column, and these ionised species are detected on an electrode.

Over the course of thousands of samples run by the research group during the year of measurements presented hereafter, the detector's sensitivity gradually decreased. This arises from end contamination at the exit of the column and contamination of the detector's electrodes.

A plot of all samples run on the GC over the course of seven months is presented in Figure 130. It is evident that the sensitivity has decreased over time. As such, the calibration curve (Figure 121), prepared at the early stages of these experiments, does not provide an accurate measure of hydrogen present. In reality, the hydrogen evolution rates of samples measured later are likely considerably higher than those calculated using this calibration curve.

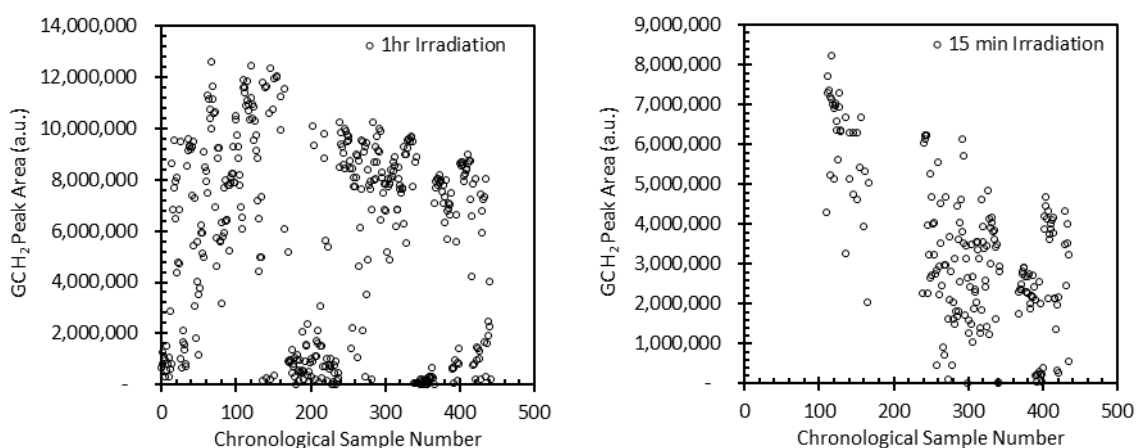


Figure 130: H₂ peak areas vs sample number in chronological order over the course of one year of use. a) H₂ peak areas after 1 hr irradiation in which time the headspace is expected to become saturated for highly active samples (see Figure 122). b) H₂ peak areas for samples irradiated for 15 minutes also demonstrate a decay of peak intensity over the course of long-term use.

Unfortunately, the detector contamination and sensitivity depletion went unnoticed until the final couple of months of practical work. Subsequent attempts to fix this issue were eventually made. This involved trimming the end of the column, cleaning the injection needle, and baking the column/detector at high temperatures for a prolonged period to desorb contaminants from their surfaces. Once refurbished, the maximum hydrogen peak area increased from 8,000,000 to 30,000,000. New calibration curves were then obtained.

The high throughput irradiation allows for the simultaneous irradiation of 48 headspace vials. The HS-20 autosampler is capable of queuing and auto-running 90 samples per batch. It is assumed that the detector's sensitivity does not change appreciably throughout a single batch. As such, samples that are measured in any one particular batch are comparable to one another. All graphs presented in this results chapter only compare HER rates for samples recorded in the same batch.

3.4.1.6.1 Disclaimer 2: Modified GC Method Post-Maintenance

As discussed above, the GC system underwent maintenance work towards the end of the experimental period of this research. Following this maintenance work, the sensitivity of the BID detector increased by an order of magnitude. Resultingly, the detector became saturated at very low concentrations of H₂.

Whereas the initial calibration curve measured H₂ concentrations up to 14 µmol ml⁻¹ (Figure 121), the new calibration was limited to a maximum concentration of 2 µmol ml⁻¹ to prevent detector saturation. Although this problem was later rectified by changing the injection method from direct to split injection and adding a purge flow, some results reported in the following section correspond to the period when lower headspace concentrations were necessary. As such, the second sample irradiation was only five minutes long. GC Peak areas during these experiments were also less reliable than before: H₂ peak positions would randomly shift, and the peak shape would be distorted. However, the peak area would remain similar to the expected values. Samples tested under these conditions are highlighted in the text.

3.5 DFT Computational Modelling

3.5.1 DBTS-PhFx

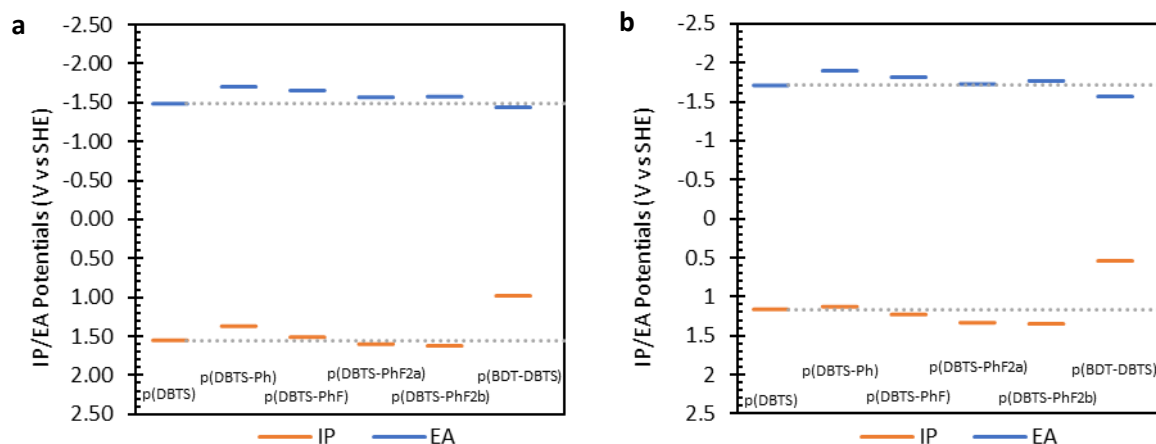


Figure 131: Computational calculations of the IP and EA potentials of DBTS-PhFx polymers. a) DFT calculations (B3LYP/DNP level of theory) performed in this work, b) xTB-IPEA calculations performed in reference.¹⁸² Dotted grey line corresponds to the IP and EA values for the DBTS-DBTS homopolymer.

The IP and EA potentials of the DBTS-PhFx series of polymers have been calculated using DFT at the B3LYP/DNP level of theory. The results from these calculations are presented in Figure 131a. Since the same co-polymers were also screened in the high-throughput study, the predicted IP and EA potentials from this earlier work are presented in Figure 131b. The two data sets are in close agreement, with the DFT-predicted values lying at slightly more positive potentials relative to the SHE and predicted to have slightly wider fundamental gaps.

In both cases, the EA potentials of the DBTS-PhFx copolymers, representing their LUMO energy levels, are close to that of the p(DBTS) homopolymer. Increasing fluorine content is expected to lower the LUMO energy level relative to the nonfluorinated DBTS-Ph co-polymer and closer to the p(DBTS) homopolymer.

In Chapter 2, it was predicted that the closer in energy that the p(DBTS) and p(DBTS-X) LUMOs lie to one another, the more delocalised the LUMO, and hence the photoelectron, will be along the polymer backbone. The same can be predicted regarding their HOMO energies relative to that of the P(DBTS). This trend is exemplified in Figures 132-137, in which the geometry-optimised structures are presented alongside the frontier molecular orbitals for each polymer in the DBTS-PhFx series.

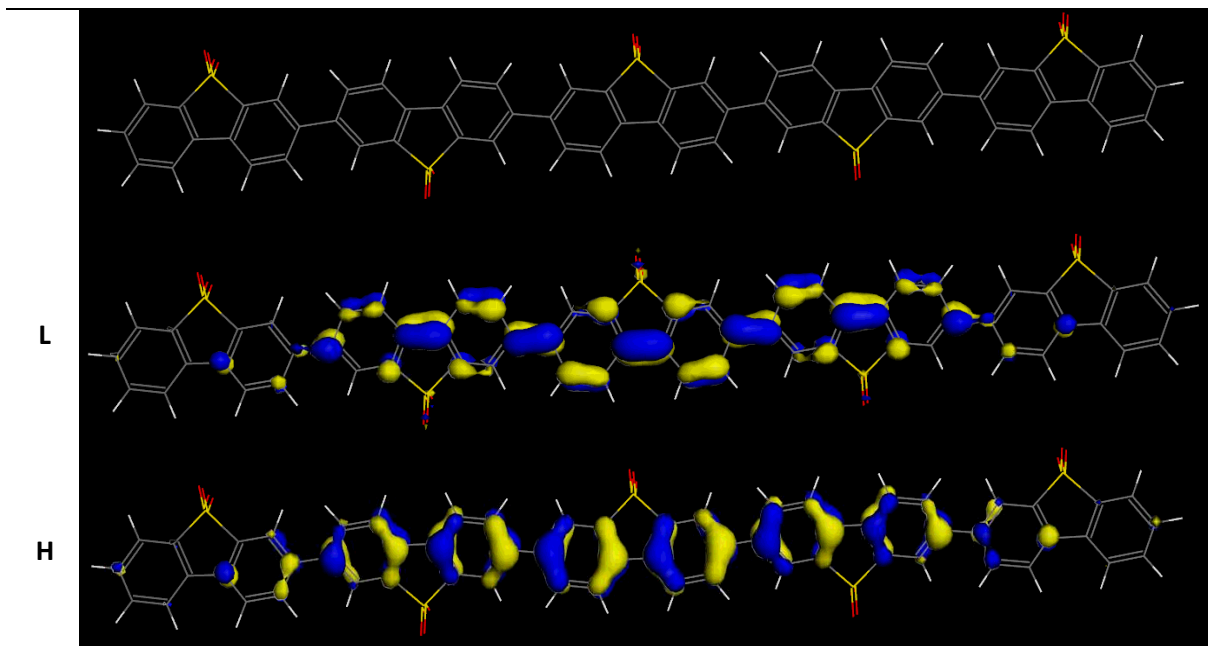


Figure 132: Optimised geometry of DBTS-DBTS and associated HOMO (H) and LUMO (L) frontier molecular orbital distribution.

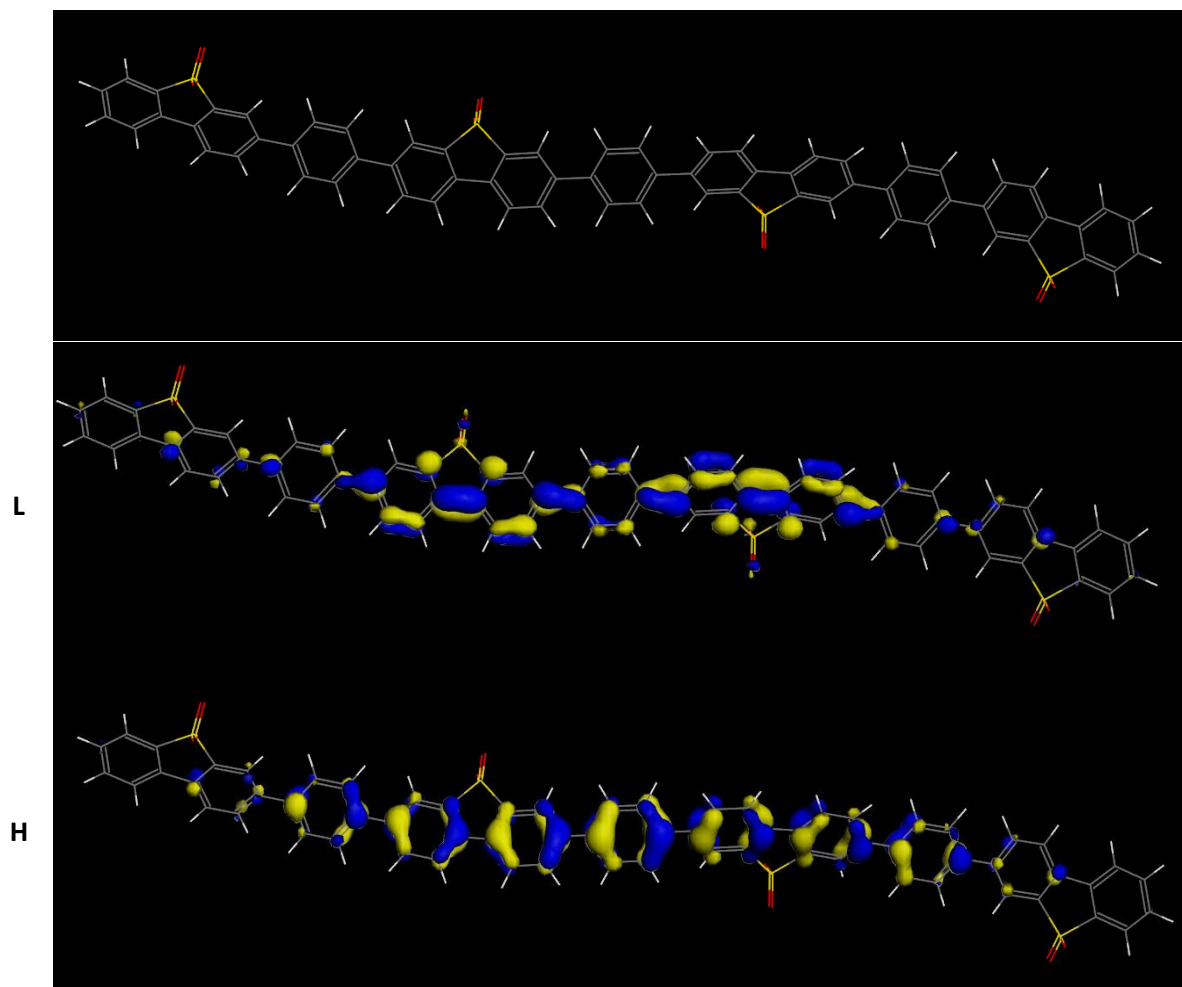


Figure 133: Optimised geometry of DBTS-Ph and associated HOMO (H) and LUMO (L) frontier molecular orbital distribution.

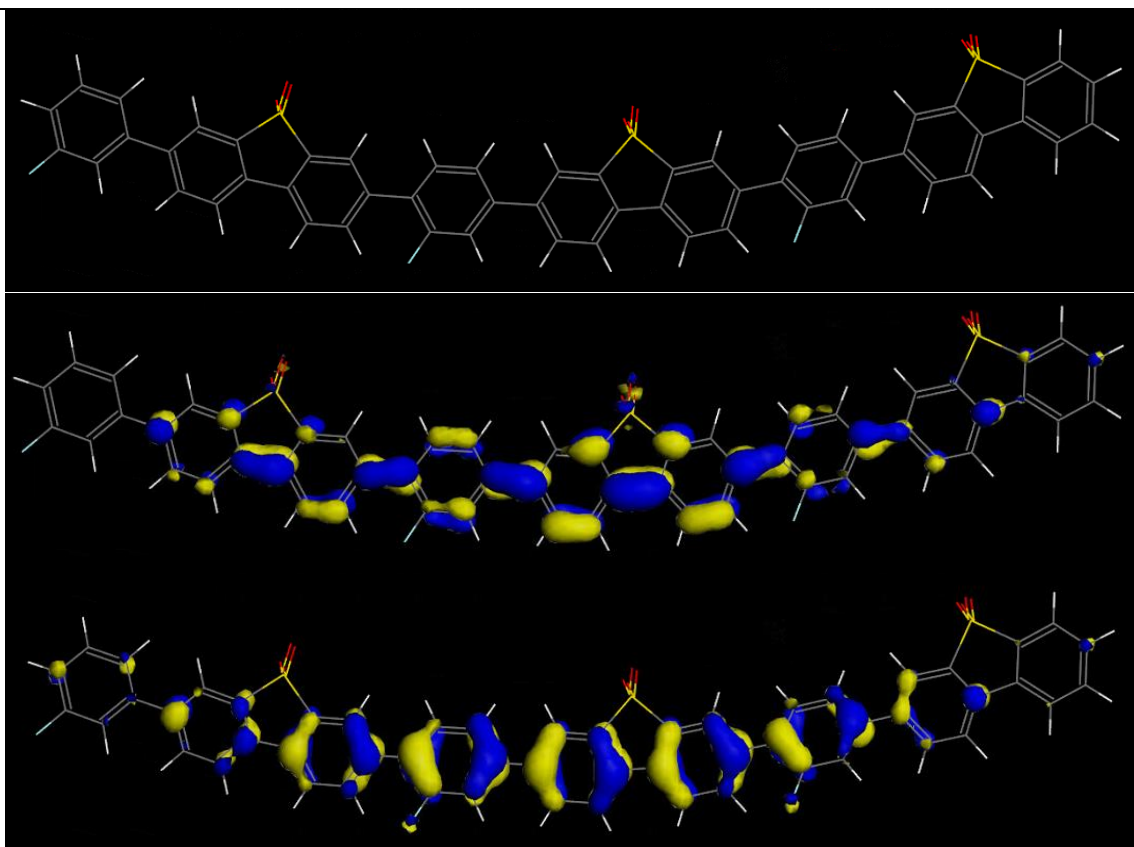


Figure 134: Optimised geometry of DBTS-PhF and associated HOMO (H) and LUMO (L) frontier molecular orbital distribution.

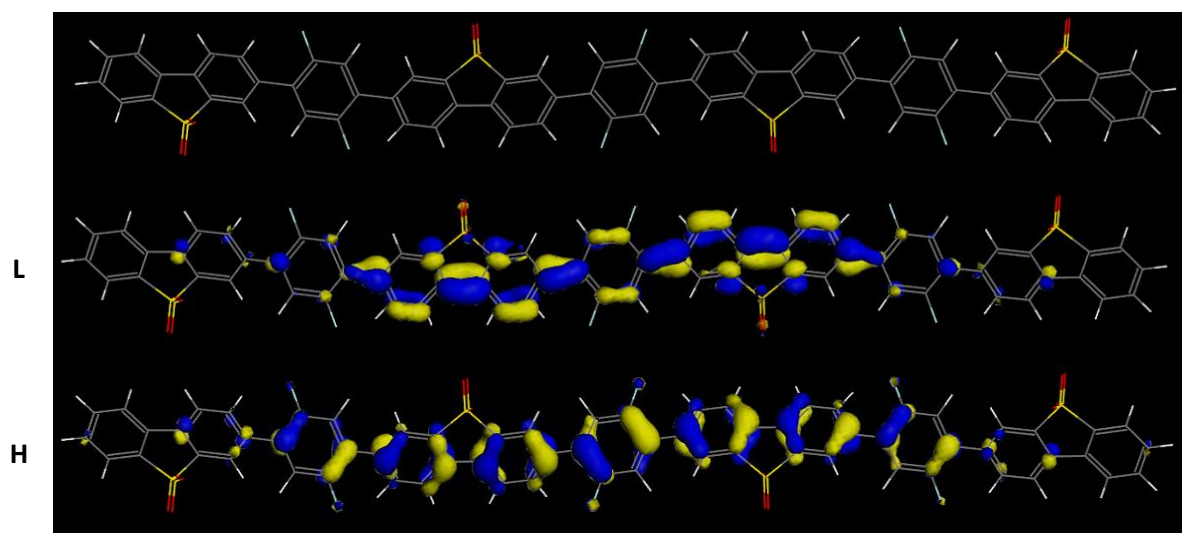


Figure 135: Optimised geometry of DBTS-PhF2a and associated HOMO (H) and LUMO (L) frontier molecular orbital distribution.

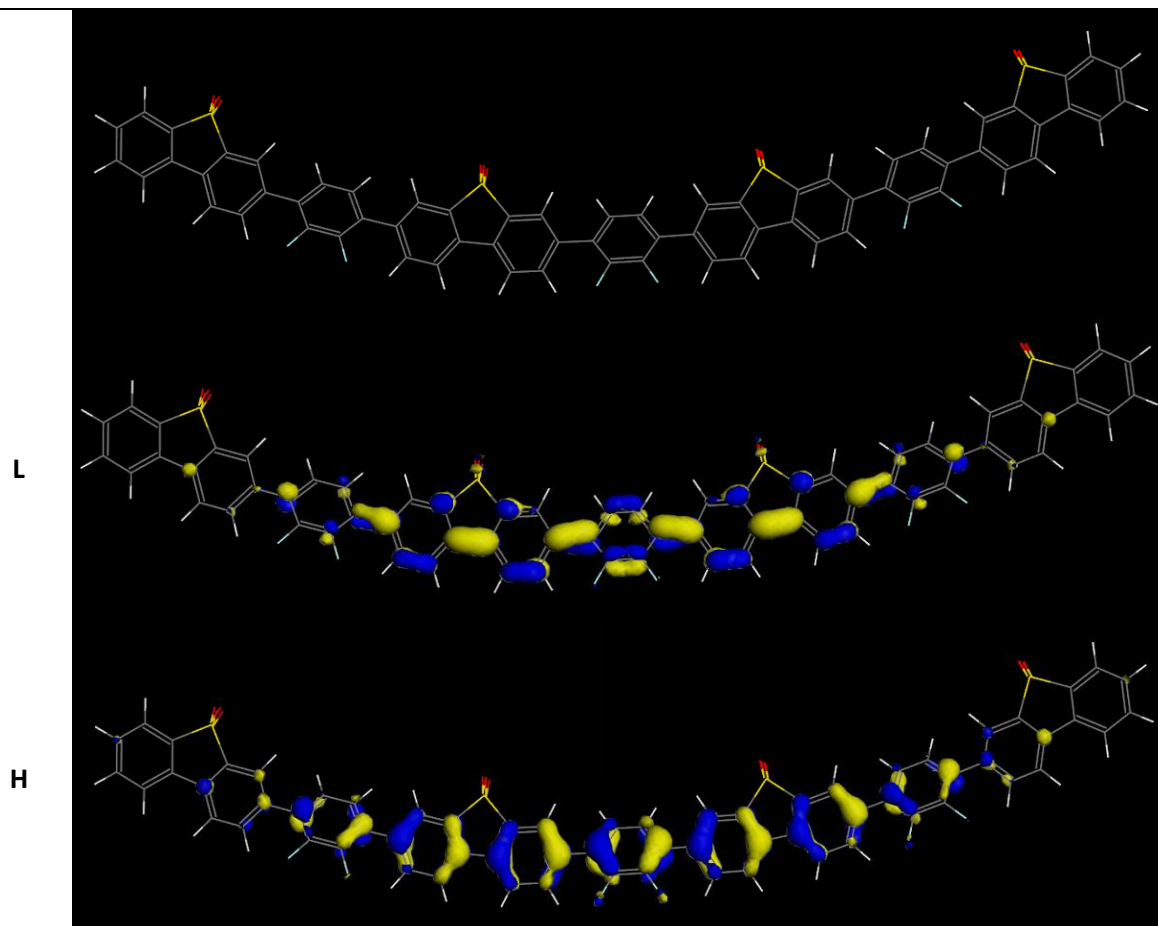


Figure 136: Optimised geometry of DBTS-PhF2b and associated HOMO (H) and LUMO (L) frontier molecular orbital distribution.

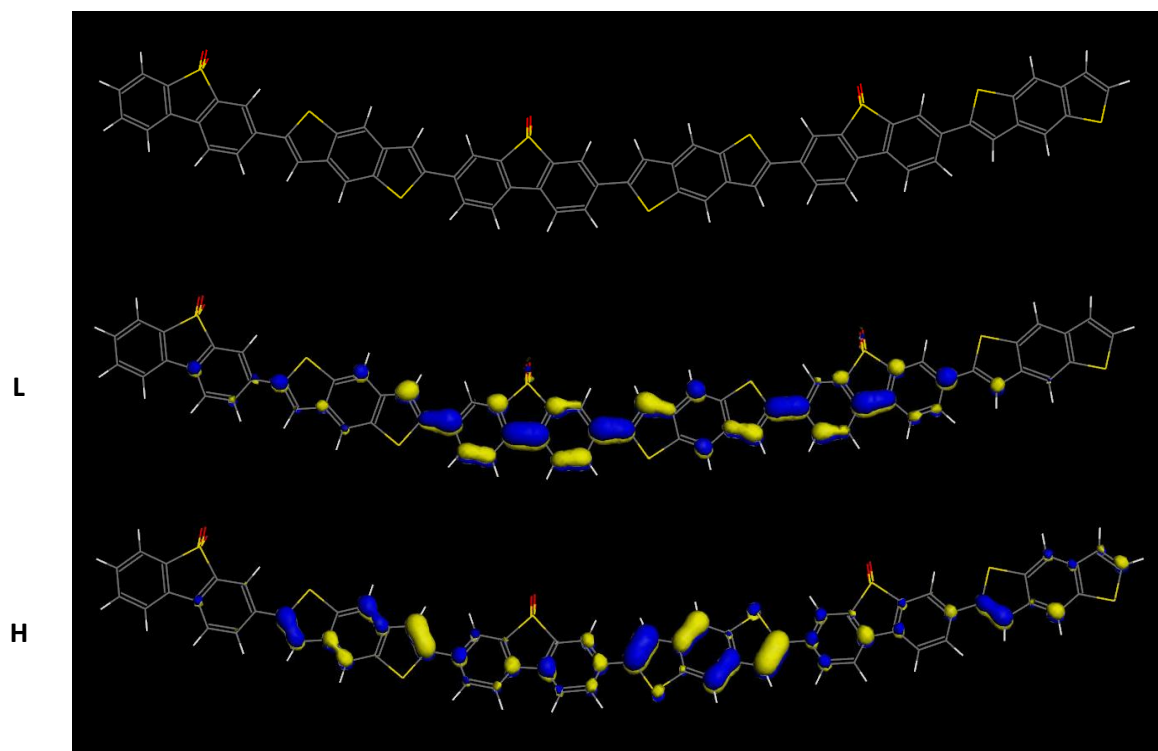


Figure 137: Optimised geometry of DBTS-BDT and associated HOMO (H) and LUMO (L) frontier molecular orbital distribution.

Some interesting trends can be observed when considering the optimised geometry of these polymers. In each case, the phenylene C-F bonds are always oriented in the opposite direction from the nearest sulfone group. This factor leads to substantially different 3D geometries for p(DBTS-PhF2a) and p(DBTS-PhF2b). Presumably, this geometric constraint arises by minimising electrostatic repulsive forces between neighbouring dipoles. In these cases, the structural disorder resulting from a distribution of dihedral angles in the semi-crystalline solid state may produce a broader band of energetic states that could aid exciton migration through the bulk material via FRET.

The optimised geometry for p(DBTS-BDT) is entirely co-planar since the dihedral angles between neighbouring monomer units are all zero degrees. This geometry should enhance charge transfer between moieties, charge separation, and oscillator strength. However, such structures are also prone to particle agglomeration resulting from π - π stacking between polymer chains.

The LUMO orbital of p(DBTS-Ph) is particularly noteworthy compared to its fluorinated derivatives. In the case of the former (Figure 133) there is substantially less orbital density on the phenylene linker. In contrast, Figures 123, 124, and 125 show an increased LUMO orbital density on the phenylene co-monomer. However, this effect is minimal since these polymers have similar IP and EA potentials.

Figure 137 demonstrates this trend with respect to the HOMO orbital density. P(DBTS-BDT) has a considerably more negative IP potential than p(DBTS). The HOMO is expected to be predominantly located on the BDT moiety, as is observed in this Figure 139. Meanwhile, the LUMO is expected to be delocalised and evenly distributed across both monomers, which is also observed.

To highlight this point further, Figure 138 presents the IP and EA potentials of p(DBTS-DBT) containing the dibenzothiophene (DBT) monomer relative to the p(DBTS) homopolymer. This monomer is electron-donating, and its IP and EA potentials are both more negative than p(DBTS). As such, the HOMO and LUMO orbitals are expected to be more localised on the BDT and DBTS moieties, respectively. Figure 139 presents the frontier orbitals for this copolymer, and their distributions agree with this prediction.

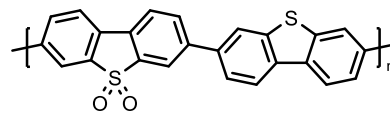
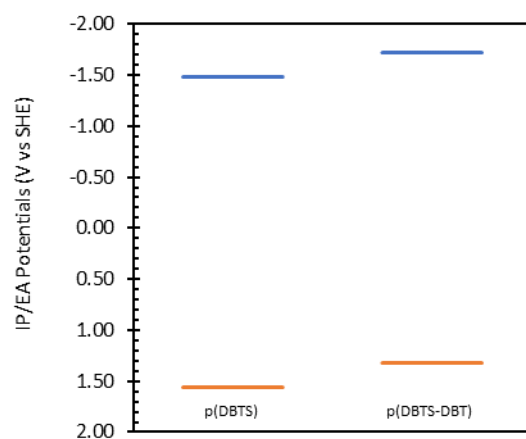


Figure 138: Computational calculations of the IP and EA potentials of DBTS-DBT co-polymer vs that of DBTS-DBTS homopolymers. DFT calculations (B3LYP/DNP level of theory). Lewis structure of DBTS-DBT is presented on the right.

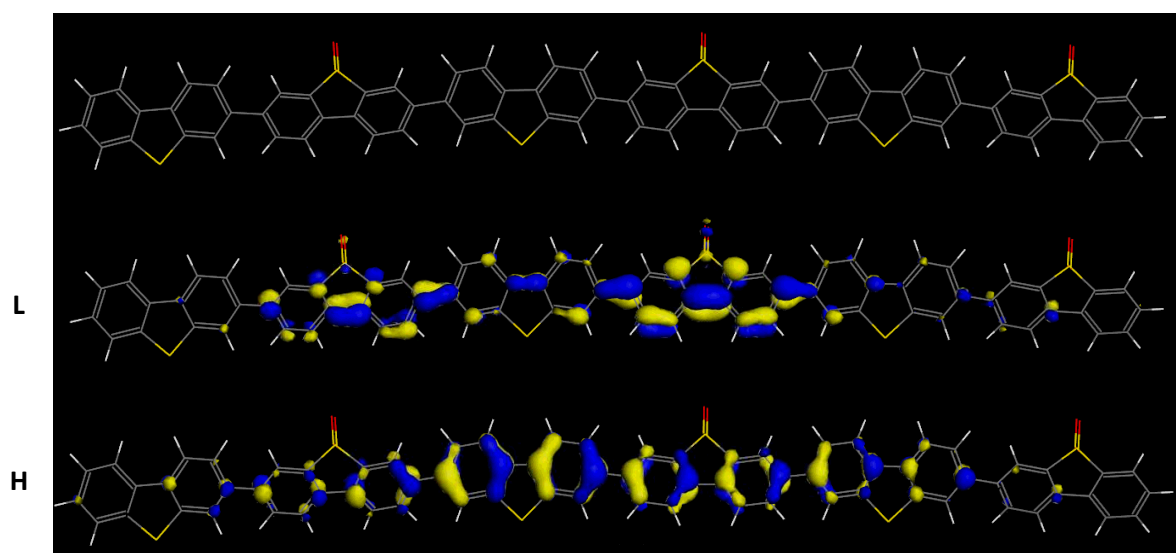


Figure 139: Optimised geometry of DBTS-DBT and associated HOMO (H) and LUMO (L) frontier molecular orbital distribution.

3.5.2 BDT-PhFx and DBTS-PhFx-BDT

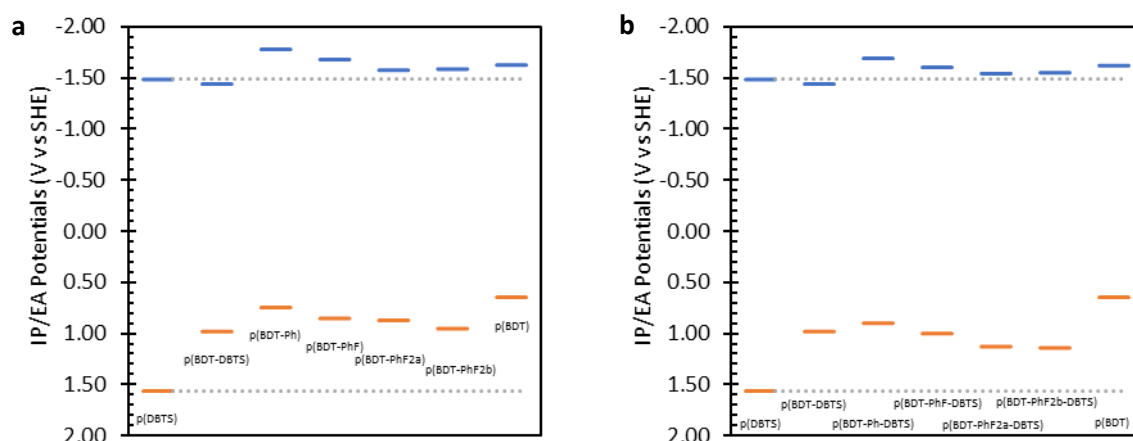


Figure 140: Computational calculations of the IP and EA potentials of (a) BDT-PhFx co-polymer and (b) DBTS-PhFx-BDT ternary co-polymers. DFT calculations performed using B3LYP/DNP level of theory.

The IP and EA potentials of the BDT-PhFx binary copolymers and the DBTS-PhFx-BDT ternary copolymers are presented in Figures 140a and 140b, respectively. Introducing the DBTS moiety into the BDT-PhFx polymers is not expected to change any IP or EA values significantly. As such, the bandgaps of the ternary polymers are expected to be largely unchanged relative to their BDT-PhFx counterpart. Introducing phenylene linkers between the BDT and DBTS moieties is expected to result in a slightly wider bandgap, which may benefit its photocatalytic activity as the overpotential for TEA oxidation increases.

The optimised geometries and frontier orbitals for the ternary polymers are presented in Figures 141-144. As expected, based on their IP and EA potentials, the HOMO is located on the BDT and PhFx moieties, and the LUMOs are delocalised over all three moieties. As the fluorine content increases, the HOMO of the ternary polymer lowers in energy relative to the p(BDT) homopolymer. This difference in energy is associated with an increased HOMO density on the BDT donor unit and decreased density on the phenylene units. Based on their predicted electronic structure, these ternary polymers remain promising candidates for photocatalytic hydrogen evolution.

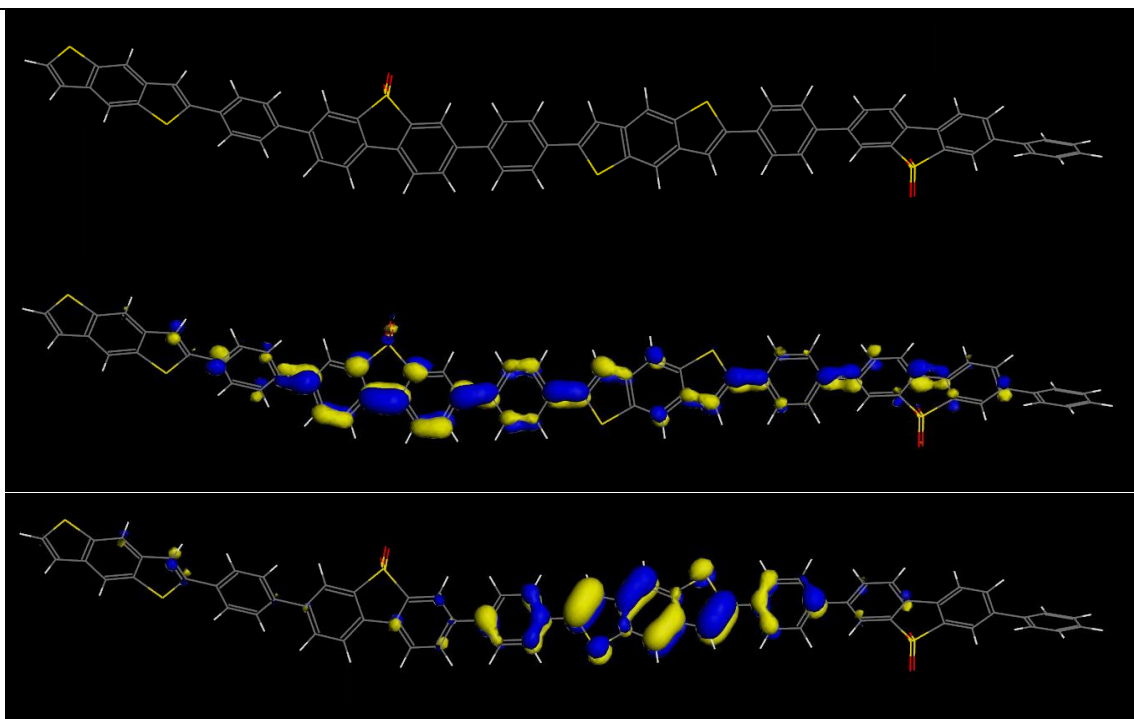


Figure 141: Optimised geometry of DBTS-Ph-BDT and associated HOMO (H) and LUMO (L) frontier molecular orbital distribution.

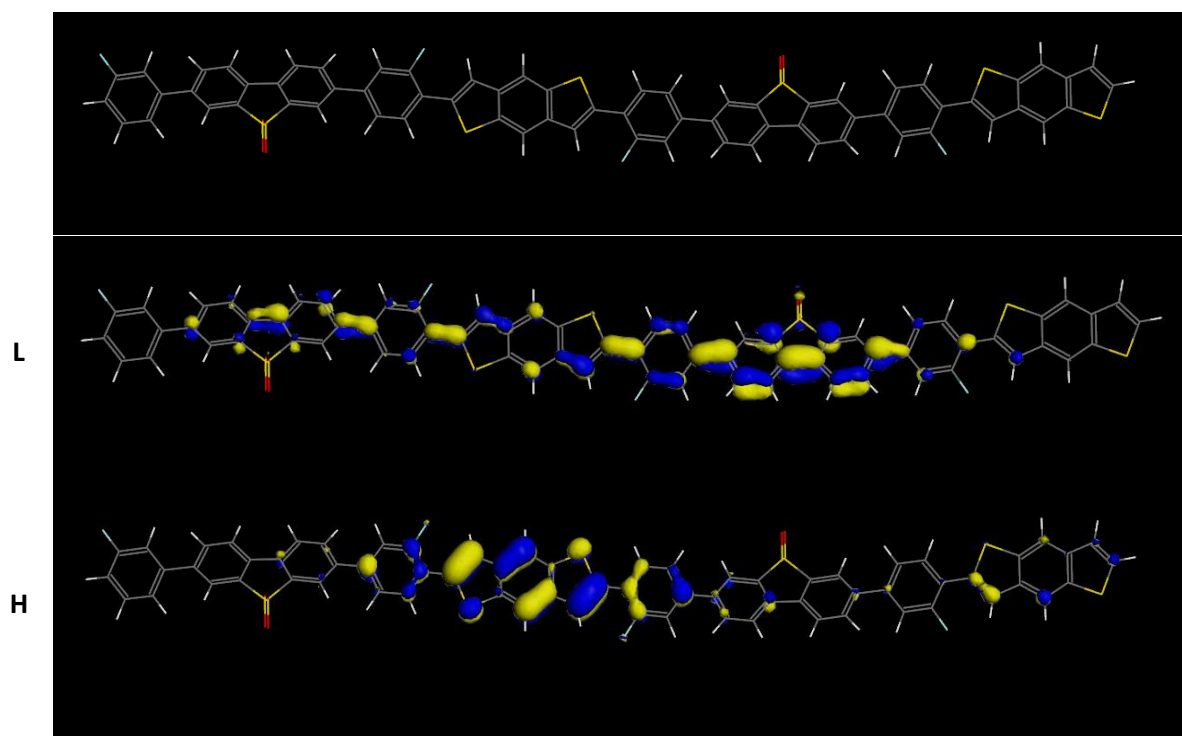


Figure 142: Optimised geometry of DBTS-PhF-BDT and associated HOMO (H) and LUMO (L) frontier molecular orbital distribution.

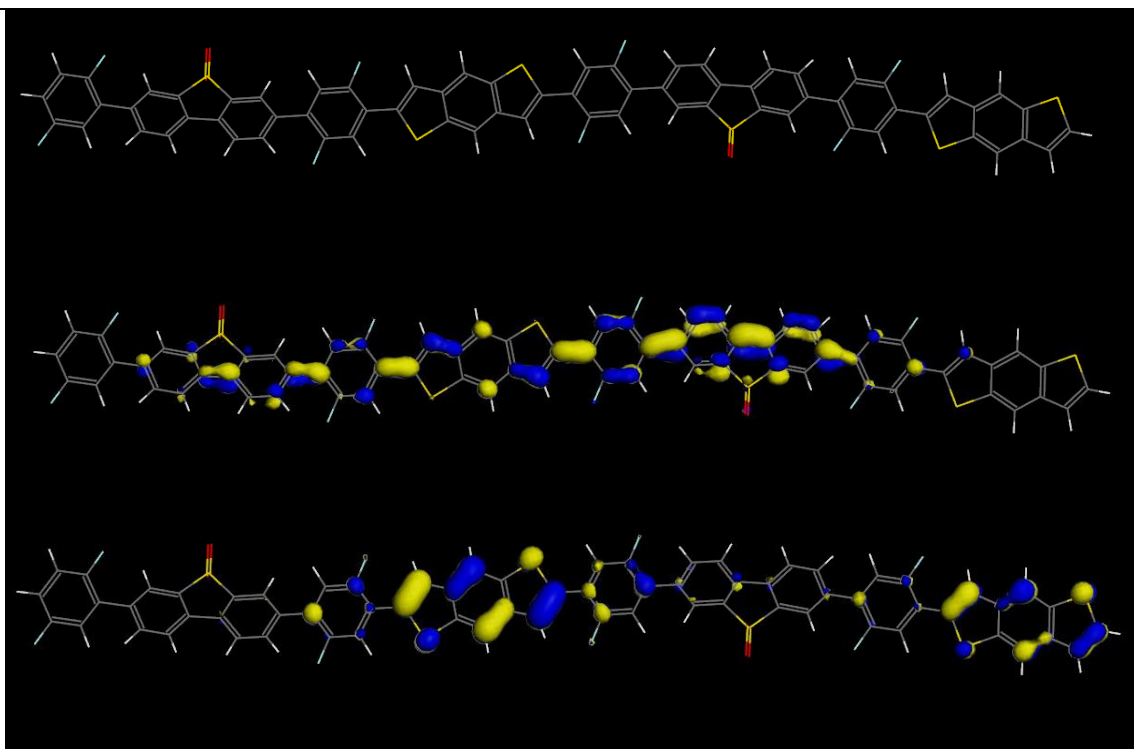


Figure 143: Optimised geometry of DBTS-PhF2a-BDT and associated HOMO (H) and LUMO (L) frontier molecular orbital distribution.

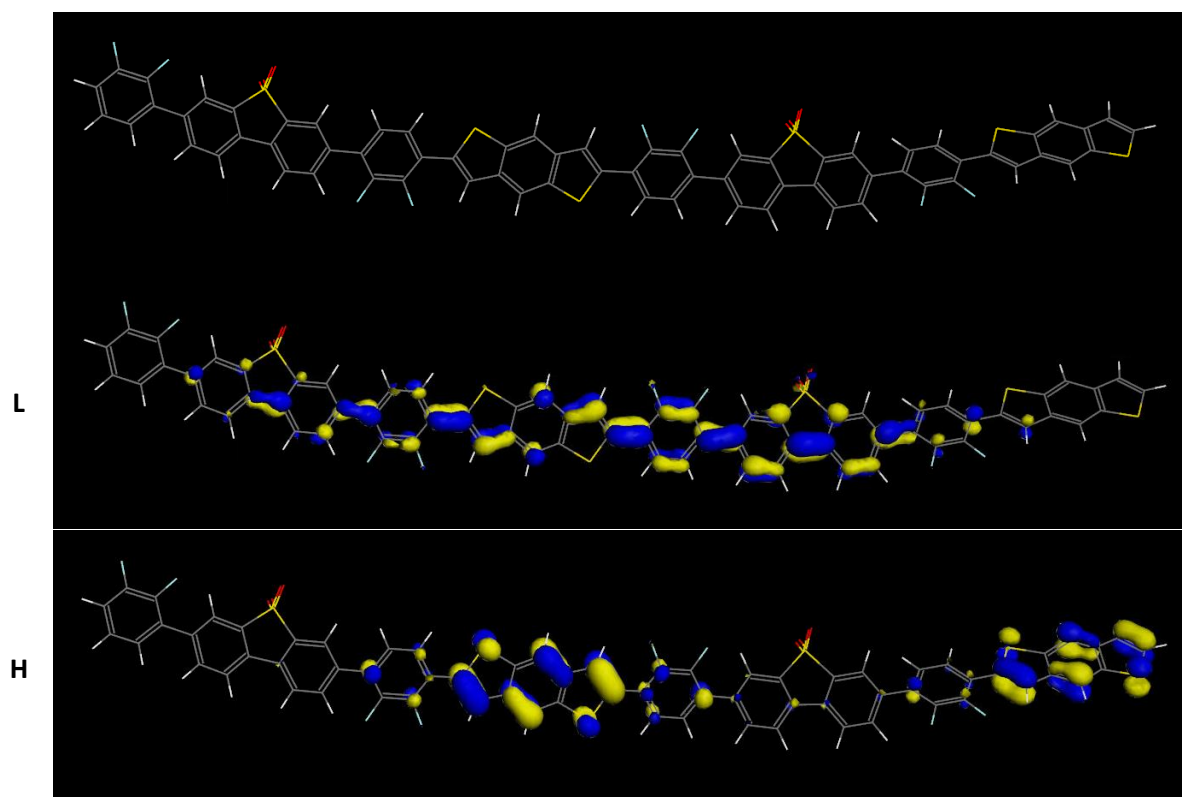


Figure 144: Optimised geometry of DBTS-PhF2b-BDT and associated HOMO (H) and LUMO (L) frontier molecular orbital distribution.

3.6 Dibenzothiophene Sulphone Co-polymers

3.6.1 Initial Synthesis Conditions

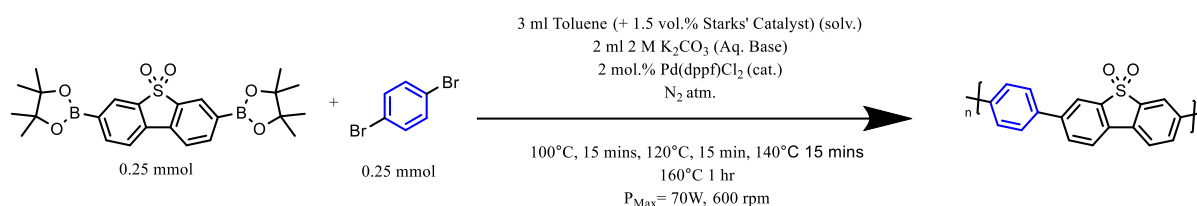


Figure 145: Initial reaction conditions for DBTS-PhFx polymers. Microwave-assisted Suzuki-Miyaura polycondensation reaction. Blue aromatic dibromide represents the variable selection of dibromide monomeric precursors investigated.

Following the work by Y. Bai *et al.*,²¹⁰ the DBTS-PhFx series of polymers were prepared using the conditions outlined in Figure 145. In contrast to the earlier work, 2M potassium carbonate was used as the base instead of 2M tetrabutylammonium acetate, and 2 mol.% of the palladium catalyst was used instead of 0.66 mol%. For the reaction conditions highlighted above, the reaction mixture is biphasic as the toluene and aqueous K_2CO_3 solution phase separate. 1.5 vol% of Aliquot 336 is added to the toluene used in these experiments to act as a phase transfer catalyst (PTC). Aliquot 336, also known as Starks' Catalyst, is a quaternary ammonium salt containing long aliphatic hydrocarbon chains that allow ions of the base to be transported into the organic phase.

Due to the safety measures installed in the Biotage Initiator+ microwave reactor, early reaction attempts were challenging. This is because the reactor automatically shuts down if a sudden pressure spike is detected. Due to the biphasic nature of the reaction, which is performed above the boiling point of water, the aqueous phase began to boil and cause these spikes when heated too quickly. Water is also very polar and therefore absorbs microwave radiation efficiently. This might have contributed to the pressure spikes if water was superheated and suddenly vaporised within the emulsion generated upon stirring. The microwave power was limited to 70 W, and a stepwise heating profile was programmed to circumvent this problem. The new heating profile reached 160 °C by intermediary steps of 100 °C, 120 °C, and 140 °C, at which points the reaction mixture was held for 15 minutes each.

Interestingly, the reactions that ended early due to pressure spikes still successfully produced the polymer products. Solid precipitates resembling the final polymer had already appeared within two minutes of microwave-assisted heating, during which the temperature had not yet risen above 120 degrees. This highlights the power of microwave synthesis, whereby a three-day solvothermal reaction can be sped up to a couple of minutes.

3.6.1.1 Appearance

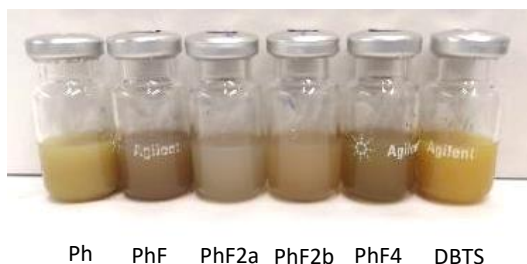


Figure 146: Image of DBTS-PhFx polymers dispersed in 1:1:1 TEA/MeOH/H₂O solution (5 mg in 5 ml). Samples were synthesised at temperatures up to 160 °C from Toluene/K₂CO₃.

Figure 146 contains a photograph of these polymers dispersed in in a 1:1:1 mixture of water, methanol, and triethylamine. The polymer concentration is 5 mg ml⁻¹.

The appearance of these polymers is expected to be bright yellow in their pure forms. The muddy brown colour observed for these samples indicates that the product is of low purity. Whilst these could be purified further by Soxhlet extraction, it is a lengthy three-day process that would have severely negated the fast, high-throughput nature of the microwave synthesis approach. Furthermore, these polymers are insoluble in all organic solvents, and while Soxhlet extraction can improve the purity, it cannot remove all impurities. The yields of these samples are given on the secondary axis of Figure 147. Several samples were synthesised in yields that exceeded their theoretical maximum, reinforcing the notion of low purity. Notably, the co-polymers containing PhF and PhF4 phenyl units are particularly dark. These two samples are also the ones with the lowest HER rates.

Once polymers have precipitated, they can no longer increase their chain length. The temperature of 160°C was selected to maximise the solubility of monomers and short-chain intermediary oligomers in the organic solvent. However, since these polymers are insoluble, gel permeation chromatography could not be used to determine their chain lengths and polydispersity to verify this.

3.6.1.2 Photocatalytic Activity

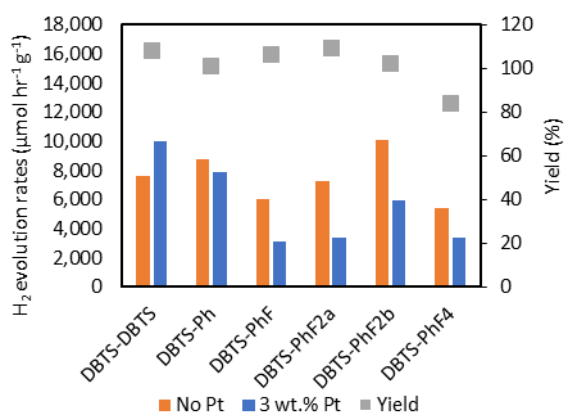


Figure 147: HER for DBTS-PhF_x polymers synthesised in this study before and after the photodeposition of Pt co-catalyst. Synthesis yields are presented on the secondary axis.

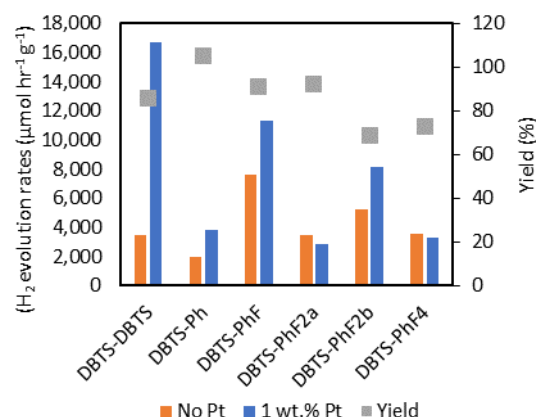


Figure 148: HER for DBTS-PhF_x polymers synthesised by Bai *et al.* before and after the photodeposition of Pt co-catalyst. Synthesis yields are presented on the secondary axis. Data retrieved from reference ¹⁸².

These polymers were tested for their hydrogen evolution rates from a 1:1:1 mixture of water, methanol, and triethylamine. Each polymer was tested as prepared and with 3 wt.% Pt co-catalyst photodeposited onto its surface. The resulting HER rates, and the associated synthesis yields are presented in Figure 147. For a direct comparison with the samples produced by Bai *et al.* discussed in Chapter 2, their results are presented in Figure 148. These rates should be directly comparable since they were tested under the same conditions using the same experimental setup.

Clearly, by synthesising the same polymers using 2M K₂CO₃ as the base compared with 1M tetrabutyl ammonium acetate (NBu₄Oac, TBAA) and using a higher concentration of the cross-coupling catalyst, the structure-activity trends regarding the photocatalytic hydrogen evolution activity change significantly. Whereas Bai's results suggest that DBTS-PhF is the most active of the phenylene copolymers, this work suggests that it is the least active. Meanwhile, DBTS-Ph and DBTS-PhF2a show reasonable photocatalytic activities under these new synthesis conditions, whereas they performed poorly under the old ones.

The Pt loading concentration of 3 wt.% was selected as this loading is common in the literature for organic photocatalysts.^{232,233} However, DBTS-DBTS (P10) is the only polymer amongst this initial set which showed an increase in activity with respect to co-catalyst loading. Furthermore, this increase is negligible compared to the increase in activity of over 300% that was activity observed by Bai *et al.* for the same material. As observed in Figure 147, adding a Pt co-catalyst resulted in decreased activity for all samples containing a phenylene co-monomer, regardless of fluorine content. This decrease in

activity is likely arises as a result of high residual palladium concentrations combined with an excess loading of additional platinum. The unexpectedly dark colour of these polymers also suggests high residual palladium concentrations.

For both sets of these data, samples were irradiated with simulated sunlight for an hour before the headspace gas concentrations were determined. As discussed in section 3.3 (methods), it was later realised that extended exposures lead to the determination of unreliable hydrogen evolution rates as the headspace pressure builds up.

3.6.2 Lower Reaction Temperature

Reactions that failed to reach temperature still resulted in the formation of polymeric precipitates. These were often lighter in colour than those obtained after reaching 160 °C and were heated for the full time. Therefore, the effect of reducing the reaction temperature to 120 °C was investigated for DBTS-DBTS and DBTS-PhF4. These polymers were also tested with a range of co-catalyst loading concentrations. These results are presented in Figure 149. For these experiments, the sample irradiation time was reduced to 30 minutes.

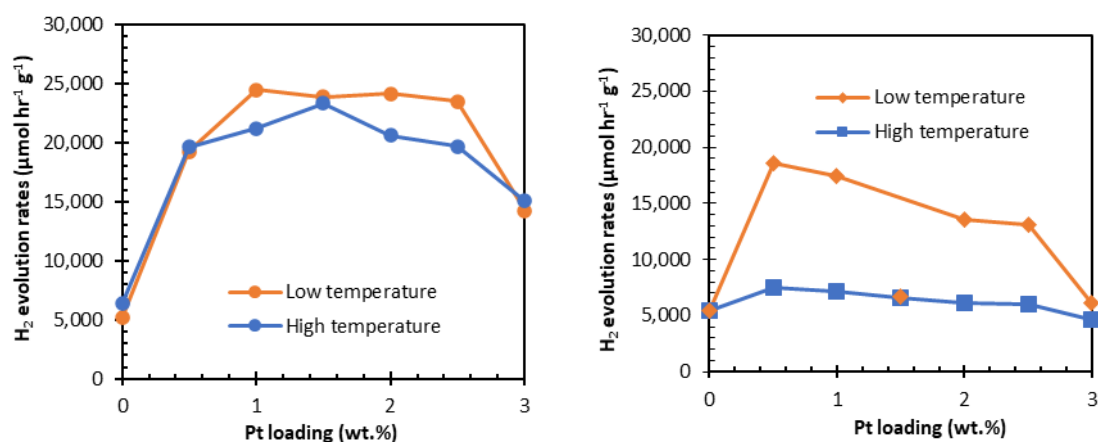


Figure 149: H₂ evolution rates for DBTS-DBTS (left) and DBTS-PhF4 (right) when loaded with different amounts of Pt co-catalyst. Two synthesis conditions are presented, corresponding to a lower temperature of 120 °C and a higher temperature of 160 °C. Samples were synthesised in the presence of 2 mol% Pd(dppf)Cl₂ catalyst.

These results clearly indicate that lower reaction temperatures during the microwave synthesis process result in higher HER rates when tested under sacrificial conditions. However, the two polymers' responses to co-catalyst loading differed significantly. Although the lower temperature did improve the efficiency of the DBTS-DBTS homopolymer, the effect of temperature was far more significant on DBTS-PhF4.

Regardless of the synthesis temperature, the HER activity of DBTS-DBTS jumped significantly from 6 mmol hr⁻¹ g⁻¹ to 20 mmol hr⁻¹ g⁻¹ upon photodepositing 0.5 wt.% Pt. This polymer reached a maximum HER of nearly 25 mmol hr⁻¹ g⁻¹ when loaded with 1 wt.% Pt. Although it appears that additional Pt content above this amount did not significantly impact the photocatalytic activity, it should be noted that the headspace concentrations remain remarkably high, despite reducing the irradiation time to 30 minutes. The accurate measure of the HER rates from these samples may be even higher but require shorter irradiation times to avoid the impact high headspace pressure.

When synthesised at 160 °C, DBTS-PhF4 exhibits a small increase in photocatalytic activity in response to small loadings of Pt co-catalyst. The largest increase in rate was observed when loaded with 0.5 wt.% Pt, whereas the photodeposition of 3 wt.% Pt resulted in a slight decreased photocatalytic activity relative to the pristine sample. However, when synthesised at the lower temperature of 120 °C, the photocatalytic activity increased from 5 mmol hr⁻¹ g⁻¹ for the pristine sample to 18 mmol hr⁻¹ g⁻¹ when loaded with 0.5 wt.% Pt. As with the sample synthesised at the higher temperature, increasing the Pt content above 0.5 wt.% decreased activity.

These results highlight that DBTS-PhF4 is far more sensitive to the reaction temperature and the co-catalyst loading content than DBTS-DBTS. It is likely that the high reaction temperature and high Pt loadings of the other DBTS-PhFx polymers prepared in section 3.6.1 are responsible for their poor photocatalytic performances, which worsened upon co-catalyst loading.

3.6.3 Residual Palladium from Suzuki-coupling Catalyst

Failed Suzuki reactions result in the formation of metallic palladium black that turns the organic phase dark.²³⁴ One hypothesis to explain the lower photocatalytic activity of polymers synthesised at 160 °C compared to 120 °C is that the higher temperatures result in more significant amounts of residual palladium leftover from the cross-coupling catalyst. This hypothesis is supported by the darker colour of the polymers synthesised at higher temperatures.

The palladium ends up embedded in the bulk of the polymer matrix and the polymer particle surface. In many cases, surface palladium acts as a cocatalyst for photocatalytic hydrogen evolution,¹⁵⁵ but it is unclear how effective palladium is as a surface-loaded co-catalyst compared to platinum. Bulk palladium, however, can be detrimental to photocatalytic activity. In this form, palladium acts as an electron trap that does not promote chemical reactions since photogenerated charges cannot reach

the surface. Since these polymers are insoluble, removing residual palladium by purification is very challenging. Some purification methods, such as Soxhlet extractions in hot organic solvents, have been successful at reducing palladium content in insoluble polymers. However, these methods are time-consuming and cannot eradicate palladium entirely.⁶²

The discrepancy between the response of DBTS-DBTS and DBTS-PhF4 to the synthesis temperature may originate from differing interactions of these polymers with residual palladium. In the case of DBTS-DBTS, long-lived negatively-charged polarons have been identified via transient absorption spectroscopy, TAS.^{235,236} This study indicated that electron transfer to residual palladium clusters is slow for this polymer. By contrast, the same paper identified that for other polymer photocatalysts, namely P8BT, charge transfer to residual palladium clusters occurs on the femto-nanosecond timescale.

If we assume that charge transfer to palladium occurs rapidly in DBTS-PhF4 and slowly in DBTS-DBTS, the discrepancy between the activities of these two polymers can be explained. For DBTS-DBTS, the photocatalytic activity and its response to Pt-loading remain similar for the synthesis at the two temperatures. This is because charge transfer to palladium is slow regardless of palladium concentration. Upon Pt photodeposition, charge transfer preferentially occurs into surface-loaded platinum particles instead of bulk palladium and the photocatalytic activity is significantly improved.

Meanwhile, for DBTS-PhF4, higher palladium content in samples prepared at 160 °C would lead to greater charge extraction into bulk palladium sites instead of surface-loaded platinum. This would result in more charge recombination and a lower HER rate. Lower quantities of palladium in the sample prepared at 120 °C would result in fewer trapped charges and more charge extraction into platinum, where subsequent proton reduction and hydrogen evolution occur.

To investigate the importance of the palladium cross-coupling catalyst concentration on the photocatalytic activity, DBTS-PhF was re-synthesised from reaction mixtures containing varying concentrations of the Pd(dppf)Cl₂ catalyst.

3.6.3.1 Role of Residual Palladium

For this investigation, DBTS-PhF was chosen. This is because the activity of the PhF co-polymer synthesised under the initial conditions (section 3.6.1) decreased upon the addition of Pt. Meanwhile, when synthesised by Bai *et al.*, the activity of this polymer increased with respect to Pt loading.

Four samples of DBTS-PhF were synthesised using four different amounts of Pd(dppf)Cl₂ catalyst in the reaction mixture: 0.33, 0.66, 1, and 2 mol%. These syntheses were carried out at 120°C. Onto each of these polymers, several different loadings of platinum were photodeposited from 0.5 – 2 wt.%. The resulting HER rates are presented in Figure 150. Since these polymers were synthesised at lower temperatures, the photocatalytic activity was significantly improved compared to the same polymer when synthesised at 160°C. Following an initial 1-hour irradiation in which it is assumed all of the platinum is photodeposited, the samples were degassed and irradiated for 15 additional minutes, after which the headspace gas composition was determined.

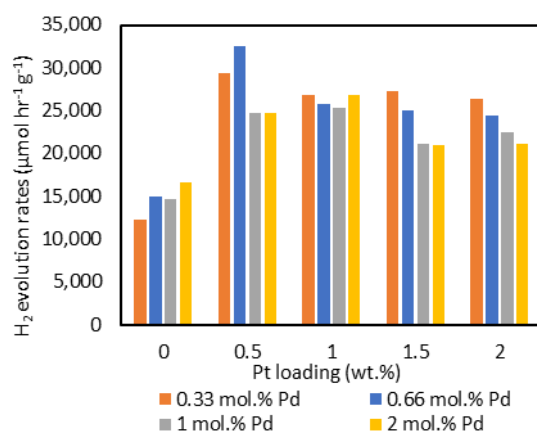


Figure 150: H₂ evolution rates for DBTS-PhF when loaded with different amounts of Pt co-catalyst after being synthesised in the presence of different loadings of Pd(dppf)Cl₂ catalyst.

Both the 0.33 and 0.66 mol% Pd samples exhibited higher photocatalytic activities and experienced the same trend with respect to Pt content. Firstly, the activity increased from 12-15 mmol hr⁻¹ g⁻¹ to record highs of 28 – 33 mmol hr⁻¹ g⁻¹ once loaded with 0.5 wt.% Pt. Further loading of 1 wt.% Pt resulted in decreased activity (~26 mmol hr⁻¹ g⁻¹) which remained largely invariant at 1.5 and 2 wt.% Pt. Without platinum, the polymers prepared with more palladium were slightly more active than those prepared with less, implying greater Pd content which acts as the only co-catalyst for these samples.

The highest activity was observed for the sample prepared using 0.66 mol% Pd and loaded with 0.5 wt.% Pt. This record HER of 32.4 mmol hr⁻¹ g⁻¹ is very high and is the most significant rate observed throughout our studies. This rate significantly surpasses all activities measured across the 99 samples prepared in the previous high-throughput work.

As discussed in section 3.3.4, mass normalised rates cannot easily be compared with results from other groups. When normalising for the approximate irradiation area of 6.7 cm² this equates to a hydrogen evolution rate of 24.2 μmol hr⁻¹ cm⁻², or 242 mmol hr⁻¹ m⁻². However, even when area-normalised comparison of results is difficult. For example, Cheng *et al.* recently reported record mass-normalised photocatalytic hydrogen evolution rates of 303.7 mmol hr⁻¹ g⁻¹.²³⁷ The area-normalised rate can be calculated as 715 mmol hr⁻¹ m⁻². However, their experimental setup uses a different light source (300W Xe arc lamp with 420 nm cutoff filter), and the photocatalysis reaction vessel is placed under vacuum to minimise the amount hydrogen dissolved. Furthermore, their reaction conditions also involve different co-solvents and different sacrificial reagents which were shown to be essential in enhancing the photocatalysis rates.

Unfortunately, this high rate was not successfully reproduced when attempting to re-synthesising this polymer on later occasions. However, the decrease in sensitivity of the GC detector over time could be the root cause of this (see section 3.4.1.6.)

For lower Pd catalyst concentrations, a more significant weighing error is introduced. Since these reactions are being performed on the 0.25 mmol scale, Pd(dppf)Cl₂ catalyst was weighed out to between 0.6 - 2.4 ± 0.1 mg. Hence this weighing procedure introduces errors on the scale of 17% for the lower masses. Despite the range of palladium catalyst content in the reaction mixtures, all samples were obtained in yields of 98% or higher.

3.6.4 Updated Synthesis Procedure

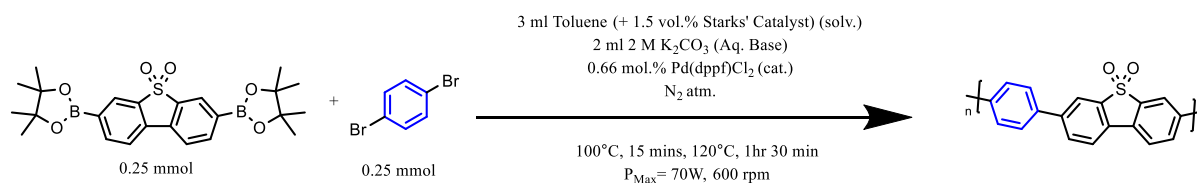


Figure 151: Reaction conditions for DBTS-PhFx polymers using a lower temperature and lower quantity of palladium catalyst. Microwave-assisted Suzuki-Miyaura polycondensation reaction. Blue aromatic dibromide represents the variable selection of dibromide monomeric precursors investigated.

Following the results from the previous sections, the DBTS-PhFx series of polymers were re-synthesised using the conditions outlined in Figure 151. The slightly higher Pd catalyst content of 0.66 mol% was used instead of the lowest concentration to reduce the error and variation in Pd content at these small synthesis scales. These polymers were dispersed in a 1:1:1 mixture of water, MeOH, and TEA for HER experiments. In all experiments involving a Pt cocatalyst, 0.5 wt.% Pt was added in the form of an aqueous H_2PtCl_6 solution prior to the first irradiation. All samples were initially irradiated for 1 hour, degassed, and subsequently irradiated for an additional 15 minutes before the headspace composition was tested. These samples are pictured in Figure 153, and the photocatalytic activities are presented in Figure 152. Compared with the initial reaction conditions (Figure 146), lower temperatures and palladium content resulted in brighter polymers, indicating higher purity products.

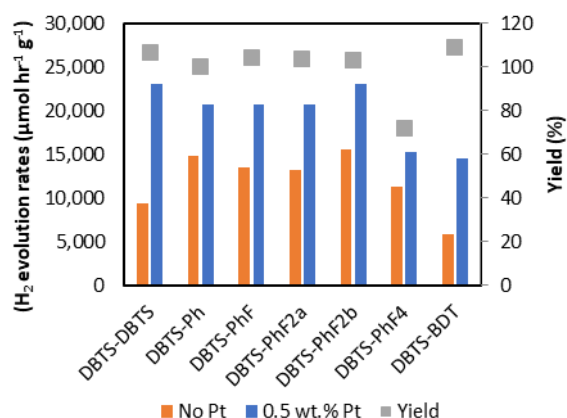


Figure 152: HER rates of DBTS-PhFx polymers synthesised under optimised conditions with and without Pt loading.

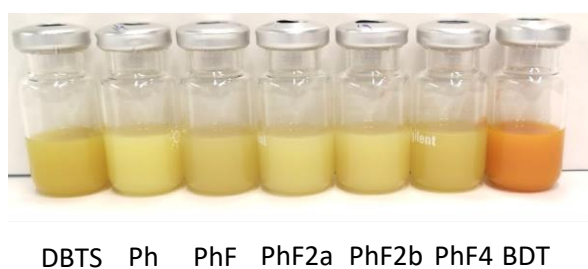


Figure 153: Image of DBTS-PhFx polymers synthesised under new conditions. 5 mg of the polymers dispersed in 5 ml of 1:1:1 TEA/MeOH/ H_2O solution.

The HER activities for these polymers are presented in Figure 152 and demonstrate significant improvements compared to the same polymers prepared under the initial reaction conditions. In each case, the photocatalytic activity improves after photodepositing 0.5 wt.% platinum as a co-catalyst. However, DBTS-PhFx co-polymers with phenylene linkers are more active before adding platinum and show a smaller relative increase in activity after adding platinum compared to the DBTS-DBTS and

DBTS-BDT polymers. This difference is likely due to the different rates of charge extraction into residual palladium via the phenylene units. However, DBTS-PhF polymers discussed in 3.6.3.1 gave rise to activities that doubled upon adding 0.5 wt.%. Despite being synthesised under identical conditions, the DBTS-PhF sample within this set achieved substantially lower HER rates with a smaller relative increase in activity upon Pt deposition. Visual inspection of DBTS-PhF, as presented in Figure 153, shows a darker polymer than those around it, potentially indicating higher residual palladium content. DBTS-PhF4 also showed higher activity for the pristine polymer and lower activity for the Pt-loaded one compared to the DBTS-PhF4 sample prepared in section 3.6.2. Further characterisation would be required to understand these changes fully.

The DBTS-PhFx polymers do not exhibit a clear trend in photocatalytic activity with respect to fluorine content. DBTS-Ph, DBTS-PhF, and DBTS-PhF2a all demonstrate the same photocatalytic HER rates once loaded with Pt, all of which were slightly lower than the DBTS-DBTS homo-polymer. Despite being expected to have the same band edge potentials as DBTS-PhF2a, DBTS-PhF2b exhibited improved photocatalytic activities comparable to the DBTS-DBTS homopolymer. This polymer also showed the highest activity in the absence of platinum. Of the fluorinated polymers, DBTS-PhF4 produced the least hydrogen. However, it is unclear if this reduced activity originates from the polymer's physical and electronic structure or if this arises from the additional impurities that are likely to be present, given that this polymer was synthesised with a lower yield.

The co-polymer DBTS-BDT has the smallest bandgap, as indicated by its orange colour. However, the additional absorption of the solar spectrum did not increase the photocatalytic activity. This polymer also does not appear to benefit from its donor-acceptor backbone structure. The results of the DFT calculations indicated that the band edge potentials are close to the minimum required for photocatalytic oxidation of TEA. Resultingly, this polymer may not have an appropriate overpotential to drive the reactions efficiently.

3.6.4.1 Optoelectronic Characterisation

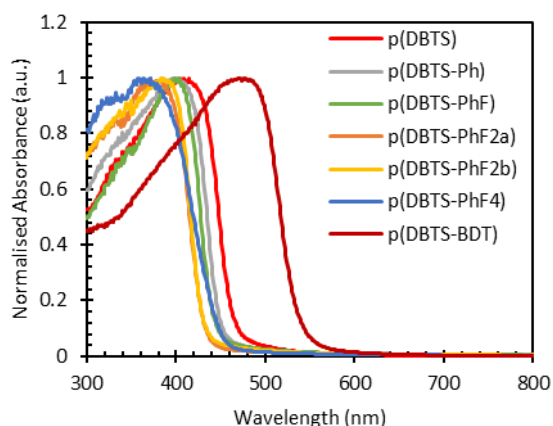


Figure 154: UV/Vis diffuse reflectance spectra of DBTS-PhFx polymers synthesised under modified conditions.

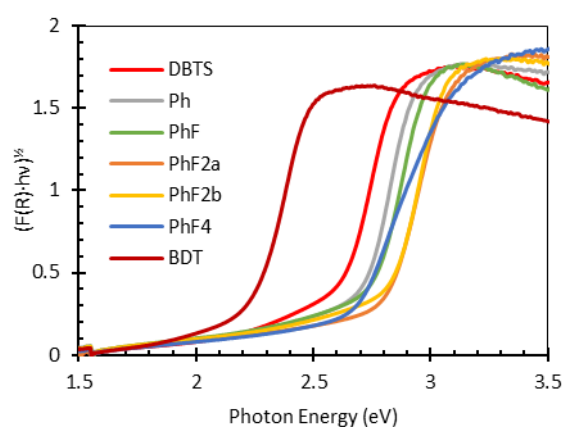


Figure 155: Tauc plot of DBTS-PhFx polymers synthesised under modified conditions for optical bandgap determination.

UV/Vis diffuse reflection spectra were recorded for the DBTS-PhFx photocatalysts and converted into $F(R)$, which is proportional to the absorption coefficient, and subsequently normalised. These DRS spectra are presented in Figure 154. The bandgaps have been calculated using the Tauc relation and extrapolating the linear section of the band edge to its intersection with the x-axis (Figure 155).

According to the DFT calculations, the fundamental gap is expected to increase by approximately 0.1 eV after introducing two fluorine substituents onto the phenyl ring of DBTS-Ph. The measured values demonstrate that the optical bandgap does increase. However, it increases by almost double the amount.

Unusually, despite its absorption maximum being located at the shortest wavelengths, the measured optical bandgap of DBTS-PhF4 is smaller than the other copolymers owing to an additional absorption feature located in the tail. The exact origin of this absorption is unclear. However, tetrafluorophenylene units exhibit unusual electrostatic interactions since the centre of the benzene ring becomes electron depleted rather than electron-rich, as is typically expected in aromatic systems. This may lead to increased long-range order via π - π stacking of adjacent aromatic rings or introduce charge transfer states.^{238–240} The DBTS-PhF4 polymer was also obtained in the lowest yield and only exhibited a small increase in photocatalytic activity upon Pt deposition. As such, this shoulder feature may also arise due to higher residual palladium concentrations or an increased concentration of sub-bandgap states.

Compared with the optical bandgap determined by Bai *et al.*¹⁸² for the same materials, these samples exhibited slightly wider bandgaps, with the exception of DBTS-PhF4. This can likely be attributed to the lower temperatures, which produced a purer, more pristine polymer with fewer sub-bandgap states arising from impurities.

Table 21: UV/Vis DRS measured optical bandgap and DFT-calculated fundamental bandgaps for DBTS-PhFx photocatalysts discussed in this section.

Sample	Optical Bandgap		Calculations			Hydrogen evolution rates		Yield
	This work	Literature ¹⁸²	EA	IP	E _F	No Pt	0.5 wt.% Pt	
	eV	eV	V vs SHE	V vs SHE	eV	μmol hr ⁻¹ g ⁻¹	μmol hr ⁻¹ g ⁻¹	%
DBTS-DBTS	2.58	2.51	1.56	-1.49	3.05	9,378	23,088	107
DBTS-Ph	2.69	2.45	1.38	-1.70	3.08	14,770	20,777	100
DBTS-PhF	2.72	2.65	1.52	-1.66	3.18	13,580	20,660	104
DBTS-PhF2a	2.78	2.70	1.61	-1.57	3.18	13,283	20,734	104
DBTS-PhF2b	2.80	2.69	1.63	-1.58	3.21	15,510	23,016	103
DBTS-PhF4	2.63	2.81	-	-	-	11,329	15,282	72
DBTS-BDT	2.22	2.18	0.98	-1.44	2.43	5,850	14,483	109

3.6.5 Alternative Reaction Conditions

3.6.5.1 Organic Solvent: Toluene (3 ml), Aqueous Base: 2M TBAA (2 ml)

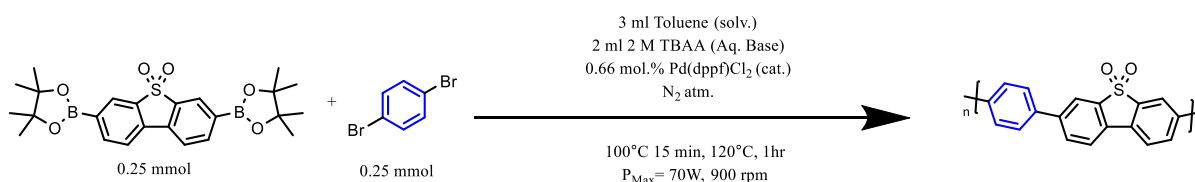


Figure 156: Modified reaction conditions for DBTS-PhFx polymers using 2M TBAA as the base. Microwave-assisted Suzuki-Miyaura polycondensation reaction. Blue aromatic dibromide represents the variable selection of dibromide monomeric precursors investigated.

Following the optimisation of reaction temperature and Pd catalyst concentration, the following experiments investigated the selection of organic solvent, aqueous base, and their relative proportions in the synthesis reaction mixture. The first modification investigated was the substitution of 2M K₂CO₃ with 2M TBAA as the aqueous base. The PTC was not used in this reaction mixture since TBAA itself is a tetra alkyl ammonium salt that improves miscibility between the organic and aqueous phases. The reaction conditions are summarised in Figure 156.

A photograph of the resulting polymers, dispersed in a 1:1:1 mixture of H₂O/MeOH/TEA (5 mg polymer in 5 ml), is shown in Figure 157. Compared with the equivalent polymers synthesised from Toluene/2M K₂CO₃, these polymers appear to have a slight brown tinge that implies lower purity.

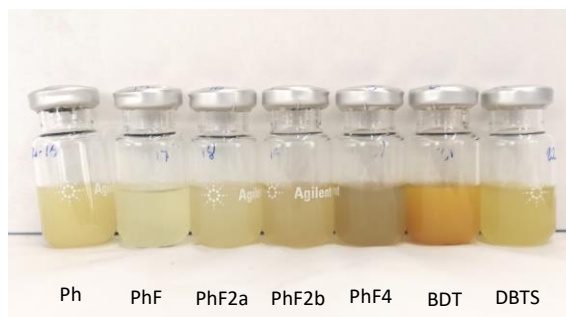


Figure 157: Image of DBTS-PhFx photocatalysts synthesised from a toluene/TBAA reaction mixture dispersed in 1:1:1 (v/v) mixture of MeOH/H₂O/TEA.

TBAA was the chosen base in the work conducted by Bai *et al.* for their high throughput work.¹⁸² As such, this is an opportunity to compare the two sets of data directly and investigate the impact of the lower reaction temperature. The two sets of hydrogen evolution results are compared side-by-side in Figures 158 and 159.

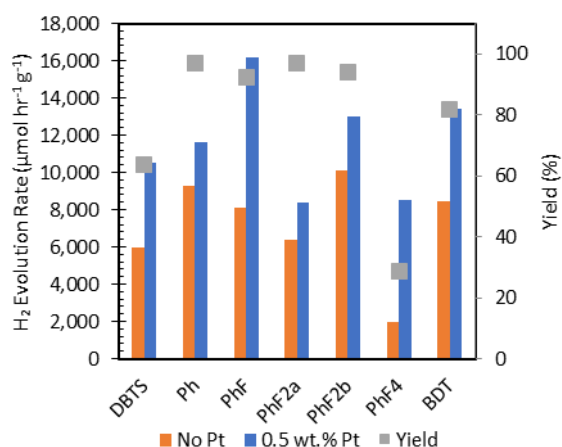


Figure 158: Photocatalytic hydrogen evolution rates for DBTS-PhFx Polymers synthesised in this section using toluene as the organic solvent and 2M TBAA as the base.

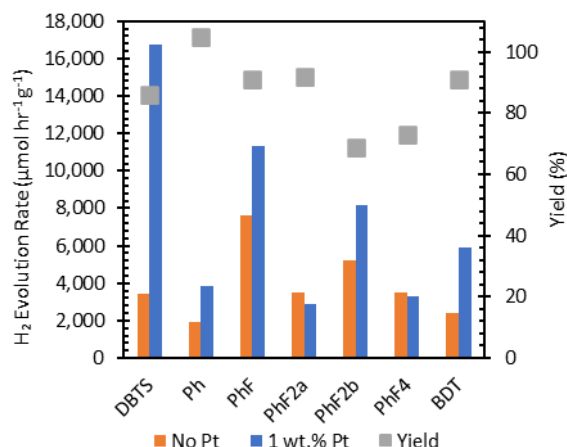


Figure 159: Photocatalytic hydrogen evolution rates for DBTS-PhFx Polymers synthesised by Bai *et al.* using toluene as solvent and 1.5M TBAA as the base. Data reproduced from reference¹⁸²

By directly comparing the two sets of data, one observes a consistent pattern of photocatalytic activity with respect to the fluorinated phenylene co-monomer after loading with a Pt co-catalyst. The hierarchy of photocatalytic rates in both cases is as follows: DBTS-PhF > DBTS-PhF2b > DBTS-Ph > DBTS-PhF2a ≈ DBTS-PhF4. In each of these cases, the hydrogen evolution rates are larger than those prepared by Bai *et al.* The new lower-temperature DBTS-BDT co-polymer is also more photocatalytically active than its counterpart reported in the literature. However, the previously-reported DBTS-DBTS homopolymer was more active than the one synthesised in this study.

All samples synthesised in the Toluene/TBAA reaction mixture at the lower temperature of 120°C exhibit increases in activity following the photodeposition of 0.5 wt.% Pt, indicating lower palladium concentrations in the cases of DBTS-PhF2a and DBTS-PhF2b. However, compared with the samples synthesised in Toluene/K₂CO₃ in the previous section, these polymers were substantially less active. Based on the visual appearance of the two sets of polymers, this may be attributed to the lower purity of the polymers synthesised using TBAA as the base.

These results demonstrate why comparing the photocatalytic activities of identical polymers synthesised under similar conditions is particularly difficult, even when tested on the same experimental photocatalysis setup. Minor changes to the synthesis conditions can significantly impact the photocatalytic activity without substantially altering the synthesis yields.

3.6.5.2 Organic Solvent: 1,4-dioxane (3 ml), Aqueous Base: 2M TBAA (2 ml)²

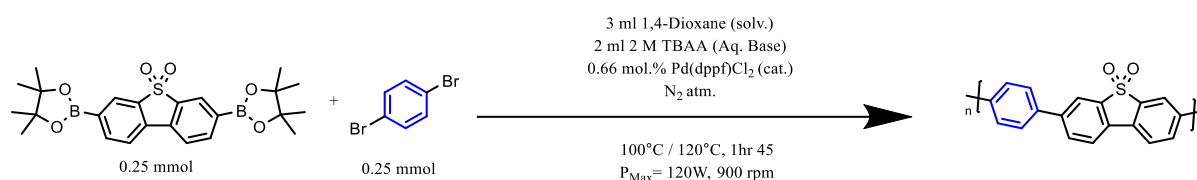


Figure 160: Modified reaction conditions for DBTS-PhFx polymers using 1,4-dioxane as the organic solvent and 2M TBAA as base. Microwave-assisted Suzuki-Miyaura polycondensation reaction. Blue aromatic dibromide represents the variable selection of dibromide monomeric precursors investigated.

One of the principal advantages of using TBAA as the base is that it is soluble in aqueous and organic media and aids the degree of mixing between the two phases. This solvent/base combination was selected because of the successful synthesis of BDT-PhF4 using these reaction conditions, as will be discussed in section 3.7. Two different reaction temperatures (100°C and 120°C) were also tested using this solvent/base combination to investigate if the photocatalytic activity can be enhanced further by even lower reaction temperatures. This solvent/base reaction mixture required a higher microwave power to heat it effectively.

² These samples were tested for their photocatalytic activities using a modified method. Please see section 3.4.1.6.1 for details.

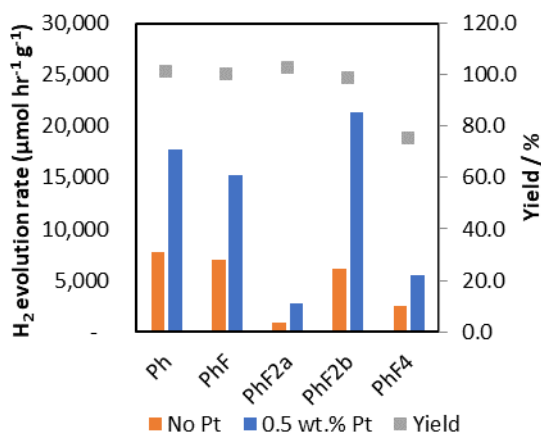


Figure 161: HER rates and synthesis yields for DBTS-PhFx co-polymers synthesised from dioxane/TBAA reaction mixture at 120°C

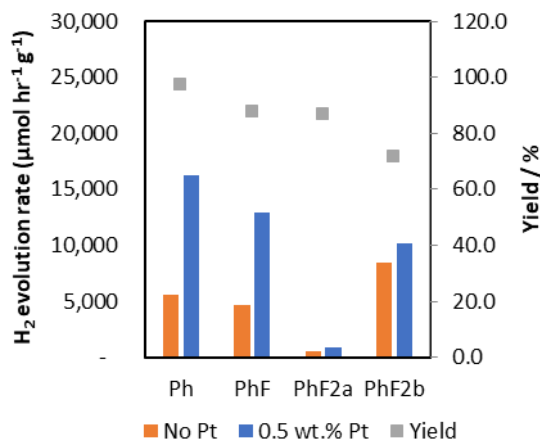


Figure 162: HER rates and synthesis yields for DBTS-PhFx co-polymers synthesised from dioxane/TBAA reaction mixture at 100°C.

The hydrogen evolution activities observed in Figures 161 and 162 demonstrate that, when using 1,4-dioxane as an organic solvent and 2M TBAA as the base (3 ml organic solvent 2 ml aqueous base), DBTS-PhFx polymers synthesised at the higher temperature of 120°C consistently produced hydrogen at a faster rate than those synthesised at the lower temperature. The yields were also consistently higher, implying that the reaction may not have gone to completion at the lower temperature. Lower reaction temperatures may also have led to shorter oligomeric polymer chain lengths if the reagent and intermediates' solubilities are reduced.

In both cases, DBTS-PhF2a significantly underperformed compared to the other polymers. This is particularly interesting compared to DBTS-PhF2b, as both polymers are predicted to have near-identical optoelectronic properties, including optical bandgap and band edge potentials. DBTS-PhF2b, when synthesised at 120°C is the most active photocatalyst with rates reaching 21.3 mmol hr⁻¹ g⁻¹. DBTS-Ph and DBTS-PhF also achieve rates of 17.7 mmol hr⁻¹ g⁻¹ and 15.2 mmol hr⁻¹ g⁻¹. These three samples are more active than the equivalent polymers synthesised from toluene/TBAA. However, DBTS-PhF2a and DBTS-PhF4 are less active. These are the same polymers that exhibited significant palladium contamination in the work published by Bai *et al.*¹⁸²

Interestingly, the photocatalytic activities of these samples increased dramatically after photodepositing the Pt co-catalyst. However, these samples were tested for their photocatalytic activity under slightly different conditions due to a limited supply of parts and technical issues with the gas chromatography system, as discussed in sections 3.3.4.2.1 **Error! Reference source not found.** and 3.4.1.6.1. The initial photodeposition period was performed with an ambient atmosphere. The

presence of oxygen at this stage may have led to the degradation of the polymer in the absence of a platinum co-catalyst.

3.6.5.3 Organic Solvent: Toluene (4.5 ml), Aqueous Base: 2M K₂CO₃ (0.5 ml)³

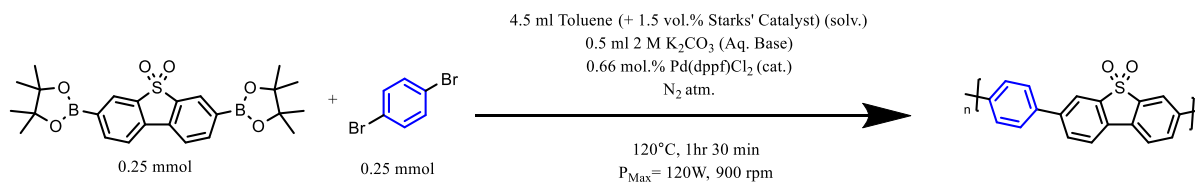


Figure 163: Modified reaction conditions for DBTS-PhFx polymers using toluene as the organic solvent and 2M K₂CO₃ as base. The ratio of organic solvent to aqueous base has been modified to 9:1, the intermittent heating step has been removed, and the maximum microwave power increased to 120 W. Microwave-assisted Suzuki-Miyaura polycondensation reaction. Blue aromatic dibromide represents the variable selection of dibromide monomeric precursors investigated.

The next modification to the reaction conditions involved reducing the volume of the aqueous phase. For these samples, 4.5 ml of toluene containing 1.5 vol% phase transfer catalyst was used as the organic solvent and 0.5 ml of 2M K₂CO₃ as the base. Compared to the reaction conditions used in section 3.6.4 (3:2 volume ratio), the smaller amount of water allows the microwave power to be increased from 70 W to 120 W. The requirement for an intermediary 15-minute heating step at 100 °C was also made redundant, as no large pressure spikes led the reactor to shut down. The new reaction conditions only contain four base equivalents compared to the starting reagents and only two equivalents compared to the number of moles of the reactive functional groups.

The resulting photocatalytic activities and the reaction yields are presented in Figure 164. The yields for the DBTS-PhFx polymers prepared via this method remain over 100% of the theoretical yield for all samples, except DBTS-PhF₄, which was obtained with an 80% yield – 8% more than from the 3:2 reaction mixture.

PhF₄-Br₂ may be susceptible to side reactions due to the presence of four strongly electronegative substituents. Whilst electronegative dibromides are favourable for Suzuki coupling, homocoupling and dehalogenation reactions may also occur.^{241,242} 1,2,4,5-tetrafluorobenzene is often used in direct arylation reactions where palladium-assisted carbon-carbon coupling reactions occur between Ar-Br and Ar-H units.²⁴³

³ These samples were tested for their photocatalytic activities using the modified method. Please see 3.3.4.2.1 and 3.4.1.6.1 for details.

The remaining yields over 100% are consistent with earlier DBTS-PhFx reactions and indicate that impurities are present. The yield calculation only considers the molecular mass of the polymer's repeat unit and assumes that the masses of the chain ends are negligible. Due to the insoluble nature of the resulting polymers, it is likely that shorter polymer chains are obtained and that the end groups of the polymer chains are a combination of heavy bromines, boronic acid pinacol esters, and palladium catalyst intermediates.

The impact of these chain ends on the photocatalytic activity is not well understood. However, studies from OPV research suggest that they may be detrimental to the optoelectronic properties of conjugated polymer photocatalysts.²⁴⁴ Since these polymers are insoluble, adding mono-brominated (or mono-boronic acid) reagents at the end of the reaction to cap the polymer chains is not impossible.

Other contaminants may include byproducts and unreacted reagents that were not entirely removed during the washing process. Due to the high-throughput approach and a focus on photocatalytic activity, the polymers were only washed with cold water and methanol. They were not further purified by Soxhlet extraction in chloroform or tetrahydrofuran, THF, despite this being a common practice in the literature.²⁴⁵

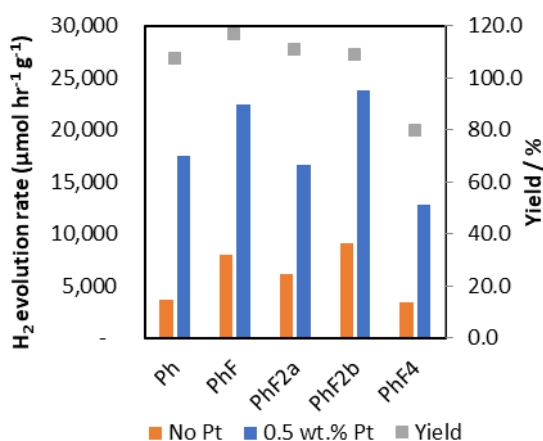


Figure 164: HER rates and synthesis yields for DBTS-PhFx co-polymers synthesised from Toluene/ K_2CO_3 using the modified solvent/base ratio.

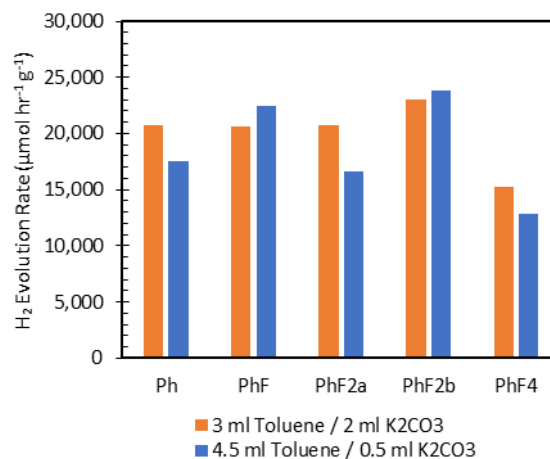


Figure 165: Comparison of HER rates for DBTS-PhFx polymers after loading with 0.5 wt.% Pt when synthesised from a Toluene/ K_2CO_3 reaction mixture with different solvent/aqueous base volume ratios.

Regarding the structure-activity relationships, these reaction conditions give rise to polymers exhibiting a different trend from those obtained from the 3:2 Toluene/ $2M K_2CO_3$ reaction mixture, as shown in Figure 165. DBTS-PhF and DBTS-PhF2b produced the most hydrogen under the sacrificial reagent conditions. All samples exhibited significant increases in activity after the photodeposition of

Pt, indicating that the residual palladium concentrations in these samples may be low. The photocatalytic activity of DBTS-PhF4 may still be inhibited by contaminants associated with its lower yield.

It is difficult to attribute the differences in activity between these samples and the equivalent polymers synthesised earlier solely to the 3:2 reaction mixture. These reactions were also performed with a higher microwave power and were directly heated to 120 °C without initially being held at 100 °C for 15 minutes. This may have impacted the reaction rate, average chain length, particle size, morphology, crystallinity, and residual palladium content.

Another consideration is the modified process by which the HER was recorded: the initial 1hr irradiation for Pt photodeposition was completed under an oxygen atmosphere. DBTS-Ph, also known in the literature as P7, has previously demonstrated the ability to drive the photocatalytic reduction of oxygen to form hydrogen peroxide.²⁴⁶ Hydrogen peroxide is highly reactive,²⁴⁶ and other polymeric photocatalysts known for hydrogen peroxide production have short lifetimes due to limited stability in its presence.²⁴⁷ It is plausible that upon irradiation in the presence of oxygen, the DBTS-PhFx polymers produced hydrogen peroxide, which degraded and deactivated the polymers. Such deactivation would significantly lower HER activity in the subsequent tests.

3.6.5.4 Organic Solvent: N,N-dimethylformamide (4.5 ml), Aqueous Base: 2M K₂CO₃ (0.5 ml)⁴

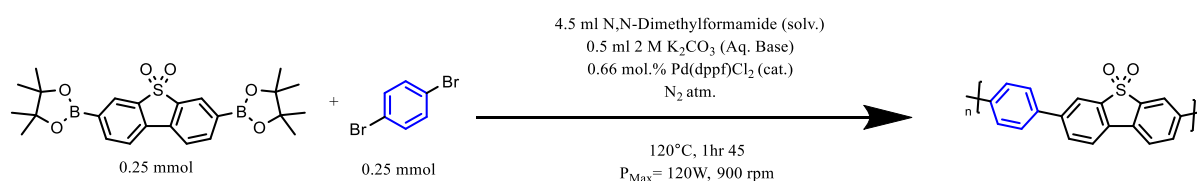


Figure 166: Modified reaction conditions for DBTS-PhFx polymers using DMF as the organic solvent and 2M K₂CO₃ as base. The ratio of organic solvent to aqueous base has been modified to 9:1, the intermittent heating step has been removed, and the maximum microwave power increased to 120 W. Microwave-assisted Suzuki-Miyaura polycondensation reaction. Blue aromatic dibromide represents the variable selection of dibromide monomeric precursors investigated.

The final set of reaction conditions investigated involved using N,N-dimethylformamide (DMF) as the organic solvent and 2M K₂CO₃ as the base. These reaction conditions mirror those typically used for the three-day solvothermal synthesis route frequently used in the literature. DMF was ruled out as a potential solvent in the initial microwave-assisted high-throughput experiment, as it heated too fast

⁴ These samples were tested for their photocatalytic activities using the modified method. Please see 3.3.4.2.1 and 3.4.1.6.1 for details.

under microwave heating and triggered pressure spikes.¹⁸² However, pressure spikes were eliminated from the Toluene/TBAA reaction during heating by increasing the proportion of the organic phase relative to the aqueous phase. The same approach was used here. This approach also resulted in a smooth heating profile with no pressure spikes for this DMF/K₂CO₃ reaction mixture.

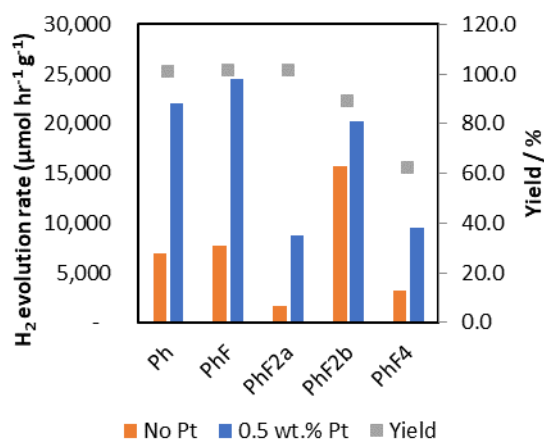


Figure 167: HER rates and synthesis yields for DBTS-PhFx co-polymers synthesised from DMF/K₂CO₃ using the modified solvent/base ratio.

As with many of the other reaction conditions, DBTS-Ph, DBTS-PhF, and DBTS-PhF2b are the most active photocatalysts. However, their relative ranking is once again different. DBTS-PhF2a and DBTS-PhF4 exhibit significantly lower photocatalytic activities. As is also the case for all other reaction conditions, DBTS-PhF4 is synthesised with a lower yield.

The photocatalytic activities of DBTS-Ph and DBTS-PhF each increase from 7.0 and 7.8 mmol hr⁻¹ g⁻¹ to 22.1 and 24.5 mmol hr⁻¹ g⁻¹, respectively, after photodepositing 0.5 wt.% Pt. Both of these values are larger than the equivalent polymers synthesised from toluene/K₂CO₃. However, the initial photocatalytic activity of DBTS-PhF2b is 15.8 mmol hr⁻¹ g⁻¹ but only increases to 20.3 mmol hr⁻¹ g⁻¹. The origin of this behaviour is unknown. Attempts were made to digest the polymers in nitric acid in preparation for ICP elemental analysis to determine the residual palladium content. Unfortunately, the polymers were not successfully digested.

3.6.6 Alternative Photocatalytic Reactions

3.6.6.1 Photocatalytic H₂O₂ Production

These DBTS-PhFx polymers synthesised in Toluene/TBAA were also tested for photocatalytic hydrogen peroxide production. In this photocatalytic reaction, photogenerated electrons reduce oxygen to form

H₂O₂ rather than reducing protons to form H₂. In an ideal overall water-splitting system, oxygen will also be present. It is, therefore, important to monitor how these polymers behave in the presence of oxygen.

Whilst photocatalytic hydrogen peroxide production is a promising area of research in itself,²⁴⁸ the photocatalytic reduction of oxygen is also a process that competes directly with the photocatalytic reduction of protons and can decrease the apparent quantum yields. Furthermore, peroxide species are highly reactive and are known to degrade polymers that have demonstrated the ability to produce it photocatalytically.²⁴⁷

To test for photocatalytic hydrogen peroxide production, 3 mg photocatalyst was dispersed in 5 ml deionised water, capped, and irradiated for 1.5 hours. Peroxide testing strips were used to test the water immediately after irradiation to gauge an approximate hydrogen peroxide production rate. The results of the test strips are photographed in Figure 168.

All DBTS-PhFx polymers produced some hydrogen peroxide photocatalytically. However, the photocatalytic reaction may only take place if the holes are also being consumed. This implies either water oxidation or polymer degradation (self-oxidation) is taking place. If the former is true, then it is suggestive that these polymers may be capable of achieving overall water splitting.

The second row of test strips in Figure 168 represents the same polymers tested for hydrogen peroxide production when dispersed in 10 vol% ethanol. Ethanol acts as a sacrificial electron donor similar to TEA in hydrogen evolution experiments.

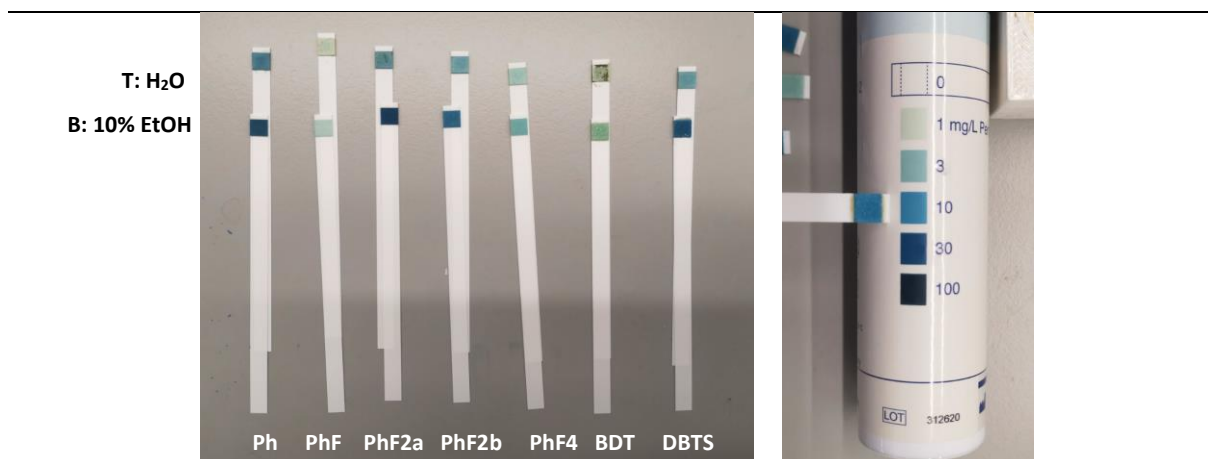


Figure 168: Hydrogen peroxide dip stick test results after dispersing 3 mg of DBTS-PhFx polymers in 5 ml of deionised water (top row) and 20 vol% ethanol (bottom row) and irradiating with AM1.5G solar simulated light for 1.5 hours under an oxygenated atmosphere. The polymers selected for this study were synthesised from a toluene/TBAA reaction mixture. Image on the right provides a colour scale for the results.

Interestingly, the two polymers which produced the least hydrogen peroxide are DBTS-PhF and DBTS-PhF4. These polymers correspond to the same two that presented the most significant jump in photocatalytic hydrogen production after photodepositing platinum (Figure 158). It is also worth noting that DBTS-PhF2a produced more hydrogen peroxide than DBTS-PhF2b, which is the reverse of the trend observed for hydrogen evolution reactions.

These results raise questions regarding the role of impurities. In particular, that of residual palladium since small increases in photocatalytic activity upon photocatalyst loading may be associated with higher levels of residual palladium. This would suggest that the polymers containing the most residual palladium also produce the most hydrogen peroxide and that residual Pd may be an effective co-catalyst for H₂O₂ production in these polymers. However, further experiments would be required to confirm this hypothesis.

Although inorganic photocatalysts do not typically produce H₂O₂ photocatalytically, overall water splitting does compete with the back reaction whereby oxygen is reduced, hydrogen is oxidised, and water is reformed. Noble metal catalysts are effective at both water splitting and oxygen reduction. In this domain, metal co-catalysts such as rhodium and platinum are coated with chromium (III) oxide, Cr₂O₃, through which oxygen does not diffuse.^{46,249,250} Employing this method on organic photocatalysts may lead to more stable polymer photocatalysts in the presence of oxygen.

Although H₂O₂ was produced photocatalytically for these samples in an oxygenated atmosphere, these samples did not produce hydrogen under an inert atmosphere. This generates important questions

regarding the oxidation reaction mechanism for these polymers. Typically, it is expected that the water oxidation/oxygen evolution reaction consumes holes. As such, these polymers are promising candidates for overall water splitting. Since the oxygen reduction reaction is more energetically favourable than the hydrogen evolution reaction, further work must be done to identify an ideal co-catalyst or combination of co-catalysts to encourage hydrogen evolution whilst inhibiting the reduction of photogenerated oxygen.

3.7 Benzo[1,2-b:4,5-b']dithiophene Co-polymers (BDT-PhFx)

Benzodithiophene co-polymer analogues of the DBTS-PhFx series were also synthesised. DFT calculations predicted that these polymers would have smaller bandgaps and could drive the HER when paired with the correct sacrificial reagents. Photocatalytic hydrogen evolution, however, may not occur when using TEA or TEOA as sacrificial reagents due to the small oxidation overpotential generating a weak thermodynamic driving force. Polymer photocatalysts with narrower bandgaps are required if overall STH efficiencies are to be improved.

Whereas benzene is a weak electron donor, it becomes significantly more electron-withdrawing as the fluorine content increases. Since BDT is a donor unit, the BDT-PhFx polymers have a donor-acceptor structure which may lead to more efficient charge separation, delocalisation, and a weaker exciton binding energy.^{58,60}

3.7.1 Organic Solvent: Toluene (3 ml), Aqueous Base: 2M K₂CO₃ (2 ml)

Initial attempts to synthesise the BDT-PhFx polymers used were initially synthesised at 120 °C in a mixture of toluene and aqueous K₂CO₃ following the success of this method in section 3.6.4. This reaction scheme is presented in Figure 169.

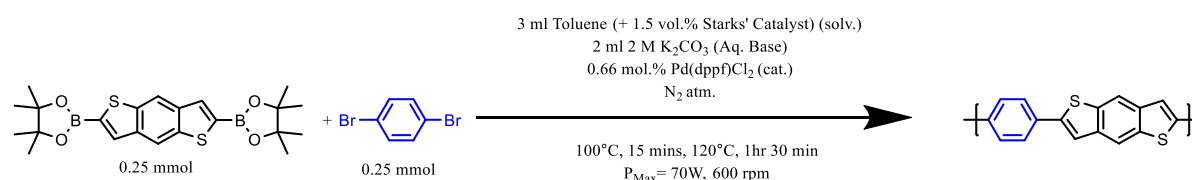


Figure 169: Initial reaction conditions for BDT-PhFx polymers using a toluene/K₂CO₃ reaction mixture in a 3:2 ratio. Microwave-assisted Suzuki-Miyaura polycondensation reaction. Blue aromatic dibromide represents the variable selection of dibromide monomeric precursors investigated.

Comparing BDT-PhFx yields (Figure 170) with those obtained for BDTS-PhFx polymers, the PhF4 polymers are synthesised in the lowest yields in both cases. However, BDT-PhFx polymers are more severely affected as yields decrease consistently with fluorine content. As this trend depends on both the boronate and dibromide species, it is reasonable to assume that the turnover-limiting step of the catalysis cycle involves an intermediate involving both units, i.e. during the isomerisation or reductive elimination steps. Dehalogenation and homocoupling side reactions are commonplace in SMC coupling reactions that can lead to low yields of the desired product.^{234,251}

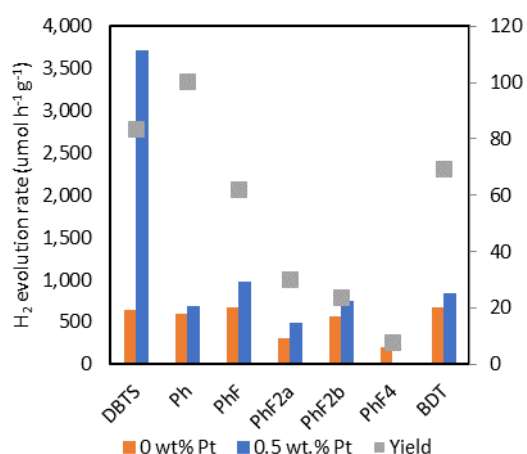


Figure 170: HER of BDT-PhF_x polymers. The yield is presented as the line chart on the secondary axis. Polymers were synthesised using 3 ml toluene, 2 ml 2M K₂CO₃, and 0.66 mol.% Pd(dppf)Cl₂. Heated at 120 °C for 1.5 hours.

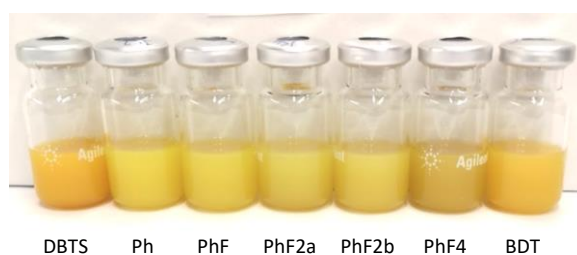


Figure 171: Image of 5 mg of BDT-PhF_x polymers dispersed in 5 ml of 1:1:1 TEA/MeOH/H₂O solution. Polymers were synthesised using 3 ml toluene, 2 ml 2M K₂CO₃, and 0.66 mol.% Pd(dppf)Cl₂. Heated at 120 °C for 1.5 hours.

Without using advanced catalysts, the PhF₄-Br₂ monomer should be highly susceptible to oxidative addition. Tetrafluorobenzene is strongly electron-withdrawing and has been used for direct arylation reactions, which proceed without any halide leaving groups.²⁴³ It is worth noting that Ar-F bonds are very strong and do not undergo Suzuki coupling reactions.

The appearance of these polymers is shown in the photograph in Figure 171. BDT-DBTS and BDT-BDT each have narrower bandgaps compared to the BDT-PhF_x co-polymers, as indicated by their orange colour. With the exception of Pt-loaded BDT-DBTS, the photocatalytic activities of the BDT-copolymers are approximately 1 mmol hr⁻¹ g⁻¹ or below. Increases in activity upon deposition of Pt for the remaining polymers are marginal.

The low photocatalytic activities of the BDT-PhF_x polymers may arise because of the high-energy HOMO that is expected to lie very close to the one-electron charge transfer oxidation potential of TEA. The DFT-predicted potentials have been reproduced in Figure 172. However, if this is the case, increasing photocatalytic activities would be expected with increasing fluorine content since fluorine lowers the IP and the IP of BDT-PhF_{2b} is predicted to be similar to that of BDT-DBTS.

A second cause of the low photocatalytic activity may be associated with the increasingly poor synthesis yields with increasing fluorine content. As observed amongst the 99 polymers analysed in Chapter 2, low yields are typically associated with lower photocatalytic activity. Despite being the most

active photocatalyst of the set, BDT-DBTS (synthesised from BDT-B(pin)₂ and DBTS-Br₂) is also notably less active (3.7 mmol hr⁻¹ g⁻¹) than the DBTS-BDT equivalent polymer (synthesised from DBTS-B(pin)₂ and BDT-Br₂) reported in section 3.6.4 synthesised under the same conditions (14.5 mmol hr⁻¹ g⁻¹). These results imply that the reaction mixture containing Toluene/K₂CO₃ is not optimal for achieving polymers with high photocatalytic activities when using BDT-B(pin)₂ as a reagent.

The final potential explanation for the poor photocatalytic activities of BDT-PhFx polymers is simply that they do not contain the DBTS monomer. As discussed extensively in the literature, the DBTS moiety improves the interfaces with water and TEA and enhances the rates of photoinduced charge transfer reactions accordingly.¹³⁵ Compared with the DBTS-PhFx equivalents, the BDT-PhFx polymers did not disperse well in the sacrificial reagent mixture.

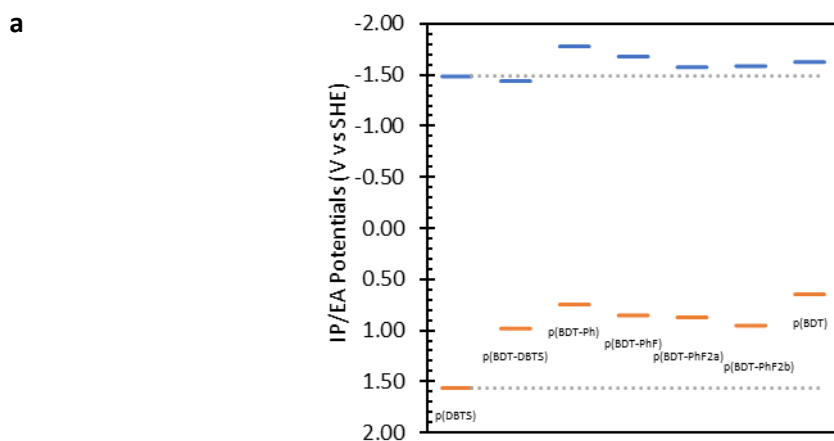


Figure 172: Computational calculations of the IP and EA potentials of BDT-PhFx co-polymers. The TEA oxidation potential lies at +0.7 V vs SHE.

3.7.2 Reaction Condition Screening

Table 22: Optimisation of BDT-PhF₄ synthesis conditions.

Sample	Catalyst	Pd (mol.%)	Solvent	Vol (mL)	Base	Vol (mL)	Additive	Temp (°C)	Time (min)	Power (W)	Yield (%)
1	Pd(dppf)Cl ₂	0.66	Toluene	3	K ₂ CO ₃	2	45 µL Aliquot 336	100 120	15 90	70	16
2	Pd(PPh ₃) ₄	0.66	Toluene	3	K ₂ CO ₃	2	45 µL Aliquot 336	100 120	15 90	70	9
3	Pd(dppf)Cl ₂	0.66	DMF	3	K ₂ CO ₃	2	-	100 120	15 90	70	10
4	Pd(dppf)Cl ₂	0.66	THF	3	K ₂ CO ₃	2	-	100 120	15 90	100	6
5	Pd(dppf)Cl ₂	0.66	1,4-Dioxane	3	K ₂ CO ₃	2	-	100 120	15 90	100	4
6	Pd(dppf)Cl ₂	0.66	Toluene	3	Cs ₂ CO ₃	2	45 µL Aliquot 336	100 120	15 90	70	12
7	Pd(dppf)Cl ₂	0.66	Toluene	3	K ₃ PO ₄	2	45 µL Aliquot 336	100 120	15 90	70	4
8	Pd(dppf)Cl ₂	0.66	Toluene	3	TBAA	2	45 µL Aliquot 336	100 120	15 90	70	71
9	Pd(dppf)Cl ₂	0.66	Toluene	3	K ₂ CO ₃	2	45 µL Aliquot 336 CuCl (0.2 mol)	100 120	15 90	70	10
10	Pd(dppf)Cl ₂	0.66	DMF	3	Cs ₂ CO ₃	2	CuCl (0.2 mol)	100 120	15 90	70	19
11	Pd(PPh ₃) ₄	0.66	Toluene	3	TBAA	2	45 µL Aliquot 336	100 120	15 90	70	-
12	Pd(PPh ₃) ₄	1.25	Toluene	3	TBAA	2	45 µL Aliquot 336	100 120	15 90	70	-
13	Pd(dppf)Cl ₂	1.10	1,4-dioxane	3	TBAA	2	-	100 120	15 90	100	52
14	Pd(dppf)Cl ₂	0.66	Toluene	4.375	TBAA	0.625	66 µL Aliquot 336	100 120	15 90	70	53
15	Pd(dppf)Cl ₂	0.8	1,4-Dioxane	4.375	TBAA	0.625	-	100 120	15 90	70	59
16	Pd(dppf)Cl ₂	0.66	1,4-Dioxane	3	TBAA	2	-	100	60	100	68
17	Pd(dppf)Cl ₂	0.66	THF	3	TBAA	2	-	100	60	100	67
18	Pd(dppf)Cl ₂	0.66	DMF	3	TBAA	2	-	100	60	100	26

As discussed above, the Toluene/K₂CO₃ reaction mixture did not produce active BDT-PhFx photocatalysts and, in the case of reactions with fluorinated phenylene dibromides, led to very low synthesis yields. This low activity may be a result of the polymer chain lengths, particle size, particle morphology, high concentrations of impurities and side products, or high levels of residual palladium.

Since BDT-PhF₄ was only synthesised with a sub-10 % yield, a study of different reaction conditions was subsequently conducted for this polymer. This study explored other palladium cross-coupling catalysts, solvents, bases, and additives. Different concentrations of base and volume ratios between organic and aqueous phases were also investigated. This screening study aimed to identify reaction conditions leading to high yields and photocatalytic activities since, as shown in Section 3.6, high yields

are not always commensurate with high photocatalytic activities. The results of this overall search are presented in Table 22.

3.7.2.1 Change of Palladium Catalyst

A key component of the reaction mixture is the choice of palladium cross-coupling catalyst. Here, 1,1-Bis(diphenylphosphino)ferrocene dichloropalladium, Pd(dppf)Cl₂, and tetrakis(triphenylphosphine) palladium(0), Pd(PPh₃)₄, are compared. Whilst many alternative catalysts are available and appropriate for Suzuki coupling, alternatives are expensive, prohibiting large-scale screening studies. Furthermore, there are no obvious alternative catalysts. Both the diboronic ester and dibromide monomer reagents are highly reactive towards Suzuki coupling and should not require advanced catalysts with more expensive ligands that are typically used to promote reactions with more challenging substrates.²⁵¹⁻²⁵³ Searches for these reagents on SciFinder and Reaxys generally report successful reactions using common palladium catalysts such as Pd(PPh₃)₄ and Pd(dppf)Cl₂.

Pd(PPh₃)₄ resulted in poor yields of BDT-PhF4. Under comparable conditions, Pd(dppf)Cl₂ consistently led to higher yields. One possible explanation arises from the fact that the dppf ligand is bidentate, resulting in a more sterically hindered palladium centre than for the Pd(PPh₃)₂ intermediate. The bidentate ligand results in a larger bite angle and increases the overlap between adjacent aryl species prior to the reductive elimination step, enhancing its rate of reaction. Furthermore, since the dppf ligand is bidentate, aryl units must bond to the metal centre in the cis-positions rather than trans-positions on the square-planar d⁸ Pd(II) intermediate. The two aryl units must be in the cis-position to enable reductive elimination.

3.7.2.2 Organic Solvent

The Suzuki polycondensation reaction was performed using four different solvents. Toluene, dimethylformamide (DMF), 1,4-Dioxane, and tetrahydrofuran (THF). These solvents were chosen as they exhibit a range of polarities. Polarity influences the miscibility of the organic and aqueous phases and controls the solubility of reagents, intermediates, and products. These reactions used 2M K₂CO₃ as the base, resulting in yields below 20%. The best-performing solvent was toluene, which only produced a 16% yield. DMF, Dioxane, and THF were all miscible with the aqueous phase.

3.7.2.3 Addition of Copper Chloride

Heteroaryl boronates are susceptible to protodeboronation reactions,^{254,255} in which the boronic acid (or boronic ester) groups are removed from precursors and oligomeric intermediates. Adding CuCl has

been shown to mitigate this issue by substituting the boronate groups in-situ and reacting with the palladium catalyst.²⁵⁶ Adding one equivalent of CuCl to the Toluene/K₂CO₃ reaction mixture did not increase the yield (10 %). Future reaction attempts may benefit from modified organoborane groups that can regulate the rate at which the functional group is hydrolysed into its boronic acid form.²⁵³

3.7.2.4 Aqueous Base

Pd-catalysed SMC reactions must be performed under basic conditions. The exact role of the base in the catalytic cycle is still widely debated.²⁵⁷ Four different bases were investigated: potassium carbonate (K₂CO₃), potassium triphosphate (K₃PO₄), Caesium carbonate (Cs₂CO₃), and tetrabutylammonium acetate, (N(Bu)₄OAc, TBAA). The base selection had the most significant impact on the yield of BDT-PhF₄. Combining 3ml of toluene with 2ml of 2M TBAA resulted in the highest observed yield of 71%. Other bases did not increase the yield.

TBAA is particularly effective due to the alkyl chains on the positively charged ammonium ion, which increase its solubility in organic solvents. The acetate ion is also reasonably soluble in organic solvents. Furthermore, TBAA is a weaker base than carbonates and phosphates.

3.7.2.5 Combined Changes

Following the improved reaction yields observed using TBAA as the base, further optimisations were conducted by combining this base with alternative solvents. Whilst Pd(PPh₃)₄ remained inactive in the presence of TBAA, yields were improved when TBAA was used in conjunction with 1,4-dioxane (52 %). However, reactions with Pd(PPh₃)₄ were still unsuccessful.

3.7.2.6 Solvent:Base Ratio

Due to a limited supply of TBAA, additional syntheses were completed with a reduced volume of the aqueous phase. 0.625 ml of 2M TBAA was added to the reaction mixture instead of 2 ml. This corresponded with a decrease in the amount of TBAA in the reaction from 4 mmol to 1.25 mmol. Since reactions were being completed on a 0.2 mmol scale, this remained more than six equivalents. Suzuki reactions are recommended to contain at least one equivalent of the base.²⁵⁸ Although the yield of the reaction conducted in toluene decreased (from 71% to 53%), it increased in 1,4-dioxane (52 – 59 %).

3.7.2.7 Reaction Time and Temperature

Throughout this synthesis optimisation procedure, it became apparent that the power-limited stepwise heating regime, developed for polymers synthesised in toluene/ K_2CO_3 (3:2), was no longer required. Using TBAA instead of K_2CO_3 prevented the sudden pressure spikes which had previously triggered the microwave reaction system to shut down. As such, the desired temperature could be attained directly using higher-power microwave radiation. The reaction time was also reduced since products were previously observed within ten minutes of microwave-assisted heating at lower temperatures following failed reactions.

The final samples were heated to 100 °C for 60 minutes using an increased power of 100W. Reducing the temperature comes with a trade-off; oligomers will be less soluble at lower temperatures, and the polymer chain length is expected to decrease as a result. However, higher temperatures also lead to impure polymers as the degradation of the reagents or the palladium catalyst is accelerated. This is evidenced by the dark inactive polymers obtained from conducting the reaction at 160 °C.

BDT-PhF4 was obtained in reasonable yields when synthesised in DMF (26%), 1,4-dioxane (68%), and THF (67%) using 2 ml of 2M TBAA as the base under these modified reaction conditions.

3.7.2.8 BDT-PhF4 Hydrogen Evolution Reaction

Following the synthesis optimisation process described above, BDT-PhF4 samples obtained at reasonable yields were tested for their photocatalytic hydrogen evolution activity. These results are presented in Figure 173.

The sample "Toluene" refers to sample 1 in Table 22 and represents the starting conditions. Most attempts to change the conditions resulted in lower yields and lower photocatalytic activities.

Although synthesis in toluene combined with TBAA led to the best yield, photocatalytic activity was not improved. Synthesis of BDT-PhF4 in 1,4-dioxane with TBAA, however, led to increased yields and increased photocatalytic activity. These reaction conditions were therefore used to prepare the remaining BDT-PhFx polymers.

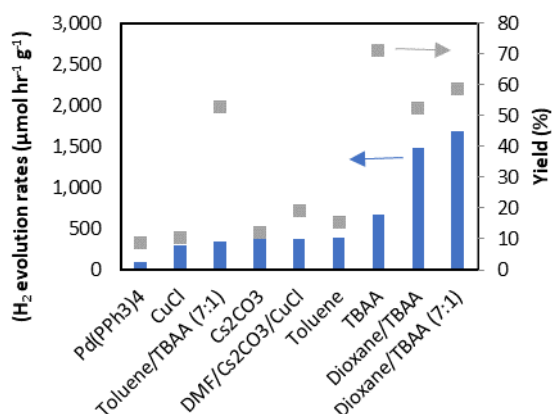


Figure 173: Comparison of photocatalytic activities for equivalent BDT-PhF4 polymers when synthesised under different conditions.

3.7.3 Organic Solvent: 1,4-Dioxane (4.375 ml), Aqueous Base: 2M TBAA (0.625 ml)

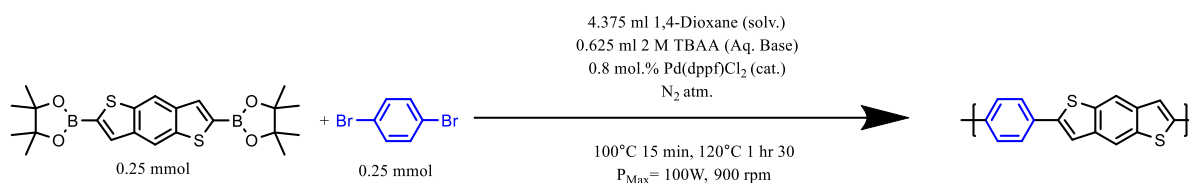


Figure 174: Modified reaction conditions for BDT-PhFx polymers using a dioxane/TBAA reaction mixture in a 7:1 ratio. Microwave-assisted Suzuki-Miyaura polycondensation reaction. Blue aromatic dibromide represents the variable selection of dibromide monomeric precursors investigated.

Following the optimisation of BDT-PhF4 for optimal yield and photocatalytic activity, the remaining polymers of the BDT-PhFx series were synthesised according to the conditions summarised in Figure 174. Unfortunately, the positive impact of running the reaction at 100 degrees with a larger TBAA content was not yet realised when these samples were synthesised. Figure 175 presents the HER for BDT-PhFx polymers synthesised using the optimised conditions, whereas HER rates for the same polymers prepared using the old (Toluene/K₂CO₃) conditions are shown in Figure 176. Yields are presented on the secondary axes. The photographs show the polymers dispersed in a 1:1:1 mixture of H₂O, MeOH, and TEA and are ordered as per the samples in the graphs above.

The new synthesis conditions result in improved yields across the PhFx co-polymers. Under the new reaction conditions, the activity of the DBTS-PhFx polymers increases with respect to fluorine content. This trend could be explained by the deeper HOMO energy levels of the fluorinated derivative that have been predicted by DFT. These deeper levels would have a greater overpotential to drive the TEA

oxidation reaction. However, BDT-DBTS and BDT-BDT exhibit poorer photocatalytic activities, despite excellent yields.

The photocatalytic activity improves for all polymers after Pt photodeposition under the new conditions. However, this increase is relatively small compared to the co-polymers containing DBTS moieties. Only BDT-DBTS exhibited a significant increase in activity after loading with Pt. Compared with the DBTS-BDT polymer synthesised from the DBTS-B(pin)₂ in section 3.6, both BDT-DBTS polymers synthesised from BDT boronic acid pinacol ester continue to underperform. These polymers are compared in Figure 177. Attempts to synthesise Ph-BDT and PhF2a-BDT analogues by reversing the boronate and bromide functional groups on the monomers were unsuccessful also attempted. These syntheses also led to improved photocatalytic activities for structurally-equivalent polymers. This trend implies that further optimisation of the reaction using alternative BDT organoborane precursors, cross-coupling catalysts, or solvent/base combinations may result in further-enhanced activities.

Based on a qualitative visual comparison between the two sets, the bandgap of BDT-PhFx polymers synthesised in 1,4-dioxane (except for BDT-DBTS) appear to be smaller than those synthesised in toluene, as they appear to be more orange and the toluene samples more yellow. This may indicate longer average polymer chain lengths for the polymers synthesised under the new conditions which would agree with the theory of improved stability of oligomeric reaction intermediates when using TBAA as the base. Changes to the absorption spectrum may also arise from the nature of aggregation in the solid state.²⁵⁹

In general, these polymers are poor photocatalysts for photocatalytic hydrogen evolution. However, this is to be expected since they do not possess the DBTS unit, which appears to be essential for photocatalytic activity. High activities for these polymers were not expected since the band gap is small, and hence they have small driving forces for driving the photocatalytic redox reactions. This necessitates fine-tuning of the band edge potentials, which the addition of fluorine appears to have achieved.

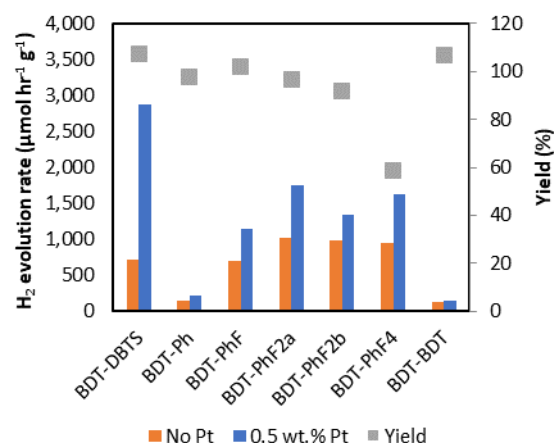


Figure 175: Top) HER rates and synthesis yields for BDT-PhFx polymers synthesised from a dioxane/TBAA reaction mixture. Bottom) Image of 5 mg of BDT-PhFx polymers dispersed in 5 ml of 1:1:1 TEA/MeOH/H₂O solution.

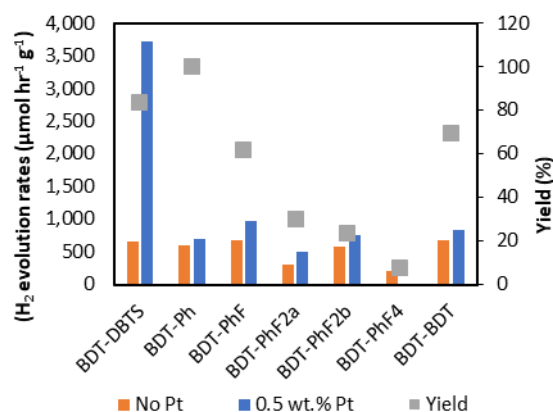


Figure 176: Top) HER rates and synthesis yields for BDT-PhFx polymers synthesised from a toluene/K₂CO₃ reaction mixture. Bottom) Image of 5 mg of same BDT-PhFx polymers dispersed in 5 ml of 1:1:1 TEA/MeOH/H₂O solution.

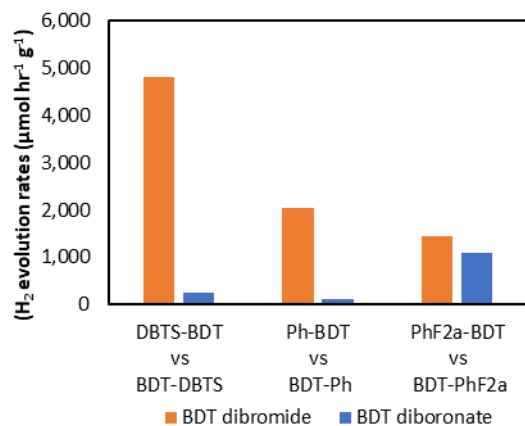


Figure 177: Comparison of photocatalytic activities for equivalent BDT-based polymers when synthesised from BDT-Br₂ (orange) and BDT-B₂pin₂. (blue) HER rates for polymers before photodeposition of 0.5 wt.% Pt.

3.7.4 Alternative Sacrificial Reagents: Ascorbic Acid / DMF

To establish if the lower activity arises from a limited driving force for TEA oxidation, further measurements of the photocatalytic activity of the BDT-DBTS and BDT-Ph polymers were performed using 0.1M ascorbic acid as the sacrificial reagent and DMF as the dispersant. 5 mg of the polymers were dispersed in 1 ml of DMF and ultrasonicated for 5 mins before adding 4ml of 1M ascorbic acid

(AA). Samples were irradiated for one hour. The basis for these reaction conditions stem from recent reports in the literature in which similar methods have resulted in extremely high photocatalytic rates.^{237,260–262}

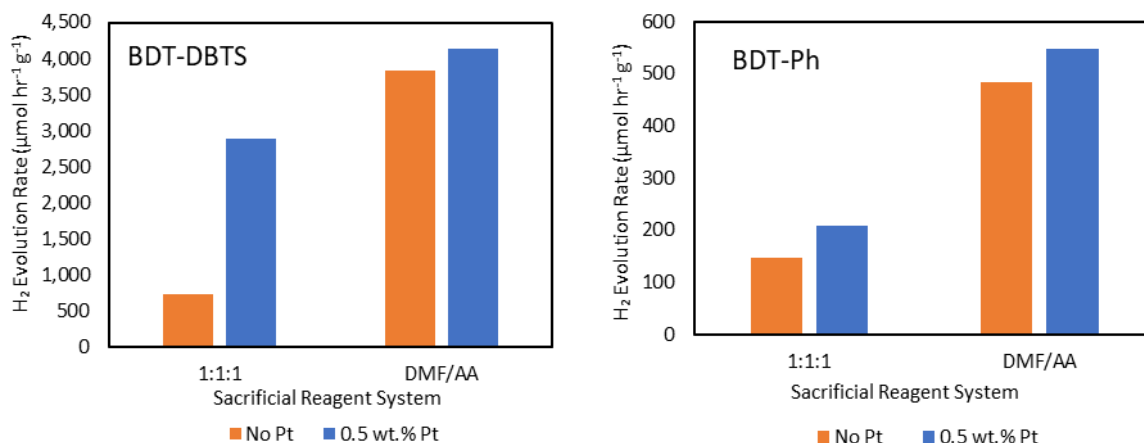


Figure 178: HER rates for the BDT-based co-polymers synthesised from a dioxane/TBAA reaction mixture. HER rates are compared when using 1:1:1 as a sacrificial reagent mixture vs an ascorbic acid/DMF sacrificial reagent mixture. A) BDT-DBTS and b) BDT-Ph polymer systems.

The results for these polymers before and after Pt photodeposition are presented in Figure 178. In both cases, the photocatalytic activity increases when using AA as the sacrificial reagent, despite not optimising the co-solvent or the pH of the reaction mixture. By contrast, when testing DBTS-Ph synthesised under the same conditions, the photocatalytic activity in the DMF/AA mixture was substantially reduced, as shown in Figure 179. These results imply that polymers containing the BDT unit may not exhibit optimal hydrogen evolution rates when using TEA as the sacrificial reagent.

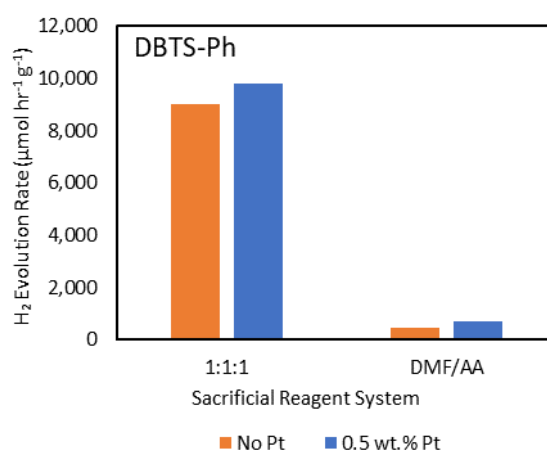


Figure 179: HER rates for the DBTS-Ph co-polymer synthesised from a dioxane/TBAA reaction mixture. HER rates are compared when using 1:1:1 as a sacrificial reagent mixture and an ascorbic acid/DMF sacrificial reagent mixture.

3.7.5 Photocatalytic Hydrogen Peroxide Production

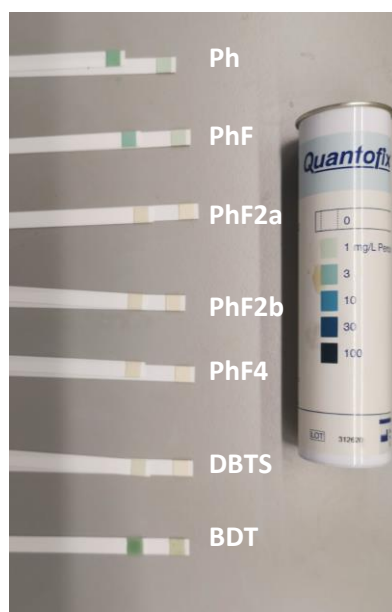


Figure 180: Hydrogen peroxide dip stick test results after dispersing 3 mg of BDT-PhFx polymers in 5 ml of deionised water (right column) and 20 vol% ethanol (left column) and irradiating with AM1.5G solar simulated light for 1.5 hours under an oxygenated atmosphere. The polymers selected for this study were synthesised from a dioxane/TBAA reaction mixture. Image on the right provides a colour scale for the results in mg L⁻¹.

As for the DBTS-PhFx polymers, the BDT-PhFx polymers were also tested for their photocatalytic hydrogen peroxide production from water and 10 vol.% ethanol solutions. Sample headspace vials were loaded with 3 mg of polymer and 5 ml of liquid before being dispersed via ultrasonication for 5 minutes. The polymer dispersions were subsequently irradiated for 1.5 hours under simulated AM 1.5G sunlight before the resulting solution was tested for peroxides using rapid dipstick tests.

As shown in Figure 180, BDT-PhFx polymers produced significantly less hydrogen peroxide than the DBTS-PhFx equivalents. In most cases, no peroxides are deemed to be present. These samples were not expected to produce any peroxide since the HOMO is higher in energy, and the 4-electron water oxidation reaction leading to oxygen evolution is thermodynamically uphill.

Interestingly, low concentrations of peroxide were detected from DBTS-BDT, DBTS-Ph, and DBTS-PhF despite these three samples being predicted to have the highest-energy HOMOs of the set. These three samples also exhibited the slowest photocatalytic hydrogen evolution rates. Contrastingly, BDT-DBTS only produces trace amounts of hydrogen peroxide despite the fact the DBTS-BDT analogue synthesised in Toluene/TBAA produced moderate amounts under the same conditions.

These results imply that photocatalytic hydrogen peroxide production might be driven by sacrificial oxidation of residual impurities and catalysed by residual palladium, at least in part. Indeed, several reports have highlighted that Pd is the most effective co-catalyst for this reaction.^{248,263} Unfortunately, attempts to determine the residual palladium concentration were unsuccessful as the polymers would not digest in nitric acid.

3.8 Ternary Polymers

The positive effects of the DBTS moiety on the photocatalytic hydrogen evolution rate is well known.^{135,264,265} It was therefore decided that DBTS-PhF_x-BDT ternary polymers should be synthesised. It is hoped that compared to the binary counterparts, the ternary system would combine the best properties: narrower bandgap of the BDT polymer with the photocatalytic activity of the DBTS polymers, whilst simultaneously allowing the band potentials to be tailored by altering the electronegativity of the fluorinated phenylene linkers.

3.8.1 Synthesis of Br-PhF_x-BDT-PhF_x-Br Intermediate

To obtain a perfectly-alternating DBTS-PhF_x-BDT polymer backbone, it would first be necessary to synthesise an intermediary dibromide or diboronic ester. Initial attempts to synthesise the monomer: Br-PhF_x-BDT-PhF_x-Br were made by reacting the BDT boronic ester with an excess of the phenylene dibromides, as outlined in Figure 181. Reacting in an excess of the dibromide monomer means that any polymerisation should be limited, as the boronates are consumed in reactions with monomers rather than oligomers.

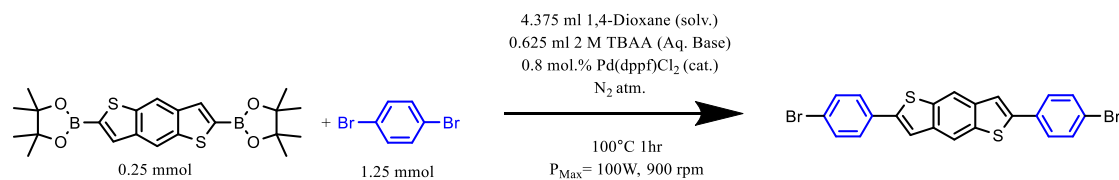


Figure 181: Initial reaction conditions used in an attempt to prepare BDT-PhF_x-Br₂ monomeric dihalide reagents using a dioxane/TBAH reaction mixture in a 7:1 ratio. The dibromide was included in the reaction mixture in excess to prevent extensive polymerisation. Microwave-assisted Suzuki-Miyaura polycondensation reaction. Blue aromatic dibromide represents the variable selection of dibromide monomeric precursors investigated.

However, as shown in Figure 182, the attempted synthesis of these monomers resulted in insoluble solids that resembled the equivalent BDT-PhF_x polymers. Unfortunately, since they were insoluble in all tested solvents, they could not be used as monomers for subsequent reaction steps.



Figure 182: Photographs of products resulting from attempted synthesis BDT-PhFx-Br₂ monomers and the DBT-PhFx polymers synthesised from stoichiometric mixtures of BDT-PhFx. Reactions were performed under similar conditions with the exception that monomers were synthesised at 100°C whereas polymers were synthesised at 120°C.

Table 23: Amount of product obtained from the attempted synthesis of BDT-PhFx monomers compared to the equivalent polymer synthesis.

Phenylene unit	p(BDT-PhFx)		Br-PhFx-BDT-PhFx-Br		
	Mass (mg)	Yield (%)	Mass (mg)	Yield (%) (If monomer)	Yield (%) (If polymer)
Ph	64.6	98	71.5	57	109
PhF	72.0	102	71.7	53	102
PhF2a	72.7	97	79.2	55	105
PhF2b	66.9	92	64.6	45	86
PhF4	49.3	59	38.7	24	46

Phenylene unit	p(DBTS-PhFx)		Br-PhFx-DBTS-PhFx-Br		
	Mass (mg)	Yield (%)	Mass (mg)	Yield (%) (If monomer)	Yield (%) (If polymer)
Ph	65.7	90	59.9	46	83

Compared to their polymeric equivalents, the monomeric series (BDT-PhFx-m) were synthesised at 100 °C instead of 120 °C. The lower temperature was selected because early synthesis attempts of BDT-Ph-m at 120 °C resulted in pressure spikes that triggered the microwave reactor to shut down. The lighter colour of the BDT-PhFx-m series compared to the BDT-PhFx polymers may result from this lower reaction temperature.

As is apparent from Table 23, the masses obtained for these monomeric species very closely resemble the yields obtained for the equivalent polymer and resemble the polymers in their physical and optical properties. It is very likely that the polymer is formed instead of the monomer, despite the excess dibromide reagent. To investigate if this failed reaction can be attributed to the BDT-diboronic acid pinacol ester, an attempt was also made to synthesise Br-Ph-DBTS-Ph-Br using the same methodology. This also resulted in an insoluble solid resembling its polymeric equivalent.

Typically, one must be very careful to ensure the correct stoichiometry of the reagents when completing polycondensation syntheses to ensure that dibromides and diboronic acid species are in a one-to-one ratio. This is on the basis that an excess of one may lead to a narrow distribution of short

oligomeric chains that are all terminated by the same leaving group. Such oligomers would be unable to react with one another to extend the polymer chain length.

The suspected formation of extended polymer chains in the presence of excess dibromide suggests that polymer formation by microwave-assisted polycondensation reactions is insensitive to the initial reagent stoichiometry. Br-PhFx-BDT-B(pin) intermediates appear to react with one another preferentially instead of the excess dibromide monomer, PhFx-Br₂.

An alternative explanation may involve the homocoupling of oligomers via the terminal bromines to generate several PhFx-PhFx links in the backbone. However, this should result in masses significantly larger than the theoretical yield for the original polymer. Since we do not see any significant increase in the solid mass obtained at the end of the reaction, this pathway appears less likely.

3.8.2 Ternary Statistical Random Co-polymer (DBTS)_n-(PhFx)_m-(BDT)_o

Computational studies of conjugated polymers indicate that the specific arrangement of monomer units along the backbone has a limited impact on the band edge potentials and bandgap.¹³⁸ DBTS-PhFx-BDT ternary polymers were therefore synthesised on a random statistical basis in a one-pot synthesis by combining DBTS-B(pin)₂, BDT-B(pin)₂, and PhFx-Br₂ reagents in a molar ratio of 1:1:2. Although other ratios of DBTS:BDT were not tested, this synthesis method could be used to explore this ternary space and optimise for photocatalytic activity. Exploring this space using the rapid microwave synthesis method would be particularly beneficial. The reaction scheme for the DBTS-PhFx-BDT series of ternary polymers is presented in Figure 183 below.

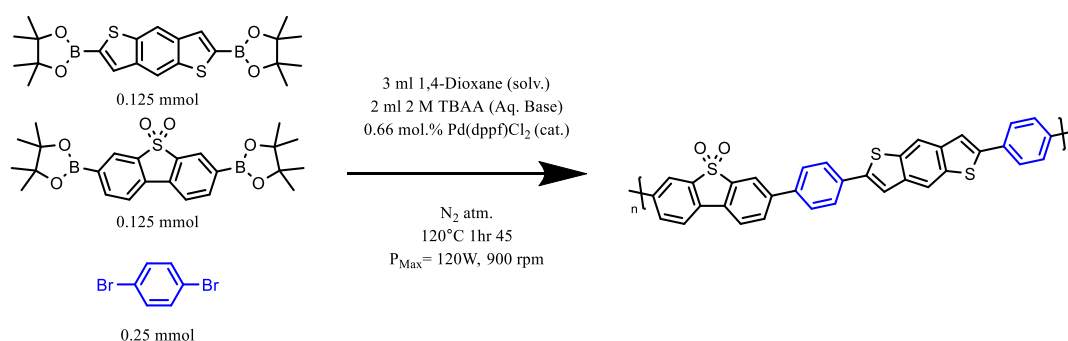


Figure 183: Reaction conditions used in an attempt to prepare statistical DBTS-PhFx-BDT ternary co-polymers using a dioxane/TBAA reaction mixture in a 3:2 ratio. Microwave-assisted Suzuki-Miyaura polycondensation reaction. Blue aromatic dibromide represents the variable selection of dibromide monomeric precursors investigated.

It is important to note that, in using this statistical method, uncertainty regarding the final polymer structure is introduced. If BDT-B(pin)₂ is far more reactive than DBTS-B(pin)₂, the first polymer chains to precipitate from the reaction mixture will be rich in BDT, whereas those synthesised later will be rich in DBTS. BDT is an electron-rich donor, whereas DBTS is an electron acceptor. The rates of Pd-catalysed Suzuki reaction are expected to differ between the two. Furthermore, the ratio of these two components in the polymer chain may also impact the length at which the chain precipitates since they have different polarities. Unfortunately, due to the insoluble nature of the polymers, gel-permeation chromatography cannot be used to determine the molecular weight distributions. For the remainder of this section, we assume a 50:50 distribution of DBTS and BDT in each polymer chain.

3.8.2.1 Appearance

The resulting polymers ranged from bright yellow to dark orange and appeared to be the exact same colours as their binary BDT-PhFx series analogues. As with the BDT-PhFx polymers, these polymers were hydrophobic, whereby dispersion in water was more challenging with increasing fluorine content. The Ph and PhF analogues dispersed fairly well in MeOH/H₂O/TEA, but dispersal in water was more challenging. The difluorinated and tetrafluorinated polymers were difficult to disperse in all solvents.

3.8.2.2 Hydrogen Evolution Study⁵

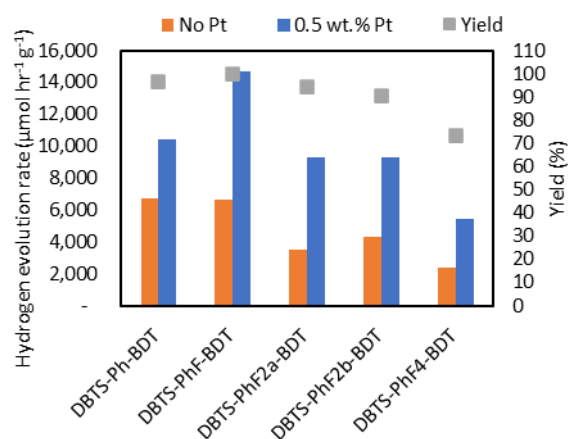


Figure 184: DBTS-PhFx-BDT polymer photocatalytic activities for H₂ evolution in MeOH/H₂O/TEA and associated synthesis yields.

⁵ These samples were tested for their photocatalytic activities using a modified method. Please see 3.3.4.2.1 and 3.4.1.6.1 for details.

The ternary polymers were tested for their hydrogen evolution photocatalytic activity. Figure 184 presents the results for these polymers. Although they did not perform as well as the equivalent DBTS-PhFx series, they did produce hydrogen at relatively high rates.

The PhF polymer was the most active, producing hydrogen at a rate of $14.6 \text{ mmol hr}^{-1} \text{ g}^{-1}$ under AM1.5G solar simulator irradiation when platinum is photodeposited. DBTS-Ph-BDT performed second best, whereas the inclusion of the difluorinated and tetrafluorinated phenylene units resulted in decreased activity.

The observed trend could be rationalised by several factors. First is the predicted redox potentials – As the number of fluorines increase, the reduction potential of a photo-excited electron decreases. The oxidation potential simultaneously increases, giving rise to similar bandgaps but different band-edge potentials. Since polymers that include the BDT moiety have smaller bandgaps, a fine balance must be found to ensure both the proton reduction and TEA oxidation can take place efficiently. The wider bandgap of the Ph and PhF polymers results in a more significant driving force for both redox reactions.

Importantly, the oxidation potential is not expected to be positive enough to oxidise water. This suggests that these polymers may be more stable with respect to degradation from H_2O_2 , which cannot be produced. Despite the photodeposition process taking place in an oxygen atmosphere, these polymers did not appear to degrade in the process as the H_2O_2 -producing DBTS-PhFx equivalents did.

As mentioned above, the fluorinated ternary polymers did not disperse nicely in solution, implying that PhF_{2x} and PhF₄ polymers are more hydrophobic. This can lead to larger particle sizes in which excitons cannot reach the surface, a lower total surface on which the reaction can take place, and a poor interface between water and the particles, which may influence the kinetics for water sorption and product desorption. This hydrophobicity may explain the reduced activity for the more fluorinated polymers.

3.9 Optoelectronic Characterisation

The optoelectronic properties of DBTS-PhFx, BDT-PhFx, and DBTS-PhFx-BDT co-polymers are investigated in this section. So that they can be compared and contrasted, only the samples synthesised under the same conditions are considered, despite the fact that DBTS-PhFx polymers are not the most active photocatalysts when synthesised under these conditions. All samples were studied via diffuse reflectance spectroscopy, steady-state fluorescence spectroscopy in the solid state and fluorescence lifetime spectroscopy in the solid state.

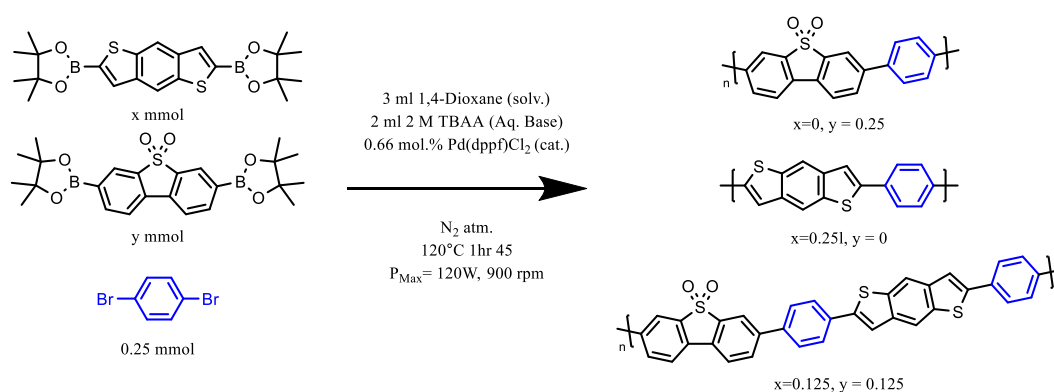


Figure 185: Reaction conditions used to re-synthesise DBTS-PhFx, BDT-PhFx, and DBTS-PhFx-BDT co-polymers using identical conditions for comparable optoelectronic characterisation. Polymers synthesised from dioxane/TBAA reaction mixtures in a 3:2 ratio. Microwave-assisted Suzuki-Miyaura polycondensation reaction. Blue aromatic dibromide represents the variable selection of dibromide monomeric precursors investigated.

It should be noted that exciton dynamics in conjugated polymers are numerous and very complicated. For a basic introduction into exciton diffusion in conjugated polymers, the reader is referred to the review by Mikhnenko *et al.*⁸² The discussions in the following sections will be based on the theory and language pioneered by Prof Barford.^{80,81,84–86,228} A particularly relevant and up-to-date summary of this theory is presented in reference⁸¹. For a very comprehensive review of exciton dynamics in all π -conjugated organic systems, the reader is referred to the recent review by Dimitriev.⁵⁵ For a discussion of excitonic effects specifically as applied to polymeric photocatalysts, see reference⁵³.

3.9.1 DBTS-PhFx

3.9.1.1 UV/Vis DRS

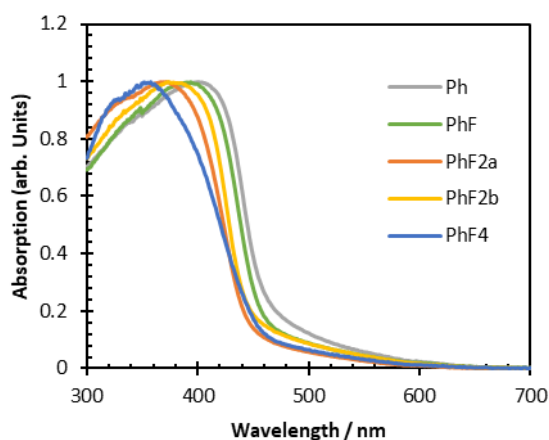


Figure 186: Normalised UV/Vis DRS spectra for DBTS-PhFx polymers synthesised from a dioxane/TBAA reaction mixture. 5 mg of polymer was blended with 55 mg of BaSO₄ to prevent complete absorption above the bandgap.

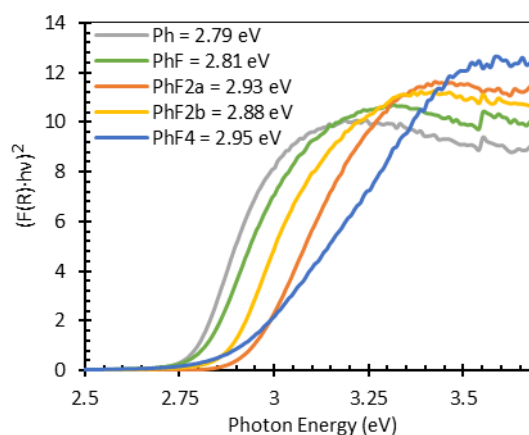


Figure 187: Tauc plot analysis for DBTS-PhFx polymers synthesised from a dioxane/TBAA reaction mixture assuming a direct bandgap.

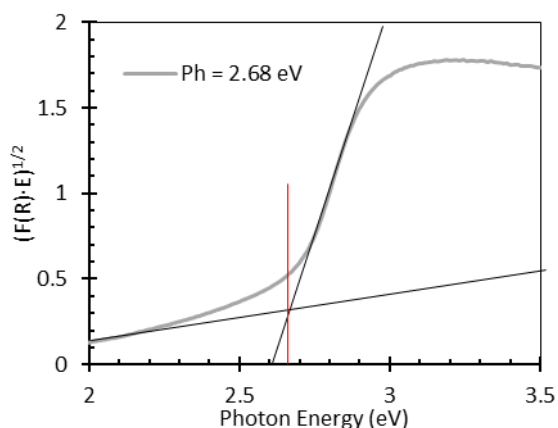


Figure 188: Tauc plot analysis for DBTS-Ph assuming an indirect bandgap. The bandgap was measured at the intersection of the two linear tangents to the curve.

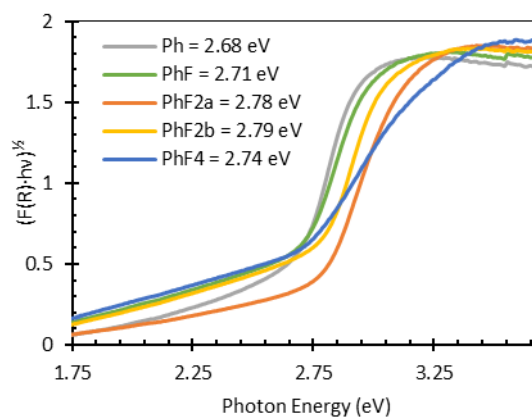


Figure 189: Tauc plot analysis for DBTS-PhFx polymers synthesised from a dioxane/TBAA reaction mixture assuming an indirect bandgap.

Diffuse reflectance spectra of the DBTS-PhFx polymers synthesised in 1,4-dioxane using 2M TBAA as the base are presented in Figure 186. Tauc plots assuming a direct bandgap are presented in Figure 187, whereas Tauc plots assuming an indirect bandgap are plotted in Figure 189. An example position from which the indirect bandgap has been determined is denoted by the red line in Figure 188; this method is in agreement with the recommended approach outlined by Makula *et al.*²⁶⁶ The experimentally determined direct and indirect bandgap values are presented in the chart legends. Both bandgaps have been reported since polymeric materials are semi-crystalline and contain a distribution of chromophores, the excitation energies of which vary according to the local polymer backbone structure, geometry, and environment.

The absorption maxima are blue-shifted with respect to increasing fluorine content. This trend is mirrored by the direct optical bandgaps. However, due to an extended absorption tail, the indirect optical bandgap of DBTS-PhF4 is determined to be smaller than that of DBTS-PhF2a and DBTS-PhF2b. This pattern agrees with the DRS measurements of the DBTS-PhFx polymers synthesised in the Toluene/K₂CO₃ reaction mixture discussed in Section 3.6.4. The origin of this absorption tail is unclear; however, it may arise from high concentrations of impurities such as palladium or from a wide distribution of local polymer structures and environments in the bulk material. The tetrafluorobenzene unit may encourage π - π stacking since the electronegative atoms produce an inverted quadrupolar dipole moment compared with an unsubstituted benzene ring.^{239,240}

The indirect bandgaps measured for the polymers synthesised from Dioxane/TBAA match those determined from Toluene/K₂CO₃, except for DBTS-PhF4, the bandgap of which is 0.1 eV wider when synthesised under the former conditions.

3.9.1.2 Steady-state Fluorescence

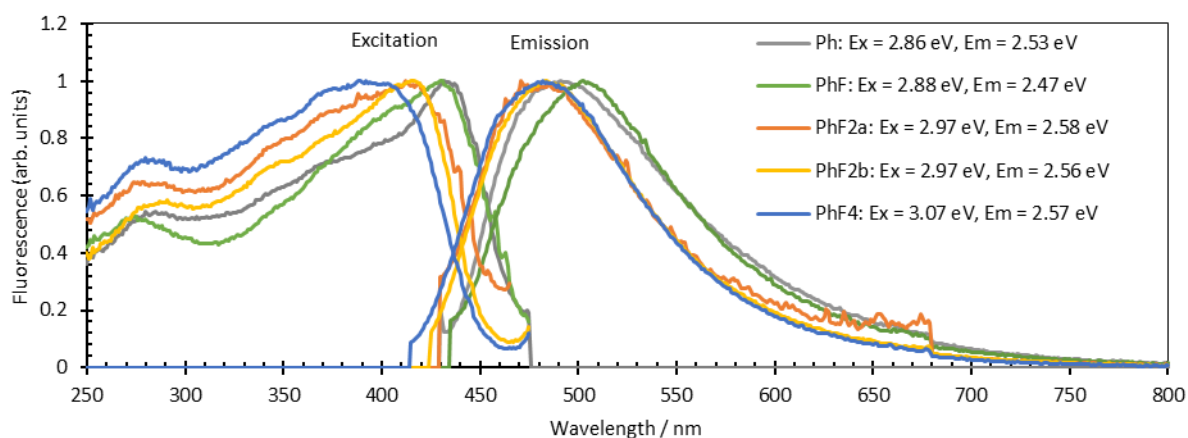


Figure 190: Solid-state steady-state fluorescence excitation and emission spectra for the DBTS-PhFx co-polymers synthesised from dioxane/TBAA. Excitation spectra are measured at the emission maxima, whereas all emission spectra are measured at a 350 nm excitation wavelength.

Steady-state fluorescence spectra for these samples are presented in Figure 190. This includes both excitation spectra and emission spectra. Excitation spectra record the fluorescence intensity at the emission maxima whilst scanning over the excitation wavelengths using a pre-sample monochromator. Emission spectra are recorded by fixing the excitation wavelength and scanning the post-sample monochromator to determine which wavelengths of light are emitted. Several excitation wavelengths of light were selected for the emission spectra of each sample. However, the shape of the emission spectrum remained invariant.

As with the absorption spectra, the excitation maxima shift to shorter wavelengths with increasing fluorine content. However, the DBTS-PhF4 sample no longer shows a lower energy absorption onset than the less fluorinated derivatives. The excitation maxima of DBTS-PhF2a and DBTS-PhF2b are identical, mirroring their indirect bandgaps. This is in direct contrast to their direct bandgaps, which differ by 0.05 eV. The excitation spectrum of DBTS-Ph is differentiated from the fluorinated derivatives by its more prominent peak shape at the band edge. This line shape broadens as more fluorine groups are added.

The excitation spectra mimic the optical absorption bandgaps, but the emission spectra are less structure-dependent. Despite similar excitation maxima, the Stokes' shift of DBTS-PhF is larger than that of DBTS-Ph. Meanwhile, the emission maxima of DBTS-PhF2a, DBTS-PhF2b, and DBTS-PhF4 are almost invariant with respect to structure. Given the widening bandgaps, this correlates with larger Stokes shifts with respect to increasing fluorine content. According to Barford *et al.* the larger shift may be associated with greater co-planarity and less torsional disorder.⁸⁵ However, the inhomogeneous broadening of the lineshapes suggests otherwise.

Vavilov's rule states that the luminescence quantum yield is independent of the excitation wavelength for molecular emitters. Kasha's rule states that emission only occurs from the vibrationally-relaxed excited state.²⁶⁷ This implies that absorption and excitation spectra should be equivalent. As can be observed in Figures 191 - 196, these conjugated polymers do not appear to satisfy these rules on first inspection, where the maxima of the excitation spectra correspond to the absorption tail. This is because the polymers emit from local exciton ground states, which are sub-gap states situated in the absorption tail.

Whilst Kasha and Vavilov's rules hold for single chromophores, conjugated polymer semiconductors represent a large distribution of non-equivalent chromophores, each with its unique absorption spectrum according to the corresponding local exciton. Furthermore, several relaxation processes compete as excitons migrate between chromophores via Forster Resonance Energy Transfer (FRET). One important consideration is the rate of electron extraction by residual palladium clusters. This results in charge separation and the formation of positively-charged polarons, which are known to quench emissions by providing a pathway for non-radiative relaxation.²⁶⁸

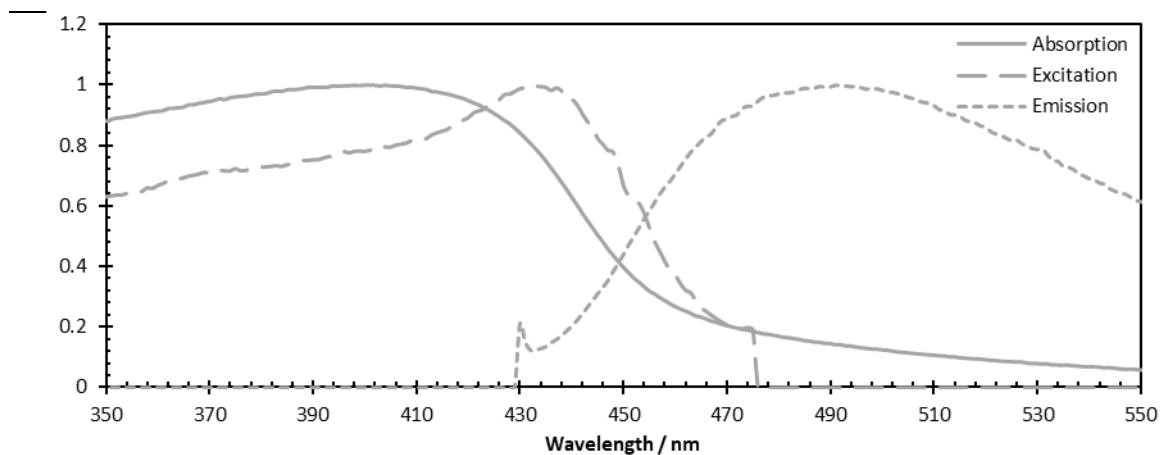


Figure 191: Normalised UV/Vis DRS, steady-state fluorescence excitation, and steady-state fluorescence emission spectra for DBTS-Ph.

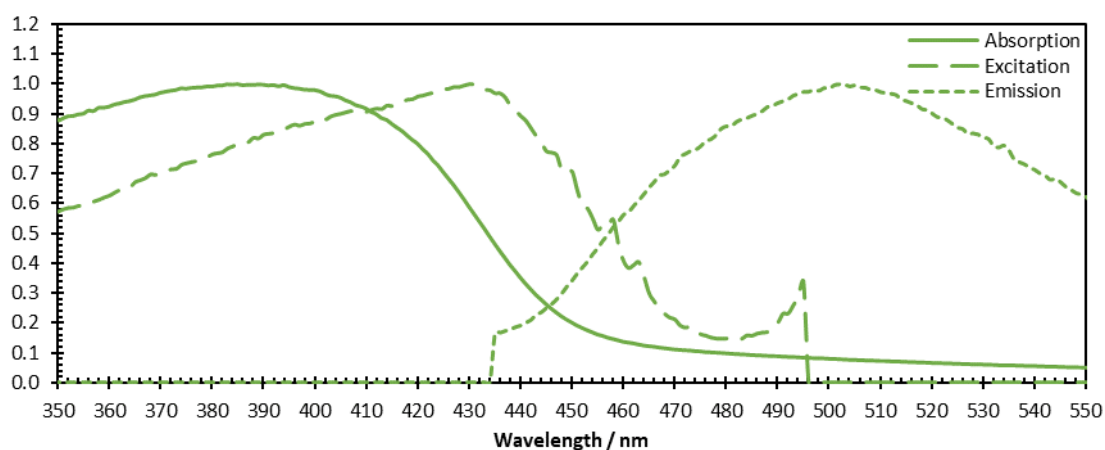


Figure 192: Normalised UV/Vis DRS, steady-state fluorescence excitation, and steady-state fluorescence emission spectra for DBTS-PhF.

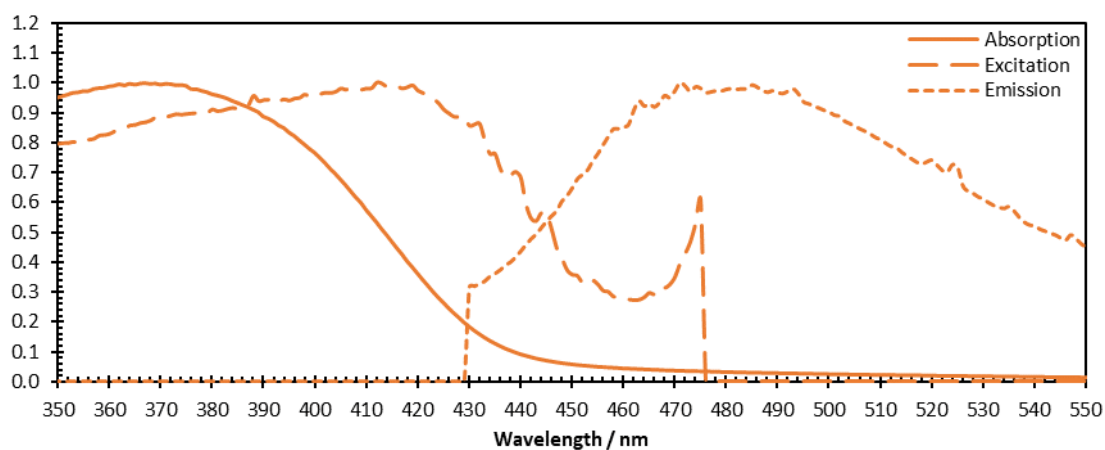


Figure 193: Normalised UV/Vis DRS, steady-state fluorescence excitation, and steady-state fluorescence emission spectra for DBTS-PhF2a.

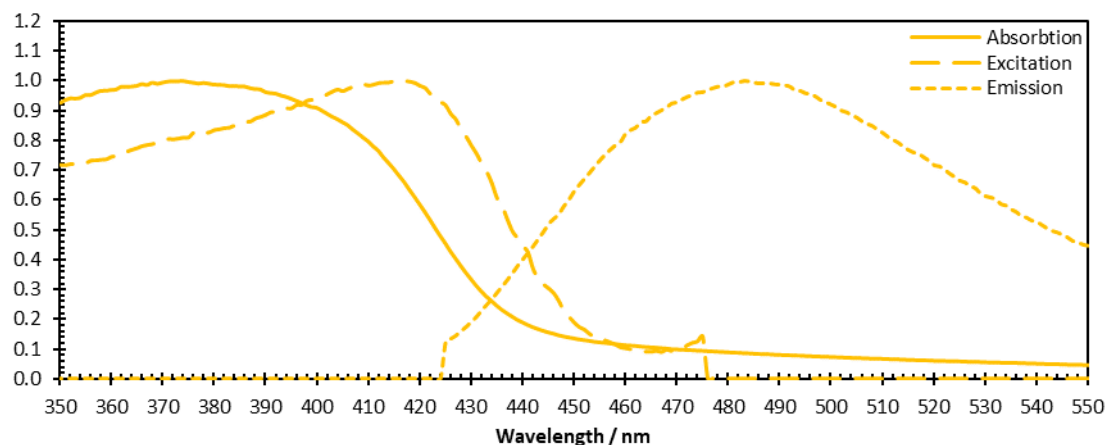


Figure 194: Normalised UV/Vis DRS, steady-state fluorescence excitation, and steady-state fluorescence emission spectra for DBTS-PhF2b.

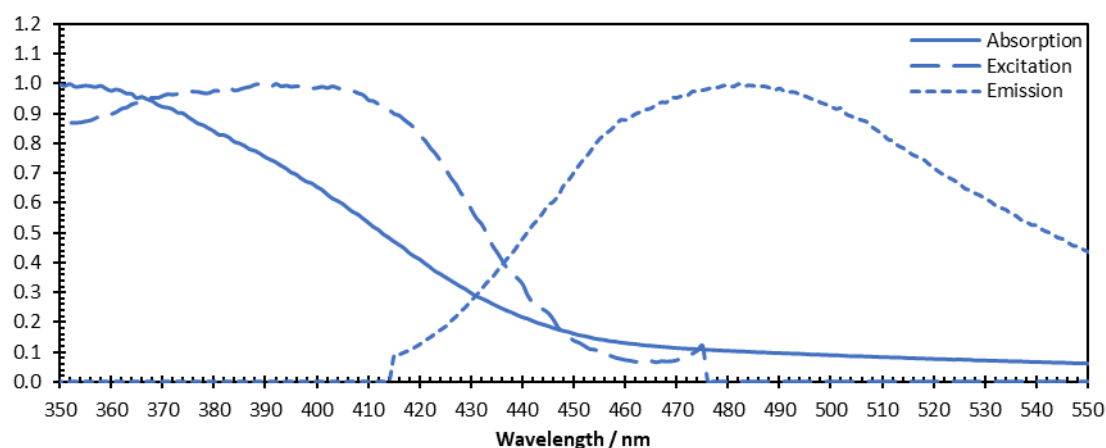


Figure 195: Normalised UV/Vis DRS, steady-state fluorescence excitation, and steady-state fluorescence emission spectra for DBTS-PhF4.

Figures 191-195 compare the DRS absorption spectra (solid lines) with the corresponding excitation (long-dashed lines) and emission spectra (short-dashed lines). All spectra were recorded in the solid state and have been normalised. Although the DRS and excitation spectra are both measurements of absorption, they are not identical. Interestingly their local maxima are located at different energies.

On first consideration, this appears to violate the Vavilov rule, which states that the photoluminescence quantum yield (PLQY) is independent of the excitation wavelength. As such, the absorption spectra and excitation spectra should be identical. Vavilov's rule is preceded by Kasha's rule, which states that photon emission will only occur from the lowest-lying excited state of a given multiplicity. Although the absorption of a high-energy photon may promote a molecule into a high-energy excited singlet state, S_n , the molecule will rapidly relax into the first singlet state, S_1 , via internal conversion before eventually relaxing back to the ground state via fluorescence. Kasha's rule holds

because the rate of internal conversion is multiple orders of magnitude faster than the rate of fluorescence, and therefore, emission from higher-order excited states is negligible. Vavilov's rule holds because IC from S_n to S_0 is also faster than other internal relaxation processes by which energy could be transferred into a different manifold, such as intersystem crossing into the triplet state.

However, when considering conjugated organic polymers in the condensed phase, it is important to remember that the local environment around each chromophore is not homogeneous. Semicrystalline polymers contain both crystalline and amorphous domains. Polymer samples contain a distribution of polymer chain lengths and defects. Each polymer chain will have a unique 3D structure resulting from a distribution of torsional angles, bond lengths, and relative orientations of monomers. Equally, each nearest neighbour of each chain will have its own unique 3D structure in space.

Furthermore, one must also consider the definition of an absorbing chromophore. A single polymer chain does not absorb a single photon. Instead, each linear polymer chain contains a distribution of chromophores along its length. Typically these absorbing chromophores will span a range of neighbouring monomers and repeat units. The electronic structure of each chromophore will not only depend on the structure and geometry of the chain within a local region along its length, but also on the external environment surrounding that local region. As such, each chromophore will absorb a slightly different wavelength of light.

Upon absorbing a photon, an exciton is formed. An exciton can be considered as a quantum mechanical quasiparticle described by its own wavefunction. After absorption, the exciton will exist in an excited state. These excited excitons will rapidly relax into a local exciton ground state (LEGS).^{54,78,81} However, unlike in homogeneous solutions of organic molecules, fluorescence does not occur from this ground state. Instead, the excitons diffuse through the material and jump from chromophore to chromophore via the Förster resonance energy transfer (FRET) mechanism.

With each jump, the energy of the exciton decreases. As the exciton energy decreases, the density of states with lower energies into which the exciton can be transferred also decreases. The lowest energy LEGS are few in number and spatially separated. Resultingly, the rate of FRET slows down and competes with the rate of radiative recombination. This is why conjugated polymers observe a red shift in the emission spectrum over the duration of the fluorescence lifetime, known as spectral diffusion.

Upon direct excitation of a LEGS, it will relax to its vibrationally relaxed state, transfer energy to lower-energy emissive LEGSs and subsequently fluoresce. However, LEGS are only located in the tail-end of the total density of exciton states and are situated below the Higher-energy excitations form Local Excited Exciton States (LEES) and Quasiextended Exciton States (QEES). Whilst LEES are considered excited states located on a single absorbing chromophore defined by a LEGS, QEES are exciton wavefunctions considered to be a linear combination of several underlying LEGS.

The highest PLQYs are observed when electronic states in the DRS UV/Vis absorption tail are excited directly. This region of the absorption spectra corresponds to the energies of the LEGS, implying that these states are strongly fluorescent. However, excitation with higher energy photons results in a smaller PLQY. This observation informs us that excitation into higher energy states will not always result in relaxation into a LEGS. Instead, there is a non-zero probability that an alternative relaxation process into a non-radiative state will occur. Some possible alternative pathways include 1) Rapid dissociation of hot excitons to form polaron pairs, 2) Rapid charge transfer to residual palladium or other impurities, 3) Energy transfer into the triplet manifold, or 4) Rapid internal conversion via coupling to the ground state.

As discussed in Chapters 6 and 9 of reference ²²⁸, the lowest-energy excited states are 1^1B_u , m^1A_g , and n^1B_u singlet states, and the 1^3B_u and 1^3A_g triplet states. These labels arise from symmetry considerations and can be used to determine which optical transitions are dipole-allowed. In centrosymmetric polymers, only the 1^1B_u state can be probed by linear spectroscopic methods. The remaining states must be investigated using nonlinear spectroscopic methods.

The 1^1B_u state can be considered a tightly-bound Frenkel-exciton with exciton binding energies of $\sim 1\text{eV}$.^{78,79,81} This is the energy band in which local excitons are considered. In p-phenylene based polymers, these excitons can be considered as $n=1$ Mott-Wannier excitons.⁸⁵

The m^1A_g states correspond to $n=2$ Mott-Wannier excitons, or charge-transfer excitons. This energy band only has a weak binding energy of $\sim 0.2\text{ eV}$ since the electrostatically-bound electron-hole pair are more spatially separated. The n^1B_u state ($n=3$ Mott-Wannier exciton) lies at the edge of the unbound electron-hole continuum. Excitons in this state have almost no electrostatic binding energy and readily dissociate into their polaron pair. Since the DBTS-PhFx co-polymers are not centrosymmetric, direct transitions to this excited state may not be forbidden by quantum mechanical selection rules.

The exact relationship between the LEES, QEES, and these higher-order polymer excited states are complicated since these concepts arise at the interface of a band theory model (Wannier excitons), molecular model (Frenkel Excitons) and the intermediate case between the two (Charge-transfer excitons).

Ultimately, the timescales for the relaxation of QEESs to LEGSs are on the order of 100 – 200 fs.⁸¹ Excess energy of these hot excitons must also be dissipated by coupling to the environment. Since these PL measurements are made in the condensed phase, QEES must therefore couple to nuclear or electronic motion in neighbouring chromophores or impurities such as residual palladium. Time-resolved transient Raman spectroscopy studies on p(DBTS-DBTS) have recently identified the formation of dissociated polaron pairs on the sub 2 ps timescale.²³⁶ The exact determination of the rate of this process was limited by the instrument response function (IRF). Therefore, these timescales agree with those expected for the relaxation of QEES. Earlier studies from OPV research have also indicated that excess energy from hot excitons aids the dissociation of charge-transfer excitons located at the D/A interface in bulk heterojunction materials.²⁶⁹ More generally, ultrafast photochemistry involving hot excited states is a growing field of interest for many processes.²⁷⁰

Without more information regarding these excitonic processes, it is difficult to conclude their impact on the photocatalytic activity. For example, further measurements are required to determine the overall photoluminescence quantum yields at different wavelengths would provide a clearer measure of the proportion of absorption events that result in energy transfer to LEGSs. Time-resolved transient absorption, time-resolved resonance Raman, and photoinduced absorption spectroscopies could provide more information about the lifetimes over which exciton and polaron states form and decay. Repeating these experiments for samples with different concentrations of residual palladium or photodeposited platinum could also provide information about charge transfer processes to these co-catalysts.

3.9.1.3 Fluorescence Lifetime

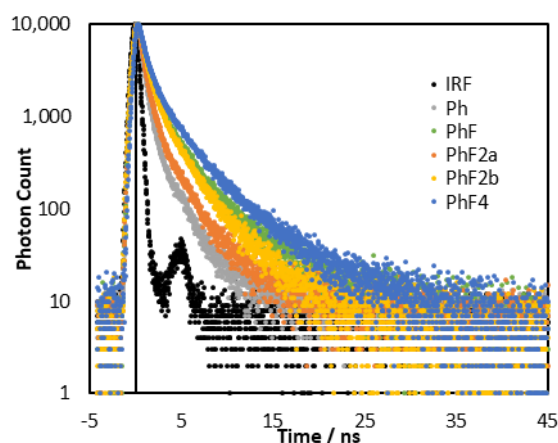


Figure 196: TCSPC fluorescence decay curves for DBTS-PhFx polymers and the instrument response function.

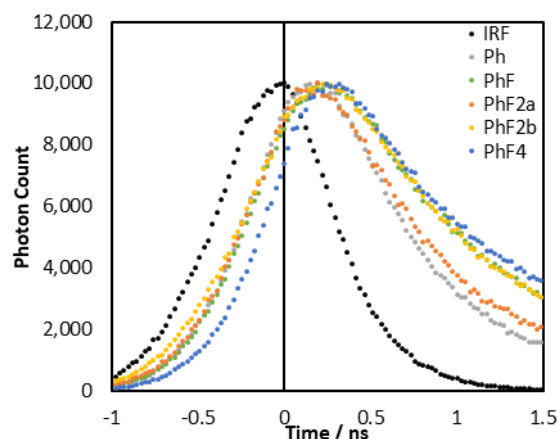


Figure 197: Fluorescence rise times and initial decay profiles for the DBTS-PhFx polymers over the first 1.5 ns after excitation.

Figures 196 and 197 show the TCSPC fluorescence spectra of the DBTS-PhFx polymers synthesised in dioxane/TBAA. All fluorescence decay measurements were fitted with triexponential functions by reconvoluting the decay function with the IRF. The weighted average lifetimes are presented in Figure 198. Although there is no clear association between weight-averaged lifetime and fluorine content, it should be noted that the non-fluorinated DBTS-Ph polymer exhibited the shortest lifetime, and the tetrafluorinated derivative DBTS-PhF4 exhibited the longest.

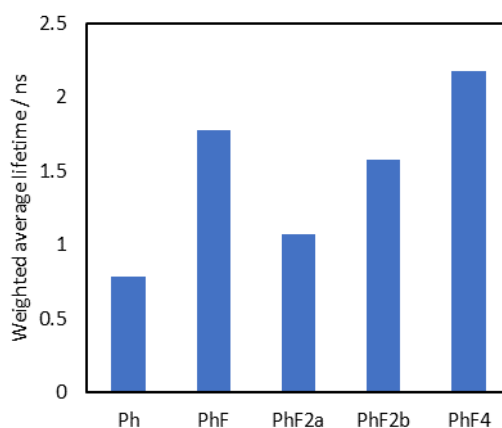


Figure 198: Weighted average fluorescence lifetimes for the DBTS-PhFx polymers resulting from reconvoluting a triexponential function with the IRF.

In Chapter 2, we highlighted that for DBTS copolymers containing fluorinated phenylene rings, the fluorescence lifetime is likely inversely correlated with the residual palladium concentration. The

exception was DBTS-PhF4, which had a long fluorescence lifetime despite a high residual palladium concentration. This discrepancy was tentatively attributed to the low-energy LUMO of DBTS-PhF4, which indicates that the thermodynamic driving force for electron extraction into Pd may be slow. The optical bandgap was the most influential factor for other phenylene-based copolymers.

Applying those observations to these samples indicates that the DBTS-PhF sample likely contains less palladium than the DBTS-PhF2a and DBTS-PhF2b samples. DBTS-PhF2a likely contains the most palladium.

A short delay was observed prior to the onset of fluorescence in each of the polymer samples, as shown in Figure 197. This time window of 200-350 ps roughly corresponds to the expected relaxation time from the excited QEES to the emissive exciton ground states. This would result in a delayed fluorescence peak as the fluorescence intensity increases exponentially at the start of the time-resolved emission. However, since such relaxation processes occur on a sub-nanosecond timescale, it is difficult to resolve the fluorescence growth from the IRF. Furthermore, small shifts in the order of picoseconds may also arise because the IRF and the fluorescence occur at different wavelengths of light, which take fractionally different optical path lengths, travel at different speeds through optical elements, and cascade slower rates in the photomultiplier tube at detection.²⁷¹ Furthermore, due to the convolution of the fluorescence intensity with the IRF, longer fluorescence lifetimes will result in a broader initial peak and a delayed maximum.

3.9.1.4 Optoelectronic Properties and Photocatalytic Activity

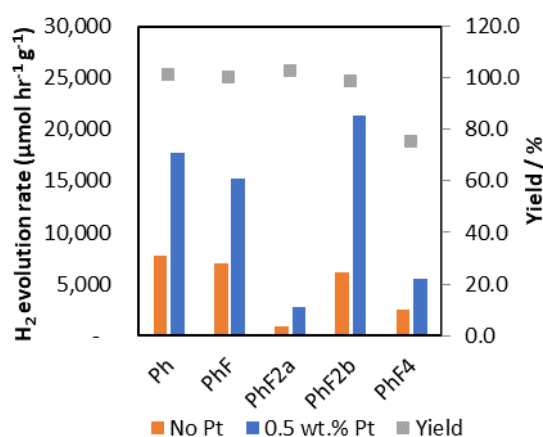


Figure 199: HER rates of the DBTS-PhFx polymers for which the optoelectronic properties have been determined and associated synthesis yields of the polymers.

It is difficult to draw conclusions regarding the impact of these optoelectronic properties on the photocatalytic hydrogen evolution activity based on the limited data gathered. Photocatalytic rates for these samples have been reproduced in Figure 199.

DBTS-PhF2a and DBTS-PhF4 drive the HER at the slowest rates. In both cases, the UV-Vis absorption spectrum contains a long tail at the low-energy edge. This then correlates with a broad fluorescence excitation spectrum peak in the region of this absorption tail. The work published by Bai *et al.* may provide some context for these observations since the same two samples produced in their work also resulted in low photocatalytic activities.¹⁸² Chapter 2 highlights that those samples were also high in residual palladium content. The DBTS-PhF2a sample prepared in this work also exhibits a short fluorescence lifetime in the condensed phase. Therefore, its other optoelectronic properties and poor photocatalytic activity may also be associated with high residual palladium concentrations.

However, contrary to this observation, DBTS-PhF exhibited a longer fluorescence lifetime than DBTS-PhF2b, despite its narrower bandgap, implying lower residual palladium concentrations. However, when comparing their photocatalytic activities, DBTS-PhF2b performed better after photodepositing platinum. This may arise because DBTS-PhF2b is inherently more active, but DBTS-PhF2b did not always outperform DBTS-PhF when synthesised using alternative reaction conditions based on other solvent-base combinations.

3.9.2 BDT-PhFx

3.9.2.1 UV/Vis DRS

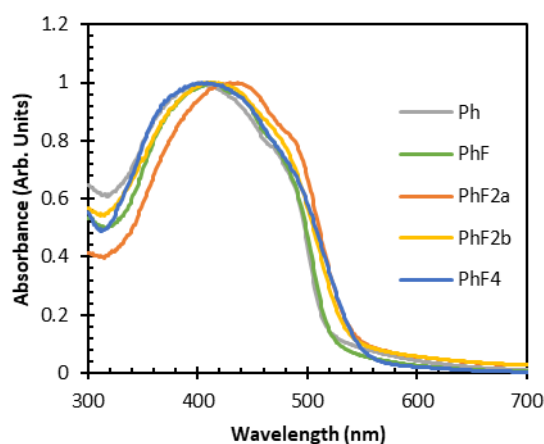


Figure 200: Normalised UV/Vis DRS spectra for BDT-PhFx polymers synthesised from a dioxane/TBAA reaction mixture. 5 mg of the polymer was blended with 55 mg of BaSO₄ to prevent complete absorption above the bandgap.

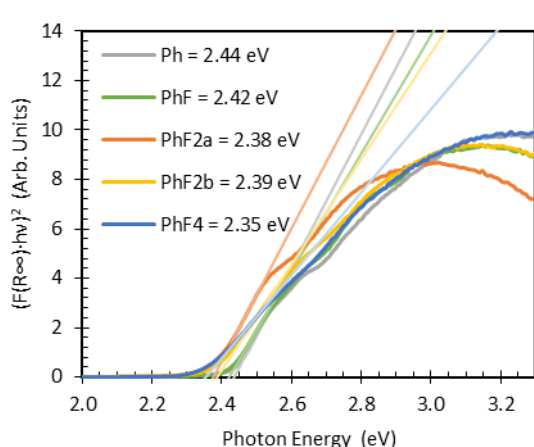


Figure 201: Tauc plot analysis for BDT-PhFx polymers synthesised from a dioxane/TBAA reaction mixture assuming a direct bandgap.

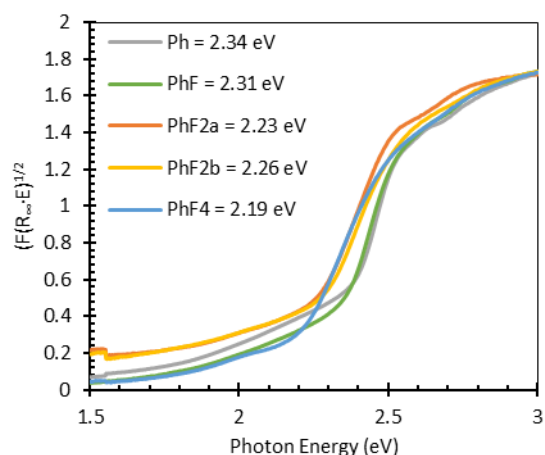


Figure 202: Tauc plot analysis for BDT-PhFx polymers synthesised from a dioxane/TBAA reaction mixture assuming an indirect bandgap.

Diffuse reflectance spectra were obtained from BDT-PhFx polymers synthesised from 1,4-dioxane and 2M TBAA at 120°C. 5 mg of each polymer was combined with 55 mg of BaSO₄ and ground together using an agate pestle and mortar to ensure absorption was maintained below unity.

The resulting absorption spectra, Tauc plot for determining the direct bandgaps, and Tauc plots for indirect bandgaps are presented in Figures 200, 201, and 202. The optical bandgaps determined via these methods are presented in the graph legends. In contrast to DBTS-PhFx polymers, the bandgap of BDT-PhFx polymers decreased with increasing fluorine content. As can be seen by comparing figures 201 and 202, Tauc plots for an indirect bandgap result in a clearer linear region at the band edge. The range of (indirect) bandgaps is narrow and spans from 2.19 eV for BDT-PhF4 to 2.34 eV for BDT-Ph.

These follow a similar pattern to the DFT calculations, which also predicted a decreasing fundamental gap on the same order of magnitude as fluorine content increases.

Each absorption spectra exhibits at least one shoulder feature between 450 and 500 nm. These were absent in the DBTS-PhFx absorption profiles and deviate from what is typically observed for traditional inorganic semiconductors. Each BDT-PhFx polymer spectra exhibits a significant absorption tail at the band edge due to optically-active local exciton ground states. However, this is particularly prevalent in the BDT-PhF4 sample. BDT-PhF4 demonstrates the lowest-energy absorption onset and the highest-energy absorption maximum within this set of polymers. This may indicate a wide distribution of exciton states and a polymer structure containing significant disorder.⁸⁵

3.9.2.2 Steady-State Fluorescence

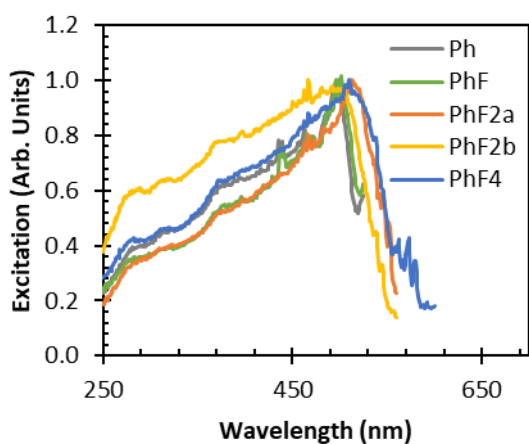


Figure 203: Solid-state steady-state fluorescence excitation spectra for the BDT-PhFx co-polymers synthesised from dioxane/TBAA. Excitation spectra are measured at the emission maxima.

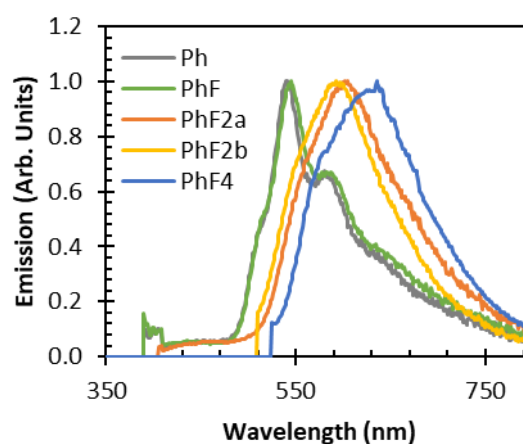


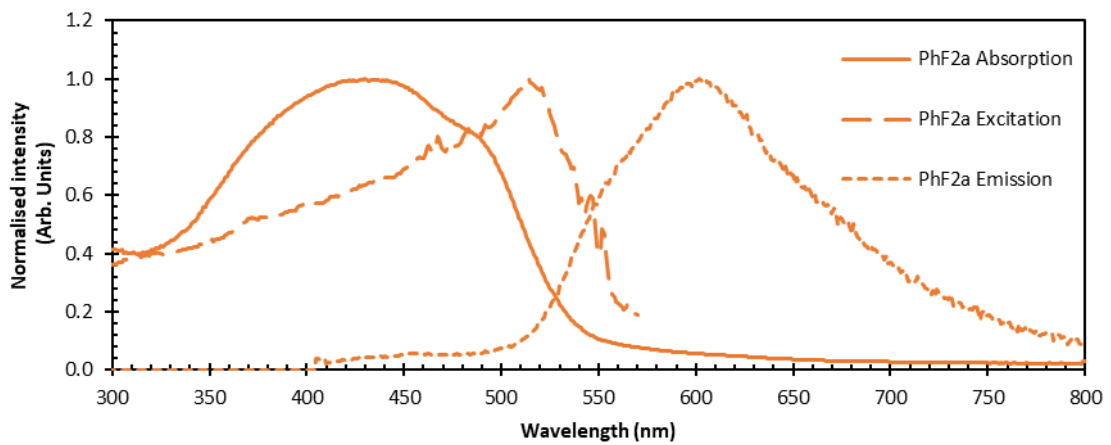
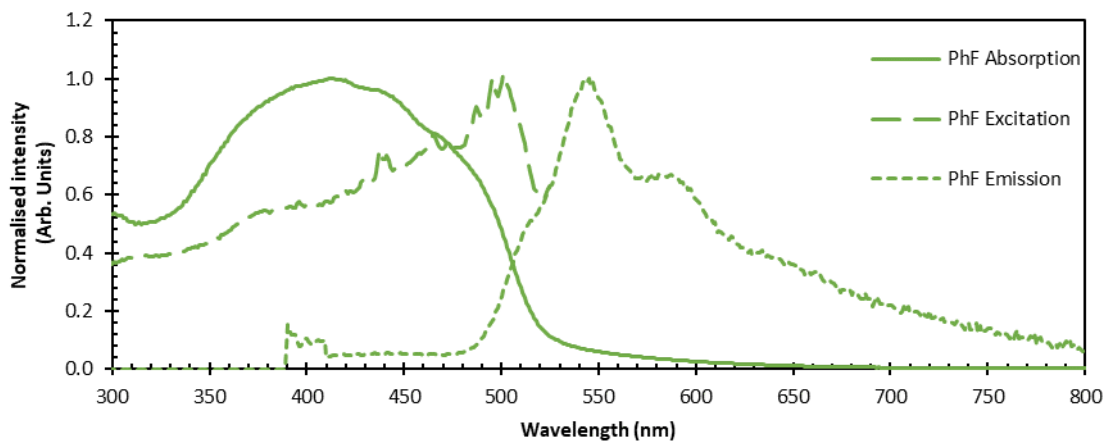
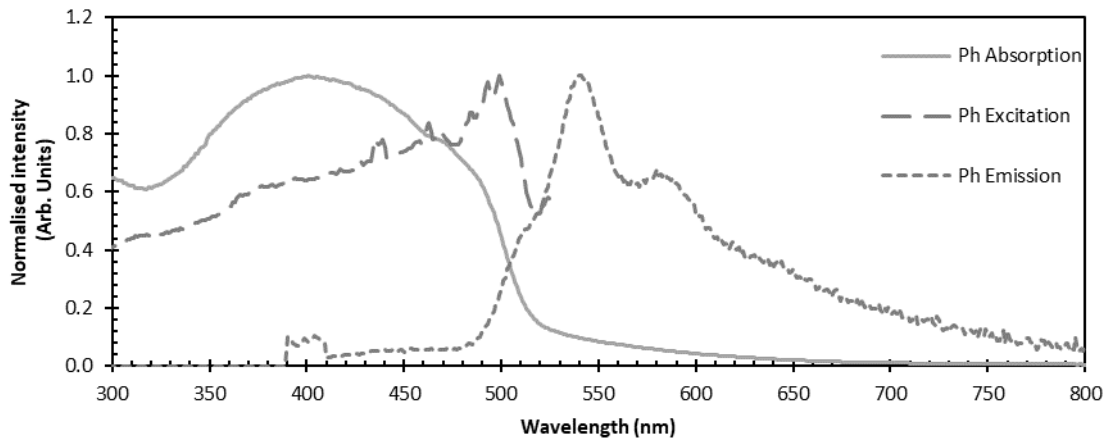
Figure 204: Solid-state steady-state fluorescence emission spectra for the BDT-PhFx co-polymers synthesised from dioxane/TBAA. Emission spectra are measured following excitation with 350 nm light.

Steady-state and time-resolved fluorescence spectra were recorded for each polymer in the solid aggregate state. Figures 203 and 204 present the steady-state fluorescence excitation and steady-state fluorescence emission spectra of the BDT-PhFx polymers, respectively. As with the absorption spectra, the excitation spectra maxima are all very close in energy, indicating similar optical bandgaps on which the electronegativity of the fluorinated phenylene groups has limited impact. Nevertheless, the same trend is observed whereby BDT-Ph is confirmed to have the largest bandgap, and BDT-PhF4 has the smallest bandgap.

The fluorescence emission spectra are more sensitive to the phenylene co-monomer. BDT-Ph and BDT-PhF present a good resolution of their vibronic structure, with the 0-0 peak exhibiting significantly greater intensities than the lower-energy 0-1 transition. This fine structure is indicative of a J-aggregate with little disorder.^{85,272} BDT-PhF2a and BDT-PhF2b each have similar emission peak shapes but are red-shifted and broader than those of BDT-Ph(F). These vibronic progressions are more indicative of an H-aggregate.^{273,274} The emission peak of BDT-PhF2a is slightly red-shifted compared to the PhF2b isomer in line with its absorption and excitation spectra. This results in similar Stokes' shifts between the two isomers. The fluorescence emission spectrum of BDT-PhF4 is further red-shifted and exhibits the largest Stokes' shift. This peak is similar in shape to the BDT-PhF2x polymers except slightly broader and less well-defined.

BDT-PhFx polymers demonstrate a clear trend whereby the emission is red-shifted with increasing electronegativity on the phenylene unit. However, the origin of this shift is unclear. In disordered conjugated polymers, the energy distribution of the LEGSs is broad, and the energy of an exciton, after migration to lower-lying exciton states, results in a red-shifted emission spectrum. The more disordered a system is, the more red-shifted its absorption is. The peak absorption is typically blue-shifted in this case. The broad absorption edge of BDT-PhF4 and large Stokes' shift indicate a significant amount of disorder. However, the corresponding excitation spectrum is not blue-shifted. It is also possible that the increased electronegativity of the fluorinated phenylene units leads to increased intramolecular charge transfer.

DFT geometry optimisation calculations for BDT-PhFx polymers imply that the preferred orientation of adjacent aromatic units in the backbone is co-planar. This geometry allows for rapid delocalisation of excitons and charges along the polymer backbone. Meanwhile, frontier molecular orbital calculations for BDT-PhFx polymers indicate that the HOMO is located on the BDT units, and the LUMO is delocalised along the backbone. Optical absorptions are likely to result in the local excitation of BDT chromophores and intramolecular charge transfer along the backbone to achieve this delocalisation, which is expected prior to photon emission/relaxation. Since BDT-PhFx polymers have Donor-Acceptor structures, this delocalisation is expected to be enhanced by increasingly electronegative phenylene units. This may also explain the red-shifted emission in BDT-PhF4 compared to BDT-Ph.



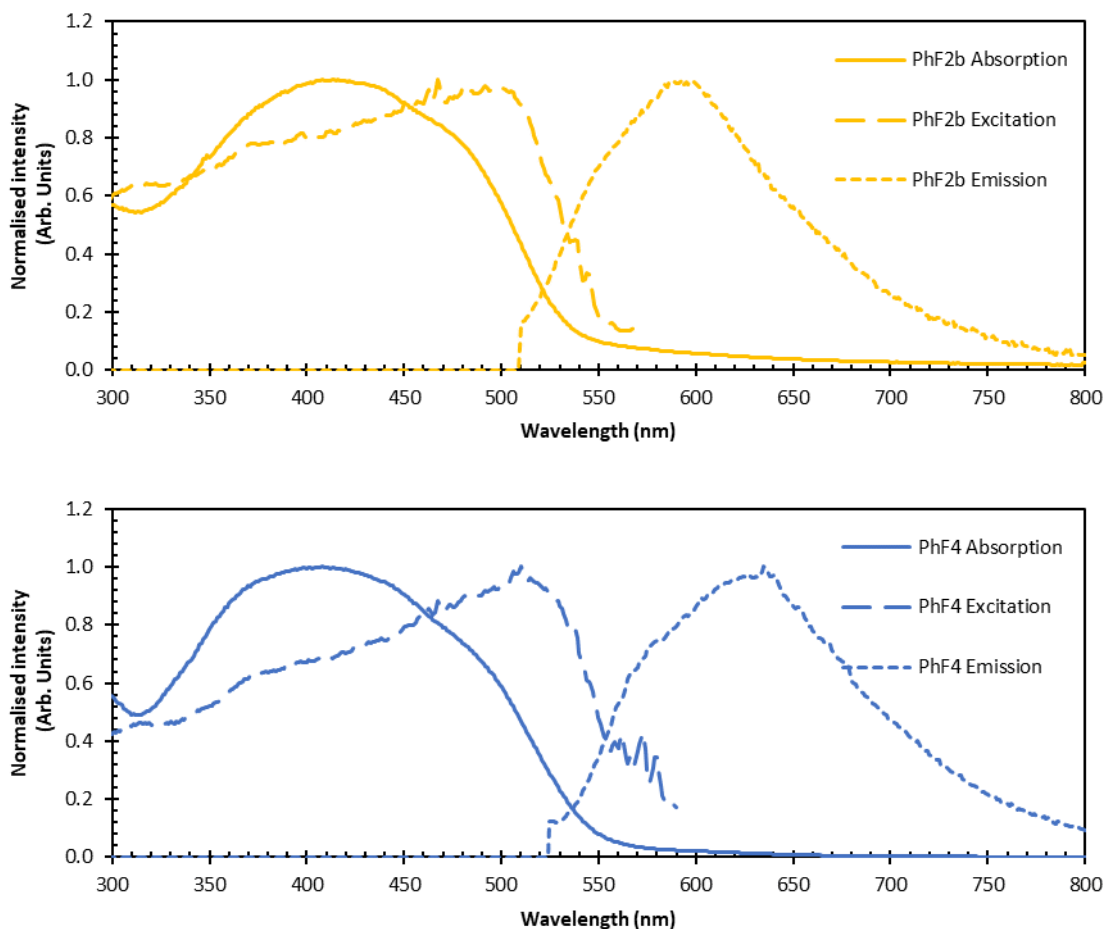


Figure 205: Normalised UV/Vis Diffuse reflectance spectra, fluorescence excitation spectra, and fluorescence emission spectra of BDT-PhFx polymers. All spectra were recorded for the samples in the solid state.

Absorption, excitation, and emission spectra are plotted for each BDT-PhFx polymer in Figure 205. As with the BDTs-PhFx series of polymers, the excitation spectra maximum corresponds to the absorption edge, indicating that emission originates from local excitons situated below the bandgap.

Excitation above the bandgap once again results in relaxation to these excitonic states. However, singlet relaxation from QEEs to LEGs in this relaxation process appears to compete with energy transfer processes from hot excitons that lead to non-radiative states. Hence, photoluminescence quantum yields for wavelengths corresponding to energies greater than the bandgap are significantly reduced. As discussed for the BDTs-PhFx series, further experiments are required to determine how this corresponds to the hydrogen evolution apparent quantum yield.

3.9.2.3 Fluorescence Lifetime

Figures 206 and 207 contain the TCSPC fluorescence decays of the BDT-PhFx polymers on a logarithmic scale and over the first 2 ns, respectively. The weight-averaged fluorescence lifetimes, obtained by reconvoluting a tri-exponential decay function with the instrument response function, are presented in Figure 208. The BDT-Ph and BDT-PhF polymers exhibit very short fluorescence lifetimes. This would result in short exciton migration distances and make it difficult for excitons to diffuse to the polymer-cocatalyst interfaces and undergo charge separation/extraction. The short lifetime of these excited states may arise due to the rapid charge extraction by residual palladium clusters. As with the DBTS-PhFx polymers, the BDT-PhF2a fluorescence has a shorter lifetime than that of BDT-PhF2b. BDT-PhF4 has a lifetime situated between the two PhF2x polymers.

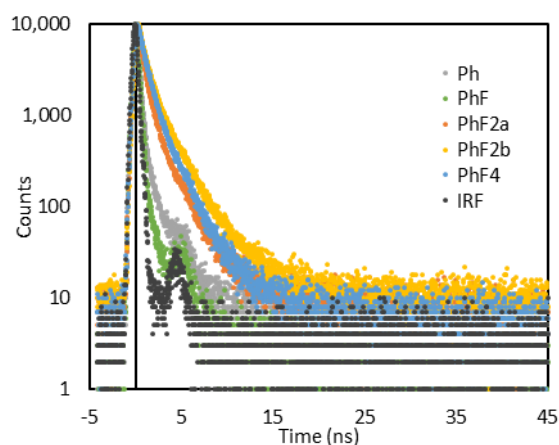


Figure 206: TCSPC fluorescence decay curves for BDT-PhFx polymers and the instrument response function.

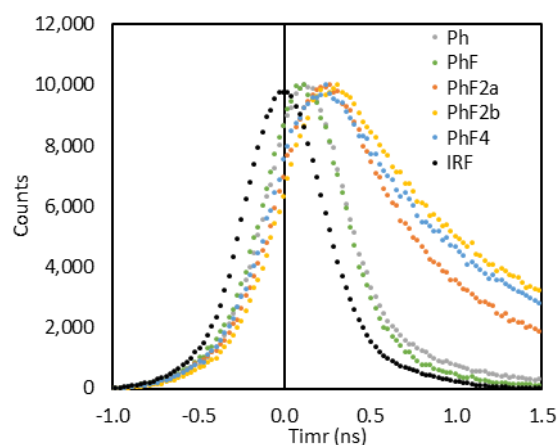


Figure 207: Fluorescence rise times and initial decay profiles for the BDT-PhFx polymers over the first 1.5 ns after excitation.

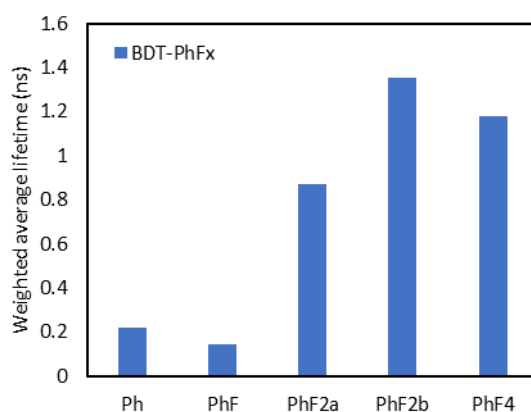


Figure 208: Weighted average fluorescence lifetimes for the BDT-PhFx polymers resulting from reconvoluting a triexponential function with the IRF.

3.9.2.4 Optoelectronics vs Photocatalytic Activity

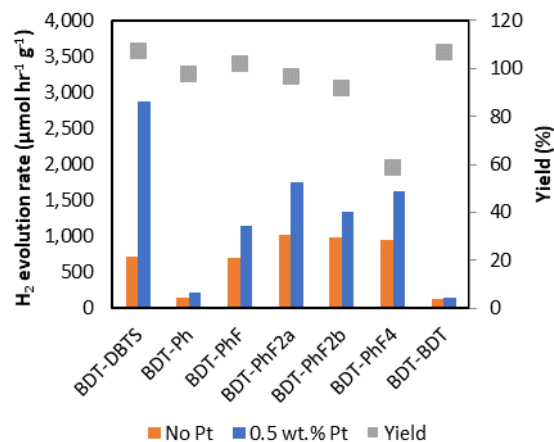


Figure 209: HER rates of the BDT-PhFx polymers for which the optoelectronic properties have been determined and associated synthesis yields of the polymers

The HER rates for the BDT-PhFx polymers investigated in this study are reproduced in Figure 209. There does not appear to be any correlation between the weight-averaged fluorescence lifetimes and the photocatalytic HER rates. For example, BDT-PhF exhibits the shortest lifetime, but its HER rate is comparable with the other BDT-PhFx polymers containing fluorine atoms. BDT-Ph, however, also exhibits a short lifetime but produces the least hydrogen.

DBTS-PhF2a is more photocatalytically active than DBTS-PhF2b, despite also exhibiting a shorter fluorescence lifetime. Interestingly, when comparing the fluorescence excitation spectra of these two polymers, DBTS-PhF2a also has a more pronounced peak at the band edge. Its DRS absorption tail at low energies is steeper, and its bandgap is slightly red-shifted. Combined, these results indicate that the 3-dimensional structure of solid-state DBTS-PhF2a may be less disordered than that of DBTS-PhF2b. The PhF2b co-polymer is also synthesised at a slightly lower yield. Since BDT-PhF4 has the lowest-lying HOMO and is most likely to drive the TEA oxidation reaction, its photocatalytic activity could potentially be improved by decreasing the disorder in the backbone. This may naturally result from improving synthesis conditions and increasing the yield.

3.9.3 DBTS-PhF_x-BDT

3.9.3.1 UV/Vis DRS

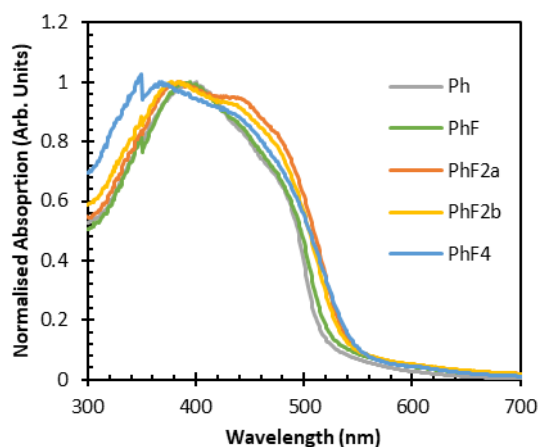


Figure 210: Normalised UV/Vis DRS spectra for DBTS-PhF_x-BDT statistical ternary co-polymers synthesised from a dioxane/TBAA reaction mixture. 5 mg of polymer was blended with 55 mg of BaSO₄ to prevent complete absorption above the bandgap.

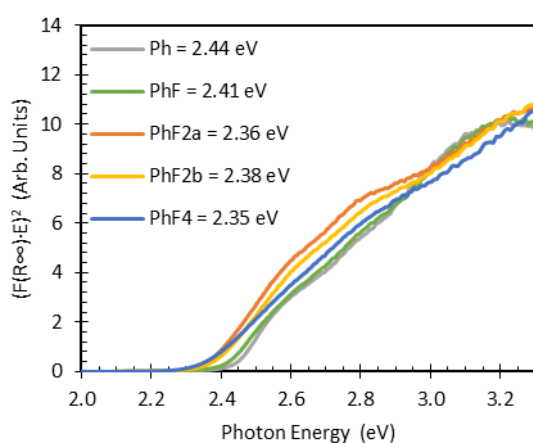


Figure 211: Tauc plot analysis for DBTS-PhF_x-BDT statistical ternary co-polymers synthesised from a dioxane/TBAA reaction mixture assuming a direct bandgap.

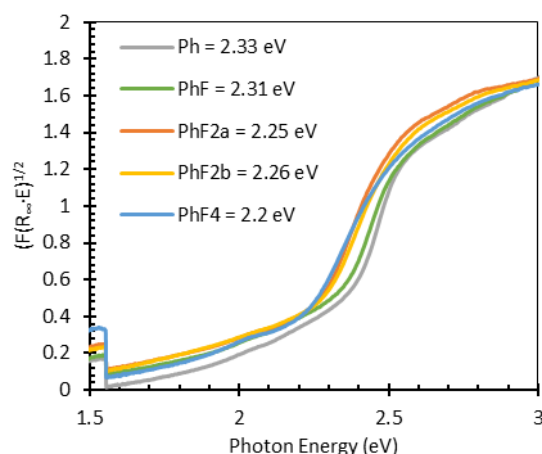


Figure 212: Tauc plot analysis for DBTS-PhF_x-BDT statistical ternary co-polymers synthesised from a dioxane/TBAA reaction mixture assuming an indirect bandgap.

Figures 211 and 212 show the UV/Vis DRS spectra of the solid polymer powder and the corresponding Tauc plot for an indirect semiconductor. The bandgaps determined for these polymers are presented in the chart legends. Except for an additional absorption feature located between 300 – 425 nm, which results in a broader absorption profile and a blue-shifted absorption maximum, the absorption spectra of these polymers are very similar to the BDT-PhF_x co-polymers. The corresponding measured optical bandgaps are almost identical to the BDT-PhF_x polymers.

In each case, the additional high-energy absorption feature is very similar in energy to the corresponding DBTS-PhF_x polymer. These shoulders can be attributed to optical transitions located on local DBTS-PhF_x chromophores. Given that a mixture of multiple bandgaps cannot be identified

and that there is no sudden steep rise in the absorption at the DBTS-PhFx absorption onset, it is likely that ternary polymers were successfully synthesised, rather than a mixture of DBTS-PhFx and BDT-PhFx binary polymers.

3.9.3.2 Steady-State Fluorescence

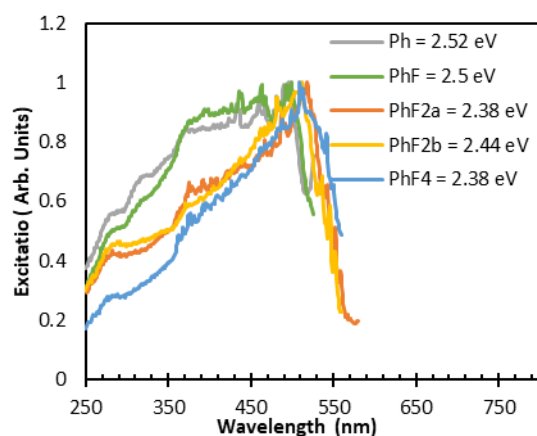


Figure 213: Solid-state steady-state fluorescence excitation spectra for the DBTS-PhFx-BDT statistical ternary copolymers synthesised from dioxane/TBAA. Excitation spectra are measured at the emission maxima.

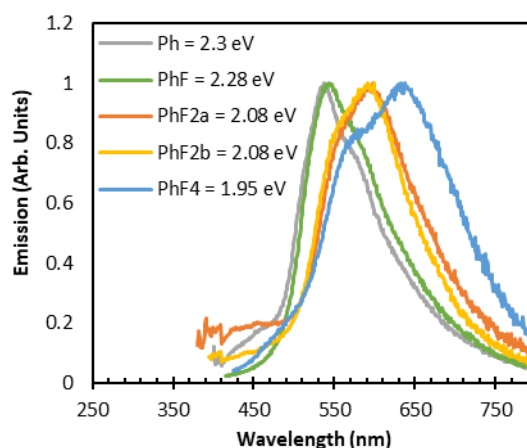
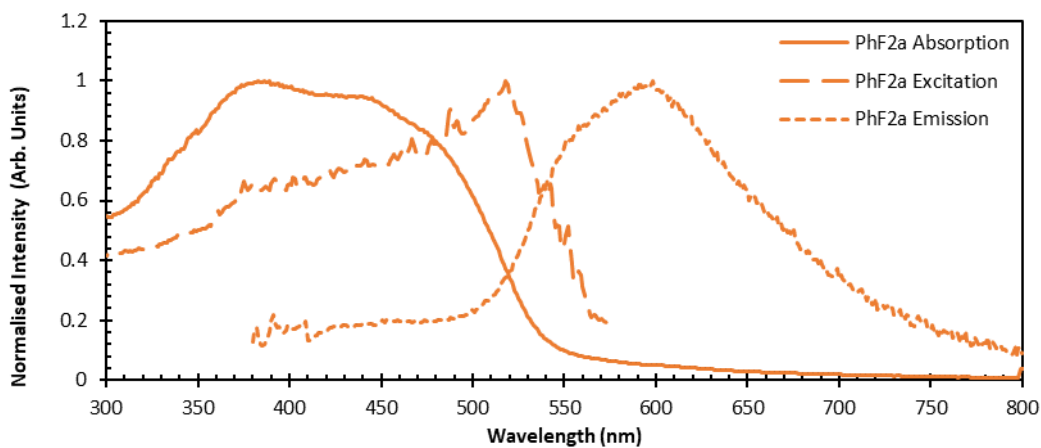
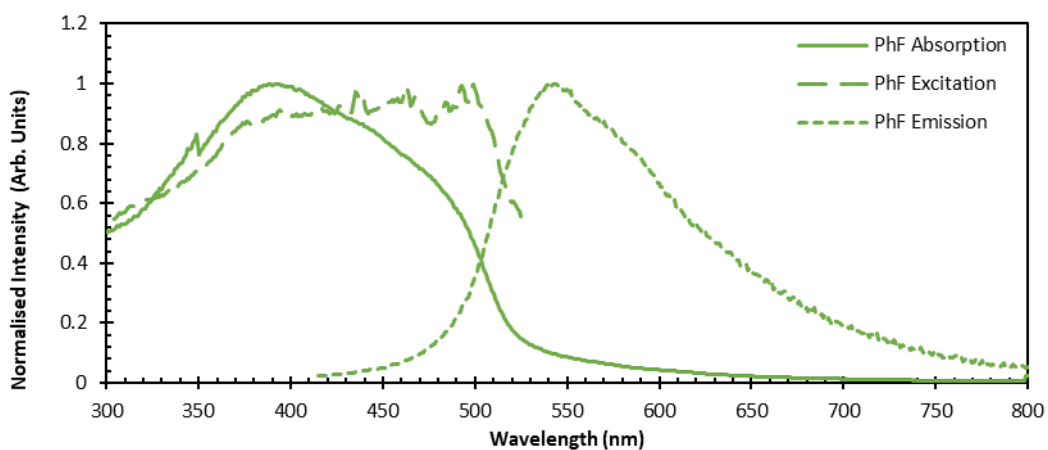
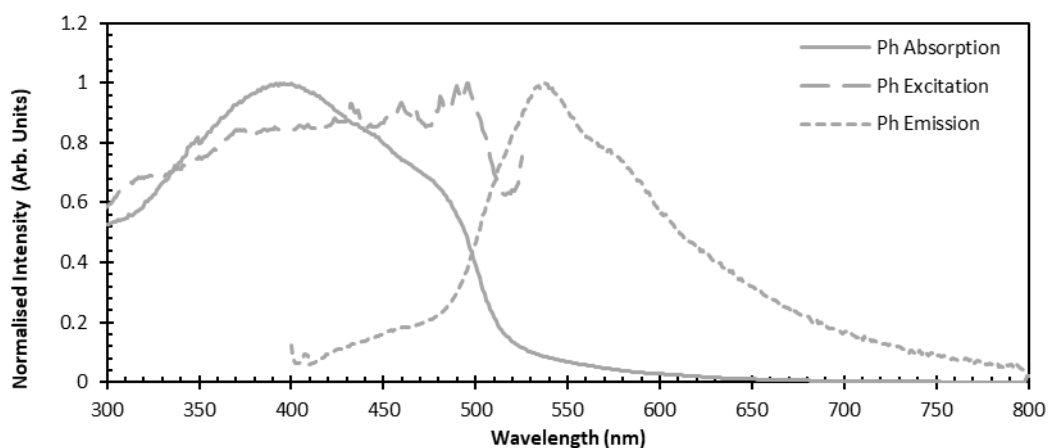


Figure 214: Solid-state steady-state fluorescence emission spectra for the DBTS-PhFx-BDT statistical ternary copolymers synthesised from dioxane/TBAA. Emission spectra are measured following excitation with 350 nm light.

Figures 213 and 214 contain the steady-state fluorescence excitation and emission spectra of the DBTS-PhFx-BDT ternary polymers, respectively. As with all of the other conjugated polymers, the excitation spectra (with fluorescence intensity measured at the corresponding emission maxima) exhibit the same trend as the absorption onset, whereby the maxima are red-shifted with respect to fluorine content. This excitation spectra maximum also overlaps with the absorption band edge. As for the other conjugated polymers, this implies that direct excitation of excitons leads to enhanced emission. In contrast, absorption above the band gap leads to increased rates of non-radiative decay.

Emission is also red-shifted with respect to increased fluorine content. The red-shifted peaks are considerably broader than those at shorter wavelengths. In each emission spectra, several features can be identified. For Ph and PhF polymers, the higher energy feature is the most intense, whereas for the PhF2x and PhF4 polymers, the second peak is the most intense. This once again implies a potential transition from and Predominantly hJ-type aggregate into an H_j-aggregate upon the addition of fluorine atoms. This implies fluorine can influence intermolecular charge transfer and chain stacking.²⁷³

As with BDT-PhFx polymers, the observed red-shift may arise from increased disorder leading to a broad distribution of excitonic states. Förster resonance energy transfer enables excitons to migrate to the lowest-energy local exciton ground states. Since disorder leads to a broad density of exciton states, the increased disorder is expected to lead to larger Stokes' shifts.



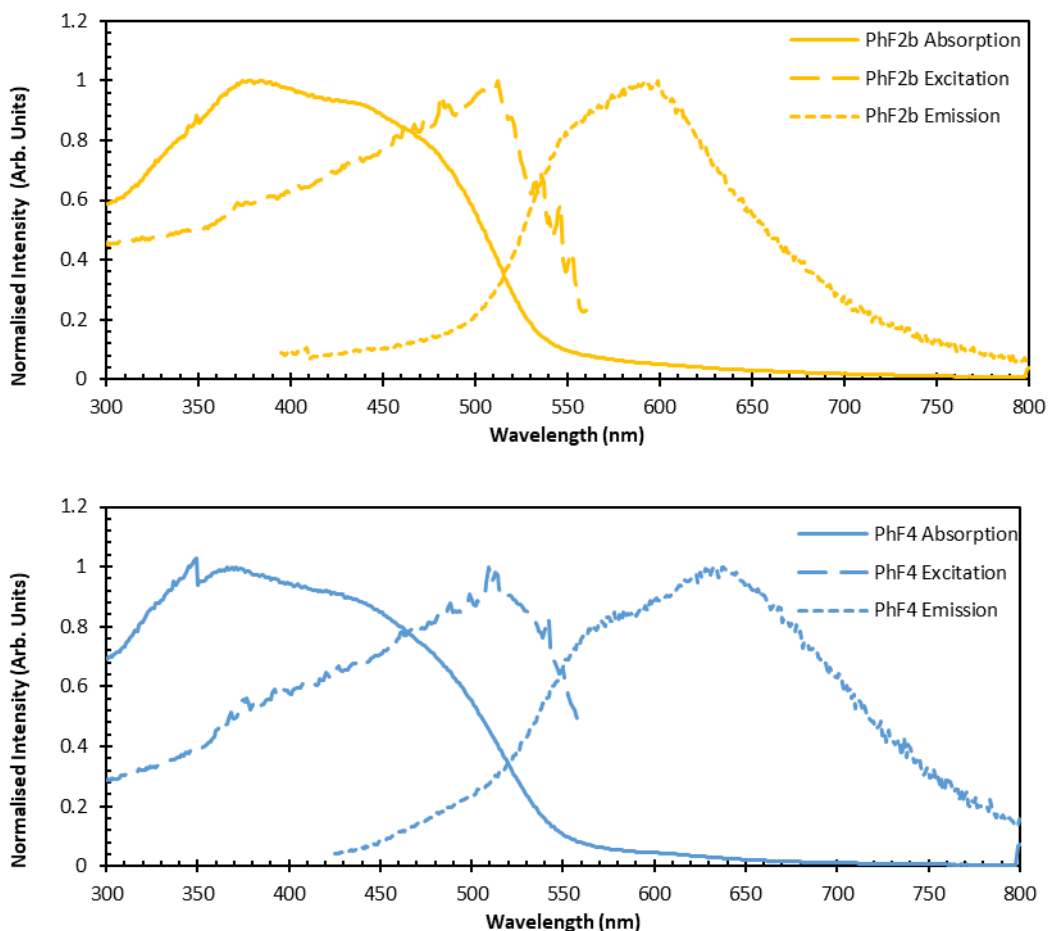


Figure 215: Normalised UV/Vis Diffuse reflectance spectra, fluorescence excitation spectra, and fluorescence emission spectra of BDT-PhFx-BDTS polymers. All samples were measured in the solid state.

The absorption, excitation, and emission spectra for each ternary polymer are presented in Figure 215. For all polymers, the fluorescence intensity increases as the photon energy approaches that of the exciton states. The local maxima correspond with the absorption edges. However, in the cases of Ph and PhF ternary polymers, the normalised fluorescence intensity upon exciting the polymer with shorter wavelengths plateaus at energies above the band gap. It remains above 0.8 until the absorption maxima. Since absorption increases over this range and fluorescence does not, this still corresponds to a decreased PLQY at higher energies. However, this does potentially imply an increased energy transfer from higher energy states to the emissive exciton states when compared to the other polymers, assuming equal photoluminescence quantum yields. However, further experiments are required to confirm this. This may partially explain these two polymers' higher hydrogen evolution rates.

3.9.3.3 Fluorescence Lifetime

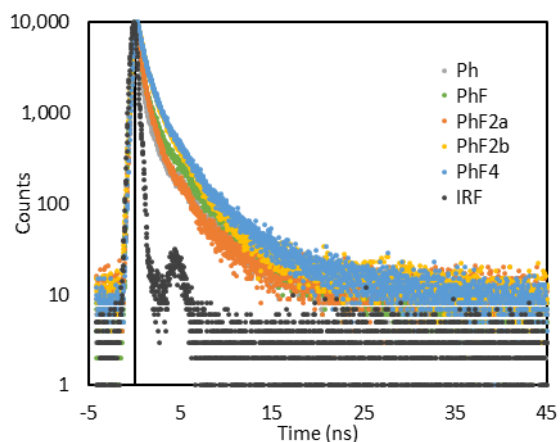


Figure 216: TCSPC fluorescence decay curves for DBTS-PhFx-BDT statistical ternary co-polymers and the instrument response function.

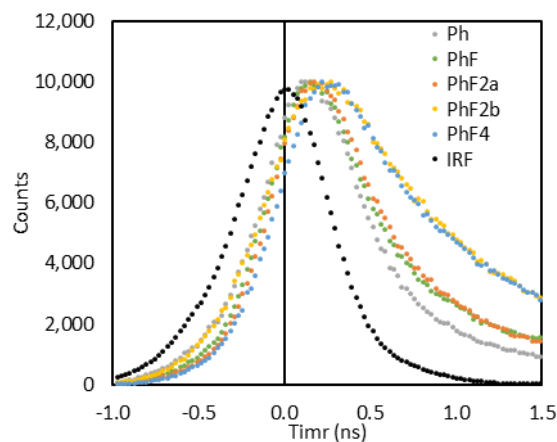


Figure 217: Fluorescence rise times and initial decay profiles for the DBTS-PhFx-BDT statistical ternary co-polymers over the first 1.5 ns after excitation.

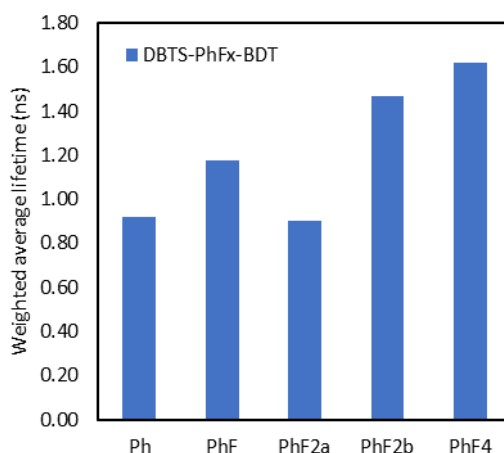


Figure 218: Weighted average fluorescence lifetimes for the DBTS-PhFx-BDT statistical ternary co-polymers resulting from reconvoluting a triexponential function with the IRF.

Whilst the absorption, excitation, and emission spectra of the ternary co-polymers are almost identical to those of the BDT-PhFx binary equivalents, there is a direct change in the fluorescence lifetimes. The lifetimes of the Ph and PhF co-polymers have increased from 0.2 and 0.15 ns to 0.9 and 1.2 ns, respectively. The lifetime of the ternary PhF2a co-polymer is similar to that observed for the binary BDT equivalent, and the PhF2b ternary polymer only increases by 0.1 ns. The PhF4 ternary polymer exhibits the longest lifetime of the set, with a lifetime of 1.6 ns.

Generally, the trend between fluorescence lifetimes and fluorine content is very similar to those observed for the DBTS-PhFx polymers. Adding fluorine to the phenylene groups results in longer

lifetimes than the unsubstituted co-polymer. Whereas in DBTS-PhFx polymers, this trend coincides with widening bandgaps, the opposite is true for DBTS-PhFx-BDT ternary co-polymers. This implies that it is indeed the presence of fluorine that makes the difference.

The results from Chapter 2 indicate that these results are also likely to be strongly correlated to the residual palladium concentrations. Indeed, this factor may be important in understanding why the PhF2a co-polymers consistently exhibit shorter fluorescence lifetimes than the PhF2b equivalents. Unfortunately, attempts to test residual palladium concentration were unsuccessful as the polymers could not be fully digested in concentrated nitric acid.

3.9.3.4 Optoelectronics vs Photocatalytic Activity

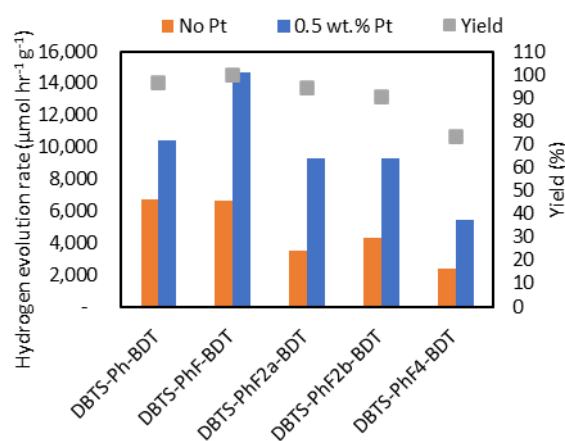


Figure 219: HER rates of the DBTS-PhFx-BDT statistical ternary co-polymers and their associated synthesis yields.

The HER rates for the DBTS-PhFx-BDT ternary co-polymers have been reproduced in Figure 219. Interestingly, it is the Ph and PhF variants that exhibit the highest photocatalytic activities following the photodeposition of 0.5 wt.% platinum, despite these polymers possessing the lowest driving force for TEA oxidation and the shortest fluorescence lifetimes.

In addition to these polymers being produced in the highest yields, these two polymers also exhibited the best-resolved vibronic structures in their steady-state fluorescence emission spectra and the smallest Stokes' shifts between excitation and emission. In these polymers, the 0-0 optical transition is the strongest, whereas in polymers with increasing fluorine content, the 0-1 transition at lower energy is the most intense.

According to Eder *et al.* a high intensity ratio of I_{0-0}/I_{0-1} corresponds to a J-type aggregate of chromophores in which the transition dipole moments align with one another along the polymer

backbone in a head-to-tail manner.²⁷⁴ Structural disorder, however, will result in peak broadening and a decrease in the magnitude of this ratio.⁸⁵ Meanwhile, when the ratio I_{0-0}/I_{0-1} is less than 1, this implies an increased proportion of chains that interact intermolecularly with one another through space in the form of an H-aggregate. In this case, excitons are spread over neighbouring chains, and the transition dipole moments in one chain point in the opposite direction to those in the neighbouring chain. This results in the 0-0 transition turning dark and an increase in the fluorescence intensity of the 0-1 transition. Likewise, the ratio of these two emission lines is closer to 1 when the polymer chain is disordered. Disorder also contributes to line broadening.

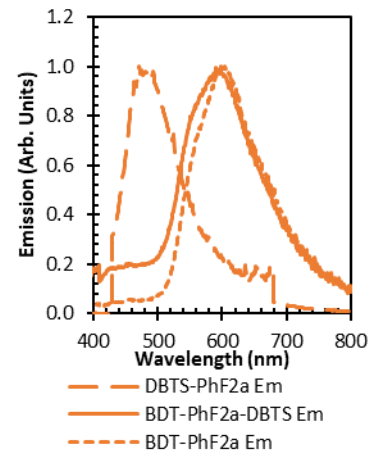
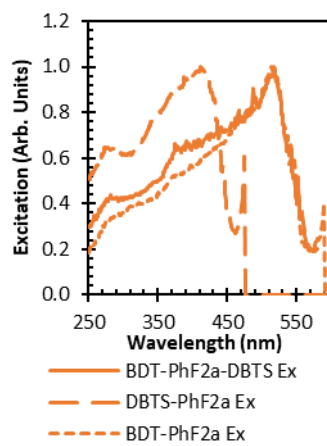
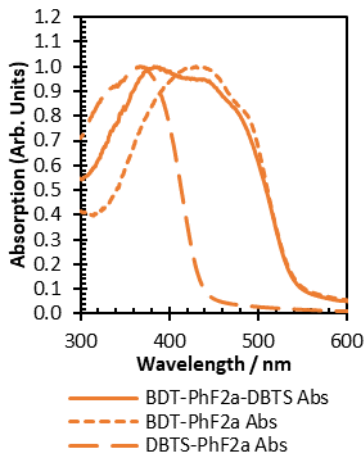
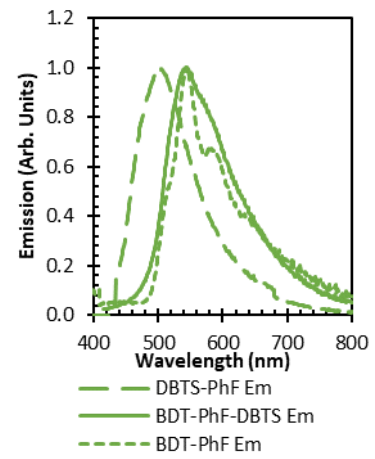
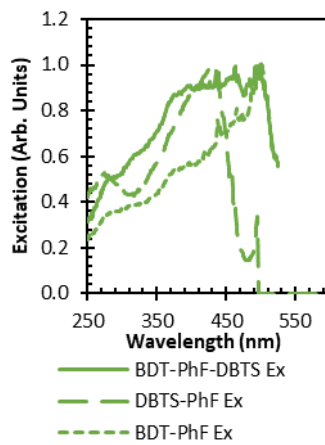
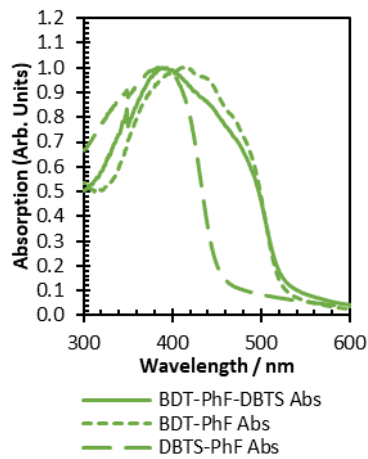
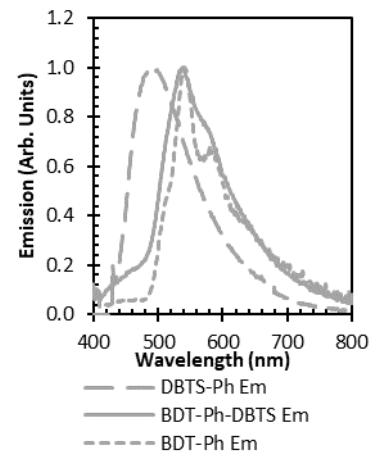
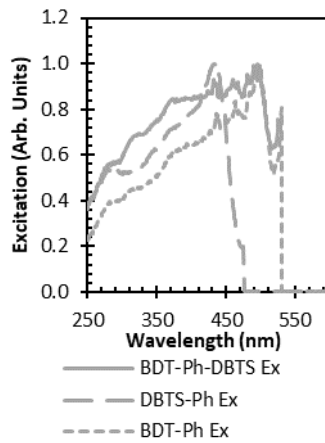
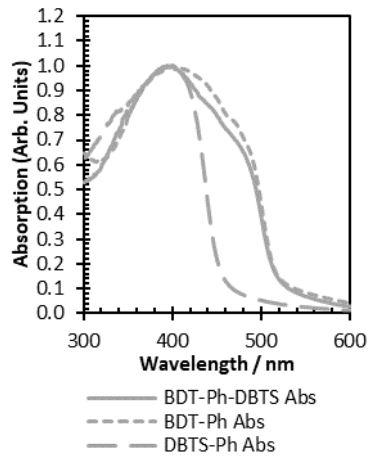
According to this interpretation, DBTS-PhFx-BDT polymers containing Ph and PhF phenylene units form J-aggregates, whereas PhF2a, PhF2b, and PhF4 polymers lead to the formation of interchain excitons and H-aggregates. Higher fluorine content also appears to lead to a greater degree of polymer disorder. Generally, H-aggregates are associated with larger Stokes' shifts and decreased photoluminescence intensity.

H-aggregates result from intermolecular charge transfer between neighbouring polymer chains. If this leads to charge separation, this may explain why fluorescence lifetimes are longer for polymers containing more fluorine atoms. However, exciton diffusion will be faster in J-aggregates since the lowest energy singlet state is emissive, and FRET depends on the coupling of transition dipole moments of optically-allowed transitions on nearby chromophores.

Photoluminescence quantum yield measurements would provide important insights into the radiative vs non-radiative relaxation rates in these systems. Coupled with non-linear spectroscopic measurements, these results would help to identify the formation of excitons, exciton polarons, and charge-separated polarons. Such measurements would provide more information about the exciton dynamics in these materials and study how these impact the resulting photocatalytic activities.

As more fluorine atoms are added to the phenylene moiety, there is expected to be an increase in intermolecular π - π stacking between electron-rich aromatic pi-systems on the DBTS and BDT units and the electron-deficient aromatic system on the fluorinated phenylene ring.

3.9.4 Binary vs Ternary Polymers



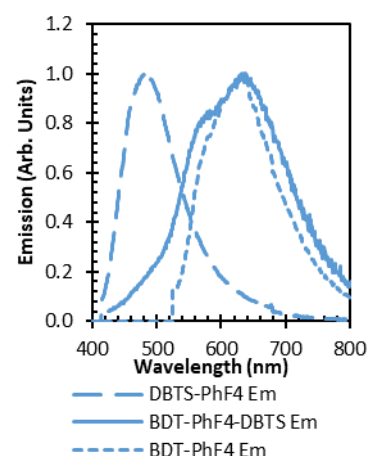
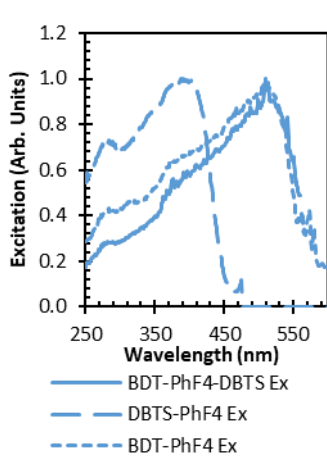
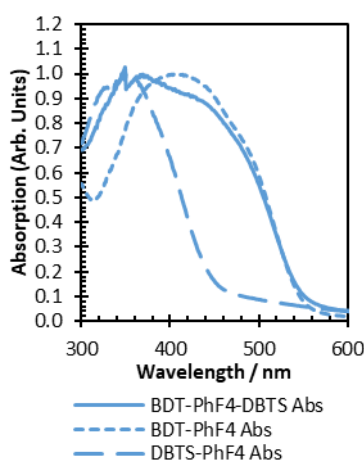
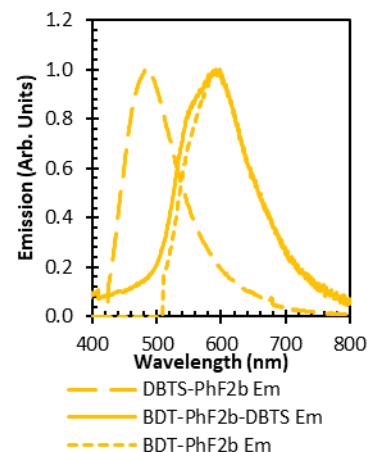
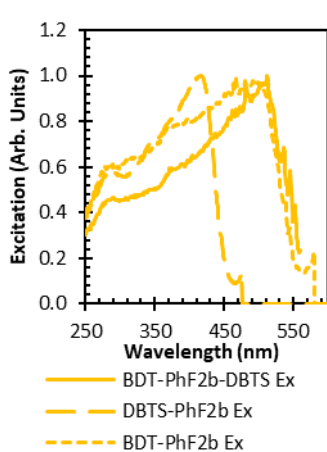
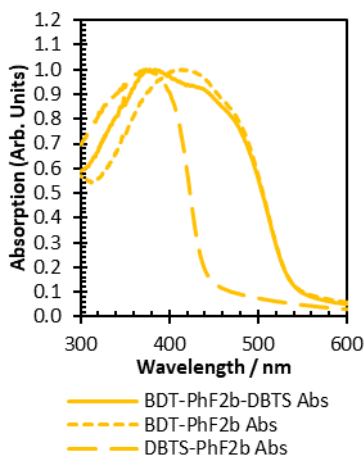


Figure 220: Comparison of normalised UV/Vis DRS spectra for the BDT, DBTS, and ternary co-polymers for each of the PhFx co-monomers.

Figure 221: Comparison of normalised fluorescence excitation spectra for the BDT, DBTS, and ternary co-polymers for each of the PhFx co-monomers.

Figure 222: Comparison of normalised fluorescence emission spectra for the BDT, DBTS, and ternary co-polymers for each of the PhFx co-monomers.

Figures 220 - 222 contain the absorption, photoluminescence excitation, and photoluminescence emission spectra for the DBTS-PhFx, BDT-PhFx, and DBTS-PhFx-BDT co-polymers for each phenylene linker unit. These graphs allow us to make a more detailed comparison between the binary and ternary derivatives. For example, the similar optoelectronic properties of BDT-PhFx (short-dashed line) and DBTS-PhFx-BDT (solid line) co-polymers become evident. However, key differences also become apparent.

In terms of the UV/vis spectra, the absorption peaks of the ternary polymers become increasingly broad as the number of fluorine atoms increases. These changes can be attributed to the fact that DBTS-PhFx bandgaps widen with added fluorine, whereas BDT-PhFx bandgaps narrow with increasing fluorine content. Both sets of chromophores contribute to the total absorption profile of the ternary polymers.

In the case of the Ph and PhF co-polymers, the excitation maxima of the DBTS and BDT binary co-polymers are close in energy. The degree of overlap between the excitation spectra of DBTS-PhFx and BDT-PhFx polymers decreases as fluorine content increases. This is because the excitation spectra of DBTS-PhFx polymers exhibit blue shifts with fluorine content, whereas the excitation spectra of BDT polymers are red-shifted. This may explain why the excitation spectra for ternary polymers containing the Ph or PhF moieties are broader than those for the ternary polymers containing more fluorine atoms.

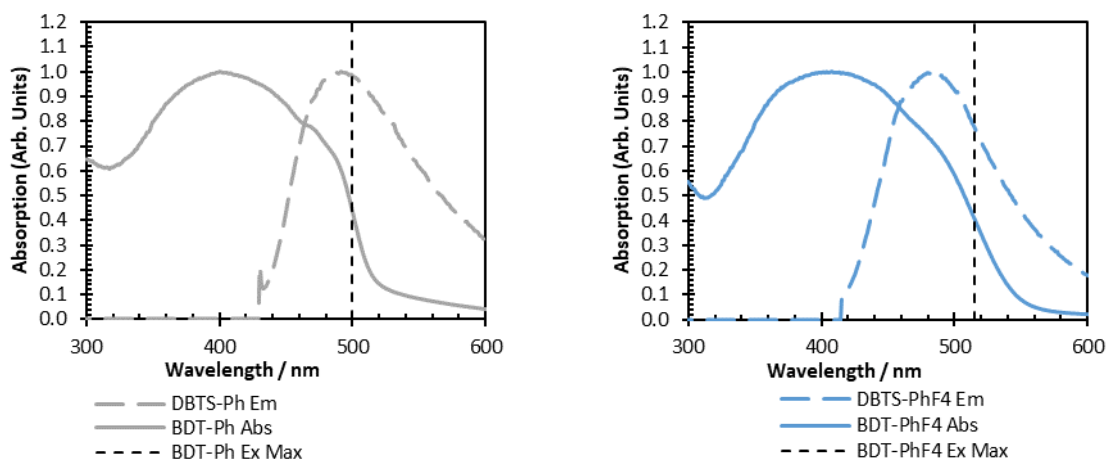


Figure 223: DBTS-PhFx emission overlap with BDT-PhFx excitation

Figure 223 demonstrates the overlap between the emission wavelengths from DBTS-PhFx chromophores and the absorption spectrum for BDT-Phx chromophores. This is shown for the Ph (Figure 223a) and PhF4 (Figure 223b) co-polymers. Vertical black dashed lines represent the maxima of the BDT-PhFx fluorescence excitation. In the case of the DBTS-Ph and BDT-Ph co-polymers, the emission from DBTS-Ph overlaps with the tail of the BDT-Ph absorption spectrum. As shown by the dotted black line, this region also corresponds to the excitation wavelengths that result in the most intense fluorescence from BDT-Ph chromophores.

By contrast, the emission spectrum of DBTS-PhF4 exhibits a greater degree of overlap with the complete absorption spectrum of BDT-PhF4 and a worse overlap with the fluorescence excitation spectrum of BDT-PhF4. Consequently, this implies that energy transfer from a DBTS-PhF4 chromophore onto a BDT-PhF4 chromophore is more likely to excite the latter into a non-emissive dark state.

When comparing the photoluminescence emission spectra, several of the ternary polymers possess a high-energy emission tail that is absent from the BDT-PhFx equivalents. These emission tails overlap

with the DBTS-PhFx emission spectra, indicating that charge transfer from DBTS-PhFx chromophores to BDT-PhFx chromophores does not always occur with 100% efficiency. This is to be expected since theoretical studies suggest that excitons will only hop between a few chromophores before emission, implying that some emission will occur from low-lying DBTS-PhFx chromophores rather than the BDT-PhFx chromophores at lower energies. This also implies that some energy is transferred by a non-FRET type process in which the emission of a photon from one chromophore is followed by the reabsorption of that photon by another chromophore with lower exciton energies.

3.9.5 Optoelectronics Discussion

On the critical parameter of hydrogen evolution rate, DBTS-PhFx polymers outperformed those containing the BDT unit. BDT-PhFx polymers are poor photocatalysts with low activities when using TEA as a sacrificial reagent. Ternary polymer photocatalyst maintained the small bandgap associated with BDT but exhibited significantly improved photocatalytic activities comparable to, but smaller than, equivalent DBTS-PhFx polymers. This reinforces previous studies that have indicated that the DBTS moiety is very important for hydrogen evolution. Such papers have pointed to the localisation of electron density on the sulfone functional groups,²⁷⁵ and others have highlighted their improved hydrophilicity.¹³⁵

Although the ternary polymers can absorb a broader range of visible light, they are also more hydrophobic, particularly as the amount of fluorine on the phenylene linker increases. This hydrophobicity likely leads to slow reaction kinetics at the water-polymer interface and large aggregated particle sizes that are difficult to disperse. Since the exciton diffusion lengths in conjugated polymers are typically on the order of 5-10 nm, large particles will result in increased rates of bulk recombination.

The band edge potentials of BDT-polymers and their ternary analogues are very similar. Although all samples are expected to possess a suitable CBM for hydrogen evolution, the ternary polymers are expected to have slightly larger bandgap due to a deeper VBM that generates a larger overpotential for the oxidation of TEA. However, in practice, both sets of polymers exhibit the same bandgap, casting some doubt over the corresponding band potentials.

Frontier orbital calculations of the ternary polymers imply that, despite the same IP/EA band potentials, the LUMO electron density is located on the DBTS unit. In contrast, the HOMO is located

on the BDT unit. The similarity in the LUMO orbital energies between binary and ternary polymers indicates that the electron density should be easily delocalised along the polymer backbone.

In the solid state, a clear discrepancy exists between the total absorption spectrum, as determined by UV/Vis DRS, and the fluorescence excitation spectrum that probes the electronic transitions from the absorption of incident photons that result in the population of optically-active excited states. These results imply that the vast majority of absorption events result in the population of non-emissive dark states. However, PLQY measurements at different wavelengths are required to determine absolute values for this process.

It is very likely that these absorption/excitation spectra discrepancies originate from the fact that polymer chains form aggregates in the solid state. These aggregates are unlikely to be distinctly H-type or J-type, but rather they will represent an HJ-aggregate in which there is a balance between short-range charge-transfer interactions arising from orbital overlap and longer-range coulombic interactions.²⁵⁹ These interactions can be both intrachain and interchain. The extent of these couplings will depend on the π - π stacking distance as well as the longitudinal and latitudinal translation vectors between the centre-of-mass transition dipole moments on nearby chromophores. This is further complicated in semicrystalline polymers, since the stacking of chromophores is not consistent in all directions as they are in molecular crystals.^{272,274}

However, in the case of BDT-containing co-polymers, including the ternary polymers, it is apparent that changing the number of fluorine atoms on the phenylene group alters the nature of this interchain stacking and the fluorescence profile transitions from one more representative of J-aggregates, as in the case of an isolated linear polymer chain, to one that contains increased H-aggregate character. This transition has also been seen in certain molecular organic semiconductors after modifying their structure.²⁷³

This work highlights the importance of understanding exciton dynamics in polymeric photocatalysts. Several questions are raised, particularly with regard to the fate of dark-state excitons. Are these excitons capable of migrating through the polymer and contributing to photocatalytic activity? Are charge-transfer excitons more easily dissociated? Are polarons trapped if formed in the bulk, or can they also migrate to the polymer particle surface?

Since polymeric photocatalysts are typically used in their solid-state heterogeneous particulate form, understanding exciton and polaron dynamics is incredibly important. Furthermore, even soluble polymers have been shown to form aggregates above critical concentrations.²⁷⁶ These results show that polymers containing fluorinated phenylene units could be interesting subjects for such fundamental spectroscopic experiments in the future.

3.10 Conclusions and Future Work

3.10.1 DBTS-PhFx

Analysis of the results from a previous high-throughput experiment in Chapter 2 revealed that DBTS co-polymers containing fluorinated phenylene co-monomers are promising photocatalysts for enhanced hydrogen evolution. In that study, none of the 99 synthesised polymers exceeded the hydrogen evolution reaction rate of the DBTS-DBTS homopolymer after the photodeposition of a 1 wt.% Pt co-catalyst when using a 1:1:1 v/v reaction mixture of MeOH/TEA/H₂O, where MeOH is a dispersant, and TEA is the sacrificial electron donor. To the best of this author's knowledge, no other linear conjugated polymer has outperformed DBTS-DBTS under these sacrificial conditions to date. However, it should be noted that photocatalysis testing setups make it challenging to compare rates produced by different research groups.

The work presented in this chapter has revealed that DBTS-PhFx polymers are capable of performing similarly to, or even better than, DBTS-DBTS under these same reaction conditions. However, the photocatalytic activities of these polymers are incredibly sensitive to the polymerisation synthesis conditions. The most active version of DBTS-DBTS that could be synthesised achieved an HER rate of 23 mmol hr⁻¹ g⁻¹. Meanwhile, the most active sample of DBTS-PhF achieved a remarkable HER rate of 33 mmol hr⁻¹ g⁻¹. However, this high rate could not be reproduced in later samples.

Photocatalytic rates of DBTS-PhFx co-polymers were improved by first reducing the reaction temperature and subsequently improved further by reducing the concentration of the palladium cross-coupling reagent. It was also found that, unlike DBTS-DBTS, co-polymers containing phenylene units were more sensitive to the platinum co-catalyst loading concentrations. Optimal HER rates were observed when loading with 0.5 wt.% Pt. However, it is possible that even lower concentrations could lead to further enhancements in these rates.

The exact relationship between photodeposited platinum and residual palladium is unclear. Results in Chapter 2 also highlighted that residual palladium concentrations are associated with limited HER rates. Charge transfer to residual palladium clusters could lead to the trapping of photogenerated charges if these clusters are embedded in the polymer matrix and not situated at the interface with water. It is also possible that energy is transferred from polymers into metal clusters via long-distance Forster-like dipole-dipole coupling rather than exciton charge separation and injection. It has been reported that this can be a dominant cause of exciton decay at the interface between organic semiconductors and metals.^{277,278}

Subsequent synthesis of DBTS-PhFx polymers under different reaction conditions has revealed that the selection of organic solvent, base, the concentration of that base, and the volume ratio of organic and aqueous phases can all influence the photocatalytic hydrogen evolution reaction rate. Samples synthesised with poor yields typically performed worse, indicating that the presence of impurities can inhibit the HER reaction. However, variations between samples obtained in high yields under different conditions were also significant.

Since the HER rates of the DBTS-PhFx polymers were dependent on the synthesis conditions, it is difficult to identify which co-polymer structure is the most active. When synthesised from a reaction mixture containing 4.5 ml DMF and 0.5 ml of 2M K₂CO₃, DBTS-Ph (22.1 mmol hr⁻¹ g⁻¹) and DBTS-PhF (24.5 mmol hr⁻¹ g⁻¹) were the most active co-polymers. When synthesised from a reaction mixture containing 4.5 ml toluene (+1.5 vol% Starks' catalyst) and 0.5 ml of 2M K₂CO₃, DBTS-PhF (22.4 mmol hr⁻¹ g⁻¹) and DBTS-PhF2b (23.9 mmol hr⁻¹ g⁻¹) were the best-performing hydrogen-evolution photocatalysts. Each of these photocatalysts performed similarly to the DBTS-DBTS homopolymer synthesised from 3 ml toluene (+ 1.5 vol.% Starks' catalyst) and 2 ml of 2M K₂CO₃ (23.0 mmol hr⁻¹ g⁻¹).

Under most conditions, DBTS-PhF and DBTS-PhF2b were the top-performing photocatalysts. DBTS-Ph also consistently produced large volumes of hydrogen. DBTS-PhF4, however, was typically synthesised with lower yields and exhibited poorer photocatalytic activities. DBTS-PhF2a was the most sensitive polymer with respect to the synthesis conditions. This polymer performed best when synthesised from toluene/2M K₂CO₃ (16.7 mmol hr⁻¹ g⁻¹). However, under all other synthesis conditions, its photocatalytic activity did not exceed 10 mmol hr⁻¹ g⁻¹. Based on the analyses of these polymers in Chapter 2, DBTS-PhF2a and DBTS-PhF4 appear to be more susceptible to incorporating larger quantities of residual palladium.

Despite being isomers of one another, DBTS-PhF2a and DBTS-PhF2b exhibited different optoelectronic properties when synthesised from a reaction mixture containing 1,4-dioxane/2M TBAA. DBTS-PhF2a exhibits a wider direct bandgap and a more shallow absorption edge. DBTS-PhF2a also exhibited a shorter fluorescence lifetime than DBTS-PhF2b. However, the indirect bandgaps, fluorescence excitation spectra maxima, and photoluminescence emission spectra are invariant. These differences are predicted to arise from increased polymer backbone disorder and a higher residual palladium concentration. However, further studies are necessary to verify this.

It is also worth noting that the PhF2a and PhF4 moieties are centrosymmetric. Unlike the PhF and PhF2b moieties, these phenylene rings do not have a permanent dipole moment. This will likely impact the polymer chain's ground state geometry and energetic distributions of different geometric configurations, intermolecular chain packing in the condensed phase, the size and magnitude of the transition dipole moments, and how the polymer chains interact with polar water molecules. Each of these factors can impact the exciton dynamics, charge separation, and charge transfer steps of the photocatalytic process.

Due to time constraints and the total number of samples prepared over a short period of time, it was not possible to perform all of the desired measurements for each polymer. Some of the most fundamental measurements that still need to be made include CHNS(F) elemental analysis, ICP-OES for Fe and Pd content, XRD for the degree of crystallinity, contact angle measurements for wettability, dynamic light scattering measurements for particle size and dispersibility, FT-IR measurements to study the different vibrational modes related to different fluorine content, solid-state NMR (C^{13} and F^{18}) could be used to confirm the structure. Electrochemical measurements could be used to determine and compare the polymer redox potentials with predicted values. Additional SEM images could be taken to investigate different surface morphologies for different reaction conditions. Physical characterisation before and after photocatalysis would also be beneficial to provide an indication of polymer stability.

From the perspective of further photocatalysis studies, longer-term measurements should be performed over 5+ hours to confirm hydrogen evolution rates. Screening studies using alternative sacrificial reagents could also provide more information about reaction mechanisms. Similarly, the mass-normalised rates provided for these polymers cannot easily be compared with results from other research groups. As such, AQY measurements at different wavelengths are required. These

measurements, alongside additional absorption and photoluminescence measurements under the same dispersion conditions, could also be used to identify whether AQYs follow the excitation or total absorption spectra, indicating if non-emissive dark states can also contribute to photocatalytic reactions.

Further experiments should also be made regarding the effect of purification on the resulting photocatalytic HER rates. Multi-day Soxhlet purifications were outside of the scope of this study since this process would have negated the rapid micro-wave assisted synthesis process. However, such purification steps in chloroform or tetrahydrofuran could be used to remove impurities such as unreacted reagents, short-chain oligomers, some residual palladium, and other unwanted byproducts. This is particularly important since the yield of many polymers exceeded 100%, indicating the presence of considerable sums of impurities.

These samples have also demonstrated the ability to produce hydrogen peroxide photocatalytically from pure water. Whilst this process is chemically promising itself, it also has promising implications for overall water-splitting applications, as H_2O_2 in pure water can only occur when holes are consumed in the oxygen evolution reaction. These results imply that further investigations into appropriate co-catalysts, such as CoOH, FeOOH, NiOOH, or IrO_2 could be used to catalyse the OER and extract photogenerated holes from the polymer. Likewise, modifications to the HER co-catalyst, such as using Pt or Rh could result in enhanced electron extraction from the polymer. If a layer of Cr_2O_3 is subsequently photodeposited on top, it may also be possible to prevent the oxygen reduction reaction and drive the hydrogen evolution reaction instead. Combined, selective photodeposition of several co-catalysts could result in organic polymers capable of driving the overall water-splitting reaction more efficiently than those currently reported in the literature. This study's high-throughput testing setup capability has significant potential for screening many combinations in various concentrations. It would also be possible to investigate the impact of using co-solvents to aid dispersion, salts to improve ionic strength, and acids and bases to control the pH.

This work has also demonstrated that polymers synthesised using a microwave-assisted reaction can be produced at high yields and exhibit very high photocatalytic hydrogen evolution rates. Compared with the traditional solvothermal synthesis approach, which takes three days per sample, reactions performed in the microwave are completed within one hour. This reaction time could likely be reduced considerably further. Initial problems regarding pressure spikes and rapid solvent heating were overcome by limiting the microwave power and decreasing the volume of water relative to that of the

organic solvent. By changing these factors, it was possible to use a DMF/K₂CO₃ reaction mixture without needing an intermediary heating step, a method previously ruled out by Bai *et al.* in their high-throughput study.

Whilst the data collected by Bai *et al.* in their high throughput study was instrumental in informing this work, this work has demonstrated that optimal reaction and testing conditions were not used. For example, their samples were synthesised at 160°C and used TBAA as the reaction base. This work has demonstrated that these reaction conditions are conducive to impure polymers with significantly inhibited photocatalytic activities, even when synthesised at high yields. Furthermore, photocatalysis measurements were performed over a 1 hr irradiation. This has been shown to saturate the headspace vials and provide underestimated results. Their Pt-loaded samples also contained 1 wt.% Pt, whereas this work has shown that even lower concentrations can further improve photocatalytic activity for polymers other than DBTS-DBTS. The good performance of DBTS-DBTS despite non-ideal reaction conditions indicates that charge transfer rates to high concentrations of residual palladium are slow. However, this is not guaranteed for other DBTS-containing co-polymers. Fluorescence lifetime, photoinduced absorption, transient absorption, and transient Raman spectroscopies could be used to provide more information about the formation and lifetimes of polaron pairs, polarons, charge transfer excitons, Frenkel excitons, and negatively-charged palladium clusters.

3.10.2 Binary vs Ternary Polymers

This chapter has also investigated the BDT-PhFx set of linear binary co-polymers and the DBTS-PhFx-BDT set of linear ternary co-polymers. These polymers were synthesised from the BDT-B(Pin)₂ diboronic acid bis pinacol ester precursor. This resulted in poor synthetic yields for most polymers, which decreased further upon introducing additional fluorine atoms. This reduction in yield is attributed to the likely protodeborylation reaction of the oligomeric intermediates. As such, future improvements could be made in the future by using alternative boronate leaving groups or by investigating the use of alternative palladium catalysts for Suzuki cross-coupling.

Reasonable yields were obtained by using TBAA as the aqueous base. It is not clear why this is the case, but it is a weaker base than K₂CO₃ and K₃PO₄, and is highly soluble in organic solvents, acting as a phase-transfer catalyst in some cases. The best photocatalytic activities and yields were obtained when BDT-based co-polymers were synthesised using 1,4-dioxane as the solvent. All polymers across

these two sets were synthesised under these conditions, despite the fact that DBTS-PhFx polymers synthesised under the same conditions produced underperforming photocatalysts.

The photocatalytic activities of the BDT-PhFx polymers were low. However, this was to be expected since these polymers were not predicted to have appreciable driving forces for TEA oxidation and do not have the DBTS unit known to be influential in TEA oxidation, improving the surface contact with water, and driving the HER. BDT-PhFx polymers demonstrated interesting optical properties with respect to fluorine content. BDT-Ph and BDT-PhFx exhibited extremely short fluorescence lifetimes and an emission spectrum with a well-defined vibronic structure indicative of a J-aggregate with a low degree of disorder. Meanwhile, as the number of fluorine atoms on the phenylene unit increased, fluorescence became increasingly red-shifted. The steady-state fluorescence emission vibronic structure also changed such that the 0-1 transition was more intense than the 0-0 transition, indicative of an H-type aggregate. This confirms that fluorine units can not only be used to fine-tune the optical band gap and band edge potentials, but can also influence the long-range interchain stacking geometries.

The ternary DBTS-PhFx-BDT linear co-polymers were also prepared from a 1,4-dioxane/2M TBAA reaction mixture. However, these polymers were prepared statistically, containing 50% DBTS and 50% BDT units linked by the phenylene moieties. Attempts to synthesise precursors that would guarantee an alternating co-polymer with a well-defined repeat structure were unsuccessful. The UV/Vis DRS, photoluminescence excitation and photoluminescence emission spectra in the solid state closely mirrored those of the BDT-PhFx equivalents. The resulting direct and indirect bandgaps were identical. However, minor differences in line shape, such as increased peak broadening, were observed. However, ternary polymers exhibited increased fluorescence lifetimes.

The ternary polymers also exhibited photocatalytic hydrogen evolution rates that were considerably more active than those of the BDT-PhFx polymers. However, relative to the DBTS-PhFx polymers synthesised under the same conditions, the results were mixed, with some of the ternary polymers outperforming the DBTS-PhFx equivalent. However, when compared with the photocatalytic HER rates for the DBTS-PhFx polymers synthesised under their optimal conditions, DBTS-PhFx polymers consistently outperformed the ternary polymers.

Despite this lower activity, these results are very promising regarding future investigations. In particular, these rates were observed using TEA as the sacrificial reagent despite not having ideal

oxidation potentials. Repeat experiments using ascorbic acid or other reagents and co-solvent dispersants could lead to improved photocatalytic reactions. Improved activities could also be achieved by altering the reaction conditions if TBAA could be replaced whilst maintaining a high synthesis yield. Furthermore, since these polymers have been prepared with a 50/50 mix of DBTS/BDT, this method could also be used to investigate alternative ratios. Previous reports have demonstrated that as little as 5% of a co-monomer can significantly impact the resulting hydrogen evolution activities.¹⁶⁵

DFT studies have also demonstrated that the LUMOs of DBTS, BDT, and PhFx homopolymers are close in energy to one another. As such, the LUMO is delocalised along the polymer chain in these ternary systems. This means that all three components can contribute to the charge transfer steps of a photogenerated electron into a co-catalyst such as platinum without adding excessive driving force that would irreversibly inject the charge into bulk residual palladium clusters.

Chapter 4: Hybrid Photocatalysts

4.1 Introduction

The high exciton binding energy in semiconducting polymers results in short-lived excitons that recombine on the pico-to-nanosecond timescale, limiting their photocatalytic efficiency considerably.^{279,280} The high HER activities observed for these polymers under sacrificial conditions have been attributed to the formation of longer-lived polarons formed after the rapid charge extraction mediated by sacrificial reagents at the polymer-solution interface.^{281,282} Whilst significant advances are being made with respect to hydrogen evolution under sacrificial conditions,^{66,67,69,70,237,260,262,283} the current direction of research risks optimising polymers for their performance with sacrificial reagents, rather than focussing on ways in which they may be used to enable overall water splitting, OWS.^{72,284}

In the absence of a sacrificial reagent, i.e. in pure water, holes are not rapidly extracted since the four-electron water oxidation reaction is slow. Without hole transfer to generate a negative-charge polaron, the excited state is short-lived, and photocatalysis rates are reduced. In the presence of oxygen, the HER competes with the more energetically favourable two-electron oxygen reduction reaction that forms hydrogen peroxide. If the reduction potential for the holes is positive enough, excitons may also preferentially oxidise water to form hydrogen peroxide instead of producing oxygen. The common half-reactions are presented in Table 24. According to the Nernst equation, these reduction potentials become more negative at higher pH values, as they depend on the activities of the H⁺ and OH⁻ ions. This equation predicts a -0.59 mV shift in redox potentials per unit of pH.

Table 24: Reduction potentials of common half-reactions in aqueous solutions and their pH dependencies

Reduction half reactions		Reduction potential vs SHE (V)				
		pH 0	pH 3	pH 7	pH 10	pH 14
$O_2 + H^+ + e^- \rightleftharpoons \cdot OOH$	(24)	-0.13	-0.31	-0.54	-0.72	-0.96
$2H^+ + 2e^- \rightarrow H_2$	(25)	+0.00	-0.18	-0.41	-0.59	-0.83
$O_2 + 2H^+ + 2e^- \rightarrow H_2O_2$	(26)	+0.68	0.50	0.27	0.09	-0.15
$O_2 + 4H^+ + 4e^- \rightleftharpoons 2H_2O$	(27)	+1.23	1.05	0.82	0.64	0.40
$H_2O_2 + 2H^+ + 2e^- \rightleftharpoons 2H_2O$	(28)	+1.77	1.59	1.36	1.18	0.94

To ensure efficient water-splitting systems, an alternative route to charge separation and extraction is required that does not depend on the use of SRs. One method is through the engineering of co-catalysts. For example, Pt is more effective at driving the hydrogen evolution reaction, whereas Pd is the preferred co-catalyst for oxygen reduction.^{248,285} However, pioneering work with inorganic photocatalysts has identified that core-shell co-catalysts with a metallic core and outer Cr₂O₃ layer can

be used to enable water transport to the cocatalyst but prevent oxygen diffusion.^{45,46} To this author's knowledge, this method has not yet been applied to organic photocatalysts.

Likewise, several co-catalysts have been investigated to catalyse the four-electron water oxidation reaction to enhance oxygen evolution. The most common water oxidation co-catalyst is cobalt oxide¹⁶¹, and several polymeric photocatalysts have exhibited slow oxygen evolution reactions when using AgNO₃ as a sacrificial electron donor.^{98,261,286}

Polymers capable of driving overall water splitting without any sacrificial reagent are very rare.^{160,287–290} The photocatalysis rates also remain several orders of magnitude slower than the best hydrogen evolution rates observed and do not always produce hydrogen and oxygen in a 2:1 ratio, implying self-oxidation or competitive oxygen reduction.²⁹¹ However, Bai *et al.* have demonstrated overall water splitting from DBTS-DBTS homopolymer for the first time by using an IrO₂ co-catalyst to drive the oxygen evolution reaction.¹⁶⁰ and residual palladium as the hydrogen evolution co-catalyst, demonstrating that these polymers have promise outside of sacrificial hydrogen evolution.

Alternatively, polymeric photocatalysts have been used in Z-schemes to drive the overall water-splitting reaction when paired with inorganic oxygen evolution photocatalysts such as BiVO₄ when and using a solution-based redox mediator for charge transport.²⁹² However, these systems are not ideal since the redox mediation must diffuse between photocatalyst particles and its reverse photooxidation and reduction can compete with hydrogen and oxygen evolution reactions.

Current efforts are being placed on the construction of direct heterojunction Z-scheme photocatalysts.^{293–296} However, many of these focus on graphitic carbon nitrides as the organic component, which are typically less active and less versatile than linear polymers, COFS, and microporous polymers.

In this chapter, we investigate the formation of organic/inorganic hybrid photocatalysts for overall water-splitting applications via in-situ polymerisation methods. Some of the polymers discussed in the previous chapter are synthesised in the presence of inorganic photocatalysts in an attempt to form a direct heterojunction Z-scheme. Two oxides are investigated, the highly-efficient overall water-splitting photocatalysts, Al-doped SrTiO₃, and the narrower bandgap oxygen evolution oxide photocatalyst BiVO₄.

4.2 Rationale and Hybrid Design

4.2.1 Design

Preferential band alignment between the two semiconductors can generate a heterojunction in which photogenerated charges in the organic material will be extracted from their exciton pairs and injected into the inorganic material. Theoretically, this may leave behind the charged polymeric polaron with longer lifetimes and greater redox potentials. A simplified band structure indicating a potential charge migration pathway for polymer/BiVO₄ and polymer/Al:SrTiO₃ hybrids are presented in Figure 224 according to the alignment between the Polymer HOMO/LUMO energies and the oxide band edges.

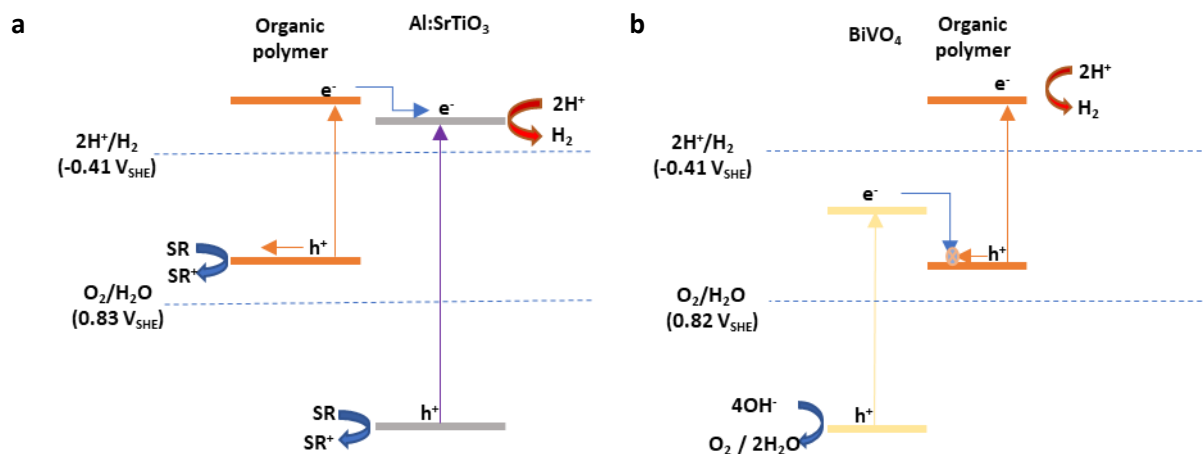


Figure 224: Energy level diagrams for theoretical organic/inorganic hybrid photocatalysts containing conjugated polymer and oxide components. a) A polymer-sensitized wide-bandgap oxide hybrid photocatalyst for enhanced HER rates. b) Organic/inorganic hybrid Z-scheme using a polymer as the hydrogen evolution photocatalyst and BiVO₄ as the oxygen evolution catalyst.

Two hybrid photocatalyst systems are investigated. The first investigates the possibility of injecting electrons from the polymer into the conduction band of flux-synthesised, Al-doped SrTiO₃ (Al:STO) in a system that may act as a polymer-sensitized photocatalyst or as a type II heterojunction. The second hybrid system combined hydrogen-evolving polymeric photocatalysts with oxygen-evolving BiVO₄. This system is envisaged to behave as an overall water-splitting Z-scheme photocatalyst.

Most hybrid systems involving oxide semiconductors reported in the literature use TiO₂ as the default inorganic component. Indeed, TiO₂ has been successfully dye-sensitized to enhance visible light absorption,^{297–304} and TiO₂-based polymer hybrid photocatalysts have also been reported.^{305–312} However, enhancements in sacrificial hydrogen evolution have been limited, and there have not been any reports of enhanced overall water-splitting activity. Likewise, studies into organic/inorganic hybrids based on SrTiO₃ have been very limited.^{313,314}

In particular, no attempts have been made to prepare hybrid materials based on Al-doped, flux-synthesised SrTiO₃ nanocrystals. Al:STO, when prepared in this manner and paired with the optimal cocatalysts, is a remarkable photocatalyst capable of driving the overall water-splitting reaction with

an apparent quantum yield of 96% using UV-radiation.³⁸ Its high activity is attributed to its faceted single-crystal nanoparticles. Charge separation is achieved by a natural inbuilt potential difference across the different crystallographic directions, which leads to selective photodeposition of different co-catalysts on each facet. When the hydrogen-evolution Rh cocatalyst is coated with a Cr₂O₃ shell, the O₂ reduction backreaction is inhibited. The high degree of crystallinity combined with faceted nanostructure results in low defect concentrations and extraordinarily long excited state lifetimes on the order of milliseconds.⁴⁴

The main problem associated with this Al:STO photocatalyst is that it only absorbs in the UV-vis region, so its overall solar-to-hydrogen conversion efficiency is significantly inhibited. By combining a polymer sensitizer with Al:STO particles, it is hoped that rapid charge injection from the polymer into the Al:STO CB may lead to extended excited state lifetimes and enhanced hydrogen evolution rates on the oxide surface by polymer sensitisation by building a type-II heterojunction.

The second set of hybrid photocatalysts involves combining hydrogen evolution polymers with the oxygen evolution catalyst BiVO₄. Whereas most oxide photocatalysts have very wide band gaps and only absorb in the UV region, the bandgap of BiVO₄ is only 2.4 eV and absorbs visible light. Furthermore, it is stable and has a deep enough VBM to drive the oxygen evolution reaction. However, its CBM is also low in energy and not appropriate for driving the hydrogen evolution reaction. These factors make it an ideal candidate for overall water-splitting Z-schemes.^{315–318}

One of the main inhibiting factors that inhibit the water oxidation reaction on BiVO₄ catalysts is the sluggish charge carrier dynamics.^{319,320} However, similar to the methods employed to enhance Al:STO photocatalysts, recent progress has also been made with regard to faceted crystals on which co-catalysts can be selectively photodeposited.³²⁰

Polymer-sensitised Al:STO is unlikely to drive the overall water-splitting reaction since holes will accumulate on the organic components with non-ideal potentials for water oxidation. However, unlike for dye-sensitised oxides, it may be possible to construct a ternary hybrid photocatalyst system in which the polymer acts as a conductive medium between the two oxides. The theoretical flow of photogenerated charges in a ternary hybrid system is modelled in Figure 225a.

Figure 225b depicts the ideal appearance of these ternary hybrid systems. This would include a micro-sized BiVO₄ crystal coated in an ultrathin polymer layer and decorated with oxide nanoparticles. The

polymer's surface area per gram is anticipated to be significantly enhanced by coating inorganic particles. Since exciton lifetimes and diffusion lengths are very short in organic semiconductors, polymer domains with smaller dimensions should result in significantly reduced rates of bulk electron-hole recombination. However, rates of surface recombination may become more apparent.

Following the successful preparation of DBTS-DBTS/TiO₂ hybrids by Shu *et al.*,³⁰⁹ we use a similar *in-situ* polymerisation method to fabricate polymer/Al:SrTiO₃ and polymer/BiVO₄ hybrid photocatalysts by adding the oxide particles to the reaction mixture during the microwave-assisted polymerisation reactions. Other groups have also demonstrated the successful formation of organic/inorganic heterojunctions using in-situ polymerisation methods.^{321–323}

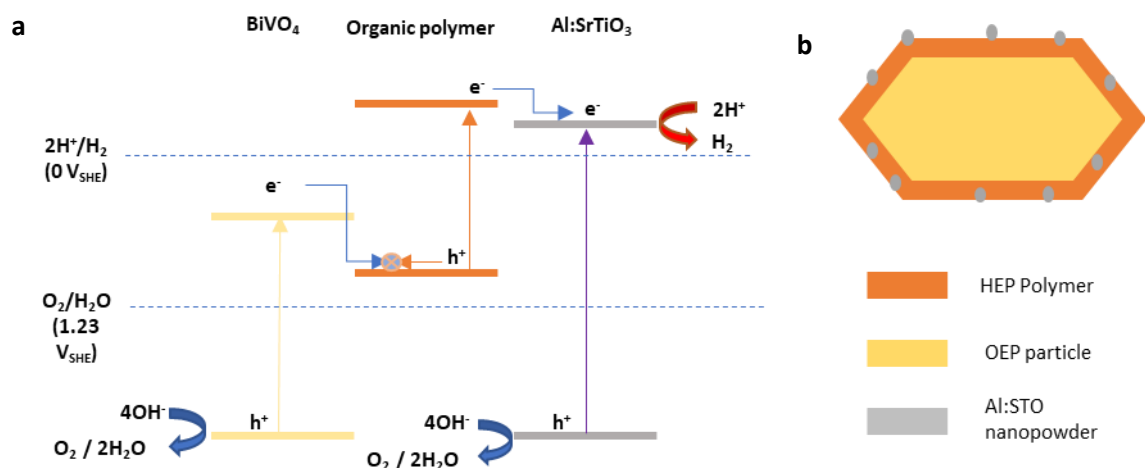


Figure 225: a) Energy level diagram for a theoretical multiscale and multicomponent hybrid photocatalyst that combines a polymeric component with two oxide photocatalysts. b) Hypothetical multiscale hybrid photocatalyst system containing large BiVO₄ crystals coated in a thin layer of polymer and decorated with Al:STO nanoparticles.

4.2.2 Polymer/Oxide Energy Level Alignment

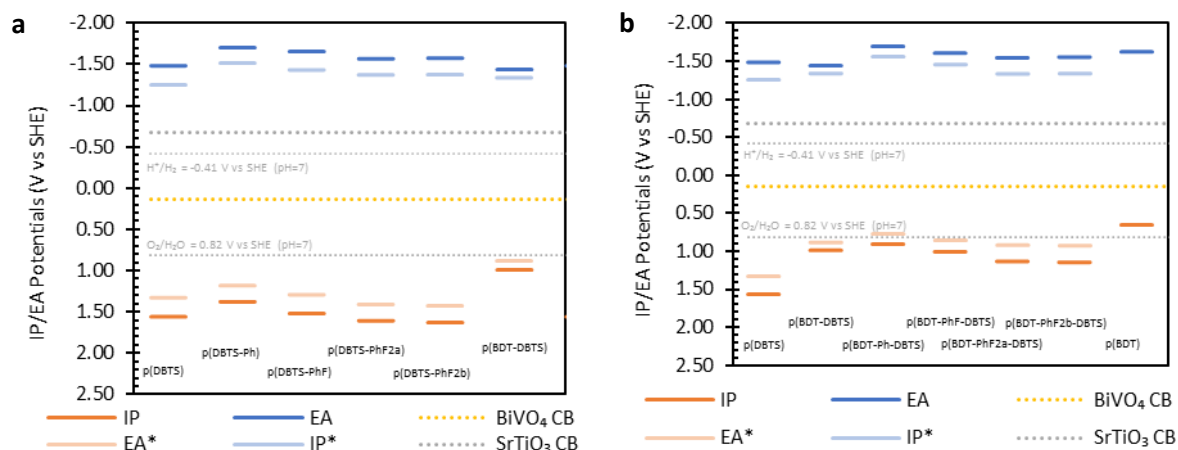


Figure 226: Energy level diagrams for the polymers investigated in Chapter 3 with their estimated IP* and EA* potentials as calculated from the initial EA and IP values and the experimentally-determined indirect optical bandgaps. Bold dotted

grey line represents the CBM of SrTiO₃ at pH=7 as estimated by the Bulter-Ginley method. Bold dotted yellow line represents the CBM of BiVO₄ at pH=7 as estimated by the Bulter-Ginley method. a) DBTS-PhFx polymers, and b) DBTS-PhFx-BDT ternary co-polymers. The redox potentials for water at pH=7 are also highlighted.

Figure 226 contains the IP and EA of the DBTS-PhFx binary polymers and DBTS-PhFx-BDT ternary polymers, respectively, as determined via DFT in Chapter 3. EA* and IP* potentials have also been calculated by taking the difference between the fundamental gap and the measured indirect optical bandgap and shifting the IP and EA potentials equally in opposite directions to maintain the polymer's mid-bandgap position.

These plots also contain the CB potentials for SrTiO₃ and BiVO₄ as predicted using the Butler and Ginley method.³²⁴ Briefly, this involves calculating the geometric mean of the Mulliken electronegativities for the constituent atoms and taking this value as the mid-bandgap potential. The CBM and VBM are then calculated according to their bandgaps. These band potentials correspond to the band edge positions at the point of zero charge (pzc). The pzc corresponds to the pH of the aqueous solution at which the [OH⁻] and [H⁺] concentrations around the surface of the particles are equal, and the particle surfaces contain no net charge. As such, the predicted band positions were further modified according to the Nernst equation to simulate their positions at pH=7.³²⁵

Using the Mulliken electronegativities of the constituent atoms clearly comes with associated limitations. Primarily, these band edge positions are estimated without any reference to the crystal structure or arrangement of atoms. Although experimental methods exist to measure the CB, VB, and Fermi-level positions of semiconductors, such as photoelectron spectroscopy, inverse photoelectron spectroscopy, and the electrochemical Mott-Schottky analysis via electron impedance spectroscopy, literature values for these materials vary widely.^{41,326–328}

The plots in Figure 226 indicate that all of the polymers investigated in Chapter 3 possess LUMO energies higher than the CBM of SrTiO₃ and HOMO energies lower than the CB of BiVO₄. As such, these remain promising candidates from which to form hybrid photocatalysts. These charts also indicate that DBTS-PhFx polymers have favourable band alignments to drive the overall water-splitting reaction.

4.2.3 Type of Heterojunction

Figure 226 only plots the band edge potentials of the inorganic photocatalysts relative to the IP and EA energies of the organic components. Although favourable alignment at this stage is important, the

band edge potentials at a solid-state heterojunction will shift as the Fermi levels of the component systems align and thermodynamic equilibrium is reached. This is achieved by net charge transfer across the interface.

Band alignment between two heterogeneous semiconductors across an interface can first be achieved by first aligning the vacuum levels and defining the HOMO/VBM, LUMO/CBM, and Fermi levels (E_F) positions of each component relative to this level, via their IP, EA, and work function (ϕ). According to the Anderson model, thermodynamic equilibrium is attained through charge transfer of electrons and holes between the two semiconductors across the interface. The band potentials shift relative to one another, and the semiconductors each build up a space-charge layer, represented by band bending. This is the same basic principle behind the construction of a p-n junction in silicon semiconductors.³²⁹

However, the Anderson-Model fails in many cases. In reality, the vacuum levels are not aligned. Instead, it exhibits a discontinuous break resulting from potential difference that forms across the interface between the two components. This is known as the interfacial dipole potential, δ .^{330,331} Resultingly, the extent of band bending observed in real systems, particularly those involving organic semiconductors, is a combination of a large interface dipole paired with a far smaller degree of band bending. This band level alignment approach is summarised in Figure 227, which has been reproduced from the work by Muench *et al.*³³²

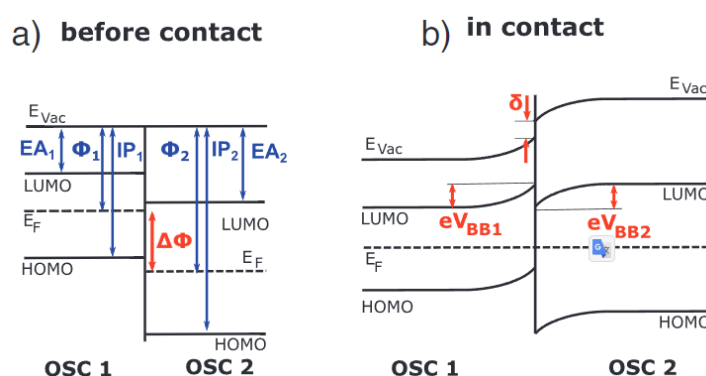


Figure 227: Band alignment at the interface between two organic semiconductors. Reproduced from Muench *et al.*³³²

Recent work has demonstrated that there is a linear relationship between the size of the interface dipole and the potential difference between work function of a semiconductor and the IP of an ultra-thin layer of organic materials.^{333,334} Muench *et al.* further developed this body of work by studying 40 different organic-organic and organic-inorganic interface systems via photoelectron spectroscopy.³³² Their work not only considered the interface dipole at the interface of a bulk semiconductor and a molecular monolayer, but also considered the interface between two bulk semiconductors in order to

study the resulting band bending in organic semiconductors. They conclude that, as a general rule, 60% of the difference in work function between the two semiconductors is accounted for by the interfacial dipole potential, whereas the remaining 40% required to achieve thermal equilibrium and Fermi level alignment arises from band bending.

In this section, we will consider hypothetical heterojunctions that may form between the organic and inorganic components of the theoretical hybrid system. Diagrams have been prepared using the Anderson model in order to highlight the general forces of motion that would be acting on charges as the result of forming a space charge layer. As discussed above, this model is not entirely accurate as interfacial dipoles exist and complicate the picture. In reality, the extent to which interfacial dipole potentials dominate the Fermi level alignment will depend on specific structural or electronic bonding interactions at the interfaces and the presence, nature, and concentrations of various defects and dopants in both semiconductor components.

Two hypothetical interfaces between an organic photocatalyst and Al:STO are presented in Figures 228 and 229. In the first case, the Fermi level of Al:STO lies higher in energy than that of the polymer. In this case, Al:STO potentials shifts downwards, and the polymer potentials shift upwards. As with a p-n junction, this generates a favourable electric field at the interface through which photoexcited electrons will be transferred into the Al:STO CB and holes are transported from Al:STO into the organic polymer. This is known as a Type-II heterojunction.

Undoped SrTiO₃ is non-stoichiometric and is better represented by the formula SrTiO_{3-x} due to the presence of Ti³⁺ impurities and oxygen vacancies that balance each other out. This introduces partially filled Ti³⁺ 3d orbitals into the bandgap that results in an n-doped material. As such, the Fermi level of SrTiO₃ lies very close to the CBM and a Type-II heterojunction is likely.

The HOMOs of the DBTS-PhFx polymers are expected to be capable of driving the oxygen evolution reaction. As such, a Type-II heterojunction between these polymers and Al:STO could theoretically result in a situation in which oxygen evolution rate at the polymer/water interface are observed. However, this would depend on the rate at which photogenerated charges are separated, the rate electrons are extracted, and on the lifetime/stability of the P⁺ polaron.

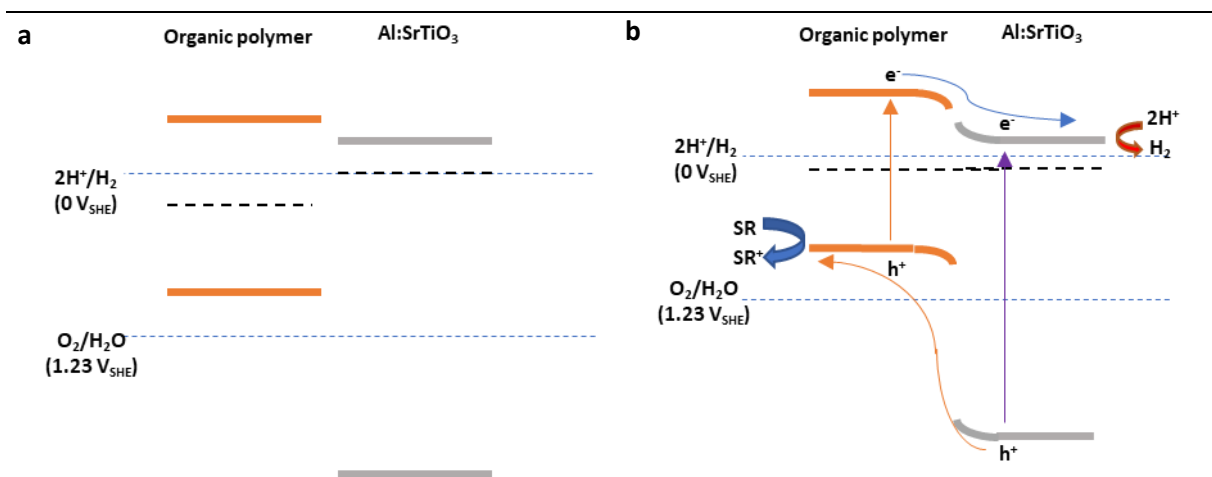


Figure 228: A pn-type heterojunction at the interface between an intrinsic polymeric semiconductor and n-type Al:SrTiO₃. Band bending will only enable favourable energy transfer across the interface if the Fermi level of Al:STO is more at a negative potential than the Fermi level of the organic polymer.

Whilst the above situation would be an ideal band alignment, the electronic structure of Al:STO is different from that of pristine SrTiO₃. Ti³⁺ defects are the primary cause of the low photocatalytic activity of undoped SrTiO₃.⁴¹ Al³⁺ dopants substitute Ti³⁺ ions and the associated defect levels from the middle of the bandgap are removed. However, this also lowers the Fermi level, making the material less n-doped. Excess Al³⁺ may even introduce p-doped character via the formation of additional oxygen vacancies.^{41,42,335,336}

Resultingly, the polymer-Al:SrTiO₃ band alignment may better resemble that of a Z-scheme photocatalyst as presented in Figure 229. In this situation, the relative positions of the polymer's LUMO and Al:STO CB are inverted. As such, the oxide would either inject electrons into the polymer or recombine with the polymer's holes. In this situation, the in-built electric field of the space-charge layer would result in an enhanced photogenerated charge separation at the interface and, when combined with thin layers of polymer on a STO substrate, could lead to enhanced photocatalytic hydrogen production rates on the polymer surface. Overall water splitting may also occur in this situation. However, the rate would still be limited by the rate of exciton generation in Al:STO due to its large bandgap.

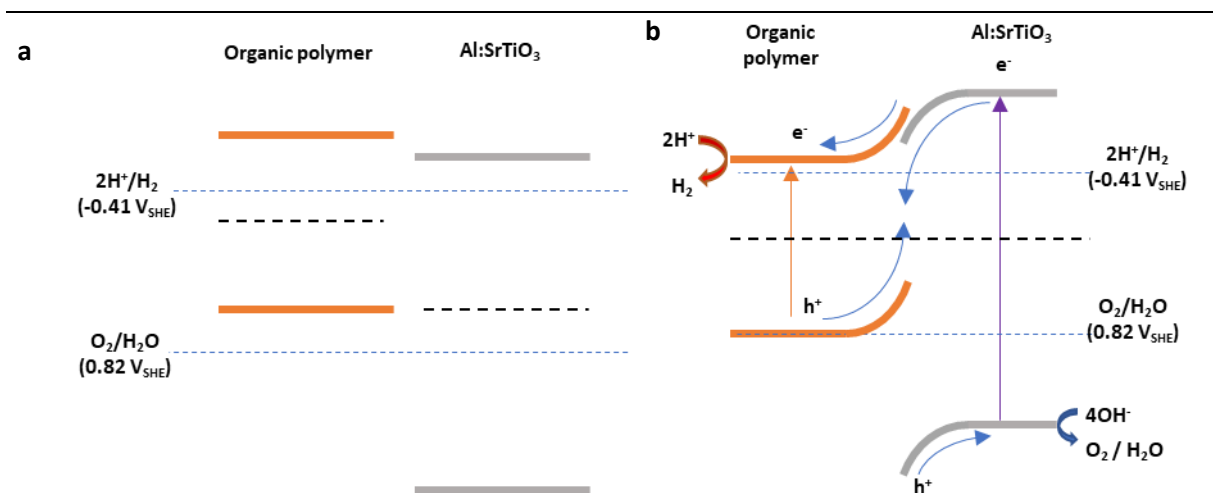


Figure 229: An np-type heterojunction at the interface between an intrinsic polymeric semiconductor and an intrinsic Al:SrTiO₃ semiconductor. Band bending would lead to the formation of a Z-scheme type interface in which hydrogen evolution takes place on the polymeric component and oxygen evolution on the surface of the oxide particles.

The predicted band alignment between the organic polymer and BiVO₄ is presented in Figure 230. This setup is predicted to be a Z-scheme type structure in which hydrogen evolution takes place on the polymer and oxygen evolution on BiVO₄.

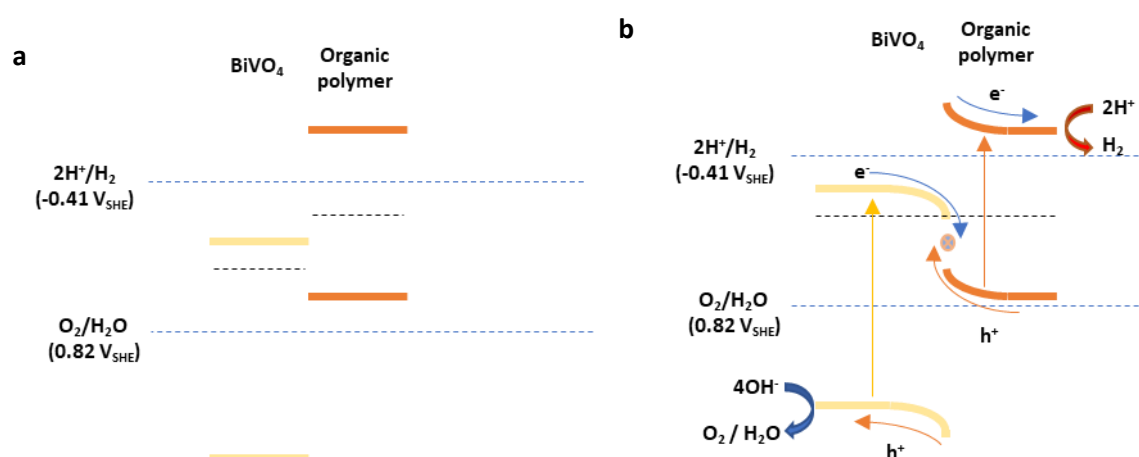


Figure 230: A heterojunction at the interface between an intrinsic polymeric semiconductor and n-type BiVO₄ semiconductor. Band bending after Fermi level alignment would lead to the formation of a Z-scheme type interface in which hydrogen evolution takes place on the polymeric component and oxygen evolution on the surface of the oxide particles.

4.3 Side Chains and Oxide Anchoring Groups: A DFT Study.

Although favourable band alignment and interfaces are plausible, realising them is incredibly challenging. Firstly, a good interface between the organic and inorganic components is necessary. The subsequent work focuses on the in-situ polymerisation method. However, it is also worth considering how the polymer structure may be modified to enhance the charge transfer process from a theoretical

perspective. In this section, we will consider the impact of adding side chains on the BDT unit in the co-polymer DBTS-BDT inspired by methods frequently used in dye-sensitised solar cells and dye-sensitised oxide photocatalysts.

Most dye-sensitised oxide photocatalyst operate on the basis of injecting electrons from the dye into CB of the oxide material. Typically, dyes will have a D- π -A structure in which the HOMO is located on a donor unit, and the LUMO is localised on an acceptor unit. The acceptor unit typically contains an anchoring group through which it can bind to an oxide surface. In the excited state, LUMO is occupied by a photoelectron. The anchoring group enhances the orbital overlap between the LUMO and the oxide CB, and consequently facilitates charge transfer.

This concept is theoretically applied to the DBTS-BDT/BiVO₄ hybrid material using DFT calculations. As discussed in Chapter 3, the BDT unit is versatile because the central benzene ring can be easily functionalised with conjugated side chains.^{146,212,213} In contrast with the dye-sensitised photocatalysts, these conjugated side chains containing oxide anchoring groups are designed to accept electrons from the oxide rather than inject electrons into it. As such, it is beneficial that the BDT unit is functionalised since the HOMO is predominantly located on it. Likewise, the selected π -conjugated side chain is the electron-donating thiophene unit.

Figure 231a contains the five theoretical side chain groups comprised of a thiophene π -linker and various common anchoring groups. The DFT-predicted IP and EA potentials are presented in Figure 231b. The calculations were performed using the same methodology outlined for the calculations in Chapter 3.

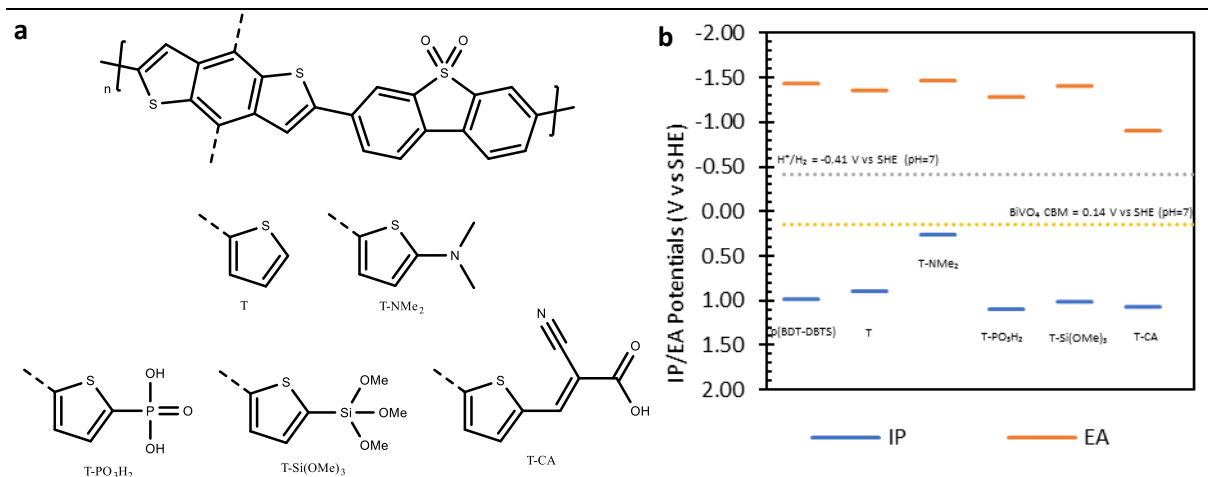


Figure 231: a) Structures of DBTS-BDT-T-A co-polymers investigated in this theoretical study. Thiophene side chains are modified with various oxide anchoring groups common in dyes used for dye-sensitised solar cells and dye-sensitised photocatalysts. b) DFT calculations of ground state IP and EA potentials for DBTS-BDT-T-A co-polymers. Calculations performed to the B3LYP/DNP level of theory using Materials Studio.

As can be seen in the energy level diagram, all polymers are predicted to be capable of driving the hydrogen evolution reaction and accepting an electron from the CB of BiVO₄. The polymer containing a thiophene unit without an anchoring group is predicted to have a slightly smaller bandgap, but relatively unchanged band potentials. T-PO₃H₂ and T-Si(OMe)₃ are also predicted to have very similar HOMO and LUMO energies implying that these anchoring groups are neither strongly electron-accepting or electron-donating.

When modified with the T-NMe₂ anchoring group, the HOMO is shifted significantly to lower binding energies indicating that it is localised on the side chains. This is expected since the nitrogen atom contains non-bonding p-orbitals that are conjugated with the poly backbone. The T-NMe₂ side chain is particularly promising as an appropriate anchoring group on an oxygen-evolving inorganic photocatalyst in a hybrid Z-scheme.

Meanwhile, the LUMO is lowered when the thiophene side chain is modified with an electron-accepting anchoring group in the form of T-AC, which contains the acrylonitrile group. This electronic structure implies that the LUMO is now located on the side chains. This unit would therefore be more useful in the polymer/Al:STO hybrid materials where the aim is to inject electrons. This polymer also has a D- π -A structure that connects the BDT unit in the backbone to the oxide surface.

These energy potentials agree directly with the frontier orbitals presented in Figures 232-236. Importantly, the LUMO is delocalised along the polymer backbone including on the BDT donor unit. This is because the EA potentials for p(DBTS) and p(BDT) are very similar. As such, HOMO and LUMO

have substantial orbital overlaps on the central benzene of the BDT unit, regardless of the selection of the side chain, and photogenerated electrons can be readily transported along the polymer backbone. The only exception to this is p(DBTS-BDT)-T-AC, in which the LUMO is situated on the electron-accepting side chains.

DBTS-BDT co-polymers containing conjugated thiophene side-chains on the BDT units have very promising electronic structures and orbital potentials for hybrid photocatalyst applications. Incorporating PhF_x linkers in the polymer backbone could further enhance these properties by fine-tuning the bandgap and the band edge potentials. Unfortunately, these polymers have only been discussed theoretically in this thesis, as there was not enough time to attempt their synthesis.

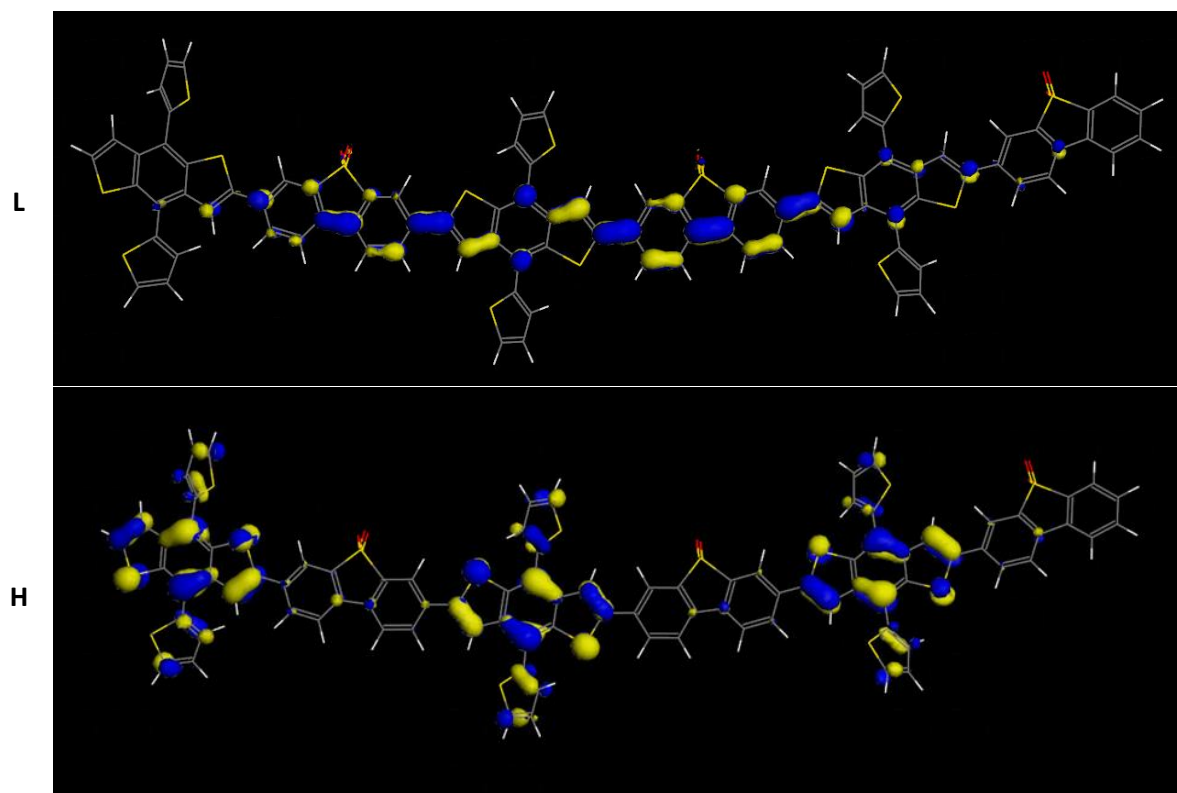
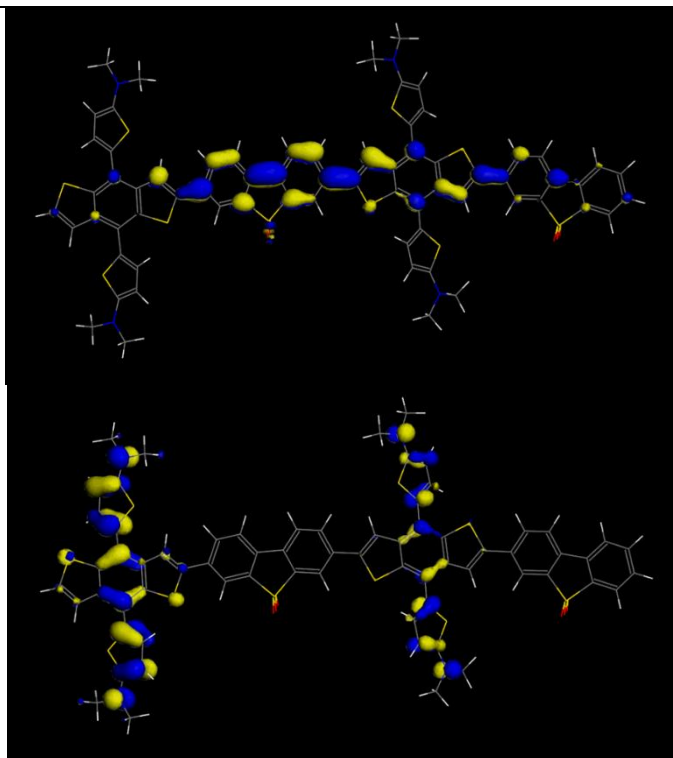


Figure 232: Equilibrium geometry and frontier orbitals of DBTS-Ph-T. Calculated using DFT at the B3LYP/DNP level.

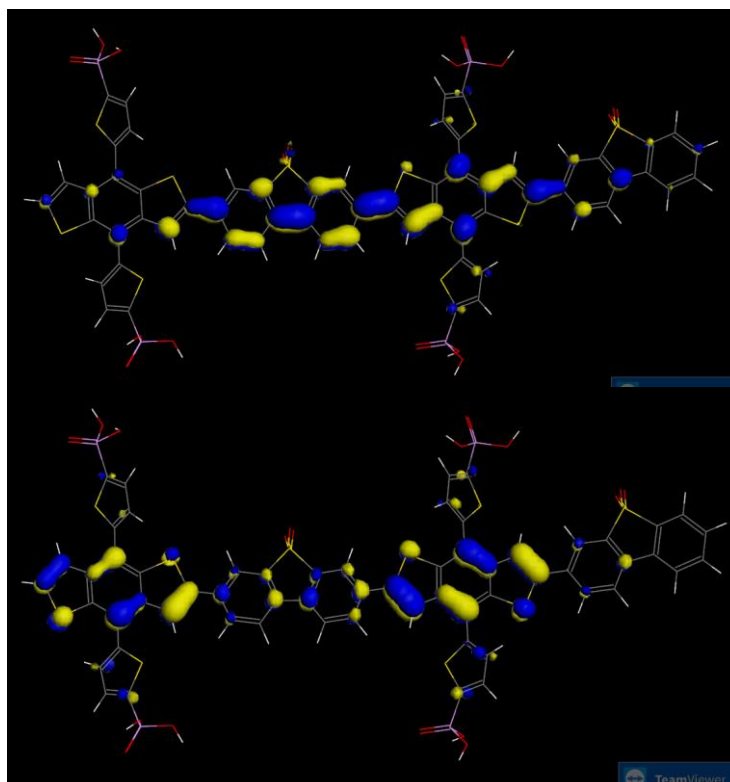
L



H

Figure 233: Equilibrium geometry and frontier orbitals of DBTS-Ph-T-NMe₂. Calculated using DFT at the B3LYP/DNP level.

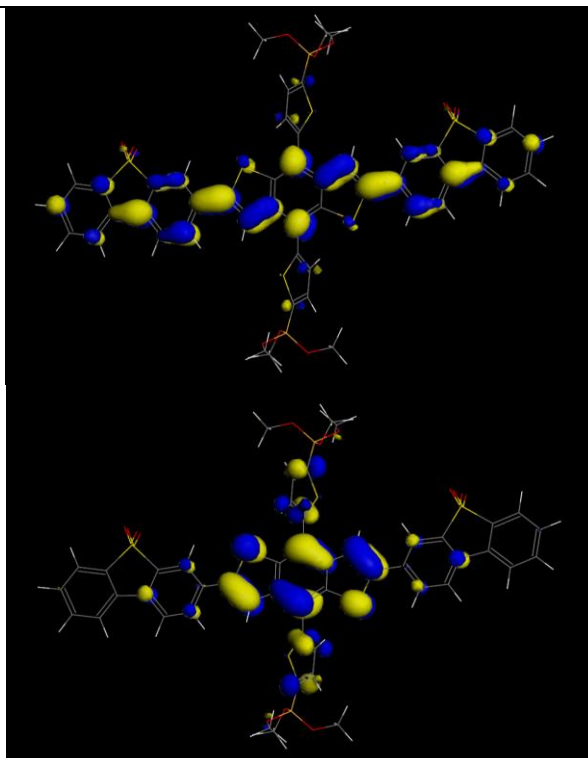
L



H

Figure 234: Equilibrium geometry and frontier orbitals of DBTS-Ph-T-P(OH)₂O. Calculated using DFT at the B3LYP/DNP level.

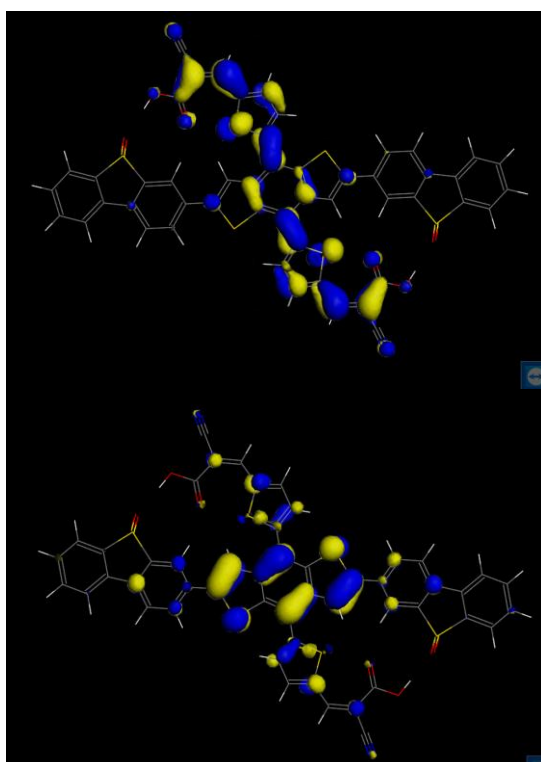
L



H

Figure 235: Equilibrium geometry and frontier orbitals of DBTS-Ph-T-Si(OMe)₃. Calculated using DFT at the B3LYP/DNP level.

L



H

Figure 236: Equilibrium geometry and frontier orbitals of DBTS-Ph-T-AC. Calculated using DFT at the B3LYP/DNP level.

4.4 Chapter Outline

Section 4.5 contains the methodology used throughout this chapter. Section 4.6 is dedicated to optimising the flux synthesis conditions of Al:SrTiO₃. A high-quality sample of the best-performing material was kindly provided by Prof. Kazunari Domen's team, which was used as a point of reference. The highly active photocatalyst are challenging to reproduce. As such, this section describes how comparable results were obtained and investigates how to make the process more reliable.

Section 4.7 discusses the in-situ polymerisation reaction and its optimisation with regard to photocatalytic activity. Sections 4.9 and 4.10 discuss Al:STO hybrid materials, using p(DBTS-DBTS) and p(DBTS-Ph) as example polymers, respectively. Sections 4.10 and 4.11 focus on BiVO₄ hybrid photocatalysts using p(DBTS-DBTS) and p(DBTS-BDT) as polymer candidates, respectively.

4.5 Methods

4.5.1 Inorganic Photocatalysts

4.5.1.1 Flux-treated Al-doped SrTiO₃

1g of SrTiO₃ (99.97%, <100nm, nanografi) was weighed out into each of two large (105ml) cylindrical alumina crucibles (99.9%, Almath Crucibles), to which 110 mg of Al₂O₃ nanopowder (99.9%, Merck/Sigma Aldrich) and 10g of SrCl₂ (99%, Alfa Aesar) was added. The powders were ground together using an agate pestle and mortar before being returned to the crucible. The two lidded 105 ml crucibles were placed inside a larger 800 ml cylindrical crucible (99% Almath), which was also lidded to prevent spillage. This setup is presented in Figure 237. The large crucible was placed inside a muffle furnace (1300 CFS, Carbolite), and the samples were heated to a range of 1000 °C to 1150 °C at a ramp rate of five degrees per minute. The samples were left at temperature for 10 hours before being left to cool back to room temperature. Once cool, samples were washed with deionised water and filtered through 0.2 µm nylon filter papers (Whatmann) using a Buchner filtration setup. Each sample was ultrasonically dispersed in large volumes of deionised water three times to ensure the complete dissolution of residual SrCl₂. The resulting powders were dried in a vacuum oven at 90°C overnight.

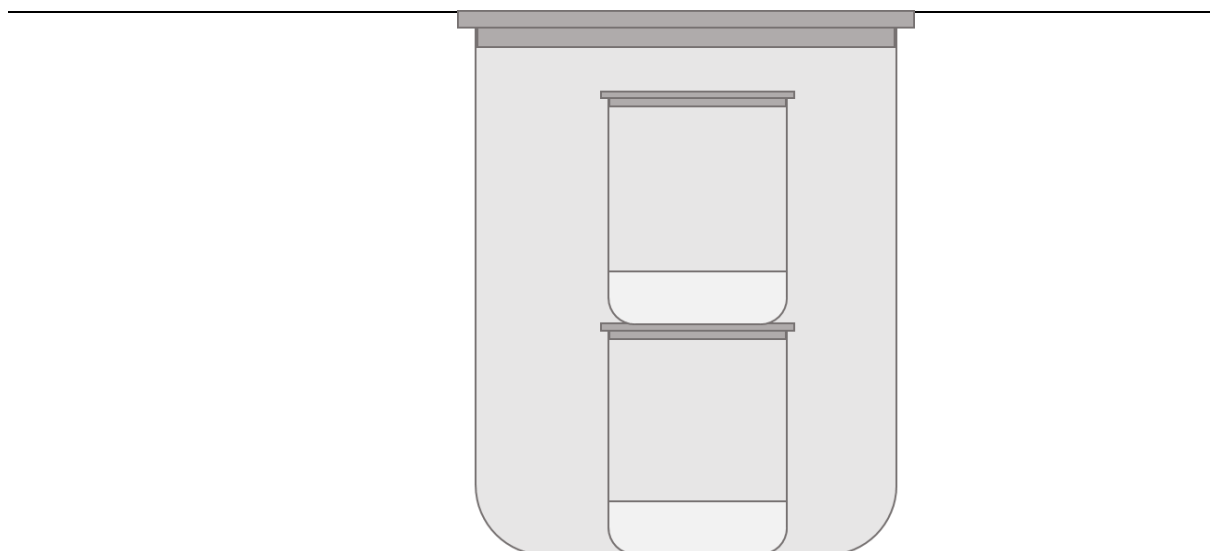


Figure 237: Diagram of nested alumina crucible setup used for the flux synthesis of Al:STO. 1 g of Al:STO is prepared in each crucible. Two batches are prepared simultaneously so that reproducibility could be tested.

4.5.1.2 Co-catalyst Impregnation

The RhCrO_x co-catalyst deposition was performed via a simple impregnation step whereby 0.2 mmol dm^{-3} solutions of Na_3RhCl_6 and $\text{Cr}(\text{NO}_3)_3 \cdot 9\text{H}_2\text{O}$ were prepared. Between 0.5 mL and 2 mL of each solution was added to 0.1 g of the photocatalyst, and the solution made up to 4 mL with water inside a 23mm open-topped vial. The solution was then evaporated at $80 \text{ }^\circ\text{C}$ under constant stirring over several hours. The deposited RhCrO_x residues were then oxidised in a furnace at $350 \text{ }^\circ\text{C}$ for one hour. These values obtained a range of Rh:Cr ratios and surface loadings ranging from 0.05 wt% to 2 wt% of each metal.

For the co-catalyst ageing experiments, Rh and Cr solutions were left in a cupboard, and new co-catalyst loaded STO samples were prepared each day over a week-long period.

4.5.1.3 Co-catalyst Photodeposition

Rh, Cr_2O_3 and CoO_x were sequentially photodeposited on the photocatalyst surfaces in varying concentrations and ratios using the high-throughput photocatalysis setup described in Chapter 3. The precursor components for the three metallic species are $\text{Na}_3\text{RhCl}_6 \cdot 9\text{H}_2\text{O}$ (Sigma Aldrich), K_2CrO_4 (Sigma Aldrich) and $\text{Co}(\text{NO}_3)_2 \cdot 6\text{H}_2\text{O}$. Solutions were made containing 0.1 mg ml^{-1} of each metallic cation concentration. The Rh solution was first added to the headspace reaction vial containing 5 mg of photocatalyst dispersed in 5 ml of water or an alternative sacrificial reagent mixture. The vial was capped and irradiated for 20 minutes using a 12"x12" wide area AAA solar simulator (Oriel, Newport,

1200W Xe arc lamp equipped with an AM1.5G filter) the light intensity was measured to be 1000 W m⁻². The vials were de-capped, and the chromium solution is added before a subsequent 20 min irradiation. Finally, this process is repeated with the added cobalt co-catalyst precursor solution.

4.5.1.4 Synthesis of BiVO₄

Faceted anisotropic BiVO₄ was synthesised via a hydrothermal method according to the literature process outlined in references^{320,337} Briefly, 10 mmol NH₄VO₃ and 10 mmol Bi(NO₃)₃·5H₂O were dissolved in 2M HNO₃. The pH of the solution was subsequently adjusted to pH=0.5 by adding ammonia solution. The reaction mixture was stirred under cold conditions for approximately 3 hours during which time a bright yellow precipitate was formed. This mixture was subsequently added to a Teflon-lined autoclave and heated for 10 hours at 473K.

4.5.2 Hybrid Organic-Inorganic Photocatalysts

4.5.2.1 In-situ Polymerisation

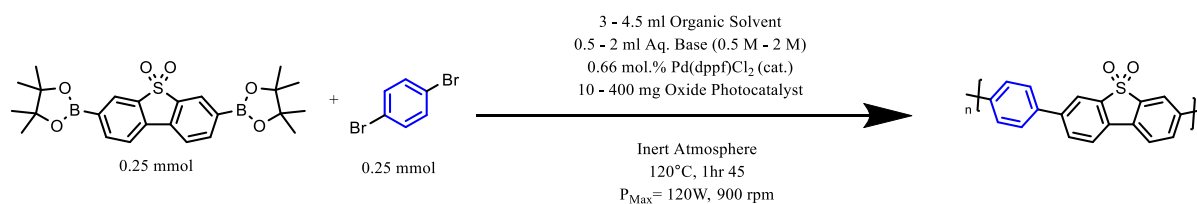


Figure 238: General reaction conditions used attempts to prepare organic/inorganic hybrid photocatalysts via *in-situ* polymerisation via microwave-assisted Suzuki-Miyaura polycondensation. Blue aromatic dibromide represents the variable selection of dibromide monomeric precursors investigated.

Hybrid photocatalysts were prepared via *in-situ* polymerisation. This was achieved using the same microwave-assisted polymerisation method explored in Chapter 3 with the exception that 10 – 400 mg of oxide was also added to the reaction mixture before heating. The oxide was dispersed in the reaction mixture by ultrasonication for 5 minutes before placing the vials into the Biotage Initiator+ automatic sampler. As in Chapter 3, a range of reaction conditions were also considered for the hybrid samples. However, the basic reaction conditions used are summarised in Figure 238.

4.5.2.2 Hydrogen Evolution Testing and Co-catalyst Photodeposition

5 mg of the co-catalyst-loaded photocatalyst powders were added to high throughput silica vials to which 5mL of deionised water (or a mixture of water, sacrificial reagent, and organic solvent) was added and then the vials capped with a rubber seal crimping lid. The suspension was then degassed by bubbling N₂ gas through the vial for 5 minutes via inlet/outlet needles perforating the rubber lid. Co-catalysts were loaded vis photodeposition, as explained for the purely inorganic samples.

4.5.2.3 SEM Imaging and EDS Mapping

Scanning electron microscopy (SEM, Hitachi) analysis was used to determine the success of preparing a hybrid via EDS mapping. For this analysis, powder was deposited on a sticky carbon tape, and silver paste was applied around the edge to ensure conductivity. Sputter-coated (Quorum Technologies, Q150T ES) with metallic chromium target for 30 seconds operating with a sputtering current of 120mA to obtain a coating of approximately 10nm. The sample was then transferred to the SEM after a minimal time reduce the level of chromium layer oxidation. For high-resolution imaging, a working distance of between five and ten millimetres and an acceleration voltage of five kilovolts was used. For chemical analysis, inbuilt energy-dispersive X-ray spectroscopy was used. In this set-up, a working distance of 15mm is used alongside an acceleration voltage of 20 kV. EDS maps were analysed using the Oxford Instruments AztecOne software.

4.6 Flux Synthesised Al:STO

Al:STO was selected as the oxide photocatalyst due to recent progress that has demonstrated that it is capable of achieving AQYs approaching 100% at 375 nm.³⁸ As such, it is hoped that any charges that are successfully injected from the polymer into its CB will go on to participate in the hydrogen evolution reaction with a high probability.

Al:STO nanocrystals are prepared by initially grinding high-purity SrTiO₃ together with an Al₂O₃ nanopowder, combining them with a large excess of SrCl₂, and heating the mixture to very high temperatures in high-purity Al₂O₃ crucibles. At these elevated temperatures, the SrCl₂ is molten and dissolves the SrTiO₃. A limited amount of Al₂O₃ is also dissolved in the flux from the added nanopowder and the crucible.⁴³ As the molten mixture cools, the SrTiO₃ recrystallises into highly-crystalline faceted nanopowders.

These nanocrystals are converted into efficient UV-active photocatalysts for overall water splitting, OWS, by adding Rh, Cr₂O₃, and CoO_x co-catalysts. This is either achieved via photodeposition or the impregnation method.⁴⁵ This latter method involves impregnation method, in which Al:STO particles are calcined following their dispersal in, and subsequent evaporation of, metal salt solutions.

The high AQY of these materials in the UV region is attributed to several synergistic factors. Al³⁺ substitute self-doped Ti³⁺ ions that arise from the natural non-stoichiometry of SrTiO_{3-δ}, which contains

an appreciable amount of oxygen vacancies.³³⁸ The Ti^{3+} ions introduce occupied 3d orbitals into the bandgap, which negatively impacts photocatalytic activity. Meanwhile, energy levels attributable to Al^{3+} ions are located in the electronic bands.⁴¹

In the absence of Al_2O_3 , when aluminium doping only arises from the crucible, Domen found that the resulting Al:STO crystals were 1-2 μm across. In contrast, in the presence of the Al_2O_3 nanopowder, they are approximately 100 nm in diameter. One hypothesis for this observation is that the nanopowder particles act as re-crystallisation seeds. The small size leads to a large surface area-to-volume ratio which is beneficial for dispersion properties and surface photocatalysis.

The faceted nanocrystals possess exposed {100}, {111}, and {110} crystallographic facets. The electronic band structure of crystalline materials depends on the crystallographic direction. This leads to crystallographic surfaces with different surface energies and work functions. It also results in an inbuilt electric field inside the crystal which can drive electron-hole charge separation. Photodeposition studies involving reduction and oxidation processes have identified facet-selective photodeposition sites, giving rise to spatially separated oxygen-evolution and hydrogen evolution reaction sites.³⁸

The final factor that leads to improved photocatalytic activity is the choice of co-catalyst. Rhodium is another platinum-group metal that binds hydrogen, water, and oxygen on its surface with appropriate energy to allow for efficient reaction rates of hydrogen evolution on its surface. However, Rh is equally efficient at driving the reverse reaction, i.e. the oxygen reduction reaction, which decreases the overall water-splitting efficiency. To overcome this, Domen's group use a core-shell structure for the co-catalyst in which metallic Rh nanoparticles are coated by chromium oxide, Cr_2O_3 . Molecular oxygen cannot diffuse through Cr_2O_3 , and the ORR is prevented. This is achieved by sequential photodeposition.⁴⁷ The photocatalytic activity was further improved by adding cobalt oxide, CoO, as an oxygen evolution co-catalyst. Upon photodeposition, Rh/ Cr_2O_3 co-catalysts are deposited on one facet surface, whereas CoO_x deposits onto another.³⁸

These photocatalysts also demonstrate long-term stability, particularly when a thin layer of TiO_2 is photodeposited on the surface. A panel of this material has demonstrated stable photocatalytic activity over 1,000 hours.⁴⁰

The preparation of this material with high levels of photocatalytic activity proved to be highly challenging. This is in agreement with other research groups that have struggled to reproduce these materials with the same degree of photocatalytic activity.⁴¹ Professor Domen's group kindly provided a reference sample of their most active material for us to compare activities with. This section discusses challenges encountered while attempting to reproduce this material. The flux-synthesised Al-doped SrTiO₃ is herein referred to as Al:STO.

In an attempt to reproduce this leading photocatalyst and understand how different factors impact the final activity, several steps were taken to optimise the synthesis and achieve a photocatalytic activity closest to the Domen reference sample. The flux reaction temperature, reaction time, the purity of the reagents, aluminium doping content, and the co-catalyst loading method were each studied. The results of these experiments are presented over the following subsections.

4.6.1 Purity of Reagents

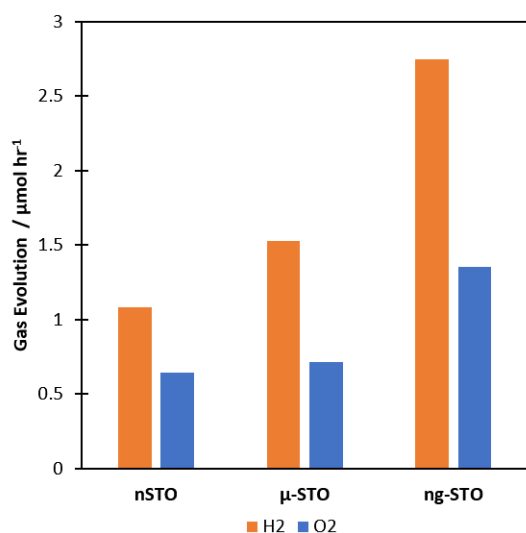


Figure 239: HER and OER rates for flux-synthesised Al:STO samples prepared from different SrTiO₃ precursors. n-STO, µ-STO, and ng-STO refer to the 99% nanopowder (Sigma), 99% micropowder (Sigma), and 99.97% nanopowders (nanografi) discussed in the main text. Samples targeted 4% Al doping and were impregnated with a RhCr_x co-catalyst before testing.

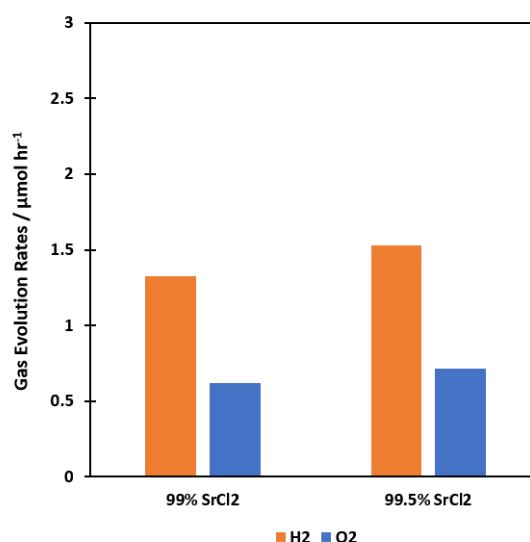


Figure 240: HER and OER rates for flux-synthesised Al:STO samples prepared from different purities of SrCl₂ salt used as the molten flux reagent. Samples prepared using the µ-STO precursor and heated to 1000°C for 10hrs.

The purity of reagents was first investigated. Three different sources of SrTiO₃ were used. A 99% purity micro powder, a 99% nanopowder, and a 99.97% nanopowder (nanografi, 100 nm). As shown in Figure 239, the highest-purity starting material resulted in higher photocatalytic activities. These samples were only prepared at 1000 °C as earlier attempts at higher temperatures resulted in a chemical spill inside the furnace.

The purity of the SrCl₂ flux was also investigated. Figure 240 shows that this may also have a small effect on the final photocatalytic activity. This is expected since single crystal inorganic semiconductors are highly sensitive to impurities that may act as traps electron or hole traps that reduce the photocatalyst efficiency.

4.6.2 Temperature

As can be seen in Figure 241, the photocatalytic activity of Al:STO is dependent on the temperature of the flux treatment. The samples heated at 1150 °C for ten hours produced the greatest amount of hydrogen (and oxygen). Each sample was prepared twice since the synthesis process is largely unreliable. However, it should be noted that except for the sample prepared at 1150 °C the two samples were in good agreement with one another. This highlights that synthesis on a one-gram scale is preferential for reproducibility compared to work completed in previous years.

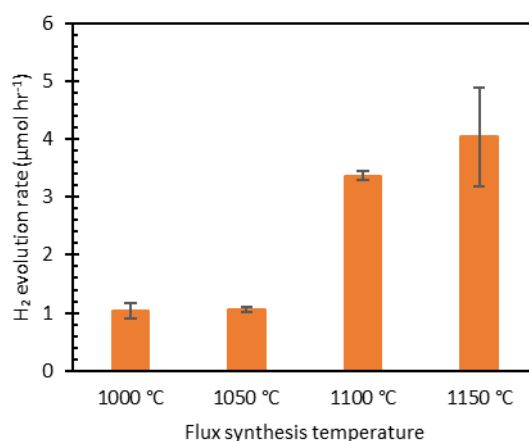


Figure 241: Photocatalytic HER rates for Al:STO samples prepared at different temperatures. Samples prepared using the ng-STO precursor and 99% SrCl₂.

Early experiments only heated the samples to 1000 °C since higher temperatures led to SrCl₂ overflowing from the crucible. The new setup using crucibles inside of another crucible was used so that any overflow does not corrode away the inside chamber of the furnace. However, no overflow was observed at any temperature. This likely implies that early overflowing might have been due to new crucibles with a rougher surface that led to nucleation, from the shape/size of the crucible used, that increasing the scale of the reaction stabilises the flux, or that the inside of the large crucible did not reach the same temperatures as the rest of the furnace.

Figure 240 shows the results from loading RhCrO_x onto the surface of the photocatalyst using the same stock solutions of Na_3RhCl_6 and $\text{Cr}(\text{NO}_3)_3$ for four days in a row. Four samples of each photocatalyst base were taken and averaged out for this experiment since results vary widely between batches made using the same conditions. A clear trend of decreasing activity was observed in both sets of samples. This experiment also confirms that the samples prepared at 1150 °C are, on average, more active than those prepared at 1100 °C.

4.6.3 Al:STO Co-catalysts

4.6.3.1 Impregnation Method

Initial experiments using the impregnation method did not yield photocatalytic activities that resembled the same photocatalysts as prepared by the Domen group, despite using the highest purity grade of reagents available and optimising the reaction temperature. Although these factors likely influence the particle size, purity and crystallinity, Al:STO does not achieve water splitting unless it is loaded with the appropriate co-catalysts at the correct concentration. As such, these variables were subsequently investigated in an attempt to reproduce activities reported in the literature.⁴⁶

Al:STO nanocrystals were initially loaded with the mixed metal oxide co-catalyst, RhCrO_x , via the impregnation method. The rhodium source was trisodium hexachlororhodate, $\text{Na}_3\text{RhCl}_6 \cdot x\text{H}_2\text{O}$, and the Chromium precursor was chromium nitrate, $\text{Cr}(\text{NO}_3)_2 \cdot 9\text{H}_2\text{O}$. These precursors were dissolved in water to a metal concentration of 1 mg ml⁻¹. An appropriate amount of the metal precursor solutions were then loaded onto Al:STO that had been synthesised at different temperatures. The resulting slurries were placed into a sand bath and heated to 60 °C under constant stirring to remove the water and coat the particles evenly. The metal salts were calcined at 350 °C for one hour to form the resulting oxides.

The stability of the precursor solutions was investigated. Stock solutions containing 1 mg ml⁻¹ of the metal ion were prepared and used to load a RhCrO_x co-catalyst onto eight Al:STO samples daily over four days. Figure 242 shows how the hydrogen evolution rates for the resulting samples changed with respect to the age of the precursor solution. The general trend demonstrates that the older the solution, the lower the activity. This is accompanied by the observation of Na_3RhCl_6 solution discolouration from red to yellow over time.

However, the age of the solution alone is not responsible for the variation of activity observed. Large variations of activity were observed within each batch, as indicated by the error bars. Likewise, the

lowest activities were observed for the samples prepared from one-day-old precursor solutions. Such trends likely arise from inhomogeneous stirring and evaporation rates. Although efforts were made to ensure all samples were heated to the same temperature for similar lengths of time, the position of vials in the sand bath relative to the centre of the hotplate/stirrer resulted in inconsistent stirring rates. Likewise, the depth at which sample vials were submerged into the sand bath likely influenced the exact temperature and evaporation rate, especially given condensation at the neck of the vials. Furthermore, the selection of the sample vial, from which the solution was evaporated, could not always be kept consistent due to availability. Although the evaporation method only differed marginally between samples, the range of results suggests that this process significantly impacts photocatalytic activity. As in Figure 241, the Al:STO nanocrystals synthesised at 1150°C typically outperformed those prepared at 1100°C.

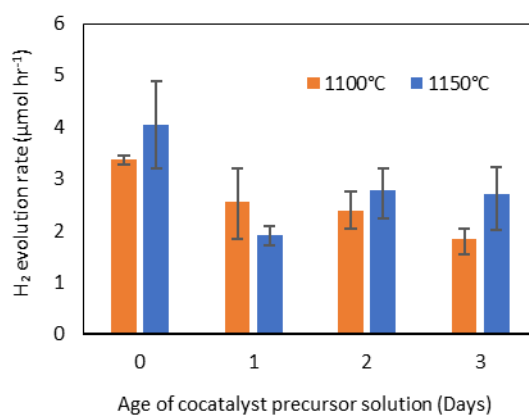


Figure 242: HER rates for flux-synthesised Al:STO samples loaded RhCrO_x co-catalyst via the impregnation method. The same Rh and Cr precursor solutions were used each day to investigate if the age of these solutions impact the quality of the resulting co-catalyst-loaded sample.

All previous samples have been loaded with 0.1 wt.% Rh, and 0.1 wt.% Cr, in agreement with the impregnation methods used in the literature.³⁹ However, the ideal ratio will be specific to the photocatalyst substrate, particularly concerning particle size and surface area. To see if the activity of the Al:STO/RhCrO_x photocatalyst could be improved by altering this ratio, a series of samples were prepared in which Rh and Cr concentrations were independently varied between 0 and 0.2 wt.% each. The resulting relative hydrogen evolution rates are presented as a bubble plot in Figure 243, whereby the area of the bubble represents the hydrogen evolution activity, and the largest bubble represents a hydrogen evolution activity of 4.5 µmol hr⁻¹. Each bubble averages two samples loaded with co-catalysts on the same day. The orange and blue samples (Al:STO prepared from flux synthesis at 1000°C and 1150°C, respectively) were prepared from different co-catalyst precursor solutions on different days.

Contrary to the literature, which suggests that both Cr and Rh are necessary for overall water splitting, the best-performing photocatalysts in Figure 243 contain little or no chromium. A general trend of decreasing activity with respect to chromium can be observed, whereas increased Rh typically resulted in increased activity until 0.15 wt.%. At high chromium content (0.15 – 0.2 wt.%) and in the absence of any chromium, a further increase in rhodium content decreased the photocatalytic activity. However, at low chromium concentrations (0.05 wt.%), the photocatalytic activity increased with additional rhodium content. The highest photocatalytic activity was observed for samples containing 0.2 wt.% Rh and 0.05 wt.% Cr, and corresponded to a HER of $4.5 \mu\text{mol hr}^{-1}$. This activity remained significantly lower than the $16 \mu\text{mol hr}^{-1}$ observed for samples provided by the Domen group.

Despite the earlier measurements, no significant difference in activity was observed for the catalysts prepared at 1000°C and 1150°C in this study when loaded with the same co-catalyst concentrations. This likely arises because the co-catalyst loading was completed on different days using fresh co-catalyst stock solutions. The co-catalyst precursor solutions were evaporated from the 1000°C samples in a sand bath. In contrast, for the 1150°C samples, the vials were placed into a dedicated multi-well heat-on block for sample vials.

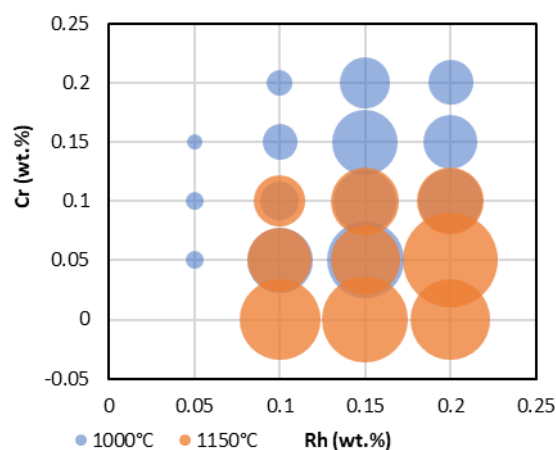


Figure 243: Photocatalytic HER rates for Al:STO loaded with different concentrations of Rh and Cr metals via the impregnation method. The largest sphere corresponds to a HER of $4.5 \mu\text{mol hr}^{-1}$.

These results show that the impregnation method is highly unreliable. The resulting activities are much lower than reported in the literature and are not easily reproducible between batches. This method appears highly sensitive to the exact method by which the precursor solutions are evaporated. The evaporation rate depends on the stirring speed, the temperature, and the choice of vessel.

Accordingly, the concentration of the precursor solution, and hence the volume of water that is required to be evaporated, is also expected to play a role. The impregnation method is likely unreliable because of the limited stability of the precursor stock solutions, particularly Na_3RhCl_6 , the aqueous solution of which becomes discoloured over time.

4.6.3.2 Photodeposition Method

The second co-catalyst loading method investigated was photodeposition. Here, metallic rhodium, chromium oxide, and cobalt oxide were sequentially photodeposited onto the Al:STO nanocrystal surfaces using AM 1.5G irradiation from the Newport Oriel AAA solar simulator. The co-catalyst precursor solutions used were 0.1 mg ml^{-1} aqueous solutions of Rh^{3+} , Cr^{6+} , and Co^{2+} from RhCl_3 , K_2CrO_4 , and $\text{Co}(\text{NO}_3)_2$, respectively. According to previous studies, the rhodium is reduced to its metal form, the chromium is reduced to form Cr_2O_3 , and the cobalt is oxidised to form CoOOH .³⁸

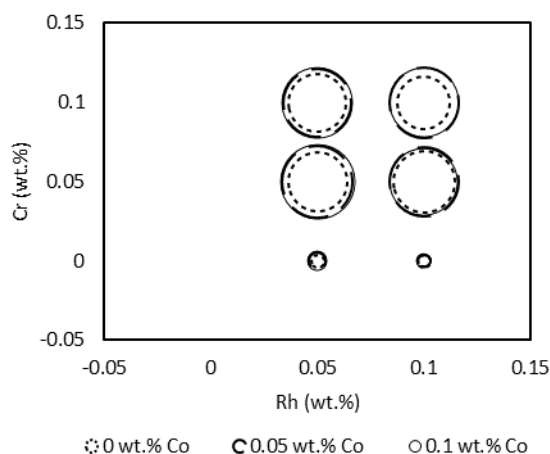


Figure 244: Photocatalytic HER rates for Al:STO loaded with different concentrations of Rh and Cr metals via the photodeposition method. The largest sphere corresponds to a HER of $12 \mu\text{mol hr}^{-1}$.

The photocatalytic hydrogen evolution activities are presented as a bubble chart in Figure 244. The largest bubble area correlates to a HER of $12 \mu\text{mol hr}^{-1}$. It becomes evident that high hydrogen evolution rates require the presence of both Rh and Cr_2O_3 . Cr_2O_3 alone does not result in overall water splitting, whereas Rh/Al:STO results in a slow rate of photocatalytic water splitting. All samples that produce hydrogen also produce oxygen in a stoichiometric amount (2:1). The presence of cobalt also enhances the OWS rate. For the samples containing all three metals, changes to the relative composition result in more minor overall efficiency improvements.

Figures 244 and 245 present the trends with respect to Co and Cr loading at different Rh concentrations. The data points in Figure 244 are an average over the two higher chromium concentrations, whereas those in Figure 245 are averaged over the two higher cobalt concentrations.

The trend with respect to Co and Cr loading appears to depend on the underlying Rh content, samples containing 0.05 wt.% Rh perform better than those containing 0.1 wt.%. At 0.05 wt.% Rh, increasing Co content from 0.05 to 0.1 wt.% increases the activity, whereas at 0.1 wt.%, the same change results in a decrease in activity. Conversely, at 0.05 wt.% Rh, increasing the Cr content from 0.05 wt.% to 0.1 wt.% decreases activity, whereas at 0.1 wt.% an equivalent change increases activity. The highest activity was observed when the Al:STO was loaded with 0.05 wt.% Rh, 0.05 wt.% Cr and 0.1 wt.% Co.

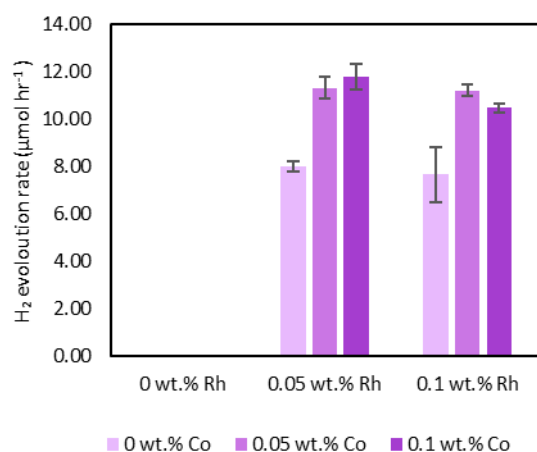


Figure 245: HER rates of STO loaded with sequentially photodeposited co-catalysts, Rh, Cr₂O₃, and CoO_x. Loadings are given in per cent weight of the metal.

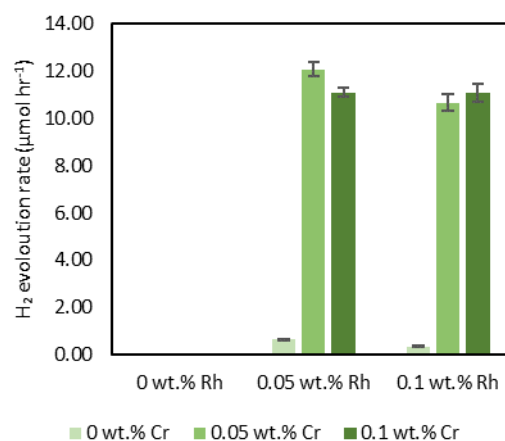


Figure 246: HER rates of STO loaded with sequentially photodeposited co-catalysts, Rh, Cr₂O₃, and CoO_x. Loadings are given in per cent weight of the metal.

The HER and OER rates for RhCrO_x/CoO_x/Al:STO photocatalysts samples prepared from the impregnation and photodeposition methods are compared in Figure 247. This Figure also contains data from the sample provided by the Domen group, as measured on our photocatalysis setup. All samples produce hydrogen and oxygen in a 2:1 stoichiometric ratio. Compared to the Domen reference sample (15.4 μmol hr⁻¹), the impregnation method only achieved 32% efficiency (4.9 μmol hr⁻¹), and the photodeposited sample achieved 80% of its activity (12.4 μmol hr⁻¹). Although the photocatalytic activity is not as high as achieved by Domen, 80% is good enough to build upon with respect to developing organic-inorganic hybrid photocatalysts. The discrepancy is likely due to the purity of reagents in the flux synthesis; the extent of reagent grinding; the size, shape, purity, and age of the alumina crucibles; and the flux heating/cooling rate. Such factors can influence the size of the resulting particles, their crystallinity, the surface area of the crystalline facets, and the exact aluminium doping concentration. For reference with the hydrogen evolution rates of the polymeric photocatalysts in the presence of TEA as a sacrificial reagent, the hydrogen evolution rate of the

Domen catalyst in pure water is $3.1 \text{ mmol hr}^{-1} \text{ g}^{-1}$ for a 5 mg sample and equates to an area-normalised rate of $2.3 \text{ } \mu\text{mol hr}^{-1} \text{ cm}^{-2}$.

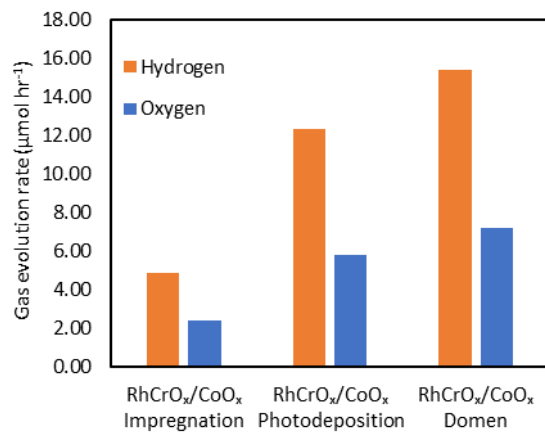


Figure 247: Hydrogen and oxygen evolution rates for Al:STO photocatalysts loaded with Rh, Cr, and Co co-catalysts by the impregnation and photodeposition methods. These samples are compared with the Domen reference sample provided by the research group in Tokyo.

4.7 In-situ Polymerisation Reaction Optimisation

This work builds upon the in-situ polymerisation method employed by Shu *et al.*³⁰⁹ to prepare hybrid organic-inorganic photocatalysts from DBTS-DBTS and TiO₂. However, significant questions regarding the mechanism by which enhanced photocatalytic activity was achieved remain unanswered. For example, it is unclear if the presence of oxide in the reaction mixture can influence the polymer's synthesis yield, chain length, polydispersity, purity, particle size, and morphology. Especially since many of these factors may influence the photocatalytic activity.

It is also unclear if a hybrid containing 10 wt.% oxide has enough oxide-liquid interface for the HER to occur at these sites. Their work also compared HER rates by using mass-normalised values and experiments were performed at a low concentration of 10 mg per 100 ml. Resultingly, the reduction of activity at higher TiO₂ loadings may have arisen from the fact that these samples contained less visible-light active polymer.

Here, using the rapid microwave-assisted synthesis method developed in chapter 4, we seek to understand if DBTS-DBTS/Al:STO hybrids can be prepared, if their activity can be optimised by varying the polymer-to-oxide ratio, if the presence of an oxide in the reaction mixture can influence the photocatalytic activity of the polymer component, and how reaction conditions influence the polymerisation yield, organic/inorganic component distribution, and photocatalytic activity.

DFT calculations predict that the EA of DBTS-DBTS results in a polymer reduction potential that lies above the CB of Al:SrTiO₃. This provides a suitable overpotential that makes exciton charge separation energetically favourable before forming an interface. As discussed earlier in this chapter, Fermi level alignment will result in band bending which may impact the rate at which charges can be extracted.

By substituting TiO₂ with Al:SrTiO₃, a superior water-splitting photocatalyst, it is anticipated that further enhancements could be obtained.

4.7.1 Reaction Conditions

4.7.1.1 Solvent

In Chapter 3 **Error! Reference source not found.**, DBTS-PhFx, BDT-PhFx, and DBTS-PhFx-BDT polymers were successfully synthesised from single-phase reaction mixtures when using TBAA as the base and 1,4-dioxane as the organic solvent. However, attempts to synthesise DBTS-DBTS and BDT-DBTS using this solvent/base combination were unsuccessful.

DBTS-DBTS was most successfully synthesised from a combination of toluene and K_2CO_3 in a biphasic reaction mixture. Whilst this is appropriate for polymer synthesis, it is unclear if this could be applied to hybrid photocatalyst preparation. To investigate this, a series of DBTS-DBTS polymers were synthesised on a 0.25 mmol scale (expected yield of 110 mg) in the presence of 10 mg of $RhCrO_x/Al:STO$ (sample F81A) using different combinations of solvent and base. This aims to replicate the 10 wt.% hybrids prepared by Shu *et al.*³⁰⁹ The resulting polymer yields are presented in Table 25.

Table 25: Initial *in-situ* preparation conditions for $RhCrO_x@Al:STO/DBTS-DBTS$ Hybrids

ID	Polymer	Al:STO sample	Mass (mg)	Solvent	Base	Yield (%)
M88	DBTS-DBTS	F77A	10	Toluene + PTC	K_2CO_3	112
M89	DBTS-DBTS	F77A	10	Toluene + PTC	K_3PO_4	102
M90	DBTS-DBTS	F77A	10	Toluene + PTC	TBAA	-
M91	DBTS-DBTS	F77A	10	Toluene	TBAA	58
M99	DBTS-DBTS	F78A	10	1,4-dioxane	K_2CO_3	62
M100	DBTS-DBTS	F77	10	DMF	K_2CO_3	59
M101	DBTS-DBTS	F77	10	THF	K_2CO_3	-
M102	DBTS-DBTS	F77	10	1,4-dioxane	K_3PO_4	-
M103	DBTS-DBTS	F77	10	DMF	K_3PO_4	67
M104	DBTS-DBTS	F77	10	1,4-dioxane	Cs_2CO_3	-
M105	DBTS-DBTS	F77	10	DMF	Cs_2CO_3	-

As in the absence of Al:STO, the synthesis of DBTS-DBTS in Toluene/ K_2CO_3 and Toluene/ K_3PO_4 ran to completion with yields over 100% as consistently observed in chapter 3. However, the residual white powder was observed in the aqueous phase, as seen in samples M88 and M89 of Figure 248. This residue was suspected to be residual strontium titanate that had not mixed with the polymer.

Single-phase reaction mixtures were obtained when toluene was combined with 2M TBAA. However, a noticeable difference arose between the M90 and M91 synthesised in the presence and absence of Aliquot 336, the phase transfer catalyst (PTC), respectively. In these reactions, TBAA, containing an aliphatic quaternary ammonium cation and an organic acetate counterion, already acts as a phase transfer catalyst to make a single-phase reaction mixture. In the presence of the PTC (M90), the palladium catalyst degraded to form palladium black, and the reaction was unsuccessful. In the absence of a PTC, a homogeneous mixture was formed. However, the polymer synthesis yield was reduced to 58%. It did not exhibit the expected bright yellow colour, implying a high concentration of

impurities, such as residual palladium, or a wider bandgap resulting from incomplete polymerisation that led to the formation of short oligomeric chains.

M99, prepared from 1,4-dioxane and 2M K_2CO_3 produced a yield of 62%. Like the Toluene/TBAA sample, this polymer was beige instead of bright yellow. M102 and M104, which also used 1,4-dioxane as the solvent paired with 2M K_3PO_4 and 2M Cs_2CO_3 , respectively, failed to produce any product as the catalyst degraded. Despite being miscible with water, the resulting reaction mixtures had phase separated. This phase separation likely arises from the saturation of soluble salts in the aqueous phase. M102, which used a THF/ K_2CO_3 reaction mixture, also failed.

The samples synthesised from DMF paired with K_2CO_3 and K_3PO_4 successfully produced a bright yellow product believed to be the desired DBTS-DBTS polymer. Despite reduced yields compared to the biphasic reactions using toluene (59% and 67% vs 112% and 102% in K_2CO_3 and K_3PO_4 , respectively), DMF remained miscible with the aqueous phase throughout the reaction. This presented the best opportunity to produce a hybrid in which the oxide particles are uniformly dispersed in the polymer matrix. It is notable, however, that the DMF/ K_3PO_4 reaction produced a white residue at the bottom of the reaction vial. Whilst most of this dissolved in the washing phase, implying that the salt byproducts were insoluble in the solvent mixture, it also contained some residual insoluble white powder believed to be Al:STO that had not been fully incorporated.



Figure 248: Post-synthesis reaction mixtures containing $RhCrO_x@Al:STO/DBTS-DBTS$ hybrid photocatalysts. Vial labels correspond to the reaction conditions outlined in Table 25. With the exceptions M100 and M103 (both prepared in water-miscible DMF) exhibited the brightest samples, whereas M88 and M89 (prepared using a biphasic toluene reaction) produced polymers in the highest yields.

SEM images and EDS maps of the resulting polymer/oxide products were recorded to determine the degree of mixing. Figure 249 presents SEM images of M88, DBTS-DBTS/Al:STO (10 wt.%) prepared

from toluene and K_2CO_3 . They demonstrate the large distribution of particle sizes from 200 μm to 1 μm in diameter. These larger particles appear to be agglomerations of smaller polymer particles on the 100 nm scale.

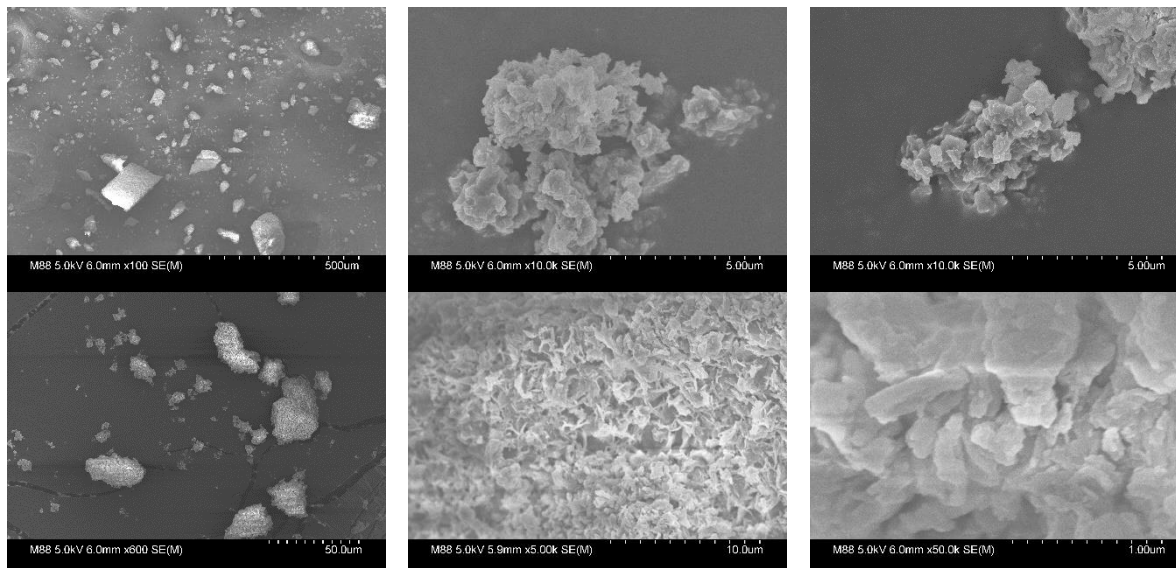


Figure 249: SEM images of hybrid sample M88 at various magnifications. Sample prepared from a biphasic reaction of 3 ml Toluene and 2 ml of 2M K_2CO_3 . Particle sizes span from 5 – 500 μm diameter.

Figure 250 contains three low-magnification images of M88 and their EDS maps from Sr $K\alpha_1$ and S $K\alpha_1$ emissions. These maps show that whilst some degree of oxide/polymer mixing does occur, this mixing is not uniform. Many polymer particles do not appear to contain much of the oxide material. Likewise, Figure 251 contains SEM images and associated EDS maps for hybrid M89, prepared from a reaction mixture of toluene and K_3PO_4 . Although some particles contain both oxide and polymer, the two are not evenly distributed.

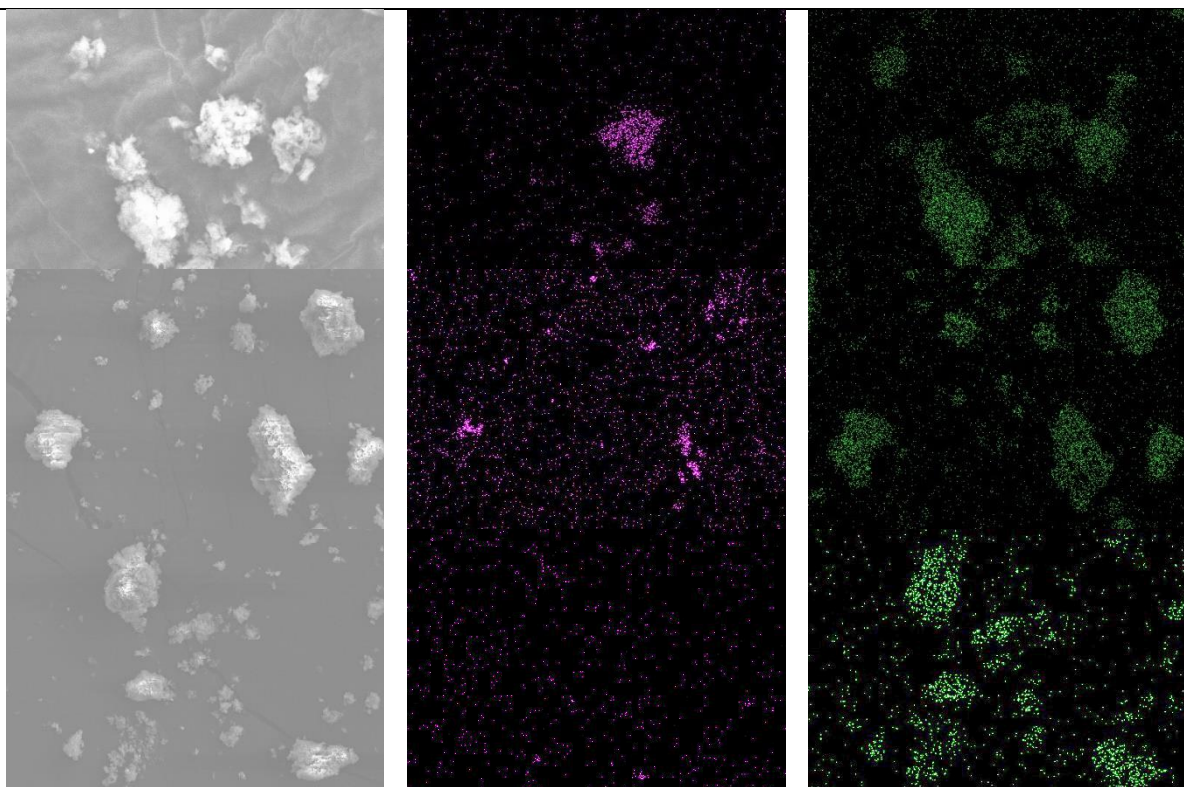


Figure 250: SEM images and EDS maps for M88, a $\text{RhCrO}_x/\text{Al:STO}/\text{DBTS-DBTS}$ hybrid photocatalyst synthesised from a biphasic reaction of 3 ml Toluene and 2 ml of 2M K_2CO_3 . EDS maps present the presence of strontium (purple) and sulfur (green) enabling identification of SrTiO_3 and polymeric components, respectively.

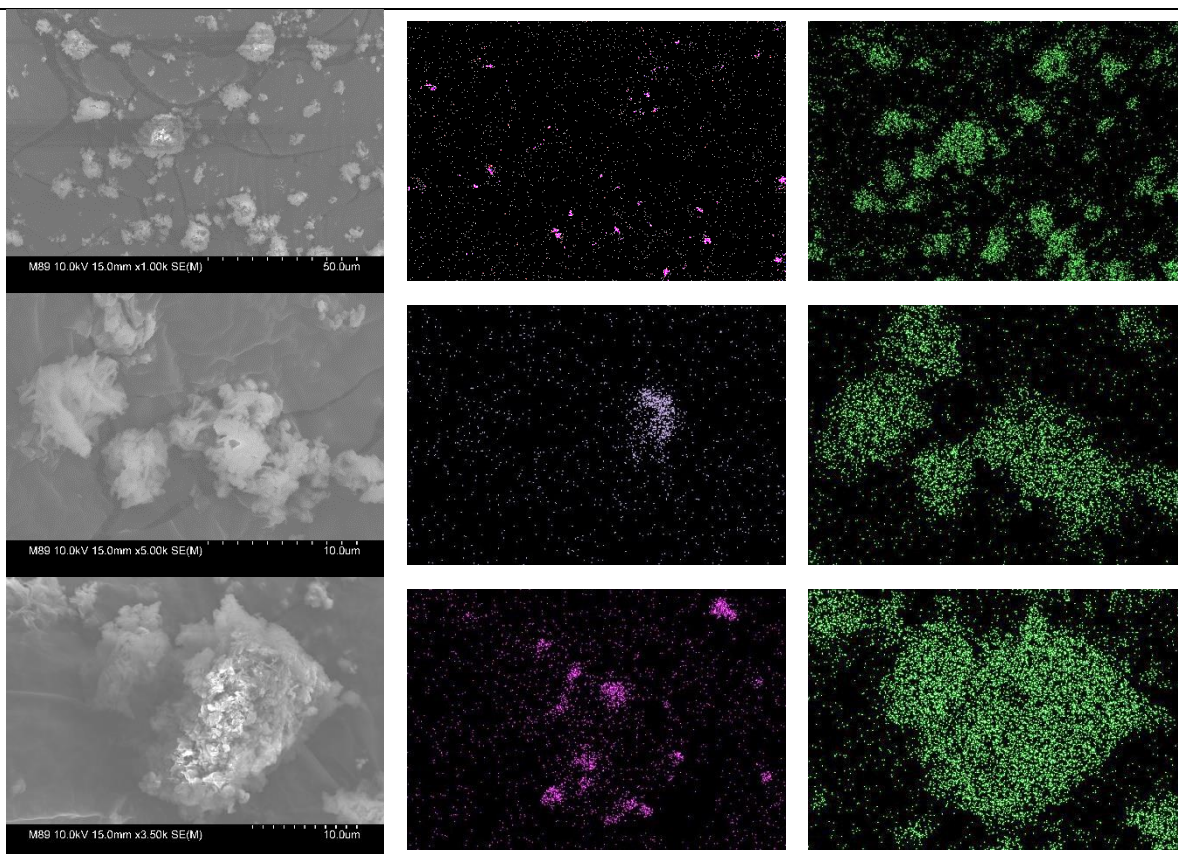


Figure 251: SEM images and EDS maps for M89, a $\text{RhCrO}_x@ \text{Al:STO/DBTS-DBTS}$ hybrid photocatalyst synthesised from a biphasic reaction of 3 ml Toluene and 2 ml of 2M K_3PO_4 . EDS maps present the presence of strontium (purple) and sulfur (green) enabling identification of SrTiO_3 and polymeric components, respectively.

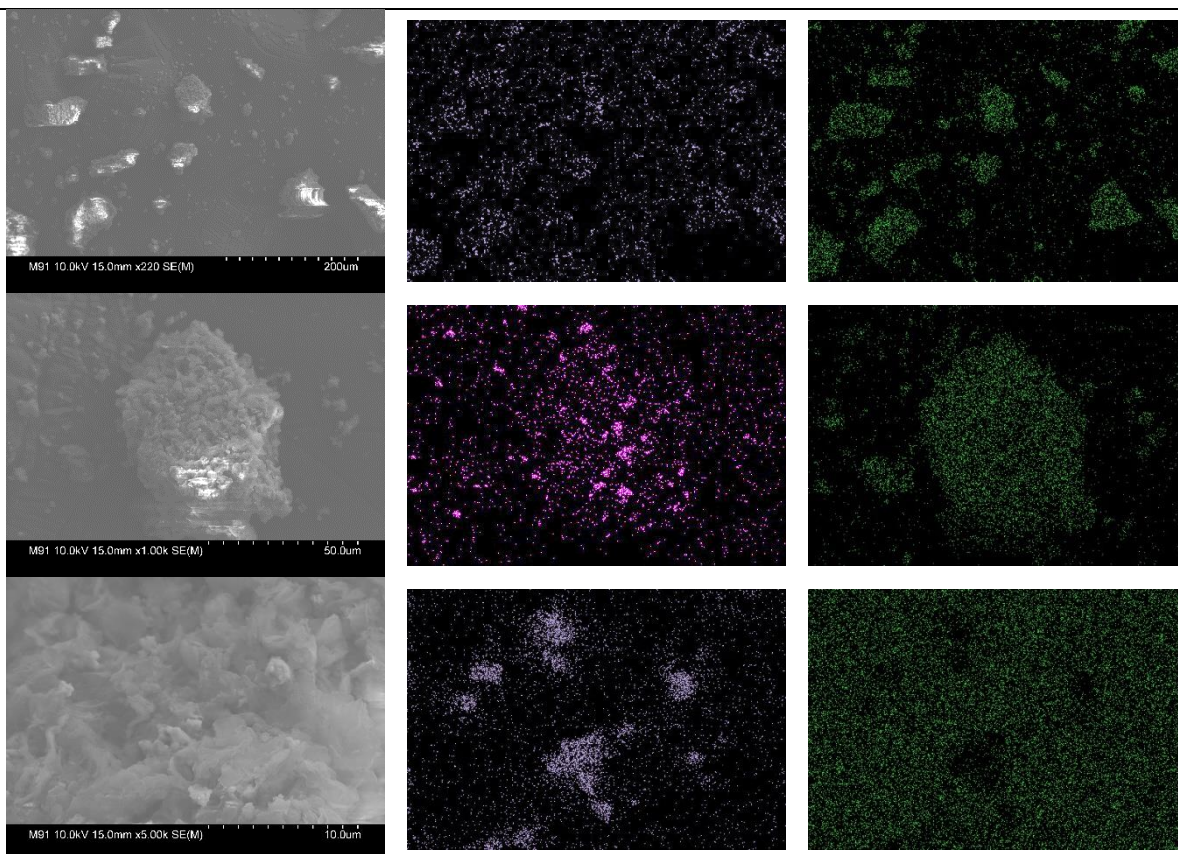


Figure 252: SEM images and EDS maps for M91, a $\text{RhCrO}_x@Al:STO/DBTS-DBTS$ hybrid photocatalyst synthesised from a monophasic reaction mixture of 3 ml Toluene and 2 ml of 2M TBAA. EDS maps present the presence of strontium (purple) and sulfur (green), enabling identification of SrTiO_3 and polymeric components, respectively.

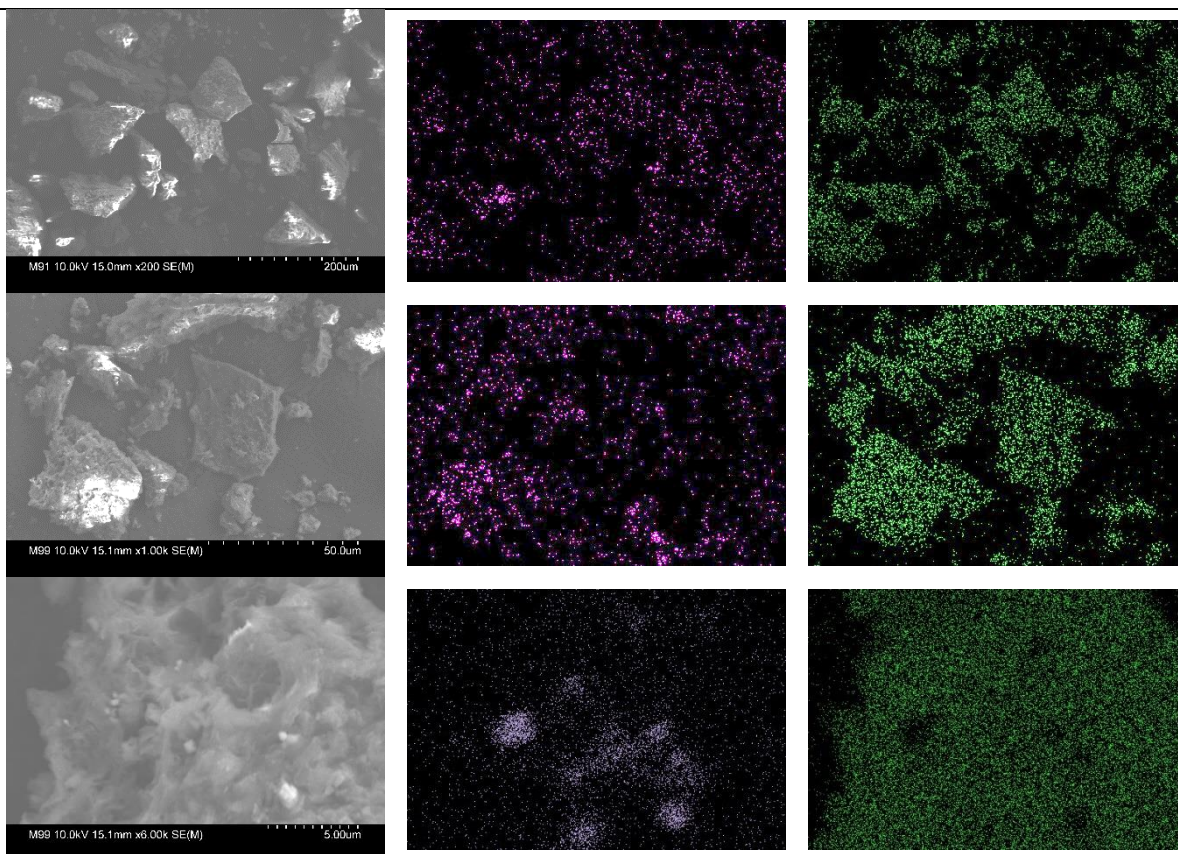


Figure 253: SEM images and EDS maps for M99, a $\text{RhCrO}_x\text{@Al:STO/DBTS-DBTS}$ hybrid photocatalyst synthesised from a monophasic reaction mixture of 3 ml 1,4-dioxane and 2 ml of 2M K_2CO_3 . EDS maps present the presence of strontium (purple) and sulfur (green), enabling identification of SrTiO_3 and polymeric components, respectively.

Figures 252 and 253 contain SEM images and EDS maps of hybrid DBTS-DBTS/Al:STO samples M91 and M99 synthesised in single-phase reaction mixtures of toluene/TBAA and Dioxane/ K_2CO_3 . In the low-magnification images of these samples, it is more challenging to see the strontium distribution. At higher magnifications, it becomes apparent that this is because the oxide is more evenly distributed throughout the polymer particles and is not concentrated in smaller clusters. These maps support the hypothesis that a biphasic reaction prevents the formation of homogeneous hybrid photocatalysts.

The hybrid photocatalysts were subsequently tested for their hydrogen evolution photocatalytic activities using a 1:1:1 mixture of $\text{H}_2\text{O}:\text{MeOH}:\text{TEA}$, whereby methanol acts as a co-solvent to aid dispersion and TEA is the sacrificial electron donor. The resulting hydrogen evolution rates are presented in Figure 254. The reaction yield is also plotted as grey data points on the secondary axis.

These data suggest that the highest hydrogen evolution reaction rates are achieved by the samples prepared from toluene in combination with K_2CO_3 . This is closely followed by the toluene/ K_3PO_4 reaction mixture. These two samples also produced the DBTS-DBTS polymer in the highest yields.

However, these hybrids exhibited the poorest oxide incorporation. In comparison with the DBTS-DBTS samples synthesised from a toluene/ K_2CO_3 reaction mixture in the absence of Al:STO, as presented in Chapter 3, these polymers exhibit higher activities before platinum loading via photodeposition but lower activities afterwards.

The remaining hybrids, in which the solvent and base combinations led to a single-phase reaction mixture, were all synthesised in lower yields, between 60% and 70%. These samples also exhibited poorer photocatalytic hydrogen evolution rates. The 1,4-dioxane/ K_2CO_3 reaction mixture generated the poorest photocatalyst, and samples prepared from the DMF/base mixtures exhibited the greatest percentage increase in activity after loading with a platinum co-catalyst.

As observed in Chapters 2 and 3, lower yields often correlate with poorer photocatalytic activities. Whilst the lower yields may originate from the single-phase reaction mixture, which could significantly impact factors such as the rates of reactions, the reagent solubility, the catalyst stability, the local concentrations, and the pH, we must also consider the impact that the oxide has on the reaction.

In the case of M88 and M89, these reactions took place using F77A as the Al:STO photocatalyst. This sample (synthesised at 1100 °C for 10 hours, 4 mol% Al) already contains the $RhCrO_x$ co-catalyst from the impregnation method (0.1 wt.% Rh and 0.1 wt.% Cr). The presence of this co-catalyst, some of which will have been incorporated into the polymer matrix, may account for the higher activity before the photodeposition of Pt (compared with the pristine polymer) and the relatively lower activity afterwards. This suggests a similar role for the Rh co-catalyst in DBTS-DBTS as for the residual Pd in DBTS- PhF_x polymers. M91 (Toluene/TBAA) and M99 (Dioxane/ K_2CO_3) were also synthesised in the

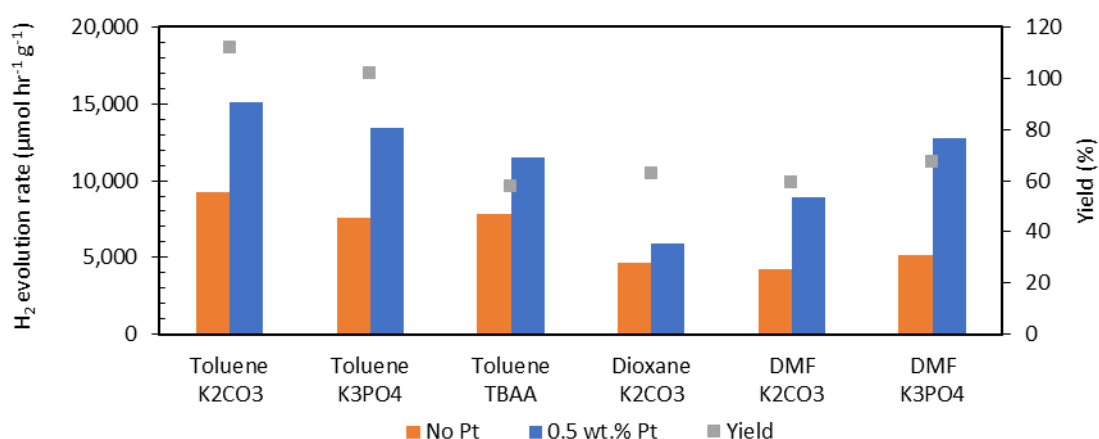


Figure 254: HER rates of Al:STO/DBTS-DBTS hybrid photocatalysts containing 10 wt.% Al:STO. Before and after Pt photodeposition. Approximate polymer synthesis yields are provided on the secondary axis.

presence of co-catalyst loaded oxides. These samples also exhibited small increases in activity following the photodeposition of Pt.

M100 (DMF/K₂CO₃) and M103 (DMF/K₃PO₄) were synthesised in the presence of F77, the same Al:STO oxide without any co-catalyst. This decision was made due to the small quantity of F77A remaining in the belief that the resulting hybrid formation would be unchanged. These polymers produced the brightest yellow photocatalysts, which also exhibited significant improvements in photocatalytic activity after photodepositing Pt. However, despite the brighter colour, the yields remained low, and the resulting photocatalytic activity was also lower than the toluene-based equivalent synthesis conditions.

While the SEM images show promise concerning the formation of polymer/oxide hybrid particles by in-situ polymerisation, these results do not demonstrate that charge transfer between the two components can occur. It is possible, however, that M100 and M109 exhibited reduced photocatalytic activities because of charge extraction into oxide particles which are subsequently unable to drive the surface photoredox reaction because there is no co-catalyst present. It is also possible that oxide particles are dispersed inside the bulk of the polymer, and water cannot reach their surfaces. This generates a similar problem to that of residual palladium, which traps photogenerated charges but cannot drive the hydrogen evolution reaction.

4.7.1.2 Solvent-to-base Ratio

To determine if the oxide, photocatalyst, or reaction mixtures are responsible for the reduced yields and lower photocatalytic activity, further testing on the DBTS-DBTS/Al:STO hybrid synthesised in DMF/Base_(aq) reaction mixtures was undertaken. The first step involved changing the DMF-to-aqueous Base volume ratios and the concentration of the base.

By introducing a higher volume percentage of DMF in the miscible reaction mixture, it is hoped that the solubility of the reagents, intermediates and oligomeric intermediary products can be increased. The parameters investigated and resulting polymer synthesis yields are presented in Table 26. Pictures of the reaction mixture after microwave heating are presented in Figure 255 and the same samples after isolating the product are presented in Figure 259.

Table 26 : RhCrO_x@Al:STO/DBTS-DBTS hybrids containing 10 wt.% Al:STO synthesised in DMF/K₂CO₃ reaction mixtures

ID	Polymer	Oxide	Mass (mg)	solvent	Vol (ml)	Base	Concentration (mol dm ⁻³)	Vol (ml)	Yield (%)
M118	DBTS-DBTS	F81A	10	DMF	3	K ₂ CO ₃	1	2	56
M119	DBTS-DBTS	F81A	10	DMF	4	K ₂ CO ₃	2	1	103
M120	DBTS-DBTS	F81A	10	DMF	4	K ₂ CO ₃	1	1	93
M121	DBTS-DBTS	F81A	10	DMF	3	K ₂ CO ₃	2	2	39
M122	DBTS-DBTS	F81A	10	DMF	3	K ₂ CO ₃	0.5	2	79
M123	DBTS-DBTS	-	-	DMF	3	K ₂ CO ₃	2	2	98
M124	DBTS-DBTS	F81A	10	DMF	4.5	K ₂ CO ₃	1	0.5	101

Regarding the yields, a significant contrast can be observed between M123 (2ml 2M K₂CO₃, No Al:STO, 98%) and M121 (2ml 2M K₂CO₃, 10 mg F81A, 39%) where the only difference arises from the presence of Al:STO nanoparticles. Interestingly, M100 (2ml 2M K₂CO₃, 10 mg F77, 59%), in which F77 is not pre-loaded with co-catalyst, was synthesised at a yield between the two. This indicates that the presence of oxide will reduce the polymer synthesis yield, and when the oxide is pre-loaded with RhCrO_x co-catalysts, the reaction is inhibited further.

When maintaining the 3:2 solvent/base ratio, the yields can be improved by decreasing the concentration of the base. Reaction mixtures containing 2ml of 2M, 1M, and 0.5M K₂CO₃ (in the presence of 10 mg co-catalyst-loaded F81A) resulted in yields of 39%, 56%, and 79%, respectively. Reducing the amount of base in the reaction mixture by decreasing the volume of base added also resulted in significantly improved yields, regardless of the concentration of the aqueous base. Reaction mixtures containing 2 ml, 1 ml, and 0.5 ml of 1M K₂CO₃ resulted in yields of 56%, 93%, and 101%, respectively. This difference is even more significant when using 2 M K₂CO₃, where reaction in 2 ml of 2M K₂CO₃ (M121) produces a dark impure polymer with a 39% yield and that in 1 ml of 2M K₂CO₃ (M119) resulted in a 103% yield. All reactions in lower volumes of base also resulted in brighter yellow polymer products.



Figure 255: $\text{RhCrO}_x@/\text{Al:STO}/\text{DBTS-DBTS}$ hybrids containing 10 wt.% Al:STO synthesised in $\text{DMF}/\text{K}_2\text{CO}_3$ reaction mixtures with various solvent/base volume ratios and base concentrations See Table 26 for details. a) Reaction mixtures following microwave synthesis, b) Samples after being isolated, washed with water and MeOH and dried in a vacuum oven overnight.

The resulting hydrogen evolution rates from these hybrids are plotted alongside the polymer yields in Figure 256. This graph also includes data for M100 (2ml 2M K_2CO_3 , 10 mg F77). These data have also been recorded from 11ml Agilent headspace vials containing 5ml of 1:1:1 ($\text{H}_2\text{O}/\text{MeOH}/\text{TEA}$) solution and 5 mg of photocatalyst. The vials have an approximate cross section of 6.7 cm^2 .

A clear correlation between synthesis yield and photocatalytic activity can be observed. For samples synthesised from 2 ml 2 M K_2CO_3 , the photocatalytic activity mimics the pattern observed for yields whereby the activity reduces in the presence of oxide and even further when that oxide is pre-loaded with a co-catalyst. The hybrids in which polymers were synthesised in the highest yields, M119 (1 ml 2M K_2CO_3 , F81A, 103%) and M120 (1 ml 1M K_2CO_3 , F81A, 93%), also produced the best-performing photocatalysts. These results reinforce the hypothesis that impurities from the reaction significantly hinder photocatalytic performance. They also highlight that future studies should make additional efforts to purify the resulting polymers via methods such as Soxhlet extraction.

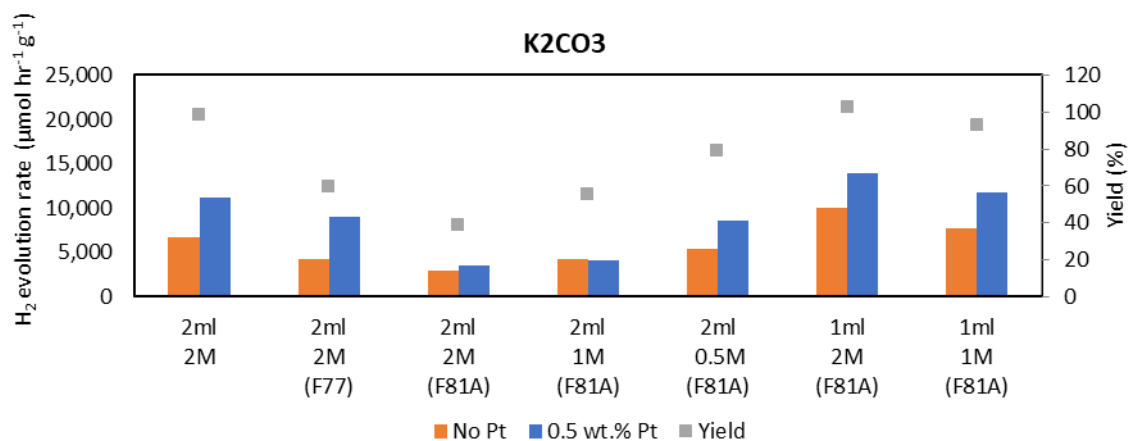


Figure 256: HER rates of Al:STO/DBTS-DBTS hybrid photocatalysts containing 10 wt.% Al:STO following synthesis in various DMF:[K₂CO₃] ratios and base concentrations. HER rates Before and after Pt photodeposition. Approximate polymer synthesis yields are provided on the secondary axis. X-axis labels present the volume and concentration of K₂CO₃ used for each sample. Sample label in brackets refers to the sample of flux-synthesised Al:STO used in the hybrid. The presence of absence of an 'A' denotes whether or not the Al:STO sample was pre-impregnated with a RhCrO_x co-catalyst.

The polymer, in the absence of Al:STO, M123 (2 ml 2M K₂CO₃, 98%), is synthesised at very high yields. Despite this, however, its photocatalytic activity is significantly lower than DBTS-DBTS synthesised from toluene/K₂CO₃. This implies that lower yields alone are not responsible for the reduced activities observed in Figure 254. These lower activities must, therefore, arise from solvent effects, such as reduced solubility resulting in shorter polymer chains. Different amounts of residual palladium and alternative particle size and morphologies are also possible. Hybrids prepared in higher DMF:H₂O ratios also produced the highest-performing photocatalysts.

As in Figure 254, the relative increases in activity with respect to Pt photodeposition were small. This is in direct contrast to the DBTS-DBTS polymers synthesised from toluene/K₂CO₃. This may result from the Rh and Cr co-catalysts on the oxide particles' surface or from the impurities and palladium content incorporated into the polymer matrix due to the choice of solvent and base.

4.7.1.3 DBTS-DBTS Polymer in DMF/K₂CO₃

The polymer, DBTS-DBTS, in the absence of Al:STO, was subsequently synthesised at several different combinations of DMF:H₂O ratios and concentrations of K₂CO₃. These were prepared on a smaller scale (0.125 mmol) and in a larger volume of liquid (10 ml). The parameters and resulting yields are presented in Table 27. The resulting HER activities are presented in Figure 257.

These results demonstrate that, in the absence of Al:STO, the DMF:Base ratio has little impact on the yield and photocatalytic activity. However, on average, the percentage increase in activity upon loading with Pt co-catalyst is larger for these samples than the hybrids synthesised with F81A. However, the final activities of Pt-loaded catalysts are similar. This observation is in line with the hypothesis that rhodium co-catalyst from the oxide particle surfaces may become incorporated into the polymer matrix during synthesis.

Table 27: DBTS-DBTS polymers synthesised from DMF/K₂CO₃ reaction mixtures containing various concentrations and volumes of the aqueous base phase.

Polymer	solvent	Vol (ml)	Base	Concentration (mol dm ⁻³)	Vol (ml)	Yield (%)
DBTS-DBTS	DMF	9	K ₂ CO ₃	2	1	70
DBTS-DBTS	DMF	9	K ₂ CO ₃	1	1	87
DBTS-DBTS	DMF	9	K ₂ CO ₃	0.5	1	85
DBTS-DBTS	DMF	8	K ₂ CO ₃	2	2	84
DBTS-DBTS	DMF	8	K ₂ CO ₃	1	2	86
DBTS-DBTS	DMF	8	K ₂ CO ₃	0.5	2	83

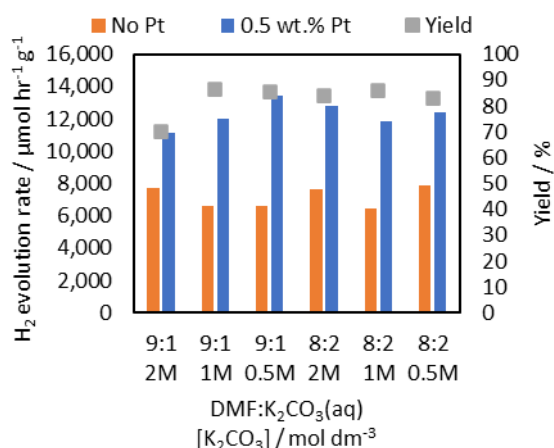


Figure 257: HER rates with and without 0.5 wt.% Pt co-catalyst for DBTS-DBTS polymers synthesised from DMF/K₂CO₃ reaction mixtures containing various concentrations and volumes of the aqueous base phase. Synthesis yields are also presented on the secondary axis.

4.7.1.4 DMF:K₃PO₄

Table 28: Al:STO/DBTS-DBTS Hybrid samples containing 10 wt.% Al:STO synthesised from various DMF:[K₃PO₄] reaction solutions.

ID	Polymer	Oxide	Mass (mg)	solvent	Vol (ml)	Base	Concentration (mol dm ⁻³)	Vol (ml)	Yield (%)
M108	DBTS-DBTS	Al:STO	10	DMF	3	K ₃ PO ₄	2	2	67
M109	DBTS-DBTS	Al:STO	10	DMF	3	K ₃ PO ₄	1	2	64
M110	DBTS-DBTS	Al:STO	10	DMF	4	K ₃ PO ₄	2	1	93
M111	DBTS-DBTS	Al:STO	10	DMF	4	K ₃ PO ₄	1	1	83

The initial results from Figure 254 also indicated that K_3PO_4 may be a better base for the reaction than K_2CO_3 . Four additional samples were synthesised to investigate the impact of base concentration and organic-to-aqueous phase ratios for reactions involving K_3PO_4 . The selected conditions and resulting yields are listed in Table 28.

As with the initial study, reactions involving K_3PO_4 as the base resulted in a dense white residue that sank to the bottom of the reaction vials following microwave heating (see Figure 258). This residue is believed to be phosphate salt byproducts from the reaction mixture that are less soluble in the DMF/ H_2O reaction mixture than their carbonate alternatives. However, this phase separation may also result in inhomogeneous mixing of oxide and polymer components within the hybrid product.

As in the case of using the K_2CO_3 base, reactions mixtures containing 3 ml DMF and 2 ml aqueous base resulted in darker hybrid products and reduced yields (see Figure Figure 258). When this ratio was changed to 4 ml DMF and 1 ml aqueous base, the polymers were brighter in colour and produced in a greater yield. In both cases, reducing the concentration from 2M to 1M slightly reduced the yield. Yields were also lower for K_3PO_4 than for K_2CO_3 .



Figure 258: Al:STO/DBTS-DBTS Hybrid samples containing 10 wt.% Al:STO synthesised from various DMF:[K_3PO_4] reaction solutions. a) Hybrids dispersed in reaction mixture after completion of the microwave-assisted polycondensation reaction, b) Hybrid samples after isolating, washing, and drying.

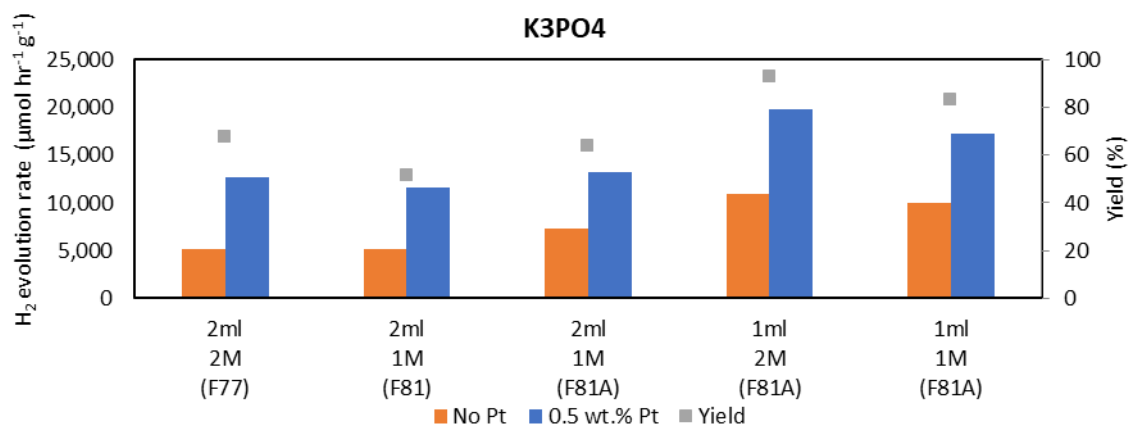


Figure 259: HER rates for Al:STO/DBTS-DBTS Hybrid samples containing 10 wt.% Al:STO synthesised from various DMF:[K₃PO₄] reaction solutions. Yields are presented on the secondary axis. X-axis labels present the volume and concentration of K₃PO₄ used for each sample. Sample label in brackets refers to the sample of flux-synthesised Al:STO used in the hybrid. The presence or absence of an 'A' denotes whether or not the Al:STO sample was pre-impregnated with a RhCrO_x co-catalyst.

Figure 259 contains the HER data for the DBTS-DBTS@F81A 10 wt.% hybrids prepared from DMF/K₃PO₄ reaction mixtures. As with the DMF/K₂CO₃ samples, the relationship between reaction yield and photocatalytic activity is clear. Lower yields always result in lower activities. The higher yields were also obtained at higher DMF:H₂O ratios. For these two samples, the highest activity was observed when using a higher concentration of K₃PO₄.

Compared to K₂CO₃, the HER rates are significantly higher when the reaction is conducted in the presence of K₃PO₄. These rates are comparable to those observed for DBTS-DBTS synthesised from toluene/K₂CO₃ reaction mixtures. Given the high yields and uncompromised activity compared with the pure polymer, indicating that the polymer is of high purity and not subject to reduced activity from byproducts, K₃PO₄ appears to be a highly promising base in the preparation of DBTS-DBTS/oxide hybrid photocatalysts. Furthermore, these photocatalysts also showed significant relative improvements in activity after photodepositing a Pt co-catalyst, despite Rh/Cr₂O₃ being present on the oxide particle surfaces.

However, since some unincorporated Al:STO residue was identified amongst the white aqueous phase that had separated in the reaction, this raises questions regarding the complete incorporation of oxides into the hybrid materials. For this reason, and for a more direct comparison with the literature methods,³⁰⁹ DMF/K₂CO₃ was the selected reaction medium for further in-situ hybrid photocatalysts preparation reactions. Furthermore, attempts to synthesise the co-polymer DBTS-Ph2a in DMF/K₃PO₄

mixtures had resulted in impure products, low yields, and low activities when compared with DMF/K₂CO₃. DMF/K₂CO₃ was therefore selected as a more appropriate reaction mixture for subsequent experiments since several other polymers would be prepared in addition to DBTS-DBTS.

4.8 DBTS-DBTS/Al:STO

Following the successful distribution of oxide particles into a polymer matrix using the DMF/K₂CO₃ reaction mixture, further DBTS-DBTS/Al:STO hybrid samples must be prepared with various polymer and oxide component ratios. Although previous research has suggested that a 10 wt.% loading of TiO₂ resulted in a significant increase in activity,³⁰⁹ further improvements in area-normalised HER rates may be obtained by increasing the oxide content further. Work presented in Chapter 3 and the previous section suggests that altering the polymerisation reaction conditions, including via the addition of oxide particles, can significantly impact the resulting photocatalytic activities of the polymer component. Therefore, any enhancement may not be directly attributable to charge transfer at the hybrid interface.

Hybrids containing only 10 wt.% oxide present an inherent issue with regard to the distribution of oxide particles. SEM images show that oxide nanoparticles are distributed both on the surface and inside the bulk of larger polymer particles. This is unsurprising given the low oxide loading concentration and the higher density of SrTiO₃ compared with the polymer. However, organic polymer exciton diffusion lengths are only anticipated to be on the order of 5 – 10 nm. As such, only a small percentage of photogenerated excitons will be capable of diffusing to the interface before extraction can occur. Furthermore, the oxide particles located in the polymer bulk may be capable of trapping electrons that are unable to react further with water due to their inaccessible surfaces.

4.8.1 Synthesis and Physical Characterisation

Four further hybrid samples of DBTS-DBTS/Al:STO were subsequently synthesised containing 50%, 100%, 150%, and 200% relative weights of the oxide component compared with the theoretical polymer yield. The polymer syntheses were conducted on the 0.25 mmol scale in 4.5 ml DMF and 0.5 ml of 1M K₂CO₃. Pd(dppf)Cl₂ was selected as the Suzuki cross-coupling catalyst with a 0.66 mol% loading. The microwave syntheses were conducted at 120 °C for 1.5 hr, and the microwave power was limited to 120 W. The reaction conditions and obtained yields are presented in Table 29.

The DMF:K₂CO₃ ratio was chosen because yields were improved at higher concentrations of DMF. The base concentration was selected to be 1 M because reactions using 2 M K₂CO₃ resulted in the deposition of some oxide particles on the reaction vial walls rather than being entirely incorporated into the hybrid product (see Figure 255). Furthermore, 0.5 ml of 1M results in the addition of 0.5 mmol of base molecules. This is 2 equivalents of base per unit of the monomer reagents and hence 1

Table 29: RhCrOx@Al:STO/DBTS-DBTS Hybrid samples containing 10 – 900 wt.% Al:STO synthesised from DMF/K₂CO₃ reaction solutions and a 9:1 ratio of organic solvent to aqueous base.

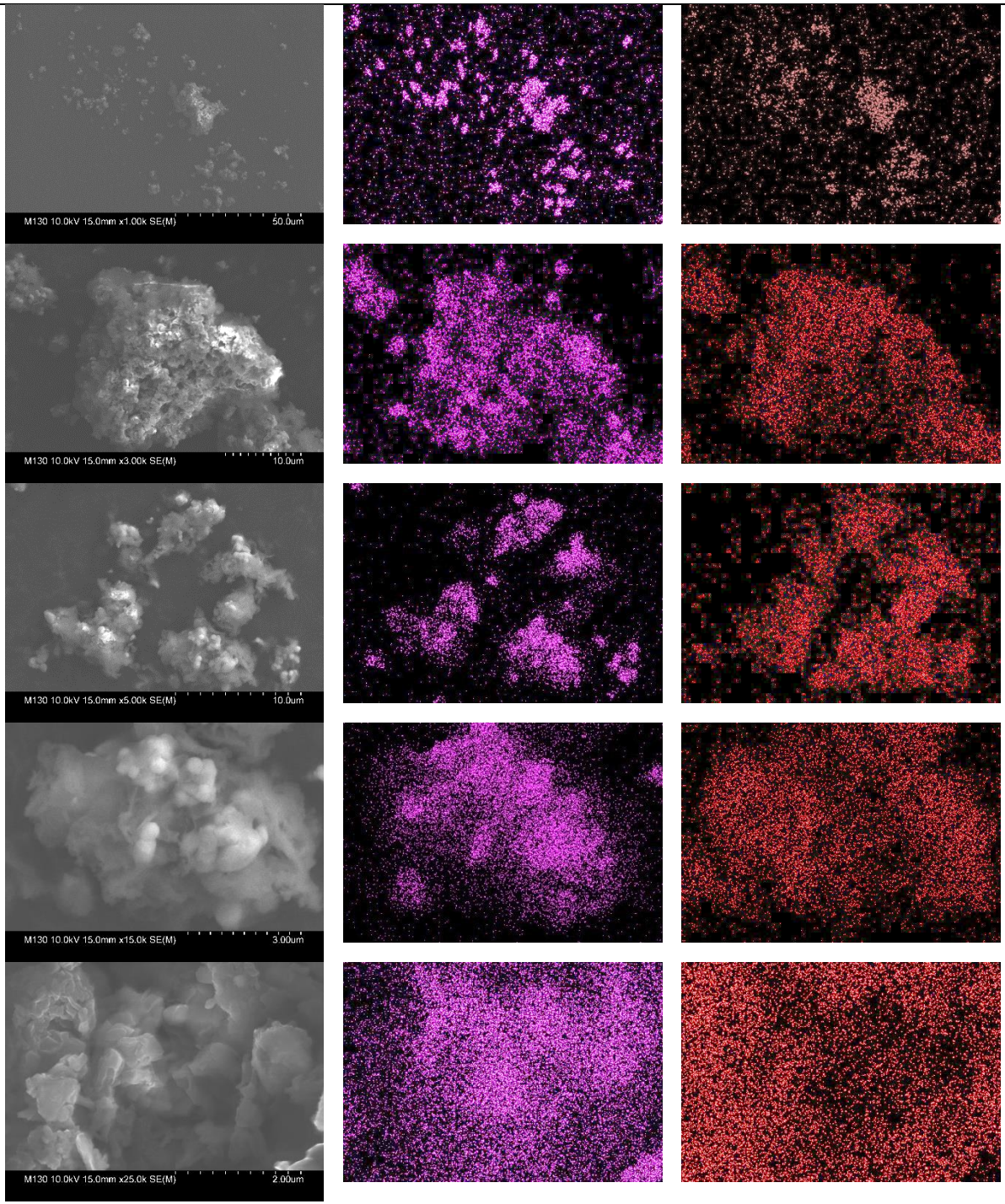
ID	Polymer	Oxide	Mass (mg)	solvent	Vol (ml)	Base	Concentration (mol dm ⁻³)	Vol (ml)	Yield (%)
M124	DBTS-DBTS	F81A	10	DMF	4.5	K ₂ CO ₃	1	0.5	101
M130	DBTS-DBTS	F81A	200	DMF	4.5	K ₂ CO ₃	1	0.5	81
M131	DBTS-DBTS	F81A	150	DMF	4.5	K ₂ CO ₃	1	0.5	75
M132	DBTS-DBTS	F81A	100	DMF	4.5	K ₂ CO ₃	1	0.5	97
M133	DBTS-DBTS	F81A	50	DMF	4.5	K ₂ CO ₃	1	0.5	93
M154 ^[a]	DBTS-DBTS	F81B	450	DMF	4.5	K ₂ CO ₃	1	0.5	27

[a] The DBTS-DBTS component of M154 was synthesised on the 0.125 mmol scale, since such large quantities of the oxide were required to achieve a 9:1 ratio.

equivalent of the functional groups. Previous reactions containing 2 ml of 2 M base for the same scale reaction included an excess of base sixteen times the concentration of the monomer reagents. Typical Suzuki reactions only require 2-3 equivalents of base for the reaction to run successfully.²⁵¹

The reactions ran to completion and produced bright yellow homogeneous mixtures. The polymers were obtained in high yields between 75% and 101%. On average, the yield decreases as the amount of oxide present in the reaction mixture increases. SEM images and EDS maps of the resulting hybrid materials are presented in Figures 260 to 262. As can be seen in these images, the Al:STO nanoparticles are well dispersed inside the DBTS-DBTS polymer matrix. At lower oxide concentrations, more pure polymer domains appear. However, even at 200 wt.% Al:STO, a greater volume of polymer is present and much of the oxide is embedded in the bulk of polymer particles. This implies that even higher ratios may be required to ensure a thin polymer layer surrounds oxide particles as per the desired model. It also remains unclear how well the two phases will adhere to one another following ultrasonication and irradiation.

The polymer component of M154 was only synthesised with a 27% yield. However, it should be stated that this yield assumes that no solids were lost during the transfer and washing stages of the reaction work-up, i.e. 450 mg of the 465 mg product obtained are assumed to be oxide. The yield measure is further exaggerated since the polymerisation reaction was performed on a 0.125 mmol scale with a theoretical yield of 55 mg. In this case, each milligram of product lost during workup and transfer equates to a drop in polymerisation yield of almost 2%. As such it is difficult to determine what the true reaction yield was and what the final polymer content is in the final hybrid polymer. Resultingly, the polymer content of M154 is likely to lie somewhere between 3 and 10 wt.%.

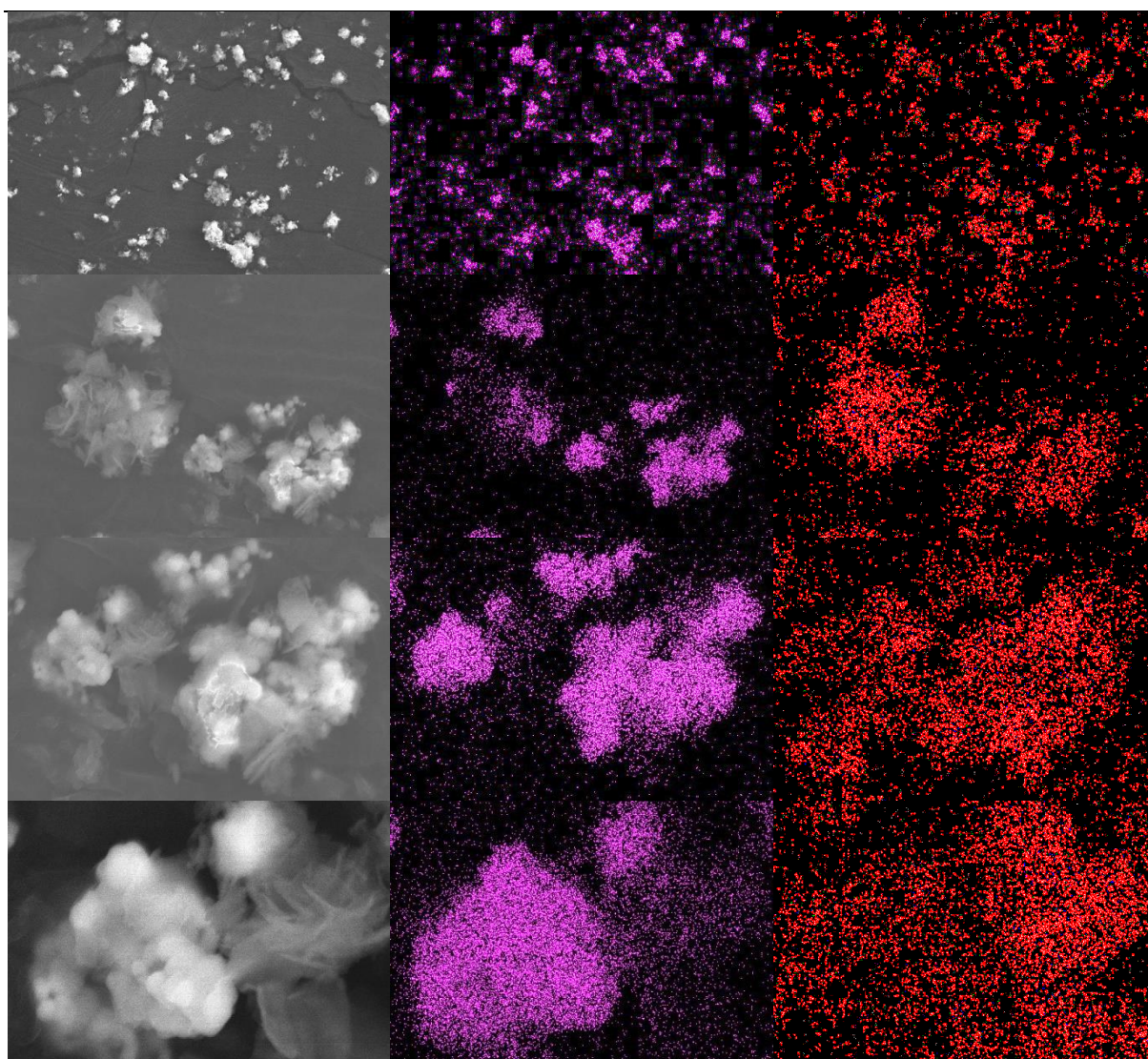


SEM Images

EDS map Sr K α 1

EDS map S K α 1

Figure 260: SEM images and EDS maps of RhCrOx@Al:STO/DBTS-DBTS hybrid photocatalyst M130. M130 contains a target Al:STO content of 67 wt.%, assuming a 100% polymer synthesis yield.



SEM Images

EDS map Sr Kα1

EDS map S Kα1

Figure 261: SEM images and EDS maps of RhCrO_x@Al:STO/DBTS-DBTS hybrid photocatalyst M131. M131 contains a target Al:STO content of 60 wt.%, assuming a 100% polymer synthesis yield.

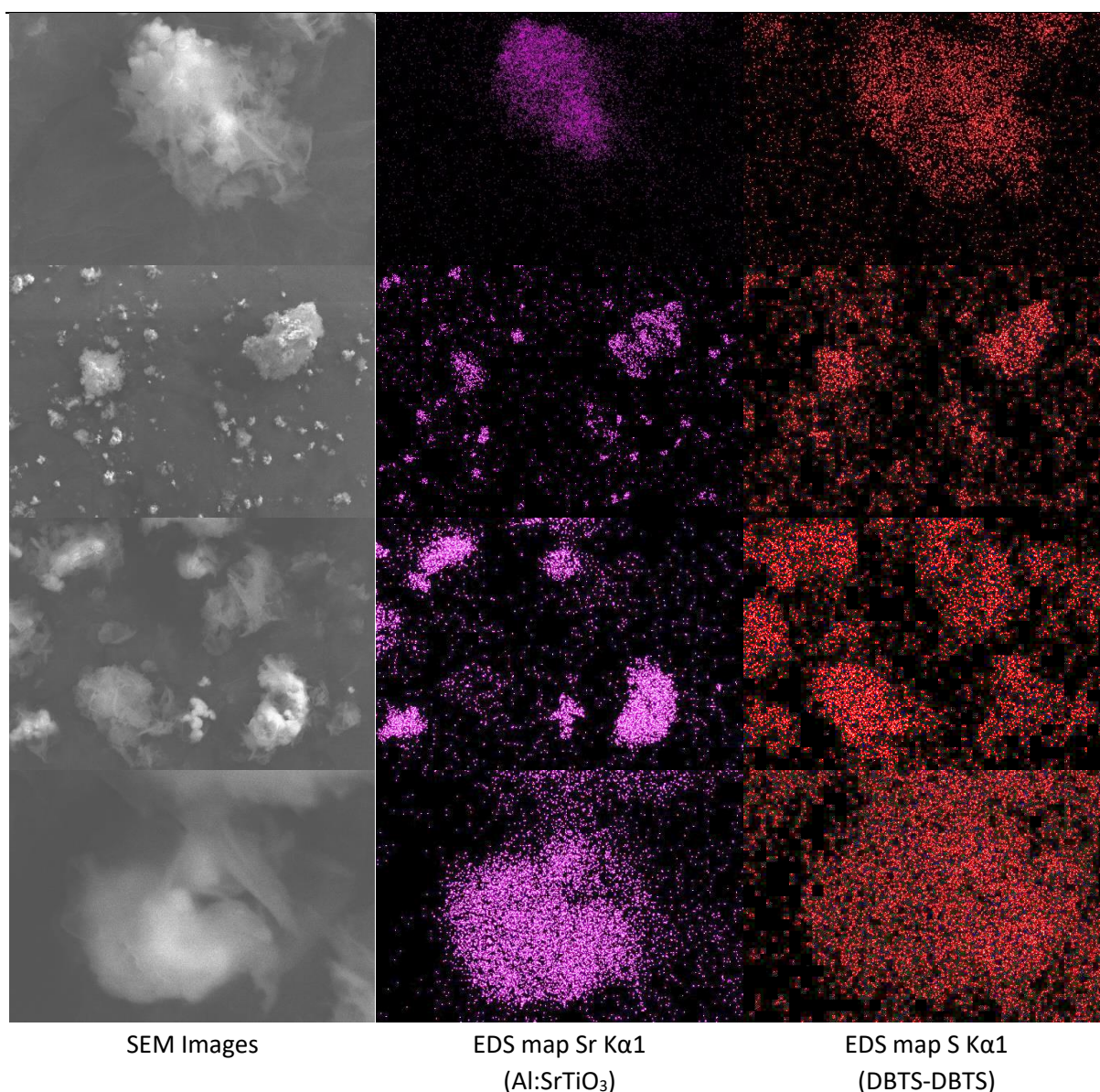


Figure 262: SEM images and EDS maps of RhCrOx@Al:STO/DBTS-DBTS hybrid photocatalyst M133. M133 contains a target Al:STO content of 33 wt.%, assuming a 100% polymer synthesis yield.

4.8.2 Area-normalised vs Mass-normalised Photocatalytic Activities.

Before testing these hybrid materials for their photocatalytic activity, it is important to highlight issues regarding the reliability of using mass-normalised hydrogen evolution rates to compare photocatalysts. Whilst high mass-normalised photocatalytic efficiencies can imply a cheap and hence more commercially-viable product, it is inherently very challenging to compare different materials for their overall photocatalytic activity.

Nowhere is this more apparent than hybrid photocatalysts. Strontium titanate has a density of 5.13 g cm^{-3} ,³³⁹ meanwhile the semicrystalline polymer DBTS-DBTS, which is only composed of the lighter elements C,H,S, and O, is considerably less dense. Furthermore, Al:STO only absorbs light in the UV-region of the spectrum. As such, for a hybrid material that only contains 10 wt.% polymer, 50 mg of the hybrid photocatalyst is required to achieve the same visible light absorption as 5 mg of the pure polymer.

To investigate the importance of this, the photocatalytic performance of M154 (90 – 97% Al:STO) was tested with different loadings of the photocatalyst from 5 to 60 mg. These samples were dispersed in 5 ml of a 1:1:1 mixture of MeOH, H₂O, and TEA. The resulting hydrogen evolution rates, in $\mu\text{mol hr}^{-1}$ for this sample are presented in Figure 263.

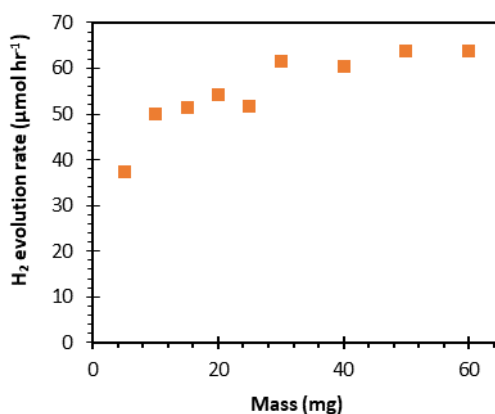


Figure 263: Absolute HER of RhCrO_x@Al:STO/DBTS-DBTS hybrid photocatalyst, M154, containing ~95 wt.% Al:STO, for different photocatalyst mass loading concentrations.

As expected, the hydrogen evolution rate over a constant area increases with the amount of photocatalyst dispersed. However, this increase is not linear and tends asymptotically to a saturation value. This is because at high concentrations, the solution becomes saturated and all of the incident light that can be absorbed is absorbed according to the Beer-Lambert law.

By assuming a 10 wt.% polymer content, it is possible to compare the photocatalytic activity of the hybrid photocatalyst M154 with the pure polymer prepared under the same conditions, M141, for a given mass of polymer. Figure 264 contains the HER rates for M141, M141 + 0.5 wt.% Pt, and M154 for masses of polymer from 0.5 to 5 mg. M154 was measured up to 60 mg of hybrid as the true polymer content of this photocatalyst is unknown and likely to be lower than 10 wt.%.

The pristine polymer follows the same trend as was observed for the hybrid photocatalyst. The hydrogen evolution rate for a given irradiation area increases asymptotically to a saturation value. This confirms that previous studies on DBTS-DBTS, in which 5 mg of polymer was weighed out, are taken in the saturation regime. It is expected that all other polymers synthesised in chapter exhibit similar absorption coefficients and that 5 mg is comfortably in the saturation regime for all of them, ensuring the results comparable.

Although the hybrid material outperforms the pristine polymer, the difference of only $8.5 \mu\text{mol hr}^{-1}$ is of a similar magnitude to the photocatalytic activity of the oxide component F81A and indicates that this hybrid material is no more active than a simple mixture of the two components would be. The hybrid photocatalyst also remains considerably less active than the pristine polymer after loading with 0.5 wt.% of platinum as a co-catalyst.

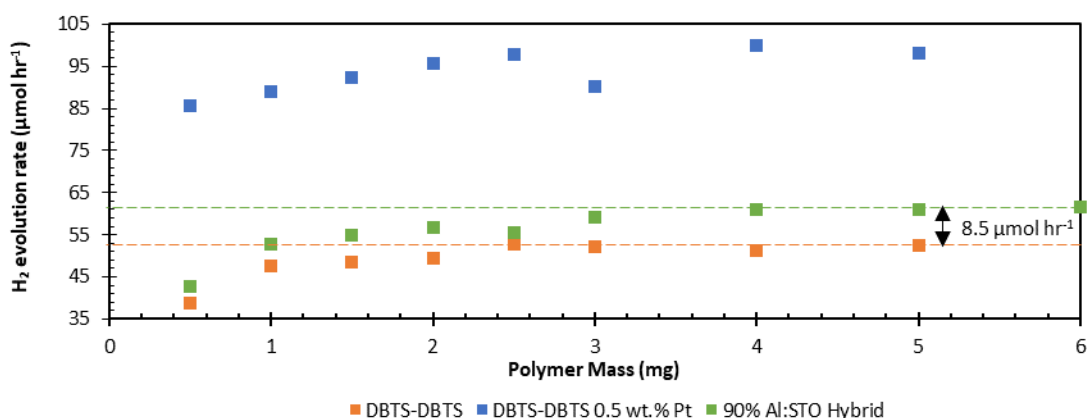


Figure 264: Absolute HER of $\text{RhCrO}_x/\text{Al:STO}/\text{DBTS-DBTS}$ hybrid photocatalyst, M154, containing a target Al:STO content of 90 wt.%, plotted against the approximate weight of the organic polymer component assuming a 100% polymer synthesis yield. HER rates for DBTS-DBTS before and after Pt photodeposition are also presented for different mass dispersions of the polymer.

To reinforce the issue surrounding mass-normalised photocatalytic activities, the same data have been converted to their mass-normalised rates, μmol per unit mass of total photocatalyst, and are presented in Figure 265. Despite having the lowest solar-to-hydrogen conversion efficiency, the vials containing the least photocatalyst produced the highest mass-normalised rates since the HER does not scale linearly with mass. Likewise, for a given irradiation area, the hybrid material produced a greater absolute quantity of hydrogen than the pristine polymer but exhibits significantly lower mass-normalised HER rates due the sample only containing 10 wt.% polymer. When dispersing 0.5 mg of DBTS-DBTS and loading it with 0.5 wt.% Pt, mass-normalised HER rates of over $170 \text{ mmol hr}^{-1} \text{ g}^{-1}$ were

obtained. Such values are comparable to the highest recorded in the literature for sacrificial hydrogen evolution.²³⁷ It is therefore vital that all future published research should include data regarding the concentration of photocatalyst, the irradiation area, and ideally be measured in the saturation regime. STH and AQY data are also more reliable for comparing photocatalysts prepared by different research groups.

Unfortunately, the setup used does not enable reliable area-normalised data since solutions are dispersed in cylindrical vials and the incident light path length is not consistent across the irradiated area. However, the irradiation area can be approximated as 6.7 cm² with an average path length of 0.75 cm.

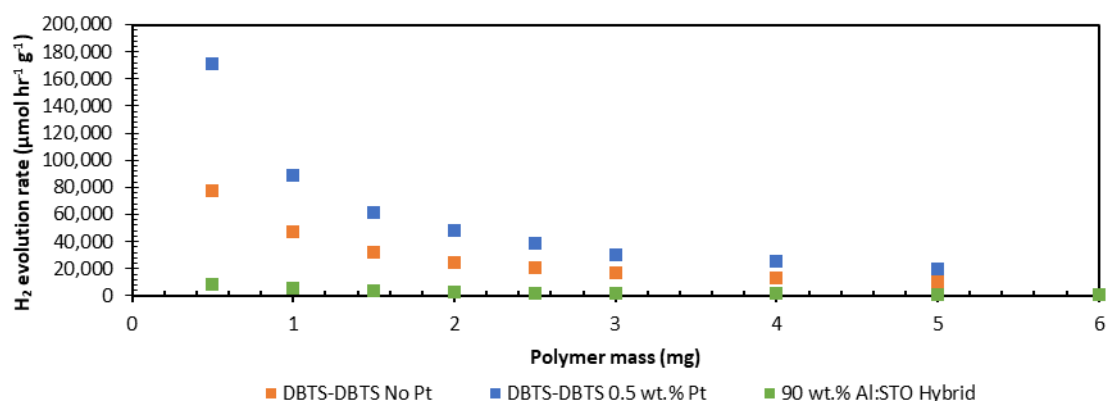


Figure 265: Mass-normalised HER rates of RhCrO_x@Al:STO/DBTS-DBTS hybrid photocatalyst, M154, containing a target Al:STO content of 90 wt.%, plotted against the approximate weight of the organic polymer component assuming a 100% polymer synthesis yield. Mass normalised HER rates for DBTS-DBTS before and after Pt photodeposition are also presented for different mass loadings of the polymer.

4.8.3 Sacrificial Hydrogen Evolution

The remaining DBTS-DBTS/Al:STO hybrids were tested for their hydrogen evolution photocatalytic activity with and without the photodeposition of a platinum co-catalyst. Unlike earlier measurements, in which 5 mg of the photocatalyst was loaded into each headspace vial, samples M130 – M133 were loaded such that approximately 5 mg of the polymer was present in each sample. In the case of M130, in which the polymer was synthesised with an 81% yield and contained 200 mg of F81A, 16.2 mg of the hybrid material was weighed into each vial. M154, representing the sample containing 90 wt.% Al:STO, was only weighed out with an equivalent of 3 mg polymer. This is because it was produced at a smaller scale and the polymerisation reaction yield was lower. Figure 266 contains the photocatalytic hydrogen evolution activity data from these samples when dispersed in 5 ml of a 1:1:1 mixture. The

data is not normalised according to the mass of the photocatalyst. The platinum co-catalyst was loaded as 0.5 wt.% of the total photocatalyst mass.

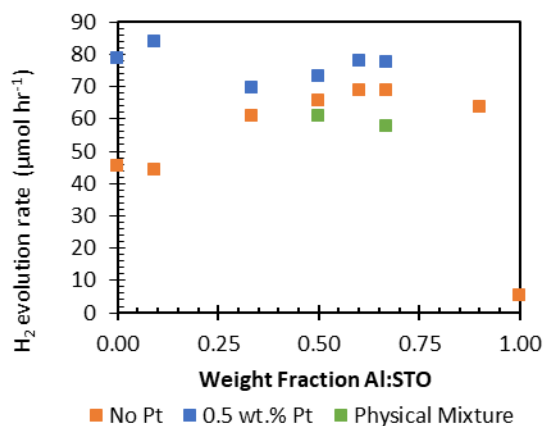


Figure 266: Absolute HER rates for $\text{RhCrO}_x@$ Al:STO/DBTS-DBTS hybrid photocatalysts containing different weight fractions of Al:STO before and after loading with 0.5 wt.% Pt. Dispersions were prepared such that vials contain approximately 5 mg of the polymer component. HER rates for two non-hybrid physical mixtures are also presented (No Pt).

In the absence of a platinum co-catalyst, the HER rates increased as the Al:STO content increased. The exception being of the hybrid containing 90 wt.% Al:STO. However, this sample only contained 3mg of polymer instead of 5mg. Non-hybrid physical mixtures of F81A and DBTS-DBTS were also tested. Whilst these also achieved photocatalytic activities greater than the sum of their components, they remained less active than their hybrid equivalents. There was also no increase in activity with respect to increasing the proportion of oxide in the mixture. However, these samples only exhibited small increases in activity after loading with a platinum co-catalyst. Furthermore, the Pt-loaded pristine polymer sample exhibited the highest photocatalytic performance.

The origin of the improved photocatalytic activity in hybrid photocatalysts remains unclear. Whilst it is hoped that the primary increase results from charge transfer between the organic and inorganic components, many other factors could be acting together to explain the observation. The first set of factors relates to the physical structure of the hybrids, whereas the second set correspond to the chemical composition of the organic polymer phase.

When the polymer is dispersed across the surfaces of an excess of inorganic particles, there are fewer large polymer particles in which bulk charge recombination events can occur. Instead, the polymer primarily exists as smaller particles and thin layers coating oxide particles and hence gives rise to an increased surface area-to-volume ratio. The polymer's surface morphology may also be influenced by

the presence of oxide particles in the reaction mixture. However, there is limited evidence for this in the SEM images. Generally, however, decreasing the bulk recombination rate in polymers is essential given the short exciton lifetimes in organic semiconductors. However, an increase in activity resulting from this would be observable regardless of the chemical composition of the inorganic powder substrate and not indicative of hybrid charge transfer.

The presence of inorganic photocatalysts within the polymerisation reaction mixture may influence the average molecular weight of the polymer, its polydispersity, as well as the composition, distribution, and concentration of byproducts and impurities such as residual palladium. Furthermore, since a photocatalyst that had been pre-loaded with a RhCrO_x co-catalyst was used, increased oxide content in the reaction mixture would also have led to an increased residual rhodium content in the polymer phase. This increase could explain why the activity of Pt-free hybrid catalysts increases with respect to oxide content, and why further Pt-loading on the photocatalyst surface only results marginal additional gains.

4.8.4 Change of Sacrificial Reagent

Previous HER measurements have all been performed from a dispersion of photocatalyst in a 1:1:1 mixture of TEA, water, and MeOH. However, this does not provide much information regarding the effectiveness of charge transfer from polymer to the oxide conduction band, since DBTS-DBTS is already highly active under these conditions. To gather more information about the photocatalytic activity of the hybrids systems, the same systems were also tested for hydrogen when dispersed in a 20 vol% solution of MeOH. MeOH does not act as an efficient hole scavenger for DBTS-DBTS. However, $\text{RhCrO}_x/\text{Al:STO}$ is capable of sacrificial hydrogen evolution in its presence. Dispersions containing physical mixtures of the two photocatalysts were also prepared for comparison. All samples were prepared to contain approximately 5 mg of polymer, with the exception of the pure Al:STO sample, which only contains 5 mg of F81A. The resulting hydrogen evolution rates are presented in Figure 267.

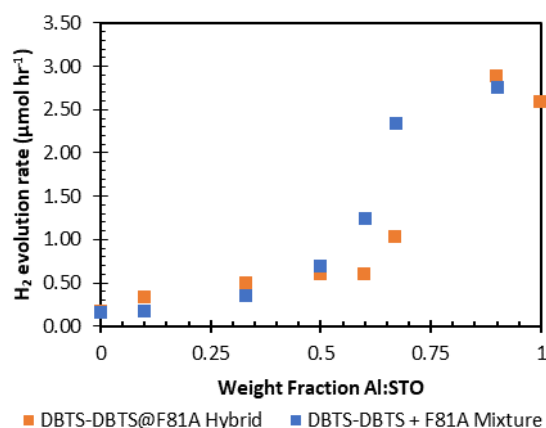


Figure 267: Absolute HER rates for $\text{RhCrO}_x/\text{Al:STO}/\text{DBTS-DBTS}$ hybrid photocatalysts containing different weight fractions of Al:STO using 20 vol.% MeOH as the sacrificial reagent solution. Dispersions were prepared such that vials contain approximately 5 mg of the polymer component. HER rates for mass-equivalent non-hybrid physical mixtures are also presented. Photocatalysts are not loaded with additional Pt co-catalysts.

As the mass percentage of the oxide increases, so does the rate of hydrogen evolution. Compared to the pure Al:STO sample, all hybrids and mixtures, with the exception of those containing 90% Al:STO, performed worse than the inorganic photocatalyst by itself material. The reduced photocatalytic activity likely arises because of competitive absorption of the incident UV light. The samples containing 10% and 33% Al:STO also contain less than 5 mg of the oxide and so the maximum absorption by the oxide component is limited further. However, the lower rate of the 50 wt.% samples, containing 5 mg polymer and 5 mg oxide, are particularly notable.

Compared with the organic/inorganic mixtures, the hybrid photocatalysts respond differently to the oxide content. At high oxide content (60 and 67 wt.% Al:STO), the physical mixture is more active than the hybrid photocatalysts. If the hydrogen evolution and methanol reduction reactions are assumed to take place on the oxide surface, this can be rationalised by a reduction in exposed oxide surfaces following the embedding of oxide particles in the polymer matrix. The oxide particles may also have lost some of their co-catalyst coatings during the in-situ polymerisation.

Hybrids containing 90% Al:STO are expected to have a significant proportion of exposed oxide surfaces and so this material performs similarly to pure $\text{RhCrO}_x/\text{Al:STO}$. Since this sample is expected to contain 27 mg oxide and 3 mg polymer, competitive absorption of incident UV light is minimised. However, this hybrid performs slightly better than both the pure oxide and the oxide/polymer mixture. This can likely be explained by the increased surface area of the polymer, which leads to an increased

contribution by the polymer component. However, interfacial charge separation and injection of electrons from the polymer into the oxide may also be possible.

Based on observations listed above, the hybrids that contain small amounts of oxide (10 and 33%) are expected to perform worse than the physical mixtures, since there is less oxide surface area available than in the case of the physical mixture. However, the hybrid photocatalysts perform better. This difference may arise from a weighing error. The 10% mixture contains 5 mg polymer, but only 0.5 mg of the oxide. Since the weighing scales are only accurate to 0.1 mg and there is a risk of losing material during transfer stages, there is a large uncertainty regarding the absolute oxide content in the mixture tested. Likewise, the 33% mixture contains 5 mg polymer but only 1.7 mg of the oxide.

A second possible explanation for this is that the polymer may utilise MeOH as a sacrificial reagent more efficiently after loading with either Rh, or Cr co-catalysts. By completing the polymerisation reaction in the presence of co-catalyst loaded oxide particles, residual co-catalyst may find its way into the polymer matrix and enhance the hydrogen evolution activity of the polymer component in this system, even at exceptionally low concentration. Charge transfer between the organic and inorganic phases may possibly also lead to enhanced rates in these hybrid materials. However, the results from hybrids containing higher oxide loadings imply that this is unlikely.

Overall, it appears unlikely that the formation of DBTS-DBTS/RhCrO_x-Al:STO hybrid photocatalyst particles leads to enhanced photocatalytic activity via a direct charge separation and transfer at the interface. However, further experiments including the synthesis of hybrid materials which have not been pre-loaded with co-catalysts is required. This can be achieved by photodepositing the relevant co-catalysts after hybrid preparation.

4.8.5 Overall Water Splitting

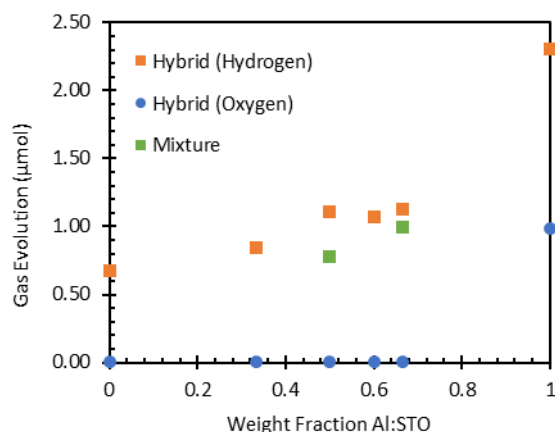


Figure 268: Absolute HER and OER rates for $\text{RhCrO}_x/\text{Al:STO}/\text{DBTS-DBTS}$ hybrid photocatalysts containing different weight fractions of Al:STO when dispersed in pure water without any sacrificial reagents. Dispersions were prepared such that vials contain approximately 5 mg of the polymer component. HER rates of two mass-equivalent non-hybrid physical mixtures are also presented (green squares). Photocatalysts are not loaded with additional Pt co-catalysts. Samples irradiated for 2 hours using AM1.5G solar-simulated irradiation.

These $\text{RhCrO}_x/\text{Al:STO}/\text{DBTS-DBTS}$ co-polymers were subsequently tested for their overall water splitting photocatalytic activities. The results of these samples, along with those for pure DBTS-DBTS and $\text{RhCrO}_x/\text{Al:STO}$ are presented in Figure 268. Physical mixtures of DBTS/DBTS + Al:STO were also compared for the 50% and 67% mass ratios. Sample vials contained approximately 5 mg of polymer each.

The hydrogen evolution rates for the hybrid materials closely mirror those of the same hybrid materials dispersed in MeOH. These values are only marginally larger than for the pure DBTS-DBTS polymer. However, there was no oxygen detected for any of these systems, indicating that the oxygen reduction reaction is taking place. It is unclear if the hydrogen originated due to photogenerated electrons that result from the sacrificial oxidation of impurities, oxidation of water, or oxidation of itself.

Physical mixtures of DBTS-DBTS + Al:STO produced less hydrogen than the equivalent hybrids. This may be because of the increased surface area of the polymeric components in hybrid systems rather than any indication of charge transfer. There was also no oxygen detected in these physical mixtures, indicating that any oxygen produced by the Al:STO component was subsequently reduced.

4.8.6 Photocatalytic Hydrogen Peroxide Production

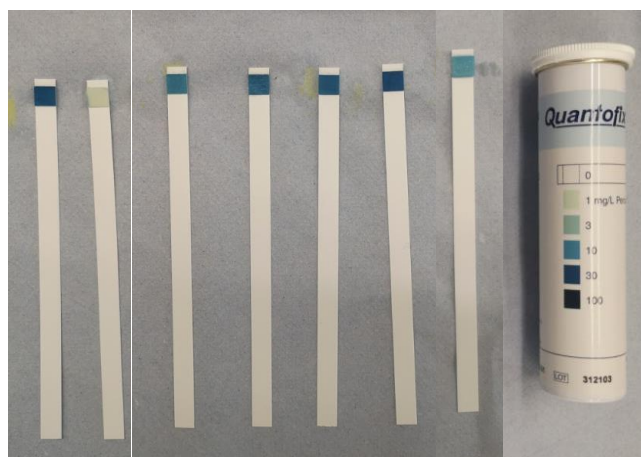


Figure 269: Hydrogen peroxide dip stick test for DBTS-DBTS/Al:STO hybrid photocatalysts. Samples from left to right: DBTS-DBTS, Al:STO, 67 wt% Al:STO Hybrid, 60 wt.% Hybrid, 50 wt.% Al:STO, 33 wt.% Al:STO, 50 wt.% Mixture. Test conditions: 5 mg equivalent polymer dispersed in 5 ml deionised water via ultrasonication. Irradiated for 2 hours with solar simulated lights. Vials were not degassed so to maintain an oxygenated atmosphere.

To confirm whether oxygen reduction is taking place, the same hybrid samples were dispersed in water and irradiated under an oxygenated atmosphere for two hours. The resulting H_2O_2 concentrations as determined by a dipstick test are presented in Figure 269.

Notably, Al:STO by itself does not produce hydrogen peroxide, The 50/50 mixture resulted in low peroxide concentrations, and the hybrid materials exhibited H_2O_2 production rates between that of pure DBTS-DBTS and the 50/50 physical mixture. Increased oxide content resulted in lower peroxide concentrations. As such, this trend is the opposite of that observed for H_2 evolution for pure water.

It is difficult to provide a full interpretation of these results. The low H_2O_2 concentration of the physical mixture may imply that exposed oxide surface leads to degradation of any generated peroxide species. However this may also result from the competitive absorption of UV-irradiation by oxide and polymer components.

By contrast the 50/50 hybrid sample produced significant amounts of H_2O_2 that were almost comparable to that observed in DBTS-DBTS. Likewise, this has several possible explanations. The first relates to the fact that there is very little oxide surface exposed due to encapsulation by the polymeric component. This could negate any peroxide degradation processes and lead to increased absorption by the organic phase relative to the oxide since light must first pass through the polymer before reaching the oxide particle. However, it is also possible that the enhanced H_2O_2 production rate of the hybrid material relates to photogenerated charge injection from the oxide component into the

polymer or accelerated charge separation/extraction due to inbuilt electric fields at the interface, such as in Z-scheme setup.

4.8.7 Discussion

The performance of these hybrid materials provides some information regarding the type of heterojunction formed between Al:STO and the DBTS-DBTS homopolymer. However, overall, the exact relationship remains very unclear, particularly since the photocatalytic activities of the physical mixtures did not behave as expected.

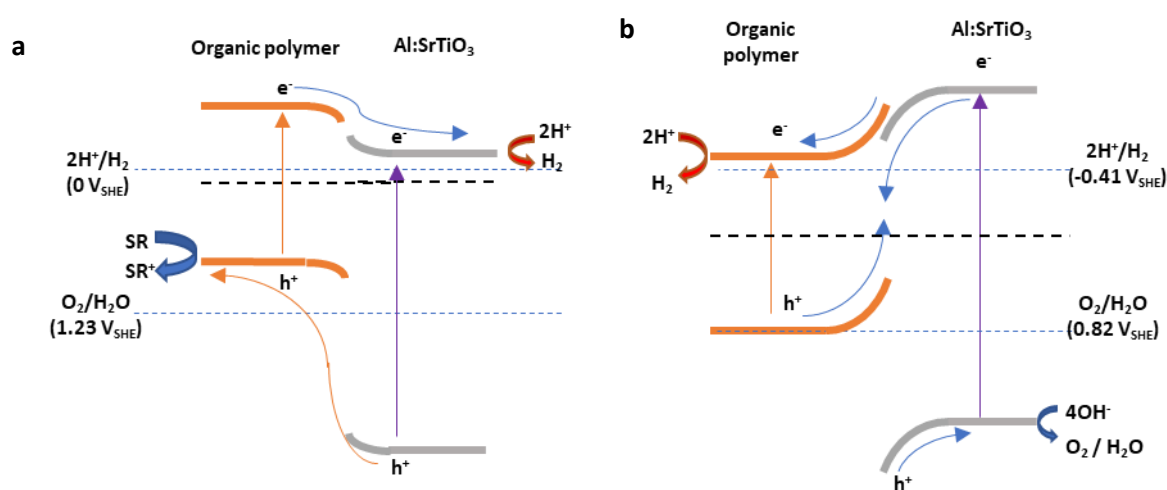


Figure 270: Theoretical band alignments, band bending, and charge transfer pathways at the interface of an organic polymer and Al:STO. a) Type-II heterojunction, b) Z-scheme heterojunction. Accurate determination of band alignment is not possible without further XPS measurements.

Figure 270 contains the two theoretical heterojunction models described in section 4.2: the type II heterojunction, and the Z-scheme heterojunction. Results from the sacrificial reagent solution containing TEA imply that a type II heterojunction may have been formed. This is because enhanced photocatalytic activities are observed under sacrificial conditions for the hybrid materials, whereas Al:STO by itself does not appear to be capable of driving sacrificial hydrogen evolution under these strongly alkaline conditions. Holes, therefore, must be consumed from the surface of the polymeric material.

Photocatalytic activity when using MeOH also appears to agree with this prediction of a Type II heterojunction. The polymer appears to be incapable of driving sacrificial oxidation of methanol. Therefore, if holes are transferred from the oxide to the polymer, MeOH oxidation on the oxide surface is inhibited. This trend is only reversed in the hybrid sample containing 90% Al:STO by mass.

By contrast, photocatalytic activity of the hybrids would be expected to match that of pure Al:STO if the heterojunction was a Z-scheme type.

Photocatalytic activities of the hybrid materials in pure water reinforce the observations in MeOH as there is no sign of oxygen evolution from the surface of Al:STO. However, the possibility of oxygen evolution followed by oxygen reduction cannot be ruled out, as the hybrid materials also demonstrate the capability of photocatalytic hydrogen peroxide production.

In both MeOH and deionised water, trace amounts of hydrogen are detected. It is unclear if this arises from low activities for overall water splitting followed by rapid oxygen reduction, if holes are consumed by another process. Possibilities for alternative processes include self-oxidation and degradation of the polymer or sacrificial oxidation of trace impurities. The increased hydrogen evolution from the hybrid materials relative to the pristine polymer is consistent with an increased polymer surface area.

Although trends for the hybrid materials imply a type II heterojunction, these results are complicated by the trends observed for the physical mixtures of polymer and oxide. These samples contained Al:STO and DBTS-DBTS particles that were independently loaded into the headspace vials and mixed via ultrasonication before testing for photocatalytic activity. It was initially assumed that the two photocatalyst components would behave independently. In this case, photocatalytic activities would only be affected in terms of competitive absorption of UV-light with photon energies above the bandgap of Al:STO.

In MeOH, the hydrogen evolution rates of the physical mixtures only compete with pure Al:STO (5 mg oxide) when samples contain more than 10 mg of oxide alongside 5 mg of polymer. This could be explained by competitive absorption given that the polymers do not contain heavy elements and do contain very strongly absorbing chromophores. As such, even when the mass ratio is 1:1, most of the UV light is absorbed by the polymeric component.

However, when tested in a 1:1:1 solution, these physical mixtures exhibited photocatalytic activities greater than the sum of their two parts. This is particularly surprising since Al:STO by itself cannot achieve sacrificial hydrogen evolution under these conditions. It is possible that charge transfer between polymer and oxide particles is also achieved for physical mixtures. This may occur if Van de

Waals and electrostatic interactions between charged particle surfaces result in physical contacts and the formation of heterojunctions.

The behaviour of the physical mixtures in pure water is also notable. In these cases, hydrogen evolution from the physical mixtures is slower than that observed from the equivalent hybrid photocatalysts. Furthermore, no oxygen was observed from these physical mixtures. These observations are contrary to those for the same mixtures dispersed in 20 % v/v MeOH which implied that a physical mixture containing 5 mg polymer and 10 mg oxide should drive the overall water splitting reaction at a similar rate to that of 5 mg of oxide by itself. Even if the oxygen is consumed by the oxygen reduction reaction, the hydrogen evolution reaction should be greater in the physical mixtures. This implies that the presence of polymer inhibits the hydrogen evolution reaction on the oxide surface.

As mentioned above, this may happen because of the formation of a heterojunction via electrostatic interactions between particles. However, an alternative explanation is that energy transfer from the Al:STO nanoparticles to the polymer occurs via Förster Resonance Energy Transfer. This is a through-space energy transfer mechanism, the distance-based probability of which scales as $1/R^6$, making it a relatively long-distance energy transfer mechanism.

Enhanced hydrogen evolution is observed for physical mixtures in MeOH, but not in pure water. The reason for this is unclear. The primary difference between these two systems is the photocatalytic oxidation reaction. It is therefore plausible that the rate of oxidation of MeOH competes with the rate of energy transfer via FRET, but the $4 h^+$ oxidation of water is slower and so FRET takes place more rapidly. The polymer also disperses more readily in MeOH. This may have an impact on whether the polymer and oxide particles agglomerate or disperse. As such this would have an impact on both FRET and the formation of VdW interfaces.

It is also important to consider the results from the hydrogen peroxide tests, since these are also performed in deionised water. If the hybrid materials operate via a type II heterojunction mechanism, electrons will be transferred from the higher-energy DBTS-DBTS LUMO to the CB of SrTiO₃. Since hydrogen peroxide production does not take place at the Al:STO/water interface, the hydrogen peroxide dip-stick results imply that this charge transfer process does not occur. Thus these results cast doubt on the prospect of a type II heterojunction.

The 5mg/5mg physical mixture produces substantially less hydrogen peroxide than just 5 mg of the polymer. This implies competitive absorption of UV-radiation amongst the two components even at low concentrations and reinforces the probability that the low activity of the 5/5 physical mixture in MeOH does not arise due to competitive absorption, but because the oxide excited state is quenched.

However, the 5/5 physical mixture also produces less hydrogen peroxide than both the 5/5 and 10/5 hybrids. These results imply one of two things. Either the rate of hydrogen peroxide production is increased due to increased polymer surface area, or that electrons are being transported across the heterojunction from the oxide and injected into the polymer.

An alternative heterojunction not considered until now is that of a Type I heterojunction. These heterojunctions occur when the band edge potentials of a wide bandgap semiconductor straddle those of a narrow bandgap semiconductor. It could be argued that, instead of forming a Z-scheme heterojunction, DBTS-DBTS/Al:STO hybrid materials form a type I heterojunction. A simplified model of how electrons would move across such a junction are provided in Figure 271.

In the case of a type I heterojunction, all photogenerated charges are injected into the polymeric component. This structure could potentially explain why hybrids exhibit improved photocatalytic activity with TEA, reduced photocatalytic activity with MeOH and show no evidence of overall water splitting whilst also being capable of driving the ORR to produce hydrogen peroxide.

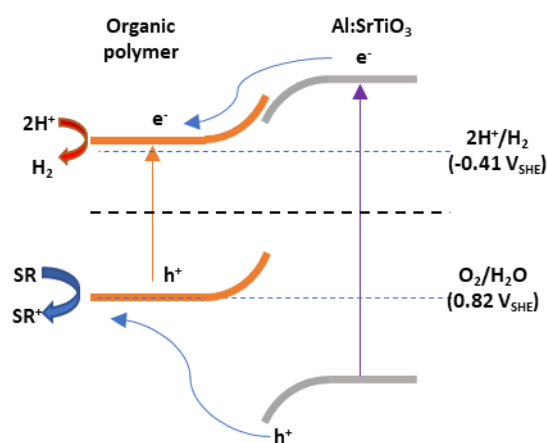


Figure 271: Theoretical band alignment, band bending, and charge transfer pathway at the interface of an organic polymer and Al:STO if a Type-I interface is formed. These heterojunctions form as a result of a wide bandgap semiconductor with band edges that straddle those of a narrow bandgap semiconductor material.

These photocatalysis results indicate that hybrid materials exhibit enhanced polymer-centred photooxidation and photoreduction reactions. The results from physical mixtures imply that the excited state of the oxide nanoparticles is quenched, even when a direct heterojunction is unlikely. As

such, it is incredibly challenging to confirm the cause of the enhanced activities in the hybrid materials and further studies are required to confirm if a type I heterojunction is formed.

The increased activity of the hybrid materials relative to the homopolymer may also arise because of increased polymer surface areas. Alternatively, residual concentrations of Rh co-catalyst may become impregnated into the polymer matrix during the in-situ polymerisation reaction. Synthesis optimisation of hybrid materials also shows that photocatalytic activities of conjugated polymers are sensitive to the synthesis conditions in which the polymers were prepared, including in the presence of Al:STO. Not only does this suggest that Rh and Cr are likely present in the hybrid materials to varying degrees, but polymer purity, chain length, and residual palladium concentrations may also be affected.

Residual co-catalyst concentrations are likely responsible for why sacrificial photocatalytic activity without Pt increases as the amount of RhCrO_x/Al:STO is present in the reaction mixture. This also explains why the increase in photocatalytic activity is dampened as additional Pt is photodeposited on the surface, as this would be in agreement with results from Chapters 2 and 3.

4.9 DBTS-Ph/Al:STO

Following the initial results of DBTS-DBTS/RhCrO_x-Al:STO hybrid materials, further hybrid materials were prepared by combining the polymer DBTS-Ph and the pristine Al:STO without a RhCrO_x co-catalyst pre-impregnated onto its surface. DBTS-Ph was selected as a potentially more promising candidate for the formation of a successful hybrid since it is calculated to have the highest-lying LUMO energy level of the polymers investigated in Chapter 3. It is hoped that the increased reduction potential, which also correlates with the wider optical bandgap observed for this material, would provide a greater driving force for charge extraction into the CB of Al:STO.

A hybrid containing 90 wt.% of Al:STO was selected, since this ratio was shown to correlate with an appropriate amount of oxide surface exposed in the case of the corresponding DBTS-DBTS hybrid materials. By spreading the polymer content across the surfaces of such a large amount of oxide also minimises the number of large polymer particles and maximises that chance that any one point within the polymeric phase is within one exciton diffusion length of an oxide-polymer interface.

Hybrid photocatalyst M187 was prepared from 4.5ml of DMF and 0.5 ml of 2M K₂CO₃ solution. It was heated to 120 °C for 1 hr 45 min under constant stirring. The DBTS-Ph polymer was synthesised on a 1.25 mmol scale with a theoretical yield of 36 mg in the presence of 327 mg of F85, a 4 mol.% Al-doped

SrTiO₃ photocatalyst that was prepared by the flux method on a 10g scale by heating for 48 hours at 1150°C with SrCl₂ and Al₂O₃ nanopowder. After subtracting the added Al:STO, 25 mg of polymer was determined to have been obtained, equalling a yield of 69%.

4.9.1 Pt-loading Study

Earlier attempts to load the hybrid photocatalysts with a photodeposited co-catalysts used 0.5 wt.% Pt. This follows the Pt-loading optimisation study in chapter 3. However, for this hybrid material, in which the polymer only constitutes 10% of the mass, it is unlikely that a blanket 0.5 wt.% loading would be optimal. Furthermore, the optimal loading for photodeposited co-catalysts on Al:STO was determined to be 0.05 wt.% Rh, 0.05 wt.% Cr, and 0.1 wt.% Co. Combined this only contains 0.2 wt.% metal and indicates that a further reduction in catalyst loading concentration may lead to enhanced photocatalytic activities, even for the pure polymeric material.

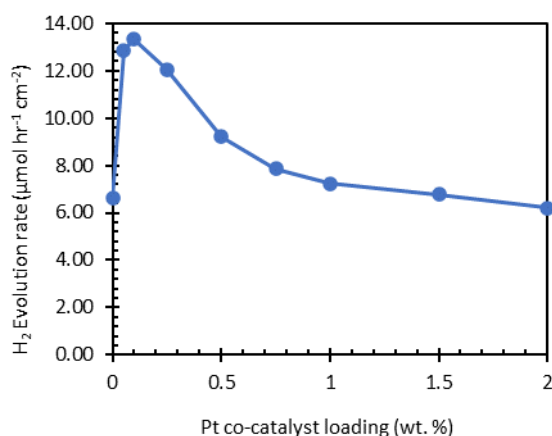


Figure 272: Area-normalised HER rates for the Al:STO/DBTS hybrid photocatalyst, M187, containing 90 wt.% Al:STO with a range of Pt-loading concentrations.

Nine samples containing 10 mg of the 90 wt.% DBTS-Ph/Al:STO hybrid material were prepared, each sample was loaded with 0 – 2 wt.% platinum during a 1-hour photodeposition period. The samples were recapped, degassed, and irradiated for a further 15 minutes before testing the headspace gas composition using the high-throughput GC setup. HER testing was undertaken in a 1:1:1 solution using TEA as the sacrificial reagent. The resulting area-normalised HER rates are presented in Figure 272. The highest HER rate is obtained when the hybrid photocatalyst is loaded with 0.1 wt.% Pt. However, this exhibits a very similar rate as when loaded with 0.05 wt.%.

Since the inorganic particles were shown to perform best when loaded with 0.05 wt.% Rh, this concentration was chosen for all future reactions involving this hybrid material. At this concentration, 10 mg of the photocatalyst contains 1 mg polymer, 9 mg oxide, and 5 μg of Pt. As a proportion of polymer content, this loading is equivalent to 0.5 wt.% and therefore consistent with the results in chapter 3. Further tests of Pt loading on the pristine polymer would be required to determine the optimal concentration in the non-hybrid case.

It should be noted that by only loading 10 mg into each headspace vial, the polymer is not likely to be operating at its highest area-normalised efficiency. However, since the polymer was prepared on a small scale and several more tests involving it had been planned, it was deemed that conserving the product was more important than using 50 mg material in each vial.

Whereas loading with 0.1 wt.% Pt more than doubled the photocatalytic activity from 6.4 to 13.4 $\mu\text{mol hr}^{-1} \text{cm}^{-2}$, a 109% increase, loading the photocatalyst with 0.5 wt.% Pt only lead to a moderate improvement to 9.0 $\mu\text{mol hr}^{-1} \text{cm}^{-2}$, a 40% improvement. These results suggest that the low photocatalytic activities of DBTS-DBTS/RhCrO_x-Al:STO hybrids following photodeposition of 0.5 wt.% Pt (see section 4.8.3), may have resulted from loading too much Pt co-catalyst. However, DBTS-DBTS has previously demonstrated that high Pt loading does not particularly inhibit its photocatalytic activity, (see Section 3.6.3). As such, this lower increase is likely still tentatively attributed to residual rhodium and chromium resulting from the synthesis procedure involving RhCrO_x/Al:STO. However, further investigations are required to confirm this.

Whilst it is unclear how residual Rh would affect the Pt-activity dependence of DBTS-Ph/Al:STO had F85 been loaded with the co-catalysts prior to in-situ polymerisation, the evidence so far supports the hypothesis that residual rhodium interferes with charge transfer to photodeposited Pt in the case of DBTS-DBTS/Al:STO.

4.9.2 Sacrificial Reagent-Dependent Activity

Section 4.9.1 successful demonstrates that the hybrid material M187 can successfully achieve sacrificial hydrogen evolution from a 1:1:1 mixture of MeOH, TEA, and H₂O. However, it is very difficult to identify if charge transfer between the organic and inorganic components has been achieved in the hybrid. As such, this hybrid photocatalyst was tested with a range of alternative sacrificial reagent combinations (water, 20% MeOH, 5% TEA, and H₂O/MeOH/TEA) and with different co-catalysts (None, 0.05 wt.% Pt, Cr₂O₃(0.1 wt.% Cr)/Pt(0.05 wt.%), and Cr₂O₃(0.1 wt.% Cr)/Rh(0.05 wt.%)). Reactions in

pure water were also loaded with 0.1 wt.% Co in the form of CoOH to enhance the oxygen evolution reaction and improve the overall water splitting activity.

The resulting photocatalytic hydrogen evolution rates are presented in Figure 273. The HER rates are particularly enhanced in the presence of TEA and are further enhanced in the 1:1:1 where MeOH is believed to improve the wettability and dispersibility of polymeric photocatalysts and acts as a hole scavenger for the oxide component. When Pt and Rh co-catalysts are combined with Cr, the hydrogen evolution activities in the presence of TEA increases. This indicates that sequential photodeposition involving Cr may be an effective way to improve photocatalytic activity of polymeric photocatalysts.

Additionally, the hybrid material can achieve hydrogen evolution from pure water when Rh/Cr or Pt/Cr are deposited on the surface. This indicates that sufficient oxide surface is accessible to the water molecules and highlights the potential of Pt as a co-catalyst for Al:STO more generally. However, to determine if any enhancement is achieved by the formation of a hybrid material compared with the individual components, further experiments were required.

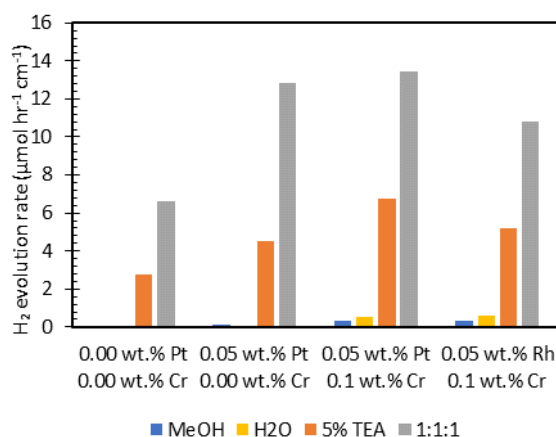


Figure 273: Area-normalised HER rates for the Al:STO/DBTS hybrid photocatalyst, M187, containing 90 wt.% Al:STO when dispersed in a range of different sacrificial reagents and when loaded with Rh and Cr co-catalysts via sequential photodeposition.

4.9.3 Sequential Photodeposition of Co-catalysts

The DBTS-Ph polymer (M181, synthesised under the same conditions), Al:STO (F85), a physical mixture of the two, and the hybrid photocatalyst (M187) were subsequently tested for hydrogen evolution in the presence of 5% TEA. Following the sequential photodeposition of Pt and Cr. Unfortunately, it was not possible to perform this experiment in a 1:1:1 solution due to limited availability of TEA at the time and research time constraints.

The results of this experiment are presented in Figure 274. Unfortunately, the HER did not improve with the formation of the hybrid in comparison with the polymer or the physical mixture. These results imply that the hydrogen evolution from the hybrid material originates entirely from the polymer component and that the presence of the oxide does not provide any benefit to the overall efficiency and charge transfer into the oxide CB appears to have been unlikely. The slight decrease in activity for the hybrid and mixture samples can be attributed to partial absorption of the UV portion of incident light that is absorbed by Al:STO.

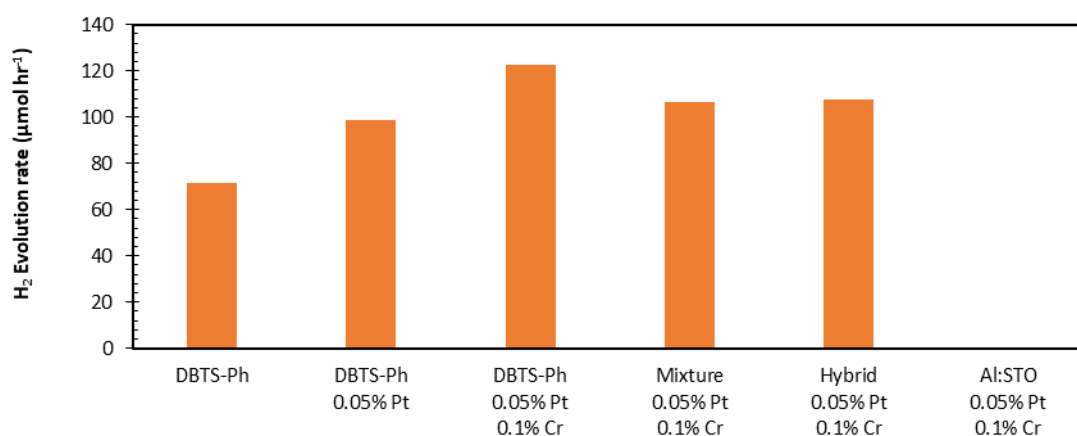


Figure 274: Area-normalised HER rates for the co-polymer DBTS-Ph photocatalyst, M181, synthesised under the same conditions as the hybrid polymer. 5 vol% TEA solution was used as the sacrificial reagent and the polymer was loaded with Rh and Cr co-catalysts via sequential photodeposition. These photocatalytic activities are compared with physical mixture, the hybrid photocatalyst (M187), and Al:STO samples tested under the same conditions.

One problem with using TEA as the sacrificial reagent is such that the co-catalysts may preferentially deposit onto the polymer surface over that of the oxide component since TEA is a hole scavenger for the polymer and not for Al:STO. Without metal on the oxide surface, it would not be possible for these particles to participate in the photoredox reactions. However, in the absence of a hole scavenger, the opposite is true, whereby Pt⁶⁺ and Rh³⁺ can only be photoreduced by electrons in the oxide since holes are slowly consumed by water to produce oxygen.

4.9.4 Overall Water Splitting

F85, M181, a mixture of the two, and M187, the hybrid, were subsequently tested for their overall water splitting activity from pure water. These photocatalysts were tested after loading with Pt/Cr/Co and Rh/Cr/Co. The resulting hydrogen and oxygen evolution rates from this experiment are presented in Figure 275.

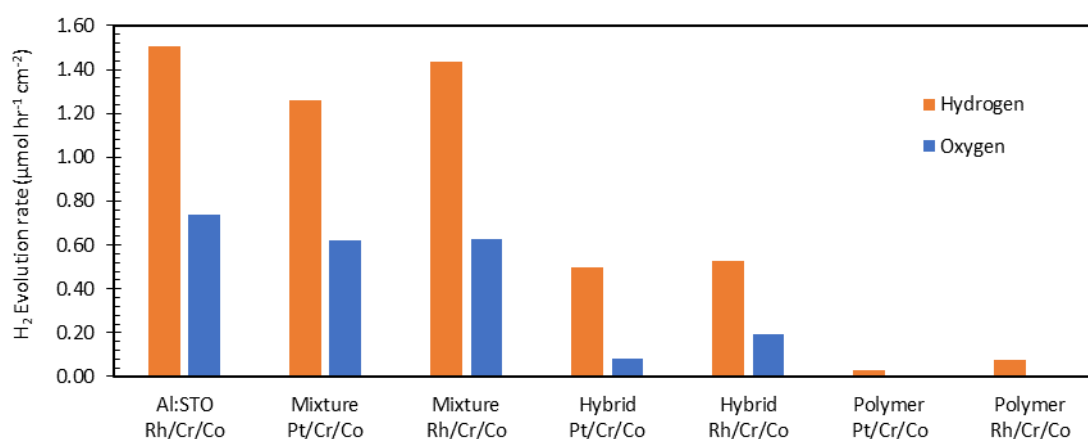


Figure 275: Photocatalytic OWS activity of Al:STO, a physical mixture of Al:STO and DBTS-Ph, the hybrid photocatalyst Al:STO/DBTS-Ph, and the pure polymer DBTS-Ph. Samples were irradiated for 1 hour under AM1.5G Solar Simulated light after being dispersed in 5 ml of deionised water. Two sets of possible co-catalysts are compared: Pt/Cr₂O₃/CoO_x, and Pt/Cr₂O₃/CoO_x. Samples are loaded with 0.05 wt.% Pt/Rt, 0.1 wt.% Cr, and 0.1 wt.% Co via sequential photodeposition.

The hybrid photocatalysts present significantly lower activities for overall water splitting than either the pure oxide or the physical mixture. The cause of this is unclear, it is likely a result of a decrease in dispersibility of the polymer-coated oxide particles since DBTS-Ph is more hydrophobic than the oxide particles and oxide particles may be bound together into larger particles by the polymer matrix. Furthermore, a smaller percentage of the oxide particles will have an interface with water. Likewise, some of the co-catalyst may still have deposited on the polymer surface in preference to the oxide. It would be beneficial to repeat this experiment using MeOH as the sacrificial reagent, since the 90% DBTS-DBTS/Al:STO hybrid photocatalyst performed as well as the isolated inorganic component and the physical mixture.

It is possible that the reduced activity in the hybrid photocatalysts compared to the physical mixtures arises from interfacial charge transfer. If the hybrid operates like a type-II heterojunction, electron injection from the polymer into the oxide may be accompanied by hole extraction from the oxide into the polymer given its more negative HOMO potential, as demonstrated in Figure 276. As the polymer cannot drive the oxygen evolution reaction at a high rate, the positively charged polaron may subsequently recombine with photogenerated electrons in the Al:STO. Although this mechanism would lead to decreased OWS activity, it would indicate that interfacial charge transfer between the organic and inorganic components is possible. Transient absorption spectroscopy, through which positive polaronic species can be identified, would be a useful tool to provide further information about the charge transfer mechanism in this material.

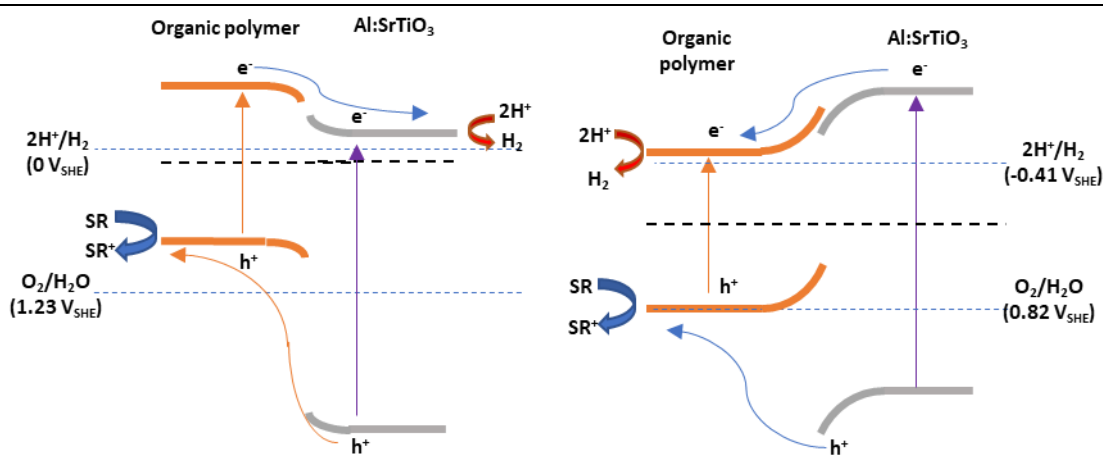


Figure 276: Possible band alignment of Type I and Type II heterojunctions that may explain why the photocatalytic activity of the hybrid photocatalyst are worse than their physical mixture equivalents.

In the absence of an inorganic component, the DBTS-Ph polymer did produce trace amounts of hydrogen gas from water. However, no oxygen was detected. Since DBTS-Ph has demonstrated the ability consume oxygen and produce hydrogen peroxide from water via a photocatalytic process it is possible that overall water splitting is achieved, and the oxygen component is subsequently consumed. Alternatively, the photogenerated holes may be consumed in the process of polymer self-oxidation, or by the oxidation of other residual impurities. These reasons may also explain why the oxygen evolution rates of the hybrid material co-loaded with Pt and Cr is low and H₂ and O₂ are not produced in a 2:1 stoichiometric ratio.

These results raise questions regarding the selection of co-catalysts. In the case of Al:STO, photodeposition of Cr₂O₃ on top of the metallic Rh particles prevents the ORR back-reaction from occurring and hence allows overall water splitting. Since more oxygen was consumed in the hybrid material when co-loading Pt/Cr compared with Rh/Cr, it may be possible to further optimise the co-catalyst loading concentrations on the pure polymer photocatalysts to prevent the ORR. Without the capability of consuming oxygen, the hydrogen peroxide production reaction ceases, and the overall water splitting reaction may be possible. Low-activity OWS has previously been observed on polymeric photocatalysts when loaded with an IrO₂ co-catalysts, suggesting that this phenomenon can be further optimised.¹⁶⁰

4.10 DBTS-DBTS/BiVO₄

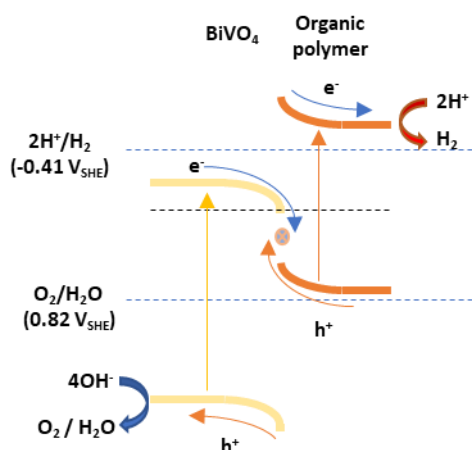


Figure 277: Energy level diagram for theoretical Z-scheme heterojunction at the interface of BiVO₄ and an organic polymer photocatalyst.

In addition to the formation of organic/inorganic hybrid photocatalysts involving Al:STO, hybrids were also prepared with BiVO₄ with the desire of synthesising direct heterojunction Z-schemes for overall water splitting. For these hybrids to work, photogenerated electrons in the BiVO₄ particles must combine with photogenerated holes in the organic phase, as per the schematic in Figure 277.

BiVO₄ was selected since it is a well-known inorganic photocatalyst capable of absorbing visible wavelengths of light and driving the oxygen evolution reaction.^{292,315} DFT calculations at the start of this chapter indicate that all of the polymers investigated in this thesis should possess HOMO energy levels that lie deeper than the CB of BiVO₄. This should enable charge transfer between the two.

Table 30: DBTS-DBTS/BiVO₄ Hybrids prepared with various Polymer:Oxide ratios

ID	Polymer	Oxide	Mass (mg)	solvent	Vol (ml)	Base	Concentration (mol dm ⁻³)	Vol (ml)	Yield (%)
M128	DBTS-DBTS	BiVO ₄	10	DMF	4.5	K ₂ CO ₃	1	0.5	97
M135	DBTS-DBTS	BiVO ₄	100	DMF	4.5	K ₂ CO ₃	1	0.5	99
M134	DBTS-DBTS	BiVO ₄	200	DMF	4.5	K ₂ CO ₃	1	0.5	50

4.10.1 Synthesis and Characterisation

DBTS-DBTS/BiVO₄ hybrid photocatalysts were prepared to contain different organic and inorganic component ratios. Al:STO only absorbs UV light and so hybrid photocatalysts based on this material benefit from a high oxide content, since this ensures the polymer is spread thinner and large oxide surface areas are exposed, without competitive absorption of visible wavelengths of light. Whilst these factors remain true for BiVO₄ and indicate that 90% oxide content may remain important in

BiVO₄-containing hybrids, this oxide, with a bandgap of 2.4 eV, will compete with the organic phase over visible light absorption.

Z-scheme photocatalysts depend on a two-photon absorption process in which photogenerated electrons in the OEP combine with photogenerated holes in the HEP. Whilst such mechanisms half the available STH efficiency, the combination of two photocatalyst components allows for a greater selection of OEP and HEP materials with narrow band gaps and tailored band-edge potentials.

BiVO₄ was synthesised using a hydrothermal method following the methodology presented by Zhao *et al.*^{320,337} In the presence of the oxide, in-situ polymerisation was successful, giving rise to a polymerisation yield of 99% when synthesising 0.25 mmol polymer (110 mg) in the presence of 100 mg of BiVO₄. However, the reaction in the presence of 200 mg of the oxide component only produced a 50% yield. It is unclear if this reaction yield is anomalous, or if an increased oxide content above a particular level consistently leads to a reduced polymerisation yield. The products resembled uniform bright yellow powders.

SEM images and EDS maps for the resulting hybrid photocatalysts are presented in Figures 278-279. As with the DBTS-DBTS hybrids containing Al:STO, those containing BiVO₄ have also successfully combined the organic and inorganic phases as all particles contain both phases. It should be noted that the EDS mapping images are comparing vanadium content and bromine content. This is because of the similar energies and resulting overlap between the M α_1 emission line of bismuth and the K series emission lines of sulphur, as highlighted in red in Table 31. Bromine can be used to identify the polymer content since the polymer chains are terminated by unreacted bromine atoms. Likewise, bromine-containing by-products and impurities also remain in the polymer phase despite several washing steps.

Table 31: X-ray emission lines for elements of interest in BiVO₄/DBTS-DBTS hybrid photocatalysts.

Element	K α_1 (eV)	K α_2	K β_1	L α_1	L α_2	L β_1	L β_2	Ly ₁	M α_1
Sulfur	2.308	2.307	2.464						
Vanadium	4.952	4.945	5.427	0.511	0.511	0.519			
Bromine	11.924	11.878	13.291	1.480	1.480	1.526			
Bismuth	77.1	74.8	87.3	10.839	10.731	13.024	12.980	15.248	2.423

It appears as though BiVO_4 may not have been synthesised with the desired morphology. In their paper, Qi *et al.* produced faceted BiVO_4 crystals on the micrometre scale.³²⁰ However, despite this, BiVO_4 has been shown to be an effective OEP in its unrefined form and this should still be capable of driving the oxygen evolution reaction.

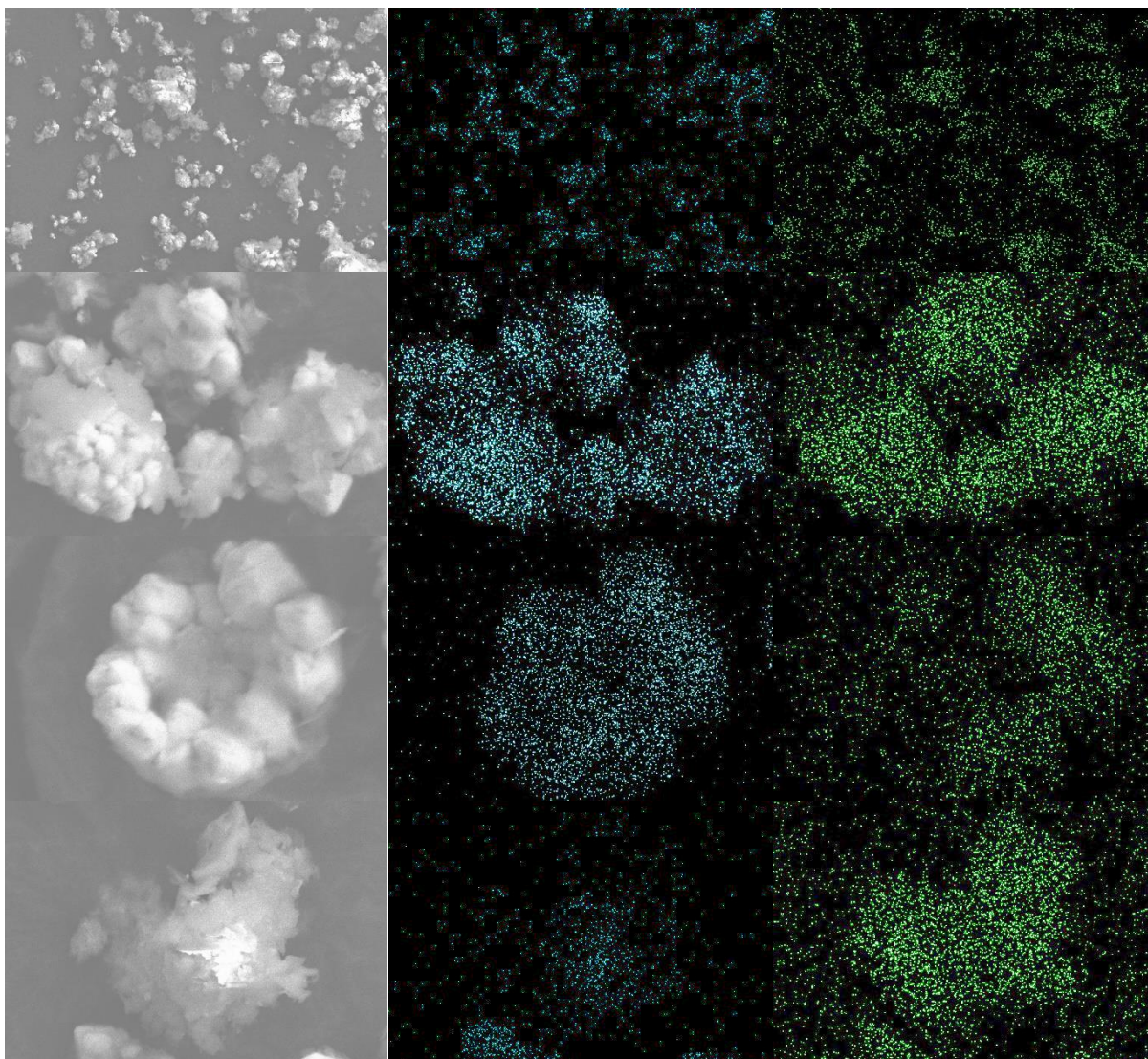


Figure 278: SEM images and EDS maps of BiVO_4 /DBTS-DBTS hybrid photocatalyst M134. M134 contains a target BiVO_4 content of 67 wt.%, assuming a 100% polymer synthesis yield. EDS maps present the distribution of vanadium (blue) and bromine (green) content relating to the oxide and polymer components, respectively.

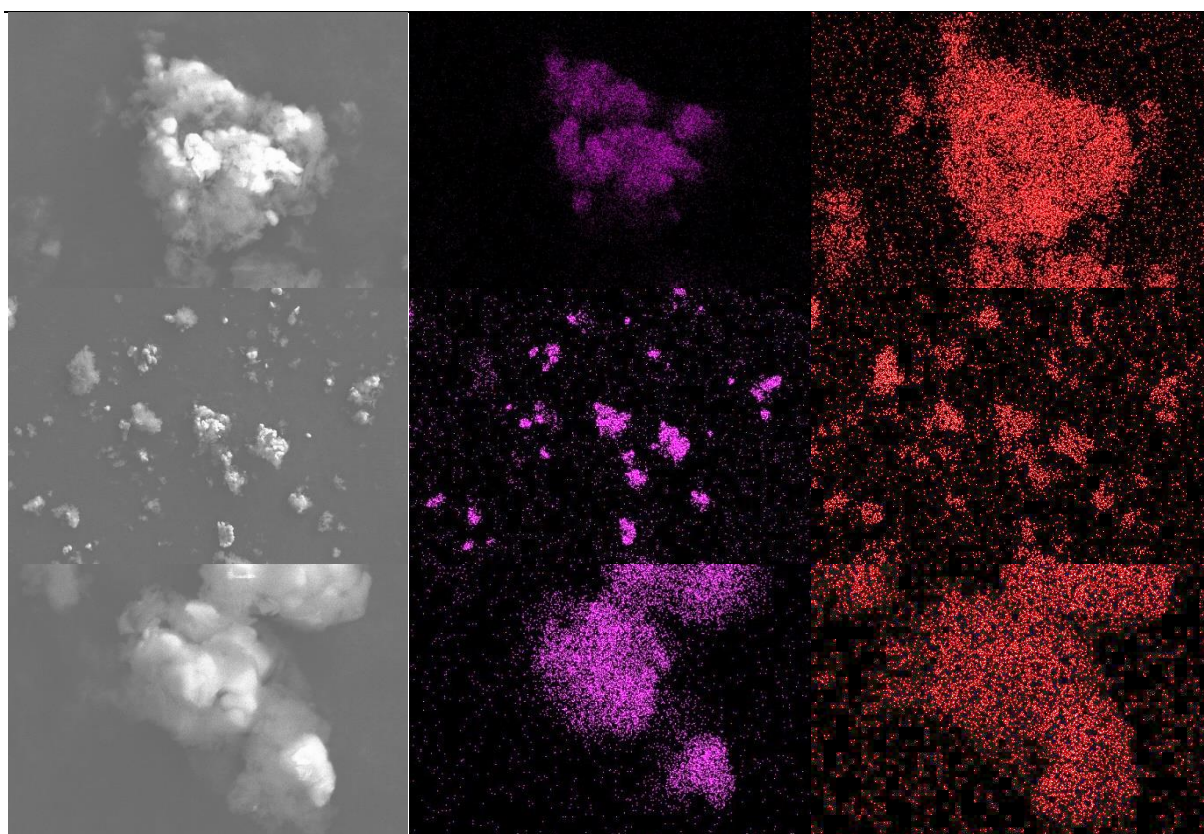


Figure 279: SEM images and EDS maps of $\text{BiVO}_4/\text{DBTS-DBTS}$ hybrid photocatalyst M135. M135 contains a target BiVO_4 content of 50 wt.%, assuming a 100% polymer synthesis yield. EDS maps present the distribution of vanadium (blue) and bromine (green) content relating to the oxide and polymer components, respectively.

4.10.2 Photocatalytic Activity

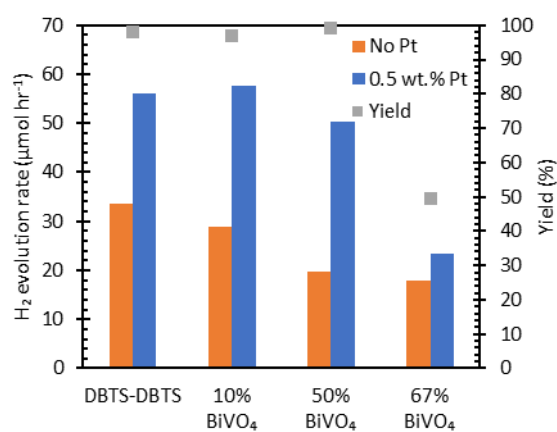


Figure 280: Absolute HER rates for $\text{BiVO}_4/\text{DBTS-DBTS}$ hybrid photocatalysts containing different weight fractions of BiVO_4 before and after loading with 0.5 wt.% Pt. Dispersions were prepared such that vials contain approximately 5 mg of the polymer component dispersed in 5 ml of a 1:1:1 v/v mixture of ($\text{H}_2\text{O}/\text{MeOH}/\text{TEA}$). Polymerisation yields are also presented on the secondary axis.

The DBTS-DBTS/BiVO₄ hybrids were tested for their hydrogen evolution activity in the presence of TEA as a sacrificial electron donor and MeOH to aid dispersion. The photocatalysts were tested with and without 0.5 wt.% Pt as a co-catalyst, and the results are presented in Figure 280.

Two sets of measurements were made. Initially, enough photocatalyst was weighed out such that the vial contained 5 mg of polymer, as per the measurements for the DBTS-DBTS/Al:STO hybrid photocatalysts. However, since both materials have similar bandgaps, the absorbable portion of incident light is likely fully absorbed by 5 mg of the overall photocatalyst, regardless of composition. As such, a secondary set of experiments were performed containing only 5mg of the hybrid photocatalysts, which gave identical results.

In the absence of a Pt co-catalyst, the pure polymer produced hydrogen at the highest rate. As more BiVO₄ is added, the activity decreased. This may be explained by the competitive absorption of visible wavelengths of light, which should half the HER production rate in an efficient Z-scheme photocatalyst. It remains unclear, however, whether BiVO₄ can extract holes from the polymer component and subsequently utilise TEA or MeOH as a hole scavengers, as would be required to prove hybrid photocatalysis action. It is possible that the BiVO₄ absorbs 50%+ of the incident light, and the polymer component operates as a standalone HER photocatalyst.

Following the photodeposition of 0.5 wt.% Pt, a slightly different trend was observed. The sample containing 10 wt.% BiVO₄ produced hydrogen at a slightly faster rate than the pure DBTS-DBTS polymer loaded with 0.5 wt.% Pt. at 50 wt.% BiVO₄, this decreased slightly, but the percent increase compared with the sample without a co-catalyst remained more significant than the pristine polymer. The 67% sample, which may contain up to 80 wt.% BiVO₄, experienced a very small increase in activity after Pt deposition.

It is difficult to explain the origins of this small increase in activity with respect to Pt on the 67 wt.% sample. One possible explanation is that the Pt selectively deposits on the organic phase of the hybrid material. In this case, 0.5 wt.% of the total could equate to as much as 2.5 wt.% of the polymer mass. However, Pt deposition studies on DBTS-DBTS in Chapter 3 did not indicate that the polymer is sensitive to Pt loading concentration. Alternatively, with a greater proportion of exposed oxide surface area in the high oxide fraction hybrids, the Pt may have predominantly deposited on the BiVO₄ crystals and not on the polymer.

Finally, as observed in section 4.7.1.3, low polymerisation reaction yields may correlate with reduced photocatalytic activity when performing in-situ polymerisation reactions. High concentrations of impurities combined with high Pt loading content could also detrimentally affect the photocatalytic activity in this sample. There is no obvious explanation for this difference in activity that can be attributed to the formation of a hybrid interface in which holes formed in the polymer are scavenged by electrons in BiVO_4 , as this process is not dependent on the platinum co-catalyst.

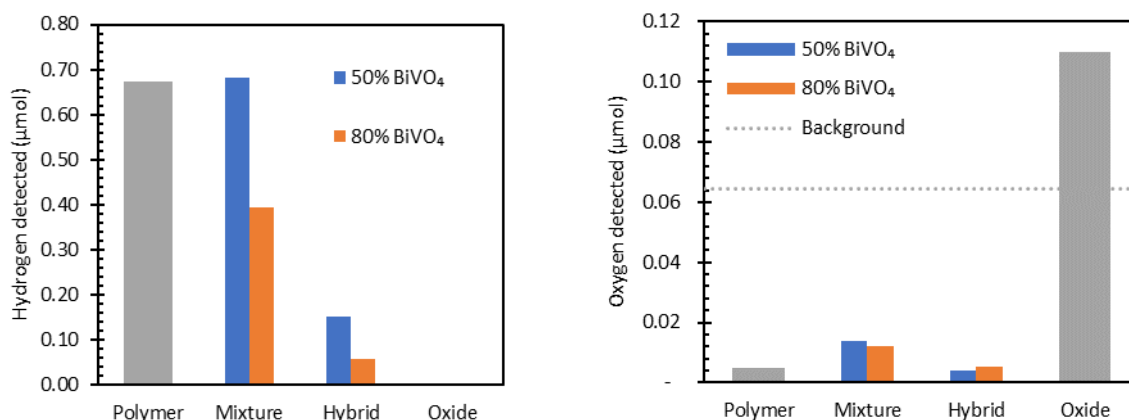


Figure 281: Absolute concentrations of H_2 (a) and O_2 (b) detected after DBTS-DBTS, DBTS-DBTS+ BiVO_4 physical mixtures, BiVO_4 /DBTS-DBTS hybrids, and BiVO_4 were tested for their overall water splitting photocatalytic activity. Samples were dispersed in 5 ml of deionised water, capped, degassed, ultrasonicated, and subsequently irradiated for 1 hour. Physical mixture and hybrid samples contain an equivalent of 5 mg of the polymeric component assuming 100% polymer synthesis. Background oxygen content detected from vials only containing 5 ml of deionised H_2O is presented as a dotted grey line in figure (b). This value is an average measurement from three vials that were also ultrasonicated and irradiated for the same length of time.

To determine if a successful Z-scheme hybrid has been obtained, the DBTS-DBTS/ BiVO_4 hybrid samples were tested for their ability to perform overall water splitting. The hydrogen and oxygen content in the headspace of the vials following 2 hours of irradiation are presented in Figures 281.

All samples containing the polymer produced trace amounts of hydrogen following irradiation in pure water. However, as in the case of DBTS-Ph, there was no corresponding production of oxygen. Conversely, oxygen levels had decreased compared with reference samples containing 5 ml of pure water, indicating that any oxygen that may have been produced was likely consumed in the formation of hydrogen peroxide. The lack of trace levels of oxygen suggests that OWS has not been achieved and implies that holes may have been consumed by polymer self-oxidation or in the oxidation of impurities. Additional hydrogen gas may also have been evolved as a by-product from any of these oxidative processes. BiVO_4 produced no hydrogen and oxygen levels were only marginally higher than

expected background levels, generating uncertainty regarding the formation of oxygen vs natural variation.

Hybrid samples produced less oxygen than their physical mixture counterparts. In both cases, the amount of hydrogen produced decreased with increasing oxide content. The latter can be explained by considering that a smaller proportion of incident light is absorbed by the polymer in the presence of increasing oxide content. The former observation, however, requires further examination.

When dispersed on oxide particle surfaces, it is expected that the polymer would exhibit an increased surface area and a reduced rate of bulk recombination events. However, these events would lead to the expectation of increased hydrogen production, rather than the observed reduction. If the hydrogen evolves from photocatalytic proton reduction (i.e. the HER), any extraction of holes by BiVO_4 would be expected to drive result in increased hydrogen content as BiVO_4 acts like a hole scavenger and oxygen content would also increase as the polymer acts as an electron acceptor. This reduction in activity is therefore unlikely to result from the formation of a Z-scheme type interface.

The most probable explanation for the observed results is that the hydrogen produced originates from polymer or impurity degradation upon irradiation, a process that occurs slower due to the synthesis of the polymer in the presence of BiVO_4 . Two immediate possible explanations arise including the possibility that the modified synthesis process has reduced the concentration of impurities, or that the oxide/polymer interface acts as an exciton trap that accelerates the rate of recombination of photogenerated excitons. However, further experiments would be required to validate these hypotheses.

4.11 DBTS-BDT/ BiVO_4

Since DBTS-DBTS/ BiVO_4 did not generate a successful Z-scheme photocatalyst, a hybrid based on DBTS-BDT was investigated. Since the LUMO of the DBTS-BDT polymer is concentrated on the BDT unit, and its energy lies close to the CB of BiVO_4 , this combination may be better suited to interfacial charge transfer between the organic and inorganic components.

Table 32: Reaction conditions and table of samples based on DBTS-BDT/ BiVO_4 Hybrids with various Polymer/oxide weight ratios.

ID	Polymer	Oxide	Mass (mg)	solvent	Vol (ml)	Base	Concentration (mol dm^{-3})	Vol (ml)
M208	DBTS-BDT	BiVO_4	0	DMF	4.5	K_2CO_3	2	0.5
M209	DBTS-BDT	BiVO_4	20	DMF	4.5	K_2CO_3	2	0.5
M210	DBTS-BDT	BiVO_4	40	DMF	4.5	K_2CO_3	2	0.5
M211	DBTS-BDT	BiVO_4	60	DMF	4.5	K_2CO_3	2	0.5
M212	DBTS-BDT	BiVO_4	80	DMF	4.5	K_2CO_3	2	0.5
M213	DBTS-BDT	BiVO_4	90	DMF	4.5	K_2CO_3	2	0.5

The hydrogen and oxygen gas levels in the headspace vials following one hour of irradiation are presented in Figures 282 and 283, respectively. These photocatalysts were tested with and without a 0.5 wt.% Pt co-catalyst. Without Pt co-catalyst, these hybrid materials produced trace amounts of hydrogen gas. However, the quantities are even smaller than the residual amount detected from DBTS-DBTS/ BiVO_4 hybrids and are on the order of nanomoles, close to the limit of the BID detector. Hybrids containing a greater weight fraction of oxide produced the most hydrogen gas, with the 80 wt.% sample producing the highest levels. However, once loaded with platinum the hydrogen concentration reduces to negligible amounts that could not easily be quantified above the background noise. Compared with the blank reference samples, all hybrid sample vials contained reduced amounts of oxygen following irradiation. Samples that consumed the most oxygen typically also produced the most hydrogen. The addition of platinum did not significantly inhibit oxygen consumption.

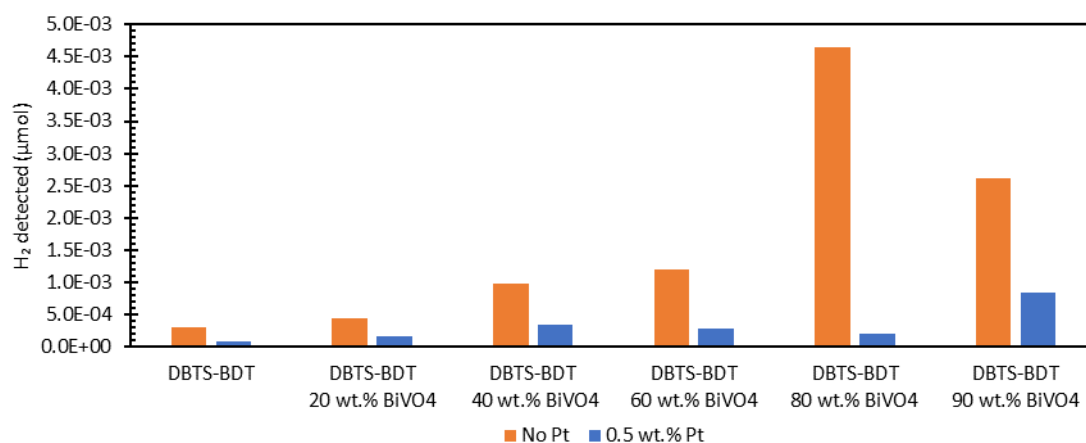


Figure 282: Absolute concentrations of H_2 detected after DBTS-BDT hybrid photocatalysts were tested for their overall water splitting photocatalytic activity. Samples were dispersed in 5 ml of deionised water, capped, degassed, ultrasonicated, and subsequently irradiated for 1 hour. Samples contain an equivalent of 5 mg of the polymeric component assuming 100% polymer synthesis. H_2 content was also determined for the samples after photodeposition of 0.5 wt.% Pt.

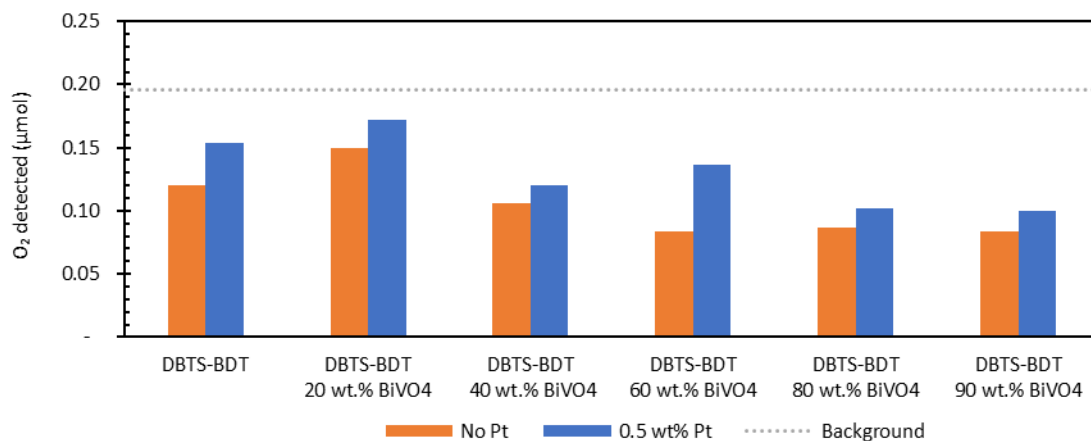


Figure 283: Absolute concentrations of O₂ detected after DBTS-BDT hybrid photocatalysts were tested for their overall water splitting photocatalytic activity. Samples were dispersed in 5 ml of deionised water, capped, degassed, ultrasonicated, and subsequently irradiated for 1 hour. Samples contain an equivalent of 5 mg of the polymeric component assuming 100% polymer synthesis. O₂ content was also determined for the samples after photodeposition of 0.5 wt.% Pt. Background oxygen content detected from vials only containing 5 ml of deionised H₂O is presented as a dotted grey line. This value is an average measurement from three vials that were also ultrasonicated and irradiated for the same length of time.

These results clearly demonstrate that DBTS-BDT/BiVO₄ hybrids cannot achieve overall water splitting from pure water. As in the case of DBTS-DBTS polymers, the hydrogen content may arise from the photodegradation of the polymer. Given that this increases in cases where more polymer is in contact with the oxide, it is possible that the polymer is degraded by the oxide component. The addition of platinum, therefore, may protect the polymer against photodegradation by acting as a trap for photogenerated electrons. Likewise, oxygen may be depleted by various oxygen reduction reaction pathways that produce by-products such as peroxide species, hydroxide ions, or water. Given that the oxide, by itself, produces oxygen, and isolated polymer only consumes trace amounts of oxygen, these results suggest that the hybrid material achieves ORR more efficiently than the individual components. Whilst this is not a promising result for OWS, this may indicate some degree of successful interfacial charge transfer and suggests that these materials may work effectively in photocatalytic hydrogen peroxide production reactions. However, further investigations would be required to confirm this.

4.12 Conclusions and Future Work

In this chapter, attempts have been made to prepare organic-inorganic hybrid photocatalysts. Polymer-sensitised photocatalysts were prepared by pairing Al-doped SrTiO₃ with DBTS-DBTS and DBTS-Ph. S-scheme hybrid photocatalysts based on a BiVO₄ as an OEP, and either DBTS-DBTS or DBTS-BDT as the HEP are also prepared. Hybrids were synthesised by in-situ microwave-assisted polymerisation.

Suzuki-Miyaura polycondensation reactions require a reaction mixture involving an aqueous base and an organic solvent. As observed in Chapter 3, these reaction parameters can have a significant impact on the photocatalytic activity of the resulting polymer, even when high polymerisation yields are obtained across several combinations. High throughput microwave-assisted synthesis allowed several polymerisation reaction conditions to be screened for the synthesis of DBTS-DBTS polymer in the presence of small quantities of RhCrO_x/Al:SrTiO₃ inorganic photocatalyst.

In biphasic reaction mixtures consisting of toluene and aqueous bases, hybrid particles did not form successfully as the organic and inorganic components had an affinity to opposite phases. Monophasic reaction mixtures based on water-miscible organic solvents successfully overcame this issue but produced polymeric photocatalysts with reduced activities. In some cases, the polymerisation reaction only produced lower yields and lower activities in the presence of the inorganic component, indicating that it may play an active role in the polycondensation reaction.

The most promising results were obtained from reactions performed using DMF as the organic solvent. Further optimisations of the ratio of organic and aqueous components, and the overall concentration of base improved polymer yields and photocatalytic activities. Increased volume fractions of the organic phase consistently produced higher quality polymers as indicated by high yields, bright yellow appearance, and high photocatalytic activities. This can be attributed to the increased solubility of the reagents, intermediaries and products involved in the polymerisation reaction. Decreased miscibility arising from high concentrations of the base in the aqueous phase resulted in minor phase separation, and the products appeared to incorporate less of the oxide into the hybrid product.

When using K₃PO₄ as the base in these reactions, the resulting DBTS-DBTS polymer exhibited higher photocatalytic activities despite similar yields as those synthesised in the presence of K₂CO₃. However, they also exhibited some phase separation and incomplete oxide incorporation into the hybrid product. As such, K₂CO₃ was selected for further hybrid syntheses, a decision reinforced by the poor performance of DBTS-PhF2a synthesised in DMF/K₃PO₄.

Without a Pt co-catalyst, hybrid photocatalysts containing DBTS-DBTS and RhCrO_x/Al:STO outperformed the pure DBTS-DBTS polymer when tested for sacrificial hydrogen evolution from a mixture of H₂O, MeOH, and TEA in a 1:1:1 volume ratio under AM 1.5G solar irradiation. Though

enhanced, these activities remained lower than those of the pristine polymer when loaded with a Pt co-catalyst. Photodeposition of Pt onto the hybrid materials only marginally enhanced their photocatalytic activity.

Whilst promising, the improved activity for oxides without Pt does not prove that the hybrids operate according to a polymer-to-oxide heterojunction charge transfer model. The initial screening experiments highlighted that in the presence of Al:STO, the resulting polymerisation yield and photocatalytic activity are highly sensitive to the reaction conditions. This is particularly the case with respect to the volume ratio of organic and aqueous solvents, the selection of base, and its concentration. As such, the increased activities in hybrids may only arise due to the secondary effects of adding oxide to the reaction mixture. These may include increased surface area, altered surface morphology, or a lower concentration of impurities. Furthermore, the incorporation of pre-loaded Rh and Cr co-catalysts from the oxide surface into the polymer matrix may have been responsible for the enhanced activity. Further experiments involving the preparation of DBTS-DBTS/Al:STO hybrids without Rh and Cr co-catalysts pre-loaded onto their surfaces would be interesting for comparison.

DBTS-Ph/Al:STO hybrids were synthesised. It was hoped that the more negative LUMO of the polymer compared with DBTS-DBTS would enable more efficient charge transfer across the heterojunction interface into the CB of Al:STO. Co-catalysts were loaded via photodeposition methods following the *in-situ* polymerisation. As such, they were loaded across the organic and inorganic phases indiscriminately.

In a 5% TEA mixture, the photocatalytic activity of the hybrid photocatalyst performed the same as the physical mixture and worse than the polymer by itself. Since cocatalysts are necessary for photocatalytic activity on the oxide surface, the samples were only compared after the photodeposition of Pt and Cr co-catalysts.

In contrast to earlier samples of DBTS-Ph, the polymer was loaded with 0.05 wt.% Pt instead of 0.5%. Despite, the lower loading, the activity increased significantly. The photocatalytic activity was further enhanced by the sequential photodeposition of Cr₂O₃. Further studies are required to identify the optimal Pt/Cr loading concentrations on the organic polymer photocatalysts. Likewise, Rh should also be investigated as an alternative co-catalyst for polymeric photocatalysts.

Given its role as a co-catalyst on Al:STO, Cr₂O₃ may also prevent the oxygen reduction reaction from occurring on the surface of polymeric photocatalysts. DBTS-Ph is known to produce H₂O₂ from pure water. However, the polymer appears to degrade over time in the presence of this strongly oxidising chemical. Therefore, the presence of Cr₂O₃ could also improve the stability of polymeric photocatalysts. Although the photodeposition of 0.05% Pt, 0.1% Cr, and 0.1% Co on DBTS-Ph did not enable overall water splitting from pure water, it is plausible that polymers may be modified to drive this reaction by further optimisation of co-catalysts in various ratios.

The DBTS-Ph/Al:STO-90 hybrid photocatalyst achieved overall water splitting. However, this was to a lesser degree than the Al:STO photocatalyst by itself. The reduction of activity of the hybrid in pure water compared with the physical mixture implies that charges may be transferred from the oxide into the organic phase, which is inactive under the same conditions. Depending on the nature of the heterojunction, and particularly the band bending at the interface, it is also possible that the interface acts as a trap and recombination centre that reduces the AQY of the inorganic component.

Hybrids consisting of polymeric photocatalysts and BiVO₄ were prepared with the hope of achieving overall water splitting via a direct heterojunction Z-scheme. However, neither DBTS-DBTS/BiVO₄ nor DBTS-BDT/BiVO₄ hybrids successfully achieved overall water splitting from pure water. In both cases, trace levels of hydrogen were detected in the vial headspace following irradiation, but the background concentration of oxygen had decreased. Evidence of charge transfer between organic and inorganic components was inconclusive. Further photocatalysis tests would be required to determine if co-catalysts, co-solvents, or pH-regulating additives could enable OWS in these hybrid materials.

Overall, attempts to prepare polymer-sensitised hydrogen evolution photocatalysts and organic/inorganic direct heterojunction Z-schemes have been unsuccessful, despite DFT calculations that suggest favourable band alignments. These results demonstrate that favourable redox potentials alone cannot predict photocatalytic activity.

Future designs of direct heterojunction Z-schemes should pay particular attention to the semiconductor physics at the heterojunction interface. It may be possible to encourage favourable charge transfer by doping the individual components, applying a tertiary interfacial layer on the oxide surface via methods such as ALD, or modifying the side chains of the polymer backbone to mimic the D- π -A structures that successfully enhance charge transfer in dye-sensitised photocatalysts and solar cells.

Chapter 5: Conclusions and Future Work

This thesis has focussed on the rational design and synthesis of linear conjugated co-polymer photocatalysts for solar-driven hydrogen production from water. Particular focus has been placed on the potential for bandgap engineering using fluorinated phenylene moieties as co-monomers and π -linkers in D- π -A type co-polymers. Finally, this research has also considered how this approach could be used to prepare organic/inorganic hybrid Z-scheme photocatalysts for direct-heterojunction overall water splitting.

This chapter initially summarises each chapter's content and highlights this work's primary research outcomes. Individual impact areas are subsequently discussed, focusing on the results obtained, their potential implications, and the additional work required before these results could be published. The potential for larger-scale, longer-term research projects based on these results is also discussed.

Unfortunately, due to personal circumstances, the impact of the pandemic was acutely felt and substantially impacted the progress of this project. Resultingly, all of the practical work presented in Chapters 2 and 3 was completed within one year of study. This included four months of part-time work to enable the safe implementation of social distancing measures, followed by only eight months of full-time research. Despite the limited timeframe and starting from a position of having no prior research experience in organic synthesis, over 210 samples were prepared. Each sample was isolated and washed manually before being tested for its photocatalytic activity under various conditions.

Consequently, much of the work presented only lays a foundation for future investigations and is not yet ready for publication. This is largely because insufficient time was available to perform the required measurements. In some cases, initial attempts were made to obtain particularly important data, but were unsuccessful. Further attempts were prevented by time constraints. Measurements that fall into this latter category include ICP-OES measurements for residual palladium determination and electrochemical measurements to determine the polymer oxidation and reduction potentials experimentally.

The computational components of this project also arose out of a necessity to work from home for an additional extended period during the pandemic due to personal circumstances. This work was also performed without prior research experience in computational chemistry.

5.1 Summary of Content

Chapter 1 provided the global context for this research, from the climate crisis and the role of green hydrogen in decarbonisation to the current state-of-the-art research developments in the field of organic photocatalysis. In Chapter 2, a detailed structure-activity analysis of a large pre-published dataset has been carried out. This sample library, consisting of 99 unique DBTS-based linear co-polymers, contained computationally-predicted data for each polymer: ionisation energies, electron affinities, optical bandgaps, and oscillator strengths; and physical characterisation data: Synthesis yield, optical bandgap, crystallinity, transmissivity, fluorescence lifetime, residual palladium content, and, most importantly, photocatalytic activity. Whilst these data were previously published and analysed using machine-learning algorithms, in-depth structure-activity analyses were not included. This analysis revealed several new relationships and trends that were previously unidentified. The full computational results from a wider set of 704 DBTS-copolymers were subsequently screened according to these trends to identify which new polymers are the most promising targets for future investigations.

Based on the new relationships identified in Chapter 2, three sets of linear co-polymers were subsequently selected for computational and physical investigations in Chapter 3. The first set, DBTS-PhF_x, contained a set of five DBTS-Ph co-polymers with a different number of fluorine units on the phenylene unit. This set also contained the DBTS-DBTS homopolymer and the DBTS-BDT co-polymer. All seven of these polymers were part of the initial high-throughput experiment. However, they were selected as reference materials, so the impact of reaction conditions on the photocatalytic activity could be further investigated and compared with the published HER rates. It was also hoped that a clearer understanding of the role of fluorine could be determined. The second set of polymers, BDT-PhF_x, contained the electron-donating BDT unit. These binary co-polymers were investigated as in anticipation of the third set of co-polymers, DBTS-PhF_x-BDT. The purpose of investigating these ternary polymers was to consider the impact of introducing a π -linker to separate the donor and acceptor units and investigate how the band structure can be engineered by varying the substituents on this phenylene unit.

Chapter 4 builds upon the work of Chapter 3 by selecting some of these polymers and attempting to prepare hybrid photocatalysts via the in-situ polymerisation method. Here, DFT calculations confirmed the suitability of the polymer band edge positions with regard to forming favourable heterojunction interfaces with Al-doped SrTiO₃ and BiVO₄. These two inorganic oxides were selected since they are cheap, stable, and have proven photocatalytic activities as overall water-splitting and oxygen-

evolution photocatalysts, respectively. A theoretical DFT investigation was also completed into the impact of introducing conjugated side chains modified with oxide anchoring groups onto the BDT unit. Hybrid materials based on DBTS-DBTS, DBTS-Ph, and DBTS-BDT were subsequently prepared and tested for their photocatalytic hydrogen evolution under sacrificial conditions and their photocatalytic overall water-splitting activities.

5.2 Research Outcomes

Although no publications have currently arisen from this project, it has nonetheless contributed to the field. This work has introduced novel polymer design concepts, identified new structure-activity relationships, presented a list of promising polymers for future investigation, provided an insight into detrimental effects of residual palladium, identified the magnitude of impact that different high-yield synthesis conditions can have on the photocatalytic activities, highlighted the positive impact of using microwave-assisted organic synthesis to screen reaction conditions rapidly, introduced a novel concept for hybrid organic/inorganic photocatalysts, attempted the first known preparation of hybrids based on flux-synthesised Al-doped SrTiO₃, made a convincing case for lowering the typical co-catalyst loading concentrations and investigating alternative non-platinum alternatives, and has highlighted the potential benefits of using sequential photodeposition of multiple co-catalysts in these photocatalytic systems. Overall this work has laid the foundation for several new promising research directions in the field of organic photocatalysts for water-splitting applications.

5.3 Impact Area I: Polymer Design

One of the major research outcomes of this project relates to an improved set of rules with which to predict DBTS co-polymers with high photocatalytic activities based on computationally predicted ionisation potentials (IP), electron affinities (EA), and oscillator strengths (f).

5.3.1 Predicted Optical Bandgap

Firstly, among the 99 polymers successfully synthesised, this work has highlighted that it is possible to correlate the computationally-determined IP and EA potentials with the measured optical bandgaps and, therefore, accurately predict the optical bandgaps of future linear photocatalysts to within ± 0.25 eV and a mean average deviation of just ± 0.11 eV. This is unexpected since ground state IP and EA energies do not account for the exciton binding energies. Typically, optical bandgaps can only be determined by solving (or approximating) the time-dependent Schrödinger equation that allows computations involving the excited state.

The fundamental gap is given by the difference between the ionisation energy and the electron affinity. This value differs from the optical gap by the exciton binding energy that arises from the electrostatic interaction of a photogenerated electron-hole pair. This results in optical gaps that are approximately 0.1 – 1 eV lower in energy compared to the fundamental gap. The strength of the exciton binding energy in any given polymer is determined by both its physical and electronic structure. Exciton binding energies are determined by the spatial separation between the electron and hole. Co-planar polymers reduce this by giving rise to larger chromophores over which the exciton will delocalise, whereas Donor-Acceptor co-polymers reduce this energy by spatially separating the exciton pair by locating them on separate moieties.

The library of polymers investigated includes pairing the DBTS-accepting monomer with a wide of co-monomers from across the spectrum from strongly donating to strongly accepting. As such, exciton binding energy will predominantly be determined by the resulting electronic structure. The position of the IP and EA potentials calculated for the DBTS-X copolymers relative to the DBTS-DBTS homopolymer provides vital information regarding the strength of the electron accepting or donating character of the co-monomer.

The fundamental gap was correlated with the optical gap by applying individual linear correction functions to the calculated IP and EA potentials after observing that the magnitude of the difference between the fundamental gap and the optical gap varies linearly with respect to each component. To a first approximation, this shows that the IP and EA energies calculated using the computationally-inexpensive extended tight-binding method only differ from their true values according to a linear correction term. This is in agreement with the observations by Zwijnenburg *et al.* who showed that the xTB values are linearly correlated with the results predicted by the more expensive DFT methods using the CAM-B3LYP hybrid functionals and the large 6-31G(d,p) basis set.¹⁸⁸

However, the fact that this linear relationship holds with respect to the optical bandgap implies that the exciton binding energy may also vary linearly with respect to the IP and EA potentials. As such, the linear correction terms also account for this variation. An alternative explanation stems from the possibility that, for DBTS-X co-polymers, the magnitude of the exciton binding energy is relatively invariant with respect to the structure of the co-monomer. In this case, the IP/EA calibration terms would predict an average exciton binding energy for all co-polymers, and the distribution of measured optical gaps relative to the newly calculated ones represent the distribution of exciton binding

energies relative to this constant, i.e. the binding energies vary within a mean average deviation of just 0.07 eV.

When applying these calibration equations to the results from a smaller set of non-DBTS co-polymers, the optical gaps were all consistently overestimated by a small amount. It is possible that this shift arises from different average exciton binding energies. However, these polymers included seven non-DBTS monomers co-polymerised with a set of five co-monomers. As such, a wider range of exciton binding energies may have been expected. Alternatively, these differences may have arisen from differences in the dielectric constant inside the bulk polymer material. The DBTS monomer is the most polar of the set. However, IP and EA values, which are sensitive to the dielectric environment, were calculated by assuming a constant dielectric environment for all polymers.

After calculating the optical bandgaps for each polymer, it was subsequently possible to predict the IP* and EA* potentials of the excited state polymers based on the predicted IP and EA potentials and the difference between the fundamental gap and predicted optical gap. This approach assumes that the Fermi potential, which lies half way between the predicted IP and EA potentials, is correctly determined by the xTB-IPEA calculations.

Although this work only definitively shows that this approach is applicable to linear conjugated polymers containing the DBTS-unit, promising results from the small set of non-DBTS co-polymers implies that this method can likely be applied to a wider set of organic semiconductors. However, this must first be confirmed on a larger set of experimental results.

If proven to be applicable to a wider range of co-polymers, this approach may also be applicable to other conjugated organic polymers such as CMPs, CTFs, and COFs. Fast inexpensive computational methods with which optical bandgaps (and consequently excited state potentials) of complicated organic semiconductors can be determined significantly enhances the applications of high-throughput virtual screening. Not only could this be applied for bandgap engineering of organic photocatalysts, but also for alternative polymer optoelectronic systems such as OPVs, OLEDs, or organic transparent conductors.

Future attempts to build on this calibration equation may also want to consider the incorporation of additional terms that reflect the differences in polarity, and hence bulk dielectric constant, of the polymer. Furthermore, consistent and accurate methods of optical bandgap determination are

required. As shown in Chapter 3, we recommend using the Tauc plot assuming an indirect bandgap, as only this method produced a linear portion of the graph for all of the polymers synthesised in that chapter. The exact exponent used in the Tauc analysis method used by Bai *et al.* is unclear. However, several of the optical bandgaps were incorrectly determined in their work due to poor fits of the linear section.

5.3.2 Optical Bandgap, Fluorescence Lifetime, and Photocatalytic Activity

Importantly, Chapter 2 highlighted that narrow bandgap materials exhibit significantly shorter fluorescence lifetimes. Short fluorescence lifetimes were also directly associated with poor photocatalytic performances and limited increases in photocatalytic activity after the photodeposition of a platinum co-catalyst. The short lifetimes are attributed to the energy-gap law which states that the rate of non-radiative relaxation via internal conversion to the ground state is inversely proportional to the energy difference between the ground and first excited state. This observation explains why, despite absorbing a greater proportion of incident light, narrow bandgap polymers exhibited lower photocatalytic activities.

The most notable exceptions to this rule were the DBTS co-polymers containing thiophene-based co-monomers. Despite having very narrow bandgaps and short lifetimes, these polymers exhibited reasonably high photocatalytic activities which increased moderately after photodepositing Pt. These exceptions are believed to arise because of their unique electronic structure.

5.3.3 Acceptors, Donators and Orbital (De)localisation

The IP and EA potentials are very closely linked to the electron donating and accepting characteristics of a given polymer. A good electron donator is a moiety from which a valent electron can be easily removed. In terms of organic monomers, 5-membered heterocycles are good electron donators since the heteroatom stabilises a positive charge, whilst negative charges are delocalised, as demonstrated by resonance structures. Consequently, electron-donating moieties have smaller ionisation energies (less-positive ionisation potentials). For similar reasons, these same moieties are less stable when negatively charged, and so have smaller electron affinities (more negative electron affinity potentials).

In Chapter 2 we redefined the reference point from which to consider the calculated IP and EA potentials of the DBTS copolymers. Instead of reporting these values relative to the SHE, we conclude that more information can be gained by considering them with respect to those of the DBTS-DBTS

homopolymer. If the Fermi potential of the co-polymer is more negative relative to that of DBTS-DBTS, the co-monomer is electron donating. Likewise if the Fermi potential is more positive, then the co-monomer is electron withdrawing.

Since the IP and EA energies are largely synonymous with the HOMO and LUMO frontier orbital energies, the relative position of these energies with respect to those of the DBTS-DBTS homopolymer is shown to be particularly informative. When the LUMO is considerably higher in energy than that of DBTS, the electron density will be localised on the DBTS moiety. Likewise when the LUMO is lower in energy then electron density will be localised on the co-monomer. The closer the LUMO lies to that of DBTS-DBTS, the more delocalised along the polymer chain it will be. The same logic can be applied to the relative HOMO energies.

These considerations are particularly important in the context of photocatalysis, since the excited state is comprised of two Singly-Occupied Molecular Orbitals (SOMOs) following the promotion of one electron from the HOMO into the LUMO. The rates of photocatalytic charge transfer steps, therefore, do not only depend on the absolute IP and EA potentials of a polymer, but also on the distribution of electronic charge within these two SOMOs along the polymer backbone. This hypothesis was confirmed using DFT frontier orbital analysis in Chapters 3 and 4.

This theoretical approach can explain the different photocatalytic activities of the DBTS co-polymers before and after photodeposition of a platinum co-catalyst. In the absence of a platinum co-catalyst, charge transfer from DBTS-DBTS to residual palladium is the rate determining step for sacrificial photocatalytic hydrogen evolution. However, LUMO density becomes more localised onto the DBTS moiety in D-A co-polymers in which DBTS is the acceptor. This makes the EA potential more negative and introduces a greater driving force for the charge transfer reaction to take place faster and these polymers produce more hydrogen.

However, platinum has a larger work function than palladium and therefore charge transfer to platinum is considerably faster than to palladium. As such, following the photodeposition of Pt, the impact of increased driving force from a more negative EA in these D-A polymers is more. Resultingly these polymers have high photocatalytic activities using residual palladium, but this does not significantly increase after photodepositing Platinum.

The opposite trend can be seen in polymers in which the LUMO is close in energy to that of the DBTS-DBTS homopolymer. In these cases, electron density is delocalised across both the DBTS moiety and the co-monomer. As such, despite having similar EA potentials, the photocatalytic rates in the presence of residual palladium as the only co-catalyst are distinctively varied. This is because charge transfer from the DBTS unit to palladium is slow, but charge transfer from the co-monomer to palladium is also possible. The rate of this charge transfer is highly dependent on the structure of the co-monomer. The high photocatalytic activity of the DBTS-PhFx polymers with residual palladium likely arises from this effect.

Meanwhile, almost all of the polymers with LUMO energies close to that of DBTS-DBTS also exhibit improved photocatalytic activities after photodepositing platinum. Most notably, this includes DBTS-DBTS itself, co-polymers containing thiophene-based monomers, the DBTS-PhFx polymers, and DBTS-PhCN.

A consequence of this observation is that future polymer photocatalyst designs should not only target polymers with the most negative electron affinities relative to the SHE. Instead, IP and EA potentials of co-polymer should be considered relative to those predicted for the two corresponding homopolymers. It may also be preferable to target polymers with slightly less negative EA potentials, since rapid charge transfer to residual palladium is not always beneficial.

When residual palladium clusters are immobilised inside the bulk polymer, they may trap electrons and prevent those charges from being used in the hydrogen evolution reaction. Palladium has also been shown to be a less effective co-catalyst for hydrogen evolution than platinum. It has also been shown to be more effective as an oxygen reduction co-catalyst for hydrogen peroxide production which may inhibit these polymers from performing as overall water splitting photocatalysts. This work has also identified that the maximum photocatalytic activity after Pt photodeposition is limited by the residual palladium concentration, regardless of the LUMO energy. Furthermore, most samples also demonstrate shorter fluorescence lifetimes with higher palladium concentrations.

5.3.4 Delocalisation, Co-planarity, and Oscillator Strength

Whilst the predicted IP and EA potentials can be useful in predicting optical bandgaps, fluorescence lifetimes, HOMO and LUMO orbital distributions, and how a polymer might behave with different co-catalysts, these factors alone are not enough to identify which theoretical polymers should make highly active photocatalysts. For this reason, a detailed structure-activity analysis of the 99 DBTS-X copolymers was performed in Chapter 2.

Global analysis of the full set of polymers identified a general relationship between polymers with large oscillator strengths and high photocatalytic activities. However, the detailed structural analysis allows chemists to predict which polymer designs will exhibit these large oscillator strengths based on structural considerations alone. Furthermore, this analysis also helps to identify which structures with small oscillator strengths may still be highly active, and which structures with high oscillator strengths will not.

The first factor determining the size of the oscillator strength is the number of conjugated aromatic rings that lie parallel to the direction of the polymer backbone. The monomer linkage positions must also be arranged such that charges can be freely delocalised along the polymer backbone, as indicated by resonance structures. For example, a para-linked biphenylene co-monomer will have a larger oscillator strength than a DBTS copolymer containing a single para-phenylene unit. A terphenylene monomer will give an even larger oscillator strength. However, meta-linked phenylene co-polymers will have smaller oscillator strengths since delocalisation of charges across both adjacent monomers is not allowed by resonance considerations.

Despite having a larger oscillator strength the photocatalytic activity of the biphenylene co-polymer is not more active than the phenylene monomer. This is because of the freely-rotating dihedral angle around the bond connecting the two p-phenylene rings, which shortens the delocalisation length of the exciton along the polymer backbone. This allows us to introduce an additional constraint for designing active polymer photocatalysts: co-polymers with large oscillator strengths arising from multiple aromatic rings must also ensure that these rings are co-planar. This constraint increases delocalisation length whilst reducing the total number of freely-rotating dihedral bonds.

Most of the top performing photocatalysts adhere to these rules: this includes the highly active DBTS copolymers containing carbazole, dibenzothiophene, fluorene, and polyaromatic hydrocarbon

macrocycle co-monomers. Importantly, these rules only hold when the long axis of the polyaromatic monomer unit is aligned with the polymer backbone.

Co-monomers containing only one aromatic ring, such as those containing only one p-phenylene based unit along the direction of the backbone, have smaller oscillator strengths. However, within this set, the same trend is observed in which larger oscillator strengths are a prerequisite for higher photocatalytic activities. Amongst these samples larger oscillator strengths appear to correlate with samples in which the EA and IP potentials are closest to that of DBTS-DBTS.

5.3.5 New Polymer Designs

One of the major outcomes of Chapter 2 is the identification of 107 linear DBTS -based polymers with the most promising physical and electronic structures for highly active hydrogen evolution photocatalysts. Of these, 29 had been synthesised in the initial high-throughput study, 19 of which placed amongst the top 25 photocatalysts tested after photodeposition of platinum. Several others had clearly been inhibited by high palladium concentrations, low yields, or low dispersibilities. Furthermore, others only met the oscillator strength screening criteria because they contained multiple aromatic rings that were not coplanar.

Resultingly, this work presents 78 brand new linear co-polymers that are expected to be highly active photocatalysts. These polymers are presented in Chapter 2. Some of the most promising candidates for further investigations are highlighted in the discussion therein.

5.4 Impact Area II: Optimised Organic Photocatalysts

In the work published by Bai *et al.* the most active DBTS-based photocatalyst following the photodeposition of Pt was the homopolymer DBTS-DBTS itself. However, the work outlined in Chapter 2 identified trends associating low photocatalytic activities with high palladium concentrations and poor synthetic yields.

Amongst the results presented by Bai *et al.* were several equivalent polymers synthesised by different conditions. Co-polymers derived from the DBTS-Br₂ monomeric reagent were compared with structurally identical co-polymers synthesised from the DBTS-B(pin)₂ monomeric reagent. The choice of starting material had a very dramatic effect on the final photocatalytic activity. Amongst the

characteristics recorded, the synthesis conditions influenced the synthesis yield, and the polymer dispersibility. Residual palladium concentrations were not measured for the DBTS-Br₂ polymers.

It was subsequently hypothesized that modifying the reaction conditions for some of the most promising DBTS co-polymer photocatalysts may lead to improved photocatalytic activities exceeding that produced by the DBTS-DBTS homopolymer after photodeposition of platinum. This was one of the major focusses of Chapter 3.

5.4.1 DBTS-PhFx Polymers

DBTS-PhFx co-polymers were selected for this investigation since they have LUMO energies close to that of DBTS-DBTS. In the high-throughput study, some of these samples exhibited high photocatalytic activity before Pt addition but also exhibited reasonable increases in activity afterwards. They also showed particularly strong sensitivity to residual palladium concentrations.

Synthesis and testing conditions were subsequently optimised. Multiple reactions were rapidly performed using microwave-assisted polymerisation, highlighting the potential of this tool to screen reaction conditions and perform high-throughput sample preparation.

Under optimal synthesis conditions, the photocatalytic activities of two of these polymers were found to exceed that of the Pt-loaded DBTS-DBTS homopolymer. These were DBTS-PhF and DBTS-PhF2b. Optimal photocatalytic activities were obtained by decreasing the concentration of the palladium co-catalyst, reducing the reaction temperature from 160°C to 120°C, changing the base from TBAA to K₂CO₃ or K₃PO₄, and increasing the ratio of organic solvent to water from 3:2 to 9:1.

The selection of organic solvent and aqueous base proved to have a very significant impact on the resulting photocatalytic activities, despite obtaining the polymers in very high yields. However, different conditions were optimal for each polymer. For example, a biphasic reaction in Toluene/ 2M K₂CO₃ produced the most active samples of DBTS-PhF2a and DBTS-PhF2b, whereas more active samples of DBTS-Ph and DBTE-PhF were obtained from a reaction mixture of DMF/2M K₂CO₃.

DBTS-PhF2a and DBTS-PhF4 consistently underperformed relative to the other polymers in the series. DBTS-PhF2a was particularly sensitive to reaction conditions. It is hypothesised that this arises due to the amount of residual palladium trapped in these polymers. However, further experiments are required to prove this.

DBTS-PhF4 was consistently synthesised with lower yields than the other polymers in the series. It is also expected to have a relatively low energy LUMO, indicating less electron density on the DBTS moiety. This is also expected to influence the rate at which charges are transferred from this polymer to either residual palladium or photodeposited platinum. Its direct bandgap indicates wider optical bandgap than the other polymers, but strong and extended absorption tail below this bandgap indicates an extensive network of exciton states arising from considerable disorder. Resultingly its indirect bandgap is smaller than the other DBTs-PhFx polymers. The PhF4 unit is also considerably more electronegative and may result in favourable π - π stacking interactions with nearby polymer chains, which could influence its optical properties.

Unlike PhF2a and PhF4, the PhF and PhF2b are moieties are not symmetric. This may contribute to a polar backbone that improves the interface with water. This may also impact the transition dipole moments and influence the symmetry-driven selection rules regarding dipole allowed or dipole forbidden optical transitions. Alternatively, the non-symmetric nature of these units is also expected to introduce a broader range of conformational energies of the constituent chromophores. This may impact the rate at which excitons diffuse through the material.

Ultimately, further characterisation is required of these samples before these findings could be published. Firstly, UV/Vis, steady state fluorescence, and fluorescence lifetime measurements are required for each sample under each set of reaction conditions are required. CHNS(F) elemental analysis is required to determine the purity of the polymers. Likewise, ICP-OES measurements are required to determine the quantity of residual palladium and/or iron in each sample. FT-IR analysis would provide information about which functional groups are present. Solid-state ^{13}C or ^{18}F NMR measurements could provide additional verification of the structure. Extended photocatalysis measurements over 5 – 8 hours would provide information about stability. Electrochemistry measurements could provide information about the redox potentials and flatband potentials. Contact angle measurements would provide information about wettability, whereas dynamic light scattering measurements would provide information about particle size and dispersibility. SEM images could be used to investigate morphological differences based on reaction conditions. Non-linear optical spectroscopies such as photoinduced absorption spectroscopy, transient absorption spectroscopy, and transient Raman spectroscopy could provide information regarding polaron formation and charge transfer rates to sacrificial reagent, palladium, or platinum. Finally, since these polymers were only washed with water and methanol, the impact of purification by Soxhlet extraction should be considered. Likewise, polymer synthesis using an alternative palladium catalyst would be necessary to

identify any effects that may arise from residual iron resulting from using the ferrocene-containing catalyst, Pd(dppf)Cl₂.

5.4.2 Co-catalysts

As implied by the initial study, DBTS-PhFx polymers proved to be particularly sensitive to residual palladium concentrations. Unexpectedly, they were also highly sensitive to the amount of platinum deposited as a co-catalyst. Many reports of organic photocatalysts use 3 wt.% Pt as a standard loading for co-catalysts. This research shows that for DBTS-PhFx polymers, increasing platinum loadings above 0.5 wt.% resulted in reduced photocatalytic activities. Subsequent studies in Chapter 4 indicated that Pt concentrations as low as 0.1 wt.% or even 0.05 wt.% may be optimal. This work also highlighted that alternative metals such as rhodium can also be used as hydrogen evolution co-catalysts in these systems.

Last-minute research presented in Chapter 4 indicated that sequential photodeposition of Rh or Pt co-catalysts followed by Cr₂O₃ and subsequently CoO_x may lead to improved activities for polymeric materials. This is a particularly fascinating and promising line of research. Notably, the DBTS-PhFx polymers are predicted to have suitable IP levels to drive the oxygen evolution reaction. This is reinforced by the fact that hydrogen peroxide is produced from pure water in an oxygenated atmosphere. As such, identifying the correct levels of Pt (or Rh), Cr, and Co may lead to the possibility of enhanced overall water splitting activity, as observed in Al:STO, if the chromium oxide layer prevents the diffusion of oxygen to the co-catalyst surface sites.

Further analysis is also required to determine which factors are the most important when driving the photocatalytic hydrogen peroxide production reaction. This in itself is a highly interesting field of research with great promise, despite the fact that this reaction competes with that of the hydrogen evolution reaction. Hypothetically, reducing the amount of residual palladium may also reduce the rate of hydrogen peroxide production and aid the potential of these polymers to be used as overall water splitting photocatalysts. Likewise, IrO₂ should also be investigated as an oxygen evolution co-catalyst to be used in tandem with the others listed above.

Serendipitously, a potential relationship between photodeposited platinum co-catalysts and polymer stability in oxygen was also identified. Due to a limited supply of disposable caps for the headspace vials, some samples were irradiated under an oxygenated atmosphere for the first hour before being degassed, irradiated for a second time, and subsequently tested for hydrogen evolution. Amongst

these samples, the photocatalytic activity of those without an additional platinum cocatalyst appeared to decrease following oxygen exposure. Why this happens is unclear. Repeat experiments with and without oxygen are required to confirm this relationship. ICP-OES measurements to determine residual palladium levels in the samples synthesised under different conditions is also necessary to provide more information. The low activities without platinum may result from the choice of synthesis conditions that led to lower residual palladium levels. However, it is also possible that photodeposited platinum prevents the formation of peroxides. It may also increase the polymer stability in the presence of peroxides. The former would be possible if charges are preferentially transferred to platinum over palladium and the hydrogen evolution reaction occurs faster than oxygen reduction.

5.5 Impact Area III: BDT-PhFx and Ternary Polymers

Alongside the DBTS-PhFx polymers synthesised in Chapter 3, an equivalent series of BDT-PhFx binary copolymers and DBTS-PhFx-BDT ternary copolymers were also prepared. Benzodithiophene (DBT) was selected because the DBTS-BDT copolymer synthesised by Bai *et al.* in their high throughput work exhibited high photocatalytic activities, despite its small bandgap and short fluorescence lifetime.

5.5.1 Polymer Design

Structurally, the BDT-moiety is promising for photocatalytic activities since it is made up of three fused coplanar aromatic rings that run parallel to the polymer backbone axis. As such, polymers containing this unit are expected to have very large oscillator strengths. It is also relatively easy to modify the BDT unit by adding side chains. Unlike when modifying the fluorene monomer, which is a common practice for adding solubilising side chains, BDT units can be modified with side chains that are π -conjugated to the polymer backbone. These can be used to improve polymer/solution interfaces, polymer/solid interfaces, prevent polymer-polymer aggregation, construct 2D conjugated microporous polymers, and fine-tune the electronic band structure.

Furthermore, the electronic structure is also highly promising. The LUMO of the BDT-BDT homopolymer lies very close in energy to that of DBTS-DBTS. As such, the co-polymer LUMO is delocalised along the polymer backbone, which should theoretically enable almost barrier-less transport of photogenerated electrons. This low-level LUMO should also result in sluggish charge transport to palladium clusters that may act as electron traps, but rapid transfer to surface deposited platinum. This is a direct point of contrast to other D-A polymers containing aromatic heterocyclic donor moieties in which the LUMO lies at higher energies.

The HOMO, however, is strongly localised on the BDT unit, which may encourage charge separation via a charge-transfer exciton intermediate with smaller exciton binding energies. The high energy HOMO combined with a relatively low energy LUMO results in a small bandgap material capable of harnessing a greater proportion of the solar spectrum.

As with the DBTS-PhFx polymers, PhFx moieties were introduced because they introduce the possibility of fine tuning the band edge potentials. These groups are also expected to make the polymer backbone more polar and enhance charge transfer rates to co-catalysts. In the context of ternary co-polymers, these π -linkers should also help to maximise the distance between the electron-hole pair generated in a charge-transfer exciton, and hence minimise the exciton binding energy to enable rapid exciton dissociation and polaron pair generation.

Frontier orbital analysis resulting from DFT studies suggests that the ternary co-polymer LUMOs are expected to be delocalised across all three moieties, enabling rapid electron delocalisation whereas the HOMO is also extended beyond the BDT unit onto the neighbouring phenylene units. The degree of this delocalisation can be controlled by controlling number of fluorines on the phenylene ring to engineer the HOMO and LUMO energies.

5.5.2 DBT-PhFx Outcomes

The optimal synthesis conditions identified for the DBTS-PhFx polymers resulted in particularly poor synthesis yields for the BDT-PhFx polymers. This is attributed to the protodeborylation mechanism of the BDT precursor and the BDT-PhFx intermediates. BDT-PhF4 was the most difficult polymer to isolate in reasonable yields. Screening several solvents, bases, catalysts, and additives using the high-throughput microwave synthesis method identified that using TBAA as the base is necessary to stabilise the reaction and obtain reasonable yields.

Photocatalytic activities of BDT-PhFx polymers was low when measuring from a sacrificial reagent solution containing a 1:1:1 volume ratio of H₂O/MeOH/TEA. This is attributed to three factors, firstly the poor dispersibility and wettability of the polymer, the weak thermodynamic driving force for TEA oxidation, and the absence of the DBTS moiety that has repeatedly been shown to enhance photocatalytic rates. BDT-PhF4 produced the highest hydrogen evolution rate. This was ascribed to it having the most positive IP and the largest driving force for TEA oxidation.

When tested for photocatalytic activity using DMF as a dispersant and ascorbic acid as an alternative sacrificial reagent (DMF/AA), the photocatalytic activity improved. This approach should be investigated further for polymers with small bandgaps and weak thermodynamic driving forces for TEA.

From the perspective of optoelectronic characterisation, BDT-PhFx polymers had wider bandgaps relative to the BDT-BDT homopolymer. Increased fluorine content resulted in narrower bandgaps. BDT-Ph and BDT-PhF exhibited remarkably short fluorescence lifetimes and their steady state fluorescence spectra exhibited a narrower distribution with a better-resolved fine structure and smaller Stokes' shifts. Further spectroscopic studies are required to better understand these observations. When combined with the poor photocatalytic activities, this indicates rapid non-radiative relaxation to the ground state via internal conversion. However, rapid charge dissociation, charge transfer to residual palladium, or energy into optically silent excited states are also possible processes prior to relaxation to the ground state.

BDT-PhF2a, BDT-PhF2b, and BDT-PhF4 all exhibited longer fluorescence lifetimes and broader steady state fluorescence emission spectra that are also substantially red-shifted with fluorine content. Although the broad, red-shifted fluorescence spectra indicate a greater degree of disorder amongst these polymers as the fluorine content increases, the longer lifetimes also indicate longer exciton diffusion lengths and potentially improved efficiency of FRET.

Despite the incredibly short fluorescence lifetime of BDT-PhF, the photocatalytic activity of this polymer remained comparable to those of the BDT-PhFx polymers containing more fluorine atoms. This suggests that the fluorescence lifetime is short because of rapid transfer to palladium or rapid charge dissociation, rather than rapid non-radiative relaxation of a local exciton to the ground state.

5.5.3 DBTS-PhFx-BDT Outcomes

Initial attempts focussed on the structured synthesis of alternating ternary co-polymers by first synthesising PhFx-BDT-PhFx-Br₂ intermediary monomers. Despite performing the reaction in a large excess of PhFx-Br₂, the polymerisation appeared to progress as normal, and the BDT-PhFx polymers were prepared instead. Subsequently, the polymers synthesised in this study are statistical co-polymers containing 50% DBTS-PhFx and 50% BDT-PhFx subunits.

DFT computations suggested that the DBTS-PhFx-BDT ternary polymers would have almost identical fundamental gaps as the equivalent BDT-PhFx polymers. This was confirmed by UV/Vis DRS and steady-state fluorescence measurements that revealed almost identical optical bandgaps between the two. The IP and EA potentials of the ternary polymers are only expected to be marginally more positive than those of the BDT-PhFx polymers.

Despite the similar bend edge potentials, the ternary polymers exhibited significantly improved photocatalytic activities compared to the BDT-PhFx equivalents. When compared with the photocatalytic activities of the equivalent DBTS-PhFx polymers synthesised under the same conditions, the PhF and PhF4 polymers produce similar amounts of hydrogen. The ternary PhF2a polymer outperforms the DBTS-PhF2a equivalent. However, DBTS-Ph and DBTS-PhF2b polymers significantly outperform the ternary equivalents.

It should be noted that Dioxane/TBAA was not an ideal reaction mixture for the synthesis of the most active DBTS-PhFx polymer photocatalysts. However, the fact that the ternary polymers exhibit photocatalytic activity on the same order of magnitude is incredibly promising, and this approach should be investigated further.

Firstly, photocatalytic activities of the ternary polymers may be limited by poor thermodynamic driving forces for TEA oxidation. Measurements using ascorbic acid should, therefore, be investigated. The activity could also be improved by modifying the reaction conditions. As has been demonstrated in this thesis, solvent selection, base selection, organic-to-aqueous phase ratios, co-catalyst selection, monomer reagent functional leaving group selection, and reaction temperature can each influence the resulting polymer's synthesis yields and photocatalytic activity independently. Purification methods are also likely to have an impact.

Photocatalysis measurements using filtered light to excite the polymer with photon energies below the bandgap of the DBTS-PhFx polymer must also be made. This would ensure that activity arises from the combined ternary structure and is not localised on phases of the polymer matrix containing DBTS-PhFx chromophores. Likewise, further characterisation is also required.

Beyond the 50/50 split of DBTS/BDT moieties investigated here, it would also be interesting to vary the feed ratio of these donor and acceptor units. Decreasing the BDT content relative to that of DBTS may introduce more DBTS-PhFx character without losing the D-A character and narrower bandgap

introduced by the BDT unit. Resultingly, these ternary polymers may lead to photocatalytic activities exceeding the sum of the constituent parts. For example, Ye *et al.* found that combining DBTS with just 5% perylene-containing DBTS co-monomer resulted in an optimal photocatalytic activity of approximately three times more active than DBTS-DBTS.¹⁶⁵ Higher concentrations of the co-monomer resulted in lower activities and band gaps that were too small. However, this study was performed without photodepositing any additional platinum co-catalyst.

From an optoelectronics perspective, not only did the optical bandgaps of the ternary polymers match those of the BDT-PhFx binary equivalents, but the trends in steady-state fluorescence spectra were also matched. The Ph and PhF ternary polymers exhibit narrow emission spectra in which the 0-0 vibrational emission peak has a larger intensity than the 1-0 emission peak. According to Barford *et al.*, the ratio of these emission peaks provides information regarding the typical chromophore size and structural disorder. As such, the ternary Ph and PhF polymers are more ordered and contain larger chromophores. Such highly ordered chains are expected to give rise to enhanced exciton transport. These features may also explain why these two polymers also exhibited the highest photocatalytic activities of the ternary polymers.

Whereas the BDT-Ph and BDT-PhF polymers also exhibited well-resolved vibrational structure in their fluorescence spectra, their fluorescence lifetimes are incredibly short. However, the fluorescence lifetimes of the ternary co-polymer equivalents are several times longer, indicating that excitons in these polymers may be able to diffuse longer distances.

Generally, the bandgaps of the fluorinated ternary polymers decrease with increasing fluorine content. However, this variation is small. Chapter 2 demonstrated that wider bandgaps result in longer lifetimes. These ternary polymers, however, show that fluorescence lifetimes in certain polymers can be extended by introducing fluorine groups.

These results suggest that fluorinated phenylene groups can enable fine-tuning of the electronic structure and may also influence polymer backbone structure, intermolecular packing structure, excited state lifetimes, exciton diffusion dynamics, and charge separation dynamics. Furthermore, all the investigated polymers demonstrated that their solid-state excitation fluorescence spectra differ significantly from their DRS-determined absorption spectra. Further spectroscopic studies on these samples could therefore be used to enhance the theoretical understanding of exciton dynamics in conjugated polymer photocatalysts.

5.6 Impact Area VI: Organic/Inorganic Hybrid Photocatalysts

5.6.1 Hybrid Photocatalyst Design

Chapter 4 focussed on the preparation of direct heterojunction organic/inorganic hybrid photocatalysts via in-situ polymerisation. This work studied two families of hybrid materials: Polymer-sensitised oxide photocatalysts for enhanced hydrogen evolution rates based on flux-synthesised Al:SrTiO₃, and polymer/oxide Z-scheme photocatalysts for overall water splitting based on BiVO₄.

DFT calculations of the polymers investigated in Chapter 2 reveal favourable band edge alignments with the respective oxide components. The theoretical potential for modifying the BDT moiety with conjugated side chains modified with oxide binding groups was also instigated in Chapter 4. This work was inspired by the molecular design of organic dyes used in dye-sensitised solar cells. This study revealed that this approach would be particularly effective for accepting photogenerated electrons from the CB of BiVO₄, since the electron-accepting HOMO orbital extends from the BDT unit onto the thiophene side chains. When these are modified with dimethylamine oxide binding groups, this conjugation extends to the binding site. Phosphoric acid and silyl binding groups do not contain significant orbital density on the binding atoms but may still enable a tighter bond with the oxide surfaces. Anchoring groups containing carboxylic and cyano functionalities are shown to be effective electron-accepting groups and would be better suited to polymer-sensitised oxide hybrid photocatalyst systems.

By coating a thin layer of polymer onto the oxide surface, it is anticipated that the rate of bulk recombination can be reduced. However, surface recombination may be enhanced. Charge separation will also be enhanced by band bending and the formation of space charge layers within the polymer semiconductor at the various interfaces.

5.6.2 Hybrid Preparation

Organic polymer photocatalysts were synthesised via microwave-assisted polycondensation reactions in the presence of the oxide particles to generate hybrid photocatalyst particles. The resulting hybrids appeared to be homogeneously mixed and exhibited direct contact between the components, as indicated by SEM micrographs and associated EDX mapping.

XPS measurements are still required to investigate the electron binding energies of core electrons to confirm band bending and charge transfer at the polymer/oxide interface. These oxides would also

benefit from dynamic light scattering measurements, adsorption isotherms, and contact angle measurements to determine particle size, surface area, and wettability, respectively.

To ensure a homogeneous mixture and apparent interface, it was important to perform the organic synthesis in a single-phase reaction mixture and hence required a water-miscible organic solvent. These samples were also very sensitive to the relative ratios of organic solvent to aqueous base, and the concentration of the aqueous base. Yields are typically correlated with photocatalytic activity, highlighting the requirement of optimal synthesis conditions. The best results were obtained when combining 4.5 mL DMF as the organic solvent with either 2M K_3PO_4 or K_2CO_3 as the selected base.

5.6.3 Hybrid Photocatalysis

Polymer-sensitised flux-synthesised aluminium-doped $SrTiO_3$ was successfully prepared using the two linear conjugated polymer photocatalysts, DBTS-DBTS and DBTS-Ph. However, since both components are active photocatalysts under different conditions, it was challenging to identify the root cause of any resulting improvements in activity.

SEM and EDX images of these hybrids indicated that homogeneous mixtures of oxide and polymer components are maintained throughout for $RhCrO_x@Al:STO/DBTS-DBTS$ hybrid photocatalyst samples containing different mass ratios of oxide and polymer. In the absence of photodeposited Pt, photocatalytic activities under sacrificial conditions increased as the ratio of oxide to polymer increased. Meanwhile, after the photodeposition of Pt, the hybrid containing 10 wt.% oxide behaved similarly to the pure polymer, but the increases in activity on hybrids with larger oxide content were limited. It is possible that these samples contained excess amounts of platinum.

The leading hypothesis for these two sets of results relates to the fact that the oxide component had been pre-loaded with a $RhCrO_x$ co-catalyst prior to the in-situ polymerisation process that generated the hybrid system. Reaction mixtures containing increased oxide also included larger amounts of rhodium. Some rhodium, therefore, is likely to be incorporated into the organic phase, where it acts as a co-catalyst. Increases in activity due to increased surface area or charge injection from the oxide particles into the polymer could also not be ruled out. Electron extraction from the polymer into the oxide is also possible. Additionally, the presence of oxide particles in the reaction mixture can also impact the quality of the resulting polymeric component. As such, increased impurity concentration or higher residual palladium content cannot be excluded as potential explanations for their photocatalytic behaviour.

These hybrid polymers did not show signs of increased photocatalytic performance using MeOH as the sacrificial reagent. Irradiation of these photocatalysts dispersed in pure water resulted in trace amounts of hydrogen but no oxygen. In the presence of oxygen, the oxygen was reduced, and hydrogen peroxide was formed. Overall these results suggest that if charge transfer occurs across the interface, it occurs via a Type-I heterojunction in which both electrons and holes are injected from the oxide component into the polymer.

DBTS-Ph/Al:STO hybrids without pre-loaded co-catalyst were subsequently prepared. Overall water splitting was observed in this hybrid after photodepositing Rh, Cr, and Co co-catalysts sequentially. However, the rate was diminished relative to physical mixtures and isolated Al:STO samples loaded with the same co-catalysts. HER rates from MeOH and TEA solutions were also conducted. However, under no conditions did the hybrid exhibit improved performances relative to the isolated organic or inorganic components.

Polymer/BiVO₄ hybrid Z-scheme photocatalysts were also prepared. However, these samples were not capable of achieving overall water splitting. Further refinement of the BiVO₄ material, such as doping and selective photodeposition of appropriate co-catalysts, is likely required.

Further spectroscopic measurements could be used to determine whether any heterojunction has been formed between the organic and inorganic components. For example, transient absorption and photoinduced absorption measurements could be used to identify the formation of excitons and track their lifetimes in pure materials relative to the hybrid system. X-ray photoelectron spectroscopy measurements would also provide valuable information regarding whether any band-bending due to charge transfer across an interface has occurred.

Microwave-assisted polymer synthesis has proven that it can be used to rapidly screen different polymer/oxide combinations in various ratios. As such, this process could be used for a high throughput study in which hundreds of polymers with suitable band potentials could be screened for use in hybrid photocatalyst systems. As the DFT study indicated, modifying the polymer backbones with side chains capable of anchoring to the oxide surfaces may also be a promising approach to enhance charge transfer rates across the interface.

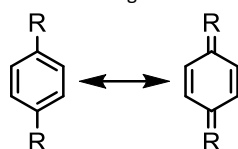
5.7 Recommended Future Work

This work has primarily focussed on linear conjugated co-polymers containing the DBTS moiety. Despite representing only a fraction of the possible organic photocatalytic systems in the literature, this work demonstrates that there remains a tremendous amount still to be learned regarding these systems. In this section, I will summarise the process that future researchers should undergo when designing new polymers in this family of materials.

Firstly, consider performing additional high-throughput computational screening studies of novel co-polymer designs. Importantly, these should also include ternary co-polymers. Ternary systems containing the DBTS unit introduce a new infinite library of potential moiety combinations. This library may be further proliferated by considering different ratios of each component and different sequential ordering of units along the backbone. As demonstrated in Chapter 3, ternary structures enable fine tuning of unique optoelectronic, physical, and chemical properties that combine those of the individual components.

When selecting which dibromide components to include in any future computational screening study, design elements highlighted in Chapter 2 may be used. As a general rule of thumb, dibromide monomers satisfying the following set of questions five should produce an effective photocatalyst when co-polymerised with DBTS.

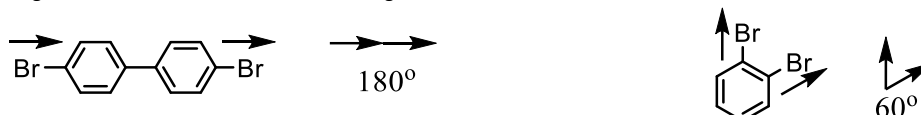
1a) Do resonance structures suggest delocalisation of electrons along the backbone of the neutral polymer?



1b) If no, do resonance structures suggest delocalisation of electrons along the backbone of the charged polymer?

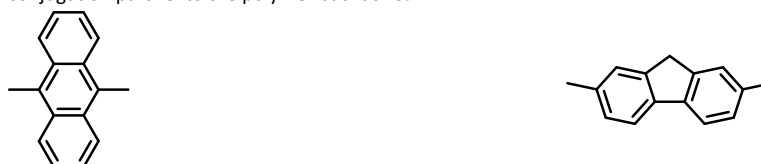


2) Is the angle between the two C-Br bonds 120° or greater?



3) Does the monomer contain more than one aromatic ring? If so, are the rings fused/co-planar?

4) Is the molecular axis of conjugation parallel to the polymer backbone?



Whether polymers with these underlying structures will be highly effective or not depends on the nature of any functional groups and the presence of aromatic heterocyclic compounds. Determining absolute rules regarding the impact of these factors is challenging without further information from computational calculations.

Using the modified xTB-IPEA extended tight binding calculations outlined in Chapter 2, accurate optical bandgaps and approximate excited state ionisation energies and electron affinities can be obtained at a low computational cost. The energies of IP* and EA* of the DBTS co-polymers relative to those of DBTS-DBTS itself would provide the most information regarding the impact of introducing heteroatoms and functional groups. Samples predicted to have large oscillator strengths ($f > 5.5$ a.u.) are typically expected to exhibit higher photocatalytic activities and longer fluorescence lifetimes.

The colour coordinated selection of co-polymers presented in **Figure 284** demonstrate how different functional groups and heteroatoms influence the HOMO and LUMO orbital energies (EA* and IP* respectively). Typically, red, grey, and purple polymers are expected to perform best as the LUMO is delocalised along the polymer backbone and the rate of charge transfer to residual palladium traps in the bulk is slow compared to the transfer of energy to photodeposited platinum. The electronic structure can be fine-tuned by adding or removing functional groups that are either electron donating (up and left) or electron withdrawing (down and right) in nature.

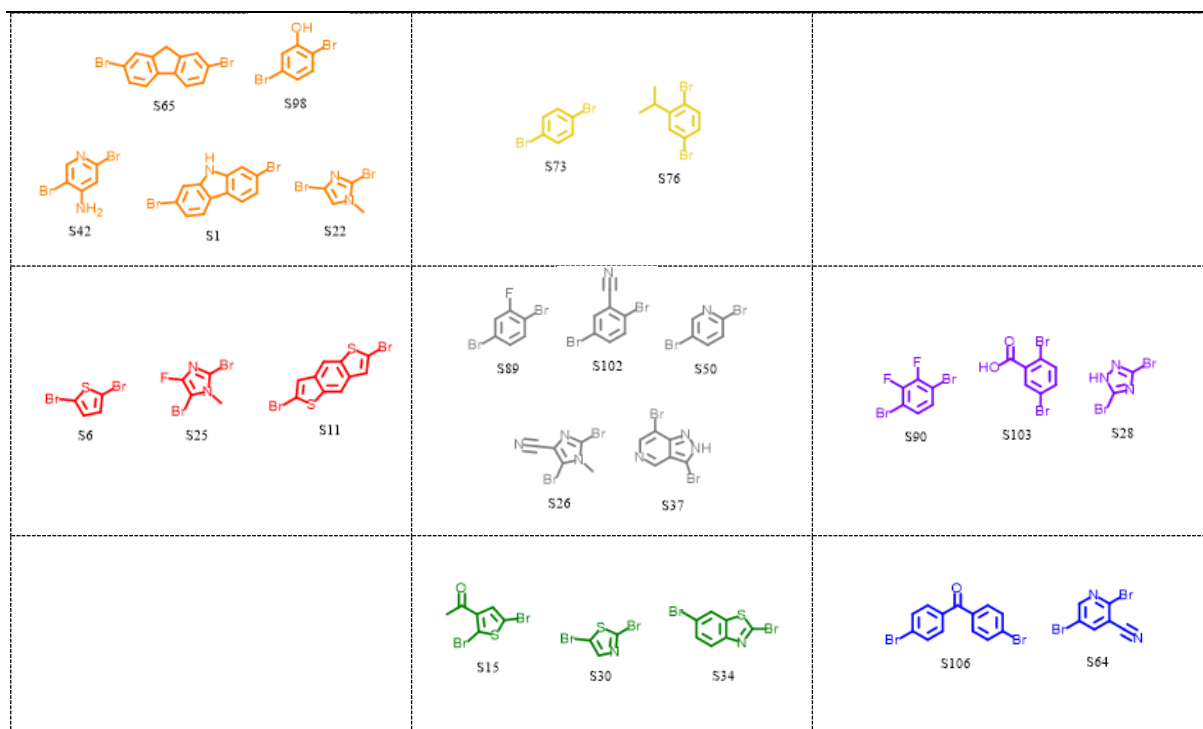


Figure 284: A selection of DBTS-X co-polymers identified as promising candidates according to the virtual screening criteria outlined in Chapter 2. Samples on the left have shallower HOMO levels than DBTS-DBTS, whereas those at the top have shallower LUMO levels than DBTS-DBTS. Likewise, the frontier orbitals of structures in the bottom right are lower in energy than DBTS-DBTS. Structures at the top left can be considered strong electron donors, whereas those at the bottom right are strong electron acceptors relative to the DBTS moiety. The orbital energies of DBTS-DBTS are predicted to match those of the grey samples closely.

The high throughput work discussed in Chapter 2 did not investigate many samples containing imidazole- or thiazole-based moieties or those containing with fused 5- and 6- member rings. These systems, which interestingly possess both electron donating and electron withdrawing groups at the same time, should be thoroughly investigated. Their favourable band energetics may also lead to high photocatalytic activities.

The work presented in this thesis, based on DBTS, BDT and PhFx moieties demonstrated that it is possible to produce DBTS-containing polymers with activities even greater than DBTS-DBTS when loaded with 0.5 wt.% Pt and tested in a 1:1:1 solution of TEA/MeOH/H₂O. Exploring now co-polymer structures based on the methodology outlined here is highly likely to result in the discovery of photocatalysts with further enhanced activities.

Another high throughput study similar to the work completed by Bai *et al.* would be very beneficial to the field. However, in addition to using the modified screening methodology and criteria, future microwave synthesis reactions should also be conducted using 4.5 ml of DMF or Toluene as the organic

solvent and 0.5 ml of 2M K_2CO_3 or K_3PO_4 as the base. Reaction temperatures should also not exceed 120°C.

When testing for sacrificial hydrogen evolution rates, these values should be reported as area-normalised values. The irradiation area should be noted and polymer dispersion concentrations of at least 1 mg ml^{-1} should be used to ensure maximum absorption of light over this region. Samples should not be irradiated for more than 15 minutes to prevent the detrimental impacts of excessive headspace pressure. Pt loading concentrations may also need to be reduced further from 0.5 wt.% to 0.1 wt% for optimal performance.

High throughput studies should also simultaneously test each photocatalyst for overall water splitting and hydrogen peroxide production. Further investigations into the use of a combination of Pt, Rh, Cr_2O_3 , and CoOOH cocatalysts (sequentially photodeposited) should be conducted in order to maximise the rate of oxygen evolution and minimise that of oxygen reduction / hydrogen peroxide production in the case of the overall water splitting reaction.

References

- (1) Hisatomi, T.; Takanabe, K.; Domen, K. Photocatalytic Water-Splitting Reaction from Catalytic and Kinetic Perspectives. *Catal Letters* **2015**, *145* (1), 95–108. <https://doi.org/10.1007/s10562-014-1397-z>.
- (2) IEA. *The Future of Hydrogen*; Paris, 2019. <https://www.iea.org/reports/the-future-of-hydrogen>.
- (3) Montoya, J. H.; Seitz, L. C.; Chakthranont, P.; Vojvodic, A.; Jaramillo, T. F.; Nørskov, J. K. Materials for Solar Fuels and Chemicals. *Nat Mater* **2017**, *16* (1), 70–81. <https://doi.org/10.1038/nmat4778>.
- (4) Lee, Q. Y.; Li, H. Photocatalytic Degradation of Plastic Waste: A Mini Review. *Micromachines (Basel)* **2021**, *12* (8), 1–20. <https://doi.org/10.3390/mi12080907>.
- (5) Koe, W. S.; Lee, J. W.; Chong, W. C.; Pang, Y. L.; Sim, L. C. An Overview of Photocatalytic Degradation: Photocatalysts, Mechanisms, and Development of Photocatalytic Membrane. *Environmental Science and Pollution Research* **2020**, *27* (3), 2522–2565. <https://doi.org/10.1007/s11356-019-07193-5>.
- (6) Fang, S.; Rahaman, M.; Bharti, J.; Reisner, E.; Robert, M.; Ozin, G. A.; Hu, Y. H. Photocatalytic CO₂ Reduction. *Nature Reviews Methods Primers* **2023**, *3* (1), 61. <https://doi.org/10.1038/s43586-023-00243-w>.
- (7) *UK Hydrogen Strategy*; UK Government, 2021. <https://www.gov.uk/government/publications/uk-hydrogen-strategy>.
- (8) Department for Business Energy & Industrial Strategy. *Energy Security Bill factsheet: Enabling the Hydrogen Village Trial*. GOV.UK. <https://www.gov.uk/government/publications/energy-security-bill-factsheets/energy-security-bill-factsheet-enabling-the-hydrogen-village-trial> (accessed 2023-12-09).
- (9) Levinsky, H. Why Can't We Just Burn Hydrogen? Challenges When Changing Fuels in an Existing Infrastructure. *Prog Energy Combust Sci* **2021**, *84*, 100907. <https://doi.org/https://doi.org/10.1016/j.pecs.2021.100907>.
- (10) Samsun, R. C.; Rex, M.; Antoni, L.; Stolten, D. Deployment of Fuel Cell Vehicles and Hydrogen Refueling Station Infrastructure: A Global Overview and Perspectives. *Energies (Basel)* **2022**, *15* (14). <https://doi.org/10.3390/en15144975>.
- (11) IEA. *Global Supply Chains of EV Batteries*; Paris, 2022. <https://www.iea.org/reports/global-supply-chains-of-ev-batteries>.
- (12) Hydrogen UK. *Hydrogen Transport Benchmarking*; 2023. <https://hydrogen-uk.org/publication/hydrogen-transport-benchmarking/>.
- (13) Nemmour, A.; Inayat, A.; Janajreh, I.; Ghenai, C. Green Hydrogen-Based E-Fuels (E-Methane, E-Methanol, E-Ammonia) to Support Clean Energy Transition: A Literature Review. *Int J Hydrogen Energy* **2023**. <https://doi.org/https://doi.org/10.1016/j.ijhydene.2023.03.240>.
- (14) IEA. *Iron and Steel Technology Roadmap*; Paris, 2020. <https://doi.org/10.1787/3dcc2a1b-en>.
- (15) Pandit, J.; Watson, M.; Qader, A. Reduction of Greenhouse Gas Emissions in Steel Production Final Report. **2020**, No. March.
- (16) Zhang, X.; Jiao, K.; Zhang, J.; Guo, Z. A Review on Low Carbon Emissions Projects of Steel Industry in the World. *J Clean Prod* **2021**, *306*, 127259. <https://doi.org/https://doi.org/10.1016/j.jclepro.2021.127259>.
- (17) IEA. *Technology Roadmap - Low-Carbon Transition in the Cement Industry*; Paris, 2018. <https://www.iea.org/reports/technology-roadmap-low-carbon-transition-in-the-cement-industry>.
- (18) UK Government. *Hydrogen Production Costs by Production 2021*; London, 2021.
- (19) Pinaud, B. A.; Benck, J. D.; Seitz, L. C.; Forman, A. J.; Chen, Z.; Deutsch, T. G.; James, B. D.; Baum, K. N.; Baum, G. N.; Ardo, S.; Wang, H.; Miller, E.; Jaramillo, T. F. Technical and Economic Feasibility of Centralized Facilities for Solar Hydrogen Production via Photocatalysis and Photoelectrochemistry. *Energy Environ Sci* **2013**, *6* (7), 1983–2002. <https://doi.org/10.1039/c3ee40831k>.
- (20) Tsao, J.; Lewis, N.; Crabtree, G. Solar FAQs. *US department of Energy* **2006**, 1–24.
- (21) Alcácer, L. *Electronic Structure of Organic Semiconductors: Polymers and Small Molecules*; IOP Publishing, 2018. <https://doi.org/10.1088/2053-2571/aaddd8>.
- (22) NREL. *ASTM G-173-03 Data Tables*. ASTM G-173-03 Data Tables. <https://doi.org/10.1520/G0173-03R20>.

- (23) Shockley, W.; Queisser, H. J. Detailed Balance Limit of Efficiency of P-n Junction Solar Cells. *J Appl Phys* **2004**, *32* (3), 510–519. <https://doi.org/10.1063/1.1736034>.
- (24) Ross, R. T.; Hsiao, T. Limits on the Yield of Photochemical Solar Energy Conversion. *J Appl Phys* **2008**, *48* (11), 4783–4785. <https://doi.org/10.1063/1.323494>.
- (25) Nishiyama, H.; Yamada, T.; Nakabayashi, M.; Maehara, Y.; Yamaguchi, M.; Kuromiya, Y.; Nagatsuma, Y.; Tokudome, H.; Akiyama, S.; Watanabe, T.; Narushima, R.; Okunaka, S.; Shibata, N.; Takata, T.; Hisatomi, T.; Domen, K. Photocatalytic Solar Hydrogen Production from Water on a 100-M² Scale. *Nature* **2021**, *598* (7880), 304–307. <https://doi.org/10.1038/s41586-021-03907-3>.
- (26) Fujishima, A.; Honda, K. Electrochemical Photolysis of Water at a Semiconductor Electrode. *Nature* **1972**, *238* (5358), 37.
- (27) Chen, X.; Shen, S.; Guo, L.; Mao, S. S. Semiconductor-Based Photocatalytic Hydrogen Generation. *Chem Rev* **2010**, *110* (11), 6503–6570.
- (28) Zhang, P.; Wang, T.; Gong, J. Mechanistic Understanding of the Plasmonic Enhancement for Solar Water Splitting. *Advanced Materials* **2015**, *27* (36), 5328–5342. <https://doi.org/https://doi.org/10.1002/adma.201500888>.
- (29) Takata, T.; Domen, K. Defect Engineering of Photocatalysts by Doping of Alivalent Metal Cations for Efficient Water Splitting. *Journal of Physical Chemistry C* **2009**, *113* (45), 19386–19388. <https://doi.org/10.1021/jp908621e>.
- (30) Nishioka, S.; Hyodo, J.; Vequizo, J. J. M.; Yamashita, S.; Kumagai, H.; Kimoto, K.; Yamakata, A.; Yamazaki, Y.; Maeda, K. Homogeneous Electron Doping into Nonstoichiometric Strontium Titanate Improves Its Photocatalytic Activity for Hydrogen and Oxygen Evolution. *ACS Catal* **2018**, *8* (8), 7190–7200. <https://doi.org/10.1021/acscatal.8b01379>.
- (31) Hitoki, G.; Ishikawa, A.; Takata, T.; Kondo, J. N.; Hara, M.; Domen, K. Ta₃N₅ as a Novel Visible Light-Driven Photocatalyst ($\lambda < 600\text{nm}$). *Chem Lett* **2002**, No. 7, 736–737. <https://doi.org/10.1246/cl.2002.736>.
- (32) Nasir, J. A.; Rehman, Z. ur; Shah, S. N. A.; Khan, A.; Butler, I. S.; Catlow, C. R. A. Recent Developments and Perspectives in CdS-Based Photocatalysts for Water Splitting. *J Mater Chem A Mater* **2020**, *8* (40), 20752–20780. <https://doi.org/10.1039/D0TA05834C>.
- (33) Guo, L. J.; Luo, J. W.; He, T.; Wei, S. H.; Li, S. S. Photocorrosion-Limited Maximum Efficiency of Solar Photoelectrochemical Water Splitting. *Phys Rev Appl* **2018**, *10* (6), 1. <https://doi.org/10.1103/PhysRevApplied.10.064059>.
- (34) Wang, D.; Zeng, H.; Xiong, X.; Wu, M. F.; Xia, M.; Xie, M.; Zou, J. P.; Luo, S. L. Highly Efficient Charge Transfer in CdS-Covalent Organic Framework Nanocomposites for Stable Photocatalytic Hydrogen Evolution under Visible Light. *Sci Bull (Beijing)* **2020**, *65* (2), 113–122. <https://doi.org/10.1016/j.scib.2019.10.015>.
- (35) Xiao, J.; Nishimae, S.; Vequizo, J. J. M.; Nakabayashi, M.; Hisatomi, T.; Li, H.; Lin, L.; Shibata, N.; Yamakata, A.; Inoue, Y.; Domen, K. Enhanced Overall Water Splitting by a Zirconium-Doped TaON-Based Photocatalyst. *Angewandte Chemie - International Edition* **2022**, *61* (17). <https://doi.org/10.1002/anie.202116573>.
- (36) Wang, Q.; Nakabayashi, M.; Hisatomi, T.; Sun, S.; Akiyama, S.; Wang, Z.; Pan, Z.; Xiao, X.; Watanabe, T.; Yamada, T.; Shibata, N.; Takata, T.; Domen, K. Oxysulfide Photocatalyst for Visible-Light-Driven Overall Water Splitting. *Nat Mater* **2019**, *18* (8), 827–832. <https://doi.org/10.1038/s41563-019-0399-z>.
- (37) Xiao, J.; Hisatomi, T.; Domen, K. Narrow-Band-Gap Particulate Photocatalysts for One-Step-Excitation Overall Water Splitting. *Acc Chem Res* **2023**. <https://doi.org/10.1021/acs.accounts.3c00011>.
- (38) Takata, T.; Jiang, J.; Sakata, Y.; Nakabayashi, M.; Shibata, N.; Nandal, V.; Seki, K.; Hisatomi, T.; Domen, K. Photocatalytic Water Splitting with a Quantum Efficiency of Almost Unity. *Nature* **2020**, *581* (7809), 411+. <https://doi.org/10.1038/s41586-020-2278-9>.
- (39) Goto, Y.; Hisatomi, T.; Wang, Q.; Higashi, T.; Ishikiriyama, K.; Maeda, T.; Sakata, Y.; Okunaka, S.; Tokudome, H.; Katayama, M. A Particulate Photocatalyst Water-Splitting Panel for Large-Scale Solar Hydrogen Generation. *Joule* **2018**, *2* (3), 509–520.
- (40) Lyu, H.; Hisatomi, T.; Goto, Y.; Yoshida, M.; Higashi, T.; Katayama, M.; Takata, T.; Minegishi, T.; Nishiyama, H.; Yamada, T.; Sakata, Y.; Asakura, K.; Domen, K. An Al-Doped SrTiO₃ Photocatalyst Maintaining Sunlight-Driven Overall Water Splitting Activity for over 1000 h of Constant Illumination. *Chem Sci* **2019**, *10* (11), 3196–3201. <https://doi.org/10.1039/c8sc05757e>.
- (41) Zhao, Z.; Goncalves, R. V.; Barman, S. K.; Willard, E. J.; Byle, E.; Perry, R.; Wu, Z.; Huda, M. N.; Moulé, A. J.; Osterloh, F. E. Electronic Structure Basis for Enhanced Overall Water Splitting Photocatalysis with Aluminum Doped SrTiO₃ in Natural Sunlight. *Energy Environ Sci* **2019**, *12* (4), 1385–1395. <https://doi.org/10.1039/c9ee00310j>.

- (42) Zhao, Z.; Willard, E. J.; Li, H.; Wu, Z.; Castro, R. H. R.; Osterloh, F. E. Aluminum Enhances Photochemical Charge Separation in Strontium Titanate Nanocrystal Photocatalysts for Overall Water Splitting. *J Mater Chem A Mater* **2018**, *6* (33), 16170–16176.
- (43) Ham, Y.; Hisatomi, T.; Goto, Y.; Moriya, Y.; Sakata, Y.; Yamakata, A.; Kubota, J.; Domen, K. Flux-Mediated Doping of SrTiO₃ Photocatalysts for Efficient Overall Water Splitting. *J Mater Chem A Mater* **2016**, *4* (8), 3027–3033.
- (44) Yamakata, A.; Yeilin, H.; Kawaguchi, M.; Hisatomi, T.; Kubota, J.; Sakata, Y.; Domen, K. Morphology-Sensitive Trapping States of Photogenerated Charge Carriers on SrTiO₃ Particles Studied by Time-Resolved Visible to Mid-IR Absorption Spectroscopy: The Effects of Molten Salt Flux Treatments. *J Photochem Photobiol A Chem* **2015**, *313* (SI), 168–175. <https://doi.org/10.1016/j.jphotochem.2015.05.016>.
- (45) Maeda, K.; Teramura, K.; Masuda, H.; Takata, T.; Saito, N.; Inoue, Y.; Domen, K. Efficient Overall Water Splitting under Visible-Light Irradiation on (Ga_{1-x}Zn_x)(N_{1-x}O_x) Dispersed with Rh-Cr Mixed-Oxide Nanoparticles: Effect of Reaction Conditions on Photocatalytic Activity. **2006**, 13107–13112. <https://doi.org/10.1021/jp0616563>.
- (46) Chiang, T. H.; Lyu, H.; Hisatomi, T.; Goto, Y.; Takata, T.; Katayama, M.; Minegishi, T.; Domen, K. Efficient Photocatalytic Water Splitting Using Al-Doped SrTiO₃ Coloaded with Molybdenum Oxide and Rhodium-Chromium Oxide. *ACS Catal* **2018**, *8* (4), 2782–2788. <https://doi.org/10.1021/acscatal.7b04264>.
- (47) Takata, T.; Pan, C.; Nakabayashi, M.; Shibata, N.; Domen, K. Fabrication of a Core-Shell-Type Photocatalyst via Photodeposition of Group IV and v Transition Metal Oxyhydroxides: An Effective Surface Modification Method for Overall Water Splitting. *J Am Chem Soc* **2015**, *137* (30), 9627–9634. <https://doi.org/10.1021/jacs.5b04107>.
- (48) Wang, Q.; Domen, K. Particulate Photocatalysts for Light-Driven Water Splitting: Mechanisms, Challenges, and Design Strategies. *Chem Rev* **2020**, *120* (2), 919–985. <https://doi.org/10.1021/acs.chemrev.9b00201>.
- (49) Yan, C.; Dong, J.; Chen, Y.; Zhou, W.; Peng, Y.; Zhang, Y.; Wang, L. Organic Photocatalysts: From Molecular to Aggregate Level. *Nano Res* **2022**, *15* (5), 3835–3858. <https://doi.org/10.1007/s12274-022-4098-8>.
- (50) Zhao, C.; Chen, Z.; Shi, R.; Yang, X.; Zhang, T. Recent Advances in Conjugated Polymers for Visible-Light-Driven Water Splitting. *Advanced Materials* **2020**, *32* (28), 1907296. <https://doi.org/10.1002/adma.201907296>.
- (51) Dai, C.; Liu, B. Conjugated Polymers for Visible-Light-Driven Photocatalysis. *Energy Environ Sci* **2020**, *13* (1), 24–52. <https://doi.org/10.1039/c9ee01935a>.
- (52) Tamai, Y.; Ohkita, H.; Bente, H.; Ito, S. Exciton Diffusion in Conjugated Polymers: From Fundamental Understanding to Improvement in Photovoltaic Conversion Efficiency. *JOURNAL OF PHYSICAL CHEMISTRY LETTERS* **2015**, *6* (17), 3417–3428. <https://doi.org/10.1021/acs.jpcclett.5b01147>.
- (53) Wang, H.; Jin, S.; Zhang, X.; Xie, Y. Excitonic Effects in Polymeric Photocatalysts. *Angewandte Chemie International Edition* **2020**, *59* (51), 22828–22839. <https://doi.org/10.1002/anie.202002241>.
- (54) Chandross, M.; Mazumdar, S.; Jeglinski, S.; Wei, X.; Vardeny, Z. V.; Kwock, E. W.; Miller, T. M. Excitons in Poly(Para-Phenylenevinylene). *Phys Rev B* **1994**, *50* (19), 14702–14705. <https://doi.org/10.1103/PhysRevB.50.14702>.
- (55) Dimitriev, O. P. Dynamics of Excitons in Conjugated Molecules and Organic Semiconductor Systems. *Chem Rev* **2021**. <https://doi.org/10.1021/acs.chemrev.1c00648>.
- (56) Li, G.; Fu, P.; Yue, Q.; Ma, F.; Zhao, X.; Dong, S.; Han, X.; Zhou, Y.; Wang, J. Boosting Exciton Dissociation by Regulating Dielectric Constant in Covalent Organic Framework for Photocatalysis. *Chem Catalysis* **2022**, *2* (7), 1734–1747. <https://doi.org/https://doi.org/10.1016/j.checat.2022.05.002>.
- (57) Jin, X.; Price, M. B.; Finnegan, J. R.; Boott, C. E.; Richter, J. M.; Rao, A.; Menke, S. M.; Friend, R. H.; Whittell, G. R.; Manners, I. Long-Range Exciton Transport in Conjugated Polymer Nanofibers Prepared by Seeded Growth. *Science (1979)* **2018**, *360* (May), 897–900.
- (58) Leenaers, P. J.; Maufort, A. J. L. A.; Wienk, M. M.; Janssen, R. A. J. Impact of π -Conjugated Linkers on the Effective Exciton Binding Energy of Diketopyrrolopyrrole–dithienopyrrole Copolymers. *Journal of Physical Chemistry C* **2020**, *124* (50), 27403–27412. <https://doi.org/10.1021/acs.jpcc.0c08768>.
- (59) Xie, Z.; Wang, W.; Ke, X.; Cai, X.; Chen, X.; Wang, S.; Lin, W.; Wang, X. A Heptazine-Based Polymer Photocatalyst with Donor-Acceptor Configuration to Promote Exciton Dissociation and Charge Separation. *Appl Catal B* **2023**, *325*, 122312. <https://doi.org/https://doi.org/10.1016/j.apcatb.2022.122312>.
- (60) Lan, Z.-A.; Zhang, G.; Chen, X.; Zhang, Y.; Zhang, I. K. A.; Wang, X. Reducing the Exciton Binding Energy of Donor-Acceptor-Based Conjugated Polymers to Promote Charge-Induced Reactions. *ANGEWANDTE CHEMIE-INTERNATIONAL EDITION* **2019**, *58* (30), 10236–10240. <https://doi.org/10.1002/anie.201904904>.

- (61) Lan, Z.; Wu, M.; Fang, Z.; Chi, X.; Chen, X.; Zhang, Y.; Wang, X. A Fully Coplanar Donor–Acceptor Polymeric Semiconductor with Promoted Charge Separation Kinetics for Photochemistry. *Angewandte Chemie International Edition* **2021**, anie.202103992. <https://doi.org/10.1002/anie.202103992>.
- (62) Kosco, J.; Sachs, M.; Godin, R.; Kirkus, M.; Francas, L.; Bidwell, M.; Qureshi, M.; Anjum, D.; Durrant, J. R.; McCulloch, I. The Effect of Residual Palladium Catalyst Contamination on the Photocatalytic Hydrogen Evolution Activity of Conjugated Polymers. *Adv Energy Mater* **2018**, *8* (34), 1802181. <https://doi.org/10.1002/aenm.201802181>.
- (63) Sachs, M.; Cha, H.; Kosco, J.; Aitchison, C. M.; Francàs, L.; Corby, S.; Chiang, C. L.; Wilson, A. A.; Godin, R.; Fahey-Williams, A.; Cooper, A. I.; Sprick, R. S.; McCulloch, I.; Durrant, J. R. Tracking Charge Transfer to Residual Metal Clusters in Conjugated Polymers for Photocatalytic Hydrogen Evolution. *J Am Chem Soc* **2020**, *142* (34), 14574–14587. <https://doi.org/10.1021/jacs.0c06104>.
- (64) Sachs, M.; Sprick, R. S.; Pearce, D.; Hillman, S. A. J.; Monti, A.; Guilbert, A. A. Y.; Brownbill, N. J.; Dimitrov, S.; Shi, X.; Blanc, F.; Zwijnenburg, M. A.; Nelson, J.; Durrant, J. R.; Cooper, A. I. Understanding Structure-Activity Relationships in Linear Polymer Photocatalysts for Hydrogen Evolution. *Nat Commun* **2018**, *9* (1), 4968. <https://doi.org/10.1038/s41467-018-07420-6>.
- (65) Zhu, L.; Zhang, M.; Xu, J.; Li, C.; Yan, J.; Zhou, G.; Zhong, W.; Hao, T.; Song, J.; Xue, X.; Zhou, Z.; Zeng, R.; Zhu, H.; Chen, C. C.; MacKenzie, R. C. I.; Zou, Y.; Nelson, J.; Zhang, Y.; Sun, Y.; Liu, F. Single-Junction Organic Solar Cells with over 19% Efficiency Enabled by a Refined Double-Fibril Network Morphology. *Nat Mater* **2022**, *21* (6), 656–663. <https://doi.org/10.1038/s41563-022-01244-y>.
- (66) Sprick, R. S.; Little, M. A.; Cooper, A. I. Organic Heterojunctions for Direct Solar Fuel Generation. *Commun Chem* **2020**, *3* (1), 1–4. <https://doi.org/10.1038/s42004-020-0288-z>.
- (67) Kosco, J.; Bidwell, M.; Cha, H.; Martin, T.; Howells, C. T.; Sachs, M.; Anjum, D. H.; Gonzalez Lopez, S.; Zou, L.; Wadsworth, A.; Zhang, W.; Zhang, L.; Tellam, J.; Sougrat, R.; Laquai, F.; DeLongchamp, D. M.; Durrant, J. R.; McCulloch, I. Enhanced Photocatalytic Hydrogen Evolution from Organic Semiconductor Heterojunction Nanoparticles. *Nat Mater* **2020**, *19* (5), 559–565. <https://doi.org/10.1038/s41563-019-0591-1>.
- (68) Chen, J.; Dong, C.-L.; Zhao, D.; Huang, Y.-C.; Wang, X.; Samad, L.; Dang, L.; Shearer, M.; Shen, S.; Guo, L. Molecular Design of Polymer Heterojunctions for Efficient Solar-Hydrogen Conversion. *ADVANCED MATERIALS* **2017**, *29* (21). <https://doi.org/10.1002/adma.201606198>.
- (69) Yang, Y.; Li, D.; Wang, P.; Zhang, X.; Zhang, H.; Du, B.; Guo, C.; Wang, T.; Liu, D. Polymer/Non-Fullerene Acceptor Bulk Heterojunction Nanoparticles for Efficient Photocatalytic Hydrogen Production from Water. *Polymer (Guildf)* **2022**, *244* (January), 124667. <https://doi.org/10.1016/j.polymer.2022.124667>.
- (70) Kosco, J.; Gonzalez-Carrero, S.; Howells, C. T.; Fei, T.; Dong, Y.; Sougrat, R.; Harrison, G. T.; Firdaus, Y.; Sheelamantula, R.; Purushothaman, B.; Moruzzi, F.; Xu, W.; Zhao, L.; Basu, A.; De Wolf, S.; Anthopoulos, T. D.; Durrant, J. R.; McCulloch, I. Generation of Long-Lived Charges in Organic Semiconductor Heterojunction Nanoparticles for Efficient Photocatalytic Hydrogen Evolution. *Nat Energy* **2022**, *7* (April). <https://doi.org/10.1038/s41560-022-00990-2>.
- (71) Yang, H.; Li, X.; Sprick, R. S.; Cooper, A. I.; Cooper, I. A.; Cooper, A. I. Conjugated Polymer Donor–Molecular Acceptor Nanohybrids for Photocatalytic Hydrogen Evolution. *Chemical Communications* **2020**, *56* (50), 6790–6793. <https://doi.org/10.1039/D0CC00740D>.
- (72) Saunders, B.; Wilbraham, L.; Prentice, A. W.; Sprick, R. S.; Zwijnenburg, M. A. The Potential Scarcity, or Not, of Polymeric Overall Water Splitting Photocatalysts. *Sustain Energy Fuels* **2022**, *6* (9), 2233–2242. <https://doi.org/10.1039/d2se00027j>.
- (73) Patterson, J. D.; Bailey, B. C. *Solid-State Physics: Introduction to the Theory: Third Edition*; Springer International Publishing: Cham, 2019. <https://doi.org/10.1007/978-3-319-75322-5>.
- (74) Evstigneev, M. *Introduction to Semiconductor Physics and Devices*, 1st ed.; Springer International Publishing, 2022. <https://doi.org/10.1007/978-3-031-08458-4>.
- (75) Brédas, J.-L.; Marder, S. R.; André, J.-M. An Introduction to the Electronic Structure of π -Conjugated Molecules and Polymers, and to the Concept of Electronic Bands; 2016; pp 1–18. https://doi.org/10.1142/9789813148598_0001.
- (76) Barford, W. *Electronic and Optical Properties of Conjugated Polymers*, 2nd ed.; Oxford University Press: Croydon, 2013.
- (77) Anderson, P. W. Absence of Diffusion in Certain Random Lattices. *Physical Review* **1958**, *109* (5), 1492–1505. <https://doi.org/10.1103/PhysRev.109.1492>.

- (78) Malyshev, A. V.; Malyshev, V. A. Statistics of Low Energy Levels of a One-Dimensional Weakly Localized Frenkel Exciton: A Numerical Study. *Phys Rev B Condens Matter Mater Phys* **2001**, *63* (19), 1951111–1951118. <https://doi.org/10.1103/physrevb.63.195111>.
- (79) Malyshev, A. V.; Malyshev, V. A. Level and Wave Function Statistics of a Localized 1D Frenkel Exciton at the Bottom of the Band. *J Lumin* **2001**, *94–95*, 369–372. [https://doi.org/10.1016/S0022-2313\(01\)00303-9](https://doi.org/10.1016/S0022-2313(01)00303-9).
- (80) Makhov, D. V.; Barford, W. Local Exciton Ground States in Disordered Polymers. *Phys Rev B* **2010**, *81* (16), 165201. <https://doi.org/10.1103/PhysRevB.81.165201>.
- (81) Barford, W. Exciton Dynamics in Conjugated Polymer Systems. *Frontiers in Physics*. 2022. <https://www.frontiersin.org/articles/10.3389/fphy.2022.1004042>.
- (82) Mikhnenko, O. V.; Blom, P. W. M.; Nguyen, T. Q. Exciton Diffusion in Organic Semiconductors. *Energy Environ Sci* **2015**, *8* (7), 1867–1888. <https://doi.org/10.1039/c5ee00925a>.
- (83) Barford, W.; Tozer, O. R. Theory of Exciton Transfer and Diffusion in Conjugated Polymers. *Journal of Chemical Physics* **2014**, *141* (16). <https://doi.org/10.1063/1.4897986>.
- (84) Barford, W. Excitons in Conjugated Polymers: A Tale of Two Particles. *Journal of Physical Chemistry A* **2013**, *117* (13), 2665–2671. <https://doi.org/10.1021/jp310110r>.
- (85) Barford, W.; Marcus, M. Perspective: Optical Spectroscopy in π -Conjugated Polymers and How It Can Be Used to Determine Multiscale Polymer Structures. *Journal of Chemical Physics* **2017**, *146* (13). <https://doi.org/10.1063/1.4979495>.
- (86) Marcus, M.; Tozer, O. R.; Barford, W. Theory of Optical Transitions in Conjugated Polymers. II. Real Systems. *J Chem Phys* **2014**, *141* (16), 164102. <https://doi.org/10.1063/1.4897985>.
- (87) Yanagida, S.; Kabumoto, A.; Mizumoto, K.; Pac, C.; Yoshino, K. Poly(p-Phenylene)-Catalysed Photoreduction of Water. *J. Chem. Soc. Chem. Commun.* **1985**, No. 474, 474–475.
- (88) Shibata, T.; Kabumoto, A.; Shiragami, T.; Ishitani, O.; Pac, C.; Yanagida, S. Novel Visible-Light-Driven Photocatalyst. Poly(p-Phenylene)-Catalyzed Photoreductions of Water, Carbonyl Compounds, and Olefins. *Journal of Physical Chemistry* **1990**, *94* (5), 2068–2076. <https://doi.org/10.1021/j100368a063>.
- (89) Matsuoka, S.; Fujii, H.; Yamada, T.; Pac, C.; Ishida, A.; Takamuku, S.; Kusaba, M.; Nakashima, N.; Yanagida, S.; Hashimoto, K.; Sakata, T. Photocatalysis of Oligo(p-Phenylenes). Photoreductive Production of Hydrogen and Ethanol in Aqueous Triethylamine. *Journal of Physical Chemistry* **1991**, *95* (15), 5802–5808. <https://doi.org/10.1021/j100168a018>.
- (90) Wang, X.; Maeda, K.; Thomas, A.; Takanabe, K.; Xin, G.; Carlsson, J. M.; Domen, K.; Antonietti, M. A Metal-Free Polymeric Photocatalyst for Hydrogen Production from Water under Visible Light. *Nat Mater* **2009**, *8* (1), 76.
- (91) Kudo, A.; Miseki, Y. Heterogeneous Photocatalyst Materials for Water Splitting. *Chem Soc Rev* **2009**, *38* (1), 253–278. <https://doi.org/10.1039/b800489g>.
- (92) Pachaiappan, R.; Rajendran, S.; Kumar, P. S.; Vo, D.-V. N.; Hoang, T. K. A.; Cornejo-Ponce, L. Recent Advances in Carbon Nitride-Based Nanomaterials for Hydrogen Production and Storage. *Int J Hydrogen Energy* **2022**, *47* (88), 37490–37516. <https://doi.org/10.1016/j.ijhydene.2021.09.062>.
- (93) Jia, J.; Zhang, Q.; Li, K.; Zhang, Y.; Liu, E.; Li, X. Recent Advances on g-C₃N₄-Based Z-Scheme Photocatalysts: Structural Design and Photocatalytic Applications. *Int J Hydrogen Energy* **2023**, *48* (1), 196–231. <https://doi.org/https://doi.org/10.1016/j.ijhydene.2022.09.272>.
- (94) Rajput, Y.; Kumar, P.; Zhang, T. C.; Kumar, D.; Nemiwal, M. Recent Advances in G-C₃N₄-Based Photocatalysts for Hydrogen Evolution Reactions. *Int J Hydrogen Energy* **2022**, *47* (91), 38533–38555. <https://doi.org/10.1016/j.ijhydene.2022.09.038>.
- (95) Wang, S.; Zhang, J.; Li, B.; Sun, H.; Wang, S. Engineered Graphitic Carbon Nitride-Based Photocatalysts for Visible-Light-Driven Water Splitting: A Review. *Energy & Fuels* **2021**, *35* (8), 6504–6526. <https://doi.org/10.1021/acs.energyfuels.1c00503>.
- (96) Malik, R.; Tomer, V. K. State-of-the-Art Review of Morphological Advancements in Graphitic Carbon Nitride (g-CN) for Sustainable Hydrogen Production. *Renewable and Sustainable Energy Reviews* **2021**, *135*, 110235. <https://doi.org/10.1016/j.rser.2020.110235>.
- (97) Kuhn, P.; Antonietti, M.; Thomas, A. Porous, Covalent Triazine-Based Frameworks Prepared by Ionothermal Synthesis. *ANGEWANDTE CHEMIE-INTERNATIONAL EDITION* **2008**, *47* (18), 3450–3453. <https://doi.org/10.1002/anie.200705710>.

- (98) Lan, Z.-A.; Fang, Y.; Zhang, Y.; Wang, X. Photocatalytic Oxygen Evolution from Functional Triazine-Based Polymers with Tunable Band Structures. *ANGEWANDTE CHEMIE-INTERNATIONAL EDITION* **2018**, *57* (2), 470–474. <https://doi.org/10.1002/anie.201711155>.
- (99) Puthiaraj, P.; Lee, Y.-R.; Zhang, S.; Ahn, W.-S. Triazine-Based Covalent Organic Polymers: Design, Synthesis and Applications in Heterogeneous Catalysis. *J Mater Chem A Mater* **2016**, *4* (42), 16288–16311. <https://doi.org/10.1039/c6ta06089g>.
- (100) Bi, J.; Fang, W.; Li, L.; Wang, J.; Liang, S.; He, Y.; Liu, M.; Wu, L. Covalent Triazine-Based Frameworks as Visible Light Photocatalysts for the Splitting of Water. *Macromol Rapid Commun* **2015**, *36* (20), 1799–1805. <https://doi.org/10.1002/marc.201500270>.
- (101) Li, L.; Fang, W.; Zhang, P.; Bi, J.; He, Y.; Wang, J.; Su, W. Sulfur-Doped Covalent Triazine-Based Frameworks for Enhanced Photocatalytic Hydrogen Evolution from Water under Visible Light. *J Mater Chem A Mater* **2016**, *4* (32), 12402–12406. <https://doi.org/10.1039/c6ta04711d>.
- (102) Meier, C. B.; Sprick, R. S.; Monti, A.; Guiglion, P.; Lee, J.-S. M.; Zwijnenburg, M. A.; Cooper, A. I. Structure-Property Relationships for Covalent Triazine-Based Frameworks: The Effect of Spacer Length on Photocatalytic Hydrogen Evolution from Water. *Polymer (Guildf)* **2017**, *126*, 283–290. <https://doi.org/10.1016/j.polymer.2017.04.017>.
- (103) Kuecken, S.; Acharjya, A.; Zhi, L.; Schwarze, M.; Schomaecker, R.; Thomas, A. Fast Tuning of Covalent Triazine Frameworks for Photocatalytic Hydrogen Evolution. *CHEMICAL COMMUNICATIONS* **2017**, *53* (43), 5854–5857. <https://doi.org/10.1039/c7cc01827d>.
- (104) Liu, M.; Guo, L.; Jin, S.; Tan, B. Covalent Triazine Frameworks: Synthesis and Applications. *J Mater Chem A Mater* **2019**, *7* (10), 5153–5172. <https://doi.org/10.1039/c8ta12442f>.
- (105) Wang, X.; Chen, L.; Chong, S. Y.; Little, M. A.; Wu, Y.; Zhu, W. H.; Clowes, R.; Yan, Y.; Zwijnenburg, M. A.; Sprick, R. S.; Cooper, A. I. Sulfone-Containing Covalent Organic Frameworks for Photocatalytic Hydrogen Evolution from Water. *Nat Chem* **2018**, *10*. <https://doi.org/10.1038/s41557-018-0141-5>.
- (106) Feng, X.; Ding, X.; Jiang, D. Covalent Organic Frameworks. *Chem Soc Rev* **2012**, *41* (18), 6010–6022. <https://doi.org/10.1039/c2cs35157a>.
- (107) Bi, S.; Lan, Z.-A.; Paasch, S.; Zhang, W.; He, Y.; Zhang, C.; Liu, F.; Wu, D.; Zhuang, X.; Brunner, E.; Wang, X.; Zhang, F. Substantial Cyano-Substituted Fully Sp²-Carbon-Linked Framework: Metal-Free Approach and Visible-Light-Driven Hydrogen Evolution. *Adv Funct Mater* **2017**, *27* (39). <https://doi.org/10.1002/adfm.201703146>.
- (108) Pachfule, P.; Acharjya, A.; Roeser, J.; Langenhahn, T.; Schwarze, M.; Schomaecker, R.; Thomas, A.; Schmidt, J. Diacetylene Functionalized Covalent Organic Framework (COF) for Photocatalytic Hydrogen Generation. *J Am Chem Soc* **2018**, *140* (4), 1423–1427. <https://doi.org/10.1021/jacs.7b11255>.
- (109) Cote, A. P.; Benin, A. I.; Ockwig, N. W.; O’Keeffe, M.; Matzger, A. J.; Yaghi, O. M. Porous, Crystalline, Covalent Organic Frameworks. *Science (1979)* **2005**, *310* (5751), 1166–1170. <https://doi.org/10.1126/science.1120411>.
- (110) Liu, C.; Xiao, Y.; Yang, Q.; Wang, Y.; Lu, R.; Chen, Y.; Wang, C.; Yan, H. A Highly Fluorine-Functionalized 2D Covalent Organic Framework for Promoting Photocatalytic Hydrogen Evolution. *Appl Surf Sci* **2021**, *537*, 148082. <https://doi.org/10.1016/j.apsusc.2020.148082>.
- (111) Wei, P.-F.; Qi, M.-Z.; Wang, Z.-P.; Ding, S.-Y.; Yu, W.; Liu, Q.; Wang, L.-K.; Wang, H.-Z.; An, W.-K.; Wang, W. Benzoxazole-Linked Ultrastable Covalent Organic Frameworks for Photocatalysis. *J Am Chem Soc* **2018**, *140* (13), 4623–4631. <https://doi.org/10.1021/jacs.8b00571>.
- (112) Wang, X.; Chen, L.; Chong, S. Y.; Little, M. A.; Wu, Y.; Zhu, W.-H. H.; Clowes, R.; Yan, Y.; Zwijnenburg, M. A.; Sprick, R. S.; Cooper, A. I. Sulfone-Containing Covalent Organic Frameworks for Photocatalytic Hydrogen Evolution from Water. *Nat Chem* **2018**, *10* (12), 1180–1189. <https://doi.org/10.1038/s41557-018-0141-5>.
- (113) Zhi, Y.; Li, Z.; Feng, X.; Xia, H.; Zhang, Y.; Shi, Z.; Mu, Y.; Liu, X. Covalent Organic Frameworks as Metal-Free Heterogeneous Photocatalysts for Organic Transformations. *J Mater Chem A Mater* **2017**, *5* (44), 22933–22938. <https://doi.org/10.1039/c7ta07691f>.
- (114) Chen, W.; Wang, L.; Mo, D.; He, F.; Wen, Z.; Wu, X.; Xu, H.; Chen, L. Modulating Benzothiadiazole-Based Covalent Organic Frameworks via Halogenation for Enhanced Photocatalytic Water Splitting. *Angewandte Chemie International Edition* **2020**, *59* (39), 16902–16909. <https://doi.org/10.1002/anie.202006925>.
- (115) Jin, E.; Lan, Z.; Jiang, Q.; Geng, K.; Li, G.; Wang, X.; Jiang, D. 2D Sp² Carbon-Conjugated Covalent Organic Frameworks for Photocatalytic Hydrogen Production from Water. *Chem* **2019**, *5* (6), 1632–1647. <https://doi.org/10.1016/j.chempr.2019.04.015>.
- (116) Lee, J.-S. M.; Cooper, A. I. Advances in Conjugated Microporous Polymers. *Chem Rev* **2020**, *120* (4), 2171–2214. <https://doi.org/10.1021/acs.chemrev.9b00399>.

- (117) Cooper, A. I. Conjugated Microporous Polymers. *ADVANCED MATERIALS* **2009**, *21* (12), 1291–1295. <https://doi.org/10.1002/adma.200801971>.
- (118) Jiang, J.-X.; Su, F.; Niu, H.; Wood, C. D.; Campbell, N. L.; Khimyak, Y. Z.; Cooper, A. I. Conjugated Microporous Poly(Phenylene Butadiynylene)s. *CHEMICAL COMMUNICATIONS* **2008**, No. 4, 486–488. <https://doi.org/10.1039/b715563h>.
- (119) Jiang, J.-X.; Su, F.; Trewin, A.; Wood, C. D.; Campbell, N. L.; Niu, H.; Dickinson, C.; Ganin, A. Y.; Rosseinsky, M. J.; Khimyak, Y. Z.; Cooper, A. I. Conjugated Microporous Poly (Aryleneethynylene) Networks. *ANGEWANDTE CHEMIE-INTERNATIONAL EDITION* **2007**, *46* (45), 8574–8578. <https://doi.org/10.1002/anie.200701595>.
- (120) Chaoui, N.; Trunk, M.; Dawson, R.; Schmidt, J.; Thomas, A. Trends and Challenges for Microporous Polymers. *Chem Soc Rev* **2017**, *46* (11), 3302–3321. <https://doi.org/10.1039/c7cs00071e>.
- (121) Sprick, R. S.; Bonillo, B.; Sachs, M.; Clowes, R.; Durrant, J. R.; Adams, D. J.; Cooper, A. I. Extended Conjugated Microporous Polymers for Photocatalytic Hydrogen Evolution from Water. *Chemical Communications* **2016**, *52* (65), 10008–10011. <https://doi.org/10.1039/c6cc03536a>.
- (122) Xu, Y.; Mao, N.; Feng, S.; Zhang, C.; Wang, F.; Chen, Y.; Zeng, J.; Jiang, J.-X. Perylene-Containing Conjugated Microporous Polymers for Photocatalytic Hydrogen Evolution. *Macromol Chem Phys* **2017**, *218* (14). <https://doi.org/10.1002/macp.201700049>.
- (123) Wang, L.; Wan, Y.; Ding, Y.; Wu, S.; Zhang, Y.; Zhang, X.; Zhang, G.; Xiong, Y.; Wu, X.; Yang, J.; Xu, H. Conjugated Microporous Polymer Nanosheets for Overall Water Splitting Using Visible Light. *Advanced Materials* **2017**, *29* (38), 1–8. <https://doi.org/10.1002/adma.201702428>.
- (124) Zhang, K.; Kopetzki, D.; Seeberger, P. H.; Antonietti, M.; Vilela, F. Surface Area Control and Photocatalytic Activity of Conjugated Microporous Poly(Benzothiadiazole) Networks. *Angewandte Chemie - International Edition* **2013**, *52* (5), 1432–1436. <https://doi.org/10.1002/anie.201207163>.
- (125) Gao, X.; Shu, C.; Zhang, C.; Ma, W.; Ren, S.-B.; Wang, F.; Chen, Y.; Zeng, J. H.; Jiang, J.-X. Substituent Effect of Conjugated Microporous Polymers on the Photocatalytic Hydrogen Evolution Activity. *J Mater Chem A Mater* **2020**, *8* (5), 2404–2411. <https://doi.org/10.1039/C9TA13212K>.
- (126) Luo, S.; Zeng, Z.; Zeng, G.; Liu, Z.; Xiao, R.; Xu, P.; Wang, H.; Huang, D.; Liu, Y.; Shao, B.; Liang, Q.; Wang, D.; He, Q.; Qin, L.; Fu, Y. Recent Advances in Conjugated Microporous Polymers for Photocatalysis: Designs, Applications, and Prospects. *J Mater Chem A Mater* **2020**, *8* (14), 6434–6470. <https://doi.org/10.1039/d0ta01102a>.
- (127) Wang, Z.; Yang, X.; Yang, T.; Zhao, Y.; Wang, F.; Chen, Y.; Zeng, J. H.; Yan, C.; Huang, F.; Jiang, J.-X. Dibenzothiophene Dioxide Based Conjugated Microporous Polymers for Visible-Light-Driven Hydrogen Production. *ACS Catal* **2018**, *8* (9), 8590+. <https://doi.org/10.1021/acscatal.8b02607>.
- (128) Ma, B. C.; Ghasimi, S.; Landfester, K.; Vilela, F.; Zhang, K. A. I. Conjugated Microporous Polymer Nanoparticles with Enhanced Dispersibility and Water Compatibility for Photocatalytic Applications. *J Mater Chem A Mater* **2015**, *3* (31), 16064–16071. <https://doi.org/10.1039/c5ta03820k>.
- (129) Xu, Y.; Mao, N.; Zhang, C.; Wang, X.; Zeng, J.; Chen, Y.; Wang, F.; Jiang, J. X. Rational Design of Donor- π -Acceptor Conjugated Microporous Polymers for Photocatalytic Hydrogen Production. *Appl Catal B* **2018**, *228* (November 2017), 1–9. <https://doi.org/10.1016/j.apcatb.2018.01.073>.
- (130) Xu, Y.; Mao, N.; Zhang, C.; Wang, X.; Zeng, J.; Chen, Y.; Wang, F.; Jiang, J.-X. Rational Design of Donor- π -Acceptor Conjugated Microporous Polymers for Photocatalytic Hydrogen Production. *APPLIED CATALYSIS B-ENVIRONMENTAL* **2018**, *228*, 1–9. <https://doi.org/10.1016/j.apcatb.2018.01.073>.
- (131) Wang, Z. J.; Ghasimi, S.; Landfester, K.; Zhang, K. A. I. Photocatalytic Suzuki Coupling Reaction Using Conjugated Microporous Polymer with Immobilized Palladium Nanoparticles under Visible Light. *CHEMISTRY OF MATERIALS* **2015**, *27* (6), 1921–1924. <https://doi.org/10.1021/acs.chemmater.5b00516>.
- (132) Sprick, R. S.; Bai, Y.; Guilbert, A. A. Y. Y.; Zbiri, M.; Aitchison, C. M.; Wilbraham, L.; Yan, Y.; Woods, D. J.; Zwiijnenburg, M. A.; Cooper, A. I. Photocatalytic Hydrogen Evolution from Water Using Fluorene and Dibenzothiophene Sulfone-Conjugated Microporous and Linear Polymers. *CHEMISTRY OF MATERIALS* **2019**, *31* (2), 305–313. <https://doi.org/10.1021/acs.chemmater.8b02833>.
- (133) Zhao, Y.; Ma, W.; Xu, Y.; Zhang, C.; Wang, Q.; Yang, T.; Gao, X.; Wang, F.; Yan, C.; Jiang, J.-X. Effect of Linking Pattern of Dibenzothiophene-S,S-Dioxide-Containing Conjugated Microporous Polymers on the Photocatalytic Performance. *Macromolecules* **2018**, *51* (23), 9502–9508. <https://doi.org/10.1021/acs.macromol.8b02023>.
- (134) Sprick, R. S.; Bonillo, B.; Clowes, R.; Guiglian, P.; Brownbill, N. J.; Slater, B. J.; Blanc, F.; Zwiijnenburg, M. A.; Adams, D. J.; Cooper, A. I. Visible-Light-Driven Hydrogen Evolution Using Planarized Conjugated Polymer Photocatalysts. *Angewandte Chemie - International Edition* **2016**, *55* (5), 1792–1796. <https://doi.org/10.1002/anie.201510542>.

- (135) Hillman, S. A. J.; Sprick, R. S.; Pearce, D.; Woods, D. J.; Sit, W. Y.; Shi, X.; Cooper, A. I.; Durrant, J. R.; Nelson, J. Why Do Sulfone-Containing Polymer Photocatalysts Work so Well for Sacrificial Hydrogen Evolution from Water? *J Am Chem Soc* **2022**, *144* (42), 19382–19395. <https://doi.org/10.1021/jacs.2c07103>.
- (136) Aitchison, C. M.; Sachs, M.; Little, M. A.; Wilbraham, L.; Brownbill, N. J.; Kane, C. M.; Blanc, F.; Zwijnenburg, M. A.; Durrant, J. R.; Sprick, R. S.; Cooper, A. I. Structure-Activity Relationships in Well-Defined Conjugated Oligomer Photocatalysts for Hydrogen Production from Water. *Chem Sci* **2020**, *11* (33), 8744–8756. <https://doi.org/10.1039/d0sc02675a>.
- (137) Sprick, R. S.; Aitchison, C. M.; Berardo, E.; Turcani, L.; Wilbraham, L.; Alston, B. M.; Jelfs, K. E.; Zwijnenburg, M. A.; Cooper, A. I. Maximising the Hydrogen Evolution Activity in Organic Photocatalysts by Co-Polymerisation. *J Mater Chem A Mater* **2018**, *6* (25), 11994–12003. <https://doi.org/10.1039/c8ta04186e>.
- (138) Heath-Apostolopoulos, I.; Wilbraham, L.; Zwijnenburg, M. A. Computational High-Throughput Screening of Polymeric Photocatalysts: Exploring the Effect of Composition, Sequence Isomerism and Conformational Degrees of Freedom. *Faraday Discuss* **2019**, *215*, 98–110. <https://doi.org/10.1039/c8fd00171e>.
- (139) Sprick, R. S.; Wilbraham, L.; Bai, Y.; Guiglion, P.; Monti, A.; Clowes, R.; Cooper, A. I.; Zwijnenburg, M. A. Nitrogen Containing Linear Poly(Phenylene) Derivatives for Photo-Catalytic Hydrogen Evolution from Water. *Chemistry of Materials* **2018**, *30* (16), 5733–5742. <https://doi.org/10.1021/acs.chemmater.8b02501>.
- (140) Yang, C.; Ma, B. C.; Zhang, L.; Lin, S.; Ghasimi, S.; Landfester, K.; Zhang, K. A. I.; Wang, X. Molecular Engineering of Conjugated Polybenzothiadiazoles for Enhanced Hydrogen Production by Photosynthesis. *ANGEWANDTE CHEMIE-INTERNATIONAL EDITION* **2016**, *55* (32), 9202–9206. <https://doi.org/10.1002/anie.201603532>.
- (141) Sprick, R. S.; Jiang, J.-X.; Bonillo, B.; Ren, S.; Ratvijitvech, T.; Guiglion, P.; Zwijnenburg, M. A.; Adams, D. J.; Cooper, A. I. Tunable Organic Photocatalysts for Visible-Light-Driven Hydrogen Evolution. *J Am Chem Soc* **2015**, *137* (9), 3265–3270. <https://doi.org/10.1021/ja511552k>.
- (142) Cheng, G.; Bonillo, B.; Sprick, R. S.; Adams, D. J.; Hasell, T.; Cooper, A. I. Conjugated Polymers of Intrinsic Microporosity (C-PIMs). *Adv Funct Mater* **2014**, *24* (33), 5219–5224. <https://doi.org/10.1002/adfm.201401001>.
- (143) Zhang, X.-H.; Wang, X.-P.; Xiao, J.; Wang, S.-Y.; Huang, D.-K.; Ding, X.; Xiang, Y.-G.; Chen, H. Synthesis of 1,4-Diethynylbenzene-Based Conjugated Polymer Photocatalysts and Their Enhanced Visible/near-Infrared-Light-Driven Hydrogen Production Activity. *J Catal* **2017**, *350*, 64–71. <https://doi.org/10.1016/j.jcat.2017.02.026>.
- (144) Xiang, Y.; Wang, X.; Rao, L.; Wang, P.; Huang, D.; Ding, X.; Zhang, X.; Wang, S.; Chen, H.; Zhu, Y. Conjugated Polymers with Sequential Fluorination for Enhanced Photocatalytic H₂ Evolution via Proton-Coupled Electron Transfer. *ACS Energy Lett* **2018**, *3* (10), 2544–2549. <https://doi.org/10.1021/acscenergylett.8b01535>.
- (145) Woods, D. J.; Sprick, R. S.; Smith, C. L.; Cowan, A. J.; Cooper, A. I. A Solution-Processable Polymer Photocatalyst for Hydrogen Evolution from Water. *Adv Energy Mater* **2017**, *7* (22). <https://doi.org/10.1002/aenm.201700479>.
- (146) Woods, D. J.; Hillman, S. A. J.; Pearce, D.; Wilbraham, L.; Flag, L. Q.; Duffy, W.; McCulloch, I.; Durrant, J. R.; Guilbert, A. A. Y.; Zwijnenburg, M. A.; Sprick, R. S.; Nelson, J.; Cooper, A. I. Side-Chain Tuning in Conjugated Polymer Photocatalysts for Improved Hydrogen Production from Water. *Energy Environ Sci* **2020**, *13* (6), 1843–1855. <https://doi.org/10.1039/D0EE01213K>.
- (147) Hu, Z.; Wang, Z.; Zhang, X.; Tang, H.; Liu, X.; Huang, F.; Cao, Y. Conjugated Polymers with Oligoethylene Glycol Side Chains for Improved Photocatalytic Hydrogen Evolution. *iScience* **2019**, *13*, 33+. <https://doi.org/10.1016/j.isci.2019.02.007>.
- (148) Wang, L.; Fernandez-Teran, R.; Zhang, L.; Fernandes, D. L. A.; Tian, L.; Chen, H.; Tian, H.; Fernández-Terán, R.; Zhang, L.; Fernandes, D. L. A.; Tian, L.; Chen, H.; Tian, H. Organic Polymer Dots as Photocatalysts for Visible Light-Driven Hydrogen Generation. *ANGEWANDTE CHEMIE-INTERNATIONAL EDITION* **2016**, *55* (40), 12306–12310. <https://doi.org/10.1002/anie.201607018>.
- (149) Pati, P. B.; Damas, G.; Tian, L.; Fernandes, D. L. A. A.; Zhang, L.; Pehlivan, I. B.; Edvinsson, T.; Araujo, C. M.; Tian, H. An Experimental and Theoretical Study of an Efficient Polymer Nano-Photocatalyst for Hydrogen Evolution. *Energy Environ Sci* **2017**, *10* (6), 1372–1376. <https://doi.org/10.1039/c7ee00751e>.
- (150) Tseng, P.-J. J.; Chang, C.-L. L.; Chan, Y.-H. H.; Ting, L.-Y. Y.; Chen, P.-Y. Y.; Liao, C.-H. H.; Tsai, M.-L. L.; Chou, H.-H. H. Design and Synthesis of Cycloplatinated Polymer Dots as Photocatalysts for Visible-Light-Driven Hydrogen Evolution. *ACS Catal* **2018**, *8* (9), 7766–7772. <https://doi.org/10.1021/acscatal.8b01678>.
- (151) Dai, C.; Panahandeh-Fard, M.; Gong, X.; Xue, C.; Liu, B. Water-Dispersed Conjugated Polyelectrolyte for Visible-Light Hydrogen Production. *SOLAR RRL* **2019**, *3* (3). <https://doi.org/10.1002/solr.201800255>.

- (152) Aitchison, C. M.; Sprick, R. S.; Cooper, A. I. Emulsion Polymerization Derived Organic Photocatalysts for Improved Light-Driven Hydrogen Evolution. *J Mater Chem A Mater* **2019**, *7* (6), 2490–2496. <https://doi.org/10.1039/c8ta11383a>.
- (153) Yang, H.; Li, X.; Sprick, R. S.; Cooper, A. I.; Cooper, A. I. Conjugated Polymer Donor–Molecular Acceptor Nanohybrids for Photocatalytic Hydrogen Evolution. *Chemical Communications* **2020**, *56* (50), 6790–6793. <https://doi.org/10.1039/D0CC00740D>.
- (154) Kosco, J.; McCulloch, I. Residual Pd Enables Photocatalytic H₂ Evolution from Conjugated Polymers. *ACS Energy Lett* **2018**, *3* (11), 2846–2850. <https://doi.org/10.1021/acscenergylett.8b01853>.
- (155) Li, L.; Cai, Z.; Wu, Q.; Lo, W. Y.; Zhang, N.; Chen, L. X.; Yu, L. Rational Design of Porous Conjugated Polymers and Roles of Residual Palladium for Photocatalytic Hydrogen Production. *J Am Chem Soc* **2016**, *138* (24), 7681–7686. <https://doi.org/10.1021/jacs.6b03472>.
- (156) Bai, Y.; Wilbraham, L.; Slater, B. J.; Zwiijnenburg, M. A.; Sprick, R. S.; Cooper, A. I. Accelerated Discovery of Organic Polymer Photocatalysts for Hydrogen Evolution from Water through the Integration of Experiment and Theory. *J Am Chem Soc* **2019**, *141* (22), 9063–9071. <https://doi.org/10.1021/jacs.9b03591>.
- (157) Wang, Z.; Hisatomi, T.; Li, R.; Sayama, K.; Liu, G. LI Perspective Efficiency Accreditation and Testing Protocols for Particulate Photocatalysts toward Solar Fuel Production. *Joule* **2021**, 1–16. <https://doi.org/10.1016/j.joule.2021.01.001>.
- (158) Lin, S.; Huang, H.; Ma, T.; Zhang, Y. Photocatalytic Oxygen Evolution from Water Splitting. *Advanced Science* **2021**, *8* (1), 2002458. <https://doi.org/10.1002/advs.202002458>.
- (159) Rahman, M.; Tian, H.; Edvinsson, T. Revisiting the Limiting Factors for Overall Water-Splitting on Organic Photocatalysts. *ANGEWANDTE CHEMIE-INTERNATIONAL EDITION* **2020**, *59* (38), 16278–16293. <https://doi.org/10.1002/anie.202002561>.
- (160) Bai, Y.; Li, C.; Liu, L.; Yamaguchi, Y.; Bahri, M.; Yang, H.; Gardner, A.; Zwiijnenburg, M. A.; Browning, N. D.; Cowan, A. J.; Kudo, A.; Cooper, A. I.; Sprick, R. S. Photocatalytic Overall Water Splitting Under Visible Light Enabled by a Particulate Conjugated Polymer Loaded with Palladium and Iridium**. *Angewandte Chemie* **2022**, *134* (26). <https://doi.org/10.1002/ange.202201299>.
- (161) Sprick, R. S.; Chen, Z.; Cowan, A. J.; Bai, Y.; Aitchison, C. M.; Fang, Y.; Zwiijnenburg, M. A.; Cooper, A. I.; Wang, X. Water Oxidation with Cobalt-Loaded Linear Conjugated Polymer Photocatalysts. *Angewandte Chemie International Edition* **2020**, *59* (42), 18695–18700. <https://doi.org/10.1002/anie.202008000>.
- (162) Yi, F.; Yang, Q.; Li, X.; Yuan, Y.; Cao, H.; Liu, K.; Yan, H. A 1,3,5-Triazine and Benzodithiophene Based Donor-Acceptor Type Semiconducting Conjugated Polymer for Photocatalytic Overall Water Splitting. *J Solid State Chem* **2023**, *318* (November 2022), 123769. <https://doi.org/10.1016/j.jssc.2022.123769>.
- (163) Zhong, Z.; Li, R.; Lin, W.; Xu, X.; Tian, X.; Li, X.; Chen, X.; Kang, L. One-Dimensional Nanocrystals of Cobalt Perylene Diimide Polymer with in-Situ Generated FeOOH for Efficient Photocatalytic Water Oxidation. *Appl Catal B* **2020**, *260* (June 2019), 118135. <https://doi.org/10.1016/j.apcatb.2019.118135>.
- (164) Chen, X.; Wang, J.; Chai, Y.; Zhang, Z.; Zhu, Y. Efficient Photocatalytic Overall Water Splitting Induced by the Giant Internal Electric Field of a G-C₃N₄/RGO/PDIP Z-Scheme Heterojunction. *Advanced Materials* **2021**, *33* (7), 1–7. <https://doi.org/10.1002/adma.202007479>.
- (165) Ye, H.; Wang, Z.; Yang, Z.; Zhang, S.; Gong, X.; Hua, J. Bandgap Engineering of Novel Perylene[1,12-bcd]Thiophene Sulfone-Based Conjugated Co-Polymers for Significantly Enhanced Hydrogen Evolution without Co-Catalyst. *J Mater Chem A Mater* **2020**, *8* (38), 20062–20071. <https://doi.org/10.1039/D0TA07286A>.
- (166) Ye, H.; Wang, Z.; Hu, K.; Wu, W.; Gong, X.; Hua, J. FeOOH Photo-Deposited Perylene Linear Polymer with Accelerated Charge Separation for Photocatalytic Overall Water Splitting. *Sci China Chem* **2022**, *65* (1), 170–181. <https://doi.org/10.1007/s11426-021-1079-5>.
- (167) Kudo, A. Z-Scheme Photocatalyst Systems for Water Splitting under Visible Light Irradiation. *MRS Bull* **2011**, *36* (1), 32–38.
- (168) Abe, R.; Sayama, K.; Domen, K.; Arakawa, H. A New Type of Water Splitting System Composed of Two Different TiO₂ Photocatalysts (Anatase, Rutile) and a IO₃⁻/I⁻ Shuttle Redox Mediator. *Chem Phys Lett* **2001**, *344* (3–4), 339–344.
- (169) Abe, R.; Shinmei, K.; Koumura, N.; Hara, K.; Ohtani, B. Visible-Light-Induced Water Splitting Based on Two-Step Photoexcitation between Dye-Sensitized Layered Niobate and Tungsten Oxide Photocatalysts in the Presence of a Triiodide/Iodide Shuttle Redox Mediator. *J Am Chem Soc* **2013**, *135* (45), 16872–16884.

- (170) Tabata, M.; Maeda, K.; Higashi, M.; Lu, D.; Takata, T.; Abe, R.; Domen, K. Modified Ta₃N₅ Powder as a Photocatalyst for O₂ Evolution in a Two-Step Water Splitting System with an Iodate/Iodide Shuttle Redox Mediator under Visible Light. *Langmuir* **2010**, *26* (12), 9161–9165.
- (171) Sayama, K.; Mukasa, K.; Abe, R.; Abe, Y.; Arakawa, H. Stoichiometric Water Splitting into H₂ and O₂ Using a Mixture of Two Different Photocatalysts and an IO₃⁻/I⁻ Shuttle Redox Mediator under Visible Light Irradiation. *Chemical Communications* **2001**, No. 23, 2416–2417.
- (172) Iwase, A.; Ng, Y. H.; Ishiguro, Y.; Kudo, A.; Amal, R. Reduced Graphene Oxide as a Solid-State Electron Mediator in Z-Scheme Photocatalytic Water Splitting under Visible Light. *J Am Chem Soc* **2011**, *133* (29), 11054–11057.
- (173) Iwashina, K.; Iwase, A.; Ng, Y. H.; Amal, R.; Kudo, A. Z-Schematic Water Splitting into H₂ and O₂ Using Metal Sulfide as a Hydrogen-Evolving Photocatalyst and Reduced Graphene Oxide as a Solid-State Electron Mediator. *J Am Chem Soc* **2015**, *137* (2), 604–607.
- (174) Zhou, P.; Yu, J.; Jaroniec, M. All-Solid-State Z-Scheme Photocatalytic Systems. *Advanced Materials* **2014**, *26* (29), 4920–4935. <https://doi.org/10.1002/adma.201400288>.
- (175) Tada, H.; Mitsui, T.; Kiyonaga, T.; Akita, T.; Tanaka, K. All-Solid-State Z-Scheme in CdS–Au–TiO₂ Three-Component Nanojunction System. *Nat Mater* **2006**, *5* (10), 782.
- (176) Wang, Q.; Li, Y.; Hisatomi, T.; Nakabayashi, M.; Shibata, N.; Kubota, J.; Domen, K. Z-Scheme Water Splitting Using Particulate Semiconductors Immobilized onto Metal Layers for Efficient Electron Relay. *J Catal* **2015**, *328*, 308–315.
- (177) Wang, Q.; Hisatomi, T.; Katayama, M.; Takata, T.; Minegishi, T.; Kudo, A.; Yamada, T.; Domen, K. Particulate Photocatalyst Sheets for Z-Scheme Water Splitting: Advantages over Powder Suspension and Photoelectrochemical Systems and Future Challenges. *Faraday Discuss* **2017**, *197*, 491–504.
- (178) Zhang, M.; Lu, M.; Lang, Z.; Liu, J.; Liu, M.; Chang, J.; Li, L.; Shang, L.; Wang, M.; Li, S.; Lan, Y. Semiconductor/Covalent-Organic-Framework Z-Scheme Heterojunctions for Artificial Photosynthesis. *Angewandte Chemie* **2020**, *132* (16), 6562–6568. <https://doi.org/10.1002/ange.202000929>.
- (179) Xu, Q.; Zhang, L.; Cheng, B.; Fan, J.; Yu, J. S-Scheme Heterojunction Photocatalyst. *Chem* **2020**, *6* (7), 1543–1559. <https://doi.org/10.1016/j.chempr.2020.06.010>.
- (180) Ye, B.; Wang, W.; Wang, L.; Tang, H.; Hu, J.; Liu, Q. Organic-Inorganic Heterojunction Photocatalysts: From Organic Molecules to Frameworks. *Mater Sci Semicond Process* **2023**, *164* (May), 107623. <https://doi.org/10.1016/j.mssp.2023.107623>.
- (181) Jang, J. S.; Kim, H. G.; Lee, J. S. Heterojunction Semiconductors: A Strategy to Develop Efficient Photocatalytic Materials for Visible Light Water Splitting. *Catal Today* **2012**, *185* (1), 270–277.
- (182) Bai, Y.; Wilbraham, L.; Slater, B. J.; Zwijnenburg, M. A.; Sprick, R. S.; Cooper, A. I. Accelerated Discovery of Organic Polymer Photocatalysts for Hydrogen Evolution from Water through the Integration of Experiment and Theory. *J Am Chem Soc* **2019**, *141* (22), 9063–9071. <https://doi.org/10.1021/jacs.9b03591>.
- (183) Bannwarth, C.; Ehlert, S.; Grimme, S. GFN2-XTB—An Accurate and Broadly Parametrized Self-Consistent Tight-Binding Quantum Chemical Method with Multipole Electrostatics and Density-Dependent Dispersion Contributions. *J Chem Theory Comput* **2019**, *15* (3), 1652–1671. <https://doi.org/10.1021/acs.jctc.8b01176>.
- (184) Grimme, S.; Bannwarth, C. Ultra-Fast Computation of Electronic Spectra for Large Systems by Tight-Binding Based Simplified Tamm-Dancoff Approximation (STDA-XTB). *J Chem Phys* **2016**, *145* (5), 054103. <https://doi.org/10.1063/1.4959605>.
- (185) Liu, Y.; Wu, J.; Wang, F. Dibenzothiophene-S,S-Dioxide-Containing Conjugated Polymer with Hydrogen Evolution Rate up to 147 Mmol G⁻¹ H⁻¹. *Appl Catal B* **2022**, *307* (November 2021), 121144. <https://doi.org/10.1016/j.apcatb.2022.121144>.
- (186) Burger, B.; Maffettone, P. M.; Gusev, V. V.; Aitchison, C. M.; Bai, Y.; Wang, X.; Li, X.; Alston, B. M.; Li, B.; Clowes, R.; Rankin, N.; Harris, B.; Sprick, R. S.; Cooper, A. I. A Mobile Robotic Chemist. *Nature* **2020**, *583* (7815), 237–241. <https://doi.org/10.1038/s41586-020-2442-2>.
- (187) Ásgeirsson, V.; Bauer, C. A.; Grimme, S. Quantum Chemical Calculation of Electron Ionization Mass Spectra for General Organic and Inorganic Molecules. *Chem Sci* **2017**, *8* (7), 4879–4895. <https://doi.org/10.1039/C7SC00601B>.
- (188) Wilbraham, L.; Berardo, E.; Turcani, L.; Jelfs, K. E.; Zwijnenburg, M. A. High-Throughput Screening Approach for the Optoelectronic Properties of Conjugated Polymers. *J Chem Inf Model* **2018**, *58* (12), 2450–2459. <https://doi.org/10.1021/acs.jcim.8b00256>.

- (189) Guiglian, P.; Monti, A.; Zwiijnenburg, M. A. Validating a Density Functional Theory Approach for Predicting the Redox Potentials Associated with Charge Carriers and Excitons in Polymeric Photocatalysts. *The Journal of Physical Chemistry C* **2017**, *121* (3), 1498–1506. <https://doi.org/10.1021/acs.jpcc.6b11133>.
- (190) Bannwarth, C.; Grimme, S. A Simplified Time-Dependent Density Functional Theory Approach for Electronic Ultraviolet and Circular Dichroism Spectra of Very Large Molecules. *Comput Theor Chem* **2014**, *1040–1041*, 45–53. <https://doi.org/10.1016/j.comptc.2014.02.023>.
- (191) Salzner, U.; Aydin, A. Improved Prediction of Properties of π -Conjugated Oligomers with Range-Separated Hybrid Density Functionals. *J Chem Theory Comput* **2011**, *7* (8), 2568–2583. <https://doi.org/10.1021/ct2003447>.
- (192) Tauc, J. Optical Properties and Electronic Structure of Amorphous Ge and Si. *Mater Res Bull* **1968**, *3* (1), 37–46. [https://doi.org/https://doi.org/10.1016/0025-5408\(68\)90023-8](https://doi.org/https://doi.org/10.1016/0025-5408(68)90023-8).
- (193) Makuła, P.; Pacia, M.; Macyk, W. How To Correctly Determine the Band Gap Energy of Modified Semiconductor Photocatalysts Based on UV–Vis Spectra. *J Phys Chem Lett* **2018**, *9* (23), 6814–6817. <https://doi.org/10.1021/acs.jpcllett.8b02892>.
- (194) Prentice, A. W.; Zwiijnenburg, M. A. The Role of Computational Chemistry in Discovering and Understanding Organic Photocatalysts for Renewable Fuel Synthesis. *Adv Energy Mater* **2021**, *11* (29). <https://doi.org/10.1002/aenm.202100709>.
- (195) Nayak, P. K.; Periasamy, N. Calculation of Electron Affinity, Ionization Potential, Transport Gap, Optical Band Gap and Exciton Binding Energy of Organic Solids Using ‘Solvation’ Model and DFT. *Org Electron* **2009**, *10* (7), 1396–1400. <https://doi.org/10.1016/j.orgel.2009.06.011>.
- (196) Sachs, M.; Sprick, R. S.; Pearce, D.; Hillman, S. A. J. J.; Monti, A.; Guilbert, A. A. Y. Y.; Brownbill, N. J.; Dimitrov, S.; Shi, X.; Blanc, F. F.; Zwiijnenburg, M. A.; Nelson, J.; Durrant, J. R.; Cooper, A. I. Understanding Structure-Activity Relationships in Linear Polymer Photocatalysts for Hydrogen Evolution. *Nat Commun* **2018**, *9* (1), 4968. <https://doi.org/10.1038/s41467-018-07420-6>.
- (197) Meng, A.; Zhang, L.; Cheng, B.; Yu, J. Dual Cocatalysts in TiO₂ Photocatalysis. **2019**, *1807660*, 1–31. <https://doi.org/10.1002/adma.201807660>.
- (198) Beasley, C.; Kumaran Gnanamani, M.; Santillan-Jimenez, E.; Martinelli, M.; Shafer, W. D.; Hopps, S. D.; Wanninayake, N.; Kim, D.-Y. Effect of Metal Work Function on Hydrogen Production from Photocatalytic Water Splitting with MTiO₂ Catalysts. *ChemistrySelect* **2020**, *5* (3), 1013–1019. <https://doi.org/https://doi.org/10.1002/slct.201904151>.
- (199) Ran, J.; Zhang, J.; Yu, J.; Jaroniec, M.; Qiao, S. Z. Earth-Abundant Cocatalysts for Semiconductor-Based Photocatalytic Water Splitting. *Chem Soc Rev* **2014**, *43* (22), 7787–7812. <https://doi.org/10.1039/c3cs60425j>.
- (200) Sprick, R. S.; Hoyos, M.; Wrackmeyer, M. S.; Sheridan Parry, A. V.; Grace, I. M.; Lambert, C.; Navarro, O.; Turner, M. L. Extended Conjugation in Poly(Triarylamine)s: Synthesis, Structure and Impact on Field-Effect Mobility. *J Mater Chem C Mater* **2014**, *2* (32), 6520–6528. <https://doi.org/10.1039/C4TC00871E>.
- (201) Zhang, W.; Smith, J.; Hamilton, R.; Heeney, M.; Kirkpatrick, J.; Song, K.; Watkins, S. E.; Anthopoulos, T.; McCulloch, I. Systematic Improvement in Charge Carrier Mobility of Air Stable Triarylamine Copolymers. *J Am Chem Soc* **2009**, *131* (31), 10814–10815. <https://doi.org/10.1021/ja9034818>.
- (202) Merz, J.; Fink, J.; Friedrich, A.; Krummenacher, I.; Al Mamari, H. H.; Lorenzen, S.; Haehnel, M.; Eichhorn, A.; Moos, M.; Holzapfel, M.; Braunschweig, H.; Lambert, C.; Steffen, A.; Ji, L.; Marder, T. B. Pyrene Molecular Orbital Shuffle—Controlling Excited State and Redox Properties by Changing the Nature of the Frontier Orbitals. *Chemistry – A European Journal* **2017**, *23* (53), 13164–13180. <https://doi.org/https://doi.org/10.1002/chem.201702594>.
- (203) Parola, A. H.; Cohen, S. G. Effect of Solvent in the Photoreduction and Quenching of Benzophenone by Triethylamine, 1-Azabicyclo[2.2.2]-Octane and 1,4-Diazabicyclo[2.2.2]Octane. *Journal of Photochemistry* **1980**, *12* (1), 41–50. [https://doi.org/https://doi.org/10.1016/0047-2670\(80\)85079-9](https://doi.org/https://doi.org/10.1016/0047-2670(80)85079-9).
- (204) Graetzel, C. K.; Graetzel, M. Hydrogen Evolution from the Photolysis of Alcoholic Benzophenone Solutions via Redox Catalysis. *J Am Chem Soc* **1979**, *101* (26), 7741–7743. <https://doi.org/10.1021/ja00520a032>.
- (205) Li, X.; Maffettone, P. M.; Che, Y.; Liu, T.; Chen, L.; Cooper, A. I. Combining Machine Learning and High-Throughput Experimentation to Discover Photocatalytically Active Organic Molecules. *Chem Sci* **2021**, *12* (32), 10742–10754. <https://doi.org/10.1039/D1SC02150H>.
- (206) Chi, X.; Chen, Q.; Lan, Z. A.; Zhang, X.; Chen, X.; Wang, X. Structure–Property Relationship of Cyano-Functionalized Conjugated Polymers for Photocatalytic Hydrogen Production. *Chemistry - A European Journal* **2023**, *29* (2). <https://doi.org/10.1002/chem.202202734>.

- (207) Chen, B.; Yang, N.; Wang, P.; Xiang, Y.; Chen, H. Post-Side Chain Engineering of Difluorinated Benzothiadiazole-Based Conjugated Microporous Polymer for Enhanced Photocatalytic H₂ Evolution. *Appl Surf Sci* **2020**, *499*, 143865. <https://doi.org/10.1016/j.apsusc.2019.143865>.
- (208) Zhang, S.; Bauer, N. E.; Kanal, I. Y.; You, W.; Hutchison, G. R.; Meyer, T. Y. Sequence Effects in Donor-Acceptor Oligomeric Semiconductors Comprising Benzothiadiazole and Phenylenevinylene Monomers. *Macromolecules* **2017**, *50* (1), 151–161. <https://doi.org/10.1021/acs.macromol.6b02215>.
- (209) Cheng, C.; Wang, X.; Lin, Y.; He, L.; Jiang, J.-X. X.; Xu, Y.; Wang, F. The Effect of Molecular Structure and Fluorination on the Properties of Pyrene-Benzothiadiazole-Based Conjugated Polymers for Visible-Light-Driven Hydrogen Evolution. *Polym Chem* **2018**, *9* (35), 4468–4475. <https://doi.org/10.1039/c8py00722e>.
- (210) Bai, Y.; Wilbraham, L.; Slater, B. J.; Zwijnenburg, M. A.; Sprick, R. S.; Cooper, A. I. Accelerated Discovery of Organic Polymer Photocatalysts for Hydrogen Evolution from Water through the Integration of Experiment and Theory. *J Am Chem Soc* **2019**, *141* (22), 9063–9071. <https://doi.org/10.1021/jacs.9b03591>.
- (211) Alam, S.; Lee, J. Progress and Future Potential of All-Small-Molecule Organic Solar Cells Based on the Benzodithiophene Donor Material. *Molecules* **2023**, *28* (7). <https://doi.org/10.3390/molecules28073171>.
- (212) Wang, W.-R.; Li, J.; Li, Q.; Xu, Z.-W.; Liu, L.-N.; Chen, X.-Q.; Xiao, W.-J.; Yao, J.; Zhang, F.; Li, W.-S. Side-Chain-Extended Conjugation: A Strategy for Improving the Photocatalytic Hydrogen Production Performance of a Linear Conjugated Polymer. *J Mater Chem A Mater* **2021**, *9* (13), 8782–8791. <https://doi.org/10.1039/D0TA12425G>.
- (213) Elewa, A. M.; Jayakumar, J.; Huang, Y.-W.; Elsayed, M. H.; Chang, C.-L.; Ting, L.-Y.; Lin, W.-C.; Chueh, C.-C.; Chou, H.-H. Biaxially Extended Side-Chain Conjugation of Benzodithiophene-Based Polymer Dots for Superior Photocatalytic Stability under Visible-Light Irradiation. *J Environ Chem Eng* **2022**, *10* (1), 106927. <https://doi.org/https://doi.org/10.1016/j.jece.2021.106927>.
- (214) Shu, C.; Han, C.; Yang, X.; Zhang, C.; Chen, Y.; Ren, S.; Wang, F.; Huang, F.; Jiang, J. X. Boosting the Photocatalytic Hydrogen Evolution Activity for D- π -A Conjugated Microporous Polymers by Statistical Copolymerization. *Advanced Materials* **2021**, *2008498*, 1–10. <https://doi.org/10.1002/adma.202008498>.
- (215) Sun, H.; Mumby, S. J.; Maple, J. R.; Hagler, A. T. An Ab Initio CFF93 All-Atom Force Field for Polycarbonates. *J Am Chem Soc* **1994**, *116* (7), 2978–2987. <https://doi.org/10.1021/ja00086a030>.
- (216) Frenzel, J.; Oliveira, A. F.; Jardillier, N.; Heine, T.; Seifert, G. Semi-Relativistic, Self-Consistent Charge Slater-Koster Tables for Density-Functional Based Tight-Binding (DFTB) for Materials Science Simulations. *Zeolites* **2004**, *2* (3), 7.
- (217) Delley, B. From Molecules to Solids with the DMol3 Approach. *J Chem Phys* **2000**, *113* (18), 7756–7764. <https://doi.org/10.1063/1.1316015>.
- (218) Stephens, P. J.; Devlin, F. J.; Chabalowski, C. F.; Frisch, M. J. Ab Initio Calculation of Vibrational Absorption. *J Phys Chem* **1994**, *98* (45), 11623–11627.
- (219) Becke, A. D. Becke's Three Parameter Hybrid Method Using the LYP Correlation Functional. *J. Chem. Phys* **1993**, *98* (492), 5648–5652.
- (220) Lee, C.; Yang, W.; Parr, R. G. Development of the Colle-Salvetti Correlation-Energy Formula into a Functional of the Electron Density. *Phys Rev B* **1988**, *37* (2), 785–789. <https://doi.org/10.1103/PhysRevB.37.785>.
- (221) Stephens, P. J.; Devlin, F. J.; Chabalowski, C. F.; Frisch, M. J. Ab Initio Calculation of Vibrational Absorption and Circular Dichroism Spectra Using Density Functional Force Fields. *J Phys Chem* **1994**, *98* (45), 11623–11627.
- (222) Delley, B. Ground-State Enthalpies: Evaluation of Electronic Structure Approaches with Emphasis on the Density Functional Method. *J Phys Chem A* **2006**, *110* (50), 13632–13639. <https://doi.org/10.1021/jp0653611>.
- (223) Delley, B. An All-electron Numerical Method for Solving the Local Density Functional for Polyatomic Molecules. *J Chem Phys* **1990**, *92* (1), 508–517. <https://doi.org/10.1063/1.458452>.
- (224) Klamt, A.; Schuurmann, G. COSMO: A New Approach to Dielectric Screening in Solvents with Explicit Expressions for the Screening Energy and Its Gradient. *Journal of the Chemical Society, Perkin Transactions 2* **1993**, No. 5, 799–805. <https://doi.org/10.1039/P29930000799>.
- (225) Kubelka, P. New Contributions to the Optics of Intensely Light-Scattering Materials. Part I. *J. Opt. Soc. Am.* **1948**, *38* (5), 448–457. <https://doi.org/10.1364/JOSA.38.000448>.
- (226) Kaiser, C.; Sandberg, O. J.; Zarrabi, N.; Li, W.; Meredith, P.; Armin, A. A Universal Urbach Rule for Disordered Organic Semiconductors. *Nat Commun* **2021**, *12* (1), 3988. <https://doi.org/10.1038/s41467-021-24202-9>.
- (227) Zhang, C.; Mahadevan, S.; Yuan, J.; Ho, J. K. W.; Gao, Y.; Liu, W.; Zhong, H.; Yan, H.; Zou, Y.; Tsang, S.-W.; So, S. K. Unraveling Urbach Tail Effects in High-Performance Organic Photovoltaics: Dynamic vs Static Disorder. *ACS Energy Lett* **2022**, *7* (6), 1971–1979. <https://doi.org/10.1021/acsenerylett.2c00816>.

- (228) Barford, W. *Electronic and Optical Properties of Conjugated Polymers*. Oxford University Press April 11, 2013. <https://doi.org/10.1093/acprof:oso/9780199677467.001.0001>.
- (229) Wang, L.; Fernández-Terán, R.; Zhang, L.; Fernandes, D. L. A.; Tian, L.; Chen, H.; Tian, H. Organic Polymer Dots as Photocatalysts for Visible Light-Driven Hydrogen Generation. *Angewandte Chemie* **2016**, *128* (40), 12494–12498. <https://doi.org/10.1002/ange.201607018>.
- (230) Wang, Z.; Hisatomi, T.; Li, R.; Sayama, K.; Liu, G.; Domen, K.; Li, C.; Wang, L. Efficiency Accreditation and Testing Protocols for Particulate Photocatalysts toward Solar Fuel Production. *Joule* **2021**, *5* (2), 344–359. <https://doi.org/https://doi.org/10.1016/j.joule.2021.01.001>.
- (231) Goto, Y.; Hisatomi, T.; Wang, Q.; Higashi, T.; Ishikiriyama, K.; Maeda, T.; Sakata, Y.; Okunaka, S.; Tokudome, H.; Katayama, M.; Akiyama, S.; Nishiyama, H.; Inoue, Y.; Takewaki, T.; Setoyama, T.; Minegishi, T.; Takata, T.; Yamada, T.; Domen, K. A Particulate Photocatalyst Water-Splitting Panel for Large-Scale Solar Hydrogen Generation. *Joule* **2018**, *2* (3), 509–520. <https://doi.org/10.1016/j.joule.2017.12.009>.
- (232) Peterson, A. A.; Lindgren, P.; Kastlunger, G. Understanding How Platinum Excels at the Hydrogen Evolution Reaction. **2018**, *02906*, 12771.
- (233) Li, Y.; Yang, L.; He, H.; Sun, L.; Wang, H.; Fang, X.; Zhao, Y.; Zheng, D.; Qi, Y.; Li, Z.; Deng, W. In Situ Photodeposition of Platinum Clusters on a Covalent Organic Framework for Photocatalytic Hydrogen Production. *Nat Commun* **2022**, *13* (1), 1–9. <https://doi.org/10.1038/s41467-022-29076-z>.
- (234) Zeng, M.; Du, Y.; Shao, L.; Qi, C.; Zhang, X.-M. Palladium-Catalyzed Reductive Homocoupling of Aromatic Halides and Oxidation of Alcohols. *J Org Chem* **2010**, *75* (8), 2556–2563. <https://doi.org/10.1021/jo100089d>.
- (235) Sachs, M.; Sprick, R. S.; Pearce, D.; Hillman, S. A. J. J.; Monti, A.; Guilbert, A. A. Y. Y.; Brownbill, N. J.; Dimitrov, S.; Shi, X.; Blanc, F. F.; Zwiijnenburg, M. A.; Nelson, J.; Durrant, J. R.; Cooper, A. I. Understanding Structure-Activity Relationships in Linear Polymer Photocatalysts for Hydrogen Evolution. *Nat Commun* **2018**, *9* (1), 1–11. <https://doi.org/10.1038/s41467-018-07420-6>.
- (236) Piercy, V. L.; Saeed, K. H.; Prentice, A. W.; Neri, G.; Li, C.; Gardner, A. M.; Bai, Y.; Sprick, R. S.; Sazanovich, I. V.; Cooper, A. I.; Rosseinsky, M. J.; Zwiijnenburg, M. A.; Cowan, A. J. Time-Resolved Raman Spectroscopy of Polaron Formation in a Polymer Photocatalyst. *Journal of Physical Chemistry Letters* **2021**, *12* (44), 10899–10905. <https://doi.org/10.1021/acs.jpcllett.1c03073>.
- (237) Cheng, J.-Z.; Liu, L.-L.; Liao, G.; Shen, Z.-Q.; Tan, Z.-R.; Xing, Y.-Q.; Li, X.-X.; Yang, K.; Chen, L.; Liu, S.-Y. Achieving an Unprecedented Hydrogen Evolution Rate by Solvent-Exfoliated CPP-Based Photocatalysts. *J Mater Chem A Mater* **2020**, *8* (12), 5890–5899. <https://doi.org/10.1039/C9TA13514F>.
- (238) Wang, W.; Luo, L.; Sheng, P.; Zhang, J.; Zhang, Q. Multifunctional Features of Organic Charge-Transfer Complexes: Advances and Perspectives. *Chemistry - A European Journal* **2021**, *27* (2), 464–490. <https://doi.org/10.1002/chem.202002640>.
- (239) Sinnokrot, M. O.; Sherrill, C. D. Substituent Effects in π - π Interactions: Sandwich and T-Shaped Configurations. *J Am Chem Soc* **2004**, *126* (24), 7690–7697. <https://doi.org/10.1021/ja049434a>.
- (240) Bagwill, C.; Anderson, C.; Sullivan, E.; Manohara, V.; Murthy, P.; Kirkpatrick, C. C.; Stalcup, A.; Lewis, M. Predicting the Strength of Anion- π Interactions of Substituted Benzenes: The Development of Anion- π Binding Substituent Constants. *Journal of Physical Chemistry A* **2016**, *120* (46), 9235–9243. <https://doi.org/10.1021/acs.jpca.6b06276>.
- (241) Banks, B.; Cargill, M. R.; Sandford, G.; Tadeusiak, A. J.; Westemeier, H.; Yufit, D. S.; Howard, J. A. K.; Kilickiran, P.; Nelles, G. Reactions of Dibromotetrafluorobenzene Derivatives with Sodium Phenoxide Salts. Competing Hydrodebromination and SNAr Processes. *J Fluor Chem* **2010**, *131* (5), 627–634. <https://doi.org/https://doi.org/10.1016/j.jfluchem.2010.02.005>.
- (242) Orbach, M.; Choudhury, J.; Lahav, M.; Zenkina, O. v.; Diskin-Posner, Y.; Leitus, G.; Iron, M. A.; van der Boom, M. E. Palladium-Catalyzed Cross-Coupling Reactions with Fluorinated Substrates: Mechanistic Insights into the Undesired Hydrodehalogenation of Aryl Halides. *Organometallics* **2012**, *31* (4), 1271–1274. <https://doi.org/10.1021/om200898t>.
- (243) Lu, W.; Kuwabara, J.; Kanbara, T. Polycondensation of Dibromofluorene Analogues with Tetrafluorobenzene via Direct Arylation. *Macromolecules* **2011**, *44* (6), 1252–1255. <https://doi.org/10.1021/ma1028517>.
- (244) Wang, Q.; Zhang, B.; Liu, L.; Chen, Y.; Qu, Y.; Zhang, X.; Yang, J.; Xie, Z.; Geng, Y.; Wang, L.; Wang, F. Effect of End Groups on Optoelectronic Properties of Poly(9,9-Dioctylfluorene): A Study with Hexadecylfluorenes as Model Polymers. *The Journal of Physical Chemistry C* **2012**, *116* (41), 21727–21733. <https://doi.org/10.1021/jp3083369>.

- (245) Sprick, R. S.; Aitchison, C. M.; Berardo, E.; Turcani, L.; Wilbraham, L.; Alston, B. M.; Jelfs, K. E.; Zwijnenburg, M. A.; Cooper, A. I. Maximising the Hydrogen Evolution Activity in Organic Photocatalysts by Co-Polymerisation. *J Mater Chem A Mater* **2018**, *6* (25), 11994–12003. <https://doi.org/10.1039/c8ta04186e>.
- (246) Zhao, W.; Yan, P.; Li, B.; Bahri, M.; Liu, L.; Zhou, X.; Clowes, R.; Browning, N. D.; Wu, Y.; Ward, J. W.; Cooper, A. I. Accelerated Synthesis and Discovery of Covalent Organic Framework Photocatalysts for Hydrogen Peroxide Production. **2022**.
- (247) Liu, L.; Gao, M. Y.; Yang, H.; Wang, X.; Li, X.; Cooper, A. I. Linear Conjugated Polymers for Solar-Driven Hydrogen Peroxide Production: The Importance of Catalyst Stability. *J Am Chem Soc* **2021**, *143* (46), 19287–19293. <https://doi.org/10.1021/jacs.1c09979>.
- (248) Hou, H.; Zeng, X.; Zhang, X. Production of Hydrogen Peroxide by Photocatalytic Processes. *Angewandte Chemie - International Edition* **2020**, *59* (40), 17356–17376. <https://doi.org/10.1002/anie.201911609>.
- (249) Maeda, K.; Teramura, K.; Saito, N.; Inoue, Y.; Domen, K. Improvement of Photocatalytic Activity of (Ga_{1-x}Zn_x)(N_{1-x}O_x) Solid Solution for Overall Water Splitting by Co-Loading Cr and Another Transition Metal. *J Catal* **2006**, *243* (2), 303–308. <https://doi.org/https://doi.org/10.1016/j.jcat.2006.07.023>.
- (250) Wang, Q.; Domen, K. Particulate Photocatalysts for Light-Driven Water Splitting: Mechanisms, Challenges, and Design Strategies. *Chem Rev* **2020**, *120* (2), 919–985. <https://doi.org/10.1021/acs.chemrev.9b00201>.
- (251) Blakemore, D. *Suzuki – Miyaura Coupling*; 2016; Vol. 1.
- (252) Beletskaya, I. P.; Alonso, F.; Tyurin, V. The Suzuki-Miyaura Reaction after the Nobel Prize. *Coord Chem Rev* **2019**, *385*, 137–173. <https://doi.org/10.1016/j.ccr.2019.01.012>.
- (253) Lennox, A. J. J.; Lloyd-Jones, G. C. Selection of Boron Reagents for Suzuki-Miyaura Coupling. *Chem Soc Rev* **2014**, *43* (1), 412–443. <https://doi.org/10.1039/c3cs60197h>.
- (254) Hayes, H. L. D.; Wei, R.; Assante, M.; Geogheghan, K. J.; Jin, N.; Tomasi, S.; Noonan, G.; Leach, A. G.; Lloyd-Jones, G. C. Protodeboronation of (Hetero)Arylboronic Esters: Direct versus Prehydrolytic Pathways and Self-/Auto-Catalysis. *J Am Chem Soc* **2021**, *143* (36), 14814–14826. <https://doi.org/10.1021/jacs.1c06863>.
- (255) Cox, P. A.; Leach, A. G.; Campbell, A. D.; Lloyd-Jones, G. C. Protodeboronation of Heteroaromatic, Vinyl, and Cyclopropyl Boronic Acids: PH-Rate Profiles, Autocatalysis, and Disproportionation. *J Am Chem Soc* **2016**, *138* (29), 9145–9157. <https://doi.org/10.1021/jacs.6b03283>.
- (256) Deng, J. Z.; Paone, D. V.; Ginnetti, A. T.; Kurihara, H.; Dreher, S. D.; Weissman, S. A.; Stauffer, S. R.; Burgey, C. S. Copper-Facilitated Suzuki Reactions: Application to 2-Heterocyclic Boronates. *Org Lett* **2009**, *11* (2), 345–347. <https://doi.org/10.1021/ol802556f>.
- (257) Lima, C. F. R. A. C.; Rodrigues, A. S. M. C.; Silva, V. L. M.; Silva, A. M. S.; Santos, L. M. N. B. F. Role of the Base and Control of Selectivity in the Suzuki-Miyaura Cross-Coupling Reaction. *ChemCatChem* **2014**, *6* (5), 1291–1302. <https://doi.org/10.1002/cctc.201301080>.
- (258) Kadu, B. S. Suzuki-Miyaura Cross Coupling Reaction: Recent Advancements in Catalysis and Organic Synthesis. *Catal Sci Technol* **2021**, *11* (4), 1186–1221. <https://doi.org/10.1039/d0cy02059a>.
- (259) Hestand, N. J.; Spano, F. C. Expanded Theory of H- and J-Molecular Aggregates: The Effects of Vibronic Coupling and Intermolecular Charge Transfer. *Chemical Reviews*. 2018, pp 7069–7163. <https://doi.org/10.1021/acs.chemrev.7b00581>.
- (260) Cheng, J. Z.; Tan, Z. R.; Xing, Y. Q.; Shen, Z. Q.; Zhang, Y. J.; Liu, L. L.; Yang, K.; Chen, L.; Liu, S. Y. Exfoliated Conjugated Porous Polymer Nanosheets for Highly Efficient Photocatalytic Hydrogen Evolution. *J Mater Chem A Mater* **2021**, *9* (9), 5787–5795. <https://doi.org/10.1039/d0ta11479k>.
- (261) Xiang, S.; Han, C.; Shu, C.; Zhang, C.; Jiang, J. X. Structure Evolution of Thiophene-Containing Conjugated Polymer Photocatalysts for High-Efficiency Photocatalytic Hydrogen Production. *Sci China Mater* **2021**, *65* (2), 422–430. <https://doi.org/10.1007/s40843-021-1757-1>.
- (262) Liu, Y.; Wu, J.; Wang, F. Dibenzothiophene-S,S-Dioxide-Containing Conjugated Polymer with Hydrogen Evolution Rate up to 147 Mmol G⁻¹ H⁻¹. *Appl Catal B* **2022**, *307* (November 2021), 121144. <https://doi.org/10.1016/j.apcatb.2022.121144>.
- (263) Yu, W.; Hu, C.; Bai, L.; Tian, N.; Zhang, Y.; Huang, H. Photocatalytic Hydrogen Peroxide Evolution: What Is the Most Effective Strategy? *Nano Energy* **2022**, *104*, 107906. <https://doi.org/https://doi.org/10.1016/j.nanoen.2022.107906>.

- (264) Wang, X.; Chen, L.; Chong, S. Y.; Little, M. A.; Wu, Y.; Zhu, W.-H. H.; Clowes, R.; Yan, Y.; Zwiijnenburg, M. A.; Sprick, R. S.; Cooper, A. I. Sulfone-Containing Covalent Organic Frameworks for Photocatalytic Hydrogen Evolution from Water. *Nat Chem* **2018**, *10* (12), 1180–1189. <https://doi.org/10.1038/s41557-018-0141-5>.
- (265) Sprick, R. S.; Bai, Y.; Guilbert, A. A. Y. Y.; Zbiri, M.; Aitchison, C. M.; Wilbraham, L.; Yan, Y.; Woods, D. J.; Zwiijnenburg, M. A.; Cooper, A. I. Photocatalytic Hydrogen Evolution from Water Using Fluorene and Dibenzothiophene Sulfone-Conjugated Microporous and Linear Polymers. *CHEMISTRY OF MATERIALS* **2019**, *31* (2), 305–313. <https://doi.org/10.1021/acs.chemmater.8b02833>.
- (266) Makuła, P.; Pacia, M.; Macyk, W. How To Correctly Determine the Band Gap Energy of Modified Semiconductor Photocatalysts Based on UV–Vis Spectra. *J Phys Chem Lett* **2018**, *9* (23), 6814–6817. <https://doi.org/10.1021/acs.jpcclett.8b02892>.
- (267) del Valle, J. C.; Catalán, J. Kasha's Rule: A Reappraisal. *Physical Chemistry Chemical Physics* **2019**, *21* (19), 10061–10069. <https://doi.org/10.1039/C9CP00739C>.
- (268) Montilla, F.; Ruseckas, A.; Samuel, I. D. W. Exciton–Polaron Interactions in Polyfluorene Films with β -Phase. *The Journal of Physical Chemistry C* **2018**, *122* (18), 9766–9772. <https://doi.org/10.1021/acs.jpcc.8b01300>.
- (269) Pensack, R. D.; Asbury, J. B. Beyond the Adiabatic Limit: Charge Photogeneration in Organic Photovoltaic Materials. *J Phys Chem Lett* **2010**, *1* (15), 2255–2263. <https://doi.org/10.1021/jz1005225>.
- (270) Demchenko, A. P.; Tomin, V. I.; Chou, P. T. Breaking the Kasha Rule for More Efficient Photochemistry. *Chem Rev* **2017**, *117* (21), 13353–13381. <https://doi.org/10.1021/acs.chemrev.7b00110>.
- (271) Smith, D. A.; McKenzie, G.; Jones, A. C.; Smith, T. A. Analysis of Time-Correlated Single Photon Counting Data: A Comparative Evaluation of Deterministic and Probabilistic Approaches. *Methods Appl Fluoresc* **2017**, *5* (4), 42001. <https://doi.org/10.1088/2050-6120/aa8055>.
- (272) Spano, F. C.; Silva, C. H- and J-Aggregate Behavior in Polymeric Semiconductors. *Annu Rev Phys Chem* **2014**, *65*, 477–500. <https://doi.org/10.1146/annurev-physchem-040513-103639>.
- (273) Oleson, A.; Zhu, T.; Dunn, I. S.; Bialas, D.; Bai, Y.; Zhang, W.; Dai, M.; Reichman, D. R.; Tempelaar, R.; Huang, L.; Spano, F. C. Perylene Diimide-Based H_J- And H_J-Aggregates- And Prospect of Exciton Band Shape Engineering in Organic Materials. *Journal of Physical Chemistry C* **2019**, *123* (33), 20567–20578. <https://doi.org/10.1021/acs.jpcc.9b04429>.
- (274) Eder, T.; Kraus, D.; Höger, S.; Vogelsang, J.; Lupton, J. M. Vibrations Responsible for Luminescence from H_J-Aggregates of Conjugated Polymers Identified by Cryogenic Spectroscopy of Single Nanoparticles. *ACS Nano* **2022**, *16* (4), 6382–6393. <https://doi.org/10.1021/acs.nano.2c00472>.
- (275) Lan, Z.-A.; Ren, W.; Chen, X.; Zhang, Y.; Wang, X. Conjugated Donor-Acceptor Polymer Photocatalysts with Electron-Output “Tentacles” for Efficient Hydrogen Evolution. *Appl Catal B* **2019**, *245*, 596–603. <https://doi.org/10.1016/j.apcatb.2019.01.010>.
- (276) Deng, Y.; Yuan, W.; Jia, Z.; Liu, G. H- and J-Aggregation of Fluorene-Based Chromophores. *J Phys Chem B* **2014**, *118* (49), 14536–14545. <https://doi.org/10.1021/jp510520m>.
- (277) Barth, S.; Bäessler, H.; Scherf, U.; Müllen, K. Photoconduction in Thin Films of a Ladder-Type Poly-Para-Phenylene. *Chem Phys Lett* **1998**, *288* (1), 147–154. [https://doi.org/10.1016/S0009-2614\(98\)00236-X](https://doi.org/10.1016/S0009-2614(98)00236-X).
- (278) Killestreiter, H.; Bäessler, H. Exciton Reaction at an Anthracene/Metal Interface: Charge Transfer. *Chem Phys Lett* **1971**, *11* (4), 411–414. [https://doi.org/10.1016/0009-2614\(71\)80372-X](https://doi.org/10.1016/0009-2614(71)80372-X).
- (279) Rörich, I.; Mikhnenko, O. V; Gehrig, D.; Blom, P. W. M.; Crăciun, N. I. Influence of Energetic Disorder on Exciton Lifetime and Photoluminescence Efficiency in Conjugated Polymers. *J Phys Chem B* **2017**, *121* (6), 1405–1412. <https://doi.org/10.1021/acs.jpcc.6b11813>.
- (280) Dimitrov, S. D.; Schroeder, B. C.; Nielsen, C. B.; Bronstein, H.; Fei, Z.; McCulloch, I.; Heeney, M.; Durrant, J. R. Singlet Exciton Lifetimes in Conjugated Polymer Films for Organic Solar Cells. *Polymers (Basel)* **2016**, *8* (1). <https://doi.org/10.3390/polym8010014>.
- (281) Wang, Y.; Vogel, A.; Sachs, M.; Sprick, R. S.; Wilbraham, L.; Moniz, S. J. A.; Godin, R.; Zwiijnenburg, M. A.; Durrant, J. R.; Cooper, A. I.; Tang, J. Current Understanding and Challenges of Solar-Driven Hydrogen Generation Using Polymeric Photocatalysts. *Nat Energy* **2019**, *4* (9), 746–760. <https://doi.org/10.1038/s41560-019-0456-5>.
- (282) Sachs, M.; Sprick, R. S.; Pearce, D.; Hillman, S. A. J.; Monti, A.; Guilbert, A. A. Y.; Brownbill, N. J.; Dimitrov, S.; Shi, X.; Blanc, F.; Zwiijnenburg, M. A.; Nelson, J.; Durrant, J. R.; Cooper, A. I. Understanding Structure-Activity Relationships in Linear Polymer Photocatalysts for Hydrogen Evolution. *Nat Commun* **2018**, *9*. <https://doi.org/10.1038/s41467-018-07420-6>.

- (283) Yang, H.; Li, X.; Sprick, R. S.; Cooper, A. Conjugated Polymer Donor-Molecular Acceptor Nanohybrids for Photocatalytic Hydrogen Evolution. *CHEMICAL COMMUNICATIONS* **2020**, *56* (50), 6790–6793. <https://doi.org/10.1039/d0cc00740d>.
- (284) Guiglion, P.; Butchosa, C.; Zwiijnenburg, M. A. Polymeric Watersplitting Photocatalysts; a Computational Perspective on the Water Oxidation Conundrum. *J Mater Chem A Mater* **2014**, *2* (30), 11996–12004. <https://doi.org/10.1039/c4ta02044h>.
- (285) Yang, J.; Wang, D.; Han, H.; Li, C. Roles of Cocatalysts in Photocatalysis and Photoelectrocatalysis. *Acc Chem Res* **2013**, *46* (8), 1900–1909.
- (286) Wang, L.; Wan, Y.; Ding, Y.; Niu, Y.; Xiong, Y.; Wu, X.; Xu, H. Photocatalytic Oxygen Evolution from Low-Bandgap Conjugated Microporous Polymer Nanosheets: A Combined First-Principles Calculation and Experimental Study. *Nanoscale* **2017**, *9* (12), 4090–4096. <https://doi.org/10.1039/c7nr00534b>.
- (287) Lin, L.; Wang, C.; Ren, W.; Ou, H.; Zhang, Y.; Wang, X. Photocatalytic Overall Water Splitting by Conjugated Semiconductors with Crystalline Poly(Triazine Imide) Frameworks. *Chem Sci* **2017**, *8* (8), 5506–5511. <https://doi.org/10.1039/C7SC00900C>.
- (288) Wang, L.; Wan, Y.; Ding, Y.; Wu, S.; Zhang, Y.; Zhang, X.; Zhang, G.; Xiong, Y.; Wu, X.; Yang, J.; Xu, H. Conjugated Microporous Polymer Nanosheets for Overall Water Splitting Using Visible Light. *ADVANCED MATERIALS* **2017**, *29* (38), 1–8. <https://doi.org/10.1002/adma.201702428>.
- (289) Yang, Y.; Chu, X.; Zhang, H.-Y.; Zhang, R.; Liu, Y.-H.; Zhang, F.-M.; Lu, M.; Yang, Z.-D.; Lan, Y.-Q. Engineering β -Ketoamine Covalent Organic Frameworks for Photocatalytic Overall Water Splitting. *Nat Commun* **2023**, *14* (1), 593. <https://doi.org/10.1038/s41467-023-36338-x>.
- (290) Yi, F.; Yang, Q.; Li, X.; Yuan, Y.; Cao, H.; Liu, K.; Yan, H. A 1,3,5-Triazine and Benzodithiophene Based Donor-Acceptor Type Semiconducting Conjugated Polymer for Photocatalytic Overall Water Splitting. *J Solid State Chem* **2023**, *318*, 123769. <https://doi.org/10.1016/j.jssc.2022.123769>.
- (291) Wu, J.; Liu, Z.; Lin, X.; Jiang, E.; Zhang, S.; Huo, P.; Yan, Y.; Zhou, P.; Yan, Y. Breaking through Water-Splitting Bottlenecks over Carbon Nitride with Fluorination. *Nat Commun* **2022**, *13* (1), 6999. <https://doi.org/10.1038/s41467-022-34848-8>.
- (292) Bai, Y.; Nakagawa, K.; Cowan, A. J.; Aitchison, C. M.; Yamaguchi, Y.; Zwiijnenburg, M. A.; Kudo, A.; Sprick, R. S.; Cooper, A. I. Photocatalyst Z-Scheme System Composed of a Linear Conjugated Polymer and BiVO₄ for Overall Water Splitting under Visible Light. *J Mater Chem A Mater* **2020**, *8* (32), 16283–16290. <https://doi.org/10.1039/D0TA04754F>.
- (293) Wang, L.; Zheng, X.; Chen, L.; Xiong, Y.; Xu, H. Van Der Waals Heterostructures Comprised of Ultrathin Polymer Nanosheets for Efficient Z-Scheme Overall Water Splitting. *Angewandte Chemie International Edition* **2018**, *57* (13), 3454–3458. <https://doi.org/https://doi.org/10.1002/anie.201710557>.
- (294) Chen, W.; Liu, M.; Li, X.; Mao, L. Synthesis of 3D Mesoporous G-C₃N₄ for Efficient Overall Water Splitting under a Z-Scheme Photocatalytic System. *Appl Surf Sci* **2020**, *512*. <https://doi.org/10.1016/j.apsusc.2020.145782>.
- (295) Feng, J.; Bian, J.; Bai, L.; Xi, S.; Wang, Y.; Chen, C.; Jing, L. Efficient Wide-Spectrum Photocatalytic Overall Water Splitting over Ultrathin Molecular Nickel Phthalocyanine/BiVO₄ Z-Scheme Heterojunctions without Noble Metals. *Appl Catal B* **2021**, *295* (April), 120260. <https://doi.org/10.1016/j.apcatb.2021.120260>.
- (296) Chen, X.; Wang, J.; Chai, Y.; Zhang, Z.; Zhu, Y. Efficient Photocatalytic Overall Water Splitting Induced by the Giant Internal Electric Field of a G-C₃N₄/RGO/PDIP Z-Scheme Heterojunction. *Advanced Materials* **2021**, *33* (7), 1–7. <https://doi.org/10.1002/adma.202007479>.
- (297) Zani, L.; Melchionna, M.; Montini, T.; Fornasiero, P. Design of Dye-Sensitized TiO₂ Materials for Photocatalytic Hydrogen Production: Light and Shadow. *Journal of Physics: Energy* **2021**, *3* (3), 031001. <https://doi.org/10.1088/2515-7655/abe04b>.
- (298) Reginato, G.; Zani, L.; Calamante, M.; Mordini, A.; Dessi, A. Dye-Sensitized Heterogeneous Photocatalysts for Green Redox Reactions. *Eur J Inorg Chem* **2020**, *2020* (11–12, SI), 899–917. <https://doi.org/10.1002/ejic.201901174>.
- (299) Willkomm, J.; Orchard, K. L.; Reynal, A.; Pastor, E.; Durrant, J. R.; Reisner, E. Dye-Sensitized Semiconductors Modified with Molecular Catalysts for Light-Driven H₂ Production. *Chem Soc Rev* **2016**, *45* (1), 9–23. <https://doi.org/10.1039/c5cs00733j>.
- (300) Youngblood, W. J.; Anna Lee, S. H.; Maeda, K.; Mallouk, T. E. Visible Light Water Splitting Using Dye-Sensitized Oxide Semiconductors. *Acc Chem Res* **2009**, *42* (12), 1966–1973. <https://doi.org/10.1021/ar9002398>.
- (301) Zhang, X.; Peng, T.; Song, S. Recent Advances in Dye-Sensitized Semiconductor Systems for Photocatalytic Hydrogen Production. *J Mater Chem A Mater* **2016**, *4* (7), 2365–2402. <https://doi.org/10.1039/c5ta08939e>.

- (302) Ding, H.; Xu, M.; Zhang, S.; Yu, F.; Kong, K.; Shen, Z.; Hua, J. Organic Blue-Colored D-A- π -A Dye-Sensitized TiO₂ for Efficient and Stable Photocatalytic Hydrogen Evolution under Visible/near-Infrared-Light Irradiation. *Renew Energy* **2020**, *155*, 1051–1059. <https://doi.org/10.1016/j.renene.2020.04.009>.
- (303) Becerril, V. S.; Sundin, E.; Abrahamsson, M. Evidence for Conduction Band-Mediated Two-Electron Reduction of a TiO₂-Bound Catalyst Triggered by Visible Light Excitation of Co-Adsorbed Organic Dyes. *JOURNAL OF PHYSICAL CHEMISTRY C* **2018**, *122* (45), 25822–25828. <https://doi.org/10.1021/acs.jpcc.8b07669>.
- (304) Tiwari, A.; Duvva, N.; Rao, V. N.; Venkatakrishnan, S. M.; Giribabu, L.; Pal, U. Tetrathiafulvalene Scaffold-Based Sensitizer on Hierarchical Porous TiO₂: Efficient Light-Harvesting Material for Hydrogen Production. *JOURNAL OF PHYSICAL CHEMISTRY C* **2019**, *123* (1), 70–81. <https://doi.org/10.1021/acs.jpcc.8b08787>.
- (305) Liu, L.; Jiang, W.; Song, X.; Duan, Q.; Zhu, E. A Novel Strategy of Lock-in Effect between Conjugated Polymer and TiO₂ towards Dramatic Enhancement of Photocatalytic Activity under Visible Light. *Sci Rep* **2020**, *10* (1), 1–11. <https://doi.org/10.1038/s41598-020-63623-2>.
- (306) Yang, H.; Amari, H.; Liu, L.; Zhao, C.; Gao, H.; He, A.; Browning, N. D.; Little, M. A.; Sprick, R. S.; Cooper, A. I. Nano-Assemblies of a Soluble Conjugated Organic Polymer and an Inorganic Semiconductor for Sacrificial Photocatalytic Hydrogen Production from Water. *Nanoscale* **2020**, *12* (48), 24488–24494. <https://doi.org/10.1039/D0NR05801G>.
- (307) Hong, Y.; Cho, Y.; Go, E. M.; Sharma, P.; Cho, H.; Lee, B.; Lee, S. M.; Park, S. O.; Ko, M.; Kwak, S. K.; Yang, C.; Jang, J. W. Unassisted Photocatalytic H₂O₂ Production under Visible Light by Fluorinated Polymer-TiO₂ Heterojunction. *Chemical Engineering Journal* **2021**, *418* (March), 129346. <https://doi.org/10.1016/j.cej.2021.129346>.
- (308) Hou, H. J.; Zhang, X. H.; Huang, D. K.; Ding, X.; Wang, S. Y.; Yang, X. L.; Li, S. Q.; Xiang, Y. G.; Chen, H. Conjugated Microporous Poly(Benzothiadiazole)/TiO₂ Heterojunction for Visible-Light-Driven H₂ Production and Pollutant Removal. *Appl Catal B* **2017**, *203*, 513–517. <https://doi.org/10.1016/j.apcatb.2016.10.059>.
- (309) Shu, G.; Wang, Y.; Li, Y.; Zhang, S.; Jiang, J.-X.; Wang, F. A High Performance and Low Cost Poly(Dibenzothiophene-S, S -Dioxide)/TiO₂ Composite with Hydrogen Evolution Rate up to 51.5 Mmol h⁻¹ g⁻¹. *J Mater Chem A Mater* **2020**, *8* (35), 18292–18301. <https://doi.org/10.1039/D0TA06159J>.
- (310) Li, C. C.; Gao, M. Y.; Sun, X. J.; Tang, H. L.; Dong, H.; Zhang, F. M. Rational Combination of Covalent-Organic Framework and Nano TiO₂ by Covalent Bonds to Realize Dramatically Enhanced Photocatalytic Activity. *Appl Catal B* **2020**, *266* (December 2019), 118586. <https://doi.org/10.1016/j.apcatb.2020.118586>.
- (311) Valverde-González, A.; López Calixto, C. G.; Barawi, M.; Gomez-Mendoza, M.; De La Peña O'Shea, V. A.; Liras, M.; Gómez-Lor, B.; Iglesias, M. Understanding Charge Transfer Mechanism on Effective Truxene-Based Porous Polymers-TiO₂Hybrid Photocatalysts for Hydrogen Evolution. *ACS Appl Energy Mater* **2020**, *3* (5), 4411–4420. <https://doi.org/10.1021/acsaem.0c00118>.
- (312) Li, J.; Wen, X.; Zhang, Q.; Ren, S. Adsorption and Visible-Light Photodegradation of Organic Dyes with TiO₂/Conjugated Microporous Polymer Composites. *RSC Adv* **2018**, *8* (60), 34560–34565. <https://doi.org/10.1039/C8RA06491A>.
- (313) Zhu, L.; Gu, W.; Li, H.; Zou, W.; Liu, H.; Zhang, Y.; Wu, Q.; Fu, Z.; Lu, Y. Enhancing the Photocatalytic Hydrogen Production Performance of SrTiO₃ by Coating with a Hydrophilic Poloxamer. *Appl Surf Sci* **2020**, *528*. <https://doi.org/10.1016/j.apsusc.2020.146837>.
- (314) Ferreira, M. A.; da Silva, G. T. S. T.; Lopes, O. F.; Mastelaro, V. R.; Ribeiro, C.; Pires, M. J. M.; Malagutti, A. R.; Avansi, W.; Mourão, H. A. J. L. Fabrication of SrTiO₃/g-C₃N₄ Heterostructures for Visible Light-Induced Photocatalysis. *Mater Sci Semicond Process* **2020**, *108* (December 2019), 104887. <https://doi.org/10.1016/j.mssp.2019.104887>.
- (315) Han, R.; Melo, M. A.; Zhao, Z.; Wu, Z.; Osterloh, F. E. Light Intensity Dependence of Photochemical Charge Separation in the BiVO₄/Ru-SrTiO₃:Rh Direct Contact Tandem Photocatalyst for Overall Water Splitting. *Journal of Physical Chemistry C* **2020**, *124* (18), 9724–9733. <https://doi.org/10.1021/acs.jpcc.0c00772>.
- (316) Wu, X.; Zhao, J.; Guo, S.; Wang, L.; Shi, W.; Huang, H.; Liu, Y.; Kang, Z. Carbon Dot and BiVO₄ Quantum Dot Composites for Overall Water Splitting: Via a Two-Electron Pathway. *Nanoscale* **2016**, *8* (39), 17314–17321. <https://doi.org/10.1039/c6nr05864g>.
- (317) Wang, J.; Kuo, M.; Zeng, P.; Xu, L.; Chen, S.; Peng, T. Few-Layer BiVO₄ Nanosheets Decorated with SrTiO₃: Rh Nanoparticles for Highly Efficient Visible-Light-Driven Overall Water Splitting. *Appl Catal B* **2020**, *279*, 119377. <https://doi.org/10.1016/j.apcatb.2020.119377>.
- (318) Yoshino, S.; Sato, K.; Yamaguchi, Y.; Iwase, A.; Kudo, A. Z-Schematic CO₂ Reduction to CO through Interparticle Electron Transfer between SrTiO₃:Rh of a Reducing Photocatalyst and BiVO₄ of a Water Oxidation Photocatalyst under Visible Light. *ACS Appl Energy Mater* **2020**, *3* (10), 10001–10007. <https://doi.org/10.1021/acsaem.0c01684>.

- (319) Suzuki, Y.; Murthy, D. H. K.; Matsuzaki, H.; Furube, A.; Wang, Q.; Hisatomi, T.; Domen, K.; Seki, K. Rational Interpretation of Correlated Kinetics of Mobile and Trapped Charge Carriers: Analysis of Ultrafast Carrier Dynamics in BiVO₄. *JOURNAL OF PHYSICAL CHEMISTRY C* **2017**, *121* (35), 19044–19052. <https://doi.org/10.1021/acs.jpcc.7b05574>.
- (320) Qi, Y.; Zhang, J.; Kong, Y.; Zhao, Y.; Chen, S.; Li, D.; Liu, W.; Chen, Y.; Xie, T.; Cui, J.; Li, C.; Domen, K.; Zhang, F. Unraveling of Cocatalysts Photodeposited Selectively on Facets of BiVO₄ to Boost Solar Water Splitting. *Nat Commun* **2022**, *13* (1), 1–9. <https://doi.org/10.1038/s41467-022-28146-6>.
- (321) Yang, X.; Xiang, Y.; Qu, Y.; Ding, X.; Chen, H. Novel in Situ Fabrication of Conjugated Microporous Poly(Benzothiadiazole)–Bi₂MoO₆Z-Scheme Heterojunction with Enhanced Visible Light Photocatalytic Activity. *J Catal* **2017**, *345*, 319–328. <https://doi.org/10.1016/j.jcat.2016.11.014>.
- (322) Xing, Y. Q.; Tan, Z. R.; Cheng, J. Z.; Shen, Z. Q.; Zhang, Y. J.; Chen, L.; Liu, S. Y. In Situ C-H Activation-Derived Polymer@TiO₂p-n Heterojunction for Photocatalytic Hydrogen Evolution. *Sustain Energy Fuels* **2021**, *5* (20), 5166–5174. <https://doi.org/10.1039/d1se00970b>.
- (323) Xiao, Y.; Jiang, Y.; Zhou, E.; Zhang, W.; Liu, Y.; Zhang, J.; Wu, X.; Qi, Q.; Liu, Z. In-Suit Fabricating an Efficient Electronic Transport Channels via S-Scheme Polyaniline/Cd_{0.5}Zn_{0.5}S Heterojunction for Rapid Removal of Tetracycline Hydrochloride and Hydrogen Production. *J Mater Sci Technol* **2023**, *153*, 205–218. <https://doi.org/10.1016/j.jmst.2022.12.060>.
- (324) Butler, M. A.; Ginley, D. S. Prediction of Flatband Potentials at Semiconductor-Electrolyte Interfaces from Atomic Electronegativities. *J Electrochem Soc* **1978**, *125* (2), 228. <https://doi.org/10.1149/1.2131419>.
- (325) Wang, J.; Osterloh, F. E. Limiting Factors for Photochemical Charge Separation in BiVO₄/Co₃O₄, a Highly Active Photocatalyst for Water Oxidation in Sunlight. *J Mater Chem A Mater* **2014**, *2* (24), 9405–9411. <https://doi.org/10.1039/C4TA01654H>.
- (326) Cooper, J. K.; Gul, S.; Toma, F. M.; Chen, L.; Glans, P. A.; Guo, J.; Ager, J. W.; Yano, J.; Sharp, I. D. Electronic Structure of Monoclinic BiVO₄. *Chemistry of Materials* **2014**, *26* (18), 5365–5373. <https://doi.org/10.1021/cm5025074>.
- (327) Hermans, Y.; Klein, A.; Ellmer, K.; van de Krol, R.; Toupance, T.; Jaegermann, W. Energy-Band Alignment of BiVO₄ from Photoelectron Spectroscopy of Solid-State Interfaces. *The Journal of Physical Chemistry C* **2018**, *122* (36), 20861–20870. <https://doi.org/10.1021/acs.jpcc.8b06241>.
- (328) Tian, L.; Guan, X.; Dong, Y.; Zong, S.; Dai, A.; Zhang, Z.; Guo, L. Improved Overall Water Splitting for Hydrogen Production on Aluminium-Doped SrTiO₃ Photocatalyst via Tuned Surface Band Bending. *Environ Chem Lett* **2023**, *21* (3), 1257–1264. <https://doi.org/10.1007/s10311-023-01580-8>.
- (329) Anderson, R. L. Germanium-Gallium Arsenide Heterojunctions [Letter to the Editor]. *IBM J Res Dev* **1960**, *4* (3), 283–287. <https://doi.org/10.1147/rd.43.0283>.
- (330) Ishii, H.; Seki, K. Energy Level Alignment at Organic/Metal Interfaces Studied by UV Photoemission: Breakdown of Traditional Assumption of a Common Vacuum Level at the Interface. *IEEE Trans Electron Devices* **1997**, *44* (8), 1295–1301. <https://doi.org/10.1109/16.605471>.
- (331) Olthof, S.; Meerheim, R.; Schober, M.; Leo, K. Energy Level Alignment at the Interfaces in a Multilayer Organic Light-Emitting Diode Structure. *Phys Rev B* **2009**, *79* (24), 245308. <https://doi.org/10.1103/PhysRevB.79.245308>.
- (332) Muench, M.; Mankel, E.; Mayer, T.; Jaegermann, W. Phenomenological Prediction of the Band Diagram of Organic–Organic and Inorganic–Organic Heterointerfaces. *Adv Mater Technol* **2021**, *6* (2), 2000110. <https://doi.org/https://doi.org/10.1002/admt.202000110>.
- (333) Li, Y.; Li, P.; Lu, Z.-H. Mapping Energy Levels for Organic Heterojunctions. *Advanced Materials* **2017**, *29* (24), 1700414. <https://doi.org/https://doi.org/10.1002/adma.201700414>.
- (334) Greiner, M. T.; Helander, M. G.; Tang, W.-M.; Wang, Z.-B.; Qiu, J.; Lu, Z.-H. Universal Energy-Level Alignment of Molecules on Metal Oxides. *Nat Mater* **2012**, *11* (1), 76–81. <https://doi.org/10.1038/nmat3159>.
- (335) Zhang, Z.; Yates Jr, J. T. Band Bending in Semiconductors: Chemical and Physical Consequences at Surfaces and Interfaces. *Chem Rev* **2012**, *112* (10), 5520–5551.
- (336) Doughty, R. M.; Hodges, B.; Dominguez, J.; Han, R.; Zhao, Z.; Assavachin, S.; Osterloh, F. E. Fermi Level Pinning Controls Band Bending and Photochemical Charge Separation in Particles of N-SrTiO₃, n-SrTiO₃:Al, and n-GaAs:Te. *JOURNAL OF PHYSICAL CHEMISTRY C* **2020**, *124* (34), 18426–18435. <https://doi.org/10.1021/acs.jpcc.0c04989>.
- (337) Zhao, Y.; Ding, C.; Zhu, J.; Qin, W.; Tao, X.; Fan, F.; Li, R.; Li, C. A Hydrogen Farm Strategy for Scalable Solar Hydrogen Production with Particulate Photocatalysts. *Angewandte Chemie - International Edition* **2020**, *59* (24), 9653–9658. <https://doi.org/10.1002/anie.202001438>.

-
- (338) Tan, H.; Zhao, Z.; Zhu, W. Bin; Coker, E. N.; Li, B.; Zheng, M.; Yu, W.; Fan, H.; Sun, Z. Oxygen Vacancy Enhanced Photocatalytic Activity of Pervoskite SrTiO₃. *ACS Appl Mater Interfaces* **2014**, *6* (21), 19184–19190. <https://doi.org/10.1021/am5051907>.
- (339) SrTiO₃ Heat Capacity, Melting Point, Density: Datasheet from Landolt-Börnstein - Group III Condensed Matter · Volume 41E: “Ternary Compounds, Organic Semiconductors” in SpringerMaterials (https://doi.org/10.1007/10717201_531). Springer-Verlag Berlin Heidelberg. https://doi.org/10.1007/10717201_531.